Springer Series in Chemical Physics 107

Rebeca de Nalda
Luis Bañares *Editors*

Ultrafast Phenomena in Molecular Sciences

Femtosecond Physics and Chemistry

Springer

Springer Series in
CHEMICAL PHYSICS 107

Springer Series in

CHEMICAL PHYSICS

The purpose of this series is to provide comprehensive up-to-date monographs in both well established disciplines and emerging research areas within the broad fields of chemical physics and physical chemistry. The books deal with both fundamental science and applications, and may have either a theoretical or an experimental emphasis. They are aimed primarily at researchers and graduate students in chemical physics and related fields.

Rebeca de Nalda • Luis Bañares
Editors

Ultrafast Phenomena in Molecular Sciences

Femtosecond Physics and Chemistry

Springer

ISSN 0172-6218 Springer Series in Chemical Physics
ISBN 978-3-319-02050-1 ISBN 978-3-319-02051-8 (eBook)
DOI 10.1007/978-3-319-02051-8
Springer Cham Heidelberg New York Dordrecht London

Library of Congress Control Number: 2013951886

Printed on acid-free paper

Springer is part of Springer Science+Business Media (www.springer.com)

Foreword

Over the past two decades, the realm of ultrafast science has become vast and exciting and has impacted many areas of chemistry, biology and physics, and other fields such as materials science, electrical engineering, and optical communication. The explosive growth in molecular science is principally for fundamental reasons. In femtochemistry and femtobiology, chemical bonds form and break on the femtosecond time scale, and on this scale of time we can freeze the transition states at configurations never before seen. Even for nonreactive physical changes, one is observing the most elementary of molecular processes. On a time scale shorter than the vibrational and rotational periods, the ensemble behaves coherently as a single-molecule trajectory.

But these developments would not have been possible without the advent of new light sources and equally important the crystallization of some key underlying concepts that were in the beginning shrouded in fog. First was the issue of the "uncertainty principle", which had to be decisively clarified. Second was the question of whether one could sustain wave packet motion at the atomic scale of distance. In other words, would the de Broglie wavelength of the atom become sufficiently short to define classical motion—"classical atoms"—and without significant quantum spreading? This too had to be clearly demonstrated and monitored in the course of change, not only for elementary processes in molecular systems, but also during complex biological transformations. And, finally, some questions about the uniqueness and generality of the approach had to be addressed. For example, why not deduce the information from high-resolution frequency-domain methods and then Fourier transform to obtain the dynamics? It is surely now clear that transient species cannot be isolated this way, and that there is no substitute for direct real-time observations that fully exploit the intrinsic coherence of atomic and molecular motions.

Theory has enjoyed a similar explosion in areas dealing with *ab initio* electronic structures, molecular dynamics, and nonlinear spectroscopies. There has been progress in calculating potential energy surfaces of reactive systems, especially in their ground state. On excited-state surfaces, it is now feasible to map out regions of the surface where transition states and conical intersections are important for the outcome of change. For dynamics, new methods have been devised for direct view-

ing of the motion by formulating the time-dependent picture, rather than solving the time-independent Schrödinger equation and subsequently constructing a temporal picture. Analytical theory has been advanced, using time-ordered density matrices, to enable the design of multidimensional spectroscopy, the analogue of 2-D (and higher) NMR spectroscopy. The coupling between theory and experiment is evident in many of the papers in this special volume.

On the technical side, the development of direct microscopy imaging methods for visualization of dynamics and the generation of attosecond pulses for mapping electronic processes have resulted in new frontiers of research. And, the ability to design shaped and sequenced pulses to control processes of interest is stimulating numerous theoretical studies in the field. Ultrafast science is continuing in many disciplines because of the fundamental nature of the time and length scales involved. The science should be attractive to future generations of young scientists.

This volume "Ultrafast Phenomena in Molecular Sciences" edited by Rebeca de Nalda and Luis Bañares is a welcome addition to the field, especially for its emphasis on the "latest" in ultrafast molecuar science and the scope of applications possible.

Pasadena, CA, USA Ahmed Zewail

Preface

Undoubtedly the progress of Molecular Sciences has benefited from the *strong interaction* with ultrafast laser techniques and developments in the last decades. In many instances, ultrafast lasers have been employed along with technological advances as a tool to study molecular systems with the aim to understand their time evolution and, in general, to disentangle the time-resolved behavior of matter. The main idea behind the scene is to reach the time scales where molecular processes occur and to visualize their time evolution; that is, femtoseconds for nuclear motion and attoseconds for electronic motion. Interesting new phenomena have emerged however when this strong interaction between ultrashort ultraintense light and molecules has been provoked, and this has stimulated in turn new developments both experimental and theoretical to try to understand the new phenomena. This loop between applications and the appearance of new phenomena is behind the progress of the field.

This volume of Springer Series in Chemical Physics is conceived to cover the latest progress on the applications of Ultrafast Technology to Molecular Sciences, from small molecules to proteomics and molecule-surface interactions, and from conventional femtosecond laser pulses and pump-probe and charged particle detection techniques to attosecond pulses in the XUV. The attosecond and few-cycle femtosecond applications are covered in the first Chapter written by Marc Vrakking and co-workers (Chap. 1), where the measurement of molecular frame photoelectron angular distributions of high kinetic energy photoelectrons for small molecules brings the time evolution of molecular structures in the course of a photochemical event. The theoretical aspects along these lines come from the Chapter written by Fernando Martin and his co-workers (Chap. 2) focusing on a simple molecular system, the hydrogen molecule, where state-of-the-art time-dependent theoretical methods are able to provide a solid groundwork for describing and interpreting the underlying molecular dynamics observed experimentally. Larger molecules under ultraintense laser fields are presented in the Chapter written by Tomoya Okino and Kaoru Yamanouchi (Chap. 3), where coincident momentum charged-particle imaging measurements shed light into intense field induced hydrogen atom migration in small hydrocarbons. The combination between the femtosecond pump-probe technique

and charged-particle (ion or photoelectron) imaging detection with resonant or non-resonant fragment ionization is the subject covered by the following three Chapters, written by Rebeca de Nalda and Luis Bañares and their co-workers (Chap. 4), Helen Fielding and co-workers (Chap. 5) and Vasilios Stavros and co-workers (Chap. 6), where key applications to the photodynamics of polyatomic molecular systems are presented. Also theoretical support is crucial when studying such larger molecular systems, but in such cases accurate quantum mechanical treatments are intractable. In the Chapter written by Leticia González and Ignacio Solá and their co-workers (Chap. 7) an approach based on semiclassical methods to study the photodynamics of polyatomic molecular systems is presented. The extension to really large molecular systems is dealt with in the Chapter by Marcos Dantus and co-workers (Chap. 8), which is centered on femtosecond laser induced dissociation for proteomic analysis. Another aspect of photodynamics of excited states of biomolecules is the aim of the Chapter written by Marcus Motzkus and co-workers (Chap. 9). In this case, multidimensional time-resolved spectroscopy based on the non-linear broadband four-wave mixing technique using sub-20 femtosecond pulses is applied to address coherence and population dynamics in molecular excited states. Reaction dynamics in the gas-solid interface is treated in the Chapter written by Mihai Vaida and Thorsten Bernhardt (Chap. 10). In particular, the Chapter focuses on the dynamics of chemical reaction on metal oxide surfaces by using ultrashort laser pulses with a perspective to applications to photocatalytic reactions at supported metal clusters and nanoparticles. Finally, the Chapter written by Olivier Faucher and his co-workers (Chap. 11) centers on the use of non-linear coherent interactions of molecules with ultrashort laser pulses to deduce the properties of gas-phase molecules and to obtain information on the environment of molecules.

We thank all the authors for their valuable efforts to provide both a meaningful background and detailed descriptions of the research lines, and we hope that the material covered in this book provides an updated and insightful window into the broad range of areas where this field is evolving.

Madrid, Spain

Rebeca de Nalda
Luis Bañares

Contents

1 Molecular Movies from Molecular Frame Photoelectron Angular Distribution (MF-PAD) Measurements 1
Arnaud Rouzée, Ymkje Huismans, Freek Kelkensberg, Aneta Smolkowska, Julia H. Jungmann, Arjan Gijsbertsen, Wing Kiu Siu, Georg Gademann, Axel Hundertmark, Per Johnsson, and Marc J.J. Vrakking

1.1 Introduction 1
1.2 Molecular Movies Using XUV/X-Ray Photoionization 5
1.3 Molecular Movies Using Strong Field Mid-Infrared Ionization . . 14
1.4 Outlook 20
References 22

2 XUV Lasers for Ultrafast Electronic Control in H_2 25
Alicia Palacios, Paula Rivière, Alberto González-Castrillo, and Fernando Martín

2.1 Introduction 26
2.2 Experimental Set-Ups 27
2.3 Theoretical Approach and Implementation 28
2.3.1 Time-Dependent Spectral Method 29
2.4 Time-Resolved Imaging of H_2 Autoionization 32
2.5 Control and Non-linear Effects in Multiphoton Single Ionization 37
2.5.1 Control of Single Ionization Channels by Means of VUV Pulses 37
2.5.2 Non-linear Effects in $(1 + 1)$-REMPI 39
2.5.3 Probing Nuclear Wave Packets in Molecular Excited States 43
2.6 Future Perspectives 45
References 46

3 Ultrafast Dynamics of Hydrogen Atoms in Hydrocarbon Molecules in Intense Laser Fields: Hydrogen Atom Migration and Scrambling in Methylacetylene 49
Tomoya Okino and Kaoru Yamanouchi
3.1 Introduction 49
3.2 Experiment and Data Analysis 50
3.3 Three-Body Decomposition Pathways of Methylacetylene and Methyl-d_3-Acetylene 52
3.3.1 Three-Body Decomposition Pathways with CC Bond Breaking 52
3.3.2 Three-Body Decomposition Pathways with H^+ and H_2^+ Ejection 56
3.4 Summary 58
References 59

4 Femtosecond Photodissociation Dynamics by Velocity Map Imaging. The Methyl Iodide Case 61
Rebeca de Nalda, Luis Rubio-Lago, Vincent Loriot, and Luis Bañares
4.1 Introduction 61
4.2 Methodology 64
4.2.1 The Experiment: Femtosecond Velocity Map Imaging . . 64
4.2.2 The Multidimensional Analysis 67
4.3 The *A* Band 69
4.3.1 Reaction Clocking: The Resonant Experiment 70
4.3.2 Transition-State Imaging: The Non-resonant Experiment 76
4.3.3 Observation of Transient Molecular Alignment 81
4.3.4 $(CH_3I)_2$ Dimer Photodissociation Dynamics 82
4.3.5 Resonant Probing: The Role of the Optical Coupling Window 86
4.4 The *B* Band 88
4.4.1 Parent Ion Detection 89
4.4.2 Fragment Velocity Map Imaging Detection 90
4.4.3 Time-Resolved Photoelectron Imaging 93
4.5 Concluding Remarks 94
References 96

5 Time-Resolved Photoelectron Spectroscopy for Excited State Dynamics 99
Roman Spesyvtsev, Jonathan G. Underwood, and Helen H. Fielding
5.1 Introduction 99
5.2 Probing Non-adiabatic Dynamics Using Time-Resolved Photoelectron Spectroscopy 100
5.2.1 Photoelectron Spectra: Using the Cation to Map Excited State Dynamics 101

5.2.2 Photoelectron Angular Distributions: Using the Free Electron to Map Excited State Dynamics . . . 103
5.3 The Experimental Toolkit for TRPES . . . 104
5.3.1 Femtosecond Light Sources . . . 104
5.3.2 Molecular Sources . . . 106
5.3.3 Photoelectron Spectrometers . . . 107
5.4 Applications . . . 108
5.4.1 Internal Conversion and Intramolecular Vibrational Energy Redistribution . . . 108
5.4.2 Molecular Alignment . . . 109
5.4.3 Photodissociation . . . 111
5.4.4 Solvated Electrons . . . 113
5.4.5 VUV TRPES . . . 113
References . . . 114

6 Biomolecules, Photostability and $^1\pi\sigma^*$ States: Linking These with Femtochemistry . . . 119
Gareth M. Roberts and Vasilios G. Stavros
6.1 Introduction . . . 119
6.2 Excited Electronic States and Photostability . . . 120
6.2.1 H-Atom Elimination Dynamics Mediated by $^1\pi\sigma^*$ States . . . 121
6.2.2 Non-adiabatic, Adiabatic and Tunneling dynamics . . . 122
6.3 Experimental Detection of $^1\pi\sigma^*$ Mediated Dynamics . . . 123
6.3.1 Time-Resolved Time-of-Flight Mass Spectrometry . . . 124
6.3.2 Time-Resolved Velocity Map Ion Imaging . . . 125
6.4 Applications . . . 128
6.4.1 Non-adiabatic Versus Adiabatic Dynamics . . . 128
6.4.2 Comparing Dynamics in Simple Azoles . . . 130
6.4.3 Excited State H-Atom Tunneling Dynamics . . . 133
6.4.4 Competing $^1\pi\sigma^*$ Mediated Dissociation Pathways . . . 136
6.4.5 Outlook . . . 139
References . . . 140

7 Ultrafast Laser-Induced Processes Described by Ab Initio Molecular Dynamics . . . 145
Leticia González, Philipp Marquetand, Martin Richter, Jesús González-Vázquez, and Ignacio Sola
7.1 Introduction . . . 146
7.2 Methodologies for Ab Initio Molecular Dynamics . . . 148
7.2.1 Surface Hopping *vs.* Ehrenfest Dynamics . . . 148
7.2.2 Laser-Induced Dynamics: FISH *vs.* SHARC . . . 151
7.3 Examples of Laser-Free Dynamics . . . 157
7.4 Examples of Laser-Induced Dynamics . . . 159
7.4.1 Impulsive Regime . . . 159

7.4.2 Adiabatic Regime . . . 162
7.5 Summary and Prospect . . . 164
References . . . 165

8 Ultrafast Ionization and Fragmentation: From Small Molecules to Proteomic Analysis . . . 171
Marcos Dantus and Christine L. Kalcic
8.1 Ultrafast Field Ionization and Its Application to Analytical Chemistry . . . 171
8.2 Mass Spectrometry Coupled to an Ultrafast Laser Source . . . 173
8.2.1 Introduction . . . 173
8.2.2 Experimental Methods . . . 178
8.3 Results from Small Polyatomic Molecules . . . 182
8.3.1 Vibrational and Electronic Coherence . . . 182
8.3.2 Effect of Pulse Shaping . . . 183
8.4 Results from Peptides . . . 187
8.4.1 Amino Acids . . . 188
8.4.2 Aromatics . . . 193
8.4.3 Acidic/Basic Amino Acids . . . 194
8.4.4 Polar Amino Acids . . . 194
8.4.5 Non-polar Amino Acids . . . 194
8.4.6 Protein Sequencing . . . 195
8.4.7 Bond Cleavage Pathways . . . 198
8.5 Discussion and Future Outlook . . . 200
References . . . 201

9 On the Investigation of Excited State Dynamics with (Pump-)Degenerate Four Wave Mixing . . . 205
Tiago Buckup, Jan P. Kraack, Marie S. Marek, and Marcus Motzkus
9.1 Introduction . . . 205
9.2 Pump-Degenerate Four Wave Mixing . . . 207
9.2.1 Signal Generation . . . 207
9.2.2 Setup Description . . . 209
9.2.3 Role of Spectral Overlap . . . 211
9.3 Results and Discussion . . . 212
9.3.1 Assignment of Vibrational Coherence to Electronic States Using Pure DFWM . . . 212
9.3.2 Detection of Dark States . . . 218
9.3.3 Vibrational Coherence Evolution in the Excited State . . . 223
9.4 Conclusions . . . 227
References . . . 227

10 Surface-Aligned Femtochemistry: Molecular Reaction Dynamics on Oxide Surfaces . . . 231
Mihai E. Vaida and Thorsten M. Bernhardt

10.1 Introduction . . . 231
10.1.1 Surface-Aligned Chemistry . . . 233
10.1.2 Molecular Adsorption on a Single Crystalline Oxide Surface . . . 235
10.1.3 Laser-Induced Molecular Desorption and Reaction on the Magnesium Oxide Surface . . . 236
10.2 Surface Pump-Probe Fs-Laser Mass Spectrometry . . . 238
10.3 Femtosecond Dynamics of Surface Aligned Reactions . . . 240
10.3.1 Unimolecular Photodissociation . . . 241
10.3.2 Bimolecular Surface Reactions . . . 251
10.4 Conclusion and Prospects . . . 254
References . . . 255

11 Optical Diagnostics with Ultrafast and Strong Field Raman Techniques . . . 263
Frederic Chaussard, Bruno Lavorel, Edouard Hertz, and Olivier Faucher
11.1 Introduction . . . 263
11.2 Optical Diagnostic by Means of Femtosecond Spectroscopy . . . 265
11.2.1 Temperature and Concentration Measurement in Gas Mixtures Using Rotational Coherence Spectroscopy Techniques . . . 265
11.2.2 Hydrogen Rovibrational Femtosecond CARS . . . 270
11.3 Field-Free Molecular Alignment in Dissipative Environment and Strong Field Regime . . . 275
11.3.1 Alignment in a Dissipative Medium . . . 275
11.4 Conclusion . . . 279
References . . . 280

Index . . . 283

Contributors

Luis Bañares Departamento de Química Física, Facultad de Ciencias Químicas, Universidad Complutense de Madrid, Madrid, Spain

Thorsten M. Bernhardt Institute of Surface Chemistry and Catalysis, University of Ulm, Ulm, Germany

Tiago Buckup Physikalisch-Chemisches Institut, Universität Heidelberg, Heidelberg, Germany

Frederic Chaussard Laboratoire Interdisciplinaire CARNOT de Bourgogne (ICB), UMR 6303 CNRS–Université de Bourgogne, Dijon Cedex, France

Marcos Dantus Michigan State University, East Lansing, MI, USA

Rebeca de Nalda Instituto de Química Física Rocasolano, CSIC, Madrid, Spain

Olivier Faucher Laboratoire Interdisciplinaire CARNOT de Bourgogne (ICB), UMR 6303 CNRS–Université de Bourgogne, Dijon Cedex, France

Helen H. Fielding Department of Chemistry, University College London, London, UK

Georg Gademann FOM Institute AMOLF, Amsterdam, The Netherlands

Arjan Gijsbertsen FOM Institute AMOLF, Amsterdam, The Netherlands

Leticia González Institute of Theoretical Chemistry, University of Vienna, Vienna, Austria

Alberto González-Castrillo Departamento de Química, Universidad Autónoma de Madrid, Madrid, Spain

Jesús González-Vázquez Departamento de Química Física I, Universidad Complutense, Madrid, Spain

Edouard Hertz Laboratoire Interdisciplinaire CARNOT de Bourgogne (ICB), UMR 6303 CNRS–Université de Bourgogne, Dijon Cedex, France

Ymkje Huismans FOM Institute AMOLF, Amsterdam, The Netherlands

Axel Hundertmark Max-Born Institut, Berlin, Germany; FOM Institute AMOLF, Amsterdam, The Netherlands

Per Johnsson Department of Physics, Lund University, Lund, Sweden

Julia H. Jungmann FOM Institute AMOLF, Amsterdam, The Netherlands

Christine L. Kalcic Michigan State University, East Lansing, MI, USA

Freek Kelkensberg FOM Institute AMOLF, Amsterdam, The Netherlands

Jan P. Kraack Physikalisch-Chemisches Institut, Universität Heidelberg, Heidelberg, Germany

Bruno Lavorel Laboratoire Interdisciplinaire CARNOT de Bourgogne (ICB), UMR 6303 CNRS–Université de Bourgogne, Dijon Cedex, France

Vincent Loriot Instituto de Química Física Rocasolano, CSIC, Madrid, Spain; Departamento de Química Física, Facultad de Ciencias Químicas, Universidad Complutense de Madrid, Madrid, Spain

Marie S. Marek Physikalisch-Chemisches Institut, Universität Heidelberg, Heidelberg, Germany

Philipp Marquetand Institute of Theoretical Chemistry, University of Vienna, Vienna, Austria

Fernando Martín Departamento de Química, Universidad Autónoma de Madrid, Madrid, Spain; Instituto Madrileño de Estudios Avanzados en Nanociencia (IMDEA-Nanociencia), Cantoblanco, Madrid, Spain

Marcus Motzkus Physikalisch-Chemisches Institut, Universität Heidelberg, Heidelberg, Germany

Tomoya Okino Department of Chemistry, School of Science, The University of Tokyo, Bunkyo-ku, Tokyo, Japan

Alicia Palacios Departamento de Química, Universidad Autónoma de Madrid, Madrid, Spain

Martin Richter Institute of Theoretical Chemistry, University of Vienna, Vienna, Austria

Paula Rivière Departamento de Química, Universidad Autónoma de Madrid, Madrid, Spain

Gareth M. Roberts Department of Chemistry, University of Warwick, Coventry, UK

Arnaud Rouzée Max-Born Institut, Berlin, Germany; FOM Institute AMOLF, Amsterdam, The Netherlands

Luis Rubio-Lago Departamento de Química Física, Facultad de Ciencias Químicas, Universidad Complutense de Madrid, Madrid, Spain

Wing Kiu Siu FOM Institute AMOLF, Amsterdam, The Netherlands

Aneta Smolkowska FOM Institute AMOLF, Amsterdam, The Netherlands

Ignacio Sola Departamento de Química Física I, Universidad Complutense, Madrid, Spain

Roman Spesyvtsev Department of Chemistry, University College London, London, UK

Vasilios G. Stavros Department of Chemistry, University of Warwick, Coventry, UK

Jonathan G. Underwood Department of Physics and Astronomy, University College London, London, UK

Mihai E. Vaida Institute of Surface Chemistry and Catalysis, University of Ulm, Ulm, Germany

Marc J.J. Vrakking Max-Born Institut, Berlin, Germany; FOM Institute AMOLF, Amsterdam, The Netherlands

Kaoru Yamanouchi Department of Chemistry, School of Science, The University of Tokyo, Bunkyo-ku, Tokyo, Japan

Chapter 1
Molecular Movies from Molecular Frame Photoelectron Angular Distribution (MF-PAD) Measurements

Arnaud Rouzée, Ymkje Huismans, Freek Kelkensberg, Aneta Smolkowska, Julia H. Jungmann, Arjan Gijsbertsen, Wing Kiu Siu, Georg Gademann, Axel Hundertmark, Per Johnsson, and Marc J.J. Vrakking

Abstract We discuss recent and on-going experiments, where molecular frame photoelectron angular distributions (MFPADs) of high kinetic energy photoelectrons are measured in order to determine the time evolution of molecular structures in the course of a photochemical event. These experiments include, on the one hand, measurements where single XUV/X-ray photons, obtained from a free electron laser (FEL) or by means of high-harmonic generation (HHG), are used to eject a high energy photoelectron, and, on the other hand, measurements where a large number of mid-infrared photons are absorbed in the course of strong-field ionization. In the former case, first results indicate a manifestation of the both the electronic orbital and the molecular structure in the angle-resolved photoelectron distributions, while in the latter case novel holographic structures are measured that suggest that both the molecular structure and ultrafast electronic rearrangement processes can be studied with a time-resolution that reaches down into the attosecond and few-femtosecond domain.

1.1 Introduction

Much of our knowledge about matter on the nano-scale is based on studies of the interaction of matter with light. Consequently, the invention of lasers in the infrared, visible and ultra-violet parts of the wavelength spectrum has greatly benefitted our understanding of chemical and physical processes. Using lasers, very insightful ex-

A. Rouzée · A. Hundertmark · M.J.J. Vrakking (✉)
Max-Born Institut, Max Born Straße 2A, 12489 Berlin, Germany
e-mail: marc.vrakking@mbi-berlin.de

A. Rouzée · Y. Huismans · F. Kelkensberg · A. Smolkowska · J.H. Jungmann · A. Gijsbertsen · W.K. Siu · G. Gademann · A. Hundertmark · M.J.J. Vrakking
FOM Institute AMOLF, Science Park 104, 1098 XG Amsterdam, The Netherlands

P. Johnsson
Department of Physics, Lund University, P.O. Box 118, 221 00 Lund, Sweden

R. de Nalda, L. Bañares (eds.), *Ultrafast Phenomena in Molecular Sciences*,
Springer Series in Chemical Physics 107, DOI 10.1007/978-3-319-02051-8_1,

periments have become possible, which operate either in the frequency or in the time domain. The latter type of experiment has been particularly informative. Using pump-probe approaches, where a first "pump" laser pulse triggers a structural change in a molecule, and a second "probe" laser pulse interrogates the molecule after it has evolved for some time, detailed questions can be asked that are pertinent to chemical reactivity. The importance of this new research field of "femtochemistry" was recognized by the Nobel Prize in Chemistry that was awarded in 1999 to Prof. Ahmed Zewail (Caltech) [1].

In femtochemistry experiments, information about an evolving molecular structure is typically inferred by measuring how the molecular absorption spectrum (or a related quantity that can be measured, such as a photoelectron or Raman spectrum) changes as a function of pump-probe delay. If it is known how the molecular absorption spectrum depends on the molecular structure, then measuring its time-dependent changes in a pump-probe sequence can inform us about time-dependent structural changes that occur in the molecule. It follows however, that femtochemistry experiments become very challenging when wavelength-dependent spectral features are not very pronounced, or if the relation between the spectrum and the structure is not known ahead of time. Correspondingly, the level of detail that can be extracted from femtochemistry experiments is reduced when the complexity of the molecule increases.

In the last few years a number of new ideas (summarized in Fig. 1.1) have been put forward that aim to remove the above-mentioned limitations of present-day femtochemistry experiments. The common denominator in all these ideas is that they base themselves on diffraction rather than absorption, so that the requirements on pre-existing knowledge of the electronic spectroscopy of the molecule under investigation are significantly relaxed. In a diffraction experiment structural information is encoded in interference patterns that result from the way that an electron or light wave scatters. In the case of light diffraction (see Fig. 1.1a), the required wavelength to resolve interatomic distances is in the X-ray regime. Time-resolved X-ray diffraction was first developed at X-ray synchrotrons, making use of the intrinsic X-ray pulse duration of about 100 ps at typical facilities [2], and was significantly improved by the implementation of slicing facilities where time resolution into the femtosecond regime was accomplished, at the expense of a very significant reduction in the available X-ray fluence [3]. Alternatively, laser-plasma based X-ray sources have been developed that allow performing X-ray diffraction experiments with a time resolution around 100 fs [4]. Finally, time-resolved X-ray diffraction is one of the main driving forces behind the development of X-ray free electron lasers (FELs) like the LCLS at Stanford (which became operational in the fall of 2009 [5]), the SACLA X-ray FEL in Japan and the future European X-ray Free Electron Laser (XFEL) that is under construction in Hamburg. At LCLS, several remarkable results illustrating the potential of coherent diffractive imaging using X-ray FELs have already been achieved [6].

As an alternative to X-ray diffraction, the diffraction of fast electrons can be used. In doing so, an important advantage is the fact that in order for electron wavelengths to match interatomic distances significantly lower electron kinetic en-

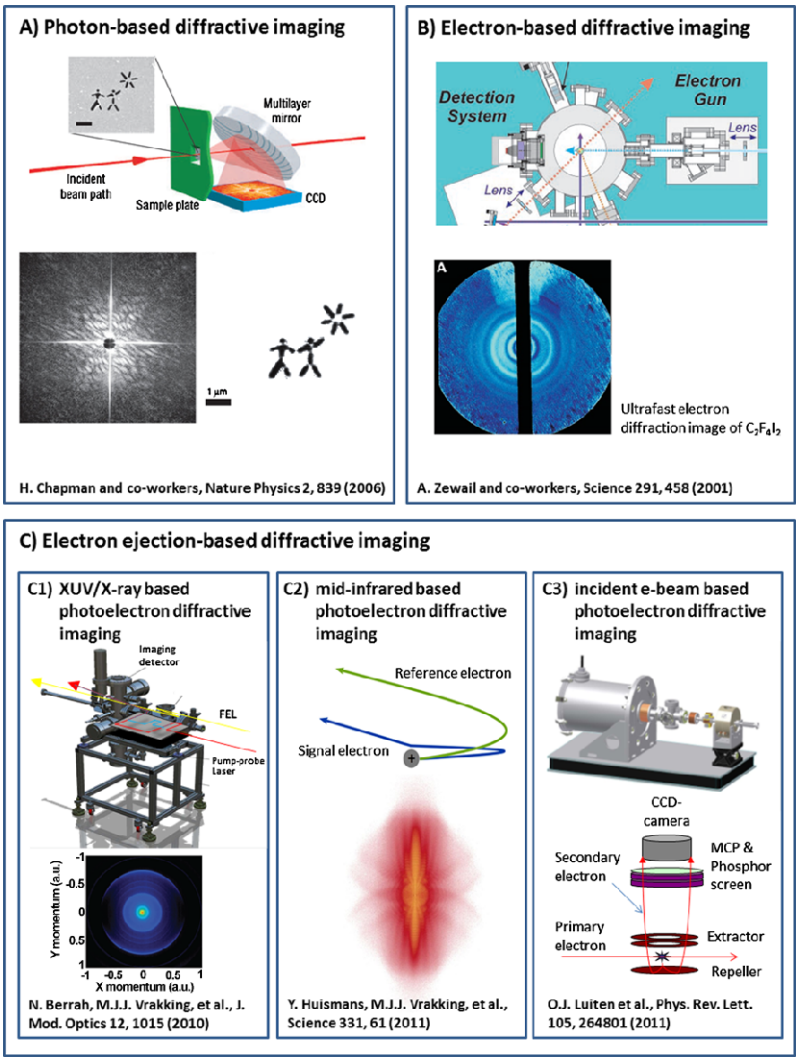

Fig. 1.1 Compilation of diffractive imaging methods. Methods A and B are based on focusing XUV/X-ray photons from a free electron laser/synchrotron or laser plasma source (**A**) or an ultrashort, laser-generated electron bunch (**B**) on a target, and subsequently recording the diffraction of the XUV/X-ray photons and electrons, respectively. In recent years these methods have been successfully implemented. XUV/X-ray diffraction imaging has—in particular—been implemented at FLASH and LCLS, while time-resolved electron diffraction using a photo-cathode source has been implemented in a number of femtosecond laser laboratories. In our research program we aim to develop methodologies for structural determination that are based on measuring diffractive properties of electrons that are extracted from a molecule upon photon or electron impact. In the former case (**C1** and **C2**) ionization is performed using single-photon ionization with an XUV/X-ray laser or multi-photon ionization with a mid-infrared laser. In the latter case (**C3**) an (e, 2e) or (e, 3e) process is used, where a fast primary electron kicks out a second or even—third electron. An overview of the photon-based experiments (**C1** and **C2**) is presented in this review

ergies are needed than the photon energy of the equivalent X-rays. The de Broglie wavelength of an electron is $\lambda_{\mathrm{DeBroglie}}(a.u.) = \pi\sqrt{2/E_{\mathrm{kin}}(a.u.)}$, where E_{kin} is the electron kinetic energy. A de Broglie wavelength of ~ 1 Angström (which, as a laser wavelength would imply the use of 12.4 keV photons!), is already achieved for electrons with a kinetic energy as low as ~ 0.15 keV. It follows that it is significantly easier to prepare the short pulse electrons that are needed for a time-resolved electron diffraction experiment with atomic resolution, than it is to prepare the short pulse X-rays that are needed for a time-resolved X-ray diffraction experiment.

Short electron pulses with kinetic energies in the 0.1–1000 keV range can be generated externally to a molecule on a photo-cathode that precedes a small accelerator. Using such a technique impressive results have been achieved by Zewail and co-workers [7–9] and by Miller and co-workers (see Fig. 1.1b) [10]. Applications have included studies of halo-ethane elimination reactions and ring opening of cyclic hydrocarbons [7], phase transitions in cuprate semiconductors [9], the transition from a monoclinic to a final tetragonal phase in crystalline vanadium dioxide [8], and laser-induced melting [10]. Already, these experiments can be performed with a time resolution of approximately 100 femtoseconds. It remains to be seen if pump-probe experiments with ca. 10 femtosecond time-resolution will become possible using this technique, although proposals to push the time resolution into the attosecond domain have already been put forward [11].

In the last few years, our research team has started working on a number of alternative methods that allow the generation of electrons with kinetic energies in the 0.1–1 keV range, two of which will be detailed in this book chapter (see Fig. 1.1c). First of all, in experiments performed at extreme ultra-violet (XUV)/X-ray FELs like the FLASH free electron laser in Hamburg (the pre-cursor of the European XFEL, which generates radiation down to 4 nm) and at LCLS, we have explored the generation of fast electrons by XUV/X-ray photo-ionization as a means to study time-resolved molecular dynamics. Like the time-resolved X-ray diffraction studies mentioned above, this work may be seen as a natural continuation of earlier synchrotron-based experiments, where ideas to use XUV/X-ray radiation for "illuminating a molecule from within" were developed about a decade ago [12, 13]. A progress report on the extension of these ideas to the time domain will be presented below. Secondly, in experiments performed at the mid-infrared free electron laser FELICE (Free Electron Laser for Intra-Cavity Experiments) in the Netherlands, we have investigated strong-field ionization at wavelengths ranging between 4 and 40 μm. Under these conditions, considerable ponderomotive acceleration of the electrons that are freed in the ionization event sets the stage for laser-driven re-collisions with the target from which the electrons are ionized, allowing the experimental measurement of photoelectron holograms that encode both molecular structure and dynamics [14]. These experiments are discussed in the present chapter as well. We note that in future we are furthermore planning experiments where 0.1–1 keV electrons that can encode molecular structures will be ejected from (time-evolving) molecules by means of a collision of the molecule with a 100 keV electron beam that is similar to the elec-

tron beams that are used for the ultrafast electron diffraction experiments mentioned above [15]. The key difference here will be that the diffractive information is to be encoded in the ejection of secondary or tertiary electrons from the molecule, rather than onto the diffraction of the incident high-energy electron beam.

The organization of the present chapter is as follows. In Sect. 1.2 we present our efforts on using XUV/X-ray single-photon ionization as a means to generate fast photoelectrons that encode a (time-evolving) molecular structure. We present the status of our work at FLASH and LCLS, where we have performed alignment-pump-probe experiments, where a first, alignment laser pulse dynamically aligns the molecule under investigation, a pump laser pulse photo-excites the molecule and the FEL pulse ionizes the molecule at a variable time delay, as well as recent experiments where a high-harmonic generation (HHG) source was used to generate a comb of XUV laser frequencies reaching up to 50 eV, and where photoionization of a series of small molecules provided insight into the contribution of different molecular orbitals and the onset of the emergence of structural information. In Sect. 1.3 we present results from our experiments on (atomic) strong field ionization at mid-infrared wavelengths ranging from 4 to 40 μm, where holographic interferences in the measured photoelectron momentum distributions suggest a route towards a novel technique for measuring (time-resolved) molecular, structural information.

1.2 Molecular Movies Using XUV/X-Ray Photoionization

In the last few years two novel XUV/X-ray short-pulse light sources have come to the forefront that have significantly changed the opportunities that experimentalists in atomic and molecular physics research can avail themselves of. On the one hand, HHG has been developed into a technique that can be implemented in moderate-scale laser laboratories on the basis of commercially available, mJoule-level, femtosecond lasers [16–18]. When the pulses from these lasers are focused onto a dense, gas phase, atomic or molecular target, XUV/X-ray light pulses are formed by means of an interaction that is commonly described in terms of a three-step mechanism, where the laser first ionizes the atom/molecule under consideration, then accelerates the ionized electrons and finally drives the electron back towards the ion left behind, where a recombination can occur that is accompanied by the emission of XUV/X-ray light [19]. Since this process repeats for every half-cycle of the driving laser field, the output frequencies are restricted to odd harmonics of the driver laser frequency, explaining the name of the technique. On the other hand, several XUV/X-ray FEL user facilities have recently become available that provide femtosecond XUV/X-ray pulses with pulse energies that are well beyond the reach of present-day HHG schemes. The first examples of such facilities have been the Tesla Test Facility (TTF) and FLASH in Hamburg [20]. More recently, the LCLS at Stanford has come into operation as the world´s first hard X-ray FEL user facility [5].

The interest in the use of these novel XUV/X-ray light sources in atomic and molecular physics can be rationalized both in the time and frequency domain. Viewed in the time domain, the inherently short optical periods of XUV/X-ray light ($\tau_{\text{optical}} = \lambda/c$, where λ is the wavelength and c is the speed of light), allows the synthesis of pulses with unprecedented pulse durations, accessing the sub-femtosecond i.e. attosecond domain [17, 18, 21]. Such pulses are ideal for the investigation of electron dynamics on its natural timescale. The generation of attosecond laser pulses requires the availability of a process that generates light in the XUV/X-ray regime over a large enough bandwidth ($\Delta E \geq 5$ eV) and with an appropriate phase relationship between the different frequency components contained within the pulse. This is precisely what the HHG process does, given the one-to-one relationship between the ionization time within the optical cycle of the driving infrared laser, the kinetic energy at the time of the electron-ion re-collision and the photon energy produced. Under typical HHG conditions, XUV/X-ray bandwidths in excess of 20 eV are easily achieved, and the pulse duration is determined by the chirp that is generated in the HHG process. The shortest pulses reported to date are about 80 attoseconds long [22], and it is to be expected that the existence of even shorter pulses will soon be demonstrated. So far, pulses obtained at XUV/X-ray FELs are still in the femtosecond domain, but ideas exist that would allow to significantly shorten the pulses [23]. At LCLS, X-ray laser pulses with a pulse duration below 10 fs have already been achieved [24].

Viewed in the frequency domain, the short wavelength and thus intrinsic high photon energy of XUV/X-ray light sources creates the ability to produce high energy photoelectrons. As we will discuss, this allows configuring molecular pump-probe experiments where photoelectrons are produced with kinetic energies where the de Broglie wavelength becomes comparable to or smaller than the internuclear distances in the molecule, so that the angular distribution of the ejected photoelectron encodes information on the molecular structure. Mentioning the time domain, attosecond science context is highly relevant here, since the intensive and widespread efforts to develop and characterize attosecond light pulses have largely been responsible for the emergence of the experimental protocols that need to be used when MFPADs are to be measured using XUV/X-ray light generated by HHG. Motivated by the requirements for attosecond science experiments, it has become possible to develop interferometrically stable multi-color pump-probe setups, with appropriate optics that can be used to image, focus, split and recombine the XUV/X-ray light beam. An example of such a setup is shown in Fig. 1.2 and corresponds to the setup that is in operation at the Max Born Institute (MBI) in Berlin.

If one wishes to time-resolve the evolution of internuclear distances in a molecule (in other words, make a "molecular movie") using photoelectrons that are ejected from the molecule using XUV/X-ray light, then it is imperative that the photoelectron angular distribution is observed in the molecular frame. One way to do this is by making use of a so-called reaction microscope [25], where the 3D momentum of ejected photoelectrons is measured in coincidence with the 3D momentum of fragment ions that are formed, and where in the axial recoil approximation the lat-

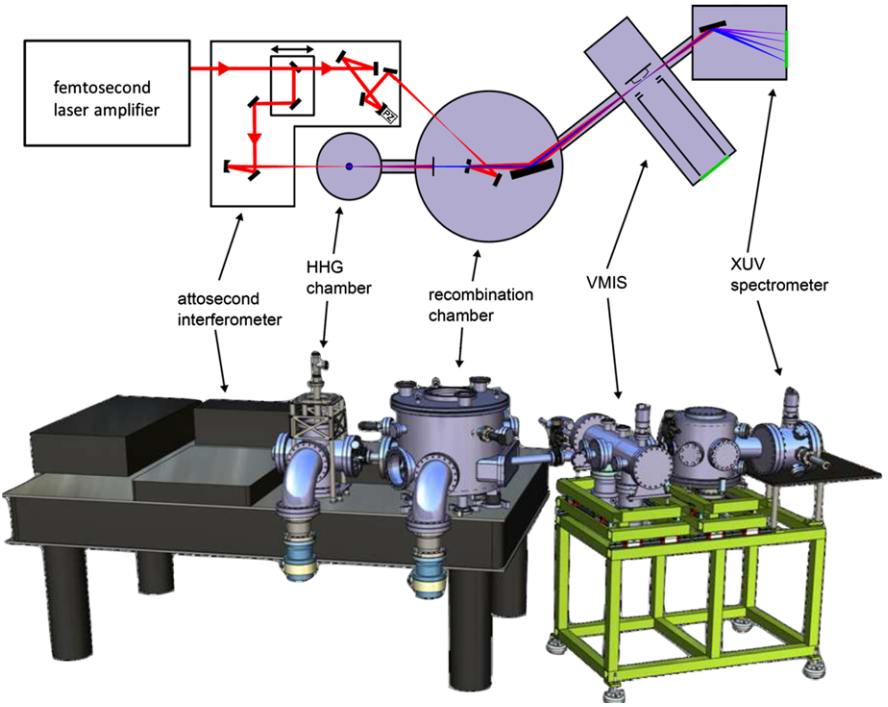

Fig. 1.2 The attosecond pump-probe setup at the Max-Born Institute (MBI). The output of a Ti:Sa laser is split into two beams, that form the two arms of a Mach-Zehnder interferometer. In one arm the laser is focused into a HHG gas cell. Following the HHG process and removal of the IR light and the generated low-order harmonics by means of a filter, this arm is recombined with the other arm in a recombination chamber. The co-linearly propagating XUV and IR beams are brought to a common focus in the center of a velocity map imaging spectrometer (VMIS) by using a toroidal mirror. Finally, an XUV spectrometer that follows the VMIS monitors the harmonic spectrum. In the experiments presented in this chapter, the IR beam was used to dynamically align CO_2, O_2, N_2 and CO molecules. The XUV ionized the aligned molecules, and the VMIS was used to record angle- and energy-resolved photoelectrons and fragment ions resulting from this ionization process

ter allow to determine the 3D orientation of the molecule at the time of ionization. A disadvantage of the use of reaction microscopes is the fact that the coincidence requirements imply that at most one electron-ion pair can be measured per laser shot, meaning that at the typical kHz repetition rates of HHG driver lasers the total amount of time needed to perform an experiment becomes prohibitive. Therefore, in our research we have focused our attention on another approach, namely one where a macroscopic molecular sample is dynamically aligned prior to the pump-probe experiment by means of the interaction with a short alignment laser pulse. By dynamic alignment we understand the re-orientation of a molecule in the laboratory frame that results from the torque that an intense laser field exerts on the molecule as a result of the interaction of the laser-induced dipole with the laser field [26]. Two

distinguishable variants exist, namely adiabatic alignment, where the molecule is exposed to a laser pulse that is significantly longer than the rotational period of the molecule [27], and impulsive alignment, where the molecule is exposed to a laser pulse that is significantly shorter than the rotational period [28]. The advantage of the latter method is that it leads to the formation of aligned molecular samples under laser field-free conditions (i.e. after the alignment laser pulse is over), although with a degree of alignment that is lower than in the adiabatic case. Hybrid schemes combining adiabatic and impulsive alignment have also been proposed [29], and—in combination with state-selection techniques—allow the preparation of molecular samples with a very high-degree of alignment and orientation [30] that can be used in experiments aimed at observing the emission of photoelectrons in the molecular frame.

Recently the experimental setup shown in Fig. 1.2 has been used to perform such an experiment [31]. A series of small molecules (CO_2, N_2, O_2 and CO) were exposed to the sequence of an IR laser pulse that dynamically aligned the molecules and an XUV pulse generated by HHG that ionized the molecules at a variable time delay. Photoelectrons and fragment ions resulting from the latter photoionization process were recorded on a velocity map imaging detector, i.e. accelerated towards a two-dimensional detector consisting of a set of micro-channel plates, a phosphor screen and a CCD camera, thereby allowing the measurement of a 2D projection of the 3D velocity distribution. The 3D velocity distribution was determined from the 2D projection by means of an iterative Abel inversion routine [32]. An important feature of the experiment was the fact that a very high count rate could be achieved (up to ca. 10^6 counts/second), due to the use of a very efficient gas injection system, which was integrated in the repeller electrode of the velocity map imaging spectrometer [33]. This allowed achieving very high signal-to-noise ratios in the data acquisition, which were crucial for observing the small differences in the photoelectron angular distribution of aligned and non-aligned (or anti-aligned) molecules.

Figure 1.3 provides an overview of the dynamic alignment that was achieved in the experiment. The experimental angular distributions of high energy O^+, resp. N^+ fragments resulting from XUV-induced dissociative ionization and/or Coulomb explosion are plotted as a function of the time delay between the impulsive alignment by the IR laser and the XUV ionization by the HHG laser. The angular distributions are expressed by means of $\langle \cos^2 \theta_{2D} \rangle$, where θ_{2D} is the angle between the measured velocity of the fragment ion in the plane of the 2D detector and the common polarization axis of the XUV and IR beams. Perfect alignment of the molecular axes corresponds to $\theta_{2D} = 0$, whereas $\theta_{2D} = \pi/2$ corresponds to molecules that are anti-aligned, i.e. having their internuclear axis perpendicular to the polarization axis of the alignment laser. θ_{2D} is not to be confused with θ, the angle between the 3D fragment ion velocity and the laser polarization axis. The degree of molecular alignment is given by $\langle \cos^2 \theta \rangle$.

As Fig. 1.3 shows, an IR-laser induced alignment occurs shortly after the excitation by the IR laser pulse, and is then followed by a series of alignment revivals

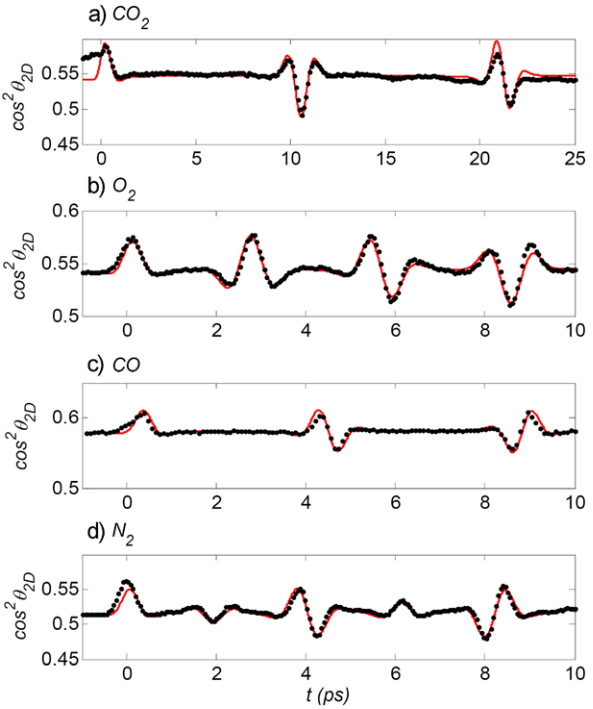

Fig. 1.3 (**a**)–(**d**) Experimental (*black dots*) and theoretical (*red lines*) alignment of CO_2, O_2, CO and N_2, as a function of the time delay between the IR alignment laser and the XUV ionization laser. The numerical calculations are based on the method described in [65] and allow a determination of the rotational temperature of the molecular sample and the average intensity of the IR beam in the XUV focus

that occur at regular time intervals determined by the rotational constants of the molecules under investigation. The approximately 300 fs long IR laser pulse imparts a kick on a timescale that is short compared to the rotational period of the molecule (i.e. $\tau_{\text{laser}} \ll \tau_{\text{rot}}$). Consequently, a rotational wave packet is formed that evolves under field-free conditions once the alignment laser field has ended and that periodically re-aligns and anti-aligns due to the re-phasing of the rotational components. The maximum degree of alignment in Fig. 1.3 corresponds to $\langle \cos^2\theta \rangle \approx 0.5$, and is not very high. This is due to the finite rotational cooling experienced by the gas leaving the capillary in the repeller electrode. Fitting of the experimental alignment distributions to theoretical results (red curves in Fig. 1.3) suggests a rotational temperature ranging from 75 K for the case of CO_2 to 37 K for the case of N_2. However, the achieved difference in the alignment and anti-alignment is sufficient for obtaining high quality differential photoelectron distributions that are acquired by taking the difference between a photoelectron measurement at a delay where the molecules are maximally aligned, and one at a delay where the molecules are maximally anti-aligned. The result of this procedure is shown for CO_2 in Fig. 1.4. Figure 1.4a first of all shows a 2D slice through the 3D XUV-only photoelectron kinetic energy and angular distribution that is measured without the IR-alignment laser. A large number of rings are observed due to the participation of harmonics H11–H29 in the experiment, as well as the fact that at least 4 orbitals contribute to the ionization (the HOMO ($X^2\Sigma_g$, $IP = 13.8$ eV), the HOMO-1 ($A^2\Pi_u$, $IP = 17.6$ eV), the HOMO-2 ($B^2\Sigma_u$, $IP = 18.1$ eV) and the HOMO-3

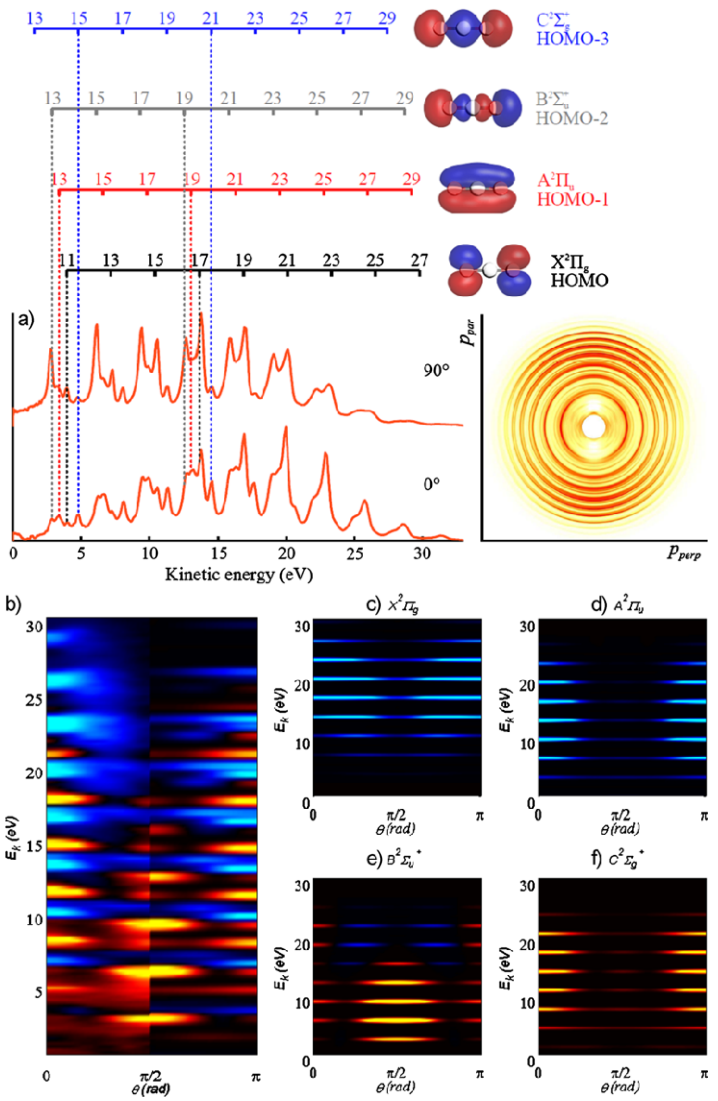

Fig. 1.4 (**a**) XUV-only ionization of CO_2, involving contributions from harmonics H11 to H29. The *bottom left panel* shows a 2D slice through the 3D photoelectron momentum distribution obtained after Abel inversion of the experimental data. The *bottom right panel* shows the integrated photoelectron spectrum along (*top*) and perpendicular (*bottom*) to the laser polarization; (**b**) comparison between the experimental and theoretical differential angular and kinetic energy distribution that is obtained by taking the difference between the photoelectron momentum distributions obtained for maximally aligned and maximally anti-aligned CO_2 molecules; (**c**–**f**) calculated evolution of the differential photoelectron angular distributions as a function of the photoelectron kinetic energy, for the four ionization channels observed in the experiment. (*Light*)*blue color* means a negative value, implying that the efficiency for signal for aligned molecules is less than that for anti-aligned molecules, whereas *red/yellow color* implies a positive value, implying that the signal is increased when the molecule is aligned

($C^2\Sigma_g$, $IP = 19.4$ eV)). When the ionization by the XUV laser pulse is preceded by the IR alignment laser, appreciable changes occur in the measured photoelectron momentum distributions. This is reflected in the experimental contour plot (left side) shown in Fig. 1.4b, where the afore-mentioned differential photoelectron kinetic energy and angular distribution is plotted as a function of the kinetic energy and the angle of ejection of the photoelectron with respect to the laser polarization axis. The differential photoelectron kinetic energy and angular distribution shows all the rings that are visible in the 2D slice in Fig. 1.4a, and moreover shows that the differences between the measurements for aligned and anti-aligned molecules sensitively depend both on the orbital that is ionized and the electron kinetic energy. To begin with, the influence of the ionized orbital manifests itself in the total photoelectron yield. The yield of electrons from the HOMO and HOMO-1 orbitals is suppressed when the molecules are aligned compared to when the molecules are anti-aligned, whereas the yield of photoelectrons corresponding to the HOMO-3 increases when the molecules are aligned. Ionization of the HOMO-2 favors aligned molecules at low photoelectron kinetic energies, but this behavior reverses above a kinetic energy of 15 eV, when anti-aligned molecules ionize more efficiently.

The dependence of the ionization on the alignment/anti-alignment of the molecular sample informs about the perpendicular resp. parallel character of the ionizing transition. When the photoionization occurs by means of a parallel transition the ionization efficiency of molecules that are aligned parallel to the laser polarization axis will be higher than that of molecules that are anti-aligned. In this case, the symmetry of the final (molecular ion + electron) state will be Σ_u. Similarly, when the photo-ionization occurs by means of a perpendicular transition, the ionization efficiency of molecules that are aligned perpendicular to the laser polarization axis will be higher than that of molecules that are aligned along the polarization axis and the symmetry of the final (molecular ion + electron) state will be Π_u. Based on the experimental data the conclusion can be drawn that the HOMO and HOMO-1 of CO_2 ionize by means of a perpendicular transition, and the HOMO-3 by means of a parallel transition. The ionization of the HOMO-2 is predominantly parallel at low energies (up to a photoelectron kinetic energy of 15 eV) and then changes to predominantly perpendicular.

The experimental results can be well-reproduced by an electron-molecule quantum scattering method that was previously also successfully applied to calculate MFPADs recorded with synchrotron radiation [34, 35]. This method is based on the multichannel Schwinger configuration interaction method (MCSCI), where the initial state and the final ionic states are represented as configuration interaction (CI) wave functions. Calculated differential photoelectron kinetic energy and angular distributions (making use of the alignment distributions provided by the experimental fits of the time-dependent molecular alignment, see Fig. 1.3) are shown in the contour plot shown on the right side of Fig. 1.4b, as well as in Figs. 1.4c–f, where the theoretical differential photoelectron kinetic energy and angular distributions are plotted separately for the four most important orbitals that contribute to the ionization signal. The overall agreement between the experimental and theoretical data is very satisfactory.

In the final (molecular ion + electron) state the symmetry of the wavefunction is determined both by the electronic state of the ion and that of the continuum electron. The wave function of a photoelectron ejected by single photon ionization can be expressed as a superposition of partial waves that are characterized by the angular momentum l of the photoelectron and a symmetry index λ that describes the projection of this angular momentum on the molecular axis; for $\lambda = 0$ the states are designated as σ and for $\lambda = 1$ as π. In practice, the partial-wave expansion converges at relatively small l ($l < 4$, or in usual notation s, p, d and f partial waves). In addition, the dipolar $u \longleftrightarrow g$ selection rule restricts the electron in the continuum to ungerade symmetry for the final ionic states $X^2\Sigma_g$ and $C^2\Sigma_g$ (which implies that only odd angular momenta appear in the partial wave expansion of the outgoing electron) and to gerade symmetry for the final ionic states $A^2\Pi_u$ and $B^2\Sigma_u$ (which means that only even angular momenta appear in the partial wave expansion of the outgoing electron). One cannot extract the partial wave decomposition of the electronic wave packet from the experimental results due to the low degree of alignment. The experimental result can only put constraints on the possible decomposition of the electronic wavepacket into partial waves. For the ionization leading to the final $X^2\Sigma_g$ ground ionic state for instance, where the wave packet is mainly composed of $l = 1, 3$ (p and f waves), the pronounced positive contribution along the laser polarization axis that is observed both theoretically and experimentally suggests that the photoelectron partial wave decomposition contains a strong contribution from the p-partial wave. The computational results support this notion, but also suggest an important role for f-wave photo-emission.

One of the most significant results that follows from the experimental and theoretical contour plots shown in Fig. 1.4b–f is the fact that the differential photoelectron angular distributions clearly depend on the kinetic energy of the outgoing electron. This may be interpreted as a manifestation of the onset of structural information in the photoelectron angular distributions. Although the photoelectron kinetic energies are still too low to observe readily interpretable diffraction patterns, and although the differential photoelectron angular distributions are heavily affected by the extensive angular averaging that occurs as a result of the rather modest degree of alignment and anti-alignment in the experiment, this result provides the rationalization for attempts to extend these results to higher photon energies. Extending the use of HHG sources, this may become possible in the near future by the use of different generating gasses with a higher cut-off (He or Ne, rather than Ar) in the HHG process [36], and/or by performing HHG with a longer wavelength driver wavelength [37] or making use of a multi-color field [38].

Alternatively, higher photon energies may be accessed by performing the experiment at one of the emerging XUV/X-ray FEL facilities, which moreover have the advantage that they offer a peak brightness which exceeds that of HHG sources by many orders of magnitude. FELs like FLASH and LCLS offer more than 10^{12} photons/pulse at photon energies ranging from ca. 0.04 to 10 keV. However, the advantages of FELs over HHG come at the expense of a lack of coherence and the difficulty to synchronize other laser sources to the FEL. The former is not a serious problem in molecular pump-probe experiments aiming at femtosecond time resolution,

whereas the latter implies that in experiments requiring high time-resolution additional measurements (e.g. electro-optical measurements [39] or cross-correlation schemes based on transient X-ray induced reflectivity modification [40]) are needed to measure the jitter between the FEL and a 2nd laser on a shot-by-shot basis. Moreover, the development of new protocols is required that allow to find the temporal and spatial overlap of the FEL laser beam and the other laser beam(s) that are used in the experiment. The availability of a velocity map imaging spectrometer provides very useful opportunities for doing this, given that the detector can be used both in a spatial and a velocity map imaging mode, while at the same time providing high quality time-of-flight information [41].

The alignment-pump-probe approach with velocity map imaging detection of high energy photoelectrons described above is in principle very suitable for application at FELs. In contrast with the use of a reaction microscope, the velocity map imaging technique allows the recording of rather large signals before space-charge distortions of the measured angular and velocity distribution set in. For example, when an FEL is focused to a spot diameter of about 100 μm and intersects the molecular beam containing the target molecules over a length of about 1 mm, then as many as 10^3 photoelectrons can be generated and measured per laser shot, before one exceeds the empirical threshold of ca. 10^8 photoelectrons/cm^3 where space charge effects start to cause serious problems.

Our first activity at the FLASH FEL was to introduce the use of velocity map imaging (VMI) [42, 43]. As far as the use of XUV/X-ray photoionization for the time-resolved observation of molecular dynamics is concerned, we have so far developed an alignment-pump-probe experiment where small molecules like Br_2 are dynamically aligned using the fundamental 800 nm wavelength of a Ti:Sa laser, photo-dissociated using the 2nd harmonic of this laser [44] and then ionized by the FEL. Figure 1.5(a)–(c) shows 2D momentum maps of Br^{2+} fragments in the presence of only the FEL (a), with both the 400 nm and the FEL beam present (b), and when all three pulses are present (c) [45, 46]. In the presence of the FEL pulse, the 2D velocity distribution is composed of concentric rings originating from dissociative ionization and Coulomb explosion of the molecule. The prominent new contribution observed in Fig. 1.5(b) results from the ionization by the FEL pulse of fragments of the dissociation initiated by the 400 nm pulse. When adding the 800 nm pulse, the angular distribution peaks along the laser polarization axis (see Fig. 1.5(c)), which indicates that the molecules are aligned prior to dissociation and ionization. First attempts have been made to record photoelectron angular distributions under these conditions. Figure 1.5(d) shows a differential photoelectron momentum map similar to the data shown in Fig. 1.4, where in the present case the difference is shown between a photoelectron momentum map recorded before and after dissociation by the 400 nm photo-excitation laser pulse. From the difference image a clear signature of the result of the dissociation process can be identified through the shift of the resulting photoelectron energies and changes in the angular distribution of photoelectrons from the 3d shell. Recording of photoelectron data with the time resolution required for a complete investigation of the Br_2 dissociation dynamics has not been completed yet.

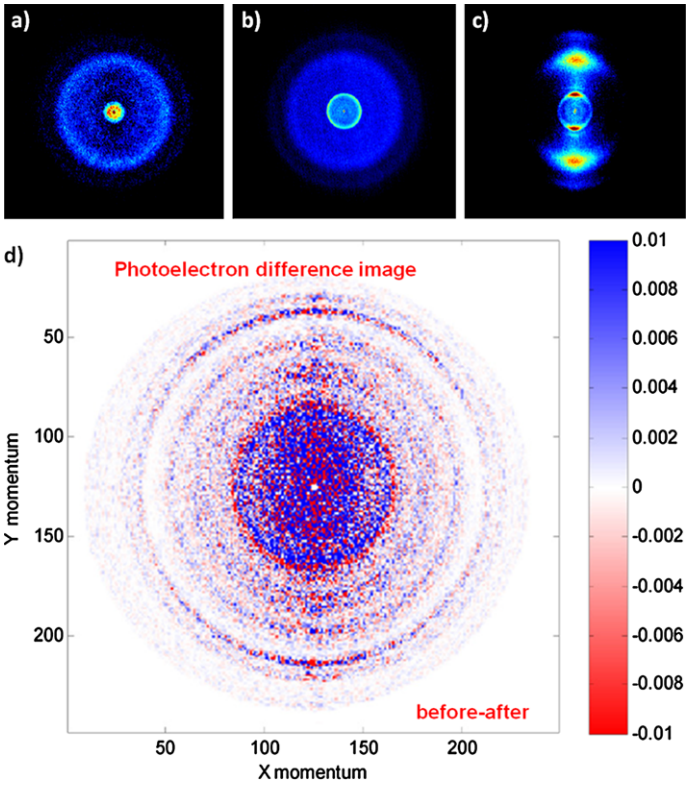

Fig. 1.5 (**a**)–(**c**) Br^{2+} ions resulting from dissociative ionization of Br_2 by 13 nm light from FLASH. In (**a**), the FEL pulse alone is impinging on the molecules, resulting in fragmentation through dissociative ionization (central ring) or Coulomb explosion (outer two rings). In (**b**), the FEL pulse is preceded by a 400 nm pump pulse which induces dissociation of the neutral molecule, resulting in a sharp central ring. In (**c**), an IR alignment pulse is sent in 1 ps before the other two pulses, impulsively aligning the molecule and resulting in a momentum distribution that is peaked along the laser polarization axis; (**d**) differential photoelectron momentum map, showing the difference between a photoelectron map for dissociated and non-dissociated Br_2 molecules

1.3 Molecular Movies Using Strong Field Mid-Infrared Ionization

In the experiments described in the previous section, high-energy electrons were generated by high energy XUV/X-ray single photon ionization. However, this is not the only way that electrons can acquire a high kinetic energy. Alternatively, electrons can be accelerated to high kinetic energies using ponderomotive acceleration in an intense laser field. In this case the energy acquired by the electron scales with $I_{\text{laser}}\lambda^2_{\text{laser}}$, where I_{laser} is the intensity of the laser and λ_{laser} is the laser wavelength. It follows that ponderomotive acceleration is particularly relevant for lasers operating in the mid-infrared wavelength range.

The use of mid-infrared strong-field ionization as a means of probing molecular dynamics is a research field that is only now being first attempted in a number of laboratories. However, there exists already a highly relevant body of work concerned with how HHG, beyond its use as a source of coherent XUV light, can be used to study atomic and molecular structure and time-resolved dynamics, by measuring the harmonic emission as a function of molecular alignment. These experiments, which have come to be known as "orbital tomography" or "harmonic imaging" experiments, probe the molecular structure since they are sensitive to multi-particle interference effects [47], and allow to re-construct the amplitude and phase of the orbital from which the ionized electron was removed [48]. Of particular interest have also been recent experimental and theoretical works showing that attosecond time-scale electron dynamics in molecular ions can be probed [49], as well as experiments where the breaking of a molecular bond was followed by monitoring the harmonic emission from the dissociating molecule as a function of time [50].

In the harmonic imaging experiments, the available observables are typically the amplitude and phase of a limited number (typ. 5–10) of harmonics. Alternatively, outcomes of the electron-ion re-collision that do not involve photon emission, but where the electron elastically or inelastically scatters off the ion, can be measured. Measurements of 2D photoelectron momentum distributions in principle provide a very rich observable, since every distinguishable final momentum of the electron (p_z, p_x), where p_z is the momentum along the polarization axis and p_x the momentum orthogonal to it, may be viewed as an independent measurement. Scattering of re-collision electrons from different constituent atoms within a molecule may lead to diffraction patterns characterized by constructive and destructive interferences that appear at specific final momenta [51, 52]. In addition, the interference between scattered and non-scattered, laser-ionized electrons leads to holographic interferences that provide further opportunities for the retrieval of dynamical and structural information.

The first experimental observation of the above-mentioned holographic interference structures was recently made in an experiment where metastable Xe atoms were ionized using 7 μm radiation from the FELICE FEL at Rijnhuizen in the Netherlands (see Fig. 1.6) [14]. 2D photoelectron momentum maps were measured with the help of a velocity map imaging spectrometer that was integrated into the FEL cavity. Under the influence of the FEL the outermost electron is pulled out of the atom along the polarization axis and starts an oscillatory motion in the laser field. The outer turning point of this oscillatory motion can be viewed as an electron source (at a distance of about 20 Angströms from the atom!) from which electron waves are emitted that reach the detector either with or without interacting with the ion from which they are produced. In the former case we are justified in thinking of the electron wave as a signal wave that encodes information about the ion, while in the latter case we are justified in thinking of the electron wave as a reference wave. In this sense, the experiment records a hologram that can in principle be used to retrieve information about the atomic or molecular target from which the electron was extracted.

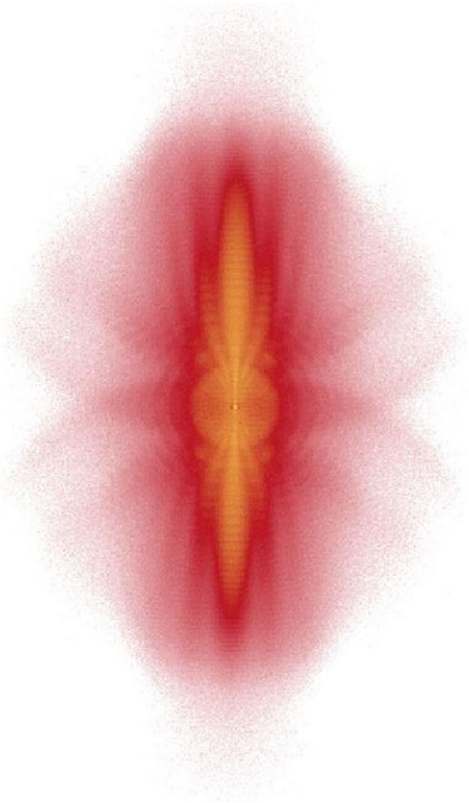

Fig. 1.6 Cut through the 3D photoelectron momentum distribution recorded for the ionization of metastable Xenon atoms by 7 μm FELICE radiation, showing the appearance of side-lobes that result from a holographic interference between electrons that scatter off the Xe^+ ion and electrons that do not. In the image, the *vertical axis* corresponds to the polarization axis of the FELICE free electron laser. The peak intensity of the FELICE laser was 7×10^{11} W/cm^2. The image shown here is the result of a 4-hour long measurement. The dynamic range in the image extends over 4 orders of magnitude

The observation of photoelectron holograms in strong-field ionization at mid-infrared wavelengths was quite unexpected, since prior to the experiment the conventional wisdom in the strong-field laser community was that with substantial scaling of the laser wavelength towards the mid-infrared the efficiency of the electron-ion re-collision would dramatically diminish. This is the reason, for example, why it is experimentally observed that the efficiency of HHG drops as function of driver wavelength with approximately $\lambda^{-(5-6)}$. However, the recent results that we have obtained at FELICE have shown that, as a result of Coulomb focussing of the electron trajectories, substantial re-collision amplitudes remain observable for wavelengths as long as 40 μm (!), where holograms such as the one shown in Fig. 1.6 could readily be observed. It is noteworthy that the photoelectron holograms observed in strong-field ionization are strongly related to interferograms that we have observed about a decade ago in velocity map imaging experiments on threshold photoionization of atoms in a weak DC electric field [53, 54]. In this case the interferences are caused by the fact that in a DC electric field there exist an infinite number of classical trajectories connecting the atom and a particular point on the detector, differing in the number of returns of the electron to the ionic core prior to ionization. Similarly, in the present strong-field holography case there are—in principle—an infinite number of trajectories that differ in the number of times that a laser-driven glancing re-

collision takes place. Evidence for the occurrence of multiple/late re-collisions was explicitly observed in [14]. The late re-collisions correspond to trajectories where the electron, after being pulled out of the atom in a particular half-cycle, misses the ion on the first, or even second re-collision opportunity, so that the scattering event that leads to a substantial change in the electron momentum only occurs on the second, or even third re-collision opportunity.

The hologram in Fig. 1.6 can on the one hand be viewed as a 'static' measurement with the potential to determine a molecular structure. Since, however, this measurement is completed within the pulse duration of the mid-infrared ionization laser, it can be easily extended to the monitoring of time-dependent structural changes in molecules, provided that the mid-infrared laser sources can be constructed with a pulse duration that is commensurate with the time-dependent molecular structural changes of interest. With the availability of 30–50 fs mid-infrared laser pulses these two requirements can readily be reconciled. At the same time, a single hologram such as shown in Fig. 1.6 already contains time-dependent information on ultrafast electron dynamics, due to the way that the time of ionization and the time of the re-collision with the ion directly determine the final momentum. This is very similar to the operating principle of the attosecond streak camera, that is commonly used in attosecond science to characterize attosecond laser pulses and to record time-dependent events on the attosecond timescale [55, 56]. In this manner, the holography experiment allows to obtain information on the ionization dynamics and ultrafast 'hole dynamics' in the molecular ion left behind that is on the sub- or few-femtosecond timescale.

In order to arrive at the interpretation of the side-lobes in Fig. 1.6 in terms of a holographic interference between a signal and reference electron wave, a number of numerical methods were used. The side-lobes are reproduced when the time-dependent Schrödinger equation (TDSE) is solved in the single active electron (SAE)-approximation [57], but this does not provide any physical insight yet. A deeper understanding can be obtained when using methods that are based on the strong-field approximation (SFA), which has already been invoked in the explanation of many strong-field phenomena [58]. In the SFA, one assumes that prior to ionization the laser field has a negligible interaction with the electron compared to the interaction of the electron with the atomic or molecular ion core, and that after ionization, which is assumed to occur by means of a tunneling process, the situation is reversed, i.e. the motion of the electron is then entirely governed by the interaction of the electron with the laser field. These assumptions allow one to explain, for example, the high-energy cut-off that is observed in HHG [19]. SFA in its simplest form cannot explain the holographic interferences that are observed in Fig. 1.6, since it does not include the Coulomb interaction of the electron with the ion from which it as extracted and the changes in the electron momentum that are induced by electron-ion recollisions that occur under the influence of the oscillatory laser field. A suitable method to include the Coulomb interaction into SFA was introduced by Bauer and Prophuzhenko [59, 60], making use of the fact that within an SFA framework strong field ionization can be numerically evaluated using the application of a saddle-point method [61], which regards ionization resulting in a given final momentum (p_z, p_x) as arising from a finite number of distinct ionization events, which

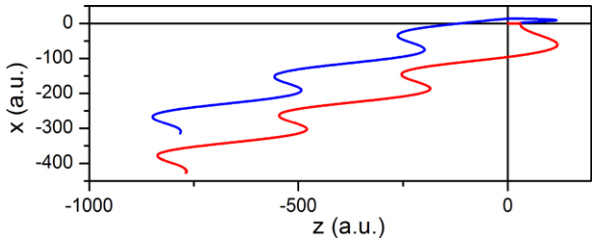

Fig. 1.7 The role of re-collision in strong-field ionization: two trajectories that lead to the formation of electrons with a final momentum $p_x = -0.01$ a.u., $p_z = -0.46$ a.u. in the ionization of metastable Xe atoms by a 7×10^{11} W/cm^2, 7 μm laser field. The *red trajectory* corresponds to an electron that only weakly interacts with the ionic core, while the *blue trajectory* corresponds to an electron that strongly interactions with ion and undergoes Coulomb focusing. As a result, the radial velocity along the *blue trajectory*, which is initially in the upward direction, is converted into a velocity in the downward direction, allowing this trajectory to interfere on the detector with the *red trajectory*

are accompanied by distinct trajectories that take the electron from the atom or molecule to the detector. When the Coulomb interaction is taken into account during the evaluation of these trajectories, the Coulomb-Corrected SFA (CCSFA) method results [59, 60], which correctly predicts the influence of the Coulomb interaction on the final momentum that the electron acquires and on the phase evolution (in the combined Coulomb and laser field) that the electron experiences on its way to the detector. Hence both the influence of the Coulomb interaction and the possibility for the occurrence of momentum-changing electron-ion re-collisions are automatically included in this method, which therefore allows to correctly predict the location of the holographic interferences. Inspection of the trajectories that are responsible for the emergence of interference maxima and minima illustrates the holographic principle (see Fig. 1.7) and clearly shows that the interference at a given final momentum occurs as a result of the coexistence of non-scattering (i.e. reference) and strongly re-scattering (i.e. signal) trajectories. In addition, the CCSFA method clearly allows to recognize the vital role of the Coulomb interaction, since for the holographic interference to occur it is necessary that the transverse momentum p_x is reversed when the electron interacts with the ion in the course of the re-collision (see Fig. 1.7).

As an intermediate approach between the application of SFA, which is too simplistic since it neglects re-scattering, and the CCSFA method, which relies on the numerical integration of large numbers of electron trajectories, we have also applied a generalized SFA method. This method does not include the Coulomb interaction, but does include re-collisions of electrons that are driven away from and back towards the ion with zero transverse momentum, and the scattering of these electrons into a spherical wave upon returning to the ion core. The advantage of this method is that it can be treated analytically, and allows to determine that the phase difference $\Delta\phi$ between the scattered and non-scattered electron waves that causes the holographic interference is dominated by a term, $\Delta\phi \approx -\frac{1}{2}p_x^2(t_C - t_0^{\text{ref}})$ where, t_C is the moment of the electron-ion re-collision and t_0^{ref} corresponds to the time that the reference wavepacket starts tunneling through the barrier. This expression

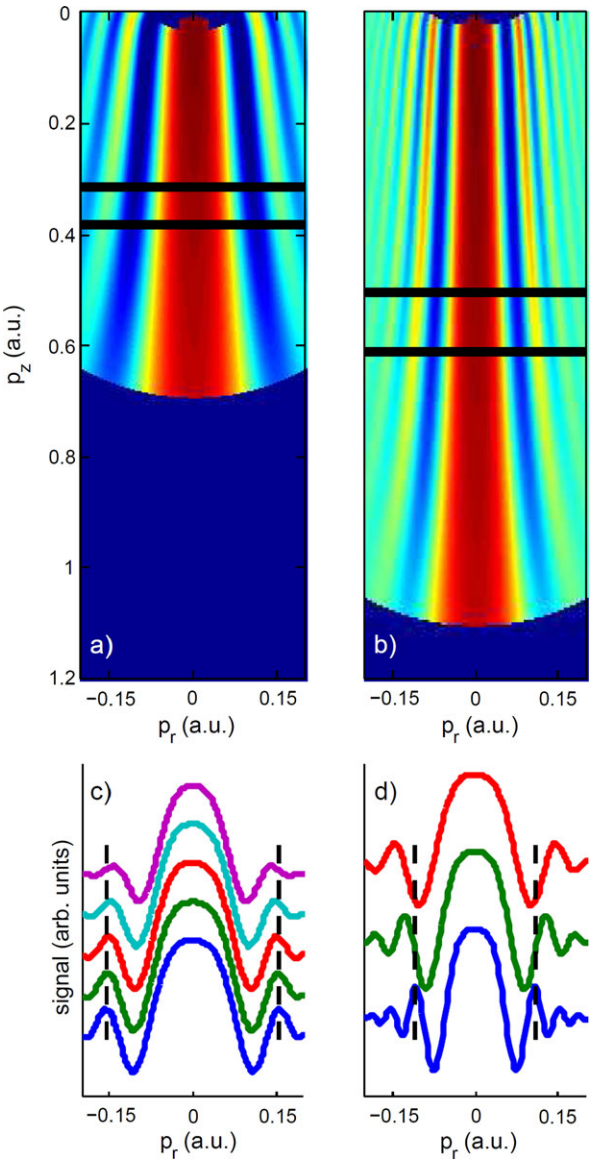

Fig. 1.8 Dependence of the holographic interference on the peak intensity and wavelength of the ionizing laser pulse: (**a**) interference fringes in the ionization of metastable Xe atoms by a 7 μm laser field with an intensity $I = 7.1 \times 10^{11}$ W/cm^2 (*lila*), 5.5×10^{11} W/cm^2 (*cyan*), 4.5×10^{11} W/cm^2 (*red*), 3.2×10^{11} W/cm^2 (*green*) and 1.9×10^{11} W/cm^2 (*blue*); the contourplot shows the two-dimensional momentum map calculated for $I = 7.1 \times 10^{11}$ W/cm^2; (**b**) interference fringes in the ionization of metastable Xe atoms as a function of the laser wavelength while keeping the ponderomotive energy constant. *Curves* are shown for $\lambda = 16$ μm and $I = 3.4 \times 10^{11}$ W/cm^2 (*blue*), for $\lambda = 11$ μm and $I = 4.4 \times 10^{11}$ W/cm^2 (*green*) and for $\lambda = 8$ μm and $I = 5.4 \times 10^{11}$ W/cm^2 (*red*). In all cases the line-outs are evaluated at $p_z = 0.5$ $p_{z,\text{cut-off}}$, where the latter value corresponds to the momentum along the polarization axis at the $2U_p$ cut-off energy; the momentum map shows the result calculated for $\lambda = 16$ μm

for $\Delta\phi$ allows to predict the dependence of the holographic interference pattern on the intensity and wavelength of the laser. The dependence on the intensity of the mid-infrared laser is very modest. When the intensity changes, the values of t_C and t_0^{ref} that lead to the production of a photoelectron with final momentum $(p_z,\ p_x)$ only change by very small amounts, suggesting that the interference pattern is very robust with regards to changes in the peak laser intensity and explaining why the holographic interference patterns easily survive the temporal and spatial averaging

that, under experimental conditions, inevitably takes place in a laser focus. These arguments are corroborated by the calculations shown in Fig. 1.8(a), which show the result of generalized SFA calculations for the ionization of metastable Xe atoms by a 7 μm laser with an peak intensity ranging from 1.9×10^{11}–7×10^{11} W/cm^2 [62]. For a constant value of p_z, the interference pattern hardly changes as a function of the intensity. This is very different when the wavelength of the ionizing laser is changed. To illustrate this, Fig. 1.8(b) shows a series of calculations where the holographic interference is calculated as a function of the laser wavelength under conditions where the ponderomotive energy (and thus the value of p_z where the high-energy cut-off is observed in the photoelectron spectrum) stays constant. Figure 1.8(b) clearly shows that with increasing laser wavelength the spacing of the holographic interference fringes narrows, due to the fact that the difference between t_C and t_0^{ref} scales linearly with laser wavelength, leading to a doubling of the phase difference between the reference and signal electron wave at a fixed position in the momentum map [62].

1.4 Outlook

It is in the nature of scientific development that advances are often stimulated by the emergence of novel technological capabilities. In this respect, the molecular sciences are no exception. At present, the emergence of intense, short pulse light sources outside the traditional near-infrared to near-UV wavelength range promises the development of novel techniques that address time-dependent dynamics and that do not rely so much on molecular photo-absorption as on diffraction of laser light or the photoelectrons that can be generated using these sources.

On the one hand, at an increasing number of places around the world, XUV/X-ray free electron laser sources are being constructed and coming available, that deliver ultrashort XUV/X-ray laser pulses with unprecedented fluences and peak intensities, that can be used to develop new ways to study time-resolved molecular dynamics based on use of the diffractive properties of energetic photoelectrons that are ejected from time-evolving molecules upon photo-ionization. In the last few years pump-probe protocols have been developed that allow to first dynamically align a molecule of interest, thereby fixing its orientational degrees of freedom in the laboratory frame, before addressing the molecule with a pump pulse that initiates the photo-dynamics of interest and the XUV/X-ray laser pulse that ionizes the molecule and/or fragments resulting from the photo-excitation. In combination with sophisticated 2D or even 3D energy—and angle-resolved photoelectron and—ion detection strategies this promises to lead to the emergence of a novel way of studying photo-chemical events that complements the present absorption-based techniques. There are remaining problems that need to be solved, such as the challenge of adequately synchronizing the FEL light with the output

of the other laser sources that are needed in such an experiment, but rapid advances are being made, and with the more wide-spread use of seeded FEL operation we may expect that in a few years these experiments can be routinely performed. At the same time, continued progress in the capabilities of HHG sources suggests that certain classes of experiments can also be transported to smaller-scale laser laboratories. Some examples of this have been given in the present chapter.

On the other hand, continued progress in the generation of near- and mid-infrared radiation promises the ability to develop novel spectroscopic techniques that are based on the interaction of ponderomotively accelerated photoelectrons with photo-excited and time-evolving molecules. In the present chapter, we have presented one example of this emerging field and have described the presence of holographic interferences in the strong field ionization of metastable Xe atoms using 7 μm laser radiation from a mid-infrared FEL. It is to be expected that the exploration of molecular strong field ionization will soon be investigated in this wavelength range, paving the way for novel spectroscopic techniques for monitoring time-dependent molecular dynamics as well. In doing so, it is very likely that the essence of the results that were obtained so far at an FEL can be transported to smaller-scale laser laboratories. Already, with existing parametric generators and amplifiers it is possible to generate sufficient amounts of radiation in the 3–4 μm wavelength range that studies of strong-field ionization of time-evolving molecules can be confidently attempted. Furthermore, currently on-going developments aimed at the development of high repetition rate optical parametric chirped pulse amplification (OPCPA) laser systems in this wavelength range [63, 64] suggest that the time is not far that sophisticated experimental strategies involving alignment, photo-excitation and mid-infrared strong-field probing of the molecular dynamics can be attempted at 0.1–1 MHz repetition rate, inviting the use of coincident photoelectron-fragment ion detection strategies that allow to measure high quality MFPADs.

The results presented in this chapter represent a starting point of a novel research area that will require significant effort in the coming years, but then also promises to lead to major novel insights into the way that molecular systems behave in response to incident radiation fields.

Acknowledgements Apart from the work shown in Fig. 1.5, the present chapter draws heavily from a number of previously published research papers, in particular Refs. [14, 31, 45, 62]. Consequently, the work presented in this chapter would not have been possible without the considerable efforts from a large number of people who contributed to these original publications on the basis of a scientific collaboration. We particularly want to thank Prof. R. Lucchese (Texas A&M Univerisity, College Station), M. Lucchini (Politecnico di Milano), Dr. S. Duesterer, Dr. N. Stojanovic, Dr. H. Redlin and the staff at the FLASH FEL in Hamburg, Dr. Ph. Wernet (HZB Berlin), Dr. M. Gensch (DESY Rossendorf), Prof. K. Ueda (Tohoku University, Sendai), Dr. A. van der Meer, Dr. B. Redlich, Dr. G. Berden and Dr. J. Bakker and the staff at the FELICE FEL in Rijnhuizen, Dr. F. Lépine and C. Cauchy (Université de Lyon), Dr. S. Zamith (Université Paul Sabatier, Toulouse), Dr. T. Martchenko (Université Paris 06), Prof. H.G. Muller (AMOLF, Amsterdam), Prof. K. Schafer (LSU, Baton Rouge), Prof. M.Yu Ivanov and Dr. O. Smirnova (MBI, Berlin), Prof. D. Bauer (Rostock University) and Prof. S. Prophuzhenko (Moscow University).

References

1. A.H. Zewail, Femtochemistry: atomic-scale dynamics of the chemical bond using ultrafast lasers (Nobel lecture). Angew. Chem., Int. Ed. Engl. **39**(15), 2587–2631 (2000)
2. F. Schotte et al., Watching a protein as it functions with 150-ps time-resolved X-ray crystallography. Science **300**(5627), 1944–1947 (2003)
3. C. Bressler et al., Femtosecond XANES study of the light-induced spin crossover dynamics in an iron(II) complex. Science **323**(5913), 489–492 (2009)
4. M. Woerner et al., Concerted electron and proton transfer in ionic crystals mapped by femtosecond X-ray powder diffraction. J. Chem. Phys. **133**(6) (2010)
5. P. Emma et al., First lasing and operation of an angstrom-wavelength free-electron laser. Nat. Photonics **4**(9), 641–647 (2010)
6. H.N. Chapman et al., Femtosecond X-ray protein nanocrystallography. Nature **470**(7332), 73–77 (2011)
7. H. Ihee et al., Direct imaging of transient molecular structures with ultrafast diffraction. Science **291**(5503), 458–462 (2001)
8. P. Baum, D.S. Yang, A.H. Zewail, 4D visualization of transitional structures in phase transformations by electron diffraction. Science **318**(5851), 788–792 (2007)
9. N. Gedik et al., Nonequilibrium phase transitions in cuprates observed by ultrafast electron crystallography. Science **316**(5823), 425–429 (2007)
10. B.J. Siwick et al., An atomic-level view of melting using femtosecond electron diffraction. Science **302**(5649), 1382–1385 (2003)
11. P. Baum, A.H. Zewail, Attosecond electron pulses for 4D diffraction and microscopy. Proc. Natl. Acad. Sci. USA **104**(47), 18409–18414 (2007)
12. A. Landers et al., Photoelectron diffraction mapping: molecules illuminated from within. Phys. Rev. Lett. **87**(1), e013002 (2001)
13. F. Krasniqi et al., Imaging molecules from within: ultrafast angstrom-scale structure determination of molecules via photoelectron holography using free-electron lasers. Phys. Rev. A **81**(3), 033411 (2010)
14. Y. Huismans et al., Time-resolved holography with photoelectrons. Science **331**(6013), 61–64 (2011)
15. T. van Oudheusden et al., Compression of subrelativistic space-charge-dominated electron bunches for single-shot femtosecond electron diffraction. Phys. Rev. Lett. **105**(26) (2010)
16. T. Brabec, F. Krausz, Intense few-cycle laser fields: frontiers of nonlinear optics. Rev. Mod. Phys. **72**(2), 545–591 (2000)
17. P. Agostini, L.F. DiMauro, The physics of attosecond light pulses. Rep. Prog. Phys. **67**(6), 813–855 (2004)
18. F. Krausz, M. Ivanov, Attosecond physics. Rev. Mod. Phys. **81**(1), 163–234 (2009)
19. P.B. Corkum, Plasma perspective on strong-field multiphoton ionization. Phys. Rev. Lett. **71**(13), 1994–1997 (1993)
20. W. Ackermann et al., Operation of a free-electron laser from the extreme ultraviolet to the water window. Nat. Photonics **1**(6), 336–342 (2007)
21. M.F. Kling, M.J.J. Vrakking, Attosecond electron dynamics. Annu. Rev. Phys. Chem. **59**, 463–492 (2008)
22. E. Goulielmakis et al., Attosecond control and measurement: lightwave electronics. Science **317**(5839), 769–775 (2007)
23. P. Emma et al., Femtosecond and subfemtosecond X-ray pulses from a self-amplified spontaneous-emission-based free-electron laser. Phys. Rev. Lett. **92**(7) (2004)
24. J.N. Galayda et al., X-ray free-electron lasers-present and future capabilities. J. Opt. Soc. Am. B, Opt. Phys. **27**(11), B106–B118 (2010)
25. J. Ullrich et al., Recoil-ion and electron momentum spectroscopy: reaction-microscopes. Rep. Prog. Phys. **66**(9), 1463–1545 (2003)
26. H. Stapelfeldt, T. Seideman, Colloquium: aligning molecules with strong laser pulses. Rev. Mod. Phys. **75**(2), 543–557 (2003)

27. J.J. Larsen et al., Aligning molecules with intense nonresonant laser fields. J. Chem. Phys. **111**(17), 7774–7781 (1999)
28. F. Rosca-Pruna, M.J.J. Vrakking, Experimental observation of revival structures in picosecond laser-induced alignment of I-2. Phys. Rev. Lett. **87**(15), 153902 (2001)
29. S. Guerin, A. Rouzee, E. Hertz, Ultimate field-free molecular alignment by combined adiabatic-impulsive field design. Phys. Rev. A **77**(4), 041404(R) (2008)
30. O. Ghafur et al., Impulsive orientation and alignment of quantum-state-selected NO molecules. Nat. Phys. **5**(4), 289–293 (2009)
31. F. Kelkensberg et al., XUV ionization of aligned molecules. Phys. Rev. A **84**(5), 051404 (2011)
32. M.J.J. Vrakking, An iterative procedure for the inversion of two-dimensional ion/photoelectron imaging experiments. Rev. Sci. Instrum. **72**(11), 4084–4089 (2001)
33. O. Ghafur et al., A velocity map imaging detector with an integrated gas injection system. Rev. Sci. Instrum. **80**(3), 033110 (2009)
34. R.R. Lucchese, K. Takatsuka, V. Mckoy, Applications of the Schwinger variational principle to electron molecule collisions and molecular photoionization. Phys. Rep. **131**(3), 147–221 (1986)
35. R.R. Lucchese et al., Polar and azimuthal dependence of the molecular frame photoelectron angular distributions of spatially oriented linear molecules. Phys. Rev. A **65**(2), 020702 (2002)
36. C.G. Wahlstrom et al., High-order harmonic-generation in rare-gases with an intense short-pulse laser. Phys. Rev. A **48**(6), 4709–4720 (1993)
37. P. Colosimo et al., Scaling strong-field interactions towards the classical limit. Nat. Phys. **4**(5), 386–389 (2008)
38. W.Y. Hong et al., Broadband water window supercontinuum generation with a tailored mid-IR pulse in neutral media. Opt. Lett. **34**(14), 2102–2104 (2009)
39. I. Wilke et al., Single-shot electron-beam bunch length measurements. Phys. Rev. Lett. **88**(12), 124801 (2002)
40. C. Gahl et al., A femtosecond X-ray/optical cross-correlator. Nat. Photonics **2**(3), 165–169 (2008)
41. P. Johnsson et al., Characterization of a two-color pump probe setup at FLASH using a velocity map imaging spectrometer. Opt. Lett. **35**(24), 4163–4165 (2010)
42. P. Johnsson et al., Velocity map imaging of atomic and molecular processes at the free electron laser in Hamburg (FLASH). J. Mod. Opt. **55**(16), 2693–2709 (2008)
43. A. Rouzee et al., Angle-resolved photoelectron spectroscopy of sequential three-photon triple ionization of neon at 90.5 eV photon energy. Phys. Rev. A **83**(3) (2011)
44. L. Nugent-Glandorf et al., Ultrafast time-resolved soft X-ray photoelectron spectroscopy of dissociating Br-2. Phys. Rev. Lett. **8719**(19), 193002 (2001)
45. N. Berrah et al., Non-linear processes in the interaction of atoms and molecules with intense EUV and X-ray fields from SASE free electron lasers (FELs). J. Mod. Opt. **57**(12), 1015–1040 (2010)
46. A. Rouzée et al., Towards imaging of ultrafast molecular dynamics using FELs. J. Phys. B **46**, 164029 (2013)
47. T. Kanai, S. Minemoto, H. Sakai, Quantum interference during high-order harmonic generation from aligned molecules. Nature **435**(7041), 470–474 (2005)
48. J. Itatani et al., Tomographic imaging of molecular orbitals. Nature **432**(7019), 867–871 (2004)
49. O. Smirnova et al., High harmonic interferometry of multi-electron dynamics in molecules. Nature **460**(7258), 972–977 (2009)
50. H.J. Worner et al., Following a chemical reaction using high-harmonic interferometry. Nature **466**(7306), 604–607 (2010)
51. M. Spanner et al., Reading diffraction images in strong field ionization of diatomic molecules. J. Phys. B, At. Mol. Opt. Phys. **37**(12), L243–L250 (2004)
52. M. Meckel et al., Laser-induced electron tunneling and diffraction. Science **320**(5882), 1478–1482 (2008)

53. C. Nicole et al., Photoionization microscopy. Phys. Rev. Lett. **88**(13), 133001 (2002)
54. F. Lepine et al., Atomic photoionization processes under magnification. Phys. Rev. A **70**(3), 033417 (2004)
55. J. Itatani et al., Attosecond streak camera. Phys. Rev. Lett. **88**(17), 173903 (2002)
56. R. Kienberger et al., Atomic transient recorder. Nature **427**(6977), 817–821 (2004)
57. H.G. Muller, An efficient propagation scheme for the time-dependent Schrodinger equation in the velocity gauge. Laser Phys. **9**(1), 138–148 (1999)
58. H.R. Reiss, Effect of an intense electromagnetic field on a weakly bound system. Phys. Rev. A **22**(5), 1786–1813 (1980)
59. S.V. Popruzhenko, D. Bauer, Strong field approximation for systems with Coulomb interaction. J. Mod. Opt. **55**(16), 2573–2589 (2008)
60. S.V. Popruzhenko, G.G. Paulus, D. Bauer, Coulomb-corrected quantum trajectories in strong-field ionization. Phys. Rev. A **77**(5), 053409 (2008)
61. W. Becker et al., Above-threshold ionization: from classical features to quantum effects. Adv. At. Mol. Opt. Phys. **48**, 35–98 (2002)
62. Y. Huismans et al., Scaling laws for photoelectron holography in the mid-infrared wavelength regime. Phys. Rev. Lett. **109**, 013002 (2012)
63. O. Chalus et al., Six-cycle mid-infrared source with 3.8 μJ at 100 kHz. Opt. Lett. **35**(19), 3204–3206 (2010)
64. C. Erny et al., High-repetition-rate optical parametric chirped-pulse amplifier producing 1-μJ, sub-100-fs pulses in the mid-infrared. Opt. Express **17**(3), 1340–1345 (2009)
65. A. Rouzée, Thesis. University of Burgundy (2007)

Chapter 2
XUV Lasers for Ultrafast Electronic Control in H_2

Alicia Palacios, Paula Rivière, Alberto González-Castrillo, and Fernando Martín

Abstract Manipulation and control of molecular electron dynamics is currently in the spotlight for numerous multidisciplinary applications in physics, chemistry and biology. During the last decade, free electron lasers and sources based on high-order harmonic generation have been successfully developed to enable the generation of femtosecond and attosecond intense radiation pulses in the ultraviolet and soft X-ray regions. These tools have lead to an outbreak of pump-probe experiments suited to explore structural dynamics in atoms and molecules with spatial and temporal resolutions on the atomic length and intrinsic electronic time scales, respectively. Such experiments, using hydrogen molecules (H_2, D_2) as prototypical examples, have been performed to study molecular dissociative single and multi-photon ionization, photon-induced symmetry breaking in molecular dissociation, and time-resolved imaging of coherent nuclear wave-packets. The counterpart state-of-the-art time-dependent theoretical methods, able to provide a solid groundwork for describing and interpreting the underlying ultrafast physical molecular dynamics in such experiments, are still scarce. The difficulty is to achieve an accurate description accounting for the full dimensionality of the problem. A proper treatment of nuclear degrees of freedom is already indispensable to study multiphoton single ionization of diatomic molecules. This is discussed in the present manuscript in different applications. We first examine the role of the coupled electronic and nuclear motions in problems that probe coherent nuclear wave-packets using intense UV pulses and in resonance-enhanced multiphoton single ionization (REMPI) processes, whose rates are underestimated when using approaches within the fixed nuclei approximation. Later, we show that for highly intense fields the presence of vibrational structure leads to step-ladder Rabi oscillations that are probed in the REMPI probabilities. Finally, we demonstrate the suitability of these time-dependent full-dimensional treatments to provide time-resolved images of autoionization of H_2, following the

A. Palacios (✉) · P. Rivière · A. González-Castrillo · F. Martín
Departamento de Química, Universidad Autónoma de Madrid, 28049 Madrid, Spain
e-mail: alicia.palacios@uam.es

F. Martín
Instituto Madrileño de Estudios Avanzados en Nanociencia (IMDEA-Nanociencia), 28049 Cantoblanco, Madrid, Spain

R. de Nalda, L. Bañares (eds.), *Ultrafast Phenomena in Molecular Sciences*, Springer Series in Chemical Physics 107, DOI 10.1007/978-3-319-02051-8_2,

time evolution of both electron and proton distributions after the interaction with ultrashort pulses.

2.1 Introduction

The success of the new generation of laser sources in providing intense femtosecond (1 fs $= 10^{-15}$ s) and attosecond (1 as $= 10^{-18}$ s) pulses opens the door to manipulation and control of molecular electron dynamics. The last two decades have witnessed a qualitative step forward on laser assisted applications in physics, chemistry and biology [1–3]. First pump-probe experiments using 10–100 fs laser pulses were able to retrieve information with atomic time and space resolutions. The development of femtochemistry research, awarded with the Nobel Prize in Chemistry in 1999 [4], led to images at the time scale of nuclear motion allowing us to unravel the dynamics of chemical bond breaking and formation and intramolecular processes [2]. The more recent breakthroughs in x-ray free electron laser (XFEL) sources that combine high peak power with few-fs pulses made it possible to explore an even wider variety of ultrafast phenomena [5–8]. In line with those, high-harmonic generation (HHG) techniques soon made the attosecond science sprout [9–12], with the commitment to achieve actual snapshots of electron motion, with laser pulse durations down to hundreds of as. Today's ultrafast scientific community is rapidly improving experimental techniques leading to an increasing number of studies in attosecond electron dynamics in atomic and molecular targets. Extensive literature of the state-of-the-art attosecond science are given in [13–16]. The exceptional potential of the current laser technology thus challenges theoretical methods to provide a solid groundwork to understand and interpret the mechanisms that are responsible for a wealth of laser-induced processes. Despite the equally impressive developments in supercomputing capabilities, substantial efforts are still necessary to achieve full dimensional accurate theoretical descriptions of these processes in multielectron atoms and molecules. The need for deep insights on the fundamental physics that governs ultrafast laser-matter interactions make the simplest molecules (H_2, D_2) the ideal targets of study. The richness on the information that photo-induced excitation and ionization of these prototypical molecules provide is incomparable, being the only systems where the coupled motion of nuclei and electrons (including electron correlation effects) can be tackled from ab initio quantum treatments. Detailed reviews on ultrafast dynamics in hydrogen molecules can be found in [17–19].

The aim of this manuscript is to provide a survey on the latest experimental and theoretical achievements on excitation and ionization of hydrogen molecules by UV/XUV ultrashort laser pulses. We particularly focus on those processes that can eventually lead to control of autoionization and multiphoton single-ionization processes in molecules by acting at the few-fs and sub-fs time scales. We examine in detail the mechanisms that are triggered at different frequencies by tuning the laser parameters (pulse length, laser intensity, etc) and that indeed allow to manipulate the

relative importance of different ionization channels. We also present theoretical predictions on phenomena induced by intense XUV fs laser pulses that are inexistent in atoms.

This document is organized as follows. Section 2.2 briefly reviews the experiments performed in the last few years on single and double ionization of hydrogen molecules subject to different radiation sources. In Sect. 2.3, we report the most relevant theoretical contributions aimed at exploring excitation and ionization of H_2, followed by a brief description of the time-dependent theoretical methods employed for the calculations presented here. Sections 2.4 and 2.5 discuss in detail some of these theoretical results in the framework of the current and future laser capabilities. We conclude with a short discussion on the current limitations of these methods to describe ultrafast molecular phenomena and on upcoming studies devoted to understand fundamental concepts in small molecules.

2.2 Experimental Set-Ups

A complete understanding of molecular photoionization, even in the simplest systems, is not yet accomplished. Ionization and dissociation may take place simultaneously in time-scales of few femtoseconds (fs) and several competing channels may be favored/suppressed by tuning the radiation parameters. Synchrotron radiation sources have been used to explore photoionization of H_2, with particular interest in the region where doubly excited states (DES) are significantly populated ($60 > \omega > 25$ eV). Interference phenomena due to the coupled motion of electrons and nuclei have been observed in single photoionization of H_2. For instance, synchrotron radiation experiments, with diverse light and detection arrangements, have explored the anisotropies in the angular distributions of emitted electrons, which are the consequence of autoionization from different DES [20–23]. Also, a noticeable number of works have focused on photodissociation of DES into two neutral fragments [24–31]. These last works measure the fluorescence from the decay of excited H atoms, which enables to distinguish dissociation arising from vibrationally excited states of the ion H_2^+ from that arising from DES that dissociate faster than they ionize. Synchrotron radiation experiments have thus provided a significant amount of structural information that allows one to disentangle the complexity of molecular photoionization.

Nevertheless, emerging pulsed radiation sources are required for a time-resolved imaging of the molecular dynamics that eventually may lead to manipulation and control of these processes. High harmonic generation (HHG) techniques or free-electron laser (FEL) and X-ray FEL sources are able to generate intense ultrashort laser pulses in the UV and XUV regions. In the last few years, diverse pump-probe experiments have provided images with unprecedented time and spatial resolution on photo-induced atomic and molecular dynamics. In this context, pioneering experiments using XUV pulses were performed in two-photon single ionization of hydrogen molecules [32], where dissociative above threshold ionization (ATI) was explored.

Facilities as FLASH in Hamburg or LCLS in Stanford nowadays produce pulses in the x-ray region with durations as short as a few fs [7]. With the advent of detection techniques such as recoil-ion and electron momentum spectroscopy [5], it is possible to detect in coincidence all charged fragments arising from atomic and molecular fragmentation processes. Combinations of these experimental set-ups have recently provided a time-resolved picture of the Coulomb break-up of D_2 after absorption of two XUV photons [33, 34]. On the other hand, HHG techniques have demonstrated to be able to generate trains of attosecond (as) [10, 35] and isolated as [12] XUV pulses. These pulses are ideal to trigger ionization processes in atoms and molecules, whose field-free evolution can be subsequently tracked at the electronic time scale (hundreds of as). Experimental set-ups combining such sources with IR fields have led to the first observations of time-resolved images of electron localization in single ionization of H_2 and D_2 [36–38]. Despite the relatively large experimental efforts devoted to study molecular photoionization in hydrogen molecules, further investigations should also shed light on a number of unexplored processes, such as those involving the dynamics of highly correlated singly excited states, or those involving DES that are not optically allowed in photoionization (i.e., that are not accessible by absorption of a single photon).

2.3 Theoretical Approach and Implementation

Solid ab-initio theoretical methods able to describe the interaction of pulsed radiation with molecules are still under development. A full treatment that accurately accounts for all degrees of freedom (electronic and nuclear motion, including electron correlation) remains a challenge, even for the simplest molecules. As a consequence, apart from low dimensional models, most formalisms have been devoted to H_2^+ (see [18, 19] and references therein). Few groups have reported electronic correlated calculations on diatomic homonuclear molecules, and most of them have tackled the problem by using methods within the fixed nuclei approximation (FNA) [39–42], or assuming that the electronic dipole transition moments are independent of the internuclear distance [43, 44]. The first fully correlated calculations accounting for the complete dimensionality of electronic and vibrational motions as well as for interferences between all open direct and resonant ionization channels in H_2 and D_2 photoionization were performed within a time-independent approach [45–48]. Although restricted to single photoionization with monochromatic radiation, the methodology provided, for the first time, an accurate description of molecular autoionization (lifetimes, dissociative and photoionization cross sections, etc). Recently, this method has provided solid theoretical support to a large variety of experiments performed with synchrotron radiation [21–23, 30]. Its Feshbach-like treatment [49] allows for a proper description of the electronic continuum of the molecule and constitutes the skeleton for latter theoretical developments in the time domain. In particular, the representation of molecular stationary states presented below in this section is based on this formalism.

The advent of ultrashort laser technology, producing actual time-resolved pictures of electron dynamics in small molecules [16, 18, 19, 50], posed the challenge for homologous time-dependent theoretical approaches. Full dimensional methods in the time domain have been recently developed, thus opening the way to explore multiphoton single ionization processes on hydrogen molecules subject to ultrashort pulses [51–54]. The essence of these methods is given in this section. Further methodological and computational details can be found in [54].

Despite the demonstrated suitability of existing methods for a large number of fundamental problems induced by diverse radiation sources in hydrogen molecules, the study of double ionization by including the nuclear motion remains an unresolved matter. The main difficulties, which particularly make spectral methods ill-suited, are the large size of the problem and the correct description of the full-body Coulomb break-up. Within the FNA, several attempts to solve one-photon double ionization of H_2 have made use of close-coupling methods [55–58] or pure numerical representations of the wave packet [59–61]. In reference [62], the nuclear motion was taken into account within the Born-Oppenheimer (BO) approximation. These numerical approaches are promising and, although still restricted to the FNA or the BO approximation, they have already provided first results on two-photon double ionization of H_2 [63–65], for which experiments were recently carried out [33, 34]. In spite of the good qualitative agreement shown with experimental data, the theoretical calculations reported in [33, 34] assumed the separability of each photon absorption, thus preventing a quantitative comparison. Undoubtedly, further theoretical and computational efforts are still required to describe molecular multiphoton double ionization and the molecular motion associated with it.

In the following, we focus on molecular single ionization processes induced by UV and XUV ultrashort pulses, which demand time-dependent, full dimensional theoretical approaches. The theoretical methodology here described has been presented in detail in previous works. The fundaments to compute the molecular structure within the Feshbach theory can be found in [45, 66]. The latter developments of this formalism within a time-dependent treatment are explained in [53, 54]. We next summarize the key steps in the theoretical method and its current implementation. Atomic units are used throughout unless otherwise indicated.

2.3.1 Time-Dependent Spectral Method

The time-dependent (non relativistic) Schrödinger equation (TDSE) for the hydrogen molecule is written as:

$$i\frac{\partial}{\partial t}\Phi(\mathbf{r}, R, t) = \hat{H}(\mathbf{r}, R, t)\Phi(\mathbf{r}, R, t), \tag{2.1}$$

where $\mathbf{r}$ stands for the electronic coordinates (both $\mathbf{r}_1$ and $\mathbf{r}_2$) and R is the internuclear distance. The total Hamiltonian is separated in two terms, $\hat{H}(\mathbf{r}, R, t) = \hat{H}_0(\mathbf{r}, R) + \hat{V}(\mathbf{r}, t)$, where $\hat{H}_0$ is the time-independent field-free Hamiltonian of H_2,

and $\hat{V}(\mathbf{r}, t)$ the interaction potential with the field. The laser-molecule interaction is treated under the dipole approximation and the electromagnetic field is written within the semiclassical approximation, which are valid for the wavelengths used in the present work, in the UV and XUV regions.

In the dipole approximation, and in the velocity gauge, the laser-molecule interaction is written in terms of the momentum operator of the electron $\hat{\mathbf{p}}$ and the vector potential $\hat{\mathbf{A}}(t)$. For a single pulse with a central photon energy ω and a total pulse duration T, $\hat{\mathbf{A}}(t)$ can be expressed as:

$$\hat{\mathbf{A}}(t) = \begin{cases} A_0 F(t) \sin(\omega t)\hat{\varepsilon} & t \in [0, T] \\ 0 & \text{elsewhere,} \end{cases} \tag{2.2}$$

where $\hat{\epsilon}$ is the polarization vector. We use a sine squared temporal envelope for the finite pulse $F(t) = \sin^2(\pi t/T)$. The field-free Hamiltonian $\hat{H}_0$ is given by

$$\hat{H}_0(\mathbf{r}, R) = \hat{T}(R) + \hat{H}_{el}(\mathbf{r}, R), \tag{2.3}$$

where $\hat{T}(R) = -\hat{\nabla}_R^2/2\mu$ is the nuclear kinetic energy, μ the reduced mass of the nuclei, and $\hat{H}_{el}$ is the electronic Hamiltonian including the nucleus-nucleus repulsion potential term. Mass polarization, relativistic corrections terms and non-adiabatic couplings are neglected. The time-dependent wave function in Eq. (2.1) is expanded in a basis of fully correlated vibronic states of the isolated molecule:

$$\begin{aligned} \Phi(\mathbf{r}, R, t) = &\sum_n \sum\!\!\!\!\!\!\int_{v_n} C_{nv_n}(t)\Psi_{nv_n}(\mathbf{r}, R)e^{-iW_{nv_n}t} \\ &+ \sum_\alpha \sum_{\ell_\alpha} \int d\varepsilon_\alpha \sum\!\!\!\!\!\!\int_{v_\alpha} C^{\ell_\alpha}_{\alpha\varepsilon_\alpha v_\alpha}(t)\Psi^{\ell_\alpha}_{\alpha\varepsilon_\alpha v_\alpha}(\mathbf{r}, R)e^{-iW_{\varepsilon_\alpha v_\alpha}t} \\ &+ \sum_r \sum\!\!\!\!\!\!\int_{v_r} C_{rv_r}(t)\Psi_{rv_r}(\mathbf{r}, R)e^{-iW_{rv_r}t} \end{aligned} \tag{2.4}$$

where $\Psi_{nv_n}(\mathbf{r}, R)$ corresponds to the n bound electronic state of H_2 at its v_n (bound or dissociative) vibrational state, $\Psi_{rv_r}(\mathbf{r}, R)$ is a resonant electronic state (at its v_r vibrational state) lying above the ionization threshold, and $\Psi^{\ell_\alpha}_{\varepsilon_\alpha v_\alpha}(\mathbf{r}, R)$ is an electronic continuum state of energy ε_α in the α ionization channel at its v_α (bound or dissociative) vibrational state for an angular momentum ℓ_α of the ejected electron. The symbol $\sum\!\!\!\!\!\!\int$ indicates a summation over bound states plus an integral over the dissociative ones, and W_x is the total energy of each vibronic state. These stationary states are evaluated within the Born-Oppenheimer approximation and, therefore, they are written as products of an electronic and a vibrational wave function. Thus we first compute the electronic states which parametrically depend on the internuclear distance. Then, from the resulting potential energy curves, we calculate the vibrational structure associated to each electronic state.

The electronic structure is obtained within the Feshbach formalism [49]. The bound electronic states are obtained by directly solving the eigenvalue problem,

$$\hat{H}_{el}(\mathbf{r}, R)\phi_n(\mathbf{r}, R) = \mathscr{E}_n(R)\phi_n(\mathbf{r}, R), \tag{2.5}$$

whereas the representation of continuum and autoionizing electronic states uses the Feshbach subspaces. Two orthogonal complementary subspaces are defined ($\hat{Q} + \hat{P} = 1$) respectively containing the resonant ($\hat{Q}$) and non-resonant ($\hat{P}$) contribution to the continuum electronic wave function at a given energy. Note that precisely the use of two subspaces, respectively holding the electronic continuum and the doubly excited states (DES) embedded in that continuum, makes the method suitable for a straightforward time-resolved tracing of the DES decay. We then solve the electronic eigenvalue problem for each subspace:

$$[\hat{Q}\,\hat{H}_{el}\,\hat{Q}]\phi_r(\mathbf{r}, R) = \mathscr{E}_r(R)\phi_r(\mathbf{r}, R), \tag{2.6}$$

$$[\hat{P}\,\hat{H}_{el}\,\hat{P}]\phi_{\alpha,\ell_\alpha,\varepsilon}(\mathbf{r}, R) = \mathscr{E}_{\alpha,\varepsilon}(R)\phi_{\alpha,\ell_\alpha,\varepsilon}(\mathbf{r}, R). \tag{2.7}$$

The eigenvalue equations for the bound states [Eq. (2.5)] and the resonant component of the continuum [Eq. (2.6)] are solved using a configuration interaction method in a basis of H_2^+ orbitals, whereas the non-resonant continuum electronic states, Eq. (2.7), are calculated using a multichannel L^2 close-coupling procedure [66, 67]. The basis set of H_2^+ orbitals are written as single center expansions using spherical harmonics for the angular part and B-spline basis functions for the radial part [68, 69]. The results presented in following sections have been obtained using angular momenta expansions up to $\ell = 16$, and up to 180 B-splines functions of order $k = 8$ in a box of size 60 a.u., which is large enough to avoid unphysical reflections. For the close-coupling procedure, angular momenta of the ejected electron are included up to $l_\alpha = 7$, for each α electronic state in the discretized continua associated to each ionization threshold of the H_2^+ molecule.

Once the electronic structure is obtained in a given grid of internuclear distances, we solve the one-dimensional Schrödinger equation to calculate the nuclear wave functions $\chi_{v_i}(R)$:

$$\left[\hat{T}(R) + \mathscr{E}_x(R)\right]\chi_{v_x}(R) = W_{x,v_x}\ \chi_{v_x}(R) \tag{2.8}$$

where x stands for a bound, resonant or continuum electronic state, and $\mathscr{E}_x$ is the corresponding potential energy curve previously obtained. For the results here presented, the basis for the nuclear wave functions had up to 300 B-splines defined in a box of size 12 a.u.

By projecting onto the basis of vibronic states, the TDSE defined in Eq. (2.1) is reduced to a system of coupled differential equations that can be solved using ordinary integration procedures. A sixth-order Runge-Kutta algorithm, implemented in PETSc libraries [70], is used for the integration.

Excitation and ionization amplitudes are extracted by projecting the propagated time-dependent wave packet into the excitation or ionization final states. Since the

wave packet is written in terms of the stationary states of the system, the expansion coefficients directly give the corresponding amplitudes, which allows for a straightforward analysis of the spectral components (total, energy- and angle-differential) in the wave packet. Therefore, for a given final energy $W_{\varepsilon_\alpha v_\alpha}$, and a given energy sharing for nuclei (E_{v_α}) and electrons (ε_α) such as $W_{\varepsilon_\alpha v_\alpha} = E_{v_\alpha} + \varepsilon_\alpha$, the ionization probability is:

$$\frac{d^2 P^{\ell_\alpha}(E_{v_\alpha}, \varepsilon_\alpha, T)}{dE_{v_\alpha} d\varepsilon_\alpha} = \left| C^{\ell_\alpha}_{\alpha \varepsilon_\alpha v_\alpha}(t = t_{max}) \right|^2, \tag{2.9}$$

where ℓ_α stands for the ℓ angular momentum contribution of the ejected electron in the α ionization threshold, and T is the pulse length. The upper time limit in the Runge-Kutta integration of the TDSE is t_{max}, and it should be chosen such $t_{max} > T$. It is important to note that the asymptotic limit is only reached when autoionization of significantly populated DES has occurred, which implies $t_{max} > T + \tau_{max}$, being τ_{max} the largest lifetime of those DES. This topic is further discussed and illustrated in Sect. 2.4.

The theoretical calculations presented in the next Sections are performed for linearly polarized light parallel to the molecular axis. According with dipole selection rules, the only relevant molecular states are those with total symmetry Σ_g^+ and Σ_u^+. The potential energy curves of those states are shown in Fig. 2.1 of Sect. 2.4.

2.4 Time-Resolved Imaging of H_2 Autoionization

Several molecular-dynamics processes involve DES. Autoionization receives particular attention because of its key role in electron scattering and photoionization. Given the complexity of accounting for all degrees of freedom to properly describe molecular autoionization, most experimental and theoretical studies on characterization, structure and mechanisms of molecular DES have used the simplest possible targets (H_2, D_2). DES are highly correlated electronic states (both electrons are simultaneously excited by absorption of one or more photons) and decay into the background continuum in a time scale comparable to that of nuclear motion. As it will be shown in the present work, through the evaluation of the competing dissociative and non-dissociative ionization channels, one can obtain relevant information on the role of the combined nuclear motion with electron correlation in the DES of the hydrogen molecule.

The potential energy curves for H_2 are shown in Fig. 2.1. In full thick lines, there appear the ground state of the neutral molecule ($X^1\Sigma_g^+$), the six lowest single ionization thresholds of H_2^+ ($1s\sigma_g$, $2p\sigma_u$, $2p\pi_u$, $2s\sigma_g$, $3p\sigma_u$ and $3d\sigma_g$), and the double ionization threshold (the $1/R$ potential curve corresponding to the full Coulomb break up of the system). The lowest singly excited states of $^1\Sigma_g^+$ and $^1\Sigma_u^+$ symmetries are also plotted. The DES of H_2 lie above its first ionization threshold. Each one of the higher ionization thresholds have associated series of DES (labeled as Q_n). In Fig. 2.1, there are only shown the first two series, Q_1 and Q_2, converging

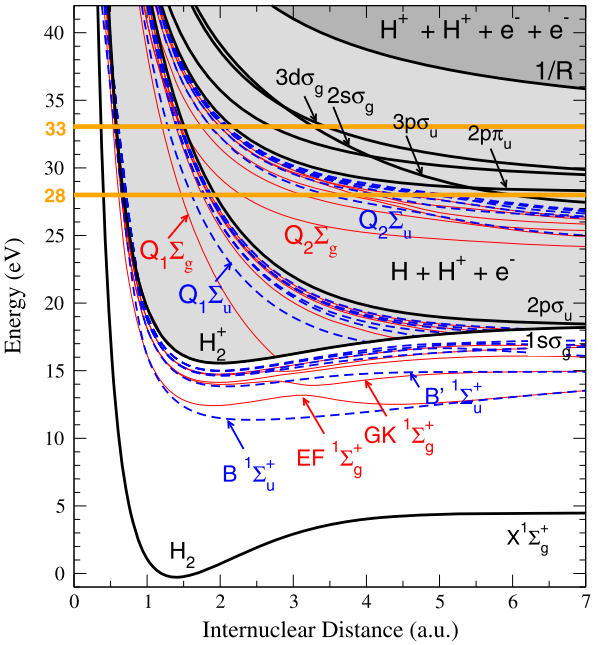

Fig. 2.1 Potential energy curves of H_2. The lowest $^1\Sigma_g^+$ and $^1\Sigma_u^+$ single excited states of the neutral are plotted and accordingly labeled. *Thick full lines* correspond to the ground state of H_2 ($X^1\Sigma_g^+$), the consecutive ionization thresholds (i.e., the six lowest H_2^+ electronic states) and the double ionization threshold ($1/R$) for the full break up of the molecule ($H^+ + H^+ + e^- + e^-$). *Shadowed areas* indicate the single and double electronic continua, respectively. Embedded in the single electronic continua the first two series of DES, Q_1 and Q_2, are represented. The two *horizontal thick lines* at 28 and 33 eV, indicate the photon energies used for the results presented in this section

into the $2p\sigma_u$ and $2p\pi_u$ thresholds respectively. As it is shown, the potential energy curves of the DES of H_2 are purely repulsive. After population of DES by single or multiphoton absorption, several channels associated to autoionization properties compete: DES can either dissociate into neutral atoms (H(nl)+H(nl′)) or ionic fragments ($H^+ + H^-$), or autoionize into the non-dissociative ($H_2^{**} \rightarrow H_2^+ + e^-$) and dissociative ($H_2^{**} \rightarrow H + H^+ + e^-$) electronic continua.

The first experimental evidence of the doubly excited states of H_2 appeared in the 1960's [71], detecting dissociation into neutral fragments after electron impact. However, only twenty years later, experimental measurements on photodissociation were available [24, 25, 28] and the first theoretical calculations of their potential energy curves were obtained [72]. In the 1990's, several theoretical works focused on the characterization of these states by obtaining energy positions, autoionization widths [45, 47, 48, 73] and photoionization cross sections [45, 47, 48, 74, 75]. Only very recently, combined experimental and theoretical works have shown the existence of different interference phenomena in the autoionization process involving both electrons and nuclei: in randomly oriented molecules subject to linearly po-

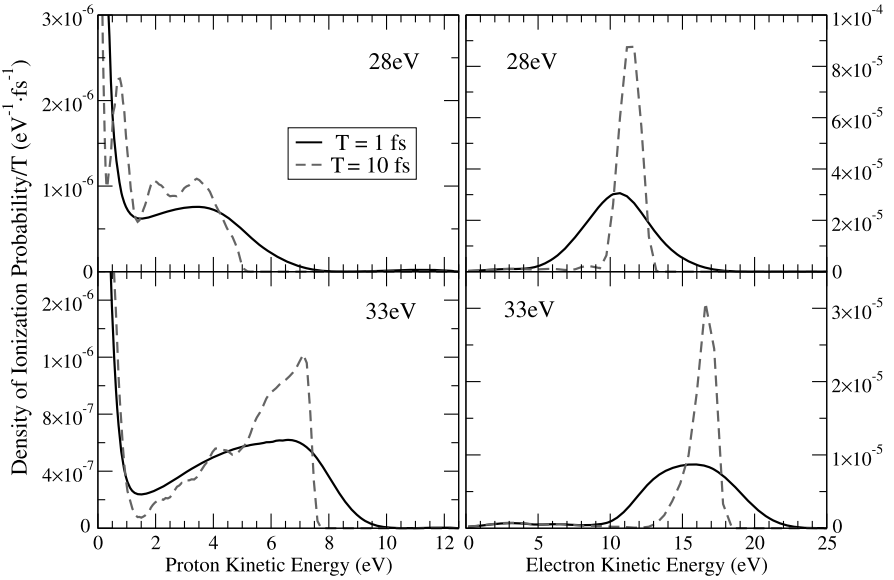

Fig. 2.2 Density of ionization probability as a function of proton (*left panels*) and electron (*right panels*) kinetic energy release. Results are plotted for two different pulse durations, 1 and 10 fs, and two central photon energies, 28 and 33 eV. The intensity is fixed at 10^{12} W/cm^2

larized light [23] or in aligned molecules irradiated with circularly polarized light leading to an unexpected circular dichroism in hydrogen molecules [22].

Despite the large amount of structural information on photoionization obtained by means of synchrotron radiation [20, 26, 31], characterization of these states with time-resolution requires the use of ultrashort UV/XUV pulsed radiation. In principle, pump-probe techniques using fs pulses can track the combined dynamics of molecular dissociation (nuclear motion lays in the range of tens of fs) and autoionization, which takes place in a few fs for the lowest series of DES in H_2. However, some important considerations on the time and energy domains are required. On the one hand, pulse durations shorter than those lifetimes should be used in order to subsequently trace the field free evolution of the molecular autoionization triggered after photoabsorption. On the other hand, the large energy bandwidths (few eV) of such short pulses usually imply more complicated detection techniques in order to obtain full coincidence detection of ejected fragments. This is illustrated in Fig. 2.2, which shows the ionization probabilities for two different pulse lengths, 1 fs ($< \tau_{max}$, the lifetime of the DES) and 10 fs ($> \tau_{max}$), plotted as a function of proton (left panels) and electron (right panels) kinetic energy release. As can be seen, the results present a strong dependence on the pulse duration for a given photon energy. Calculations have been performed considering a laser intensity of 10^{12} W/cm^2 for two central frequencies, 28 and 33 eV, indicated in Fig. 2.1. For 28 eV, direct photoionization and autoionization from the Q_1 series of DES, both into the first ionization threshold $1s\sigma_g$, are possible. For 33 eV, in addition to the former open

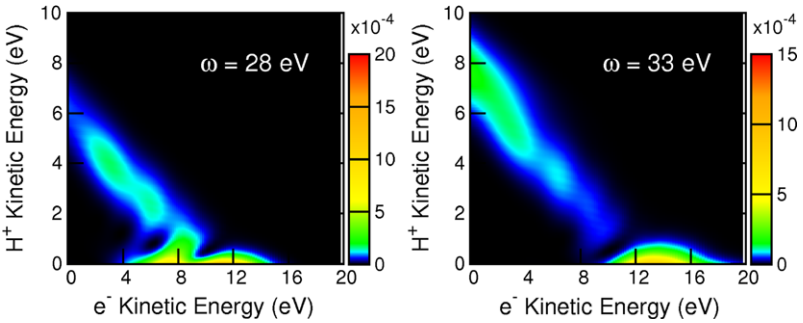

Fig. 2.3 Dissociative ionization probability as a function of proton and electron kinetic energy releases for a 1 fs pulse with a central energy of 28 eV (on the *left*) and 33 eV (on the *right*)

channels, there are also contributions from direct photoionization through the second ionization threshold ($2p\sigma_u$) and autoionization from the Q_2 series.

First, note that electron kinetic energy (EKE) distributions contain all dissociative and non-dissociative ionization channels, whereas, obviously, the proton kinetic energy (PKE) distributions only account for dissociative ionization. Nevertheless, since non-dissociative ionization is the major channel (98 %) in photoionization, it dominates in the smooth electron distributions, which reflect the energy bandwidth of the pulse. EKE distributions are centered at the expected values of excess electron energy given by the direct vertical transition from the ground state of the neutral. In contrast, PKE distributions show different structures varying with photon energy and pulse duration. As shown in Fig. 2.2, for 28 eV, the signature of autoionization of the Q_1 series appears at 2–8 eV of PKE. For a central photon energy of 33 eV, the peak at around 7 eV of PKE corresponds to the direct dissociative ionization associated to the $2p\sigma_u$ ionization threshold. The exponential decay of the probability at low proton energies correspond to direct photoionization and it equally manifests in the PKE distributions for any photon energy above the dissociative ionization potential of H_2 (18.15 eV) [45, 53]. The sharp features in the PKE distributions for a 10 fs pulse completely disappear for 1 fs, which is the consequence of the large spectral bandwidth of the pulse.

Figure 2.3 shows the dissociative ionization probabilities for a 1 fs pulse, centered at 28 eV and 33 eV respectively, as a function of both electron and proton kinetic energies. Here, it is clear that integration over electron energies with such a broad bandwidth leads to smooth PKE distributions when short pulses are used. For a 10 fs pulse (whose energy bandwidth is 0.6 eV), only narrow distributions centered at diagonal total energies of ~ 10 and ~ 15 eV appear [76], which therefore allow for the distinction of the autoionization structures after integration over electron energy. The pulse duration dependence of the PKE distributions thus partly contains information on the time scale for autoionization dynamics. For long enough pulses, the sharp signatures of autoionization appear and the PKE distribution is almost identical to that obtained with monochromatic light (i.e., in the continuous wave limit), which in the energy domain implies that $T > 1/\Gamma$, where Γ is an

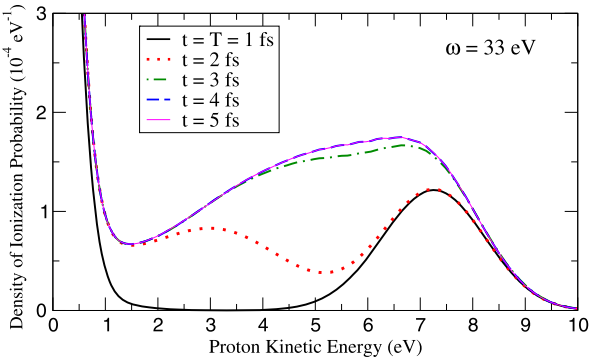

Fig. 2.4 Density of dissociative ionization probability as a function of the proton kinetic energy release for a 1 fs pulse with a central energy of 33 eV and $I = 10^{12}$ W/cm^2. Ionization probabilities has been integrated over all possible electron energies. Each *curve* corresponds to the ionization yield at different times, once the pulse is turned off

averaged autoionization width over the relevant internuclear distances. However, for pulses shorter than the average resonance lifetime ($T < 1/\Gamma$), structures are not well-defined and even disappear, therefore photoionization fragments should be measured in coincidence to obtain such information.

The previous conclusion is further visualized through a time-resolved imaging of the autoionization events. Figure 2.4 show the evolution of the PKE distributions after the interaction with a 1 fs pulse. The ionization probability increases with time in the region of intermediate PKE due to the delayed decay of the DES. The stationary limit is reached 3 fs after the end of the pulse, which is thus the lifetime of the DES that is being significantly populated (the first DES of $Q_1\,\Sigma_u$ series). Moreover, the time scales at which nuclei are moving in the DES potential energy curve are also reflected in the time tracing shown in figure 2.4. For $t = 2$ fs, autoionization leads to protons with around 3 eV. Such proton energy corresponds to an internuclear distance of ~ 1.8 a.u. in the first $Q_1\,\Sigma_u$ potential energy curve. At $t = 3$ fs, the probability has increased in the region of proton kinetic energies up to 6–7 eV, which indicates that autoionization occurs when the nuclei have moved at least 3 a.u. apart. The probability distributions at 4 and 5 fs are identical, i.e., 4 fs after the end of the pulse non appreciable autoionization takes place. These results suggest the possibility to trace molecular autoionization in time when it is launched with pulses of 3 fs duration or shorter.

State-of-the-art experimental techniques (pump-probe schemes or probe pulses through attosecond transient absorption) are currently capable of extracting such dynamical information. First experimental works using attosecond UV pump–femtosecond IR probe pulses have observed electron localization mediated by autoionization [37, 77]. Despite their success, in schemes using IR fields, unraveling contributions from different scattering channels is not an easy task. Indeed, DES of both Σ_u^+ and Σ_g^+ symmetries (the latter not optically allowed by direct photoionization) are being populated in the presence of the IR. Also, as it is usually the case, the ejected electron is driven by the IR field regardless of the state of the ion left behind. These effects may usually hide the intrinsic electron dynamics that is sought for. In this respect, the use of UV pump–UV probe schemes is an alternative that should allow one to disentangle the contributions from different ionization

channels more easily. Indeed, the short wavelength of UV/XUV pulses ensures that the dynamics of the nuclear wave packets that is being probed is entirely due to the unperturbed molecular potential [78]. These pump-probe schemes would also bring the possibility to explore the Σ_g^+ DES, as well as diverse phenomena related to transitions through singly excited states of the neutral. Such processes are discussed in the following section.

2.5 Control and Non-linear Effects in Multiphoton Single Ionization

Investigations on few-photon single ionization of hydrogen molecules are very scarce. Experimental studies are restricted to above threshold ionization processes [32, 79], and most theoretical studies, in the multiphoton regime, have made use of the fixed nuclei approximation (FNA) [40–42]. This approach is valid to quantitatively predict total few-photon ionization probabilities for photon energies below ~ 11 eV. For higher photon energies, the $(1+1)$-REMPI (resonant enhanced multiphoton ionization) channel in H_2 opens and FNA approaches underestimate ionization [51, 80]. In the region where two-photon ionization is the dominant process, the proper inclusion of the nuclear degrees of freedom in the theoretical description leads to a dramatic increase of the $(1+1)$-REMPI probability and its variation with photon energy is smoother with respect to that predicted within the FNA [see Fig. 2.5(a)]. More importantly, fully dimensional theoretical calculations have shown that, for a given range of photon energies, dissociative ionization may become the dominant process. This observation is unexpected because, in all reported studies on H_2 photoionization, dissociative ionization (DI) is always orders of magnitude smaller than non-dissociative ionization (NDI). Moreover, it indicates that by manipulating the radiation parameters one can actually control the ratio between different ionization channels. This will be discussed in the first part of this section. In the second subsection, we explore the different mechanisms that are triggered at high intensities and that allow for such control in the two-photon single ionization processes. Finally, in order to shed some more light on $(1+1)$-REMPI processes in molecules, results obtained for a pump-probe scheme with two identical UV pulses are shown in the third subsection. There, we discuss the observables that allows one to retrieve information and characterize the vibronic wave packets associated to singly excited states of the neutral.

2.5.1 Control of Single Ionization Channels by Means of VUV Pulses

The ratio between DI and NDI channels can be tailored by appropriately tuning the laser parameters. This is illustrated in Fig. 2.5, where DI, NDI and total ionization

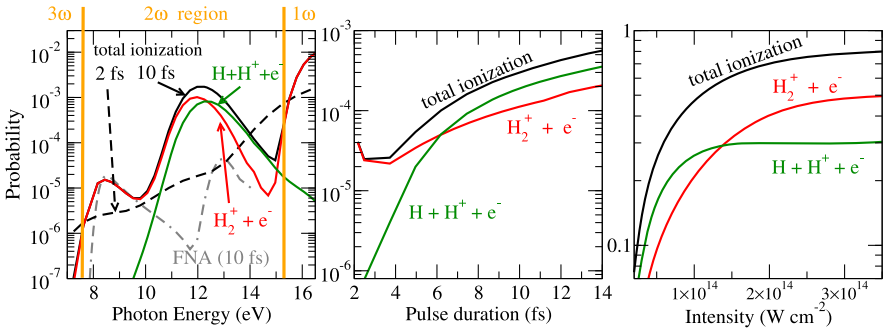

Fig. 2.5 DI, NDI and total ionization as a function of (**a**) photon energy, fixing $I = 10^{12}$ W/cm^2 and pulse durations indicated in the plot; (**b**) pulse duration, fixing $I = 10^{12}$ W/cm^2 and a photon energy of 13.3 eV; and (**c**) laser intensity, fixing the photon energy at 13.3 eV and a pulse duration of 10 fs

probabilities are shown as a function of (a) photon energy, (b) pulse duration and (c) laser intensity.

Single ionization probabilities (total, DI and NDI) as a function of photon energy are plotted [panel (a) in Fig. 2.5] for a pulse duration of 10 fs and $I = 10^{12}$ W/cm^2. For comparison, the total ionization probability obtained within the FNA at the equilibrium distance is shown for the same pulse parameters, as well as total ionization results for a 2 fs pulse and $I = 10^{12}$ W/cm^2. Around 15 eV, the one-photon single ionization threshold is reached, which manifests in a sudden increase of the total ionization probability. A significant enhancement of the total ionization probability is indeed expected at each N-photon ionization threshold. This behavior is also predicted within simple FNA treatments, as it is shown in the figure. However, besides the above mentioned underestimation of two-photon ionization in the FNA, when using pulses whose duration is of the order or shorter than the time scale of nuclear motion (i.e., below tens of fs), a proper description of the process requires to consider all degrees of freedom. Nuclear motion plays a key role when few fs pulses are used: the ionization probabilities present sharper profiles for long pulses ($T > 10$ fs, larger than the typical times for nuclear motion), while short pulses smooth the transitions between the regions where ionization by absorption of a different number of photons dominates [80, 81]. Larger energy bandwidths populate wider bands of vibrational states, effectively lowering the N-photon ionization thresholds. In particular, the unexpected prominence of DI in the photon energy region between 12.5 and 15.2 eV, shown in Fig. 2.5(a), can only be predicted by properly accounting for the nuclear motion. It is due to the favorable Franck-Condon overlaps among the potential energy curves involved in the $(1+1)$-REMPI, i.e. those between the ground state of the neutral molecule and the singly excited Σ_u^+ states, and those between these latter states and the vibronic states associated to the electronic continuum. It should be remarked that such vibrational selectivity is achieved for pulses with a relatively narrow bandwidth (of the order of the vibrational spacing; equivalently, for pulse durations of the order of the vibrational motion). This is illustrated in panel (b) of

Fig. 2.5 where the variation of DI and NDI probabilities are plotted as a function of the pulse duration for a fixed photon energy of 13.3 eV and a moderate intensity of 10^{12} W/cm^2. Both contributions vary monotonously with the pulse length, but the DI probability increases by more than two orders of magnitude when the pulse duration varies from 2 to 12 fs. Consequently, the ratio between DI and NDI can be controlled by varying the pulse duration.

The analogous behavior and control can be achieved by varying the laser intensity. It is illustrated in panel (c) of Fig. 2.5 for the same photon energy, 13.3 eV, and for a 10 fs pulse. For intensities below 10^{14} W/cm^2, DI becomes the major ionization channel. The increase of the field intensity is qualitatively equivalent to shortening the pulse duration. Increasing intensity, i.e. the amplitude of the field, ionization takes place progressively faster, making the effective pulse duration decrease. Thus, when using high intensities one loses the vibrational selectivity through the intermediate states that favors the DI channel. However, although an equivalent behavior is qualitatively achieved by tuning the pulse length or laser intensity, a very different mechanism is triggered for highly intense fields. This is further discussed in the next subsection.

2.5.2 *Non-linear Effects in (1 + 1)-REMPI*

An extensive effort has been devoted to explore the non-linear effects that arise with intense fields in the UV and XUV regions. Among them, the most well-known phenomenon is the emergence of Rabi-type oscillations between electronic states [82], which are actually responsible of the variation of the DI/NDI ratio with intensity. Rabi oscillations between atomic levels have been extensively treated in quantum mechanics textbooks [83]. The simplest picture is that of a coherent superposition of resonant quantum states in a two-level system under the influence of an external periodic field, which leads to an oscillation in the state population between the lower and the upper levels. Its frequency is given by the amplitude of the field (equivalently, the laser intensity I) and the dipole transition moment between the states (μ), such that $\Omega = \mu\sqrt{I}/\hbar$. In this context, a common description for this high-intensity regime is the Floquet picture. Within its frame, one could view the resonant states coupled by the field as "dressed" electronic states. A schematic representation of the intermediate single excited states of H_2 dressed by the field with an intensity of $2 \cdot 10^{14}$ W/cm^2 is shown in Fig. 2.6(a). One can see the characteristic Autler-Townes splitting of the states separated by an energy approximately equal to the Rabi frequency. This energy splitting induced in the intermediate states that are accessible by one-photon absorption is expected to leave its signature in the ionization signal after absorption of the second photon. In a reduced two-level picture, one would expect two well defined peaks in the electron energy differential ionization probabilities, as displayed in the scheme given in Fig. 2.6(a). In fact, simple two-level system models have been successfully applied to characterize Rabi oscillations occurring in molecular targets subject to pulses longer than the typical times for vibrational and rotational motions. These experiments used nanosecond (ns) pulses

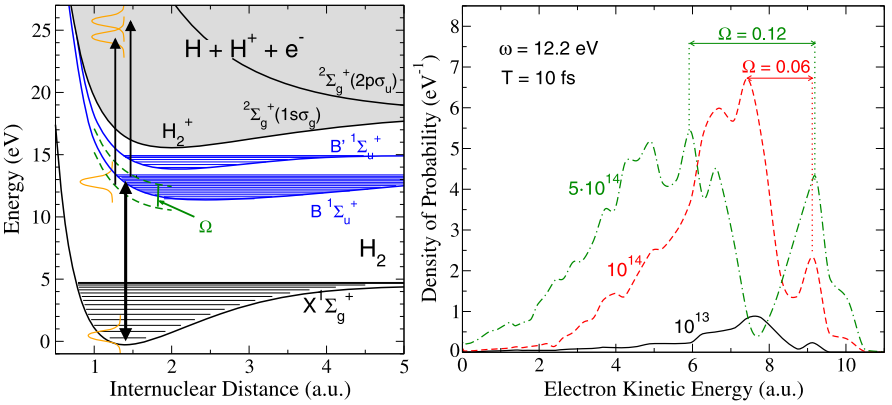

Fig. 2.6 (*Left*) Schematic representation of $(1+1)$ resonant two-photon ionization process. Rabi oscillations are pictured with a double *arrow*. The AT splitting of the first excited state, Ω, corresponds to a laser intensity of $2 \cdot 10^{14}$ W/cm^2. The pulse bandwidths are those of a 10 fs laser pulse. (*Right*) Single ionization probabilities as a function of electron energy for different laser intensities. Laser parameters are indicated

in two-color REMPI [84–86] and fluorescence pump-probe schemes [87–90]. Since ns pulses can energetically resolve individual rovibronic transitions, the process can be described by only accounting for the two significant levels. However, when short pulses are used, Rabi oscillations take place not between individual vibronic states, but between nuclear wave packets (NWPs) [44]. Therefore, the vibrational time scales, the pulse duration and laser intensity must be accordingly considered.

The first consequence of these oscillations proceeding through bands of vibronic states is the appearance of complicated patterns in the ionization signal. The AT effect is nevertheless visible in the electron energy differential ionization probabilities, which are plotted for different laser intensities in Fig. 2.6(b). Despite the complex profiles arising from the vibrational structure, they still show two differentiated peaks which are the signature of $(1+1)$-REMPI taking place through dressed single electronic excited states of the neutral. Although the energy splitting actually depends on the internuclear distance (since the electronic dipole moment does), one can approximate its value by using the transition moment value at the equilibrium internuclear distance of the neutral [$\Omega = \mu(R = 1.4\ \text{a.u.})\sqrt{I}/\hbar$]. The estimated values are in very good agreement with those extracted from the full calculation: for intensities of 10^{14} and $5 \cdot 10^{14}$ W/cm^2 the predicted values are 1.4 and 3.3 eV, respectively, and the electron spectra show splittings around 1.6 and 3.3 eV. The AT effect is not appreciable for an intensity of 10^{13} W/cm^2, whose estimated Rabi frequency is $\Omega \simeq 0.43$ eV. This is directly related to the pulse length: the spectral width of a 10 fs pulse is ~ 0.6 eV, which cannot then resolve an energy splitting of 0.43 eV. Or equivalently speaking in the time domain, 10 fs is too short to accommodate a complete Rabi oscillation for such intensity. In brief, the condition $T > 1/\Omega$ is necessary to observe the AT effect.

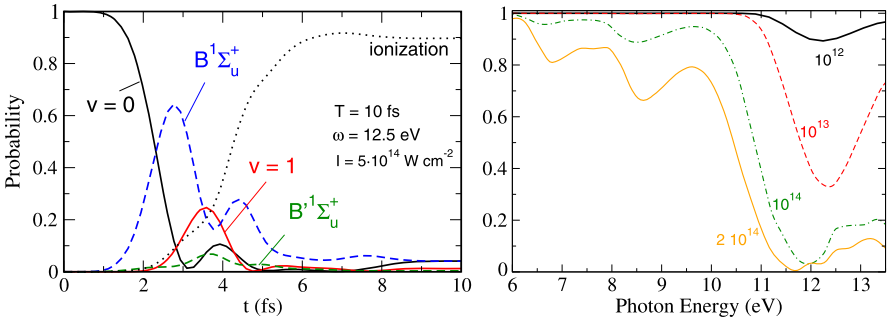

Fig. 2.7 (*Left*) Probability of finding H_2 in the $B^1\Sigma_u^+$ and $B'^1\Sigma_u^+$ excited states (all v), in the lowest vibrational states $v = 0$ and $v = 1$ of the ground state of the neutral, and total ionization probability as functions of time. Results are obtained for a photon energy of 12.5 eV, a laser intensity of $5 \cdot 10^{14}$ W/cm^2 and a pulse duration of 10 fs. Note that probabilities are only obtained for t satisfying $A(t) = 0$. (*Right*) Probability left in the ground state as a function of the photon energy for different laser intensities and a pulse duration of 10 fs

The structures in Fig. 2.6, signature of the oscillation between NWPs generated by the large bandwidth of short pulses, already prove that the picture of an isolated two-level system is no longer valid for molecular targets. The presence of nuclear motion leads to new mechanisms, inexistent in atomic targets. In fact, two-photon single ionization proceeds through a step-ladder mechanism: after each Rabi oscillation the ground state is repopulated in higher vibrational levels, therefore reaching higher and higher vibronic levels of singly excited states. As a consequence, higher vibronic final states are accessible after each oscillation, so that NDI leaves the ion in larger quantum vibrational levels and DI ejects protons (and electrons) at higher energies. This step-ladder mechanism is very apparent when the probabilities of the different vibronic states are tracked with time. In Fig. 2.7(a), the population of the lowest vibronic states of the H_2 molecule ($v = 0$ and $v = 1$ of the ground state), the excitation probability for the two first singly excited electronic states $B^1\Sigma_u^+$ and $B'^1\Sigma_u^+$ (summed over their vibrational states) and the total ionization probability are plotted as functions of time. In the first half of the first Rabi oscillation, a manifold of $B^1\Sigma_u^+$ vibrational states is populated. In the second half of the oscillation, the population goes back to the ground electronic state. As long as the pulse bandwidth is larger than the energy spacing between vibronic states ($T > 1/\Delta E_v$), not only the $v = 0$ level is populated, but also the $v > 0$ vibrational states. Thus, we observe that after the maximum probability for the $B^1\Sigma_u^+$, the $v = 1$ level starts to be populated for the first time. Then, in the first half of the second oscillation, the photon can be absorbed from the excited vibrational levels ($v > 0$) of the ground electronic state and, as a consequence, higher singly excited electronic states are reached. This is captured in the $B'^1\Sigma_u^+$ population that comes to a maximum value in this second oscillation. Consequently, the step-ladder mechanism gives access to intermediate electronic states that are hardly populated and even not accessible by direct single photon absorption. The oscillations are also reflected in the ionization probability (dotted line in Fig. 2.7(a)). Once the first Rabi oscillation is completed, the popu-

lation of the intermediate states is depleted, and, consequently, the $(1+1)$-REMPI probability exhibits a relative minimum around 3.5 fs. After 4 fs, two-photon ionization becomes the dominant process over one-photon excitation.

Furthermore, the ground state is completely depleted for the laser parameters here considered, so the ionization saturates. The population of the ground state is shown for various laser intensities and as a function of photon energy in Fig. 2.7(b). For the higher intensities, the ground state is completely depopulated in the $(1+1)$-REMPI energy region. Besides, the higher the intensity, the larger the shift of the absolute minimum to lower photon energies, which would be expected from the AT effect. As the energy splitting becomes larger (the higher the intensity, the larger Ω), the $(1+1)$-REMPI becomes accessible at lower photon energies. The other minima in the population of the ground state correspond to $(2+1)$-REMPI. At those photon energies, ~ 6 and ~ 7.5 eV, extremely high laser intensities would be required to saturate ionization. The reason lies in the character of the electronic states involved, the singly excited states of Σ_g^+ symmetry. They present double-well potential energy curves that diminish the efficiency of the transitions among their vibronic states.

At this point we have the time scales at which these phenomena are restricted. Two conditions must be fulfilled to observe the step-ladder mechanism: (i) $T > 1/\Omega$, i.e. the pulse is long enough to accommodate a complete Rabi oscillation, which is determined by the laser intensity, and (ii) $T < 1/\Delta E_v$, i.e. the pulse is short enough to populate manifolds of vibrational states. The step-ladder mechanism, which allows for higher protons to be ejected, is thus observed if the pulse duration lies between those limits ($1/\Omega < T < 1/\Delta E_v$), i.e., the electronic structure (dipole moment) and the field intensity set the lower limit, while the vibronic structure, i.e. the nuclear motion, imposes the upper one. In the H_2 molecule, the vibrational energy spacing fixes an effective upper limit of ~ 15 fs. And, for instance, the use of intensities around 10^{14} W/cm^2 impose pulse lengths above 5 fs in order to observe step-ladder Rabi oscillations in H_2 [80]. It should be noticed that, in contrast with the step-ladder mechanism, the AT effect will be observed as long as the fist condition, $T > 1/\Omega$, is satisfied. In conclusion, the manipulation of laser intensities in a range of values 10^{12}–10^{15} W/cm^2 with UV and XUV sources in the fs time scale allows for the control of ionization channels, either by modifying the relative importance of non-dissociative (NDI) or dissociative (DI) ionization processes or by suppressing and/or favoring the emission of faster electrons.

It is clear that a complete characterization of vibronic wave packets involving the intermediate singly excited states is mandatory to elucidate and design new strategies to control the above explained mechanisms. To explore the dynamics of these states, the most straightforward and experimentally affordable technique is the use of pump-probe schemes with two identical pulses. In the next section, we will use the same central frequencies employed through this work with (i) photon energies around 12 eV, where $(1+1)$-REMPI probability reaches its maximum, (ii) short pulses, to create vibronic wave packets containing an appreciable number of vibrational states, and (iii) low intensities, to avoid non-linear effects that, in principle, complicate the patterns in the probing of vibronic wave packets involving the singly

excited states. We will also explore which observables actually contain significant information to unravel the dynamics of these states.

2.5.3 Probing Nuclear Wave Packets in Molecular Excited States

The present pump-probe set-up with two identical pulses is outlined in Fig. 2.8(a). A pump pulse excites the molecular target, creating a NWP in the $B^1\Sigma_u^+$ state that field-free evolves in time until a second photon is absorbed, thus mapping it into the ionization channels.

As in the previous sections, we have chosen a photon energy of 12.2 eV, which is in resonance with the $B^1\Sigma_u^+$ electronic state in a direct vertical transition from the ground state, such that the $(1+1)$-REMPI process dominates. We use a laser intensity of 10^{12} W/cm^2, which is low enough to avoid field-induced distortion of the molecular potential, and a 2 fs pulse duration, whose broad bandwidth ensures the creation of an energetically wide vibrational wave packet. Similar experimental set-ups have been already used with XFEL sources and applied to probe the NWP dynamics launched in molecular ions by detecting the fragments after the Coulomb explosion (CE) of H_2 and D_2 [33, 34]. In principle, exploring singly excited states has the added complication of disentangling several single ionization channels (DI and NDI associated to several ionization thresholds). Also, an easy mapping into the final energy-differential observables is not trivial, in contrast with standard CE experiments in [33]. However, as we will show below, it is still possible to distinguish those channels by looking at angular-differential quantities. Indeed, by measuring the molecular frame induced asymmetries in the electron ejection in $(1+1)$-REMPI it is possible to clock the evolution of the pumped NWPs. In a delayed two-photon absorption one could expected a symmetry breaking of the ejected electrons with respect to the molecular frame as that observed in experiments on photoionization mediated through autoionization [21, 36, 37, 91, 92]. The up-down (or left-right) asymmetry of electron ejection in molecules that dissociatively ionize is a well-known process [17, 93] that arises from the superposition of two states with different parity. Such superposition is achieved in those experiments through the time-delay decay of DES. Analogously, it can be generated by a time-delayed two-photon ionization involving the single excited states of the neutral.

As schematically represented in Fig. 2.8, the pump pulse creates a NWP in the $B^1\Sigma_u^+$ single excited state. In this potential energy curve, whose oscillating period is around 25–30 fs [76], the molecule stretches. Consequently, the NWP in the $B^1\Sigma_u^+$ state travels to larger internuclear distances, such that when the probe pulse is absorbed the ionization potential to reach the second threshold ($2p\sigma_u$ state in H_2^+) is lower. Because of the purely dissociative character of the $2p\sigma_u$ ionization threshold, a direct mapping of the NWP appears in this channel, which is unfortunately obscured by the larger contribution of the first ionization threshold $1s\sigma_g$ to the DI. This is shown in Fig. 2.9(a), where the PKE distribution is plotted at different time delays. Since the $1s\sigma_g$ contribution is appreciable larger, only a subtle signature of

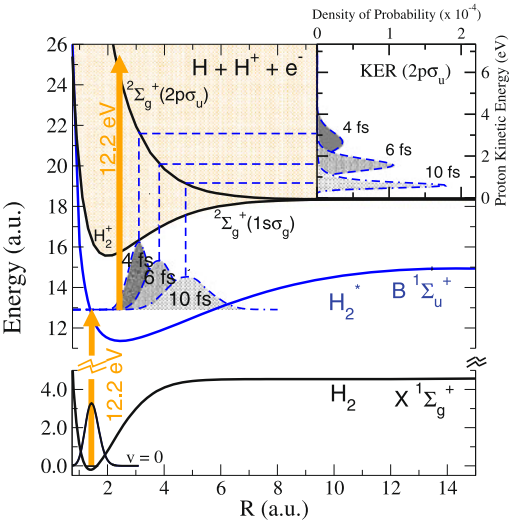

Fig. 2.8 Relevant potential energy curves for H_2 and the H_2^+ ion. Pump and probe pulses (with central frequency of 12.2 eV) are indicated with *arrows*. Calculated squared amplitudes of the NWP generated by the pump pulse after 4, 6 and 10 fs are shown as functions of the internuclear distance. *Dashed lines* indicate (i) the vertical transition from their maximum to the second ionization threshold ($2p\sigma_u$) and (ii) the expected energies in the continua connected to the actual probed kinetic energy releases shown in the *inset* for that threshold

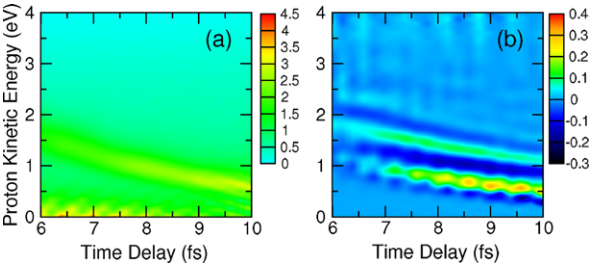

Fig. 2.9 (**a**) Dissociative single ionization probability ($\times 10^{-4}$) and (**b**) asymmetry parameter as a function of time-delay (x-axis) and proton kinetic energy (y-axis)

the $2p\sigma_u$ one, which leads to protons of lower energy as the time delay increases, is obtained in the PKE distributions. Nevertheless, the proton-electron ejection from the $2p\sigma_u$ interferes with the $1s\sigma_g$ channel for the same energy in the continuum. This superposition leads to a significant molecular frame asymmetry in the electron ejection, which indirectly uncovers the mapping of the NWP position in the $2p\sigma_u$ DI contribution. A clear image of the time evolution of the NWP pumped in the excited state of the neutral molecule is shown in the asymmetry parameter plot in Fig. 2.9(b). The asymmetry parameter is simply obtained as

$$A = (N_{up} - N_{down})/(N_{up} + N_{down}) \tag{2.10}$$

where "up" and "down" indicate the ejection of the electron respect to the proton ejection. The position of the wave packet is perfectly clocked in the asymmetry parameter as a function of the proton KER and the time delay. This is an interesting application to be tested in other molecules. It is particularly relevant because the NWP evolution is often obscured in the KER spectra due to the contribution of several ionization channels, the presence of complex structures (resulting from inter-

ferences between energy-degenerate paths) or the broad bandwidth of the ultrashort pulses.

2.6 Future Perspectives

A large diversity of photoionization problems has been explored, both theoretically and experimentally, using as prototypical molecules H_2 and D_2. As it has been widely discussed in Sects. 2.2 and 2.3, the last decade has undergone a sprout of studies on processes induced by ultrafast pulsed radiation, prompted by the new XFEL facilities and rapid developments of HHG techniques. These sources nowadays allow to explore fundamental problems in atomic and molecular physics at their intrinsic electronic and nuclear time scales. For instance, a substantial number of works have employed pump-probe set-ups, with pulses as short as a few hundreds of as, to generate time-resolved images of electronic and nuclear wave packets. However, further theoretical and experimental efforts are required to prove the ability of these technologies to not only trace, but drive and steer the electron and nuclear dynamics in atoms, molecules and, eventually, in larger systems.

This goal can only be reached through a deep knowledge of the underlying physics in the laser-induced phenomena, which makes the hydrogen molecules, i.e. the smallest multielectron molecular targets, the perfect candidates. As we have seen, autoionization studies, in which doubly excited states are populated by absorption of one or two photons, have already shed some light on the role of electron correlation combined with the nuclear motion. Moreover, existent robust theoretical methods, with demonstrated capability to predict laser-induced phenomena in hydrogen molecules, have recently given strong support for experimental measurements that have only become available with the new radiation sources. Example of those are XUV pump–IR probe experiments that have been able to achieve electron localization in H_2 and D_2 [37, 38], and XUV pump–XUV probe schemes that map nuclear wave packets created in H_2^+ into the full break up channels [33, 34]. The use of these targets as benchmarks for novel experimental set-ups require constant theoretical input. Theoretical simulations are also valuable to predict novel phenomena that may arise in laser-molecule interactions [51, 52] and to explore problems as coherent control in multiphoton ionization [94]. However, despite the flexibility and wide applicability of the methods described in this chapter, many interesting problems, even for simple molecules, still need the development of new theoretical tools. This is the case of studies on one- and few-photon double ionization processes, in which both electrons are simultaneously ejected by direct photoabsorption, or sequential absorption processes. These investigations will bring a better understanding of electron correlation effects and are encouraged by the above mentioned XUV pump–XUV probe experiments [33, 34]. In this context, theoretical and computational efforts are being currently devoted to tackled double ionization problems in hydrogen molecules. Such methodologies are also expected to be useful to explore non-linear effects induced by strong IR fields. Accurate descriptions for these problems are still scarce and will be the subject of further work in the near future.

Acknowledgements This work was accomplished with an allocation of computer time from Mare Nostrum BSC and CCC-UAM, and was partially supported by the MICINN projects FIS2010-15127, ACI2008-0777 and CSD 2007-00010, the ERA-Chemistry project PIM2010EEC-00751, the European grants MC-ITN CORINF and MC-RG ATTOTREND, the European COST Action CM0702, and the XCHEM Advanced Grant 290853 of the European Research Council. AP and PR acknowledge a Juan de la Cierva post-doctoral Contract from MICINN.

References

1. J. Seres, E. Seres, A.J. Verhoef, G. Tempea, C. Streli, P. Wobrauschek, V. Yakovlev, A. Scrinzi, C. Spielmann, F. Krausz, Nature **433**, 596 (2005)
2. A.H. Zewail, Annu. Rev. Phys. Chem. **57**(1), 65–103 (2006)
3. S. Lunnemann, A.I. Kuleff, L.S. Cederbaum, J. Chem. Phys. **129**(10), 104305 (2008)
4. A.H. Zewail, J. Phys. Chem. A **104**(24), 5660–5694 (2000)
5. J. Ullrich, R. Moshammer, A. Dorn, R. Dörner, L.P.H. Schmidt, H. Schmidt-Böcking, Rep. Prog. Phys. **66**(9), 1463–1545 (2003)
6. C. Bostedt, H.N. Chapman, J.T. Costello, J.R. Crespo López-Urrutia, S. Düsterer, S.W. Epp, J. Feldhaus, A. Föhlisch, M. Meyer, T. Möller, Nucl. Instrum. Methods Phys. Res., Sect. A, Accel. Spectrom. Detect. Assoc. Equip. **601**(1–2), 108–122 (2009)
7. A. Barty, J. Phys. B, At. Mol. Opt. Phys. **43**(19), 194014 (2010)
8. J.U.H. Chapman, J.M. Rost, J. Phys. B, At. Mol. Opt. Phys. **43**(19), 190201 (2010)
9. M. Drescher, M. Hentschel, R. Kienberger, G. Tempea, C. Spielmann, G.A. Reider, P.B. Corkum, F. Krausz, Science **291**(5510), 1923–1927 (2001)
10. M. Hentschel, R. Kienberger, C. Spielmann, G.A. Reider, N. Milosevic, T. Brabec, P. Corkum, U. Heinzmann, M. Drescher, F. Krausz, Nature **414**, 509–513 (2001)
11. P. Salières, M. Lewenstein, Meas. Sci. Technol. **12**, 1818 (2001)
12. G. Sansone, E. Benedetti, F. Calegari, C. Vozzi, L. Avaldi, R. Flammini, L. Poletto, P. Villoresi, C. Altucci, R. Velotta, S. Stagira, S. De Silvestri, M. Nisoli, Science **314**(5798), 443–446 (2006)
13. A. Scrinzi, M.Y. Ivanov, R. Kienberger, D.M. Villeneuve, J. Phys. B, At. Mol. Opt. Phys. **39**(1), 1 (2006)
14. E. Goulielmakis, V.S. Yakovlev, A.L. Cavalieri, M. Uiberacker, V. Pervak, A. Apolonski, R. Kienberger, U. Kleineberg, F. Krausz, Science **317**(5839), 769–775 (2007)
15. M.F. Kling, M.J.J. Vrakking, Annu. Rev. Phys. Chem. **59**(1), 463–492 (2008)
16. F. Krausz, M. Ivanov, Rev. Mod. Phys. **81**, 163–234 (2009)
17. B. Sheehy, B. Walker, L.F. DiMauro, Phys. Rev. Lett. **74**(24), 4799–4802 (1995)
18. J.H. Posthumus, Rep. Prog. Phys. **67**(5), 623 (2004)
19. C.R. Calvert, W.A. Bryan, W.R. Newell, I.D. Williams, Phys. Rep. **491**(1), 1–28 (2010)
20. A. Lafosse, M. Lebech, J.C. Brenot, P.M. Guyon, L. Spielberger, O. Jagutzki, J.C. Houver, D. Dowek, J. Phys. B, At. Mol. Opt. Phys. **36**(23), 4683 (2003)
21. F. Martín, J. Fernández, T. Havermeier, L. Foucar, T. Weber, K. Kreidi, M. Schöffler, L. Schmidt, T. Jahnke, O. Jagutzki, A. Czasch, E.P. Benis, T. Osipov, A.L. Landers, A. Belkacem, M.H. Prior, H. Schmidt-Böcking, C.L. Cocke, R. Dörner, Science **315**(5812), 629–633 (2007)
22. D. Dowek, J.F. Pérez-Torres, Y.J. Picard, P. Billaud, C. Elkharrat, J.C. Houver, J.L. Sanz-Vicario, F. Martín, Phys. Rev. Lett. **104**(23), 2–5 (2010)
23. T. Reddish, A. Padmanabhan, M. MacDonald, L. Zuin, J. Fernández, A. Palacios, F. Martín, Phys. Rev. Lett. **108**(2), 1–5 (2012)
24. M. Glass-Maujean, J. Chem. Phys. **85**, 4830–4834 (1986)
25. M. Glass-Maujean, J. Chem. Phys. **89**, 2839 (1988)
26. M. Glass-Maujean, H. Schmoranzer, J. Phys. B, At. Mol. Opt. Phys. **38**(8), 1093–1105 (2005)

27. E.M. García, J.A. Ruiz, S. Menmuir, E. Rachlew, P. Erman, A. Kivimäki, M. Glass-Maujean, R. Richter, M. Coreno, J. Phys. B, At. Mol. Opt. Phys. **39**(2), 205 (2006)
28. S. Arai, T. Kamosaki, M. Ukai, K. Shinsaka, Y. Hatano, Y. Ito, H. Koizumi, A. Yagishita, K. Ito, K. Tanaka, J. Chem. Phys. **88**, 3016 (1988)
29. T. Odagiri, M. Murata, M. Kato, N. Kouchi, J. Phys. B, At. Mol. Opt. Phys. **37**(19), 3909 (2004)
30. J.D. Bozek, J.E. Furst, T.J. Gay, H. Gould, A.L.D. Kilcoyne, J.R. Machacek, F. Martín, K.W. McLaughlin, J.L. Sanz-Vicario, J. Phys. B, At. Mol. Opt. Phys. **39**(23), 4871 (2006)
31. J.R. Machacek, V.M. Andrianarijaona, J.E. Furst, A.L.D. Kilcoyne, A.L. Landers, E.T. Litaker, K.W. McLaughlin, T.J. Gay, J. Phys. B, At. Mol. Opt. Phys. **44**(4), 045201 (2011)
32. K. Hoshina, A. Hishikawa, K. Kato, T. Sako, K. Yamanouchi, E.J. Takahashi, Y. Nabekawa, K. Midorikawa, J. Phys. B, At. Mol. Opt. Phys. **39**(4), 813–829 (2006)
33. Y.H. Jiang, A. Rudenko, J.F. Pérez-Torres, O. Herrwerth, L. Foucar, M. Kurka, K.U. Kühnel, M. Toppin, E. Plésiat, F. Morales, F. Martín, M. Lezius, M.F. Kling, T. Jahnke, R. Dörner, J.L. Sanz-Vicario, J. van Tilborg, A. Belkacem, M. Schulz, K. Ueda, T.J.M. Zouros, S. Düsterer, R. Treusch, C.D. Schröter, R. Moshammer, J. Ullrich, Phys. Rev. A **81**(5), 1–4 (2010)
34. Y.H. Jiang, A. Rudenko, E. Plésiat, L. Foucar, M. Kurka, K.U. Kühnel, T. Ergler, J.F. Pérez-Torres, F. Martín, O. Herrwerth, M. Lezius, M.F. Kling, J. Titze, T. Jahnke, R. Dörner, J.L. Sanz-Vicario, M. Schöffler, J. van Tilborg, A. Belkacem, K. Ueda, T.J.M. Zouros, S. Düsterer, R. Treusch, C.D. Schröter, R. Moshammer, J. Ullrich, Phys. Rev. A **81**(2), 1–4 (2010)
35. P.M. Paul, E.S. Toma, P. Breger, G. Mullot, F. Augé, P. Balcou, H.G. Muller, P. Agostini, Science **292**(5522), 1689–1692 (2001)
36. K.P. Singh, F. He, P. Ranitovic, W. Cao, S. De, D. Ray, S. Chen, U. Thumm, A. Becker, M.M. Murnane, H.C. Kapteyn, I.V. Litvinyuk, C.L. Cocke, Phys. Rev. Lett. **104**(2), 1–4 (2010)
37. G. Sansone, F. Kelkensberg, J.F. Pérez-Torres, F. Morales, M.F. Kling, W. Siu, O. Ghafur, P. Johnsson, M. Swoboda, E. Benedetti, F. Ferrari, F. Lépine, J.L. Sanz-Vicario, S. Zherebtsov, I. Znakovskaya, A. L'Huillier, M.Y. Ivanov, M. Nisoli, F. Martín, M.J.J. Vrakking, Nature **465**(7299), 763–766 (2010)
38. F. Kelkensberg, W. Siu, J.F. Pérez-Torres, F. Morales, G. Gademann, A. Rouzée, P. Johnsson, M. Lucchini, F. Calegari, J.L. Sanz-Vicario, F. Martín, M.J.J. Vrakking, Phys. Rev. Lett. **107**, 043002 (2011)
39. C.H. Greene, B. Yoo, J. Phys. Chem. **99**(6), 1711–1718 (1995)
40. J. Colgan, D. Glass, K. Higgins, P. Burke, J. Phys. B, At. Mol. Opt. Phys. **34**, 2089 (2001)
41. A. Apalategui, A. Saenz, J. Phys. B, At. Mol. Opt. Phys. **35**, 1909 (2002)
42. A. Awasthi, Y.V. Vanne, A. Saenz, J. Phys. B, At. Mol. Opt. Phys. **38**, 3973 (2005)
43. C. Meier, V. Engel, Phys. Rev. Lett. **73**, 3207–3210 (1994)
44. Z. Sun, N. Lou, Phys. Rev. Lett. **91**, 023002 (2003)
45. I. Sánchez, F. Martín, J. Chem. Phys. **106**(18), 7720 (1997)
46. I. Sánchez, F. Martín, Phys. Rev. Lett. **79**, 1654–1657 (1997)
47. I. Sánchez, F. Martín, Phys. Rev. A **57**(2), 1006–1017 (1998)
48. I. Sánchez, F. Martín, J. Chem. Phys. **110**, 6702–6713 (1999)
49. H. Feshbach, Ann. Phys. **19**, 287–313 (1962)
50. T. Brabec, F. Krausz, Rev. Mod. Phys. **72**, 545–591 (2000)
51. A. Palacios, H. Bachau, F. Martín, Phys. Rev. Lett. **96**(14), 143001 (2006)
52. A. Palacios, H. Bachau, F. Martin, Phys. Rev. A **74**(3), 1–4 (2006)
53. J. Sanz-Vicario, H. Bachau, F. Martín, Phys. Rev. A **73**(3), 1–12 (2006)
54. J. Sanzvicario, A. Palacios, J. Cardona, H. Bachau, F. Martín, J. Electron Spectrosc. Relat. Phenom. **161**(1–3), 182–187 (2007)
55. A.S. Kheifets, Phys. Rev. A **71**, 022704 (2005)
56. A.S. Kheifets, I. Bray, Phys. Rev. A **72**, 022703 (2005)
57. J. Colgan, M.S. Pindzola, F. Robicheaux, Phys. Rev. Lett. **98**, 153001 (2007)
58. T.-G. Lee, M.S. Pindzola, F. Robicheaux, J. Phys. B, At. Mol. Opt. Phys. **43**(16), 165601 (2010)

59. W. Vanroose, F. Martín, T.N. Rescigno, C.W. McCurdy, Science **310**(5755), 1787–1789 (2005)
60. L. Tao, C.W. McCurdy, T.N. Rescigno, Phys. Rev. A **82**, 023423 (2010)
61. X. Guan, K. Bartschat, B.I. Schneider, Phys. Rev. A **83**, 043403 (2011)
62. W. Vanroose, D. Horner, F. Martín, T. Rescigno, C. McCurdy, Phys. Rev. A **74**(5), 1–19 (2006)
63. J. Colgan, M.S. Pindzola, F. Robicheaux, J. Phys. B, At. Mol. Opt. Phys. **41**(12), 121002 (2008)
64. F. Morales, F. Martín, D.A. Horner, T.N. Rescigno, C.W. McCurdy, J. Phys. B, At. Mol. Opt. Phys. **42**(13), 134013 (2009)
65. X. Guan, K. Bartschat, B.I. Schneider, Phys. Rev. A **82**, 041404 (2010)
66. F. Martín, J. Phys. B, At. Mol. Opt. Phys. **32**(16), 197 (1999)
67. M. Cortés, F. Martín, J. Phys. B, At. Mol. Opt. Phys. **27**(23), 5741 (1994)
68. H. Bachau, E. Cormier, P. Decleva, J.E. Hansen, F. Martín, Rep. Prog. Phys. **64**(12), 1815 (2001)
69. A. Palacios, H. Bachau, F. Martín, J. Phys. B, At. Mol. Opt. Phys. **38**(6), 99 (2005)
70. S. Balay, J. Brown, K. Buschelman, W.D. Gropp, D. Kaushik, M.G. Knepley, L.C. McInnes, B.F. Smith, H. Zhang, PETSc web page (2011). http://www.mcs.anl.gov/petsc
71. M. Leventhal, R. Robiscoe, K. Lea, Phys. Rev. **158**(1), 49–56 (1967)
72. S.L. Guberman, J. Chem. Phys. **78**, 1404–1413 (1983)
73. L. Siebbeles, C.L. Sech, J. Phys. B, At. Mol. Opt. Phys. **27**(19), 4443 (1994)
74. I. Borges Jr, C.E. Bielschowsky, J. Phys. B, At. Mol. Opt. Phys. **33**(9), 1713 (2000)
75. I. Borges Jr., C.E. Bielschowsky, Chem. Phys. Lett. **342**, 411–416 (2001)
76. A. González-Castrillo, J.F. Pérez-Torres, A. Palacios, F. Martín, Theor. Chem. Acc. **128**(4–6), 735–742 (2010)
77. G. Sansone, F. Kelkensberg, F. Morales, J.F. Pérez-Torres, F. Martín, M.J.J. Vrakking, IEEE J. Sel. Top. Quantum Electron. **18**, 520 (2012)
78. L.A.A. Nikolopoulos, P. Lambropoulos, J. Phys. B **39**, 883–893 (2006)
79. Y. Furukawa, Y. Nabekawa, T. Okino, S. Saugout, K. Yamanouchi, K. Midorikawa, Phys. Rev. A **82**(1), 1–5 (2010)
80. A. Palacios, H. Bachau, F. Martín, Phys. Rev. A **75**(1) (2007)
81. J.F. Pérez-Torres, J.L. Sanz-Vicario, H. Bachau, F. Martín, J. Phys. B, At. Mol. Opt. Phys. **43**(1), 015204 (2010)
82. I.I. Rabi, Phys. Rev. **51**, 652 (1937)
83. L. Allen, J.H. Eberly, *Optical Resonances and Two-Level Atoms* (Wiley, New York, 1975)
84. M.A. Quesada, A.M.F. Lau, D.H. Parker, D.W. Chandler, Phys. Rev. A **36**, 4107–4110 (1987)
85. B. Girard, G.O. Sitz, R.N. Zare, N. Billy, J. Vigué, J. Chem. Phys. **97**, 26 (1992)
86. S. Xu, G. Sha, B. Jiang, W. Sun, X. Chen, C. Zhang, Chem. Phys. **100**, 6122 (1994)
87. J. Qi, G. Lazarov, X. Wang, L. Li, L.M. Narducci, A.M. Lyyra, F.C. Spano, Phys. Rev. Lett. **83**, 288–291 (1999)
88. J. Qi, F.C. Spano, T. Kirova, A. Lazoudis, J. Magnes, L. Li, L.M. Narducci, R.W. Field, A.M. Lyyra, Phys. Rev. Lett. **88**, 173003 (2002)
89. S. Ghosh, J.E. Sharping, D.G. Ouzounov, A.L. Gaeta, Phys. Rev. Lett. **94**, 093902 (2005)
90. E. Ahmed, A. Hansson, P. Qi, T. Kirova, A. Lazoudis, S. Kotochigova, A.M. Lyyra, L. Li, J. Qi, S. Magnier, J. Chem. Phys. **124**, 084308 (2006)
91. M. Kremer, B. Fischer, B. Feuerstein, V.L.B. de Jesus, V. Sharma, C. Hofrichter, A. Rudenko, U. Thumm, C.D. Schröter, R. Moshammer, J. Ullrich, Phys. Rev. Lett. **103**(21), 213003 (2009)
92. B. Fischer, M. Kremer, T. Pfeifer, B. Feuerstein, V. Sharma, U. Thumm, C. Schröter, R. Moshammer, J. Ullrich, Phys. Rev. Lett. **105**(22), 1–4 (2010)
93. E. Charron, A. Giusti-Suzor, F.H. Mies, Phys. Rev. Lett. **75**(15), 2815–2818 (1995)
94. A. González-Castrillo, A. Palacios, F. Catoire, H. Bachau, F. Martín, J. Phys. Chem. A (2012)

Chapter 3
Ultrafast Dynamics of Hydrogen Atoms in Hydrocarbon Molecules in Intense Laser Fields: Hydrogen Atom Migration and Scrambling in Methylacetylene

Tomoya Okino and Kaoru Yamanouchi

Abstract Characteristic ultrafast processes of hydrogen atom migration commonly observed in hydrocarbon molecules in an intense laser field are introduced by referring to our recent studies on three-body decomposition of methylacetylene and methyl-d_3-acetylene. Special emphases are placed on how dynamical pictures of hydrogen migration are extracted from coincidence momentum imaging (CMI) maps and proton distribution maps constructed from the CMI maps and how migrations of respective hydrogen atoms are correlated with each other, leading to ultrafast exchange and scrambling of hydrogen atoms within a hydrocarbon molecule.

3.1 Introduction

When gaseous molecules are exposed to an intense laser field ($> 10^{13}$ W/cm^2), they are multiply ionized and decomposed eventually into fragment ions through Coulomb explosion processes [1, 2]. We have shown from our series of studies that rich information of molecules interacting with an intense laser field such as ultrafast structural deformation and ultrafast hydrogen migration can be extracted from the analysis of the observed momentum vectors of fragment ions [3–22]. Among the phenomena we have found so far, ejections of triatomic hydrogen molecular ions, H_3^+, and ultrafast hydrogen migration are noteworthy. These phenomena were commonly found when hydrocarbon molecules are exposed to an intense laser field, and can be regarded as those characteristic of H and D atoms having considerably smaller mass than other heavier atoms in hydrocarbon molecules.

It is interesting to note that there are two different timescales during which hydrogen atoms move when hydrocarbon molecules are irradiated with an intense laser field. The shorter timescale is characterized by the duration of ultrashort laser

T. Okino · K. Yamanouchi (✉)
Department of Chemistry, School of Science, The University of Tokyo, 7-3-1 Hongo, Bunkyo-ku, Tokyo 113-0033, Japan
e-mail: kaoru@chem.s.u-tokyo.ac.jp

R. de Nalda, L. Bañares (eds.), *Ultrafast Phenomena in Molecular Sciences*, Springer Series in Chemical Physics 107, DOI 10.1007/978-3-319-02051-8_3,

pulses, which is of the order of 10 to 30 fs, and the longer timescale is in the rage of 0.1∼1 ps, which is of the order of a period of molecular rotation. Our pump-and-probe study of two-body decomposition of methanol exposed to an ultrashort intense laser pulse showed that "fast" hydrogen atom migration proceeds in the presence of the intense laser field whose duration is 40 fs and the "slow" hydrogen atom migration proceeds after the light field disappears [15]. The slow post-laser pulse migration can be regarded as a unimolecular decomposition process of an energized parent ion prepared by the irradiation of an ultrashort intense laser pulse. Our recent study on the ejection of H_3^+ from ethane (C_2H_6) and deuterated ethane (CH_3CD_3) excited by an intense laser field showed that six hydrogen atoms are scrambled almost statistically within the relatively long lifetime of a precursor parent ion prior to the ejection of a triatomic hydrogen molecular ion [20].

In the present study, we focus on the "fast" hydrogen atom migration processes by referring to our recent study on the three-body fragmentation processes of methylacetylene and methyl-d_3-acetylene induced by ultrashort intense laser pulses, and show on the basis of the coincidence momentum imaging maps how four H/D atoms within a parent molecule migrate in an ultrashort intense laser field.

3.2 Experiment and Data Analysis

The details of the experimental setup have been reported in our previous papers [21–23]. Typically the output of a femtosecond laser system (790 nm, 40 fs, 5 kHz) is focused with a quartz lens ($f = 150$ mm) at the point where they crossed at right angles with a molecular beam of a sample gas introduced into the ultrahigh vacuum chamber through a nickel skimmer (∅0.48 mm) from a microsyringe (∅70 μm). The laser field intensity at the focal spot is in the range of 10^{13}∼10^{14} W cm^{-2}.

The ion species ejected from the laser focal volume were extracted by three equally spaced parallel-plate electrodes in the velocity mapping configurations [24] and detected by a position sensitive detector with delay-line anodes [25]. The three dimensional momentum vectors of the respective fragment ions were determined by their time-of-flight and the position on the detector. False coincidence events originating from two or more parent molecular ions were discriminated from the true coincidence events by imposing the momentum conservation conditions. The number of detected ions was kept to be about 0.5 events per laser shot in order to secure the coincidence conditions and reduce the false coincidence events. The accumulated event number is of the order of 10^8.

The spatial distribution of a proton or deuteron within a triply charged parent molecule decomposing into three fragment ions including the proton or deuteron can be mapped by converting the observed momentum vectors of the fragment ions into the coordinate space, in which the position of the proton or deuteron with re-

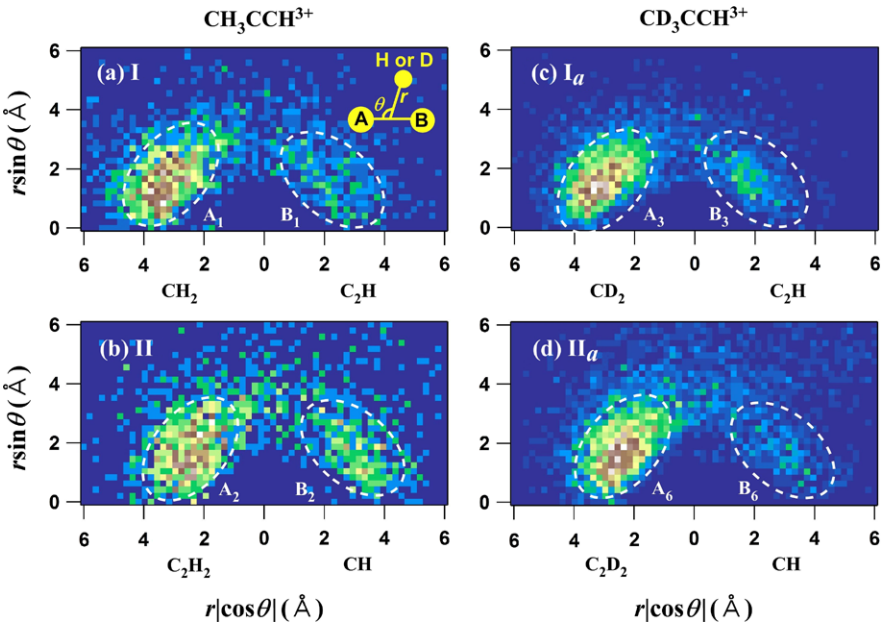

Fig. 3.1 The proton/deuteron distribution maps. (**a**) I: $H^+ + CH_2^+ + C_2H^+$. (**b**) II: $H^+ + C_2H_2^+ + CH^+$, (**c**) I_a: $D^+ + CD_2^+ + C_2H^+$, (**d**) II_a: $D^+ + C_2D_2^+ + CH^+$. The *inset figure* shows the definitions of parameters r and θ describing the geometrical structure just before the decomposition. In all of the four maps, there are two dense areas, which are labeled as A_n and B_n ($n = 1$, 2, 3, and 6)

spect to the rest of the molecule decomposing into two fragment ions is obtained in the molecular-fixed coordinate system as demonstrated in our previous paper [22].

In this analysis of the coincidence momentum data for the three-body decomposition of triply charged methylacetylene and methyl-d_3-acetylene, three geometrical parameters r_1, r_{23}, and θ are introduced to express the geometrical configuration of $C_3H_4^{3+}$ or $C_3HD_3^{3+}$ just before the Coulomb explosion as shown in the inset of Fig. 3.1(a), where r_1 is the distanced of a proton or a deuteron measured from the center of gravity of the two heavier moieties M_2 and M_3, r_{23} is the distance between the center of masses of M_2 and M_3, and θ is the angle between a proton (or a deuteron) and the axis connecting the center of masses of the two heavier moieties. The momentum vectors of the three fragment ions are calculated by numerically solving the classical equations of motion under the assumptions that (i) the repulsive Coulombic interaction is that between the point charges representing the respective fragment ions and (ii) the initial values of the velocity of the respective fragment ions are zero. The numerical calculations are repeated iteratively until the observed momentum vectors of the respective fragment ions are reproduced.

3.3 Three-Body Decomposition Pathways of Methylacetylene and Methyl-d_3-Acetylene

3.3.1 Three-Body Decomposition Pathways with CC Bond Breaking

3.3.1.1 Methylacetylene

In methylacetylene, the following two types of three-body decomposition pathways are identified in the CMI maps.

[Type I: $C_\beta C_\gamma$ bond breaking]

$$\text{I:} \quad C_3H_4^{3+} \rightarrow H^+ + C_\gamma H_2^+ + C_\alpha C_\beta H^+ \tag{3.1}$$

[Type II: $C_\alpha C_\beta$ bond breaking]

$$\text{II:} \quad C_3H_4^{3+} \rightarrow H^+ + C_\beta C_\gamma H_2^+ + C_\alpha H^+ \tag{3.2}$$

where three carbon atoms are labeled using α, β, γ as H–$C_\alpha \equiv C_\beta$–$C_\gamma H_3$.

The number of events in Pathway I (55 %) is as large as that of Pathway II (45 %). This result indicates that the $C_\beta C_\gamma$ bond breaking and the $C_\alpha C_\beta$ bond breaking occur with almost the same probabilities. It is highly probable that a proton ejected in these three-body Coulomb explosion processes is originated from a hydrogen atom which is originally bonded to the C_γ atom in the methyl group, but it may also be possible that a proton is ejected from the C_α atom in the methine group if the hydrogen migration proceeds prior to the chemical bond breaking.

The proton distribution maps of Pathway I and Pathway II are shown in Fig. 3.1(a) and 3.1(b), respectively. The proton distributions cover the entire θ range, but there are clear two dense areas labeled by A_1 and B_1 in Pathway I and A_2 and B_2 in Pathway II. The distribution A_1 shows that the protons are distributed around the CH_2^+ moiety. The distribution B_1 shows that the protons are distributed around the C_2H^+ moiety. The probability of the distribution A_1 (78 %) is much larger than that of the distribution B_1 (22 %). This result indicates that a proton is preferentially ejected from the methyl group accompanied by the $C_\beta C_\gamma$ bond breaking that is originally a single bond. The probability distribution A_2 (62 %) is much larger than that of the distribution B_2 (38 %). This result also indicates that a proton is preferentially ejected from the methyl group.

It is probable that the ejected protons are originated from the methyl group in both Pathway I and Pathway II, however, in order to identify securely whether a proton is ejected from methyl group or from methine group, we performed the CMI measurements using partially deuterated species, methyl-d_3-acetylene.

3.3.1.2 Methyl-d_3-Acetylene

In methyl-d_3-acetylene, six three-body decomposition pathways are identified in the CMI maps and three of them are categorized into Type I decomposition pathways and the rest of them are categorized into Type II decomposition pathways as

[Type I: $C_\beta C_\gamma$ bond breaking]

$$\mathrm{I}_a\colon\quad \mathrm{CD_3CCH^{3+}} \rightarrow \mathrm{D^+ + C_\gamma D_2^+ + C_\alpha C_\beta H^+} \tag{3.3}$$

$$\mathrm{I}_b\colon\quad \mathrm{CD_3CCH^{3+}} \rightarrow \mathrm{H^+ + C_\gamma D_2^+ + C_\alpha C_\beta D^+} \tag{3.4}$$

$$\mathrm{I}_c\colon\quad \mathrm{CD_3CCH^{3+}} \rightarrow \mathrm{D^+ + C_\gamma HD^+ + C_\alpha C_\beta D^+}$$
$$\mathrm{(and/or\ D^+ + C_\alpha HD^+ + C_\beta C_\gamma D^+)} \tag{3.5}$$

[Type II: $C_\alpha C_\beta$ bond breaking]

$$\mathrm{II}_a\colon\quad \mathrm{CD_3CCH^{3+}} \rightarrow \mathrm{D^+ + C_\beta C_\gamma D_2^+ + C_\alpha H^+} \tag{3.6}$$

$$\mathrm{II}_b\colon\quad \mathrm{CD_3CCH^{3+}} \rightarrow \mathrm{H^+ + C_\beta C_\gamma D_2^+ + C_\alpha D^+} \tag{3.7}$$

$$\mathrm{II}_c\colon\quad \mathrm{CD_3CCH^{3+}} \rightarrow \mathrm{D^+ + C_\beta C_\gamma HD^+ + C_\alpha D^+}$$
$$\mathrm{(and/or\ D^+ + C_\alpha C_\beta HD^+ + C_\gamma D^+)} \tag{3.8}$$

where the carbon atoms are labeled using α, β, γ as $\mathrm{H\text{–}C_\alpha \equiv C_\beta\text{–}C_\gamma D_3}$.

Confirmation of the Major Pathway The relative yields for the observed six decomposition pathways are summarized in Table 3.1. The major pathways corresponding to Pathway I and Pathway II in methylacetylene are Pathway I_a and Pathway II_a in methyl-d_3-acetylene, respectively.

The deuteron distribution maps for Pathway I_a and Pathway II_a are shown in Fig. 3.1(c) and 3.1(d). In Pathways I_a and II_a, the distributions of $\mathrm{A_3}$ and $\mathrm{A_6}$ are denser than those of $\mathrm{B_3}$ and $\mathrm{B_6}$, respectively, suggesting that the deuteron is mainly ejected from $\mathrm{CD_3}$ side. The deuteron distribution maps for Pathways I_a and II_a have the same tendency as the proton distribution maps of Pathways I and II, respectively. It supports our conjecture that the ejected proton in methylacetylene originates mainly from methyl group in Pathways I and II.

H/D Exchange The proton/deuteron distribution maps for the Pathways I_b, I_c, II_b, and II_c are shown in Fig. 3.2. The distribution $\mathrm{A_4}$ of Pathway I_b in Fig. 3.2(a) shows that the hydrogen atom in the $\mathrm{C_\alpha H}$ group migrates to the $\mathrm{C_\gamma}$ site and a deuterium atom in the $\mathrm{C_\gamma D_3}$ group migrates to the $\mathrm{C_\alpha C_\beta}$ part. Therefore, this $\mathrm{A_4}$ distribution shows a decomposition pathway accompanying the H/D exchange.

Similarly, the distribution $\mathrm{A_7}$ of Pathway II_b in Fig. 3.2(b) shows that the hydrogen atom in the $\mathrm{C_\alpha H}$ group migrates to the $\mathrm{C_\beta C_\gamma}$ part and a deuterium atom in the $\mathrm{C_\gamma D_3}$ group migrates to the $\mathrm{C_\alpha}$ site. Therefore, this $\mathrm{A_7}$ distribution also shows a decomposition pathway accompanying the H/D exchange.

Table 3.1 The event numbers of the observed three-body decomposition pathways accompanying the proton (deuteron) ejection and the yield ratios for Type I and Type II decomposition pathways.

Pathway	Event number	Ratio/%
methylacetylene		
(I): $H^+ + CH_2^+ + C_2H^+$	2008	55
(II): $H^+ + C_2H_2^+ + CH^+$	1639	45
(III): $H^+ + H_2^+ + C_3H^+$	2714	–
methyl-d_3-acetylene		
(I_a): $D^+ + CD_2^+ + C_2H^+$	3396	87
(I_b): $H^+ + CD_2^+ + C_2D^+$	357	9
(I_c): $D^+ + CHD^+ + C_2D^+$	137	4
(II_a): $D^+ + C_2D_2^+ + CH^+$	4292	86
(II_b): $H^+ + C_2D_2^+ + CD^+$	214	4
(II_c): $D^+ + C_2HD^+ + CD^+$	499	10
(III_a): $D^+ + D_2^+ + C_3H^+$	974	–
(III_b): $H^+ + D_2^+ + C_3D^+$	1664	–

H/D Exchange Long Distance These distributions, A_4 and A_7, representing the H/D exchange prior to the decomposition can be regarded as definitive evidences of the correlated motion of the H atom in the methine group and D atoms in the methyl group.

On the other hand, the distribution B_4 of Pathway I_b in Fig. 3.2(a) shows that one deuterium atom in the $C_\gamma D_3$ group migrated to the $C_\alpha C_\beta$ part. Similarly, the distribution B_7 of Pathway II_b in Fig. 3.2(b) shows that one deuterium atom in the $C_\gamma D_3$ group migrates to the C_α site.

In Pathway II_b, a proton is ejected from the methine group and the fragment ions $C_2D_2^+$ and CD^+ are generated with the $C_\alpha C_\beta$ bond breaking. It should be noted that the fragment ion CD^+ can only be generated when a deuterium atom originally in the $C_\gamma D_3$ group migrates to the C_α atom in the $C_\alpha H$ group. This can be regarded as an evidence of the migration of a deuterium atom from the C_γ site to the C_α site along the $C_\alpha C_\beta C_\gamma$ skeleton of the three carbon atoms in methyl-d_3-acetylene.

H/D Exchange and Scrambling In Pathway II_c, the fragment ions $C_\beta C_\gamma HD^+$ and $C_\alpha D^+$ are detected with D^+. This shows that one hydrogen atom migrates from the C_α site to the $C_\beta C_\gamma$ part and one deuterium atom migrates from the C_γ site to the C_α site. The distribution A_8 of Pathway II_c shown in Fig. 3.2(d) represents the decomposition pathway accompanying the H/D exchange. The distribution B_8 shows that there is an additional migration process of a deuterium atom from the C_γ site to the $C_\alpha C_\beta$ part besides the H/D exchange. This means that as many as three H/D atoms migrate prior to the decomposition. If the more than two H/D atoms migrate prior to the decomposition, the process is called as "hydrogen scrambling".

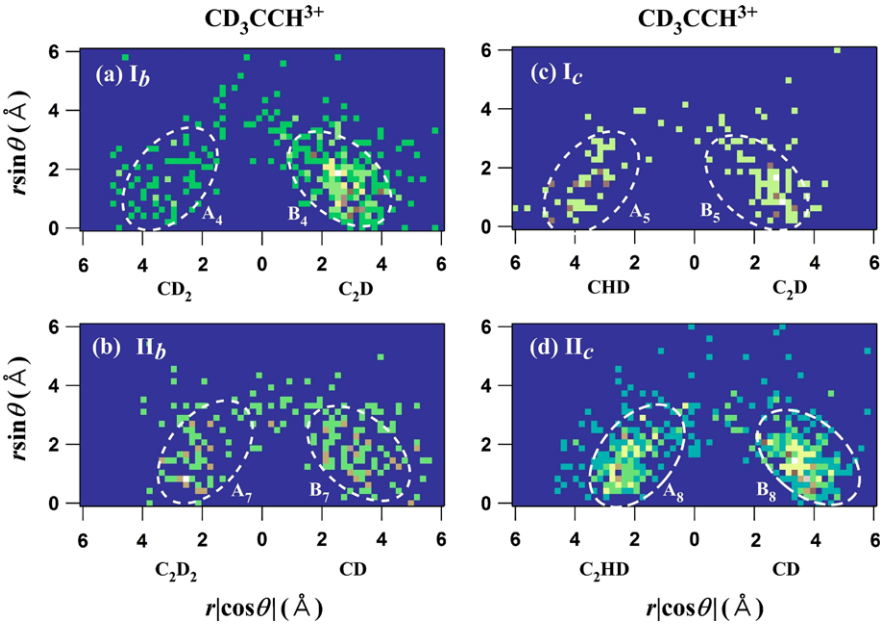

Fig. 3.2 The proton/deuteron distribution maps of the three-body decomposition pathways. (**a**) I_b: $H^+ + CD_2^+ + C_2D^+$, (**b**) I_c: $H^+ + C_2D_2^+ + CD^+$, (**c**) II_b: $D^+ + CHD^+ + C_2D^+$, (**d**) II_c: $D^+ + C_2HD^+ + CD^+$. In all the four maps, there are two dense areas, which are labeled as A_n and B_n ($n = 4$, 5, 7, and 8)

Similarly, in Pathway I_c, the fragment ions $C_\gamma HD^+$ and $C_\alpha C_\beta D^+$ are detected with D^+. This shows that one hydrogen atom migrates from the C_α site to the C_γ site and one deuterium atom migrates from the C_γ site to the $C_\alpha C_\beta$ part. The distribution A_5 in Fig. 3.2(c) represents the existence of the H/D change prior to the decomposition. In addition to the H/D exchange, the migration of another deuterium atom proceeds from the C_γ site to the $C_\alpha C_\beta$ part as represented by the distribution B_5. This means that the hydrogen atom scrambling proceeds also in Pathway I_c.

Alternative Explanation As described in the parenthesis in Eqs. (3.5) and (3.8), Pathways I_c and II_c can also be categorized into Type II and Type I decomposition pathways, respectively, as interpreted below. The distribution B_5 in Pathway I_c may represents the migration of one deuterium atom from the C_γ site to the C_α site, and the distribution A_5 represents the migration of two deuterium atoms from the C_γ site to the C_α site. Similarly, in Pathway II_c, the distribution B_8 may represent the migration of one deuterium atom form the C_γ site to the $C_\alpha C_\beta$ part and the distribution A_8 represents the migration of two deuterium atoms from the C_γ site to the $C_\alpha C_\beta$ part.

Therefore, it can securely be said that the two decomposition pathways, I_c and II_c, are interpreted as (i) the decomposition pathways with the migration of three

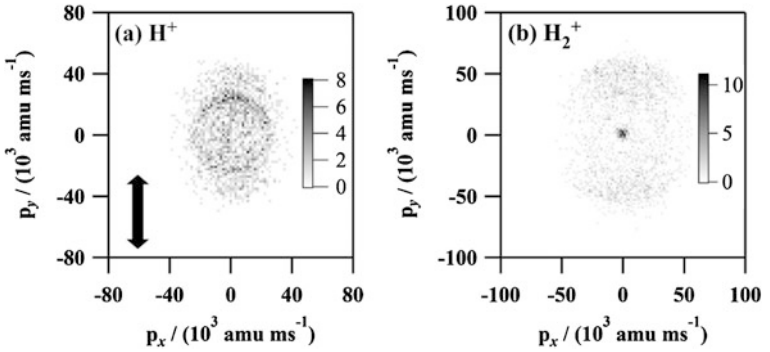

Fig. 3.3 2D CMI maps of (**a**) H^+ and (**b**) H_2^+ ejected from the three-body decomposition pathway, $C_3H_4^{3+} \rightarrow H^+ + H_2^+ + C_3H^+$. The *vertical arrow* represents the laser polarization direction

light atoms (H/D exchange and one D migration, "hydrogen scrambling") and/or (ii) the decomposition pathways with the migration of two D atoms.

3.3.2 Three-Body Decomposition Pathways with H^+ and H_2^+ Ejection

In addition to the three-body decomposition pathways shown in Sect. 3.3.1, the following three kinds of three-body decomposition pathways called Type III accompanying the ejection of H^+ (D^+) and H_2^+ (D_2^+) were identified in methylacetylene and methyl-d_3-acetylene,

$$\text{III:} \quad C_3H_4^{3+} \rightarrow H^+ + H_2^+ + C_3H^+, \tag{3.9}$$

$$\text{III}_\text{a}\text{:} \quad C_3HD_3^{3+} \rightarrow D^+ + D_2^+ + C_3H^+, \tag{3.10}$$

$$\text{III}_\text{b}\text{:} \quad C_3HD_3^{3+} \rightarrow H^+ + D_2^+ + C_3D^+, \tag{3.11}$$

In the present chapter, we focus attention on our analysis on Pathway III to show how these light ion species, H^+ and H_2^+, are ejected from triply charged methylacetylene.

The CMI maps of H^+ and H_2^+ are shown in Figs. 3.3(a) and 3.3(b), respectively. It is clearly seen in Fig. 3.3(a) for H^+ that there are two features, that is, a pair of the inner crescent type features and the other pair of the outer broadened crescent features. In Fig. 3.3(b), even though the distributions are less conspicuous than in Fig. 3.3(a), similar inner and outer pairs of the crescent features can be identified. These inner and outer crescent features identified both in the momentum distributions of H^+ and H_2^+ suggest that at least two different decomposition routes coexist in Pathway III.

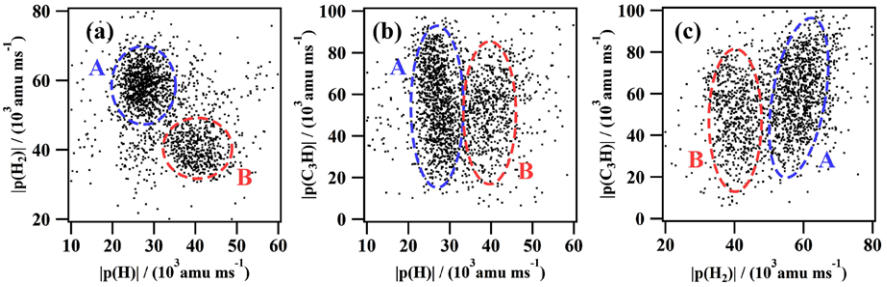

Fig. 3.4 Momentum correlation maps for (**a**) $|\mathbf{p}(\mathrm{H})| - |\mathbf{p}(\mathrm{H_2})|$, (**b**) $|\mathbf{p}(\mathrm{H})| - |\mathbf{p}(\mathrm{C_3H})|$, and (**c**) $|\mathbf{p}(\mathrm{H_2})| - |\mathbf{p}(\mathrm{C_3H})|$ in the three-body decomposition pathway, $\mathrm{C_3H_4^{3+}} \rightarrow \mathrm{H^+} + \mathrm{H_2^+} + \mathrm{C_3H^+}$. In these three correlation maps, there are two dense domains labeled by A (*blue dotted oval*) and B (*red dotted oval*) (Color figure online)

In order to examine more in detail the decomposition processes, the momentum correlation maps are constructed as shown in Figs. 3.4(a)–(c). In the correlation map of Fig. 3.4(a) representing the correlation between the absolute value of the momentum of $\mathrm{H^+}$, $|\mathbf{p}(\mathrm{H^+})|$, and that of the momentum of $\mathrm{H_2^+}$, $|\mathbf{p}(\mathrm{H_2^+})|$, there are two dense regions separated with each other; one is the distribution centered at $(|\mathbf{p}(\mathrm{H^+})|, |\mathbf{p}(\mathrm{H_2^+})|) = (26, 60)$, which is hereafter called Domain A, and the other is the distribution centered at $(|\mathbf{p}(\mathrm{H^+})|, |\mathbf{p}(\mathrm{H_2^+})|) = (40, 40)$, which is hereafter called Domain B, where the numerical values of the momentum values are represented in the momentum unit of 10^3 amu $\mathrm{m\,s^{-1}}$.

In Fig. 3.4(b) representing the correlation between $|\mathbf{p}(\mathrm{H^+})|$ and the absolute value of the momentum of $\mathrm{C_3H^+}$, $|\mathbf{p}(\mathrm{C_3H^+})|$, there are also two dense regions, but they both are stretched along the $|\mathbf{p}(\mathrm{C_3H^+})|$ axis. The region corresponding Domain A spreads in the wide momentum region of $|\mathbf{p}(\mathrm{C_3H^+})| = 20{\sim}90$, while the region corresponding Domain B spreads in the narrower region of $|\mathbf{p}(\mathrm{C_3H^+})| = 30{\sim}70$. Similarly, in Fig. 3.4(c) representing the correlation between $|\mathbf{p}(\mathrm{H^+})|$ and $|\mathbf{p}(\mathrm{C_3H^+})|$, these two domains A and B spread along the $|\mathbf{p}(\mathrm{C_3H^+})|$ can be seen.

In the three dimensional momentum correlation map in which the x, y, and z axes represent respectively $|\mathbf{p}(\mathrm{H^+})|$, $|\mathbf{p}(\mathrm{H_2^+})|$ and $|\mathbf{p}(\mathrm{C_3H^+})|$, Domain A and Domain B can be regarded as cigar type shape domains whose major axes are mostly along the z axis. Considering that the ion species ejecting "first" from a triply charged parent molecule is expected to have the larger momentum release than that ejecting "next" from the doubly charged moiety left after the first ion ejection, Domain A may represent the decomposition route in which $\mathrm{H_2^+}$ is ejected first and $\mathrm{H^+}$ is ejected next, while Domain B may represent the decomposition route in which $\mathrm{H_2^+}$ is ejected first and $\mathrm{H^+}$ is ejected next.

If the second ejection occurs long after the first ejection, the absolute momentum values of the two singly charged ions produced at the second ejection stage should become equal, and also, the spatial distribution of the momentum vector of the singly charged ion produced at the second ejection stage should become isotropic. However, as seen in Figs. 3.4(b) and 3.4(c), any distribution of data points running

along the diagonal line, representing the cases in which two singly charged ions have equal momentum releases, could not be identified. Furthermore, obviously, the pairs of the inner crescent feature in Figs. 3.3(a) and 3.3(b), showing the spatial distribution of the singly charged ion, which is supposed to have been produced from the second ejection stage, is not isotropic.

Therefore, it can be said that the ejections of the light ion species could not be separated from each other. This means that the three-body decomposition does not proceed in a *sequential* manner but in a *concerted* manner. The concerted decomposition scheme can be supported by the cigar-type shape of Domain A and Domain B in the 3D momentum space. When H^+ and H_2^+ are on the same side with respect to C_3H^+, like in the original methyl group configuration, C_3H^+ should receive large momentum recoil. On the other hand, if H^+ and H_2^+ are located on the opposite sides with respect to C_3H^+, C_3H^+ should have much smaller momentum release because C_3H^+ is sandwiched by H^+ and H_2^+. In Domain A, the largest value of $|\mathbf{p}(C_3H^+)|$ can be taken when H^+ is ejected as soon as after H_2^+ is ejected so that C_3H^+ receive the largest momentum recoil from the same side, while the smallest value of $|\mathbf{p}(C_3H^+)|$ can be taken when H^+ is ejected after H^+ is transferred to the opposite side of C_3H^+ with respect to the side of the ejecting H_2^+. This transfer of the position of H^+ can be realized by the overall rotation of H^+–C_3H^+ by about π induced by the recoil momentum received from the ejecting H_2^+ at the earlier part of the three-body decomposition. When H^+ is ejected from H^+–C_3H^+ after the π rotation, the direction of the recoil momentum received by C_3H^+ is in the opposite direction to that received at the earlier ejection of H_2^+. The continuous event distribution in Domain A indicates that there are a lot of events categorized into intermediate cases in which H^+ is ejected when the H^+–C_3H^+ moiety rotates by the angle smaller than π. In the earlier part of this *concerted* three-body decomposition, H_2^+ starts to leave and the rest of the molecule starts to rotate simultaneously, and H^+ starts to leave before H_2^+ is still in the process of the ejection. Almost exactly the same scenario can be drawn for the events in Domain B in which H^+ is ejected "earlier" than H_2^+.

3.4 Summary

In this chapter, our recent studies on ultrafast hydrogen migration processes occurring in the three-body decomposition processes of methylacetylene and methyl-d_3-acetylene induced by intense laser fields are introduced.

From the H/D distribution maps obtained for methyl-d_3-acetylene, it was revealed that a variety of different types of the H/D migration processes coexist such as (i) the migration of one H atom, (ii) the exchange between two H atoms, (iii) the migration of two H atoms, and (iv) the exchange of two H atoms and additional migration of one H atom ("hydrogen scrambling").

These processes of hydrogen migration and hydrogen scrambling are considered to be finished by the time when the enhanced ionization [26, 27] occurs from the

singly charged and/or doubly charged parent ions to the triply charged species. This is because the enhancement of the ionization is expected to occur when the C–C internuclear distance becomes approximately twice as large as the equilibrium internuclear distance, and consequently, by the time when the ionization to the triply charged stage occurs, the distance between the heavy moieties is too far for hydrogen atoms to migrate further. Considering that three-body decomposition proceeds immediately after triply charged precursor ions are produced, the probability of hydrogen migration to occur after the triple ionization should be extremely low.

In addition, a different type of three-body decomposition processes in which two light ion species such as H^+ and H_2^+ are ejected are identified for methylacetylene and methyl-d_3-acetylene. From the momentum correlation maps for methylacetylene, it was revealed that the three-body decomposition proceeds in a concerted manner so that H^+ and H_2^+ are ejected almost simultaneously. It was also shown that events in which H^+ starts to leave earlier than H_2^+ and those in which H_2^+ starts to leave earlier than H^+ coexist.

As has been shown in the present chapter as well as in our previous studies, the motions of at least two or three hydrogen atoms need to be considered simultaneously for describing hydrogen migration processes even when apparently one proton moves. The migration, exchange, and scrambling processes of hydrogen atoms occurring within a very short period of time can be characteristic phenomena commonly observed in hydrocarbon molecules when they are exposed to an intense laser field, and this highly correlated ultrafast motion of hydrogen atoms may better be treated by a theoretical method beyond Born-Oppenheimer approximation such as that developed by our group [28, 29] in which protons are represented by multiple-centered wave functions like electrons in a molecule.

Acknowledgements We thank Prof. Huailiang Xu (Jilin University) for conducting measurements and his variable comments. The present research was supported by the following three grants from the Ministry of Education, Culture, Sports, Science and Technology (MEXT), Japan; the Grant-in-Aid for Specially Promoted Research on Ultrafast Hydrogen Migration (#19002006), the Grant-in-Aid for Global COE Program for Chemistry Innovation and Special Coordination Funds for Promoting Science and Technology.

References

1. K. Yamanouchi, S.L. Chin, P. Agostini, G. Ferrante (eds.), *Progress in Ultrafast Intense Laser Science I–VI* (Springer, Heidelberg, 2006–2010)
2. J.H. Posthumus, Rep. Prog. Phys. **67**, 623 (2004)
3. A. Hishikawa, H. Hasegawa, K. Yamanouchi, Phys. Scr. T **110**, 108 (2004)
4. A. Hishikawa, H. Hasegawa, K. Yamanouchi, J. Electron Spectrosc. Relat. Phenom. **141**, 195 (2004)
5. A.S. Alnaser, I. Litvinyuk, T. Osipov, B. Ulrich, A. Landers, E. Wells, C.M. Maharjan, P. Ranitovic, I. Bochareva, D. Ray, J. Phys. B, At. Mol. Opt. Phys. **39**, S485 (2006)
6. T. Okino, Y. Furukawa, P. Liu, T. Ichikawa, R. Itakura, K. Hoshina, K. Yamanouchi, H. Nakano, Chem. Phys. Lett. **423**, 220 (2006)
7. P. Liu, T. Okino, Y. Furukawa, T. Ichikawa, R. Itakura, K. Hoshina, K. Yamanouchi, H. Nakano, Chem. Phys. Lett. **423**, 187 (2006)

8. R. Itakura, P. Liu, Y. Furukawa, T. Okino, K. Yamanouchi, H. Nakano, J. Chem. Phys. **127**, 104306 (2007)
9. A. Hishikawa, A. Matsuda, M. Fushitani, E.J. Takahashi, Phys. Rev. Lett. **99**, 258302 (2007)
10. A. Hishikawa, A. Matsuda, E.J. Takahashi, M. Fushitani, J. Chem. Phys. **128**, 084302 (2008)
11. A. Matsuda, M. Fushitani, E.J. Takahashi, A. Hishikawa, Phys. Chem. Chem. Phys. **13**, 8697 (2011)
12. H. Xu, T. Okino, K. Yamanouchi, J. Chem. Phys. **131**, 151102 (2009)
13. H. Xu, T. Okino, K. Yamanouchi, Chem. Phys. Lett. **349**, 255 (2009)
14. Y.H. Jiang, A. Rudenko, O. Herrwerth, L. Foucar, M. Kurka, K.U. Kühnel, M. Lezius, M.F. Kling, J. van Tilborg, A. Belkacem, K. Ueda, S. Düsterer, R. Treusch, C.D. Schröter, R. Moshammer, J. Ullrich, Phys. Rev. Lett. **105**, 263002 (2010)
15. H. Xu, C. Marceau, K. Nakai, T. Okino, S.L. Chin, K. Yamanouchi, J. Chem. Phys. **133**, 071103 (2010)
16. H. Xu, T. Okino, K. Nakai, K. Yamanouchi, S. Roither, X. Xie, D. Kartashov, M. Schöffler, A. Baltuska, M. Kitzler, Chem. Phys. Lett. **119**, 484 (2010)
17. J. Zhou, H.B. Schlegel, J. Phys. Chem. A **115**, 8375 (2011)
18. H. Xu, T. Okino, T. Kudou, K. Yamanouchi, S. Roither, M. Kitzler, A. Baltuska, S.L. Chin, J. Phys. Chem. A **116**, 2686 (2012)
19. L. Zhang, S. Roither, X. Xie, D. Kartashov, M. Schöffler, H. Xu, A. Iwasaki, S. Gräfe, T. Okino, K. Yamanouchi, A. Baltuska, M. Kitzler, J. Phys. B, At. Mol. Opt. Phys. **45**, 085603 (2012)
20. R. Kanya, T. Kudou, N. Schirmel, S. Miura, K.M. Weitzel, K. Hoshina, K. Yamanouchi, J. Chem. Phys. **136**, 204309 (2012)
21. T. Okino, A. Watanabe, H. Xu, K. Yamanouchi, Phys. Chem. Chem. Phys. **14**, 4230 (2012)
22. T. Okino, A. Watanabe, H. Xu, K. Yamanouchi, Phys. Chem. Chem. Phys. **14**, 10640 (2012)
23. H. Hasegawa, A. Hishikawa, K. Yamanouchi, Chem. Phys. Lett. **349**, 57 (2001)
24. A.T.J.B. Eppink, D.H. Parker, Rev. Sci. Instrum. **68**, 3477 (1997)
25. J. Ullrich, R. Moshammer, A. Dorn, R. Dörner, L.H. Schmidt, H. Schmidt-Böcking, Rep. Prog. Phys. **66**, 1463 (2003)
26. T. Zuo, A.D. Bandrauk, Phys. Rev. A **52**, R2511 (1995)
27. J.H. Posthumus, L.J. Frasinski, A.J. Giles, K. Codling, J. Phys. B, At. Mol. Opt. Phys. **28**, L349 (1995)
28. T. Kato, K. Yamanouchi, J. Chem. Phys. **131**, 164118 (2009)
29. T. Kato, K. Yamanouchi, Phys. Rev. A **85**, 034504 (2012)

Chapter 4
Femtosecond Photodissociation Dynamics by Velocity Map Imaging. The Methyl Iodide Case

Rebeca de Nalda, Luis Rubio-Lago, Vincent Loriot, and Luis Bañares

Abstract The introduction of time-resolved measurements in the femtosecond time-scale using velocity map imaging techniques of charged particles (ions and photoelectrons) in combination with resonant multiphoton ionization of the fragments for the study of the photodissociation dynamics of small polyatomic molecules is reviewed. A typical experiment consists of the measurement of a sequence of images, whose analysis requires in most cases sophisticated multidimensional fitting methods to extract all the relevant time-resolved information contained in the images. In particular, the application of these techniques to the study of the direct photodissociation (*A* band) and electronic predissociation (*B* band) of methyl iodide along with the detection and characterization of transient species and the study of cluster dissociation, as a case example for femtosecond velocity map imaging, are presented and discussed.

4.1 Introduction

In the last decades, the field of laser photochemistry has reached an important technical maturity, due to the development of versatile laser sources and powerful detection techniques. One of the followed directions has aimed to explore dynamics directly in the time scales of chemical molecular processes, which are typically in the femtosecond to picosecond range. Understanding the time required for a process to take place—if such concept is suitable of a precise definition within the realm of the microscopic world—implies the possibility of either measuring, or externally inducing, the start and finish moments of the process. In standard two-body reaction dynamics, the definition of the start of the reaction is arbitrary, given the long-range potentials involved in a chemical reaction, and this is complicated by the fact that

R. de Nalda · V. Loriot
Instituto de Química Física Rocasolano, CSIC, C/ Serrano, 119, 28006 Madrid, Spain

L. Rubio-Lago · V. Loriot · L. Bañares (✉)
Departamento de Química Física, Facultad de Ciencias Químicas, Universidad Complutense de Madrid, 28040 Madrid, Spain
e-mail: banares@quim.ucm.es

R. de Nalda, L. Bañares (eds.), *Ultrafast Phenomena in Molecular Sciences*, Springer Series in Chemical Physics 107, DOI 10.1007/978-3-319-02051-8_4,

in conventional experiments, performed with a large number of molecules, each event is characterized by its own impact parameter, relative velocities and positions, so that, for the ensemble, the origin of time is particularly ill-defined in the scale characteristic of the reaction itself.

On the contrary, photo-induced processes (photoionization, photoisomerization, photodissociation) are often termed "half reactions" [1], with an origin of time that is set by the laser pulse initiating the process. Some degree of uncertainty remains, however, due to the temporal width of the laser pulse, and thus time zero is best defined for the shortest pulse available. In practice, it is common to assign the origin of time to the maximum of the intensity envelope of the laser pulse used to induce a given process. It is the temporal width of the laser pulse that sets the time resolution and hence, the time scales that can be explored with such pulse. Even for half reactions, however, the end of the process remains considerably less well defined, and in practice, the most useful definition depends on the technique to be used as a probe of the process. If a short non-resonant laser pulse is employed as an ionization probe, transition state species can be subjected to ionization at all times, and one would have to define the "end" of the process as the time delay for which some parameter characteristic of the process (i.e. the kinetic energy distribution) reaches its asymptotic value. The situation is different if a short laser pulse, resonant with an intermediate level of a product fragment, is employed as probe in a stepwise ionization process (REMPI), or in a transition to a fluorescence emitting state. The presence of the resonance enhances the magnitude of the observable, be it fluorescence or ionization, by orders of magnitude with respect to the non-resonant case. In this instance, only if the co-fragment is distant enough, so that the targeted resonance is not shifted beyond the bandwidth of the probe laser, is the product fragment detected with high efficiency. Typically, the probe laser central wavelength is tuned to the free radical resonance, so that detection only starts when the fragments are far from each other so that the above condition is fulfilled. This is normally referred to as "the opening of the optical window". This type of measurement provides a natural definition of the "end" of the process, allowing "clocking", although it has to be noted that it is a definition that is dependent on the bandwidth of the probe laser [2]. In any case, comparison of "clocking" times in multichannel processes allows to extract information on the energy flow processes between electronic and nuclear degrees of freedom in a molecular species, and can provide valuable information on the dynamics at special regions of the potential energy surfaces like conical intersections.

The study of these fast energy distribution processes in molecules has been at the core of the discipline that has been termed Femtochemistry for the last decades [3]. In the heart of the gear of such progress, several molecular systems, which possess the valuable characteristic of being complex and yet theoretically accessible, can be found. Among them, methyl iodide, CH_3I, constitutes the five-atom paradigm [4]. Due to the high electronegativity of the halogen atom, methyl halides can be viewed as pseudo-diatomic systems (where the methyl moiety plays the role of a pseudo-atom), pseudo-triatomic (the pseudo-atom consists of the three hydrogen atoms) or full five-atom molecules, depending on the theoretical framework.

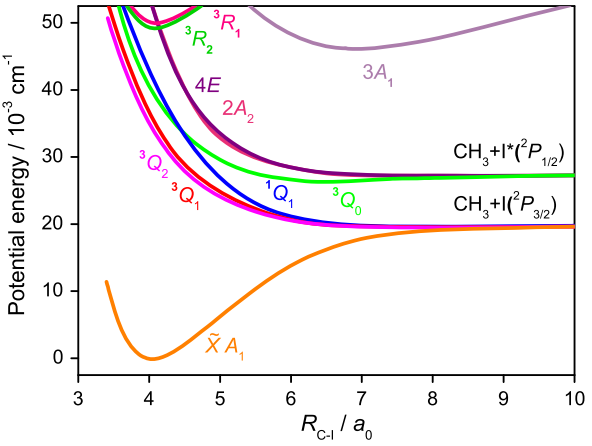

Fig. 4.1 Relevant potential energy curves for CH_3I photodissociation and electronic predissociation calculated along the reaction coordinate (C–I distance). Adapted from [5]

What makes methyl iodide more amenable to experimentalists with respect to other methyl halides, however, is related to the strong spin-orbit splitting of the iodine atom, which has several consequences. In the first place, the CH_3I absorption spectrum is notably shifted towards the red with respect to the other methyl halides. The first absorption band in methyl iodide, the *A* band, is centered at 262 nm; in methyl bromide and methyl chloride, it lies at around 200 nm and 170 nm, respectively. The difference is meaningful, since the absorption spectrum in methyl iodide can be explored in detail due to the availability of tunable laser sources, while in the other two cases, only discrete studies at particular wavelengths are feasible. In the second place, despite the structureless shape of the methyl iodide *A* band, quasi-selective excitation of any of the three bright states is possible, while in the other methyl halides, the three states are highly overlapped across the spectral range. Spectroscopic convenience is also related to the existence of a variety of readily accessible $(2+1)$ REMPI schemes for all possible products of the reaction, the methyl radical $CH_3(\tilde{X}^2A_2)$, the ground state iodine atom $I(^2P_{3/2})$ and the spin-orbit excited $I^*(^2P_{1/2})$. The second absorption band of CH_3I, also named *B* band, possesses a completely different character, and consists of transitions to lifetime broadened bound states of Rydberg character. It is an interesting example of predissociation where lifetimes critically depend on the details of the coupling to the dissociative continuum. The importance of methyl iodide in the field of photodissociation dynamics cannot be reduced to a role of testing bench. The CH_3I photodissociation process possesses its own dynamical interest, which can be explained in terms of molecular structure considerations. The C_{3v} symmetry of methyl iodide can be easily lowered to C_s with low-energy vibrations. Such change in geometry dictates the whole photochemistry both in the *A* and *B* bands, enabling curve crossings that would not be possible in C_{3v}.

In the chapter, we will describe recent results of the prompt ($\approx$ 100 fs) CH_3I and $(CH_3I)_2$ dissociation in the *A* band and the slower predissociation ($\approx$ 1 ps) in the *B* band, studied through the combination of ultrashort tunable pump-probe laser schemes with detection of velocity map ion and electron images (see Fig. 4.1 for a

view of the relevant potential energy curves). Attention will be paid to some crucial issues that are sometimes overlooked, like the applicability of REMPI schemes in ultrafast experiments, the role of laser-induced molecular alignment, or the influence of the optical coupling window on reaction "clocking" times. Additionally, we will show how these processes can be dramatically altered by the presence of a nearby molecule. The CH_3I molecule possesses a significant permanent dipole moment and readily forms clusters for sufficiently high densities and low temperatures. This chapter will show the dramatic effects of dimerization on the dissociation dynamics.

4.2 Methodology

4.2.1 The Experiment: Femtosecond Velocity Map Imaging

One of the central ingredients of the experimental strategy employed here is the use of the velocity map imaging technique, presented for the first time by Eppink and Parker in 1997 [6]. This technique permits full three-dimensional (3D) spatial resolution of the velocity distribution of charged particles, which, coupled to femtosecond pump-probe detection, leads to a complete real time elucidation of the dissociation event. Figure 4.2 shows a typical sketch of the experimental setup.

The irradiation configuration and pulse parameters (central wavelengths and energies) are chosen as a function of the experiment performed as variants of a single main rig. For most of the experiments described here the laser was a Spectra-Physics amplified Ti:sapphire system delivering 80 fs, 1 mJ pulses centered at 800 nm with 1 kHz repetition rate, but some of the later experiments (B-band) were performed with an upgraded system (50 fs, 3.5 mJ). For two-pulse experiments, the fundamental output is split into two arms, one of which is used to pump an optical parametric amplifier (OPA) tuned to generate signal pulses in the 1.2 μm–1.4 μm region, which are later frequency quadrupled to constitute a ∼3 μJ beam in the 300–340 nm region for $(2+1)$ REMPI probing of either I atoms or CH_3 fragments. In the non-resonant experiments, the OPA is not used and the ∼ 800 nm beam constitutes the probe beam, which is later recombined with the pump beam. The pump beam is generated by harmonic generation (third harmonic for the A-band, fourth for the B-band) of the second arm of the fundamental output, yielding 266 nm or 200 nm, respectively. A computer-controlled, motorized delay stage in the pump arm provides controllable delay between the pump and probe pulses with around 0.3 fs step.

For A-band studies in CH_3I, performed with a third-harmonic pump pulse, the time duration of the pump and probe pulses is estimated to be around 100 fs, limited by a ∼ 200 fs cross correlation. Later B-band studies, pumped with the fourth harmonic at 200 nm, showed a ∼ 400 fs cross correlation. The bandwidth of both pump and probe lasers is ∼ 3 nm full width at half maximum (FWHM), except the 200 nm beam used for B-band studies, with a bandwidth of only ∼ 0.3 nm FWHM. Independent polarization control in each arm is provided by the use of half-wave plates, and telescopes are used to control their focusing geometry on target. The

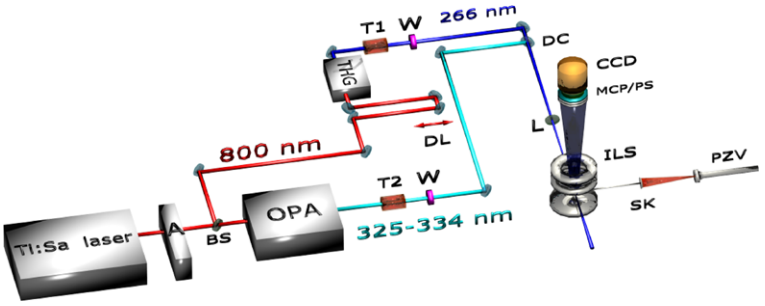

Fig. 4.2 Schematic representation of the setup for femtosecond time-resolved velocity map imaging experiments. A Ti:sapphire amplified laser system is split into two arms that provide the frequency-tripled pump beam (266 nm) and the tunable probe beam [325–334 nm, output of an optical parametric amplifier (OPA)]. (BS) Beam splitter. (A) Autocorrelator. (W) Half-wave plate. (T1, T2) Telescopes. (L) Lens. (DC) Dichroic mirror. (DL) Delay line. (PZV) 1 kHz piezoelectric valve. (SK) Skimmer. (ILS) Ion lens system. (MCP) Microchannel plate. (PS) Phosphor screen. (CCD) Charge-coupled device camera. Copropagating pump and probe femtosecond pulses are focused in the CH_3I/He molecular beam. The 3D distribution of a given fragment ion is extracted, accelerated, and projected on an imaging detector consisting of a MCP/PS coupled to a CCD camera, where the velocity map images are recorded as a function of pump-probe delay time

pump and probe laser beams are propagated into the vacuum chamber collinearly and focused with a 25 cm focal length lens into the interaction region of the chamber. Their polarization is kept parallel to the detector face to provide the cylindrical symmetry required for the procedure of Abel inversion of the ion images.

The vacuum chamber is divided into three sections: source, ionization, and detection, with differential pumping between the source chamber and the other two. The molecular beam is generated by supersonic expansion of the sample. CH_3I, kept at a temperature of 0 °C or below in ice/water or ice/salt baths, is seeded in Ar or He, at a typical total pressure of 1.5–2.5 bars, depending on signal levels, and expanded into vacuum through the 0.5 mm nozzle diameter of a 1 kHz piezoelectric home-made pulsed valve. The choice of temperature, buffer gas pressure and temporal section of the gas pulse allows control of the degree of clustering. Experiments devoted to CH_3I monomer dissociation were conducted under conditions where no clustering occurred. The molecular beam passes through a 0.5 mm skimmer that separates the source chamber from the ionization chamber. Once in the ionization chamber the molecular beam flies between the repeller and the extractor plates of a gridless ion lens electrode system, where it is intersected perpendicularly by the laser beams. The ions created in the interaction region are extracted perpendicularly towards a 60 cm time-of-flight tube at the end of which sits the detector, a dual microchannel plate (MCP) in Chevron configuration coupled to a phosphor screen. Appropriate voltages to the electrodes are applied so that velocity mapping configuration [6] is achieved, *i.e.*, all ions with the same initial velocity vector are mapped on the same point on the plane of the detector, regardless of their original position. Optimum velocity mapping conditions were obtained with $V_{\text{extractor}}/V_{\text{repeller}} = 0.785$ at $V_{\text{repeller}} = 5200$ V. By applying a gated voltage to the

front plate of the MCP, its gain is gated, so that a selective detection of ion masses can be achieved. The two-dimensional (2D) mass-selected ion images on the phosphor screen are recorded with a Peltier-cooled 12-bit CCD camera and stored in a computer. The velocity, and thus the kinetic energy, of the ions, was calibrated using methyl images produced in the A-band photodissociation of CH_3I for a long time delay between the pump and probe pulses, using the known kinetic energy release of the $CH_3(v=0) + I^*(^2P_{1/2})$ and $CH_3(v=0) + I(^2P_{3/2})$ channels [4]. In these conditions, the kinetic energy resolution of the apparatus is better than 100 meV at 1 eV kinetic energy release.

Raw images are projections of the Newton spheres characteristic of the photodissociation process on the plane of the detector. They can be Abel-inverted [7] in the case of cylindrical symmetry, which is guaranteed if the polarization axes of all lasers employed are parallel to the plane of the detector. The method used for inversion was pBasex [8], where polar coordinates are applied for the inversion. This way, the noise produced in the mathematical procedure is concentrated in the middle of the image, allowing a clean analysis of the images in the regions of interest.

Time zero, defined as the position of temporal overlap between the pump and probe lasers on target, and also their cross-correlation function, are given by the *in situ* measurement of either the parent ion transient of N,N-diethyl aniline by $(1+1')$ REMPI [4] or through multiphoton ionization of Xe [9].

The energy balance for the photodissociation of CH_3I is given by

$$h\nu - D_0 + E_i(CH_3I) = E_i(CH_3) + \mathrm{ESO}[I(^2P_{j/2})] + E_{\mathrm{kin}}(CH_3) + E_{\mathrm{kin}}(I), \quad (4.1)$$

where υ is the frequency of the photolysis laser, $D_0 = 2.41 \pm 0.03$ eV [10] is the dissociation energy of the C–I bond, $E_i(CH_3I)$ is the internal energy (rotation and vibration) of the parent molecule in the molecular beam, $E_i(CH_3)$ is the internal energy of the CH3 fragment, $E_{\mathrm{SO}}[I(^2P_{j/2})]$ is the spin-orbit energy for the iodine atom in the 2P state (for I, $E_{\mathrm{SO}} = 0$ and for I*, $E_{\mathrm{SO}} = 0.943$ eV) [10], and $E_{\mathrm{kin}}(CH_3)$ and $E_{\mathrm{kin}}(I)$ are the center-of-mass kinetic energies of the methyl and iodine fragments, respectively, which are linked by the momentum conservation law that translates into

$$m_I E_{\mathrm{kin}}(I) = m_{CH_3} E_{\mathrm{kin}}(CH_3). \quad (4.2)$$

The angular distributions for each fragment channel, obtained by radial integration of the corresponding images, have been fitted to the commonly used expression for one-photon dissociation and $(2+1)$ REMPI detection processes [11–13]:

$$I(\theta) = \frac{\sigma}{4\pi}\left[1 + \beta_2 P_2(\cos\theta) + \beta_4 P_4(\cos\theta) + \beta_6 P_6(\cos\theta)\right] \quad (4.3)$$

where θ is the angle between the photofragment recoil direction and the photolysis laser polarization direction, σ is the absorption cross section (since the experimental setup has been not calibrated for total intensities, σ is treated as a normalization fitting parameter), β_i are anisotropy parameters which reflect the dissociation dynamics and the photofragment polarization, and P_i are the Legendre polynomials of i^{th} order. If no photofragment polarization is expected, Eq. (4.3) can be truncated in $i = 2$, and in that particular case, β_2 coincides with the anisotropy parameter, β.

4.2.2 The Multidimensional Analysis

This section is devoted to details concerning image analysis for the particular case of velocity map charged particle images. It is common that the analysis of such data is carried out using methods that involve cuts or partial integrations through the multidimensional data. As a consequence, in many instances, the full information that can be extracted from the data is not totally and accurately recovered. A home-made procedure developed in our group [9] for the complete multidimensional fit of this type of data will be described here. This procedure has proven to be crucial for the extraction of all the relevant information from the images if, in addition, the temporal dimension is included, as it is the case in time-resolved velocity map imaging experiments. Some examples can be seen in [14, 15]. The key advantage of the method consists of its capability to distinguish the different overlapped contributions present in the set of images corresponding to different reaction channels of interest from secondary signals arising from other pathways.

Briefly, the method consists of an application of the well-known Levenberg–Marquardt nonlinear regression method [16–18] to n-dimensional data, but adapted to the particular case of velocity map images to find a balance between calculation speed, accuracy, and human-guided input. The procedure assumes that each image contains the sum of a number of "contributions" (related to each of the mechanisms producing a given species with a certain speed distribution). Each contribution is parameterized as a function of all variables (radius and angle for each image, but also time, for instance, to fit a time-dependent series of images) with a test functional form with physical meaning using a sufficient number of adjustable parameters. The first test functions are chosen guided by the known physical properties of the system. The least-squares procedure is then applied to the complete data collection. Inspection of the residuals (typically, also in image format), guides the choice of the second set of functional forms. An iterative procedure of this kind allows the complete parameterization of the data, and from this, quantities such as decay times, anisotropy parameters, etc. can be obtained for each contribution, with estimates of error bars. For those cases where the initial guesses for the parameters or functional forms are misguided (on the number or nature of the contributions to the image, on the time behavior of anisotropy, etc.), discrepancies can be detected easily through the use of the analysis of the residuals. It is important to note that the multidimensional nature of the fit allows the discrimination of the different contributions to the images, in a manner that a reduced-dimensionality analysis cannot achieve. In addition, there is no conceptual problem to extend the fitting procedure to n dimensions, the only limitation being computational time restrictions to analyze large quantities of data. Once the procedure has yielded an analytical expression for the complete set of data, the behavior of each "contribution" can be analyzed separately.

A typical image acquired in this type of experiments, either raw (through slice imaging), or, equivalently, mathematically inverted (through velocity-map imaging), contains, in general, a set of "contributions", by which we mean each of the possible processes or channels associated with a given type of charged particle (ion or photoelectron). Typically, a "channel" is characterized by a given kinetic energy, which,

on the image, can be measured by the distance to the center of the image, r. For the analysis of the kinetic energy distribution (ignoring the angular character), integration over the 2π angular range of the images is carried out. The signal $S(v,t)$, depending on speed (v) and time (t), is assumed to be composed of individual contributions $C_i(v,t)$, each of which has its own temporal shape as a function of time, $i(t)$, and speed distribution, $R_i(v)$. However, $C_i(v,t)$ does not need to be separable, in the sense that some of the parameters of $R_i(v)$ may be allowed to depend on time. It is assumed, in general, that these contributions do not interfere with each other, so that $S(v,t) = \Sigma_i C_i(v,t)$. Such contributions can be modeled, for instance, by asymmetric-Gaussian functions such as

$$R(v) = e^{-4\ln 2[(v-v_0)/\sigma_r]^2} H(v - v_0) + e^{-4\ln 2[(v-v_0)\sigma_l]^2} H(v_0 - v) \tag{4.4}$$

where v_0 is the position of the peak, σ_r and σ_l are the right and left widths, respectively, and $H(v)$ is the Heaviside function. The physical meaning of the asymmetry in the peaks of the speed distribution is related in most cases to the rotational temperatures of both the parent molecule and the nascent fragment, convoluted by the apparatus response function. The temporal behavior can show different functional forms depending on the type of mechanism. For the non-resonant multiphoton ionization detection, it defines a cross-correlation-type signal. For the cases where no changes in the shape of each contribution are expected as a function of time, we can write

$$C_i(v,t) = i(t) \times R_i(v) \tag{4.5}$$

The angular distribution of charged particles for a given radius provides additional information on the nature of the channel. For the type of analysis that we are describing, it simply adds another layer of complexity. Legendre polynomials, $P_n(\cos\alpha)$, represent a complete angular basis set, which has the advantage that only few terms β_n are generally sufficient to describe the anisotropy of each contribution. The anisotropy A can be written as

$$A(\alpha) = 1 + \beta_2 P_2(\cos\alpha) + \beta_4 P_4(\cos\alpha) + \cdots \tag{4.6}$$

where α is the angle between the polarization axis of the electric field and the considered direction.

In practice, a strategy that has proven most useful as a pre-treatment of the experimental data is to perform partial angular integration of the set of images in 10° steps. This way, for the 90° quadrant relevant if cylindrical symmetry holds, nine speed distributions are extracted from each image corresponding to the different angular ranges. These are stored in a 3D matrix with the dimensions speed, angular section, and time.

For best results, it is common that a global fit to all experiments performed in identical conditions is carried out. In that case, each experiment is labeled in order, and the label is taken as an additional "dimension" for the fit. Such strategy takes into account that some of the parameters (relative intensity of the multiphoton processes, time of temporal overlap, etc.) may have differing values among experimental runs, but some others (decay times, for instance) must all share a given value.

Finally, the Levenberg–Marquardt nonlinear regression method is applied to fit the parameters in the "constructed" images for least discrepancy with the experimental set of data. This methodology has proven extremely efficient for the extraction of meaningful values for physical parameters (temperatures, anisotropy parameters, population level distributions, lifetimes, cross-correlations) from the complex data provided by extended sets of images acquired in experiments.

4.3 The *A* Band

The decomposition dynamics of CH_3I upon UV photon absorption in the *A* band constitutes one of the most extensively documented cases of the consequences of non-adiabatic surface-crossing in molecular dynamics. Electronic non-adiabatic interactions, which involve the breakdown of the Born–Oppenheimer approximation, are ubiquitous and considerable theoretical and experimental efforts have been made to characterize the broad variety of possibilities. In particular, conical intersections in polyatomic molecules attract special interest [19, 20], partly because they have been identified as candidates for control under strong laser fields [21]. The effect of a conical intersection can be quite complex since it does not need to be energetically accessible to affect the molecular dynamics [22]. When the conical intersection lies close to the Franck–Condon region, as in the case of the alkyl halides in general and in CH_3I in particular, [23] the strong interaction between the involved states plays a major role on the dissociation dynamics.

The CH_3I *A*-band constitutes the lowest-energy absorption feature of the molecule and consists of a broad featureless continuum ranging from 210 to 350 nm with a maximum at about 260 nm [24]. As was first demonstrated by Mulliken and Teller [25], the lowest energy electronic excitation in CH_3I corresponds to an n–σ transition, where a non-bonding p electron of iodine is promoted to the lowest energy available anti-bonding molecular orbital [25]. The spin-orbit (SO) coupling is large, due to the presence of the heavy iodine atom, and the SO configuration can be used for the first excited electronic states [26]. Three SO states are accessible through dipole allowed transitions from the ground state: the $^3Q_1$ and $^1Q_1$ states (in Mulliken's notation) [27] through weak perpendicular transitions and the $^3Q_0$ state through a strong parallel transition [28]. The $^3Q_0$ state correlates adiabatically with $CH_3(X^2A_2) + I^*(^2P_{1/2})$ products, while the $^3Q_1$ and $^1Q_1$ states correlate with $CH_3(X^2A_2) + I(^2P_{3/2})$. From now on we will use I* and I to refer to $I^*(^2P_{1/2})$ and $I(^2P_{3/2})$, respectively, and just CH_3 to refer to $CH_3(X^2A_2)$. At the curve maximum, around 260 nm, the absorption is dominated by the $^3Q_0$ state, while transitions to the $^3Q_1$ and $^1Q_1$ states become more important towards the low energy (red) and high energy (blue) regions of the absorption band, respectively [27, 29]. The asymptotic correlation between excited surfaces and photoproducts implies that a curve crossing between the $^3Q_0$ and $^1Q_1$ states must take place close to the Franck–Condon region.

Structurally, the non-adiabatic curve crossing implies a reduction of the molecular symmetry from C_{3v} to C_s caused by e-type vibrations during the absorption

step [30, 31]. In the C_{3v} geometry, the different symmetries of the $^1Q_1(3E)$ and $^3Q_0(^2A_1)$ states disable any possible crossing. In the reduced symmetry C_s geometry, the $3E$ state splits into $4A'$ and $2A''$ components, whilst the symmetry of the $2A_1$ state is lowered to $3A'$. The avoided crossing between the distorted $3A'$ and $4A'$ states gives rise to a conical intersection. The position of the crossing point reported in the literature is strongly dependent on the level attained in the theoretical calculations.

An important feature of CH_3I dissociation in the A band, as evidenced experimentally [32], is that approximately 90 % of the available energy appears as fragments' kinetic energy, although a substantial vibrational excitation in the umbrella mode (ν_2) of CH_3 has been found. This is expected from the dramatic geometrical change of CH_3 upon dissociation, from pyramidal to planar. Excitation in the CH_3 symmetric stretch mode (ν_1) has been observed too. Methyl fragments in correlation with the ground state $I(^2P_{3/2})$ atom appear with a higher internal energy content, both vibrational and rotational than those formed in correlation with spin-orbit excited $I^*(^2P_{1/2})$.

4.3.1 Reaction Clocking: The Resonant Experiment

This section will describe experiments of the "clocking" type, *i.e.* where the reaction times for the multiple channels are the observables of interest. In the basic experiment, a pump laser is employed to promote the parent molecule to a particular excited state. A second laser, tuned to a resonant transition of a particular photoproduct, is sent to the interaction region after a controllable delay, and ionizes the product fragment of interest. The resonant probe laser opens up an optical coupling region in the potential energy surface determined by the laser bandwidth, which allows the clocking of the reaction from the initial wave packet formed in the Franck–Condon region to the free fragments in the asymptotic region. Since A-band photofragmentation happens along purely dissociative surfaces, the dynamics are of "ballistic" nature, and the signal appearance is delayed with respect to the zero of time, at a delay time that we will call the "clocking" time. The plot of the fragment ion signal intensity versus the delay between the laser pulses can typically be fitted to a Boltzmann sigmoidal curve of the form

$$S \propto \left\{1 + \exp\left(\frac{t - t_0}{t_C}\right)\right\}^{-1} \tag{4.7}$$

parameterized by a center temporal position t_0 (*i.e.*, delay time for which the intensity has reached half its asymptotic value) and a rise time constant t_C, which describes the steepness of the rise. Relative reaction times of the different channels can be defined through the differences in the center temporal position for their rise curves. Absolute determination of reaction delay times can be determined through an external reference in an independent experiment, and are subject to greater uncertainty.

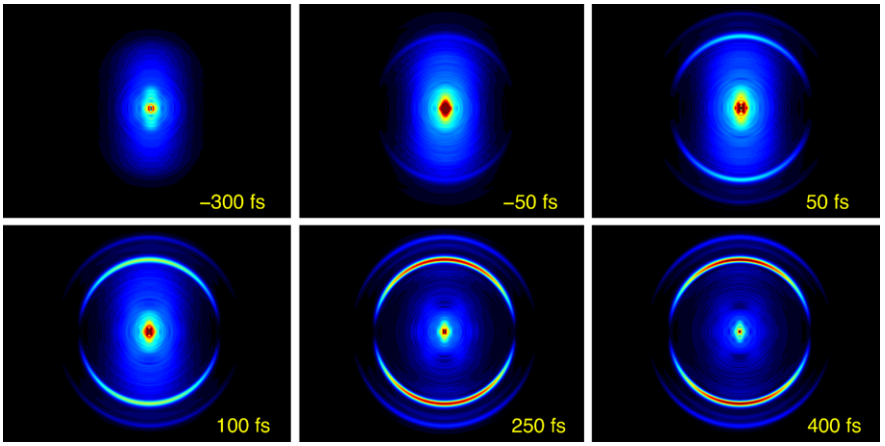

Fig. 4.3 Abel inverted CH_3^+ images obtained upon CH_3I excitation at 266 nm and CH_3 $(2+1)$ REMPI at 333.5 nm—Q branch of the $3p_z(^2A_2'' \leftarrow {}^2A_2'')0_0{}^0$ transition—-as a function of pump-probe delay time. The central structure is due to multiphoton ionization processes. Three well-defined rings appear in the image for positive delay times. The inner and outer rings correspond to vibrationless $CH_3(\nu = 0)$ formed in correlation with spin-orbit excited $I^*(^2P_{1/2})$ and ground-state $I(^2P_{3/2})$ fragments, respectively. The middle ring corresponds to the channel yielding symmetric stretch mode excited $CH_3(\nu_1 = 1)$ in correlation with the $I(^2P_{3/2})$ fragments

Upon photodissociation of methyl iodide in the A band, the appearance of either atomic iodine or CH_3 fragments can be probed by using their $(2+1)$ REMPI schemes. As a first example, we will show the results of methyl detection when photodissociation is produced at 266 nm. Probe central wavelengths are in the region 320–335 nm and can be tuned to probe the desired components of the nascent CH_3 vibrational wave packet.

Figure 4.3 shows a series of six Abel-inverted images corresponding to methyl fragments measured for different pump-probe delay times when the probe laser is tuned to 333.5 nm, corresponding to the Q branch of the $3p_z(^2A_2'' \leftarrow {}^2A_2'')0_0{}^0$ transition. The first image, acquired at -300 fs, corresponds to the situation where the probe pulse temporally precedes the pump. The unstructured contribution in the center of the image (*i.e.*, low kinetic energy), has been attributed to multiphoton ionization processes. As the pump-probe delay is increased, the appearance of rings indicates the occurrence of reaction channels with a well defined kinetic energy. Since the process is direct and takes place along a purely repulsive surface, the process is fast and can be considered completely terminated (or "asymptotic") after a time delay of approximately 400 fs.

Three rings can be observed in the images. The inner, and most intense ring, and the outer ring correspond to vibrationless $CH_3(\nu = 0)$ formed in correlation with I^* and I, respectively. It is important to note that a third, weaker ring, can be seen between the two main ones. This can be assigned to CH_3 with one quantum in the ν_1 symmetric stretch mode, in correlation with I, as derived from the measured kinetic energy. $CH_3(\nu_1 = 1)$ is visible in this experiment, contrarily to

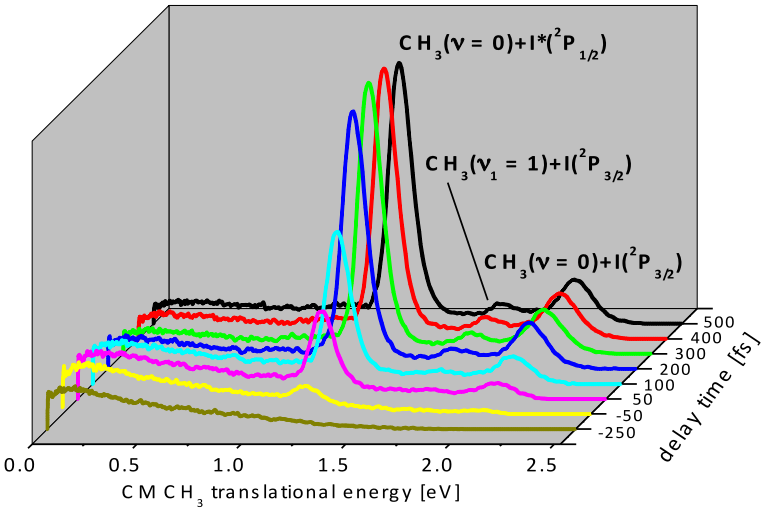

Fig. 4.4 Center-of-mass kinetic energy distributions of CH_3 upon 266 nm photodissociation of CH_3I and a $(2+1)$ REMPI process of methyl at 333.5 nm, which excites the vibrational components $0_0{}^0$ and $1_1{}^1$ of the $3p_z(^2A_2'' \leftarrow {}^2A_2'')$ Rydberg transition. The peaks correspond to the three rings in Fig. 4.1. Vibrationless methyl is visible, formed in correlation with ground $I(^2P_{3/2})$ and spin-orbit excited $I^*(^2P_{1/2})$ fragments. Methyl with one quantum in the symmetric stretch mode $\nu_1 = 1$ formed in correlation with $I(^2P_{3/2})$ is also measurable as an intermediate, weaker peak in the distributions. The results are shown as a function of the pump-probe delay time

nanosecond experiments, because the Q branch of the $3p_z(^2A_2'' \leftarrow {}^2A_2'')1_1{}^1$ transition is shifted only by 0.4 nm to the red of the $3p_z(^2A_2'' \leftarrow {}^2A_2'')0_0{}^0$ transition; that is, well within the bandwidth of the femtosecond probe laser centered at 333.5 nm. This phenomenon is quite general when performing REMPI experiments with broadband femtosecond laser pulses, where all transition resonances that lie within the bandwidth of the probe pulse can be strongly enhanced and contribute to the observed signals [4, 33].

Angular integration of the images shown in Fig. 4.3 renders the center-of-mass (CM) translational energy distributions of the CH_3 fragment, which are shown in Fig. 4.4. The three peaks in the distribution profile correspond to each of the rings present in the images of Fig. 4.3. The width of the peaks is mainly due to the rotational envelope of the probed rotational distribution, with considerably hotter character for the $CH_3(\nu = 0) + I(^2P_{3/2})$ channel than for the $CH_3(\nu = 0) + I^*(^2P_{1/2})$ channel, in agreement with previously reported results [34, 35]. Additionally, the distributions shown in Fig. 4.4 provide the branching ratio between the I and I* channels (I/I*) in correlation with vibrationless methyl. An asymptotic value of 0.11 ± 0.02 was obtained, in agreement with previous works [36–38].

Radial integration of the images across the radii corresponding to each of the rings yields angular distributions for each channel. For one-photon transitions, and in the absence of fragment alignment, we expect an angular dependence of the form $I(\theta) = (\sigma/4\pi)[1 + \beta P_2(\cos\theta)]$, where σ is the total absorption cross sec-

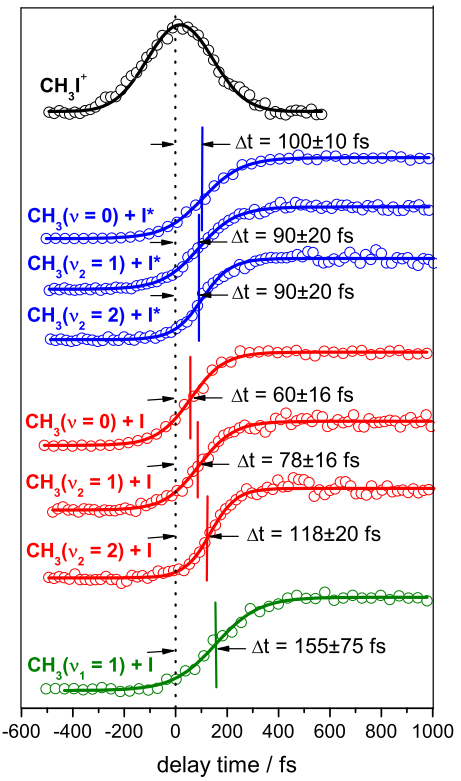

Fig. 4.5 CH_3 transients corresponding to the dissociation channels yielding $CH_3(\nu)$ in different vibrational states ($\nu = 0$, $\nu_1 = 1$, $\nu_2 = 1$ and $\nu_2 = 2$) in correlation with I and I*. The reaction times (with statistical uncertainties) are indicated in each transient. A transient corresponding to the parent molecule CH_3I^+ defining the time zero is also depicted (Color figure online)

tion, θ is the angle between the polarization axis of the photolysis laser and the fragment velocity vector, β is the anisotropy parameter, and $P_2(\cos\theta)$ is the second order Legendre polynomial. From least-squares fits to this function, asymptotic values (*i.e.*, for a long pump-probe delay time) obtained for the β parameter are 1.89 ± 0.05, 1.69 ± 0.05, and 1.84 ± 0.08 for the $CH_3(\nu = 0) + I^*(^2P_{1/2})$, $CH_3(\nu = 0) + I(^2P_{3/2})$, and $CH_3(\nu_1 = 1) + I(^2P_{3/2})$ channels, respectively, in good agreement with previous values reported in the literature. No significant changes in the anisotropy parameter are observed as a function of time with respect to that of the asymptotic region. These values could be affected by fragment alignment effects, but those are very weak for the $CH_3 0_0^0$ Q branch.

Of course the most appealing possibility of the time-resolved experiment with respect to the well understood nanosecond experiments is to watch the appearance of the fragments in the temporal window where they appear after parent molecule excitation. In order to determine the reaction times for the different channels, integration of each of the peaks in the kinetic energy distribution is performed at each time delay. Figure 4.5 shows the results obtained for the channels under study, with a more complete collection in Table 4.1 [39] at the end of this section. The figure shows that the main channel of this fragmentation reaction, yielding methyl and spin-orbit excited iodine, $CH_3(\nu = 0) + I^*(^2P_{1/2})$, takes place in approximately

100 fs. The minor channel through the non-adiabatic surface crossing, yielding $CH_3(\nu = 0) + I(^2P_{3/2})$, is complete earlier, in just 60 fs. This is expected from the higher available kinetic energy for this channel, which is translated into a larger terminal velocity and thus earlier completion. More surprisingly, the channel yielding vibrationally excited CH_3 in its symmetric stretch mode, $CH_3(\nu_1 = 1) + I(^2P_{3/2})$, is severely delayed, with a clocking time of around 150 fs.

It is interesting to note here that, as was noted by Zewail and others in seminal femtochemistry papers [2], the temporal resolution in this type of experiments is not limited by the duration of the pump and probe pulses (through their linear or nonlinear cross-correlation), but rather by the signal-to-noise ratio, and the reproducibility of the pulse temporal profiles. Sub-pulse duration temporal resolution is therefore not only possible, but routinely achieved with stable systems.

The results shown above were obtained with a probe laser centered at 333.5 nm causing a (2 + 1) REMPI transition in CH_3, corresponding to the Q branch of the $3p_z(^2A_2'' \leftarrow {}^2A_2'')0_0{}^0$ transition. Vibrationless and symmetric stretch excited methyl fragments were detected. It is well known that, upon CH_3I photolysis, the CH_3 moiety goes through a severe change in geometry, from pyramidal in the CH_3I molecule, to planar as a free fragment. As a consequence of this, an umbrella-mode (ν_2) wave packet is created in the UV photodissociation. The issue of whether C–I bond elongation precedes vibrational excitation of the methyl radical, or vice versa, could be in principle examined through the measurement of "clocking" times for different vibrational components of this wave packet. In this case, contrarily to symmetric stretch excitation, that has similar frequencies for the ground and excited $3p_z$ Rydberg state of methyl, causing the $1_1{}^1$ transition to lie spectrally close to the $0_0{}^0$ transition, the umbrella mode frequency is almost twice as large for the $3p_z$ Rydberg state than for the ground state. This causes a considerable blue shift in the resonance wavelength, which is beyond the probe laser bandwidth. By tuning the probe laser to 329.4 nm ($2_1{}^1$ transition), or to 325.8 nm ($2_2{}^2$ transition), vibrationally excited methyl with one ($\nu_2 = 1$) or two quanta ($\nu_2 = 2$) in the umbrella mode can be probed. Such an experiment was performed in the Madrid laboratory and was reported in detail in Ref. [39]. Indeed, vibrationally excited CH_3 was detected, both in pure umbrella overtones and combination bands with symmetric stretch excitation. Figure 4.5 also depicts the transients measured when detecting vibrationally excited methyl fragments.

The values obtained for the clocking of all the channels explored are shown in Table 4.1. Some of the values are consistent with arguments based solely on total available energy and final relative velocity. However, they contain an intriguing result: whereas for the adiabatic channel yielding $CH_3 + I^*(^2P_{1/2})$ the choice of the vibrational component probed does not provoke any variation of the measured clocking time, this is noticeable not the case for the non-adiabatic channel yielding $CH_3 + I(^2P_{3/2})$, where, systematically, higher-lying vibrational components seem to show a "delayed" appearance time.

These experimental results have been confronted with state-of-art theoretical calculations for the CH_3I in the A-band [39]. A wave packet model including four degrees of freedom, namely the C–I dissociation coordinate, the I–CH_3 bending

Table 4.1 Experimental and calculated absolute and relative appearance times for the different $CH_3(\nu_1, \nu_2) + I^*(I)$ dissociation channels and I/I^* branching ratios. The theoretical results are obtained applying different 4D and 3D models [39].

(ν_1, ν_2)	(0, 0)	(0, 1)	(0, 2)	(1, 0)
Experiment				
I^* channel, τ_1 (fs)	100 ± 10	90 ± 20	90 ± 20	
I channel, τ_2 (fs)	60 ± 16	78 ± 16	118 ± 20	155±75
$\tau_1 - \tau_2$ (fs)	40	12	−28	
I/I^* ratio	0.11 ± 0.02	0.45 ± 0.08	1.48 ± 0.03	
4D model				
I^* channel, τ_1 (fs)	95.5	97.1	100.9	
I channel, τ_2 (fs)	59.1	59.7	60.3	64.4
$\tau_1 - \tau_2$ (fs)	36.4	37.4	40.6	
I/I^* ratio	0.06	2.0	127	
3D model				
I^* channel, τ_1 (fs)	95.6	97.1	99.8	
I channel, τ_2 (fs)	59.1	59.8	60.6	
$\tau_1 - \tau_2$ (fs)	36.5	37.3	39.2	
I/I^* ratio	0.07	0.94	8.78	
3D model Ref. [4]				
I^* channel, τ_1 (fs)	113.8	115.6	118.5	
I channel, τ_2 (fs)	72.8	73.7	74.7	
$\tau_1 - \tau_2$ (fs)	41.0	41.9	43.8	
I/I^* ratio	0.07	0.76	4.83	

mode, the CH_3 umbrella mode, and the C–H symmetric stretch mode, has been employed to calculate the reaction times of the different dissociation channels experimentally observed. The model reproduces the experimental reaction times for the $CH_3(\nu_1, \nu_2) + I^*(^2P_{1/2})$ dissociation channels with $\nu_1 = 0$ and $\nu_2 = 0, 1, 2$, and also for the channel $CH_3(\nu_1 = 0, \nu_2 = 0) + I(^2P_{3/2})$ with notable accuracy. The model fails, however, to predict the experimental clocking times for the $CH_3(\nu_1, \nu_2) + I(^2P_{3/2})$ channels with $(\nu_1, \nu_2) = (0, 1)$, (0, 2), and (1, 0), *i.e.*, when the CH_3 fragment produced along with spin-orbit ground state I atoms is vibrationally excited. A collection of theoretical reaction times is found in Table 4.1. It seems, therefore, that the presence of the non-adiabatic crossing between the $^3Q_0$ and $^1Q_1$ surfaces causes a significant difference in the birth of the methyl vibrational wave packet in a manner that a 4D model has not been able to capture. This issue remains in darkness and shows the challenges that these time-resolved experiments in polyatomics can pose to reduced-dimensionality theoretical treatments.

4.3.2 Transition-State Imaging: The Non-resonant Experiment

It is interesting to discuss at this point the relevance of performing resonant ionization (versus non-resonant) in the probe step, given the broad spectral width and relatively high intensity of femtosecond pulses. To shed light on this issue, we will show an example for the A-band dissociation of CH_3I, described above. The methyl product formed upon the C–I bond fission is probed through ionization via two methods: resonant, $(2+1)$ REMPI, through the Q branch of the ground-to-Rydberg $3p_z(^2A_2'' \leftarrow {}^2A_2'')0_0{}^0$ transition with a 333.5 nm, as was described in the previous section, and non-resonant ionization with a moderate intensity ($\approx 10^{12}$ W/cm^2) 800 nm pulse.

Figure 4.6 shows the Abel-inverted velocity maps of CH_3 for the two experiments (non-resonant ionization in (a) and resonant $(2+1)$ ionization in (b)) in a situation where the probe laser is located at a sufficient delay so that dissociation is complete in both cases. As can be seen in the figure, the two images bear strong resemblances, with a strong inner ring that is a reflection of the $CH_3 + I^*(^2P_{1/2})$ channel, an external, weaker ring for the $CH_3 + I(^2P_{3/2})$ channel, and some intermediate structures corresponding to vibrationally excited methyl in the C–H stretch mode. It has to be noted that the overall signal intensity is considerably lower for the non-resonant experiment, even for notably higher laser intensities than in the resonant case. This is expected, due to the relatively low photon energy of the 800 nm beam, and the absence of ionization-enhancing resonances. Another important difference is the more pronounced contribution of ions with low kinetic energies that appear near the central part of the image and that are the result of competing dissociative ionization pathways. This contribution causes a decrease in contrast for the channels under study and in certain cases it may mask them beyond detection. Finally, an important consequence of the use of a non-resonant probe pulse, and one that may often be desirable, is the absence of selectivity with regards to the rovibrational components of the nascent fragments. In the case of the methyl fragment, it may quite safely be presumed that practically no selection is performed in the ionization step. Since the velocity map imaging technique allows to distinguish the degree of internal excitation through the measurement of velocities and energy conservation arguments, non-resonant probing can then be used to estimate the global energy distribution in the internal degrees of freedom of the fragments. The lack of selectivity is shown in the red curve of panel (c) of the figure, which contains kinetic energy distributions, as broadened features when compared to the resonant experiment. The difference with the resonant case, where only vibrationless methyl fragments are observed, is particularly marked in correlation with the I channel, where vibrational population inversion occurs [40]. Under the assumption that all vibrational states of methyl have the same ionization probability by the non-resonant probe laser, this result provides a direct measurement of the nascent vibrational populations. In general, this type of experiments can be employed as a measurement of the complete internal energy content of the fragment if resolution allows it.

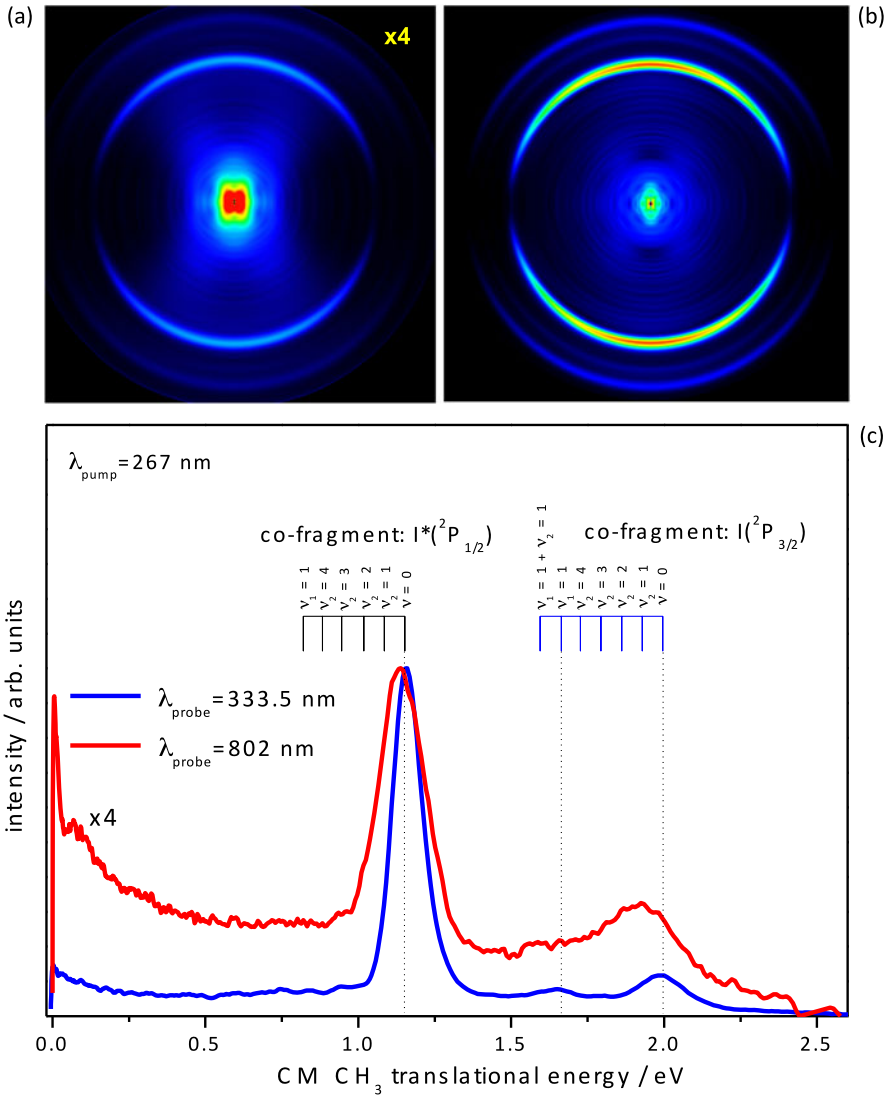

Fig. 4.6 Abel-inverted CH_3^+ images obtained upon excitation of CH_3I at 267 nm for a pump-probe delay time of 1 ps. (**a**) CH_3 detection by nonresonant multiphoton ionization at 802 nm (at least seven photons are needed). The contrast of this image has been increased by a factor of 4. (**b**) CH_3 detection by $(2+1)$ REMPI at 333.5 nm (Q branch of the $3p_z(^2A_2'' \leftarrow {}^2A_2'')0_0^0$ transition). (**c**) Asymptotic center-of-mass CH_3 kinetic energy distributions obtained at 802 nm (*red*) and 333.5 nm (*blue*) probe wavelengths together with the assignments made for the different product channels. The *curves* have been normalized to clarify the comparison

In early Femtochemistry papers [2], moderately off-resonant laser probes were identified as the key to explore the presence of transient species between reactants

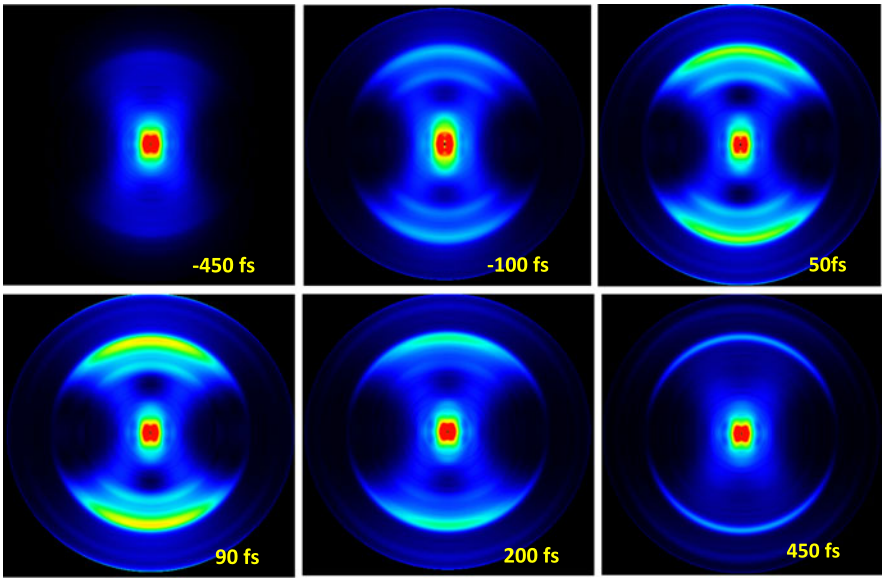

Fig. 4.7 False-color Abel-inverted CH_3^+ images obtained as a function of pump-probe delay time. Color scale is kept constant so as to highlight the changes in overall signal intensity. The image corresponding to the asymptotic case (delay time of +450 fs) is intensified by a factor of 4 with respect to the others. The most intense ring corresponds to the main $CH_3 + I^*(^2P_{1/2})$ dissociation channel. A larger radius ring, which produces a much weaker signal, can be attributed to the $CH_3 + I(^2P_{3/2})$ channel. An additional channel of lower kinetic energy (smaller radius) and strong anisotropy can be seen when pump and probe pulses overlap. The weak but clear rings that can be observed in the image taken at a delay of +450 fs corresponding to the asymptotic $CH_3 + I^*(^2P_{1/2})$ and $CH_3 + I(^2P_{3/2})$ *A*-band dissociation channels keep a similar intensity for much longer delay times

and products in the course of a photoinduced chemical reaction. The key idea was that an intermediate species would show transient resonances detuned from those of the parent or the products of the reaction. Therefore, details of the complete potential energy surfaces could be obtained from a collection of time-and-frequency resolved experiments. This idea was demonstrated for ICN and NaI [41, 42], for instance, and was at the core of the birth of Femtochemistry as a new discipline capable of observing the intermediate stages of chemical change.

A slightly different approach is presented here, where a completely off-resonance probe laser pulse is employed and information on transient species is not gained from spectral measurements, but from the recording of final kinetic energies as a function of time through the velocity map imaging technique. Figure 4.7 shows Abel-inverted CH_3 images as a function of the delay time between a UV pump that excites CH_3I to the *A*-band, and a near-IR probe at 800 nm. It is interesting to see how, for times immediately after time zero, intense contributions appear in the methyl ion images, that are not entirely dissimilar from those at the asymptotic limit. Analysis of the energy-angle-and-time resolved channels allowed us to propose that

the measurements reflect early-time dynamics of the molecular system in the *A*-band, as will be discussed below [32, 43].

The strongly enhanced signal obtained at early delay times showing a global structure with strong similarities to the asymptotic case is the main observable of this experiment. For such short times, the mechanism involves a 267 nm photon absorption in the early part of the pulse, which triggers the CH_3I *A*-band dissociation. In a fraction of molecules, the wave packet will evolve undisturbed and give rise to the neutral CH_3 and I fragments, which are amenable to be probed by a delayed 802 nm pulse at long delay times (asymptotic component). In part of the excited molecules, however, subsequent absorption of additional 267 nm photons is possible; in fact it is likely to be favoured by the presence of high-lying Rydberg states just below the ionization continuum, and only one additional 802 nm photon would be sufficient to produce CH_3I^+ in its ground state. Such $(2+1')$ process would have a strong probability due to the resonant enhancement for the 267 nm photons at one- and two-photon level, and the strong absorption probability of the 802 nm, which would produce the ion with little excess energy above the ionization potential.

Given the very rapid dissociation in the *A*-band ($\sim$ 100 fs), the transient species $[CH_3 \cdots I]^{\ddagger}$ can still absorb further 267 nm photons coming from the trailing edge of the pulse even for considerably elongated internuclear distances. If sufficient time has passed before absorption takes place, the wave packet on the *A*-band will have already split due to the early non-adiabatic crossing between the ${}^3Q_0$ and ${}^1Q_1$ surfaces, acquiring different excess kinetic energies. Upon simultaneous 267 nm and 802 nm absorption, it would be expected that the part of the wave packet evolving on the ${}^1Q_1$ surface could be promoted to the *A* excited state of CH_3I^+, which is known to undergo a fast internal conversion to the $CH_3^+ + I(^2P_{3/2})$ asymptote (ground state of the ion), and the part evolving on ${}^3Q_0$ to the *B* excited state of CH_3I^+, which would dissociate to the $CH_3^+ + I^*(^2P_{1/2})$ asymptote (see Fig. 13 of Ref. [32]).

Considering this mechanism, which is very much in the spirit of the methodology presented by Zhong and Zewail in Ref. [43], the kinetic energy finally present in the methyl ion fragment should contain two contributions. The first contribution arises from the available energy of the neutral *A*-band dissociation at a given intermediate C–I internuclear distance ($E_{\mathrm{av}}^{\ddagger}$), which will be smaller than the asymptotic available energy ($E_{\mathrm{av}}^{\mathrm{final}}$), since the wave packet cannot have reached a very long internuclear distance at the time of the second absorption (see Fig. 13 of Ref. [32]). Since the excess energy upon the ionization step will be taken by the ejected electron, the other contribution comes only from the available energy on the ionic repulsive potential surface once the wave packet has initially evolved in the neutral potential surface. The CH_3 kinetic energy shifts observed in the kinetic energy distributions shown in Fig. 4.8 indicate that the methyl fragment carries less energy close to the temporal overlap of the pump and probe pulses than in the asymptotic region (long delay time), which can be explained if the ionic dissociative surface is flatter than the neutral surface. The fact that we observe a larger shift as the delay time is shortened is an indication that the 802 nm pulse provides the time when the wave packet is frozen in the neutral dissociation surface and taken to the flatter ionic dissociative surface, where the total energy gained is bound to be lower. The broadened kinetic

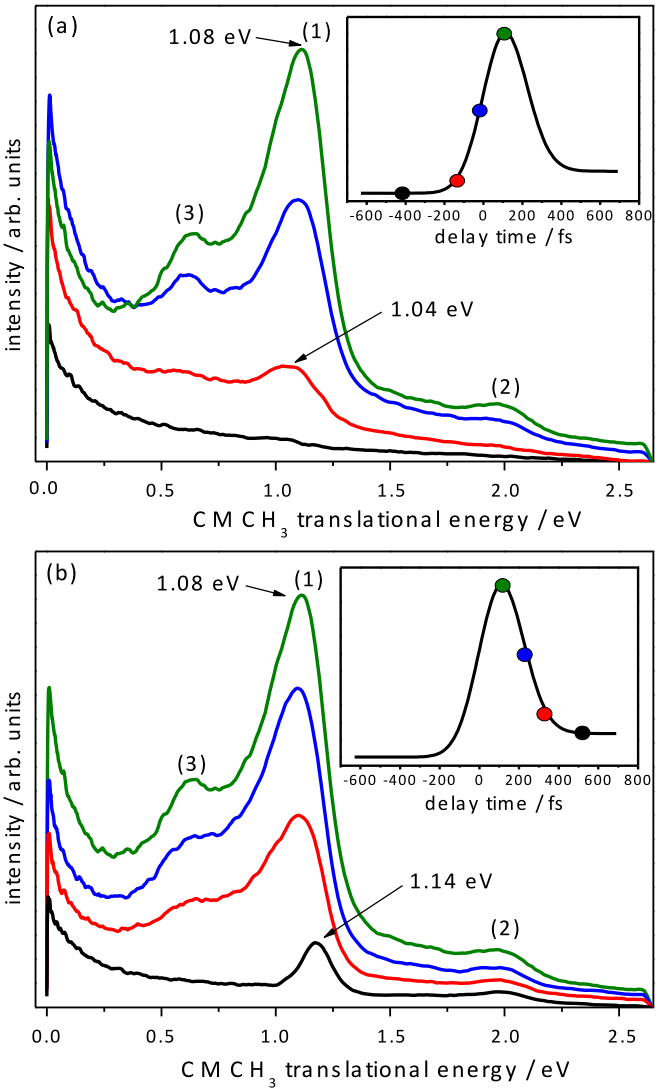

Fig. 4.8 Center-of-mass CH_3 kinetic energy distributions at selected pump-probe delay times as indicated in the *insets*, where the fitted *curve* corresponding to the transient obtained by angular integration of the ring assigned to the $CH_3 + I^*(^2P_{1/2})$ channel in the images of Fig. 4.7, is depicted along with *color circles* to clarify what delay times are represented: (**a**) from −400 to 110 fs and (**b**) from 110 to 520 fs. Peaks (1) and (2) correspond to the $CH_3 + I^*(^2P_{1/2})$ and $CH_3 + I(^2P_{3/2})$ channels, respectively. Peak (3) may correspond to a dissociative ionization channel. The labels on top of peak (1) indicate the values of the CH_3 kinetic energy at the maximum of the peak

energy distribution peaks measured for short delay times are also consistent with this mechanism, where excitation is produced in a region of the neutral dissociative

surface of rapidly changing potential, and therefore, parts of the wave packet with a range of kinetic energies will contribute for a given delay time.

The above discussion shows that a strategy based on employing an off-resonant laser probe, can go beyond the idea of finding resonances in transient species, and can profit from universal ionization at sufficiently high laser intensities, coupled to a detection technique that is sensitive to the energy content of the fragments.

4.3.3 Observation of Transient Molecular Alignment

A few words will be said here about the contribution of laser-induced molecular alignment to the fragment angular distributions observed in photodissociation processes. In general, any molecular system whose polarizability is not isotropic will show some tendency to align in the presence of an alternating electric field [44, 45], in a process where the axis of highest polarizability will tend to align along the light polarization axis. For long pulses (pulses of longer duration than the rotational period of the molecule), molecular alignment adiabatically follows the laser pulse intensity envelope, whereas for short pulses, the molecule cannot follow the envelope and, instead, coherences are created between the rotational components that give rise to recurrences, or revivals of the molecular preferential alignment [46, 47]. The two types of alignment are often termed adiabatic and impulsive alignment, respectively.

Laser-induced molecular alignment must be taken into account in all situations where the target molecule has anisotropic polarizability (as most do) and the laser intensity is high enough. In practice, typical photodissociation processes induced in the UV with moderate pulse energies are not carried out at intensities that are sufficiently high to induce an important degree of alignment. However, whenever infrared fields are added, with the purpose of inducing nonlinear effects (multiphoton absorption, Coulomb explosion, etc.), the contribution of molecular alignment to the observed angular distributions cannot be disregarded as long as the intensities are of the order of 10^{12} W/cm^2 or above.

An example of the considerations above will be shown for the case of CH_3I *A*-band dissociation, through the inspection of the angular distributions of the CH_3^+ images shown in Fig. 4.7. It is obvious simply through visual inspection that the most important contribution at times near temporal overlap between the 266 nm UV pulse and the 800 nm IR pulse is angularly narrower than the main asymptotic contribution observed at 450 fs delay. Two effects may contribute to this narrowing of the angular distribution near time zero: one is a multiphoton pump step, and the other is a dynamic alignment process of the parent molecule due to the intense 800 nm pulse [48, 49]. In order to separate these effects, a further three laser pulse experiment was performed where impulsive molecular alignment was induced using an equivalent—same energy per pulse and focusing conditions—800 nm pulse. After a controlled delay, a photodissociation experiment was performed at 266 nm, followed by an on-resonance, long delay time REMPI probing of the resulting methyl

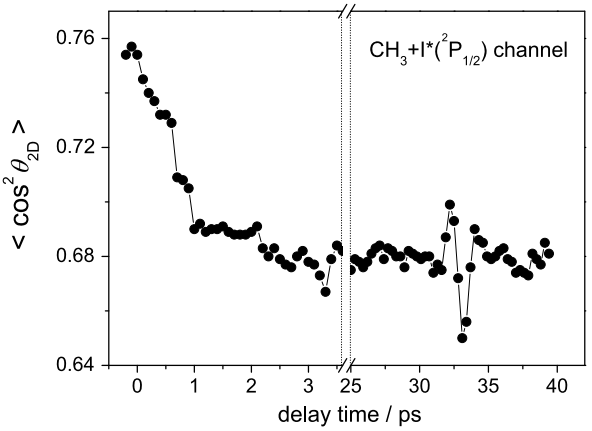

Fig. 4.9 Alignment dynamics of CH_3I represented by $\langle \cos^2 \theta_{2D} \rangle$. This quantity is derived from the intense ring in the CH_3^+ raw images assigned to the $CH_3(v = 0) + I^*(^2P_{12})$ channel measured as a function of the delay time between an IR alignment pulse (802 nm) and the excitation pulse (267 nm). The $CH_3(v = 0)$ fragment arising from the A-band photodissociation of CH_3I is probed at a long delay time (several picoseconds) by $(2 + 1)$ REMPI at 333.5 nm. The first half revival is observed at a delay time between the alignment and photolysis pulses of ≈ 32 ps, which corresponds to half of the rotational period of the molecule

fragment (as in the resonant experiment described in the first section). Figure 4.9 shows the expected value of the $\cos^2 \theta$ distribution for the main ring in the image, as a function of the delay between the strong IR pulse and the photolysis laser.

This result shows that indeed some degree of molecular alignment is obtained by the fact that, at around 32 ps, the first half revival of CH_3I is neatly observed, with the typical shape of angular recurrences. If molecular alignment were the only source of angular narrowing, it would be predicted that the variations at the half revival and at time zero should be of the same order. Therefore, the factor of 4 lower modulation observed at the revival time, compared to that at time zero indicates that, even though molecular alignment does play a partial role in the angular narrowing observed at time zero, the main attribution must be to a change in the nature of the pump laser absorption from a one-photon to a multiphoton process.

4.3.4 $(CH_3I)_2$ Dimer Photodissociation Dynamics

This section is devoted to the study of a fast photoinitiated process in a cluster through the use of a femtosecond laser pump–probe scheme and the detection of fragments in velocity map imaging conditions. Such work has been carried out on the $(CH_3I)_2$ system and constitutes the first report of its kind. A chronogram of the fragmentation process, with a detailed picture of the energy distribution including orientational features and the appearance times of the relevant channels will be presented here. As will be shown, it is demonstrated that cluster-specific behaviour

produces crucial changes even in a prompt bond fission like A-band dissociation of CH_3I.

Clusters, or aggregates, offer a unique chance to study the influence of a weakly bound environment on a photoinitiated process. The "solvent" effect does not necessarily involve subtle changes: even though, typically, inter-molecular distances in van der Waals clusters are large, several examples exist in the literature of a phenomenon known as "concerted" photochemistry, [50, 51] *i.e.* reaction routes that are only possible in clusters, since they involve reactions between constituent molecules. While concerted photochemistry is the most extreme case of cluster-specific chemistry, reactions that can take place in the isolated molecule can witness important differences when the molecule is immersed in such an environment. It is this type of study that has been undertaken, where the ultrafast ejection of a CH_3 group from a UV-irradiated methyl iodide dimer $(CH_3I)_2$ in the A-band has been analyzed and the changes with respect to the analogous process in the isolated molecule have been identified.

The expansion conditions are similar to those employed in the investigation of monomer photodissociation described above, to ensure a moderate degree of clustering, since the focus of the work is dimer dynamics, and the presence of larger clusters is undesirable. The experiment was carried out, in this case, in the middle—colder—part of the molecular beam, so that CH_3I and $(CH_3I)_2$ are the main species, with number densities of the same order of magnitude. Aggregates up to $(CH_3I)_5$ constitute a negligibly low fraction of the detected species [15].

The simultaneous presence of the monomer and the dimer has been turned to our advantage in this experiment, since the photodissociation process is amenable to study both species in only one experiment. Figure 4.10 shows the CH_3 images obtained using 267 nm pump (center of the CH_3I A-band) and 333.5 nm probe photons (for methyl detection), in monomer (Fig. 4.10a) and cluster conditions (Fig. 4.10b), acquired at asymptotic time delays. Figures 4.10c and 4.10d show the corresponding center-of-mass kinetic energy distributions. As was said above, contributions related to A-band dissociation of both the monomer and the dimer appear on the same image, due to the simultaneous presence of both species. Comparison of Figs. 4.10a and 4.10b indicates that the presence of clusters introduces three new contributions to the image. One is a broad, structureless component that can be seen approximately from 0 to ~ 3 eV and that can be fitted as the sum of two Gaussian distributions on the velocity axis, peaking at ~ 1.2 eV and ~ 3 eV. The other two are two new rings (peaks $1'$ and $2'$ in Fig. 4.10d), which appear at lower kinetic energies compared with those of the monomer (peaks 1 and 2 in Fig. 4.10d), broadened in energy and with a larger ratio between the high kinetic energy component ($I(^2P_{3/2})$ channel in the monomer) and the low kinetic energy component ($I^*(^2P_{1/2})$ channel in the monomer). For the low kinetic energy channel, the contributions from the monomer and dimer are clearly distinguishable, but this is no longer the case for the high kinetic energy channel, which appears very significantly broadened and more intense, so much that the monomer $I(^2P_{3/2})$ channel only appears as a shoulder in the high kinetic energy area of the dimer peak. The weaker $CH_3(\nu_1 = 1) + I(^2P_{3/2})$ channel (see section on A-band photodissociation) can no longer be observed in these conditions.

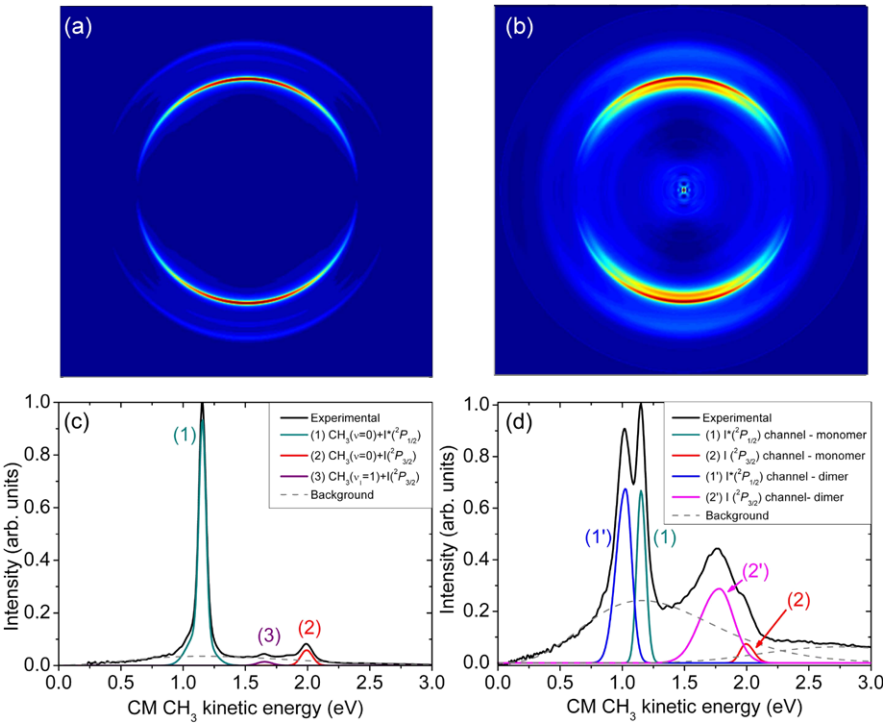

Fig. 4.10 (**a**) and (**b**) Abel inverted experimental CH_3^+ images obtained upon excitation of (**a**) CH_3I, and (**b**) a mixture of CH_3I and $(CH_3I)_2$, by two laser pulses: pump pulse at 267 nm and probe pulse, delayed by 1.5 ps, at 333.5 nm, for CH_3 $(2+1)$ REMPI. (**c**) and (**d**) Corresponding center-of-mass kinetic energy distributions of CH_3. Experimental data are shown together with simulated *curves* for the several contributions observed. The separate pump and probe laser contributions have been subtracted from the total signal in both the images and kinetic energy distributions

The experimental observations point to the idea that the two new rings observed in the CH_3^+ images correspond to *A*-band dissociation of the $(CH_3I)_2$ dimer, where the CH_3 fragment is formed in correlation with either the $[I\cdots CH_3I]$ species (high kinetic energy contribution) or the $[I^*\cdots CH_3I]$ species (low kinetic energy contribution). In this scenario, we will refer to the "$I(^2P_{3/2})$ channel" and the "$I^*(^2P_{1/2})$ channel" when describing dimer dissociation.

A-band dissociation in the dimer can appear modified for several reasons, the stabilization energy in the dimer and the different degree of rotational excitation in the outgoing fragments being the most obvious causes of change. The reduction in the kinetic energy of the CH_3 fragment in correlation with $I^*(^2P_{1/2})$ observed in this work is 0.12 ± 0.01 eV, which would correspond, in the absence of other effects, to a decrease in the total available energy of 0.13 eV. In the $I(^2P_{3/2})$ channel, we observe a shift of 0.20 ± 0.04 eV. As to the effect of rotation, it is clear from the larger energy width of the peaks associated with dimer dissociation that a sig-

nificantly larger degree of rotational excitation is present, while no distinction can be made as to whether it corresponds to the light outgoing CH_3 fragment or to the $[I/I^* \cdots ICH_3]$ co-fragment, as both imply a reduction of the total available kinetic energy.

In combination with *ab initio* calculations [15] that have produced optimized geometries for the dimer and energy values and oscillator strengths for the excited states of the *A* band of $(CH_3I)_2$, these results have provided solid understanding of the blue-shift of the *A*-band in the $(CH_3I)_2$ dimer. This shift had been reported previously and had been qualitatively understood in terms of the ground state dimer being stabilized by a dipole–dipole interaction, while the molecular dipole is weakened by the valence state transition, which involves the promotion of an electron located mainly on the I atom to an antibonding molecular orbital. With a lower dipole–dipole interaction, the dimer in the valence state will not be as stabilized as in the ground electronic state. Donaldson et al. [52] reported an experimental shift of the peak of the absorption band by around 500–1000 cm^{-1} in conditions of dimer formation with respect to monomer-only conditions. This value is compatible with the value of about 0.2 eV (1600 cm^{-1}) found here.

In addition, a significant difference in the anisotropy observed for the monomer and dimer must be noted. Through the use of the multidimensional fit procedure described in the methodology section, it has been possible to discriminate the angular character of the different contributions, with the finding that, for the $I^*(^2P_{1/2})$ channel, no loss of orientational preference happens upon dimerization, and this is in contrast with the $I(^2P_{3/2})$ channel, which shows a pronounced decrease in the observed anisotropy. The implications of this observation will be discussed below.

One more feature marks a difference between monomer and dimer dissociation results in the asymptotic situation: the dramatic increase in the $I(^2P_{3/2})/I^*(^2P_{1/2})$ ratio observed through the $CH_3(\nu = 0)$ fragment, from values of 0.14 ± 0.05 for the monomer to 0.72 ± 0.05 for the dimer. Analogous measurements were performed by tuning the probe laser to 329.5 nm and 325.8 nm, which constitute a resonant probe of $CH_3(\nu_2 = 1)$ and $CH_3(\nu_2 = 2)$, respectively (ν_2 being the umbrella mode of CH_3). A dramatic change of the $I(^2P_{3/2})/I^*(^2P_{1/2})$ ratio, in the same direction as that just described for $CH_3(\nu = 0)$, was also observed in both cases.

The decrease of the anisotropy of the $I(^2P_{3/2})$ channel in the dimer and the large change in the branching ratio need to be discussed conjointly. An increase of the $I(^2P_{3/2})/I^*(^2P_{1/2})$ ratio could be related to either a change in the main absorbing states or in the efficiency of the coupling in the non-adiabatic crossing. Since the other possibly participating states, $^1Q_1$ and $^3Q_1$, are of perpendicular nature, in contrast to the parallel $^3Q_0$ state, an examination of the change in anisotropy should permit the distinction between the two phenomena. If we consider that the $I(^2P_{3/2})$ fragment observed is originated partly through absorption to $^3Q_0$ followed by crossing to $^1Q_1$, and partly through direct absorption to one of the perpendicular states ($^3Q_1$ or $^1Q_1$), then the resulting anisotropy is expected to reflect a mixture of parallel ($\beta = 2$) and perpendicular ($\beta = -1$) character. From the observation of experimental values for the β anisotropy parameter, a

ratio of approximately 2:1 is extracted for those two routes. This is an important result, since it indicates that the participation of absorption of the perpendicular states is not negligible, as was the case for the monomer at 267 nm excitation; instead, it accounts for approximately 1/3 of the total absorption at this wavelength. However, this alone cannot account for an increase in the $I(^2P_{3/2})/I^*(^2P_{1/2})$ ratio from 0.14 ± 0.05 for the monomer to 0.72 ± 0.05 for the dimer. From the combined values of ratios and anisotropy, we conclude that the efficiency of the non-adiabatic crossing approximately doubles in the dimer with respect to the monomer.

The experimental results presented above show the richness of the information that can be obtained in relatively simple experiments. In this case, through a global approach where velocities and anisotropies are examined simultaneously, detailed information on the stabilization energy, the degree of internal energy content, the contribution of several electronic excited states to the overall absorption, and finally, the effect of dimerization on the population transfer through the non-adiabatic crossing, has been obtained.

4.3.5 Resonant Probing: The Role of the Optical Coupling Window

$(CH_3I)_2$ dimer photodissociation will be explored temporally in this section to illustrate an important feature of resonantly probed "clocking" experiments. Figure 4.11 shows the time evolution in the detection of CH_3 coming from the monomer in the $I^*(^2P_{1/2})$ channel, and also from the dimer in both the $I(^2P_{3/2})$ and $I^*(^2P_{1/2})$ channels. The time delay for free CH_3 observation is still short in the dimer ($\sim$ 220 fs), but clearly delayed with respect to monomer dissociation ($\sim$ 80 fs). If the decrease in available energy, due to the blue shift of the band, is taken into account, calculated delays of only $\sim$ 10 fs are obtained classically, indicating that this is clearly insufficient to explain the experimental measurement.

As is described in detail in Ref. [15], this case is a particularly illuminating example of the role of the probing step. In particular, it must be noted that resonant CH_3 probing is done here through a $(2+1)$ REMPI process via a Rydberg state. This is a state of spatially extended character, and during the first phases of dissociation, it is situated in the vicinity of the $[I\cdots ICH_3]$ moiety, where close-lying Rydberg states can be present. In this situation, the resonance can be significantly perturbed by the nearby presence of $[I\cdots ICH_3]$, so that the CH_3 radical would only appear as "free" after an elongated distance (i.e. time).

A simplified theoretical simulation was performed in order to assess that the delay in the measured clocking time was not due to an intrinsic difference in the photodissociation dynamics in the dimer with respect to the monomer, but to an important difference in the probing step (through the late opening of the optical coupling window) due to the extended character of the orbitals. A CASSCF calculation was performed to describe the effect of the nearby presence of the $[I\cdots ICH_3]$ species on the Rydberg electronic states of the ejected CH_3 group. A reduced model

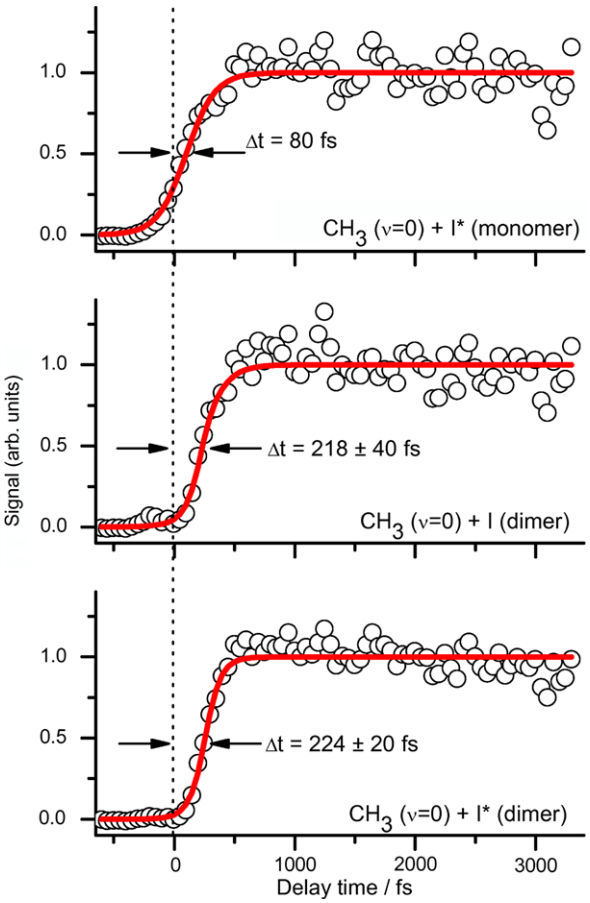

Fig. 4.11 Transients showing appearance times of the observed channels yielding $CH_3(v = 0)$ for both monomer CH_3I and cluster $(CH_3I)_2$ species. *Open circles* show the amplitudes of each of the contributions; *solid lines* show the fitted curves (Color figure online)

was employed for this purpose, where only two CH_3 groups are considered. The energy of the Rydberg $3p_z$ state was calculated as a function of the distance between the two CH_3 groups. A potential energy curve was obtained that shows significant distortion for elongated distances. This necessarily implies that the optical window for the REMPI transition employed to detect the appearance of the CH_3 fragment will not be open until the distance is sufficiently long so that this distortion is negligible (at least, of the order of the bandwidth of the probe laser). A classical 1D dynamic calculation was performed under the simplification that the CH_3 dynamics takes place on the ${}^3Q_0$ monomer surface (shifted by 0.12 eV to account for the blue shift of the band), but the probe laser absorption could only take place once the $3p_z({}^2A_2'' \leftarrow {}^2A_2'')0_0{}^0$ transition in CH_3 became resonant under the influence of the nearby presence of the other CH_3. For the estimation of the CH_3–CH_3 distances, an axial CH_3–I recoil and a head-tail geometry for the cluster were assumed. This calculation produced a delay of ~ 80 fs for the $I^*({}^2P_{1/2})$ channel with respect to the situation where distortion of the Rydberg state of CH_3

does not occur. Even though this is somewhat shorter than the experimental delay ($\sim$ 140 fs), it is clearly of the same order of magnitude, and we believe this is the main mechanism producing a delay in the apparent dissociation times for the dimer. We consider that this is a clear illustration of the fact that this effect, where a substantial delay occurs in the time opening of the optical detection window, needs to be taken into account whenever resonant probing is employed, especially for large molecules, and in particular clusters, where intermediate orbitals used for the resonant transition can be substantially modified by the nearby presence of a similar moiety.

The time-resolved work performed on the $(CH_3I)_2$ species shows that even the influence of a weakly bound environment can have profound influences on a molecular dissociation process. The phenomenon that was chosen (fast ejection of a CH_3 fragment from a $(CH_3I)_2$ dimer) would not seem prone to showing this effect, due to the extremely fast nature of the dissociation and the weak bond between the two CH_3I molecules. Nevertheless, dramatic changes both in the absorbing states and in the strength of non-adiabatic couplings between them have been detected. It is expected that these cluster-related effects will be even more important in slower processes and more tightly bound systems.

4.4 The *B* Band

The second absorption band in methyl iodide, the B band, has been by far much less studied than the more accessible A-band. It starts at around 200 nm and hence, the possibility of performing detailed spectroscopic studies with conventional lasers is restricted to the red edge of the band. The B band results from the excitation of a $5p\pi$ electron of the I atom to a $6s$ molecular Rydberg orbital. The remaining three $5p\pi$ electrons are subject to strong spin-orbit coupling, so that, in C_{3v} symmetry, the ionic core can be in the $^2\Pi_{3/2}(^2E_{3/2})$ or the $^2\Pi_{1/2}(^2E_{1/2})$ states. From the $J-j$ coupling between the ionic core states and the Rydberg electron several bound states are formed. Transitions to those related with the $^2\Pi_{3/2}(^2E_{3/2})$ core, from the ground state, constitute the B band, of perpendicular character. Discrete vibrational structure appears in the spectrum [52–56], but the lines are considerably lifetime broadened due to interaction with dissociative surfaces that belong to the A band, which causes electronic predissociation. Lifetimes of these states are in the picosecond regime and are strongly dependent on vibrational excitation in a non monotonic manner [53].

The characteristics of B-band predissociation in CH_3I, including lifetimes, anisotropy, branching ratio, and vibrational activity of the methyl fragments, have proven to be strongly dependent on the vibrational level of initial excitation in the parent molecule. The extreme sensitivity to the vibrational excitation is related to the details of the crossings between the potential energy surfaces and the spatial distributions of the wave functions at each vibrational level. Therefore, systematic measurements of the properties of this predissociation process provide challenging constraints for the theoretical description of this system. Here, we will

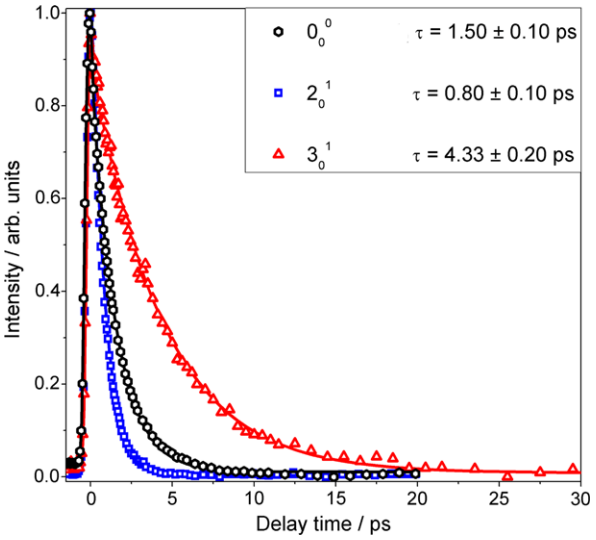

Fig. 4.12 Experimental transients corresponding to parent CH_3I decay after 201.2 nm (*black circles*, 0_0^0 band), 196.7 nm (*blue squares*, 2_0^1 band) and 199.2 nm (*red triangles*, 3_0^1 band) *B*-band excitation. Probe center wavelength was 304.5 nm. *Solid lines* correspond to the fit of the experimental data

briefly show the results obtained for three cases: the 0_0^0 transition at 201.2 nm (excitation to the vibrationless level of the Rydberg state), the 2_0^1 transition at 196.7 nm (one quantum of excitation in the umbrella mode), and the 3_0^1 transition at 199.2 nm (one quantum of excitation in the C–I stretch mode). Given the large spectral separation between these features (larger, in any case, than the laser bandwidth), the eigenstate picture is useful, since a vibronic wave packet cannot be formed.

A complete study was carried out on this system, through the time-resolved measurements of the parent ion yield, velocity map images of both the CH_3 and I fragments, obtained both with REMPI and non-resonant ionization schemes, and photoelectron imaging detection. The complete results were published in Refs. [9, 14], so here we will only review the most salient features.

4.4.1 Parent Ion Detection

The CH_3I parent decay time was measured by acquiring collections of mass-selected images as a function of delay time between the pump and the probe laser pulses. Ionization of the parent CH_3I was produced through a $(1 + 1')$ REMPI scheme. Figure 4.12 shows transients of the CH_3I^+ signal obtained for excitation at 201.2 nm (0_0^0 band), 196.7 nm (2_0^1 band), and 199.2 nm (3_0^1 band) and photoionization with a single photon of 304.5 nm. The measured lifetimes, τ, obtained through these transients, are 1.50 ± 0.10 ps, 0.80 ± 0.10 ps, and 4.33 ± 0.20 ps, respectively. As previously announced, lifetimes change drastically depending on the vibronic level and therefore on the pump wavelength.

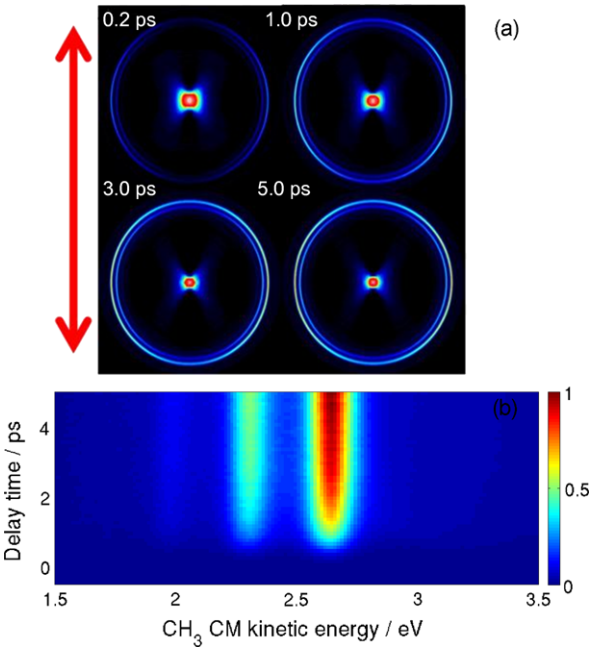

Fig. 4.13 (**a**) Sequence of Abel-inverted methyl images, in false color, for a pump-probe delay time of 0.2, 1, 3, and 5 ps for a pump laser center wavelength of 196.7 nm for B-band excitation of CH_3I to the 2_0^1 vibronic level and a probe laser center wavelength of 333.5 nm. The *double-sided arrow* indicates the polarization axes of both lasers. (**b**) 2D map of the kinetic energy distribution of the CH_3 fragment as a function of the delay time

4.4.2 Fragment Velocity Map Imaging Detection

Fragment detection (I and CH_3) was performed in velocity map imaging conditions, as a function of the delay between the pump laser pulse and the ionizing-probe pulse. Figure 4.13 shows an example of such measurement, where methyl images were acquired for a series of time delays after CH_3I excitation in the 2_0^1 transition of the B-band.

It is interesting to note that, contrarily to the dynamics expected for the A-band, caused by a prompt bond fission, in this case the appearance of the methyl fragment is mediated by a finite state lifetime, and therefore, transient behavior is expected to follow an exponential function of the form

$$S(t) \propto e^{-4\ln 2(\frac{t}{\tau_{cc}})^2} \otimes \left[\left(1 - e^{-\frac{t}{\tau}}\right) \times H(t)\right] \tag{4.8}$$

where τ is the lifetime of the initial state and τ_{cc} is the instrumental response time. It can be argued that such behavior should be temporally shifted due to the additional dissociation time along the dissociative surface. It has not been considered here because this time is negligible when compared to predissociation times in this case. Fits of the parameters in Eq. (4.8) to the integrals of the contributions visible in Fig. 4.13 provide lifetimes compatible with those obtained from parent ion yields.

As shown above for the A-band section, fragment detection with short pulses can be achieved via resonantly enhanced ionization schemes, or via non-resonant strong IR field ionization. In some cases, the application of this double approach

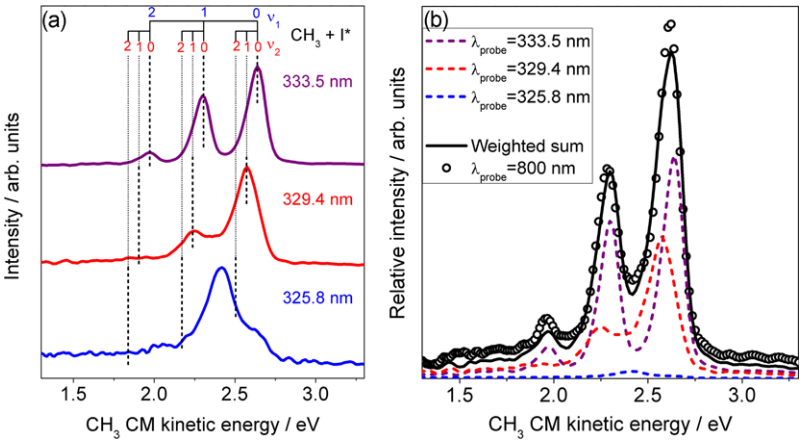

Fig. 4.14 (**a**) Center-of-mass CH_3 kinetic energy distributions measured at a pump-probe delay time of 10 ps, with a pump laser centered at 196.7 nm for B-band excitation of CH_3I to the 2_0^1 vibronic level and a probe laser centered at 333.5 nm (*top*), 329.4 nm (*middle*), and 325.8 nm (*bottom*), in resonance with the Q branch of the two-photon $3p_z(^2A_2'' \leftarrow {}^2A_2'')$ transition in CH_3 in its 0_0^0, 2_1^1, or 2_2^2 bands, respectively. (**b**) Center-of-mass CH_3 kinetic energy distribution upon B-band excitation of CH_3I at 196.7 nm to the 2_0^1 vibronic level and subsequent CH_3 non-resonant multiphoton ionization probing with pulses centered at $\approx$ 800 nm delayed by 10 ps (*open circles*). *Colored lines* contain the resonant probing distributions shown in the *left panel*, at 333.5 nm (*dashed purple*), 329.4 nm (*dashed red*), and 325.8 nm (*dashed blue*). The *solid black line* is the distribution obtained through the weighted sum of the three kinetic energy distributions for resonant CH_3 probing

allows to obtain estimates of product state distributions. We will show an example here. Figure 4.14a, shows asymptotic kinetic energy distributions for the methyl fragment formed in B-band predissociation of methyl iodide in the 2_0^1 band. The three curves correspond to the detection of methyl in its vibrationless state (0_0^0, purple curve, at 333.5 nm), one quantum in the umbrella mode (2_1^1, red curve, at 329.4 nm) and two quanta in the umbrella mode (2_2^2, blue curve, at 325.8 nm). Excitation of the symmetric stretch mode is observed simultaneously. The open circles in Fig. 4.14b contain the methyl fragment kinetic energy distribution obtained though non-resonant IR ionization. Under the assumption of similar ionization probabilities under the IR field, obtaining the best multiplicative factors for the resonant curves to fit the non-resonant curve yields estimates of nascent vibrational components of the methyl fragment [9]. As an example, Fig. 4.15 shows the relative vibrational populations extracted from the above mentioned analysis corresponding to the stretching mode excitation of the methyl fragment for the different initial vibrational states excited in the Rydberg state. The increasing vibrational activity in this mode is evident when moving from the 0_0^0 to 2_0^1 to 3_0^1 transitions.

It is interesting to note that the time-resolved velocity map imaging technique allows to monitor changes in the anisotropy of the fragment angular distribution as a function of time, and thus, in the absence of fragment alignment effects, it provides information on molecular rotation. This phenomenon has been explored for the B-

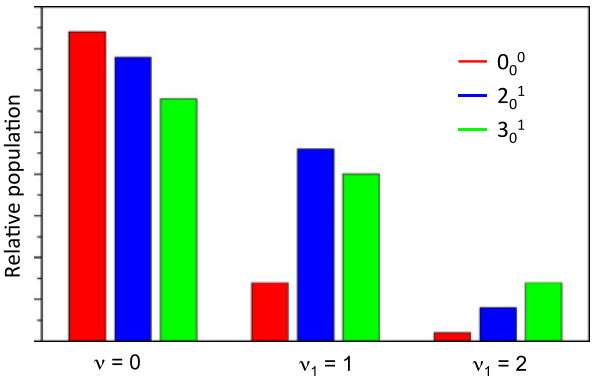

Fig. 4.15 Relative vibrational populations extracted from the fit of the data shown in Fig. 4.14 for the stretching mode of the methyl fragment arising from predissociation at the 0_0^0, 2_0^1 and 3_0^1 levels

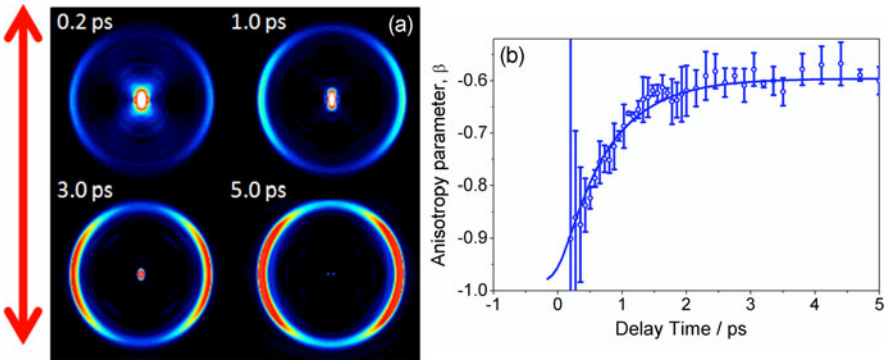

Fig. 4.16 (**a**) Sequence of Abel-inverted iodine images, in false *color*, for a pump-probe delay time of 0.2, 1, 3, and 5 ps for a pump laser center wavelength of 196.7 nm and a probe laser center wavelength of 304.5 nm. The *double-sided arrow* indicates the polarization axis of both lasers. (**b**) Experimental anisotropy transient corresponding to $I^*(^2P_{1/2})$ appearance after 196.7 nm B-band excitation of CH_3I to the 2_0^1 vibronic level. *Error bars* correspond to the standard deviation of each point obtained from the set of experimental runs (Color figure online)

band through detection of the $I^*(^2P_{1/2})$ fragment, which does not show alignment effects, because the populations of the $M_J = \pm 1/2$ must be equal [9, 57], so that its angular distribution is a reflection of parent molecular rotation.

The results of time-resolved $I^*(^2P_{1/2})$ detection can be seen in Fig. 4.16. The left panel shows iodine ion images as a function of time for the 2_0^1 transition of the CH_3I B-band. The first image, taken at 200 fs delay, shows extreme perpendicular character, with $\beta \sim -1$, reflecting the perpendicular nature of the transition. Iodine ions are thus concentrated in the equator of the sphere whose poles are defined by the polarization vector of the pump laser beam. Measuring iodine at later times shows a relaxation of this extreme anisotropy, that is, a significant number of iodine atoms appear along the poles of the sphere described above. The variation of the β parameter, defined in Eq. (4.1), as a function of time is shown quantitatively in the right panel of Fig. 4.16. The temporal scales of the anisotropy change are related to

the lifetime of the excited state, and also to the degree of rotational excitation in the parent molecule [9]. From semiclassical models, rotational temperatures of ~ 40 K are expected to account for the measured values [58, 59].

4.4.3 Time-Resolved Photoelectron Imaging

Time-resolved photoelectron velocity map imaging experiments provide additional information on the process. In this case, a pump-probe scheme has been found that allows the detection of photoelectrons originated by ionization of the parent in the excited Rydberg state (at short delay times), or those originated by REMPI of the iodine atom born after the molecule breaks (for long delays). For intermediate delays, both signals are present simultaneously and can be separated through their kinetic energies. This was achieved through a pump-probe scheme where the pump beam is centered at the desired B-band transition of the molecule, and the probe beam causes REMPI ionization in the product. In this manner, photoelectrons originated from ionization of the parent are created in a $(1 + 1')$ process, and those originated in the iodine fragment are caused by a $(1 + 2' + 1')$ process, where the first photon excites the parent molecule, and the subsequent $(2' + 1')$ process occurs in the free fragment. This is shown in Fig. 4.17, where the results corresponding to the $0_0{}^0$ and $3_0{}^1$ bands are shown in the left and right panels, respectively. In both cases, the photoelectron rings that appear most intense for short delays gradually become dimmer, with the time constant of the molecular predissociation, and the higher-radius rings due to ionization of the iodine product grow in intensity until they reach their final value, with a time constant consistent with the former. It is interesting to note that only photoelectrons due to the ionization of the iodine atom product, but not to the methyl product, are detectable, since iodine ionization is strongly enhanced due to the use of a REMPI scheme.

Photoelectron spectra obtained through angular integration of the rings in Fig. 4.17 are shown in Fig. 4.18 for early (top panels) and late times (bottom panels) for the $0_0{}^0$ band (left panels) and the $3_0{}^1$ band (right panels). In each case, they are plotted as a function of the binding energy of the corresponding species. The photoelectron spectra provide information on the initial molecular excitation, and in that sense, the results shown in panel (b) of Fig. 4.18 constitute a confirmation that the initial excitation is almost exclusively to the $\nu_3 = 1$ state. Since the potential energy surface of the B 6s [2] Rydberg state is similar to the ground state surface of the ion, transitions with $\Delta\nu = 0$ are expected to dominate [56, 60] and, therefore, the main contribution is related to the formation of CH_3I^+ with one quantum of excitation in the ν_3 mode due to initial excitation to the $\nu_3 = 1$ level of the Rydberg state. Other vibrational combinations are visible in the spectrum, but always with at least one quantum of excitation in the ν_3 mode.

As mentioned before, when acquired with a long delay time between the pump and probe laser pulses, the photoelectrons are originated from the iodine atoms resulting from dissociation. Due to the pulse bandwidth, the $(2 + 1)$ REMPI schemes

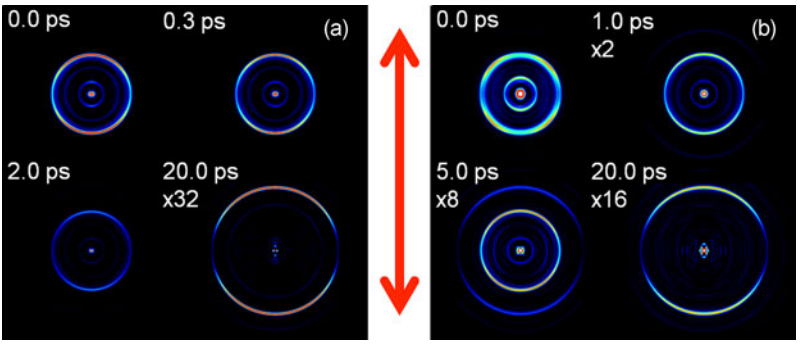

Fig. 4.17 *Left*: Sequence of Abel-inverted photoelectron images, in false color, for a pump-probe delay time of 0, 0.3, 2, and 20 ps for a pump laser center wavelength of 201.2 nm (0_0^0 band) and a probe laser center wavelength of 304.5 nm. The *double-sided arrow* indicates the polarization axis of both lasers. *Right*: Sequence of Abel-inverted photoelectron images, in false color, for a pump-probe delay time of 0, 1, 5, and 20 ps for a pump laser center wavelength of 199.2 nm (3_0^1 band) and a probe laser center wavelength of 304.5 nm. The *double-sided arrow* indicates the polarization axis of both lasers

at 304.5 nm employed are resonant for both I and I*. Evidence for I* formation is clear for both the 0_0^0 and the 3_0^1 bands; the data also suggest the minor presence of ground state iodine, which shows as a shoulder to the main I* contribution.

The combination of parent, fragment and photoelectron detection in velocity map imaging conditions, and using femtosecond pump-probe schemes with resonant and non-resonant ionization constitutes a powerful tool that can reveal the details of complex photoinduced processes, as has been shown for this case of *B*-band predissociation of CH_3I. In this case, we have measured the rapidly varying lifetimes of the vibronic states in the *B*-band, the time dependent fragment anisotropies, the internal energy content of the fragments, and we have identified new channels that had been overlooked in the past, in particular one yielding ground state iodine, and a fast channel producing spin-orbit excited iodine through direct absorption to dissociative surfaces [9].

4.5 Concluding Remarks

This chapter has presented the capabilities of femtosecond velocity map imaging schemes for the detailed description of time-resolved photodissociation dynamics and molecular photodynamics in general. The combination of femtosecond pump-probe tunable laser pulses and a 2D detection technique such as velocity mapping, and the use of selective detection of known quantum states of the product fragments using resonance-enhanced multiphoton ionization has revealed to be an excellent method through the prototype example of the CH_3I molecule, where a broad range of processes can be explored, such as direct dissociation, predissociation, the effect of conical intersections, dimerization, or laser-induced molecular alignment.

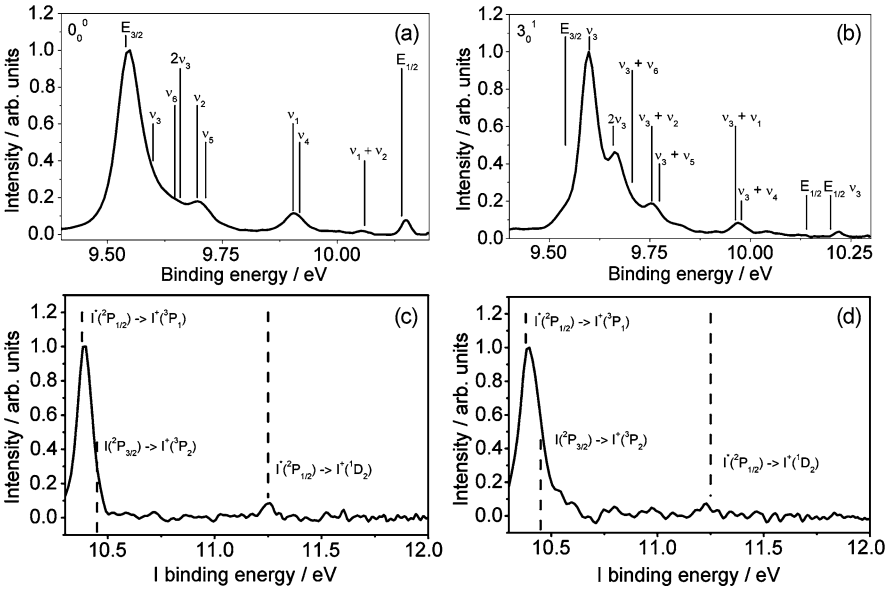

Fig. 4.18 Photoelectron spectra plotted relative to the binding energy. *Top row*: Pump-probe delay time of 400 fs (photoelectron kinetic energy distribution plotted as a function of the binding energy for the parent molecule). (**a**) Pump laser center wavelength of 201.2 nm (0_0^0 band). (**b**) Pump laser center wavelength of 199.2 nm (3_0^1 band). *Bottom row*: Pump-probe delay time of 30 ps (photoelectron kinetic energy distribution plotted as a function of the binding energy in the iodine product). (**c**) Pump laser center wavelength of 201.2 nm (0_0^0 band). (**d**) Pump laser center wavelength of 199.2 nm (3_0^1 band). In all cases, the probe laser center wavelength is 304.5 nm

Relatively minor experimental changes are required to explore other interesting phenomena with a very similar experimental scheme, like, for instance, Coulomb explosion [60, 61]. Also, the possibilities for strong-field control through the introduction of an additional IR ultrashort laser field have been explored with success [62, 63]. More and more systems are becoming amenable to be studied by femtosecond velocity map imaging, and there are now examples for small molecules like ammonia [64, 65] or larger molecules like organic chromophores [66–72]. This clearly shows the power of femtosecond velocity map imaging to investigate time-resolved molecular photodynamics.

Acknowledgements We acknowledge the contributions to the experimental and theoretical work presented in this chapter by J.G. Izquierdo, J. Durá, G.A. Amaral, J. González-Vázquez, G. Gitzinger, M.E. Corrales, G. Balerdi and A. García-Vela. This work has been financed by the Spanish MICINN and MINECO through Grants No. CTQ2008-02578, CTQ2012-37404-C02-01, the Consolider program "Science and Applications of Ultrafast Ultraintense Lasers", Grant No. CSD2007-00013, and by the European Union ITN network "Ultrafast control of quantum systems by strong laser fields-FASTQUAST" (Grant No. PITN-GA- 2008-214962). This research has been performed within the Unidad Asociada "Química Física Molecular" between Departamento de Química Física of UCM and CSIC. The facilities provided by the Centro de Láseres Ultrarrápidos (UCM) are gratefully acknowledged.

References

1. R. Schinke, *Photodissociation Dynamics* (Cambridge University Press, Cambridge, 1993)
2. M.J. Rosker, M. Dantus, A.H. Zewail, J. Chem. Phys. **89**, 6113 (1988)
3. A.H. Zewail, Pure Appl. Chem. **72**, 2219 (2000)
4. R. de Nalda, J. Durá, J.G. Izquierdo, J. González-Vázquez, L. Bañares, J. Chem. Phys. **128**, 244309 (2008). and references therein
5. A.B. Alekseyv et al., J. Chem. Phys. **134**, 044303 (2011)
6. A.T.J.B. Eppink, D.H. Parker, Rev. Sci. Instrum. **68**, 3477 (1997)
7. B.J. Whitaker, Image reconstruction: the Abel transform, in *Imaging in Chemical Dynamics*, ed. by A.G. Suits, R.E. Continetti (Am. Chem. Soc., Washington, 2000)
8. G.A. Garcia, L. Nahon, I. Powis, Rev. Sci. Instrum. **75**, 4989 (2004)
9. G. Gitzinger, M.E. Corrales, V. Loriot, R. de Nalda, L. Bañares, J. Chem. Phys. **136**, 074303 (2012)
10. A.T.J.B. Eppink, D.H. Parker, J. Chem. Phys. **109**, 4758 (1998)
11. R.N. Zare, *Angular Momentum: Understanding Spatial Aspects in Chemistry and Physics* (Wiley, New York, 1998)
12. R.N. Dixon, J. Chem. Phys. **85**, 1866 (1986)
13. T.P. Rakitzis, R.N. Zare, J. Chem. Phys. **110**, 3341 (1999)
14. G. Gitzinger, M.E. Corrales, V. Loriot, G.A. Amaral, R. de Nalda, L. Bañares, J. Chem. Phys. **132**, 234313 (2010)
15. R. de Nalda, J. Durá, J. González-Vázquez, V. Loriot, L. Bañares, Phys. Chem. Chem. Phys. **13**, 13295 (2011)
16. D.W. Marquardt, SIAM J. Appl. Math. **11**, 431 (1963)
17. Y. Bard, *Nonlinear Parameter Estimation* (Academic Press, New York, 1974)
18. N.R. Draper, H. Smith, *Applied Regression Analysis*. Wiley Series in Probability and Statistics (Wiley, New York, 1981)
19. J. González-Vázquez, L. González, I.R. Solá, J. Santamaría, J. Chem. Phys. **131**, 104302 (2009)
20. S. Nanbu, T. Ishidab, H. Nakamura, Chem. Sci. **1**, 663 (2010)
21. B.J. Sussman, D. Townsend, M.Y. Ivanov, A. Stolow, Science **314**, 278 (2006)
22. D.R. Yarkony, Rev. Mod. Phys. **68**, 985 (1996)
23. Y. Amatatsu, S. Yabushita, K. Morokuma, J. Chem. Phys. **104**, 9783 (1996)
24. A. Gedanken, M.D. Rowe, Chem. Phys. Lett. **34**, 39 (1975)
25. R.S. Mulliken, E. Teller, Phys. Rev. **61**, 283 (1942)
26. G. Herzberg, *Molecular Spectra and Molecular Structure III. Electronic Spectra and Electronic Structure of Polyatomic Molecules* (van Nostrand, Princeton, 1996)
27. R.S. Mulliken, J. Chem. Phys. **8**, 382 (1940)
28. R.S. Mulliken, Phys. Rev. **50**, 1017 (1936)
29. F.G. Godwin, C. Paterson, P.A. Gorry, Mol. Phys. **61**, 827 (1987)
30. Y. Amatatsu, K. Morokuma, S. Yabushita, J. Chem. Phys. **94**, 4858 (1991)
31. D. Person, P.W. Kash, L.J. Butler, J. Chem. Phys. **94**, 2557 (1991)
32. J. Durá, G.A. Amaral, R. de Nalda, L. Bañares, J. Chem. Phys. **131**, 134311 (2009)
33. R. de Nalda, J.G. Izquierdo, J. Durá, L. Bañares, J. Chem. Phys. **126**, 021101 (2007)
34. H. Guo, J. Chem. Phys. **96**, 6629 (1992)
35. D. Xie, H. Guo, Y. Amatatsu, R. Kosloff, J. Phys. Chem. A **104**, 1009 (2000)
36. R.O. Loo, G.E. Hall, H.-P. Haerri, P.L. Houston, J. Phys. Chem. **92**, 5 (1989)
37. D.W. Chandler, J.W. Thoman Jr., M.H.M. Janssen, D.H. Parker, Chem. Phys. Lett. **156**, 151 (1989)
38. D.W. Chandler, M.H.M. Janssen, S. Stolte, R.N. Strickland, J.W. Thoman, D.H. Parker, J. Chem. Phys. **94**, 4839 (1990)
39. A. García-Vela, R. de Nalda, J. Durá, J. González-Vázquez, L. Bañares, J. Chem. Phys. **135**, 154306 (2011)
40. G. Li, H.J. Hwang, H.C. Jung, Rev. Sci. Instrum. **76**, 023105 (2005)

41. M. Dantus, M.J. Rosker, A.H. Zewail, J. Chem. Phys. **89**, 6128 (1988)
42. T.S. Rose, M.J. Rosker, A.H. Zewail, J. Chem. Phys. **91**, 7415 (1989)
43. J. Durá, R. de Nalda, J. Álvarez, J.G. Izquierdo, G.A. Amaral, L. Bañares, ChemPhysChem **9**, 1245 (2008)
44. J.J. Larsen, H. Sakai, C.P. Safvan, I. Wendt-Larsen, H. Stapelfeldt, J. Chem. Phys. **111**, 7774 (1999)
45. B. Friedrich, D. Herschbach, Phys. Rev. Lett. **74**, 4623 (1995)
46. T. Seideman, J. Chem. Phys. **115**, 5965 (2001)
47. F. Rosca-Pruna, M.J.J. Vrakking, J. Chem. Phys. **116**, 6567 (2002)
48. H. Stapelfeld, T. Seideman, Rev. Mod. Phys. **75**, 543 (2003)
49. E. Hamilton, T. Seideman, T. Ejdrup, M.D. Poulsen, C.Z. Bisgaard, S. Viftrup, H. Stapelfeld, Phys. Rev. A **72**, 043402 (2005)
50. D.E. Folmer, E.S. Wisniewski, S.M. Hurley, A.W. Castleman Jr., Proc. Natl. Acad. Sci. USA **96**, 12980 (1999)
51. K.V. Vidma, A.V. Baklanov, E.B. Khvorostov, V.N. Ishchenko, S.A. Kochubei, A.T.J.B. Eppink, D.A. Chestakov, D.H. Parker, J. Chem. Phys. **122**, 204301 (2005)
52. D.J. Donaldson, V. Vaida, R. Naaman, J. Chem. Phys. **87**, 2522 (1987)
53. A.P. Baronavski, J.C. Owrustky, J. Chem. Phys. **108**, 3445 (1998)
54. S. Felps, P. Hochmann, P. Brint, S.P. McGlynn, J. Mol. Spectrosc. **59**, 355 (1976)
55. M.R. Dobber, W.J. Buma, C.A. de Lange, J. Chem. Phys. **99**, 836 (1993)
56. S. Eden, P. Limao-Vieira, S.V. Hoffmann, N.J. Mason, Chem. Phys. **331**, 232 (2007)
57. V.A. Shubert, M. Rednic, S.T. Pratt, J. Chem. Phys. **130**, 134306 (2009)
58. C. Jonah, J. Chem. Phys. **55**, 1915 (1971)
59. S. Yang, R. Bersohn, J. Chem. Phys. **61**, 4400 (1974)
60. Y. Wang, S. Zhang, Z. Wei, B. Zhang, J. Phys. Chem. A **112**, 3846 (2008)
61. M.E. Corrales, G. Gitzinger, J. González-Vázquez, V. Loriot, R. de Nalda, L. Bañares, J. Phys. Chem. A **116**, 2669 (2012)
62. G. Balerdi, M.E. Corrales, G. Gitzinger, J. González-Vázquez, I.R. Solá, V. Loriot, R. de Nalda, L. Bañares, EPJ Web Conf. **41**, 02035 (2013)
63. M.E. Corrales, G. Balerdi, V. Loriot, R. de Nalda, L. Bañares, Faraday Discuss. **163**, 447 (2013)
64. K.L. Wells, G. Perriam, V.G. Stavros, J. Chem. Phys. **130**, 074308 (2009)
65. N.L. Evans, H. Yu, G.M. Roberts, V.G. Stavros, S. Ullrich, Phys. Chem. Chem. Phys. **14**, 10401 (2012)
66. A. Iqbal, M.S.Y. Cheung, M.G.D. Nix, V.G. Stavros, J. Phys. Chem. A **113**, 8157 (2009)
67. A. Iqbal, V.G. Stavros, J. Phys. Chem. A **114**, 68 (2010)
68. K.L. Wells, D.J. Hadden, M.G.D. Nix, V.G. Stavros, J. Phys. Chem. Lett. **1**, 993 (2010)
69. D.J. Hadden, C.A. Williams, G.M. Roberts, V.G. Stavros, Phys. Chem. Chem. Phys. **13**, 4494 (2011)
70. G.M. Roberts, A.S. Chatterley, J.D. Young, V.G. Stavros, J. Phys. Chem. Lett. **3**, 348 (2012)
71. G.M. Roberts, C.A. Williams, J.D. Young, S. Ullrich, M.J. Paterson, V.G. Stavros, J. Am. Chem. Soc. **134**, 12578 (2012)
72. G.M. Roberts, C.A. Williams, H. Yu, A.S. Chatterley, J.D. Young, S. Ullrich, V.G. Stavros, Faraday Discuss. **163**, 95 (2013)

Chapter 5
Time-Resolved Photoelectron Spectroscopy for Excited State Dynamics

Roman Spesyvtsev, Jonathan G. Underwood, and Helen H. Fielding

Abstract This chapter provides an overview of time-resolved photoelectron spectroscopy (TRPES) for unravelling excited state dynamics in polyatomic molecules. It begins with a brief introduction to the basics of nonadiabatic dynamics in polyatomic molecules. This is followed by a description of the principles behind TRPES and a discussion of the roles of the ionisation continuum. We then describe the experimental toolkit, from light and molecule sources to photoelectron spectrometers. Finally, we describe several examples where TRPES has been employed to unravel non-adiabatic dynamics in polyatomic molecules.

5.1 Introduction

When a molecule absorbs a femtosecond pulse of UV light, it is promoted to an excited electronic state in which the nuclei are no longer in their equilibrium positions. The resulting excess vibrational energy can be redistributed within the molecule in various ways: it may undergo a photochemical reaction on the excited state (such as isomerisation, proton-transfer or electron-transfer) before relaxing back to the ground-state, or it may undergo electronic relaxation from the initially populated excited state to another state of the same multiplicity (internal conversion) or to one of different multiplicity (intersystem crossing) [1–8]. These non-radiative processes often occur at, or near to, molecular configurations where two or more electronic states are degenerate, known as conical intersections [9]. Conical intersections provide very efficient 'photochemical funnels' for the ultrafast (sub-picosecond) non-radiative decay processes that underpin the photochemistry of almost all polyatomic molecules. Such non-radiative dynamics are key to many photobiological functions, such as vision and photosynthesis, and underlie many concepts in active molecular electronics.

R. Spesyvtsev · H.H. Fielding (✉)
Department of Chemistry, University College London, London, UK
e-mail: h.h.fielding@ucl.ac.uk

J.G. Underwood
Department of Physics and Astronomy, University College London, London, UK

R. de Nalda, L. Bañares (eds.), *Ultrafast Phenomena in Molecular Sciences*,
Springer Series in Chemical Physics 107, DOI 10.1007/978-3-319-02051-8_5,

The coupling of vibrational and electronic degrees of freedom described above is a breakdown of the Born-Oppenheimer approximation (BOA). The BOA is based on the assumption that, as a result of the large difference in mass between electrons and nuclei, their motions can be considered separately, to a first approximation. Non-adiabatic coupling of electronic and nuclear motion often leads to complex, broadened absorption spectra as a result of the high density of vibrational states and strong variation of transition dipole moment with nuclear coordinate. However, photoelectron spectroscopy is sensitive to both electronic configuration and vibrational composition and, as a result, time-resolved photoelectron spectroscopy (TRPES) is an extraordinarily powerful tool for unravelling the dynamical details of ultrafast non-adiabatic processes.

TRPES has been the subject of a number of excellent reviews [10–26]; this chapter focuses on providing a brief overview of the fundamental molecular physics behind TRPES, a brief description of the experimental toolkit and some examples of applications of TRPES—some classic and some more recent.

5.2 Probing Non-adiabatic Dynamics Using Time-Resolved Photoelectron Spectroscopy

In a TRPES experiment, a molecule is promoted to an excited electronic state with an ultrashort pump pulse. A probe pulse then ionises the evolving excited state of the molecule, generating free electrons, and the electron kinetic energy and/or angular distribution of these free electrons is measured as a function of the time delay between the pump and probe laser pulses. TRPES has several practical and conceptual advantages over other pump-probe methods.

(i) Ionization is always an allowed process because the selection rules are relaxed as a result of the range of possible symmetries of the outgoing electron—there are no optically dark states in photoionization.
(ii) Very detailed information can be obtained by differential analysis of the outgoing photoelectron in terms of its kinetic energy and angular distribution; these measurements are made simultaneously in time-resolved photoelectron imaging.
(iii) Charged particle detection is extremely sensitive.
(iv) Higher order (multiphoton) processes, which can be difficult to identify in energy-integrated femtosecond experiments, are identified more easily in a photoelectron spectrum.
(v) Photoelectron-photoion coincidence measurements reveal the mass of the carrier of the photoelectron spectrum, making it possible to disentangle reaction pathways in fragmentation experiments, studies of cluster solvation effects as a function of cluster size, and studies of scalar and vector correlations in photodissociation dynamics.
(vi) As free-electron laser light sources become available, tuning the probe photon wavelength will allow ionization of not only valence and inner valence

electrons (which are accessible using conventional laser sources), but also selectively non-bonding and core electrons, and have the potential to provide a different view of the reaction dynamics.

The molecular ionization continuum provides a template for observing both excited state vibrational dynamics and evolving excited state electronic configurations. The excited state vibrational dynamics are observed *via* Franck-Condon distributions in the photoelectron spectrum, while the electronic dynamics are manifested through the cation states formed during photoionization (which have correspondingly different photoelectron energies), as well as the form of the photoelectron angular distribution. These ideas are discussed in more detail below.

5.2.1 Photoelectron Spectra: Using the Cation to Map Excited State Dynamics

The electronic states of the cation can provide a map of evolving electronic structures in the neutral state prior to ionization—in the independent electron approximation, emission of an outer electron occurs without simultaneous electronic reorganization of the 'core' (cation or neutral)—this is called the 'molecular orbital' or Koopmans' picture [27–29]. Thus, it is possible to determine the most probable electronic state of the cation following single photon ionization of a specific electronic state of the neutral molecule. The probabilities of partial ionization into specific cation electronic states can differ drastically with respect to the molecular orbital nature of the neutral electronic state being probed. For example, if an electronic configuration correlates, upon removal of a single active outer electron, to the ground electronic configuration of the cation, then the photoionization probability is generally higher than if it does not.

Figure 5.1 illustrates how the cation electronic structures can be used in (angle-integrated) time-resolved photoelectron spectroscopy to disentangle electronic dynamics from vibrational dynamics in ultrafast non-adiabatic processes. A Born-Oppenheimer, zeroth-order, optically bright state, S_n, is prepared coherently with a femtosecond pump pulse. According to the molecular orbital picture, it should ionize into the continuum associated with the D_0 state of the cation (the ground electronic state of the cation) in this example. This process gives rise to a photoelectron energy band ε_1. Non-adiabatic coupling (promoted by vibrational modes of appropriate symmetry) then transforms the zeroth-order optically bright state S_n into a lower lying zeroth-order optically dark state S_{n-1}. In this example, according to the molecular orbital picture, this state should ionize into a different continuum associated with an electronically excited state of the cation, D_1, giving rise to a photoelectron band ε_2. Thus, for a sufficiently energetic probe pulse, (*i.e.*, both ionization channels accessible energetically) the photoionisation channel will switch from ε_1 to ε_2 during the non-adiabatic process. This simple picture illustrates how the evolving excited-state electronic configuration can be monitored during a non-adiabatic process whilst following, simultaneously, the coupled nuclear dynamics

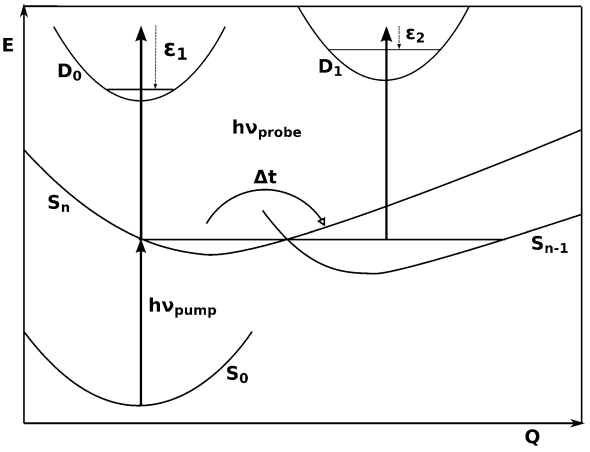

Fig. 5.1 A TRPES scheme for disentangling electronic and vibrational dynamics in an excited polyatomic molecule exhibiting Koopmans' Type I correlations, *e.g.* the neutral excited states, S_n and S_{n-1} in this example, correlate to different cation electronic states D_0 and D_1 [26]

via the evolution of the vibrational structure within each photoelectron band. The cation electronic structures are essentially acting as a 'template' for disentangling electronic dynamics from vibrational dynamics in the excited state.

If the neutral and cation electronic states have similar equilibrium geometries, each neutral vibronic state will give rise to a single peak in the photoelectron spectrum for each vibrational mode, as a result of a $\Delta\upsilon = 0$ propensity (where υ is the vibrational quantum number). However, if there is a substantial difference in the equilibrium geometries, each neutral vibronic state will give rise to a vibrational progression in the photoelectron spectrum, as a result of $\Delta\upsilon = 0, 1, 2\ldots$ transitions for each vibrational mode populated in the electronically excited state of the neutral molecule. Thus, the photoelectron spectrum will reflect the vibronic composition of the molecular wavepacket, and the time-dependence of the vibrational structure in the photoelectron spectrum reflects, directly, the nuclear motion of the molecule [30]. Of course, this Franck-Condon mapping of the vibrational dynamics onto the photoelectron spectrum will break down if the variation of the electronic ionization dipole matrix elements varies significantly with relevant nuclear coordinates, for example in a region in which vibrational autoionization is active [27, 29, 31, 32], or along a dissociative coordinate.

Two limiting cases have been proposed for Koopmans-type correlations in TRPES experiments [33, 34], and both have been observed experimentally [35, 36, 72]. The first case, Type I, is when the neutral excited states S_n and S_{n-1} correlate to different cation electronic states, as in Fig. 5.1. Even if there are large geometry changes upon internal conversion, or ionization to produce vibrational progressions, the electronic correlations will favour disentangling the vibrational dynamics from the electronic dynamics. The other limiting case, Type II, is when the neutral excited states S_n and S_{n-1} correlate equally strongly to the same cation electronic states, and so produce overlapping photoelectron bands. Although different Franck-Condon factors can allow the states S_n and S_{n-1} to be distinguished in the photoelectron spectrum [37], generally Type II ionization correlations make it more difficult to disentangle electronic and vibrational dynamics from the photoelectron spectrum. It

is in these Type II situations that measuring the time-resolved photoelectron angular distribution can be of real benefit—as discussed below, the photoelectron angular distribution reflects the evolution of the molecular electronic symmetry.

5.2.2 *Photoelectron Angular Distributions: Using the Free Electron to Map Excited State Dynamics*

The electronic states of the free electron, usually described as scattering states, are also responsible for electronic structure in the continuum. The free electron states populated during photoionization reflect angular momentum correlations and are therefore sensitive to the evolving electronic configuration and symmetry of the neutral molecule. This sensitivity is expressed in the form of the photoelectron angular distribution (PAD). As the electron leaves the molecule, it scatters from the molecular potential. As such, the scattering wave function reflects the electronic and nuclear configuration of the neutral molecule at the moment of ionization [26, 38, 39]. Hence, the PAD measured (in the molecular frame) also reflects the electronic and nuclear structure of the neutral at the moment of ionization. However, the PAD is usually measured in the laboratory frame, where the direction of electron ejection is measured in a frame which is referenced to the polarization of the probe pulse, rather than directly in the molecular frame. Although such laboratory-frame measurements carry a great deal of information, they are an average over all molecular orientations present and therefore carry less information than a measurement of the PAD in the molecular frame. Using coincidence techniques, it is possible to measure the PAD relative to a recoiling photofragment, which approaches a molecular frame PAD measurement [40–42]. A more generally applicable method for making molecular-frame PAD measurements exploits strong non-resonant laser fields to align the molecular axis, thus defining the molecular orientation prior to ionization [43].

The continuum state accessed by the probe pulse may be written as a direct product of the cation and free electron states. As with any optical transition, there are symmetry based 'selection rules' for the photoionization step. For photoionization, the requirement is that the direct product of the irreducible representations of the free electron wave function (Γ_{e^-}), the state of the ion (Γ_{M^+}), the molecular frame transition dipole moment (Γ_μ) and the neutral state (Γ_M) contains the totally symmetric irreducible representation of the molecular point group (Γ_{TS}),

$$\Gamma_{e^-} \otimes \Gamma_{M^+} \otimes \Gamma_\mu \otimes \Gamma_M \subset \Gamma_{TS}. \tag{5.1}$$

Clearly, the symmetries of the contributing photoelectron partial waves will be determined by the electronic symmetry of the electronic state undergoing ionization, as well as the molecular frame direction of the ionization transition dipole moment (which determines the possible Γ_μ), and the electronic symmetry of the cation. As

such, the evolution of the photoelectron angular distribution, which reflects the allowed symmetries of the partial waves, will reflect the evolution of the molecular electronic symmetry.

Since the symmetry of the free electron wavefunction determines the form of the PAD, the shape of the PAD will reflect (i) the electronic symmetry of the neutral molecule and (ii) the symmetries of the contributing molecular frame transition dipole moment components. Since the relative contributions of the molecular frame transition dipole moments are determined geometrically by the orientation of the molecule relative to the ionizing laser field polarization, the form of the laboratory frame PAD will reflect the distribution of molecular axis in the laboratory frame, and so will reflect the rotational dynamics of the molecule [44–50].

5.3 The Experimental Toolkit for TRPES

Virtually all polyatomic molecules have strong absorption bands in the ultraviolet (200–350 nm) and ionisation potentials in the vacuum ultraviolet (VUV) (< 150 nm). The most common form of TRPES employs a UV pump pulse to access lower lying electronically excited states and a UV probe pulse to ionise the molecule from these excited states and generate photoelectrons with electron kinetic energies in the range 0–3 eV. Generally, it is not possible to ionise a molecule that has returned to its electronic ground state using a UV probe pulse, since the molecule will have considerable excess vibrational energy and there is a $\Delta\upsilon = 0$ propensity for photoionisation. To photoionise molecules that have returned to the electronic ground-state by non-radiative decay from electronically excited states, requires a VUV probe pulse to access higher vibrational states in the ionisation continuum. Extreme ultraviolet (XUV) probe pulses allow the additional possibility of ionising core electrons; photoelectrons generated by photoionisation of the valence electrons will have high electron kinetic energies (just a few eV less than the XUV probe pulse).

5.3.1 Femtosecond Light Sources

Most TRPES experiments employ commercial femtosecond laser systems that are tuneable in the UV. Femtosecond laser technology is a research field in itself, and there are many excellent reviews available, see for example [51, 52]. The most common scheme for the production of femtosecond UV pulses is based on a Ti:Sapphire (Ti:S) laser operating at around 800 nm. A bandwidth of around 100 nm can be achieved, enabling the production of pulses as short as 10 fs. The Ti:S crystal is usually pumped using a continuous laser with an output wavelength around 525 nm. The femtosecond pulses from the Ti:S oscillator are used to seed a chirped pulse regenerative amplifier; before amplification, the seeding pulses are stretched to a

few hundreds of picoseconds to avoid non-linear processes and damage in the gain medium. Single pass amplifiers can be used to increase the pulse intensity further. After amplification, the amplified pulses are compressed back to durations of a few tens of femtoseconds. The amplifier is usually pumped by a nanosecond laser operating around 525 nm.

Harmonics of the fundamental output of the Ti:S amplifier can be obtained by frequency-doubling and sum-frequency generation processes in β-barium borate (BBO) crystals generating pulses around 400 nm, 267 nm and 200 nm. Optical parametric amplifiers (OPAs) [53, 54] are employed to generate femtosecond pulses that are tuneable throughout the UV to around 235 nm. In an OPA, the fundamental output of the Ti:S amplifier is focussed onto a Sapphire crystal to generate a white light continuum, which is then mixed with the fundamental in a BBO crystal, providing tuneable light in the range 1150 nm to 2630 nm; shorter wavelengths are generated by subsequent sum-frequency mixing and higher order harmonic generation.

The duration of a laser pulse is limited to the cycle of the laser field, which for 800 nm is a few femtoseconds but can be less than a hundred attoseconds in the XUV [55]. Attosecond XUV pulses are produced by high harmonic generation (HHG) in nonlinear gases. In principle, it is possible to use any gas, however the ionization potential of the atom or molecule has to be high enough for the HHG to compete with multiphoton ionization. The energy range and intensity profile of the XUV spectrum depends on the gas; in Ar, the spectrum ranges from 10 eV (125 nm) to around 100 eV (12.5 nm). An XUV monochromator or filters can be used to select the photon energy range for the experiment. The efficiency of HHG is usually relatively low ($\sim 10^{-6}$) yielding photon fluxes of around 10^8 photons per pulse. XUV laser sources have sufficient photon energy to ionize the ground-state of any molecule, but they also have sufficient photon energy to ionise inner valence electrons, which promises to yield complementary information.

Free electron lasers (FELs) can produce very short laser pulses with high photon energy and high brilliance [56]. FELs work by generating high quality electron pulses which are accelerated to relativistic energies and compressed to femtosecond duration before being fed into an undulator. The periodic trajectory of the electrons in the magnetic field of the undulator results in the emission of synchrotron radiation. Due to the interaction between the emitted radiation and the electrons the radiation is amplified coherently, thus, producing coherent electromagnetic radiation with a mean photon energy that is controlled by the electron energy and the undulator parameters. There are several international FEL facilities in the world, which include the European soft x-ray FEL Free-Electron Laser in Hamburg (FLASH) [57] and the USA x-ray FEL (XFEL) the Linac Coherent Light Source (LCLS) [58]. The FLASH facility generates laser pulses in the wavelength range 6.8 nm to 47 nm and pulse durations from 10 fs to 70 fs. The LCLS facility operates in the wavelength range from 0.15 nm to 2.2 nm with pulse durations from 70 fs to 500 fs. The intensity of these XUV and x-ray free electron lasers (XFELs) is currently as high as 10^{13} photons per pulse, which is several orders of magnitude larger than those obtained using XUV HHG sources. A new XFEL facility is currently under development in Hamburg, Germany. This European project aims to achieve even higher photon intensities in the wavelength range from 0.1 nm to 6.2 nm.

The relationship between pulse duration and spectral bandwidth for Gaussian pulses is restricted by the inequality,

$$\Delta\nu \cdot \Delta t \geq 0.441, \tag{5.2}$$

which can be rewritten as,

$$\Delta\lambda\ [\mathrm{nm}] \geq 1.471 \times 10^{-3} \frac{\lambda^2\ [\mathrm{nm}^2]}{\Delta t\ [\mathrm{fs}]}, \tag{5.3}$$

where $\Delta\nu$ is the spectral width (FWHM), $\Delta\lambda$ is the bandwidth (FWHM) at wavelength λ, and Δt is the pulse duration (FWHM) of the Gaussian laser pulse. Equation (5.2) stipulates that it is not possible to have infinitely good spectral resolution and time resolution simultaneously. The timescales for non-adiabatic processes range from tens of femtoseconds to hundreds of picoseconds. From Eq. (5.3), we see that the bandwidth of a 100 fs pulse at 250 nm is around 1 nm (equivalent to around 20 meV or 150 cm^{-1}) and the bandwidth of a 0.1 fs pulse at 15 nm is around 3 nm ($>$ 10 eV). Thus, planning a TRPES experiment requires careful consideration of the requirements for the photoionisation wavelength alongside the achievable temporal and spectral resolution.

Another important aspect of a TRPES experiment is the delay between the pump and probe laser pulses. This is usually controlled by changing the path length between the two pulses using optics mounted on commercial translation stages. In UV-UV and UV-VUV/XUV pump-probe experiments, the pump and probe laser pulses generally both originate from the same oscillator, which keeps the jitter well below the temporal resolution of the translation stage (typically around 0.01 fs). However, in pump-probe experiments using XFELs, UV pump and x-ray probe pulses do not have the same origin and the jitter may be significant [59].

5.3.2 Molecular Sources

In order to make time-resolved photoelectron spectroscopy measurements of isolated molecules, an expansion into a vacuum chamber is usually employed ensuring a collision-free environment. Such conditions also allow for the stringent requirements of most electron detectors which place an upper limit of around 10^{-5} mbar in the laser-molecule interaction region.

The simplest way to deliver a gas sample into the laser-molecule interaction region is to feed it through a thin needle. The gas will expand into the vacuum chamber with the highest density close to the needle tip. Such a source is not well collimated and only a small fraction of the effused molecules overlap with the laser focus. Such low number densities place a practical limit on the achievable signal-to-noise ratio in such experiments.

A more efficient way to deliver a gas sample into the laser-molecule interaction region is with a supersonic molecular beam. The gas is usually delivered through a

nozzle, which is a sealed tube with a 50–500 μm hole. The source chamber housing the nozzle is separated from the laser-molecule interaction region by a molecular skimmer with a diameter of a few millimetres, generating a high density, well-collimated molecular beam [60]. Such molecular beams have small transverse velocity and very low velocity spread in the propagation direction [61]. This reduces the number of molecules in the interaction region which have been thermalized through collision with the chamber walls and scattered back into the interaction region. In addition, the expansion process cools down vibrational and rotational motions in the molecules often leading to spectral simplification. The cooling effect is a function of the nozzle diameter, the gas pressure behind the nozzle and the carrier gas [62, 63]. A liquid nitrogen cold trap is often placed after the laser-molecule interaction region to absorb scattered molecules that pass through the interaction region.

During a TRPES experiment the laser-molecule interaction occurs for only a tiny fraction of the total time of the experiment, defined by the laser pulse duration and laser repetition rate. Therefore, most of the gas from a continuous nozzle source does not interact with the laser. The efficiency can be improved significantly by using pulsed nozzles. The pressure behind the pulsed nozzle can be as high as 100 bar whilst maintaining reasonable vacuum conditions in the photoelectron spectrometer. Such high pressures can produce very efficient cooling; for example, Even-Lavie pulsed nozzles can cool large molecules to temperatures below 1 K [64].

A more recent development is TRPES of liquid samples. Liquid jets were first developed to study evaporation of molecular monomers and dimers [65]. For TRPES in liquids, the key component is a quartz glass liquid nozzle with an aperture size around 10 μm which generates a continuous flow of liquid; after travelling a few millimetres in the vacuum the liquid jet breaks into droplets which are collected in a trap [66]. Liquid jets have been employed successfully in UV-VUV/XUV [67] and UV-UV [68] TRPES experiments.

5.3.3 Photoelectron Spectrometers

There are several different techniques for measuring photoelectron spectra. The most popular photoelectron spectrometers are based on velocity map imaging (VMI) or time of flight (ToF) methods.

ToF spectrometers measure the photoelectron spectrum by analysing the time taken for an electron to travel from the interaction region to a detector. ToF spectrometers usually employ electrostatic or magnetic fields to guide the electrons to the detector. A commonly employed ToF spectrometer is the magnetic bottle electron spectrometer [69] which has the advantage of a large collection efficiency (typically 50 %). Photoelectrons created in the molecule-laser interaction region are guided in a magnetic field toward the electron detector which is usually a microchannel plate. ToF spectrometers can be constructed to have high energy resolution over a wide range of photoelectron energies which is particularly useful for experiments

using VUV or x-ray probe pulses. Hemispherical electron energy analysers have been employed in liquid jet experiments due to their efficient differential pumping [68]. Obtaining information about photoelectron angular distributions from ToF measurements is more challenging, requiring ToF spectrometers with small solid angles of collection (and so low collection efficiency) and repeated measurements with different experimental geometries.

Velocity map imaging (VMI) allows both the photoelectron spectrum and the photoelectron angular distribution to be measured simultaneously. VMI is based on using static electric fields to project the 3D photoelectron momentum distribution created in the molecule-laser interaction region onto a 2D photoelectron image in the plane of the electron detector. The position sensitive electron detector usually comprises a microchannel plate, a phosphor screen and a charge-coupled device. The original 3D photoelectron momentum distribution can be reconstructed from 2D photoelectron image using an inversion algorithm such as an inverse Abel transform [70]. The energy resolution of a VMI apparatus depends on the electron detector resolution as well as on the focussing properties of the electrostatic lens. Energy resolution as low as $\Delta E/E = 0.38$ % can be achieved [71].

5.4 Applications

5.4.1 Internal Conversion and Intramolecular Vibrational Energy Redistribution

Femtosecond TRPES has been exploited very successfully to observe ultrafast internal conversion (IC) in a number of polyatomic molecules. A classic example is S_2/S_1 IC in the linear polyene all-*trans* 2,4,6,8-decatetraene (DT) [72]. The energy level scheme is presented in Fig. 5.2. The first optically allowed transition is to the $S_2(1^1B_u)$ state, which is a singly excited configuration, correlating electronically with the $D_0(1^2B_g)$ ground electronic state of the cation. The $S_1(2^1A_g)$ state arises from a configuration interaction between singly and doubly excited configurations and correlates electronically with the $D_1(1^2A_u)$ first electronically excited state of the cation. The photoelectron spectra presented in Fig. 5.2 show a rapid shift in electron distribution ε_1 (ionisation of S_2) to ε_2 (ionisation of S_1) with a ~400 fs timescale.

TRPES can also be exploited to follow intramolecular vibrational energy redistribution (IVR) in polyatomic molecules. An elegant example is restricted IVR in toluene [73]. The pump pulse prepares a coherent superposition of the $6a^1$ state, corresponding to one quanta of vibrational excitation in the totally symmetric ring breathing mode, and the $10b^16b^1$ state, corresponding to one quanta in the CH_3 wagging mode (10b) and one quanta in the out-of-plane C–H bending mode (16b). As a result of anharmonic coupling between these two states (a Fermi resonance) population flows between them and this is observed as oscillations in the photoelectron spectrum (Fig. 5.3). The period of the oscillation is ~ 6 ps and is inversely proportional to the energy separation of the two states in the superposition.

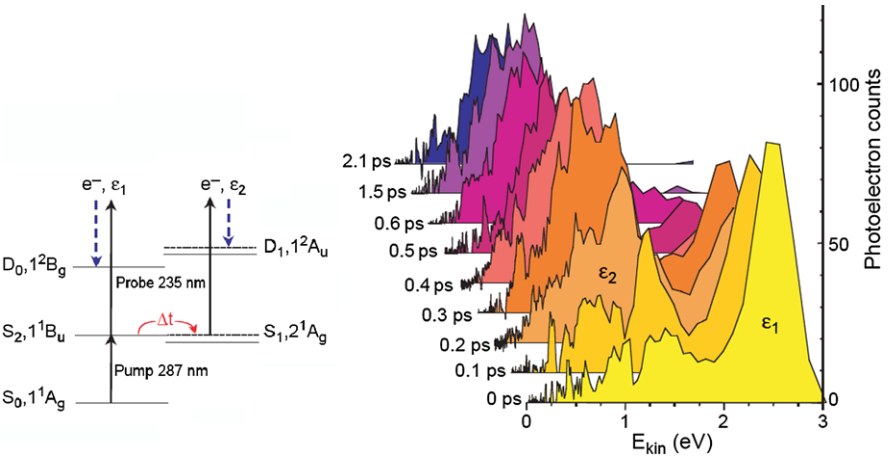

Fig. 5.2 Energy level scheme (*left*) for TRPES of DT (*right*). The narrow peak at ε_1 corresponds to ionisation of S_2 to D_0 and the broader peak at ε_2 corresponds to ionisation of S_1 to D_1 [72]

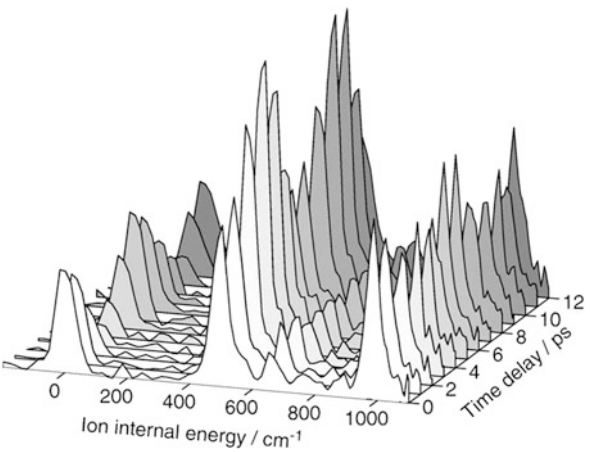

Fig. 5.3 TRPES following excitation of the $6a^1 + 10b^1 6b^1$ Fermi resonance in toluene. The ~ 6 ps oscillations in the photoelectron band observed around 500 cm^{-1} ion internal energy is out of phase with those observed at zero and 1000 cm^{-1} ion internal energy [73, 74]

5.4.2 Molecular Alignment

As mentioned in Sect. 5.2.2, photoelectron spectra and photoelectron angular distributions are sensitive to the molecular frame direction of the ionizing light polarization. Consequently, such measurements can be a sensitive probe of molecular axis alignment.

A particularly elegant illustration of the evolution of molecular alignment is observed in pyrazine. The energy level scheme is presented in Fig. 5.4. The pump pulse excites the S_1 origin of pyrazine and is probed by two-photon ionisation *via* the $3s$ and $3p_z$ Rydberg states, resulting in two distinct bands in the photoelectron spectrum. Strong spin-orbit coupling of the singlet S_1 state with the triplet T_1 state

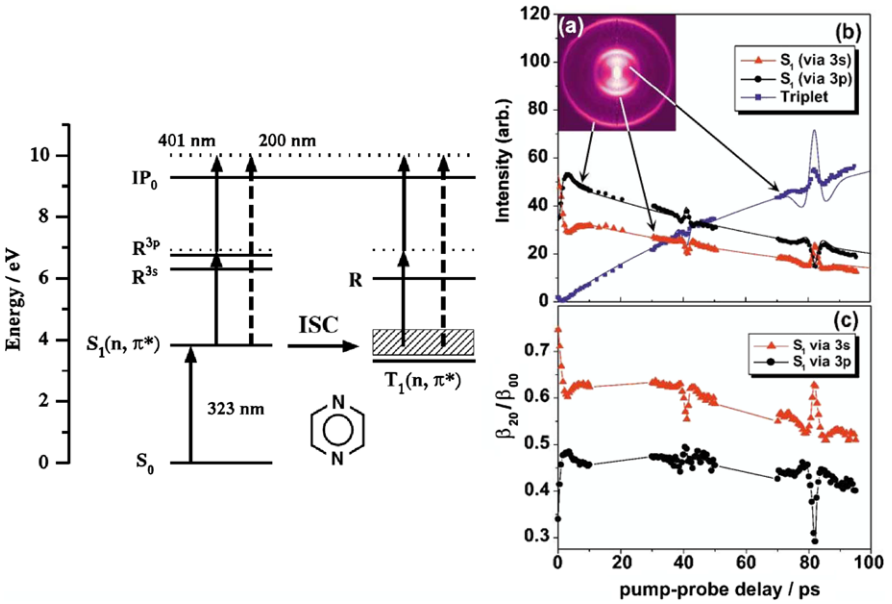

Fig. 5.4 Schematic energy level diagram for pyrazine (*left*). Inverse Abel transformed photoelectron image following initial excitation of S_1 and subsequent 2-photon ionisation, observed at a pump-probe delay of 30 ps (*inset*, *top right*). Time evolution of the photoelectron intensity (*top right*) and photoelectron angular distribution (*bottom right*) of each of the three major components of the photoelectron image: S_1 *via* 3*s* (*triangles*); S_1 *via* $3p_z$ (*circles*); T_1 [75]

results in intersystem crossing (ISC). The loss of S_1 population (higher energy photoelectrons) is accompanied by a rise in T_1 population (lowest energy photoelectron band).

The linearly polarised pump pulse creates a distribution of principal molecular axes, which is aligned with respect to the electric field. The molecules then rotate and realign at a later time, referred to as a rotational coherence. The electric field vector of the linearly polarised probe pulse is aligned so that it is parallel to that of the pump pulse. The transition dipole moments for excitation of the intermediate 3*s* and $3p_z$ Rydberg states from S_1 are parallel and perpendicular to the principal molecular axis, respectively. Therefore, the rotational coherences observed as fast oscillations in both the intensities of the photoelectron bands and their anisotropies are out of phase with one another (Fig. 5.4). Interestingly, rotational coherences are also observed in the photoelectron band corresponding to photoionisation from the triplet state, demonstrating that rotational coherence is preserved during ISC in pyrazine.

Recently, it has been demonstrated that laser-induced molecular axis alignment can be exploited to enable PAD measurements in the molecular frame during ultrafast processes, as illustrated in CS_2 [43]. In this experiment, a strong laser field is employed to align the molecular axes of ground state CS_2 molecules prior to

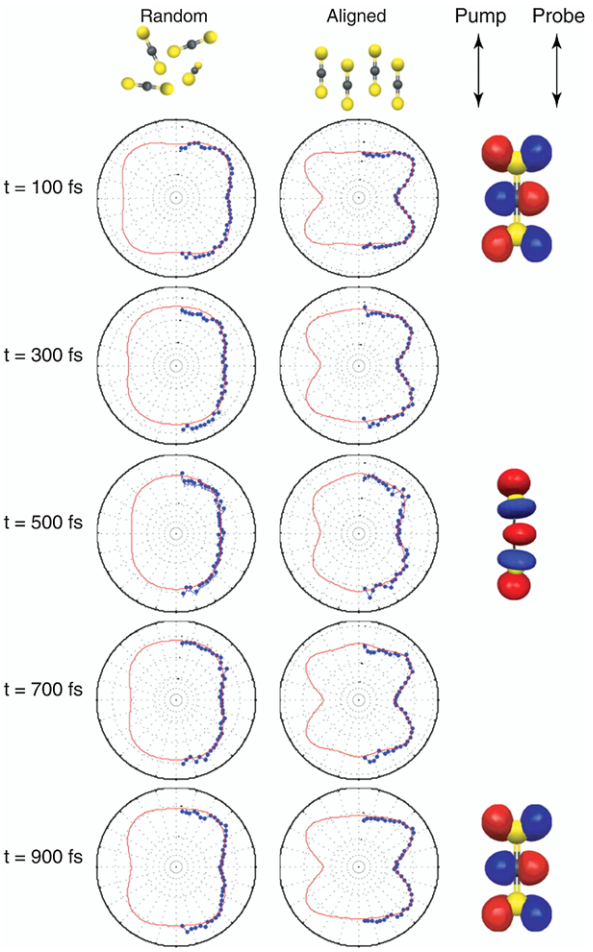

Fig. 5.5 Time-resolved PADs for unaligned (*left*) and aligned (*right*) CS_2 molecules. The laboratory frame laser polarization vectors are shown at *top right*. Also shown are the orbitals with the highest contribution to the state evolving adiabatically from the initially excited state in the Franck Condon (FC) region. *Top* and *bottom right panels* show the π^* orbital that dominates in the FC region, whereas the *middle right panel* shows the σ^* orbital that contributes at geometries that are both stretched and bent. The molecular frame PADs (aligned) reveal details of the dynamics not seen in the randomly oriented sample. Taken from [43]

the pump-probe measurement. Since the ultrafast dynamics in this molecule occur on a timescale much faster than molecular rotation, it was possible to record PADs for aligned molecules for the duration of the process under study. These molecular frame PADS, shown in Fig. 5.5, show details of the electronic dynamics which are not observable in the equivalent experiment with unaligned molecules.

5.4.3 Photodissociation

A sophisticated variant of TRPES, time-resolved photoelectron-photoion coincidence imaging spectroscopy, has been demonstrated to be a powerful tool for unravelling the mechanisms of photodissociation, as illustrated in $(NO)_2$. A schematic en-

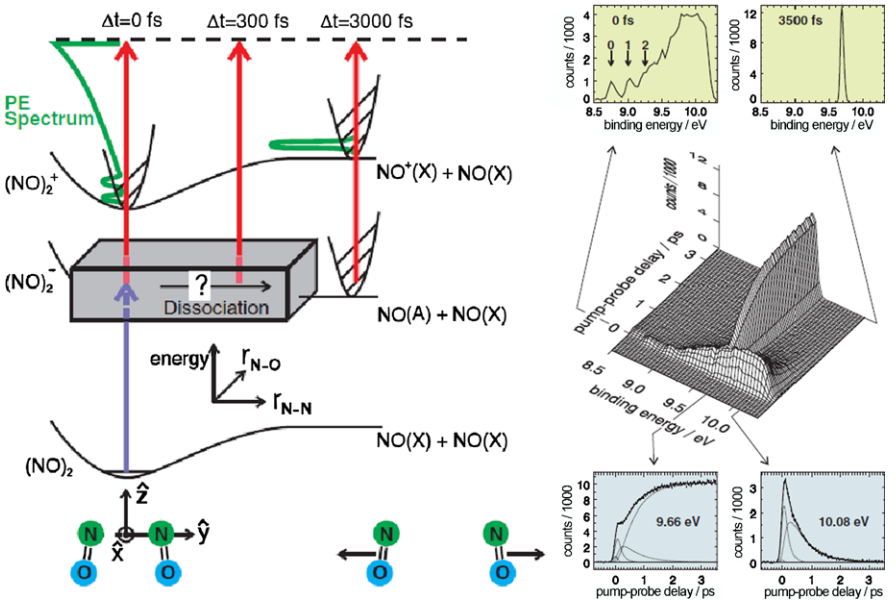

Fig. 5.6 Schematic energy level diagram of the pump-probe scheme for investigating $(NO)_2^* \rightarrow (NO)_2^{**} \rightarrow NO(A\ 3s) + NO(X)$ (*left*). TRPES (*middle right*) together with photoelectron spectra at $t = 0$ and $t = 3500$ fs (*top right*) and the time-evolutions of photoelectrons with electron kinetic energies 9.66 eV and 10.08 eV (*bottom right*) [76]

ergy level diagram is presented in Fig. 5.6: a femtosecond pump pulse promotes the dimer to an electronically excited state, $(NO)_2^*$; a femtosecond probe pulse ionises the initially excited state, the photodissociation product, NO(A $3s$), and intermediate states (represented by the grey box). At $t = 0$, the photoelectron spectrum is broad due to photoionisation from $(NO)_2^*$, whereas at long times, the photoelectron spectrum is narrow due to photoionisation from the free NO(A $3s$) photoproduct. It is not possible to fit the data using a single exponential decay for $(NO)_2^*$ and an equivalent rise for NO(A $3s$). Instead, it turns out that $(NO)_2^*$ decays with a time constant of around 590 fs and NO(A $3s$) rises with a time constant of around 140 fs.

In order to identify the intermediate state, $(NO)_2^{**}$, the momentum distributions of both the photoelectrons and photoions were recorded in coincidence. Importantly, measurement of the photoelectron momentum in coincidence with the recoiling photofragment allowed for measurement of the PAD in the frame of the recoiling photofragment. Since this photofragmentation was a rapid process, this recoil frame PAD was equivalent to the molecular frame PAD albeit averaged over rotation about the recoil axis. These experiments, supported by *ab initio* calculations, revealed that the pump pulse excites a vibrationally excited state of $(NO)_2^*$ which evolves towards an intermediate state with $3p_y$ Rydberg character, which correlates with the NO(A $3s$) + NO(X) photodissociation channel.

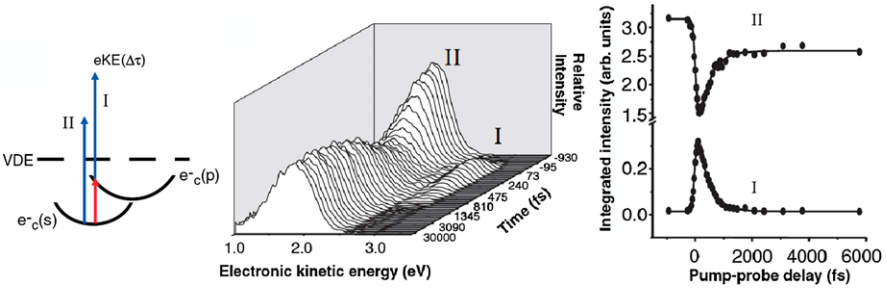

Fig. 5.7 Schematic energy level diagram for a water cluster anion (*left*). I and II correspond to two-colour resonant ionisation and direct ionisation, respectively. Time evolution of the photoelectron spectrum (*centre*) and integrated photoelectron intensity of features I and II (*right*) [77]

5.4.4 Solvated Electrons

TRPES can be employed to investigate the ultrafast dynamics of excited states of anions as well as neutral species. An interesting example is the electronic relaxation of water cluster anions [77], which are significant because they can be extrapolated to the hydrated electron in bulk solution. Figure 5.7 shows the excitation scheme: the localised ground-state population, $e^-_{\text{cluster}}(\text{s})$, is promoted to the almost degenerate excited-states, $e^-_{\text{cluster}}(\text{p})$, using an infrared femtosecond pump pulse; both the ground and excited states are subsequently ionised by an ultraviolet femtosecond probe pulse. In anions, this ionisation step is usually referred to as photodetachment. The time-resolved photoelectron spectra obtained for $(D_2O)^-_{25}$ are reproduced in Fig. 5.7. The feature at higher electron kinetic energy (labelled I in Fig. 5.7) corresponds to photodetachment from the excited state and is observed to increase in intensity during the excitation process and then decay, with a timescale of ~ 400 fs. The feature at lower electron kinetic energy (labelled II in Fig. 5.7) corresponds to photodetachment from the ground-state and is observed to decrease as the excited-state is populated and then increase as the excited-state decays back to the ground-state, on a timescale of ~ 400 fs. Thus, the timescale for internal conversion from $e^-_{\text{cluster}}(\text{p})$ to $e^-_{\text{cluster}}(\text{s})$ in $(D_2O)^-_{25}$ is determined to be ~ 400 fs.

5.4.5 VUV TRPES

A schematic diagram of a table-top laser setup that produces around 10^{10} photons per pulse in the energy range 20–30 eV, at 1 kHz, for pump-probe spectroscopy is shown in Fig. 5.8. A UV pump pulse is generated by frequency-doubling the fundamental of the amplified output of a Ti:S laser and focussed into the interaction region. High harmonics are generated in a gas cell and are also focussed into the interaction region, using a VUV mirror. The delay between the UV pump and VUV

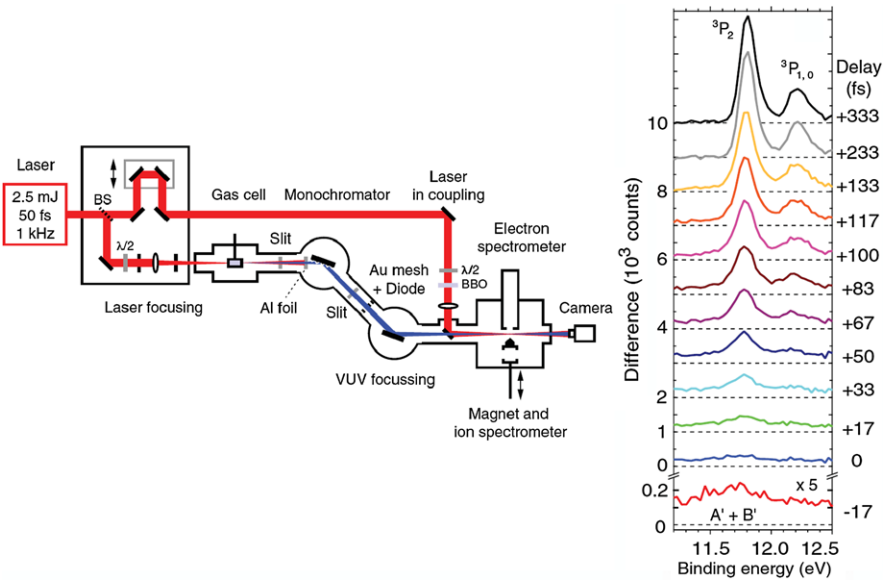

Fig. 5.8 Schematic diagram of a table-top laser setup for UV-pump-VUV-probe TRPES (*left*). TRPES of Br_2 photodissociation following excitation to Br_2^* ($^1\Pi_u$) (*right*) [78]

probe pulses is introduced by a translation stage in the path of the pump pulse. Photoelectrons are collected in a magnetic bottle spectrometer.

The capability of this setup is illustrated in the TRPES of dissociating photoexcited Br_2 molecules [79]. Br_2 is excited to the Br_2^* ($^1\Pi_u$) dissociative state using 395 nm pump pulses. Neutral molecules and Br atoms are photoionised using the VUV probe pulses. The broad photoelectron spectrum of the short-lived dissociative state, observed close to $t = 0$, evolves rapidly into comparably sharp lines resulting from photoionisation of neutral Br atoms in their ground electronic state to Br^+ ($^3P_{0,1,2}$). The application of this technique allows for a complete description of the valence electron rearrangement during bond cleavage. The availability of short pulses of VUV light greatly enhances the range of states that can be probed. In this example, much of the pump photon energy is liberated as product translational energy, and so ionization of the product states requires a VUV photon. VUV probe pulses will also allow for ionization of inner valence and core photoelectrons during ultrafast processes, potentially providing a complementary view of the dynamics to that offered by valence ionization with UV pulses.

References

1. M. Bixon, J. Jortner, J. Chem. Phys. **48**, 715 (1968)
2. J. Jortner, S.A. Rice, R.M. Hochstrasser, Adv. Photochem. **7**, 149 (1969)

3. S.R. Henry, W. Siebrand, in *Organic Molecular Photophysics*, vol. 1, ed. by J.B. Birks (Wiley, London, 1973), p. 152
4. K.F. Freed, in *Radiationless Processes in Molecules and Condensed Phases*, ed. by F.K. Fong (Springer, Berlin, 1976), p. 23
5. G. Stock, W. Domcke, Adv. Chem. Phys. **100**, 1 (1997)
6. G.A. Worth, L.S. Cederbaum, Annu. Rev. Phys. Chem. **55**, 127 (2004)
7. M. Klessinger, J. Michl, *Excited States and Photochemistry of Organic Molecules* (VCH, New York, 1994)
8. H. Köppel, W. Domcke, L.S. Cederbaum, Adv. Chem. Phys. **57**, 59 (1984)
9. S. Matsika, P. Krause, Annu. Rev. Phys. Chem. **62**(1), 621 (2011). doi:10.1146/annurev-physchem-032210-103450
10. I. Fischer, M. Vrakking, D. Villeneuve, A. Stolow, in *Femtosecond Chemistry*, ed. by M. Chergui (World Scientific, Singapore, 1996)
11. A. Stolow, Philos. Trans. R. Soc. Lond. A **356**, 345 (1998)
12. C.C. Hayden, A. Stolow, in *Advanced Physical Chemistry*, vol. 10, ed. by C.Y. Ng (World Scientific, Singapore, 2000)
13. W. Radloff, in *Advanced Physical Chemistry*, vol. 10, ed. by C.Y. Ng (World Scientific, Singapore, 2000)
14. K. Takatsuka, Y. Arasaki, K. Wang, V. McKoy, Faraday Discuss. 1–15 (2000)
15. D.M. Neumark, Annu. Rev. Phys. Chem. **52**, 255 (2001)
16. T. Suzuki, B.J. Whitaker, Int. Rev. Phys. Chem. **20**, 313 (2001)
17. T. Seideman, Annu. Rev. Phys. Chem. **53**, 41 (2002)
18. K.L. Reid, Annu. Rev. Phys. Chem. **54**, 397 (2003)
19. A. Stolow, Annu. Rev. Phys. Chem. **54**, 89 (2003)
20. A. Stolow, Int. Rev. Phys. Chem. **22**, 377 (2003)
21. T. Suzuki, Y. Seideman, M. Stener, J. Chem. Phys. **120**, 1172 (2004)
22. A. Stolow, A. Bragg, D. Neumark, Chem. Rev. **104**, 1719 (2004)
23. V. Wollenhaupt, M. Engel, T. Baumert, Annu. Rev. Phys. Chem. **56**, 25 (2005)
24. T. Suzuki, Annu. Rev. Phys. Chem. **57**, 555 (2006)
25. I.V. Hertel, W. Radloff, Rep. Prog. Phys. **69**, 1897 (2006)
26. A. Stolow, J.G. Underwood, Adv. Chem. Phys. **139**, 497 (2008)
27. J.H.D. Eland, *Photoelectron Spectroscopy*, 2nd edn. (Butterworths, London, 1984)
28. T. Koopmans, Physica **1**, 104 (1933)
29. A.M. Ellis, M. Feher, T.G. Wright, *Electronic and Photoelectron Spectroscopy. Fundamentals and Case Studies* (Cambridge University Press, Cambridge, 2005)
30. K.L. Reid, Int. Rev. Phys. Chem. **27**(4), 607 (2008)
31. R.S. Berry, J. Chem. Phys. **45**, 1228 (1966)
32. A.J. Blake, J.L. Bahr, J.H. Carver, V. Kumar, Philos. Trans. R. Soc. Lond. A **268**, 159 (1970)
33. M. Seel, W. Domcke, J. Chem. Phys. **95**, 7806 (1991)
34. M. Seel, W. Domcke, Chem. Phys. **151**, 59 (1991)
35. V. Blanchet, M.Z. Zgierski, A. Stolow, J. Chem. Phys. **114**, 1194 (2001)
36. M. Schmitt, S. Lochbrunner, J.P. Shaffer, J.J. Larsen, M.Z. Zgierski, A. Stolow, J. Chem. Phys. **114**, 1206 (2001)
37. R.S. Minns, D.S.N. Parker, T.J. Penfold, G.A. Worth, H.H. Fielding, Phys. Chem. Chem. Phys. **12**, 15607 (2010). doi:10.1039/C001671C
38. K.L. Reid, Mol. Phys. **110**(3), 131 (2012)
39. H. Park, R.N. Zare, J. Chem. Phys. **104**, 4554 (1996)
40. O. Gessner, A. Lee, J. Shaffer, H. Reisler, S. Levchenko, A. Krylov, J. Underwood, H. Shi, A. East, D. Wardlaw, E. Chrysostom, C. Hayden, A. Stolow, Science **311**, 219 (2006)
41. R.E. Continetti, C.C. Hayden, in *Modern Trends in Chemical Reaction Dynamics*, ed. by K. Liu, X. Yang. Advanced Series in Physical Chemistry, vol. 14 (World Scientific, Singapore, 2003)
42. J.A. Davies, J.E. LeClaire, R.E. Continetti, C.C. Hayden, J. Chem. Phys. **111**, 1 (1999)

43. C.Z. Bisgaard, O.J. Clarkin, G. Wu, A.M.D. Lee, O. Geßner, C.C. Hayden, A. Stolow, Science **323**(5920), 1464 (2009)
44. K.L. Reid, J.G. Underwood, J. Chem. Phys. **112**, 3643 (2000)
45. K.L. Reid, T.A. Field, M. Towrie, P. Matousek, J. Chem. Phys. **111**, 1438 (1999)
46. J.G. Underwood, K.L. Reid, J. Chem. Phys. **113**, 1067 (2000)
47. S.C. Althorpe, T. Seideman, J. Chem. Phys. **113**, 7901 (2000)
48. T. Seideman, S.C. Althorpe, J. Electron Spectrosc. Relat. Phenom. **108**, 99 (2000)
49. S.C. Althorpe, T. Seideman, J. Chem. Phys. **110**, 147 (1999)
50. M. Tsubouchi, B.J. Whitaker, L. Wang, H. Kohguchi, T. Suzuki, Phys. Rev. Lett. **86**, 4500 (2001)
51. T. Brabec, F. Krausz, Rev. Mod. Phys. **72**, 545 (2000). doi:10.1103/RevModPhys.72.545
52. U. Keller, Nature **424**, 831 (2003). doi:10.1038/nature01938
53. M. Nisoli, S.D. Silvestri, V. Magni, O. Svelto, R. Danielius, A. Piskarskas, G. Valiulis, A. Varanavicius, Opt. Lett. **19**(23), 1973 (1994). doi:10.1364/OL.19.001973
54. T. Wilhelm, J. Piel, E. Riedle, Opt. Lett. **22**(19), 1494 (1997). doi:10.1364/OL.22.001494
55. F. Krausz, M. Ivanov, Rev. Mod. Phys. **81**, 163 (2009). doi:10.1103/RevModPhys.81.163
56. M. Abd-Elmeguid et al., Tesla technical design report, part 5: The x-ray free electron laser. Tech. rep, DESY (2001)
57. K. Tiedtke, A. Azima, N. von Bargen, L. Bittner, S. Bonfigt, S. Düsterer, B. Faatz, U. Frühling, M. Gensch, C. Gerth, N. Guerassimova, U. Hahn, T. Hans, M. Hesse, K. Honkavaar, U. Jastrow, P. Juranic, S. Kapitzki, B. Keitel, T. Kracht, M. Kuhlmann, W.B. Li, M. Martins, T. Núñez, E. Plönjes, H. Redlin, E.L. Saldin, E.A. Schneidmiller, J.R. Schneider, S. Schreiber, N. Stojanovic, F. Tavella, S. Toleikis, R. Treusch, H. Weigelt, M. Wellhöfer, H. Wabnitz, M.V. Yurkov, J. Feldhaus, New J. Phys. **11**(2), 023029 (2009)
58. P. Emma, R. Akre, J. Arthur, R. Bionta, C. Bostedt, J. Bozek, A. Brachmann, P. Bucksbaum, R. Coffee, F.J. Decker, Y. Ding, D. Dowell, S. Edstrom, A. Fisher, J. Frisch, S. Gilevich, J. Hastings, G. Hays, P. Hering, Z. Huang, R. Iverson, H. Loos, M. Messerschmidt, A. Miahnahri, S. Moeller, H.D. Nuhn, G. Pile, D. Ratner, J. Rzepiela, D. Schultz, T. Smith, P. Stefan, H. Tompkins, J. Turner, J. Welch, W. White, J. Wu, G. Yocky, J. Galayda, Nat. Photonics **4**(9), 641 (2010). doi:10.1038/nphoton.2010.176
59. A. Azima, S. Dusterer, P. Radcliffe, H. Redlin, N. Stojanovic, W. Li, H. Schlarb, J. Feldhaus, D. Cubaynes, M. Meyer, J. Dardis, P. Hayden, P. Hough, V. Richardson, E.T. Kennedy, J.T. Costello, Appl. Phys. Lett. **94**(14), 144102 (2009). doi:10.1063/1.3111789
60. R. Campargue, J. Phys. Chem. **88**(20), 4466 (1984). doi:10.1021/j150664a004
61. J.B. Anderson, J.B. Fenn, Phys. Fluids **8**(5), 780 (1965). doi:10.1063/1.1761320
62. A. Amirav, U. Even, J. Jortner, Chem. Phys. **51**(1–2), 31 (1980). doi:10.1016/0301-0104(80)80077-2
63. P.M. Mayer, T. Baer, Int. J. Mass Spectrom. Ion Process. **156**(3), 133 (1996). doi:10.1016/S0168-1176(96)04422-9
64. U. Even, J. Jortner, D. Noy, N. Lavie, C. Cossart-Magos, J. Chem. Phys. **112**(18), 8068 (2000). doi:10.1063/1.481405
65. M. Faubel, T. Kisters, Nature **339**(6225), 527 (1989). doi:110.1038/339527a0
66. A. Charvat, E. Lugovoj, M. Faubel, B. Abel, Rev. Sci. Instrum. **75**(5), 1209 (2004). doi:10.1063/1.1710704
67. M. Faubel, K.R. Siefermann, Y. Liu, B. Abel, Acc. Chem. Res. **45**(1), 120 (2012). doi:10.1021/ar200154w
68. Y. Tang, H. Shen, K. Sekiguchi, N. Kurahashi, T. Mizuno, Y.I. Suzuki, T. Suzuki, Phys. Chem. Chem. Phys. **12**, 3653 (2010). doi:10.1039/B925741A
69. P. Kruit, F.H. Read, J. Phys. E, Sci. Instrum. **16**(4), 313 (1983)
70. A.T.J.B. Eppink, S. Min Wu, B.J. Whitaker, in *Imaging in Molecular Dynamics*, ed. by B.J. Whitaker (Cambridge University Press, Cambridge, 2003)
71. S.J. Cavanagh, S.T. Gibson, M.N. Gale, C.J. Dedman, E.H. Roberts, B.R. Lewis, Phys. Rev. A **76**, 052708 (2007). doi:10.1103/PhysRevA.76.052708

72. V. Blanchet, M.Z. Zgierski, T. Seideman, A. Stolow, Nature **401**, 52 (1999). doi:10.1038/43410
73. J.A. Davies, A.M. Green, K.L. Reid, Phys. Chem. Chem. Phys. **12**, 9872 (2010). doi:10.1039/C0CP00102C
74. C.J. Hammond, K.L. Reid, K.L. Ronayne, J. Chem. Phys. **124**(20), 201102 (2006). doi:10.1063/1.2204596
75. M. Tsubouchi, B.J. Whitaker, L. Wang, H. Kohguchi, T. Suzuki, Phys. Rev. Lett. **86**, 4500 (2001). doi:10.1103/PhysRevLett.86.4500
76. O. Geßner, A.M.D. Lee, J.P. Shaffer, H. Reisler, S.V. Levchenko, A.I. Krylov, J.G. Underwood, H. Shi, A.L.L. East, D.M. Wardlaw, E.t.H. Chrysostom, C.C. Hayden, A. Stolow, Science **311**(5758), 219 (2006). doi:10.1126/science.1120779
77. A.E. Bragg, J.R.R. Verlet, A. Kammrath, O. Cheshnovsky, D.M. Neumark, Science **306**(5696), 669 (2004). doi:10.1126/science.1103527
78. P. Wernet, J. Gaudin, K. Godehusen, O. Schwarzkopf, W. Eberhardt, Rev. Sci. Instrum. **82**(6), 063114 (2011). doi:10.1063/1.3600901
79. P. Wernet, M. Odelius, K. Godehusen, J. Gaudin, O. Schwarzkopf, W. Eberhardt, Phys. Rev. Lett. **103**, 013001 (2009)

Chapter 6
Biomolecules, Photostability and $^1\pi\sigma^*$ States: Linking These with Femtochemistry

Gareth M. Roberts and Vasilios G. Stavros

Abstract In an effort to illuminate why nature has chosen a particular set of biomolecular 'building-blocks' for life, a surge of gas phase experiments have recently targeted understanding why key DNA bases, amino acids and their corresponding chromophore subunits, exhibit a resistance to photochemical damage (photostability) following ultraviolet radiation absorption. The research considered in this chapter focuses on the role of dissociative $^1\pi\sigma^*$ states in photostable behavior, and in particular H-atom elimination mediated *via* these states. By probing the timescales for the appearance of these H-atoms using ultrafast lasers coupled to molecular beam methodologies, important information pertaining to the excited state dynamics of these molecules can be obtained. We also discuss how the information gleaned from these studies can be used as a 'stepping-stone' for extending this research to larger, more complex biomolecules and, ultimately, more realistic systems in solution.

6.1 Introduction

Over the years a vast arena of interdisciplinary research has strived to understand the important characteristics of many biomolecules at a molecular level. Recently though, the contemporary discipline of ultrafast biophysics has led to a number of important breakthroughs regarding our understanding of key biological processes. This has been achieved by probing the excited electronic (and vibrational) state dynamics involved in these, often complex, natural systems [1]. Whilst this is not intended to be an exhaustive list, this field has aided in intimately mapping the trigger mechanism for human vision in rhodopsin [2, 3], efficient light harvesting processes occurring within photosynthesis [4] and the origins of high fluorescence quantum yields in numerous fluorescent protein variants [5, 6]. Such feats truly emphasize how probing the excited state dynamics of biological species on an ultrafast

G.M. Roberts · V.G. Stavros (✉)
Department of Chemistry, University of Warwick, Library Road, Coventry CV4 7AL, UK
e-mail: v.stavros@warwick.ac.uk

G.M. Roberts
e-mail: g.m.roberts@warwick.ac.uk

R. de Nalda, L. Bañares (eds.), *Ultrafast Phenomena in Molecular Sciences*,
Springer Series in Chemical Physics 107, DOI 10.1007/978-3-319-02051-8_6,

timescale can provide unparalleled insights into the mechanisms underpinning a diverse range of fundamental processes in biology.

The examples mentioned above highlight how light induced biochemistry can be essential for life. In contrast though, light's interaction with living organisms can also be highly detrimental. In particular, following photoexcitation with ultraviolet (UV) radiation, the electronically excited states of UV chromophores in DNA (DNA bases) can potentially trigger ultrafast structural changes (termed photolesions), which modify or terminate its genetic function [7]. These UV triggered processes can often be the fundamental precursors to mutagenesis, carcinogenesis and apoptosis [8]. Through evolution, nature has developed methods to combat these potentially devastating UV induced photoreactions. Light triggered photolyase enzymes, for example, act as one of the final bastions of defense against UV photodamage, by actively repairing photolesion sites in DNA [9]. Fortunately, many of the molecular building-blocks nature has selected for life, particularly the DNA bases, exhibit a built-in resistance against UV triggered damage. For this reason, they are commonly classed as *photostable* species. This photostable behavior is postulated to act as one of the front-line defenses against photodamage, and is so efficient that less than 1 % of UV induced excitation processes in DNA result in the formation of photolesions [10]. Their photostability is believed to be intimately linked to how efficiently electronically excited states can undergo non-radiative relaxation back to the electronic ground state, transforming electronic energy into less harmful thermal (vibrational) energy, which can be dissipated into surrounding solvent. It is this concept of photostability, and the role that specific excited electronic states play in this behavior, which we explore further in this chapter.

6.2 Excited Electronic States and Photostability

With the themes discussed in Sect. 6.1 in mind, a large interest towards understanding the intrinsic photostability of isolated DNA bases and, more generally, molecular subunits of biomolecules (specifically UV chromophores of the DNA bases and amino acids) has ensued. The ultimate vision of this work has been to link photostability to electronic structure. Excited electronic states, by and large, are much more reactive than the ground state and proficiency for rapidly diffusing this harmful energy will invariably aid the photostability of the molecule. Over the last decade, a multitude of studies have been carried out to elicit the details of photochemical pathways that can facilitate photostable behavior. A full description of the numerous reaction pathways that have been identified to date is beyond the scope of this chapter and for further comprehensive discussion the reader is referred to references [10–13] (and references therein).

This chapter discusses the role of $^1\pi\sigma^*$ states in the excited state dynamics of heteroaromatic biomolecules and their UV chromophore subunits. In the seminal theoretical work by Sobolewski *et al*. [14], the potential role of $^1\pi\sigma^*$ states in photostability was postulated through *ab initio* electronic structure calculations. These

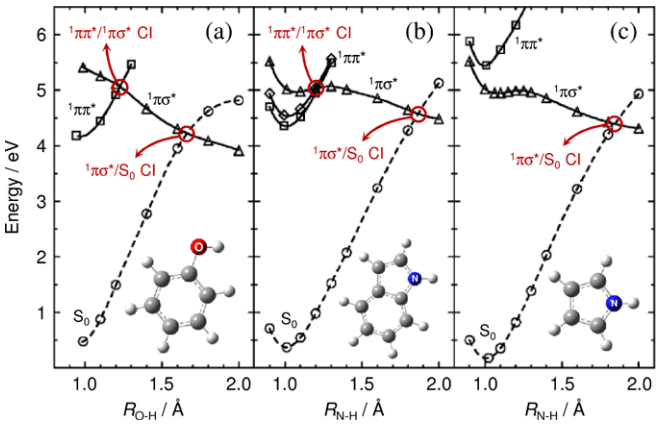

Fig. 6.1 Potential energy cuts of the S_0 ground state and lowest lying $^1\pi\pi^*$ and $^1\pi\sigma^*$ excited electronic states in (**a**) phenol, (**b**) indole and (**c**) pyrrole, as a function of the X–H stretch coordinate ($R_{X\text{–}H}$, where X = O or N). Conical intersections (CIs) are also highlighted. Figure adapted from [14]

studies indicated that $^1\pi\sigma^*$ states may offer a very simple radiationless decay pathway that contributes to the low fluorescence quantum yields observed in many heteroaromatic chromophores (beyond certain excitation energy thresholds).

Figure 6.1 depicts calculated potential energy profiles for (a) phenol, (b) indole and (c) pyrrole [14]—subunits found in tyrosine, tryptophan and hemes, respectively. With reference to these profiles, UV photon energy can be deposited into the molecule through excitation to a strongly absorbing $^1\pi\pi^*$ electronic state (formed as a result of a $\pi^* \leftarrow \pi$ transition). These molecules also possess a weakly absorbing excited electronic state of $^1\pi\sigma^*$ character, which intersects both the $^1\pi\pi^*$ state (phenol and indole, Fig. 6.1(a) and (b), respectively) and the electronic ground state (S_0), forming conical intersections (CIs) along an X–H bond coordinate, where X is typically O or N (see references [15–17] for a rigorous discussion of CIs). Sobolewski *et al.* [14] predicted that, following excitation to the $^1\pi\pi^*$ state and coupling onto the $^1\pi\sigma^*$ state (*via* a $^1\pi\pi^*/^1\pi\sigma^*$ CI), non-radiative decay along this pathway would be highly efficient due to the repulsive nature of this state, leading to either H-atom elimination or efficient relaxation to S_0 *via* a $^1\pi\sigma^*/S_0$ CI. Alternatively, it has also been demonstrated that direct excitation to the weakly absorbing $^1\pi\sigma^*$ state may also occur, leading to analogous behavior [18].

6.2.1 H-Atom Elimination Dynamics Mediated by $^1\pi\sigma^*$ States

Following the absorption of a UV photon, probing H-atom elimination from biomolecules and their subunits provides a very simple means of identifying, in part, the participation of $^1\pi\sigma^*$ states in their excited state dynamics, given that

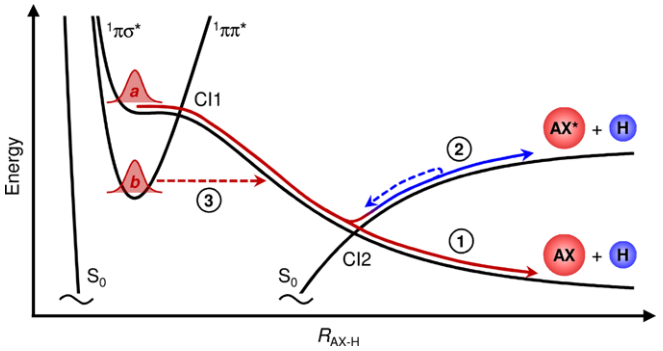

Fig. 6.2 Schematic potential energy cuts (*black*) along an AX–H bond coordinate (R_{AX-H}), depicting (1) non-adiabatic, (2) adiabatic and (3) tunneling dynamics, respectively. The details of each process are discussed in the main text. Conical intersections are labeled CI1 and CI2

these states are dissociative along X–H bond coordinates. This approach does require caution though: (i) this method is unable to provide quantitative information regarding the fraction of initially excited molecules which re-access the S_0 ground state through the $^1\pi\sigma^*/S_0$ CI; and (ii) the appearance of H-atoms is not solely indicative of $^1\pi\sigma^*$ mediated dynamics, as a range of processes, including multiphoton dissociative ionization [19, 20] and fragmentation of superexcited states [21], can also lead to the appearance of H-atoms. It is important to acknowledge that the former is currently a non-trivial issue to resolve. However, the latter can be addressed by measuring the kinetic energy (KE) of the H-atoms following photodissociation, or more commonly the total kinetic energy release (TKER). One is then able to correlate particular signatures in the TKER spectrum to H-atom elimination mediated through $^1\pi\sigma^*$ states (see Sect. 6.3.2). This was demonstrated in the pioneering work of Blank *et al*. [22] and later by Wei *et al*. [23].

6.2.2 Non-adiabatic, Adiabatic and Tunneling dynamics

H-atom elimination dynamics along $^1\pi\sigma^*$ states may involve a number of different photophysical processes. Of specific importance here are *non-adiabatic*, *adiabatic* and *tunneling* dynamics. We subsequently introduce these processes with reference to the schematic in Fig. 6.2, which depicts generic potential energy cuts along an AX–H bond, where X = a heteroatom and A = an aromatic moiety.

We begin by considering non-adiabatic behavior. With reference to wavepacket *a* in Fig. 6.2, this photo-prepared flux on the $^1\pi\pi^*$ state may pass through CI1 and proceed towards CI2 along the $^1\pi\sigma^*$ surface. Once at CI2, it can traverse through this CI non-adiabatically (process 1, solid red arrow) leading to direct AX–H bond fission, yielding H-atoms with large amounts of KE in coincidence with AX radical co-fragments. Non-adiabatic dynamics of this kind are typically characterized

by ultrafast dissociation timescales of < 100 fs (see for example [20]). Alternatively, dissociating flux can evolve adiabatically around CI2 (process 2, solid blue arrow), and generate AX radicals in an electronically excited state, AX*, together with H [19, 24]. However, in scenarios where the dissociative flux does not have enough energy to access the higher energy dissociation asymptote (*e.g.* initial photo-preparation of wavepacket *b* in Fig. 6.2), some fraction may return towards CI2 (dashed blue arrow) and non-adiabatically couple back onto S_0, forming thermally (vibrationally) hot S_0 molecules [25]. In the gas phase, these vibrationally hot S_0 species may ultimately undergo *statistical unimolecular dissociation* to generate H-atoms with low amounts of KE on a timescale as fast as picoseconds [25, 26].

A third scenario that can occur involves excited state flux tunneling through an energy barrier to access the $^1\pi\sigma^*$ surface (see for example [27–29]). Wavepacket *b* in Fig. 6.2 correlates to flux which has been photo-prepared on $^1\pi\pi^*$ below the energy of CI1. Depending on the size of the barrier area under CI1, the wave-like nature of the flux (in this instance the dissociating H-atom) may enable tunneling under CI1 (process 3, dashed red arrow) and coupling onto the $^1\pi\sigma^*$ state at extended AX–H distances (H tunneling is revisited in Sect. 6.4.3). Timescales for H-atom elimination dynamics mediated through tunneling are inherently linked to the size of the barrier and can range up to nanoseconds [29], but none-the-less, still generate high KE H-atoms as a result of subsequent dissociation on the $^1\pi\sigma^*$ surface.

In the following section we introduce experimental techniques which have been used to identify the participation of these processes in $^1\pi\sigma^*$ based dynamics, with particular focus on methods which monitor the appearance of H-atom photoproducts.

6.3 Experimental Detection of $^1\pi\sigma^*$ Mediated Dynamics

A number of spectroscopic techniques in the gas phase have been utilized to characterize $^1\pi\sigma^*$ mediated dynamics in heteroaromatic chromophores, from both a frequency- and time-domain perspective. Frequency-domain measurements can offer precise information regarding the energetics of the dissociation process and the vibrational motions involved, while time-domain measurements are often able to observe direct participation of these states and their ultrafast temporal evolution. The complementary information yielded from both domains has proved highly fruitful in understanding the role of $^1\pi\sigma^*$ states in the excited state dynamics of a broad range of biomolecules and their subunits (see for example [18, 20, 27, 29–33]). Whilst this chapter focuses on time-domain experiments, we briefly list both approaches for completeness. High resolution frequency-resolved studies have been dominated by photofragment translational spectroscopies, in particular multi-mass ion imaging [34, 35], H (Rydberg) atom photofragment translational spectroscopy [18, 36] and velocity map ion imaging [23, 37]. Time-resolved techniques have included time-resolved photoelectron spectroscopy [31, 38, 39], time-resolved mass spectrometry (TR-MS) [25, 27, 40, 41] and time-resolved velocity map ion imaging (TR-VMI)

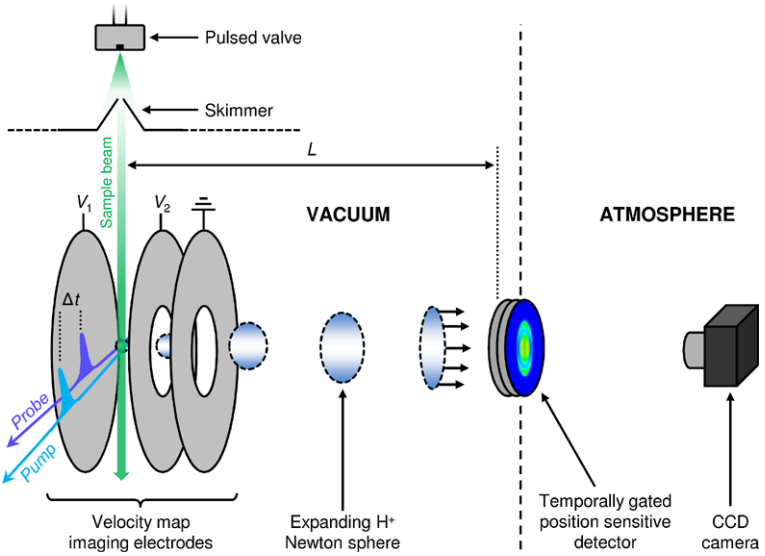

Fig. 6.3 Schematic arrangement of an ultrafast TR-VMI experiment. Further details of the TR-VMI apparatus are discussed in the main text

[20, 26, 29]. In the following sections we specifically describe the use of TR-MS and TR-VMI for probing H-atom elimination mediated by $^1\pi\sigma^*$ states in greater detail.

6.3.1 Time-Resolved Time-of-Flight Mass Spectrometry

TR-MS methods commonly utilize time-of-flight mass-spectrometers (TOF-MS). In these experiments, a skimmed molecular beam of target molecules is produced by seeding a vapor pressure of analyte into a carrier gas (*e.g.* He or Ar), which is admitted into vacuum using a pulsed valve, typically piezoelectrically [42] or solenoid [43] driven. The molecular beam pulse is intercepted perpendicularly by fs laser pulses at the centre of the TOF optics, which usually replicate the arrangement described by Wiley and McLaren [44]—such an electrode arrangement is shown in Fig. 6.3. By applying high voltages (on the order of kVs) to the TOF optics (V_1 and V_2 in Fig. 6.3), ionized photofragments are accelerated into a drift tube, with the same KE, along the time-of-flight axis, L. Whilst the KEs of the ions are the same, their velocities along the flight axis depend on mass. As a result, ions with the lightest mass arrive at the terminus of the flight tube first, followed later by heavier ions. A mass spectrum of ions, resolved by their different time-of-flights, is then collected by a detector placed at the end of the flight tube (which registers ion counts as a function of flight time). The most common type of detector is based around a

microchannel plate (MCP) assembly, which possesses very high ion detection sensitivity (> 80 % [45]).

With regards to probing the timescales for H-atom elimination, a fs pump pulse photoexcites the molecules of interest, defining the zero of time ($\Delta t = 0$) for the experiment, while a time delayed fs probe pulse, centered at 243 nm, ionizes any H-atom photoproducts through (2 + 1) resonance enhanced multiphoton ionization (REMPI), generating H^+. Both fs pump and probe pulses are typically derived from optical parametric amplifiers (OPAs) [46], commonly seeded by the output of a commercial ultrafast Ti:sapphire laser system. All ions, including H^+, are then analyzed using TOF-MS. By recording a mass spectrum at a series of different time delays (Δt) between the fs pump and probe pulses, and integrating only the H^+ counts in the mass spectrum at each Δt, the buildup of H^+ can be tracked in real time. The generated H^+ signal transient can then be modeled using appropriate functions (*e.g.* an exponential rise function convoluted with the temporal instrument response function—see Sect. 6.4.1) to obtain a time-constant, τ, for the appearance of H-atoms. However, as discussed in Sect. 6.2.1, the mere detection of H-atoms is not necessarily indicative of $^1\pi\sigma^*$ mediated dynamics. A more complete picture of $^1\pi\sigma^*$ mediated H-atom elimination can be attained using time-resolved photofragment translational spectroscopies, such as TR-VMI, which can monitor both the ultrafast appearance timescales and KEs of any H photoproducts.

6.3.2 Time-Resolved Velocity Map Ion Imaging

Charged particle imaging techniques [47] and, in particular, velocity map ion imaging (VMI) [37], have revolutionized the field of photofragment spectroscopy and are now essential methodologies used in gas phase molecular reaction dynamics [48]. One of the major advantages of VMI is that it simultaneously recovers both the recoil speed and the angular recoil trajectories (velocity vectors) of the original 3-D distribution of ionized photofragments (Newton sphere) by collecting its 2-D projection. With respect to the schematic in Fig. 6.3, VMI is typically implemented using a *gridless* Wiley-McLaren TOF electrode arrangement, which both temporally and spatially focus ions onto a *position sensitive* detector (typically a pair of MCPs coupled to a phosphor screen) placed at the terminus of a field-free flight tube. By temporally gating the detector, it is possible to collect the 2-D projection of only a specific photofragment mass of interest, m_f, based on its known TOF, t, to the detector, given by:

$$t = L\sqrt{\frac{m_f}{2eV_1}} \tag{6.1}$$

where V_1 is the voltage on the accelerator plate of the VMI arrangement, e is the elementary charge and L is the distance from the laser-molecule interaction point to the front plane of the detector. Unlike the gridded electrodes used in a standard Wiley-McLaren TOF-MS, the gridless electrodes used in VMI lead to the

formation of an electrostatic lens, which causes ionized photofragments with the same velocity vectors to be focused onto the same position of the 2-D detector plane, regardless of their initial position within the ionization volume of the focused probe laser. As a result, carefully designed VMI arrangements, in combination with high-resolution frequency-domain studies, can deliver an energy resolution down to $\Delta E/E = 0.38$ % [49]. Although this energy resolution is not achievable in ultrafast TR-VMI experiments, due to the inherently broad bandwidth of fs pulses (typically hundreds of cm^{-1}), coupling ultrafast pump-probe spectroscopy with VMI still vitally affords temporal and energy information (as well as photofragment angular recoil information—*vide infra*), regarding photodissociation mechanisms, unlike TR-MS. For completeness, we highlight that, very recently, magnetic-bottle analyzers (which are traditionally used to perform photoelectron spectroscopy [38]) have been adapted to perform time-resolved photofragment translational spectroscopy measurements on H^+ [50, 51], also delivering energy and time information about $^1\pi\sigma^*$ dynamics.

At each pump-probe time delay, Δt, the desired 1-D TKER distribution can be recovered from a measured 2-D H^+ velocity map image using image reconstruction methods [52–54]. Reconstruction algorithms return the 1-D radial (r) spectrum, which may then be converted into KE space using an appropriate Jacobian ($r^2 \propto$ KE) and a KE calibration factor. The latter is obtained by measuring photofragments from a well characterized dissociation event (*e.g.* ionizing H-atoms from photolyzed HBr [55]). The measured KE of the photofragments may finally be converted into the desired TKER scale according to:

$$\text{TKER} = \text{KE}\left(\frac{m_\text{p}}{m_\text{p} - m_\text{f}}\right) \tag{6.2}$$

where m_p is the mass of the parent molecule.

When considering $^1\pi\sigma^*$ mediated H-atom elimination dynamics, the different signal features in the derived TKER distribution can be related back to different photodissociation mechanisms. We consider this with respect to the schematic potentials in Fig. 6.4(a). Dynamics proceeding along dissociative $^1\pi\sigma^*$ states typically generate features with large TKERs [18]. For a parent species, AX–H, in its zero point vibrational level prior to photoexcitation, partitioning of the available energy into TKER during this dissociation process can be understood according to:

$$\text{TKER} = h\nu_\text{pu} - D_0(\text{AX–H}) - E_\text{elec} - E_\text{vib} \tag{6.3}$$

where $h\nu_\text{pu}$ is the pump photon energy, D_0(AX–H) is the AX–H bond strength, and E_elec and E_vib are the electronic and vibrational energies of the radical co-fragments, AX. The maximum TKER, TKER_max, after AX–H dissociation along the $^1\pi\sigma^*$ surface corresponds to a scenario where radical co-fragments are formed with zero internal energy ($E_\text{elec} = 0$ and $E_\text{vib} = 0$), following non-adiabatic dynamics through the $^1\pi\sigma^*/S_0$ CI. In this case, Eq. (6.3) simplifies to:

$$\text{TKER}_\text{max} = h\nu_\text{pu} - D_0(\text{AX–H}) \tag{6.4}$$

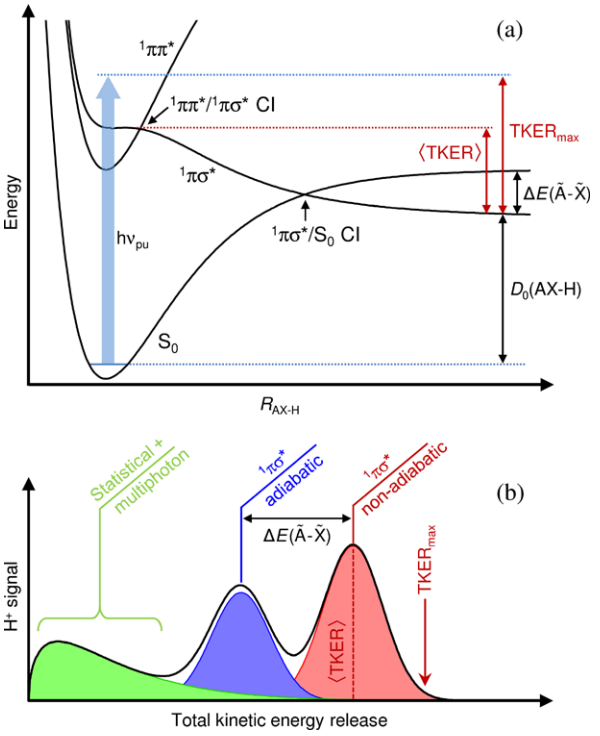

Fig. 6.4 (**a**) Schematic potential energy profiles along an AX–H bond coordinate ($R_{AX–H}$), depicting energy partitioning into TKER as a result of $^1\pi\sigma^*$ mediated dissociation, with relation to Eqs. (6.3) and (6.4). (**b**) Example profile of a TKER spectrum (*black line*) resulting from probed H-atom photoproducts, following AX–H bond fission along a $^1\pi\sigma^*$ surface

In TR-VMI studies, features associated with $^1\pi\sigma^*$ mediated AX–H fission, evolving non-adiabatically around the $^1\pi\sigma^*/S_0$ CI, typically appear as Gaussian-like profiles at high TKERs (Fig. 6.4(b), red shading). Depending on the initial $h\nu_{pu}$ energy and the energy partitioning between TKER and E_{vib}, the high energy 'tail' of these features may extend to (approximately) TKER$_{max}$ [56, 57]. As illustrated by Fig. 6.4(b), the central (mean) TKER of the non-adiabatic $^1\pi\sigma^*$ feature, ⟨TKER⟩, is related to the energy difference between the plateau region of the $^1\pi\sigma^*$ surface (caused by an avoided crossing between the $^1\pi\sigma^*$ valence state and a $^1\pi$3s Rydberg state near the vertical Franck-Condon region [18, 58]) and the dissociation asymptote—note that an alternative interpretation of ⟨TKER⟩ is required for tunneling dynamics under a $^1\pi\pi^*/^1\pi\sigma^*$ CI, as discussed in Sect. 6.4.3. Equation (6.3) also highlights that it is possible, in principle, to distinguish between non-adiabatic and adiabatic dynamics around the $^1\pi\sigma^*/S_0$ CI—the latter generates electronically excited AX co-fragments ($E_{elec} = \Delta E(\tilde{A} - \tilde{X})$), giving rise to a Gaussian-like feature which is red-shifted in TKER, relative to the location of the non-adiabatic feature, by $\Delta E(\tilde{A} - \tilde{X})$ (Fig. 6.4(b), blue shading). Similarly, H^+ signals originating from multiphoton processes and statistical unimolecular dissociation of vibrationally hot S_0 species peak at low TKERs and typically exhibit broad signal profiles peaked at low TKER (Fig. 6.4(b), green shading) [18, 26, 59, 60], allowing them to be readily distinguished from direct AX–H fission along $^1\pi\sigma^*$ surfaces. Integrating the signal associated with the $^1\pi\sigma^*$ features in the derived TKER spectra, at a series

of Δt, subsequently allows a H^+ signal transient to be constructed. This transient can finally be analyzed *via* a kinetic fit to return a timescale, τ, which solely reflects the $^1\pi\sigma^*$ mediated AX–H fission dynamics.

In addition to the combined time and energy resolution gained by TR-VMI, image reconstruction methods also return a quantitative measure of the photofragment angular distributions, which can often be a critical tool for gleaning additional information about photodissociation processes [48] (note that this is not possible when using the magnetic-bottle analyzers mentioned above). Photoexcitation will preferentially excite molecules that have their electronic transition dipole moment ($\boldsymbol{\mu}$) aligned parallel to the electric field vector of the pump laser ($\boldsymbol{\varepsilon}$), where $\boldsymbol{\varepsilon}$ is parallel to plane of the position sensitive detector. For direct dissociation along $^1\pi\sigma^*$ states, which typically occurs on a timescale much faster than parent molecule rotation (see for example [20]), the angular recoil distribution of the photofragments will be preserved, and is related to the orientation of the dissociating bond coordinate with respect to $\boldsymbol{\mu}$. For a one-photon induced dissociation process, in the limit of axial recoil, the angular distribution of photofragments, $I(\theta)$, is given by the relationship [61]:

$$I(\theta) = \frac{\sigma}{4\pi}\left[1 + \frac{\beta_2}{2}\left(3\cos^2\theta - 1\right)\right] \tag{6.5}$$

where θ is the photofragment recoil angle with respect to $\boldsymbol{\varepsilon}$, σ is the photodissociation cross-section and β_2 is the anisotropy parameter. β_2 exhibits limiting values of -1 and $+2$ in cases where $\boldsymbol{\mu}$ lies orthogonal or parallel to the dissociating bond, respectively. Non-limiting negative and positive β_2 values can arises when $\boldsymbol{\mu}$ lies at an angle between 0° and 90° with respect to the bond fission coordinate, whereas $\beta_2 = 0$ corresponds to a purely isotropic photofragment recoil distribution. $\beta_2 = 0$ can arise through either: (i) $\boldsymbol{\mu}$ lying close to an angle of 54.7° to the bond fission coordinate; or (ii) dissociation taking place on a timescale significantly slower than the timeframe for rotational decoherence of excited parent molecules. In the case of rapid direct dissociation, the value of β_2 importantly allows one to extrapolate information regarding the initially excited electronic state, provided the orientation of $\boldsymbol{\mu}$ relative to the dissociating bond coordinate is known.

In Sect. 6.4 we move on to discuss examples where TR-MS and TR-VMI methods have been applied to understanding of $^1\pi\sigma^*$ mediated dynamics in a selection of heteroaromatic species, found as subunits in a variety of photostable biomolecules.

6.4 Applications

6.4.1 Non-adiabatic Versus Adiabatic Dynamics

Clocking ultrafast timescales for $^1\pi\sigma^*$ mediated H-atom elimination dynamics from an aromatic heterocycle was first reported by Radloff and co-workers using TR-MS [25]. This work focused on elucidating the timeframes for N–H bond fission

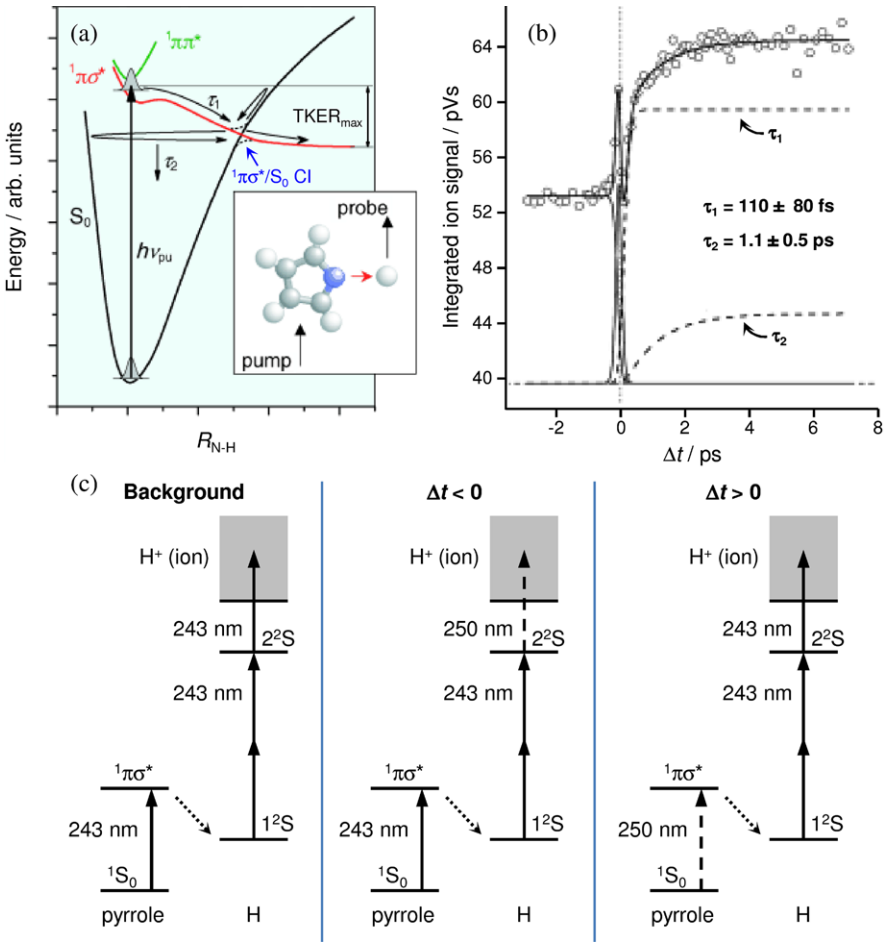

Fig. 6.5 (**a**) Schematic potential energy profiles of the S_0 ground state and lowest energy $^1\pi\pi^*$ and $^1\pi\sigma^*$ excited electronic states in pyrrole (molecular structure *inset*), with respect to the N–H bond coordinate ($R_{N\text{–}H}$). (**b**) Time-resolved H^+ signal transient (*open circles*) recorded from pyrrole using TR-MS with a 250 nm pump and 243 nm probe scheme. (**c**) Processes involved in the photolysis and ionization of H-atoms from pyrrole. Figure adapted from [25]

along the $^1\pi\sigma^*$ state in pyrrole (molecular structure shown in Fig. 6.5(a))—an aromatic subunit found in a variety of larger biomolecules, such as hemes. Figure 6.5(a) presents schematic potential energy profiles for the $S_0(^1A_1)$ ground state together with the first $^1\pi\pi^*(^1B_2)$ and $^1\pi\sigma^*(^1A_2)$ excited states in pyrrole, with respect to N–H bond length. Following excitation with a fs pump pulse centered at 250 nm, population is vibronically induced onto the $^1\pi\sigma^*$ state—a transition which is formally electric dipole forbidden in pyrrole's C_{2v} point group. This forbidden $^1\pi\sigma^*(^1A_2) \leftarrow S_0(^1A_1)$ transition gains oscillator strength by vibrational intensity borrowing from the higher lying $^1\pi\pi^*(^1B_2)$ manifold (or another higher energy

$^1\pi\pi^*$ state) [25, 62]. Using a temporally delayed fs probe pulse centered at 243 nm, the appearance timescale for any photodissociated H-atoms was subsequently monitored through (2 + 1) REMPI, enabling the detection of H^+ with TR-MS. The results of these experiments are presented in Fig. 6.5(b). For all pump-probe delays, Δt, there is a constant (time-independent) one-color background signal, generated from the 243 nm probe *via* the process depicted in the left panel of Fig. 6.5(c). At $\Delta t < 0$ ps (*i.e.* pumping with 243 nm and probing with 250 nm), some H^+ signal is generated through an inefficient two-color 'probe-pump' process (Fig. 6.5(c), middle panel). At $\Delta t = 0$ ps delay, when the fs pump and probe pulses are temporally overlapped, a sharp spike in the H^+ signal is observed (due to a combination of multiphoton absorption processes [25]), which then decays within the temporal resolution of the experiment ($\sim$ 160 fs). Finally, when $\Delta t > 0$ ps, a notable rise in signal is observed, relative to negative pump-probe delays, correlating to the appearance of photodissociated H-atoms from pyrrole at 250 nm (Fig. 6.5(c), right panel). This signal rise exhibits a bi-exponential profile with two associated time constants, τ_1 and τ_2, which take values of 110 ± 80 fs and 1.1 ± 0.5 ps, respectively. With reference to Fig. 6.5(a), the ultrafast time constant, τ_1 (110 fs), is ascribed to the timescale for direct $^1\pi\sigma^*$ mediated N–H bond fission, proceeding *via* non-adiabatic passage through the $^1\pi\sigma^*/S_0$ CI, yielding H-atoms with large amounts of KE (defined by $TKER_{max}$) in coincidence with pyrrolyl (C_4H_4N) radical co-fragments in their electronic ground state. Alternatively, as population reaches the $^1\pi\sigma^*/S_0$ CI it may evolve adiabatically, traversing the upper cone of the CI and then returning to subsequently undergo non-adiabatic coupling back into vibrationally excited ground state species. Radloff and co-workers [25] postulated that the slower τ_2 time-constant (1.1 ps) originates from this initial adiabatic behavior around $^1\pi\sigma^*/S_0$ CI, resulting in statistical elimination of H-atoms with less KE from vibrationally hot S_0 species, after some degree of intramolecular vibrational energy redistribution (IVR) in S_0.

6.4.2 Comparing Dynamics in Simple Azoles

Upon exchanging one of the ring C–H bonds in pyrrole for an N atom, the simple azole isomers imidazole and pyrazole can be formed (structures shown in Fig. 6.6), both of which belong to the lower C_s symmetry group, transforming the $^1\pi\sigma^*(A'') \leftarrow S_0(A')$ transition into an electric dipole allowed process ($A' \otimes a'' \otimes A'' \supseteq A'$). Imidazole is a common subunit of photostable biomolecules, most notably in the amino acid histidine and the purine derived DNA bases adenine and guanine. In contrast, naturally occurring pyrazole derivatives are rare [64], particularly in biomolecules which are inherently required to be photostable. In light of this, TR-VMI experiments have begun to investigate whether there are any notable differences in the UV photochemistry of these two simple azole isomers [26], particularly along their $^1\pi\sigma^*$ states, despite their qualitatively similar electronic structure [63]—Fig. 6.6 presents schematic potential energy profiles along their N–H bond coordinates.

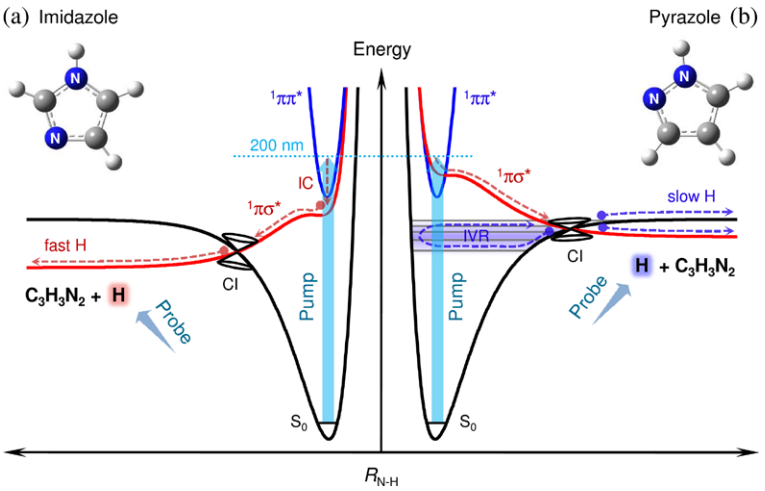

Fig. 6.6 Schematic potential energy profiles of the S_0 (*black*), $^1\pi\pi^*$ (*blue*) and $^1\pi\sigma^*$ (*red*) electronic states of (**a**) imidazole and (**b**) pyrazole (molecular structures *inset*) along their N–H bond coordinates (R_{N-H})—schematics are based on the calculated potentials in [63]. *Dashed red arrows* indicate rapid direct N–H bond fission *via* internal conversion (IC) through CIs onto the $^1\pi\sigma^*$ state, yielding high KE (fast) H-atoms. *Dashed blue lines* represent a possible pathway for IC back onto S_0 and statistical (slow) H-atom elimination following internal IVR on S_0. Figure adapted from [26]

H^+ velocity map images recorded following 200 nm excitation of imidazole and pyrazole, at delays of $\Delta t = 2.5$ and 600 ps, are shown contrasted as insets in Fig. 6.7(a) (top = 2.5 ps, bottom = 600 ps). Also presented are the TKER spectra derived from these images. The Gaussian-like features, centered at ~ 10000 cm^{-1} in both cases, correlate to probed H-atoms eliminated from the N–H bond along their $^1\pi\sigma^*$ states. In imidazole, excitation at 200 nm results in initial population of the $^1\pi\pi^*$ state, which can then couple through a CI (calculated to lie along an out-of-plane ring distortion coordinate [66]) onto the $^1\pi\sigma^*$ state, facilitating ultrafast N–H bond fission. The integrated H^+ signal transient for imidazole's $^1\pi\sigma^*$ signal feature (Fig. 6.7(b), left panel) reveals that this overall $^1\pi\pi^* \rightarrow {}^1\pi\sigma^* \rightarrow$ N–H scission process occurs in 78 ± 40 fs [65], a timescale which has been further verified through complementary time-resolved photofragment translational spectroscopy measurements by Ullrich and co-workers [51]. In pyrazole, however, an analysis of the H^+ angular recoil distribution for the $^1\pi\sigma^*$ feature in the velocity map image ($\beta_2 = -0.5$) reveals that some fraction of population is directly imparted to the $^1\pi\sigma^*$ state upon UV excitation (albeit the weak one photon absorption cross-section for this transition) [57]. Figure 6.6(b) shows how pyrazole's $^1\pi\sigma^*$ state is (i) located higher in energy than the $^1\pi\pi^*$ state and (ii) is directly accessible at 200 nm [63]. As a result, direct population of the $^1\pi\sigma^*$ state at 200 nm in pyrazole delivers extremely rapid N–H bond cleavage, supported by the sub-50 fs time-constant extracted from the transient in the right panel of Fig. 6.7(b) [57].

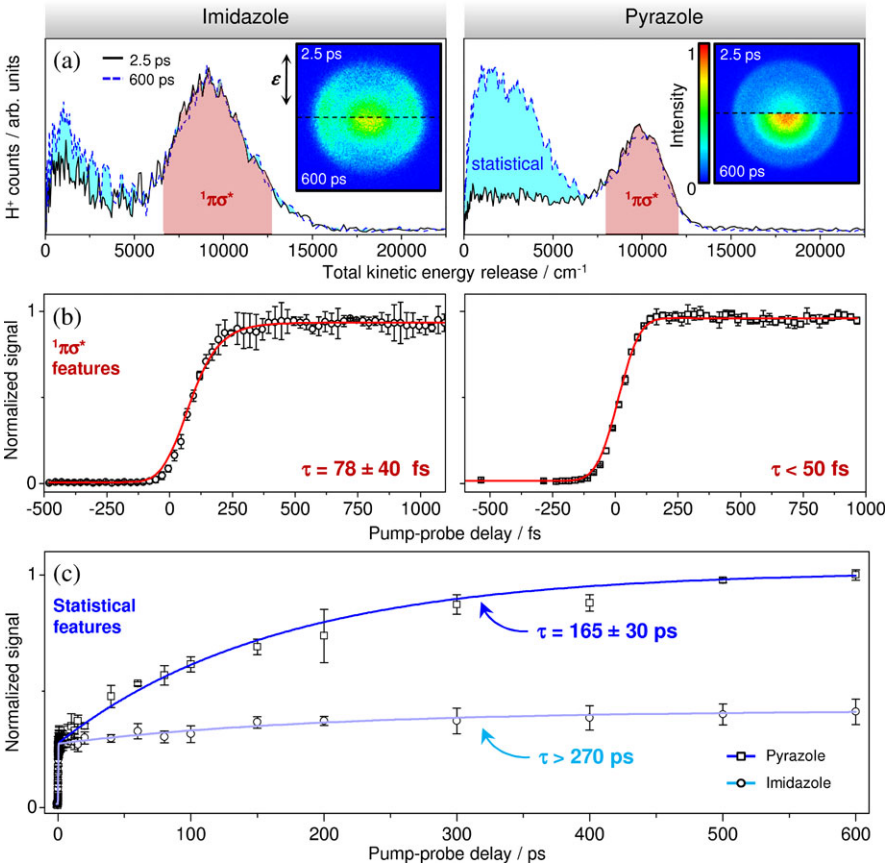

Fig. 6.7 (**a**) TKER spectra recorded at pump-probe delays of $\Delta t = 2.5$ and 600 ps for imidazole (*left*) and pyrazole (*right*). H^+ velocity map images from which the spectra are derived are provided *inset* (the *vertical arrow* indicates the electric field polarization of the pump laser, $\boldsymbol{\varepsilon}$). (**b**) Integrated H^+ signal transients and kinetic fits (*red lines*) for the $^1\pi\sigma^*$ features in imidazole (*left*) and pyrazole (*right*). (**c**) Integrated H^+ signal transients and kinetic fits (*light blue* = imidazole, *dark blue* = pyrazole) for the 'statistical' features in imidazole and pyrazole. Figure adapted from [26, 57, 65]

In pyrrole, Radloff and co-workers considered the role of slower statistical H loss from vibrationally hot S_0 species after coupling back onto S_0 at the $^1\pi\sigma^*/S_0$ CI [25]. As discussed in Sect. 6.3.2, the TKER distribution of statistically ejected H-atoms exhibits a characteristic broad signal profile, peaked at low TKER [18, 59, 60]. One of the major advantages of the TR-VMI technique over TR-MS, is that the statistical H-atom signal component can be readily discerned from signal arising from direct $^1\pi\sigma^*$ driven dynamics, due to the simultaneous provision of both temporal and energetic information. This is aptly demonstrated in imidazole and pyrazole [26]. Upon increasing Δt to hundreds of picoseconds in imidazole, a minimal increase in signal at low TKER is observed (relative to the background

multiphoton signal observed at 2.5 ps [26, 65]), and is attributed to the onset of statistical H-atom elimination from hot S_0 species. This statistical feature appears with a time-constant of > 270 ps, shown by the transient in Fig. 6.7(c) (open circles). Selective deuteration of the N–H bond (N–D) also terminates any H^+ signal, revealing that H elimination in imidazole is localized to the N–H bond coordinate, even after coupling back onto S_0 [26]. In stark contrast, pyrazole exhibits a sizable gain in statistical H^+ counts by 600 ps, relative to imidazole (see Figs. 6.7(a) and (c)), and appears with a time-constant of $\tau = 165 \pm 30$ ps. Further measurements on deuterated isotopomers of pyrazole (either exclusive deuteration of all C–H bonds (C–D) or only the N–H bond (N–D)) reveals that there is change to $\sim$ 1:1 ratio for statistical H loss from C–H:N–H coordinates in pyrazole [26] (unlike imidazole). It has been conjectured that irreversible photodamage of pyrazole through C–H bond fission and the generation of toxic free radicals may have played a role in the structural selectivity of imidazole over pyrazole in photostable biomolecules [26].

6.4.3 Excited State H-Atom Tunneling Dynamics

Over the years quantum tunneling of protons/hydrogen atoms has been implicated in a vast array of chemical [67] and biological [68] processes, such as photoacidity behavior [69, 70], alcohol dehydrogenase enzymes [71] and around the oxygen evolving complex site in photosystem II [72]. With respect to the latter, a series of proton-coupled electron-transfer reactions [73] are proposed to occur, one of which involves de-protonation of an O–H bond in a tyrosine residue *via* proton tunneling to a neighboring histidine acceptor site [72]. The residue of the amino acid tyrosine is the UV chromophore phenol, shown inset in Fig. 6.8. In recent years there has been a growing body of evidence to suggest that, over a specific UV excitation range (275–248 nm), photoexcited phenol itself exhibits a propensity for H-atom tunneling dynamics along the O–H coordinate under a $^1\pi\pi^*/^1\pi\sigma^*$ CI [27–29, 74]. It is this aspect of phenol's UV induced photochemistry which forms the topic of discussion for this section.

Calculated potential energy cuts along phenol's O–H bond coordinate by Ashfold and co-workers [28], shown in Fig. 6.8, serve to indicate how, after excitation to the zero point energy (ZPE) of the $^1\pi\pi^*$ state (275 nm), population may tunnel under the barrier formed by the $^1\pi\pi^*/^1\pi\sigma^*$ CI onto the $^1\pi\sigma^*$ state at elongated O–H bond lengths. This process subsequently gives rise to the elimination of high KE H-atoms, in coincidence with ground state phenoxyl radicals, $C_6H_5O(\tilde{X})$. Such a mechanism was first speculated in the theoretical work of Sobolewski *et al.* [14]. Later, experimental work by Pino *et al.* added further credence to this proposed tunneling mechanism [27]. This was achieved through TR-MS measurements, which compared the lifetimes extracted from parent cation signal decays following excitation to the $^1\pi\pi^*$ ZPE in a wide range of chemically substituted phenols and their hydrogen bonded complexes with NH_3. With the aid of complementary theory calculations, it was highlighted that phenol derivatives with a smaller vertical energy gap

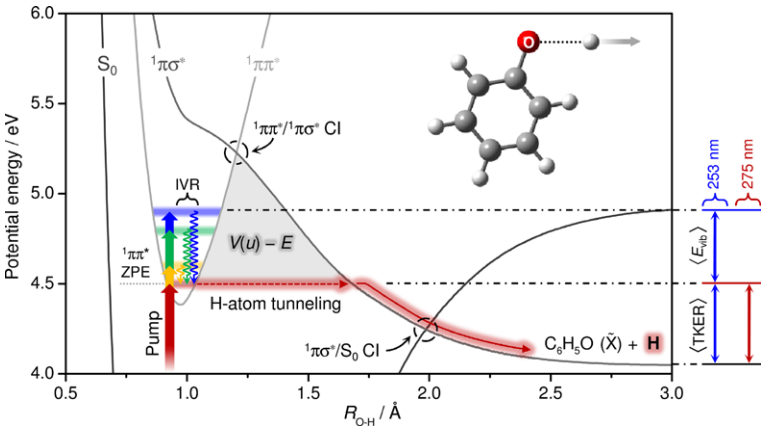

Fig. 6.8 Calculated potential energy cuts along the O–H bond coordinate (R_{O-H}) of phenol (molecular structure shown *inset*), obtained from reference [28]. Potentials were calculated at the CASPT2(10,10)/aug(O)-AVTZ level of theory. Excitation with fs pump pulses at 275 (*red*), 268 (*orange*), 258 (*green*) and 253 nm (*blue*) is indicated by the *vertical arrows*. *Wavy arrows* symbolize possible IVR back to the ZPE of the O–H stretch mode in $^1\pi\pi^*$ after excitation to modes orthogonal to the O–H stretch coordinate. The *grey shaded area*, labeled $V(u) - E$, highlights the barrier area used in 1-D BKW tunneling calculations. Figure adapted from [29]

between their $^1\pi\pi^*$ and $^1\pi\sigma^*$ states generally displayed reduced excited state lifetimes. Such an observation is in line with excited state decay dominated by tunneling under the $^1\pi\pi^*/^1\pi\sigma^*$ CI, as the excited state lifetime will be intimately linked to the size of the barrier area. Further support for this interpretation has since been garnered through frequency domain experiments, together with 2-D wavepacket calculations, by Dixon *et al.* [28], which imply that (on symmetry grounds) H tunneling is driven by the ν_{16a} mode (a ring torsion motion [75]) together with O–H stretching. Furthermore, fully deuterated phenol (C_6D_5OD) does not yield any signature of D-atom elimination *via* the $^1\pi\sigma^*$ state below the $^1\pi\pi^*/^1\pi\sigma^*$ CI [76], in line with the greatly reduced probability for D tunneling ($\sim 10^3$ times less than H [28]), allowing radiative decay processes to dominate and increase its fluorescence lifetime ($\sim$ 13 ns [77]).

Using TR-VMI, the dynamics of the excited state tunneling process in phenol can be tracked directly by monitoring the H-atom photoproducts [29]. A TKER spectrum recorded following excitation to the $^1\pi\pi^*$ ZPE at 275 nm in phenol is shown in Fig. 6.9(a) (derived from a H^+ velocity map image recorded at $\Delta t = 1.2$ ns). As with previously discussed examples, the dominant Gaussian feature centered at ~ 6000 cm^{-1} is assigned to O–H bond fission mediated by the $^1\pi\sigma^*$ state; the good accord between the predicted TKER_{max} value for this process at 275 nm (Fig. 6.9(a), vertical red arrow) and the location of the Gaussian feature confirms this interpretation. As the pump energy is increased (268–253 nm), the center of the $^1\pi\sigma^*$ feature, highlighted as $\langle$TKER$\rangle$ in Fig. 6.9(a), remains in approximately the same location (only $\sim$ 1000 cm^{-1} blue shift from 275–253 nm); this peak does, however, begin to broaden towards higher TKER, in agreement with the predicted increase in

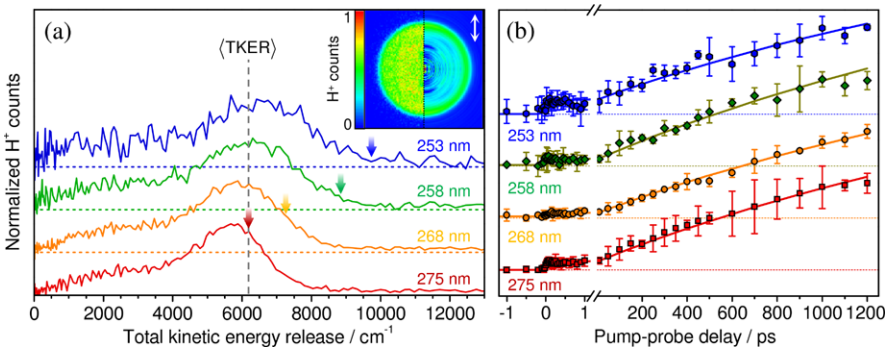

Fig. 6.9 (**a**) TKER spectra recorded following excitation with pump wavelengths centered at 275, 268, 258 and 253 nm in phenol. Spectra are recorded at a pump-probe delay of $\Delta t = 1.2$ ns. *Vertical arrows* indicate the predicted TKER_{max} for O–H bond fission *via* the $^1\pi\sigma^*$ state at the given wavelengths (see (6.4)). An example H^+ image (275 nm pump) is shown *inset*, with the polarization of the pump laser, ε, indicated by the *white arrow* (*left* = raw image, *right* = deconvoluted slice). (**b**) Integrated H^+ signal transients for the $^1\pi\sigma^*$ features in phenol. *Solid lines* represent a kinetic model obtained from 1-D BKW tunneling calculations (6.6) using the calculated potential cuts in Fig. 6.8. Figure adapted from [29]

TKER_{max} (Fig. 6.9(a), vertical arrows). With respect to the 1-D potential energy cuts along the O–H bond coordinate in Fig. 6.8, the minimal shift in ⟨TKER⟩ suggests that coupling onto $^1\pi\sigma^*$ below the $^1\pi\pi^*/^1\pi\sigma^*$ CI originates from (approximately) the same vibronic region of $^1\pi\pi^*$, irrespective of the initial excitation energy. Initially excited Franck-Condon active modes in $^1\pi\pi^*$, which are orthogonal to the O–H stretch coordinate (together with orthogonal modes populated following IVR), thus act as 'spectators' to the O–H fission process, mapping directly through into related modes (vibrational excitation) of the $C_6H_5O(\tilde{X})$ co-fragments [28]. This partitioning on the available energy between TKER and vibrational energy of the radical co-fragment, $\langle E_{\text{vib}} \rangle$, is schematically depicted on the right of Fig. 6.8 for 253 nm, relative to the scenario at 275 nm ($^1\pi\pi^*$ ZPE), where the majority of available energy is partitioned into TKER (N.B. even at 275 nm, frequency domain studies firmly indicate that $C_6H_5O(\tilde{X})$ is formed with a limited sub-set of vibrational modes, primarily an odd quanta progression of ν_{16a} in combination with ν_{18b} (an in-plane C–O wagging motion [28])). Within the context of the tunneling mechanism, the relative agreement between all ⟨TKER⟩ values and the predicted TKER_{max} for O–H fission from the $^1\pi\pi^*$ ZPE, suggests that H tunneling always proceeds from around the ZPE of the O–H stretch in $^1\pi\pi^*$ [28], possibly populated following IVR (indicated by the wavy arrows in Fig. 6.8).

Figure 6.9(b) tracks the dynamics of the $^1\pi\sigma^*$ features at the four different pump wavelengths. It is apparent that: (i) H-atom elimination dynamics have not terminated by the temporal limits of the measurements (1.2 ns) for all pump energies; and (ii) there is no apparent increase in the rate of $^1\pi\sigma^*$ mediated H elimination as the pump energy increases (within the 1.2 ns temporal window of the experiments). The latter observation accords with exclusive tunneling from the ZPE of the O–H

stretch mode in $^1\pi\pi^*$; tunneling always proceeds through the same barrier area, irrespective of the initial pump energy. Using the calculated 1-D potential energy cuts in Fig. 6.8, together with the semi-classical Brillouin-Kramers-Wentzel (BKW) formalism [78], an (upper-limit) estimate of the tunneling lifetime, τ, from the ZPE of the O–H stretch in $^1\pi\pi^*$ can be determined according to:

$$\tau = \left[\nu_{OH} \exp\left(-2\int_{u_1}^{u_2}\sqrt{\frac{2m}{\hbar^2}\big(V(u)-E\big)}du\right)\right]^{-1} \tag{6.6}$$

where u is the O–H bond coordinate, ν_{OH} is the O–H stretch frequency (3581 cm^{-1} [79]), m is the mass of H, $V(u)$ is the potential barrier through which tunneling occurs (labeled on the potentials in Fig. 6.8) and E is the KE of the H-atom—defined as the ZPE of the O–H stretch in $^1\pi\pi^*$ ($\frac{1}{2}\nu_{OH}$). This simple approach returns a value of $\tau = 2.5$ ns, in excellent agreement with an empirically derived value for τ (~ 2.4 ns [27]) as well as the measured fluorescence lifetime of the $^1\pi\pi^*$ ZPE level in phenol (~ 2.4 ns [77]). This predicted tunneling lifetime models all four H^+ signal transients in Fig. 6.9(b) (solid lines) and adds weight to the concept that the observed $^1\pi\sigma^*$ feature is born through tunneling onto $^1\pi\sigma^*$ from the ZPE of the O–H stretch mode in $^1\pi\pi^*$ at all excitation energies. Moreover, it also suggests that modes orthogonal to the O–H fission coordinate (with the exception of ν_{16a}—see [28]) have no major impact upon the effective tunneling rate. This specific picture of the excited state H-atom tunneling dynamics complements similar conclusions drawn from high resolution frequency domain measurements by Ashfold and coworkers [28], as well as more recent ultrafast time-resolved transient absorption studies of phenol dissociation in solution [74].

6.4.4 Competing $^1\pi\sigma^*$ Mediated Dissociation Pathways

As our understanding of $^1\pi\sigma^*$ dynamics in simple isolated heteroaromatics has expanded over the last decade, recent work has progressed to investigate the role of this behavior in more complex biologically relevant species [31–33, 81, 82]. In particular, there have been a small number of studies investigating competing dynamics along different $^1\pi\sigma^*$ surfaces within the same molecule. Notable subjects have included 4- and 5-hydroxyindole [83, 84], which contain both O–H and N–H bond coordinates, as well as $^1\pi\sigma^*$ driven H elimination along the amino ($N^{10}H_2$) and azole (N^9H) moieties in adenine [82]. Here, we use the model system mequinol (*para*–methoxyphenol, structure inset in Fig. 6.10) to discuss both the excitation energy dependence of competing dissociation channels, and the role of $^1\pi\sigma^*$ states localized along coordinates other than X–H bonds.

With respect to the schematic potentials shown in Fig. 6.10(a), we begin by considering H-atom elimination dynamics from the $^1\pi\sigma^*$ state located along mequinol's O–H coordinate ($^1\pi\sigma^*_{O-H}$). Note that mequinol can exist as either *trans* or *cis* rotamers (*trans* structure shown in Fig. 6.10), which are near-isoenergetic

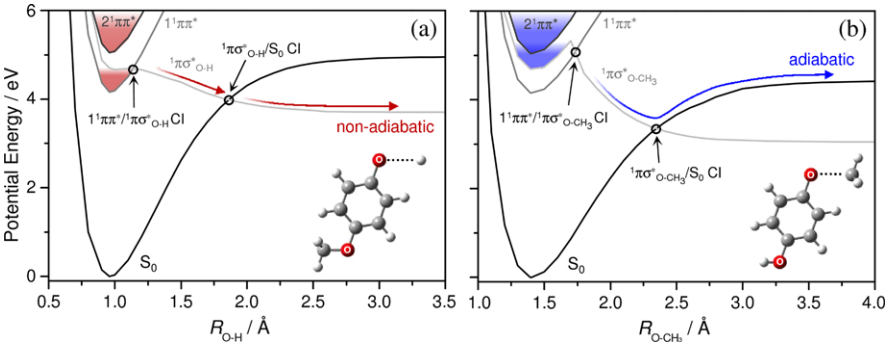

Fig. 6.10 Schematic 1-D potential energy cuts of the S_0, $1^1\pi\pi^*$, $^1\pi\sigma^*_{O–H}$ and $^1\pi\sigma^*_{O–CH_3}$ states along the (**a**) O–H ($R_{O–H}$) and (**b**) O–CH_3 ($R_{O–CH_3}$) bond coordinates of mequinol (molecular structure *inset*). The schematics are based on potentials calculated at the CASPT2(12,11)/aug-cc-pVTZ level [80]. *Shaded areas* of the potentials indicate excitation regions where subsequent $^1\pi\sigma^*_{O–H}$ (*red*) and $^1\pi\sigma^*_{O–CH_3}$ (*blue*) mediated dynamics are active. *Red arrows* indicate non-adiabatic dissociation dynamics while adiabatic dynamics are represented by *blue arrows*. Figure adapted from [80]

in S_0 ($\Delta E \sim 10$ cm^{-1} [80])—frequency-domain measurements, however, indicate that there is no significant difference in the $^1\pi\sigma^*$ governed dynamics of the two rotamers [80]. $^1\pi\sigma^*_{O–H}$ mediated H elimination in mequinol can be classified into two regimes: H tunneling (298–280 nm) and ultrafast dynamics ($\leq$ 245 nm), indicated by the red shaded regions in Fig. 6.10(a). Following excitation to the lowest energy $^1\pi\pi^*$ state ($1^1\pi\pi^*$) between $298 > \lambda > 280$ nm, dynamics proceed through tunneling under the $1^1\pi\pi^*/^1\pi\sigma^*_{O–H}$ CI, in an analogous manner to phenol (see Sect. 6.4.3). The left panel in Fig. 6.11(a) displays a representative H^+ velocity map image (inset, $\Delta t = 1.2$ ns) and TKER spectra ($\Delta t = 1$ ps and 1.2 ns), in the H tunneling regime. The $^1\pi\sigma^*_{O–H}$ feature (centered at ~ 5000 cm^{-1}) observed by 1.2 ns in the TKER spectrum correlates to H-atoms formed through non-adiabatic dissociation around the $^1\pi\sigma^*_{O–H}/S_0$ CI (Fig. 6.10(a), red arrows). A kinetic fit to this transient returns a H-atom appearance timescale of ≥ 1 ns, in qualitative agreement with an upper limit of the H tunneling lifetime obtained from calculated 1-D potentials using a simple BKW model (~ 10 ns [80]). Upon decreasing the excitation wavelength to $280 > \lambda > 245$ nm no H-atom signal is observed at either low or high TKER. The origins of this are due to competition with O–CH_3 fission dynamics, which is discussed in more detail below. Decreasing the wavelength further ($\leq$ 245 nm) accesses the higher lying $2^1\pi\pi^*$ state, at which point coupling onto the $^1\pi\sigma^*_{O–H}$ state is reactivated (Fig. 6.11(b)). At these higher energies the $^1\pi\sigma^*_{O–H}$ feature shifts to higher TKER (centered at ~ 10000 cm^{-1}) and is present by 1 ps, but remains correlated to non-adiabatic dissociation through the $^1\pi\sigma^*_{O–H}/S_0$ CI. A fit to the signal transient of this feature in Fig. 6.11(b) provides an ultrafast timescale of $\tau = 180 \pm 30$ fs for $^1\pi\sigma^*_{O–H}$ governed O–H scission, following initial excitation to $2^1\pi\pi^*$. In combination, these observations flag up a change in the mechanism for coupling onto the $^1\pi\sigma^*_{O–H}$ state, relative to the tunneling dynamics

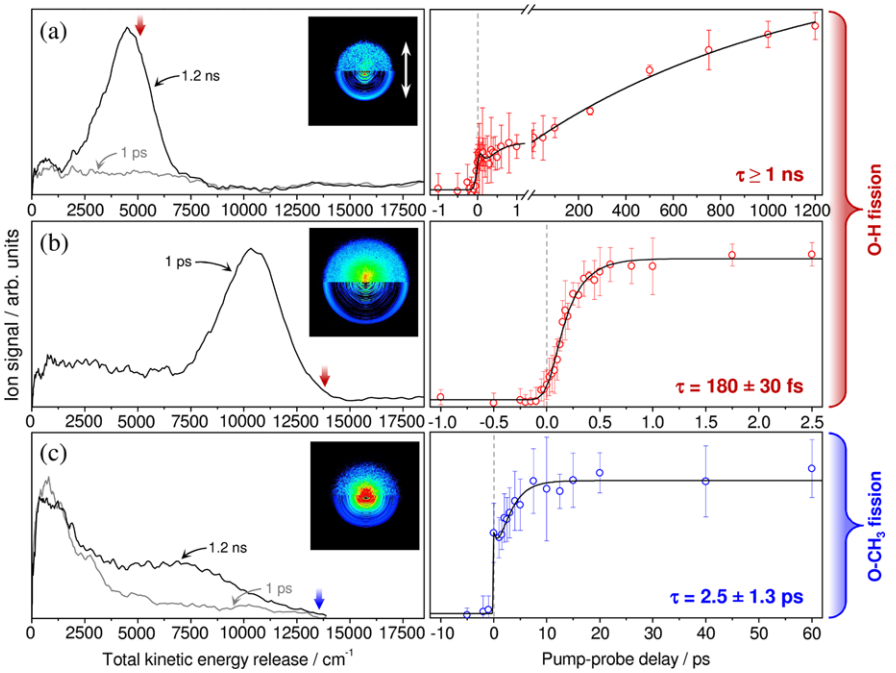

Fig. 6.11 Representative results from TR-VMI studies of O–H fission at (**a**) 298 nm and (**b**) 238 nm and O–CH_3 fission at (**c**) 238 nm in mequinol. The *left column* displays velocity map ion images ($\Delta t = 1.2$ ns) and time-resolved TKER spectra. *Vertical red arrows* indicate the predicted $TKER_{max}$ for non-adiabatic O–H fission, while the *vertical blue arrow* shows the predicted $TKER_{max}$ value for adiabatic O–CH_3 dissociation. The *right column* presents ion signal transients for the $^1\pi\sigma^*$ features. Figure adapted from [80]

at longer wavelengths. After initial excitation to $2^1\pi\pi^*$, population may either couple directly onto $^1\pi\sigma^*_{O-H}$ through a CI, or alternatively evolve through a series of $2^1\pi\pi^* \rightarrow 1^1\pi\pi^* \rightarrow {}^1\pi\sigma^*_{O-H}$ couplings. Once on $^1\pi\sigma^*_{O-H}$, transfer bond through the $1^1\pi\pi^*/{}^1\pi\sigma^*_{O-H}$ CI gives rise to non-adiabatic dissociation of the O–H bond through $^1\pi\sigma^*_{O-H}/S_0$ CI.

Recent research has demonstrated that $^1\pi\sigma^*$ dynamics are also active as a channel for CH_3 elimination, along X–CH_3 coordinates [85–88]. In mequinol there is a $^1\pi\sigma^*$ state localized along its O–CH_3 bond ($^1\pi\sigma^*_{O-CH_3}$) and electronic state potentials along this coordinate are shown in Fig. 6.10(b). Between 298–280 nm, no $^1\pi\sigma^*_{O-CH_3}$ mediated dynamics are observed. In this wavelength range excited state H tunneling dynamics dominate, whereas CH_3 tunneling under the $1^1\pi\pi^*/{}^1\pi\sigma^*_{O-CH_3}$ is not a kinetically competitive process due to the 15-times larger mass of CH_3. At wavelengths shorter than 280 nm however, dissociation along the $^1\pi\sigma^*_{O-CH_3}$ surface becomes an open channel, and representative findings from TR-VMI experiments (by REMPI probing CH_3 radical photoproducts at 333 nm [89, 90]) in this pump wavelength regime are displayed in Fig. 6.11(c). Inspection of the time-

resolved TKER spectra indicate that a $^1\pi\sigma^*_{O–CH_3}$ feature appears by 1.2 ns (centered at $\sim 7500\,cm^{-1}$), although analysis of the energetics for O–CH_3 dissociation reveals that, unlike O–H fission along $^1\pi\sigma^*_{O–H}$, CH_3 elimination occurs adiabatically with respect to the $^1\pi\sigma^*_{O–CH_3}/S_0$ CI ($TKER_{max}$ for adiabatic O–CH_3 fission is indicated by the vertical blue arrow on the left panel of Fig. 6.11(c)). These adiabatic dynamics generate ground state CH_3 radicals in coincidence with *para*-hydroxyphenoxyl radicals in their first electronically excited state, HOC_6H_4O ($\tilde{A}$). This behavior has been tentatively attributed to a geometric phase effect around the $^1\pi\sigma^*_{O–CH_3}/S_0$ CI [80]—[91] provides a broader discussion on such phenomena.

Between $280 > \lambda > 245$ nm $^1\pi\sigma^*_{O–CH_3}$ driven O–CH_3 scission prevails over any H-atom elimination processes. Unlike the $^1\pi\sigma^*_{O–H}$ state, the potentials in Fig. 6.10(b) show that $^1\pi\sigma^*_{O–CH_3}$ exhibits a quasi-bound well in the vertical Franck-Condon region (~ 0.6 eV deep), which arises from strong mixing between a $^1\pi 3s$ Rydberg state (where the 3s orbital is associated with the O atom on the O–CH_3 coordinate) and the $^1\pi\sigma^*_{O–CH_3}$ valence state (reference [58] provides a general review of Rydberg-valence mixing). As a result, excitation between $280 > \lambda > 245$ nm induces population directly into the bound 3s Rydberg well of the $^1\pi\sigma^*_{O–CH_3}$ surface, localizing electron density onto the O–CH_3 moiety, and ultimately causes O–CH_3 fission to dominate over H elimination pathways. At $\lambda \leq 245$ nm, excitation to $2^1\pi\pi^*$ occurs and subsequent dynamics along both $^1\pi\sigma^*_{O–H}$ and $^1\pi\sigma^*_{O–CH_3}$ surfaces are active. However, the right panel in Fig. 6.11(c) highlights that O–CH_3 fission *via* $^1\pi\sigma^*_{O–CH_3}$ occurs on a timescale ($\tau = 2.5 \pm 1.3$ ps) an order of magnitude slower than O–H fission along $^1\pi\sigma^*_{O–H}$ at these excitation wavelengths, indicating that the initial coupling processes onto $^1\pi\sigma^*_{O–CH_3}$ and $^1\pi\sigma^*_{O–H}$ from $2^1\pi\pi^*$ must be kinetically competitive (both < 180 fs based on the timescale recorded for $^1\pi\sigma^*_{O–H}$ driven O–H fission). The timescale differences are thus attributed to the very different topographies of the two $^1\pi\sigma^*$ states; the purely dissociative profile of $^1\pi\sigma^*_{O–H}$ enables ultrafast elimination of H-atoms in a ballistic manner, whereas time is required for population to evolve out of the quasi-bound well on $^1\pi\sigma^*_{O–CH_3}$ and adiabatically advance towards electronically excited HOC_6H_4O ($\tilde{A}$) radicals, impeding O–CH_3 fission dynamics.

These detailed TR-VMI studies of mequinol, together with previous studies on hydroxyindoles [83, 84] and adenine [82], demonstrate the feasibility of untangling competing $^1\pi\sigma^*$ mediated dynamics in more complex heteroaromatic biomolecules. Future prospects include unraveling the role of competing $^1\pi\sigma^*$ dynamics in dihydroxyindoles (subunits of photostable biological eumelanin copolymers [92–94]) and DNA nucleosides.

6.4.5 Outlook

Developing a firmer understanding of $^1\pi\sigma^*$ mediated dynamics in photoexcited DNA bases, amino acids and their subunits provides the foundations for extending

this work to a plethora of more complex systems. One can envisage that future studies will entail working towards understanding the general role that this seemingly ubiquitous mechanism plays in the UV photochemistry of larger biomolecules. In particular, the tantalizing prospects of expanding this field to: (i) probe dynamics in species such as nucleosides and nucleotides in the gas phase; and (ii) investigate the dynamics of these bio-molecular building-blocks in solution, will invariably assist in cultivating such knowledge. Progress towards achieving both of these goals is currently underway. Techniques such as electrospray ionization [95–97], laser desorption [98–101] and laser-induced acoustic desorption [102], can provide the means to entrain large biomolecules into the gas phase and by-pass issues such as thermal decomposition. Likewise, experiments in solution are beginning to showcase the transference of knowledge attained from gas phase measurements; recent ultrafast studies on phenol [74] and *para*-methylthiophenol [74, 103] in the condensed phase reveal some distinct parallels with findings from the gas phase, even though the solvent can, in principle, manipulate $^1\pi\sigma^*$ mediated behavior. Furthermore, liquid microjets [104–106] offer significant potential for applying highly differential gas phase techniques (such as time-resolved photoelectron spectroscopy) to biomolecules in the condensed phase. These are fertile grounds for new and more expansive experiments, which will undoubtedly aid in constructing a more global picture of $^1\pi\sigma^*$ driven photochemistry in the molecular building-blocks of life.

References

1. V. Sundstrom, Annu. Rev. Phys. Chem. **59**, 53–77 (2008)
2. P. Kukura, D.W. McCamant, S. Yoon, D.B. Wandschneider, R.A. Mathies, Science **310**, 1006–1009 (2005)
3. M. Garavelli, D. Polli, P. Altoe, O. Weingart, K.M. Spillane, C. Manzoni, D. Brida, G. Tomasello, G. Orlandi, P. Kukura, R.A. Mathies, G. Cerullo, Nature **467**, 440–443 (2010)
4. G.D. Scholes, G.R. Fleming, A. Olaya-Castro, R. van Grondelle, Nat. Chem. **3**, 763–774 (2011)
5. S.R. Meech, Chem. Soc. Rev. **38**, 2922–2934 (2009)
6. I.R. Lee, W. Lee, A.H. Zewail, Proc. Natl. Acad. Sci. USA **103**, 258–262 (2006)
7. W.J. Schreier, T.E. Schrader, F.O. Koller, P. Gilch, C.E. Crespo-Hernandez, V.N. Swaminathan, T. Carell, W. Zinth, B. Kohler, Science **315**, 625–629 (2007)
8. G.P. Pfeifer, Y.H. You, A. Besaratinia, Mutat. Res. **571**, 19–31 (2005)
9. J. Li, Z.Y. Liu, C. Tan, X.M. Guo, L.J. Wang, A. Sancar, D.P. Zhong, Nature **466**, 887–890 (2010)
10. C.T. Middleton, K. de La Harpe, C. Su, Y.K. Law, C.E. Crespo-Hernandez, B. Kohler, Annu. Rev. Phys. Chem. **60**, 217–239 (2009)
11. C.E. Crespo-Hernandez, B. Cohen, P.M. Hare, B. Kohler, Chem. Rev. **104**, 1977–2019 (2004)
12. S. Ullrich, T. Schultz, M.Z. Zgierski, A. Stolow, Phys. Chem. Chem. Phys. **6**, 2796–2801 (2004)
13. M. Barbatti, A.J.A. Aquino, J.J. Szymczak, D. Nachtigallova, P. Hobza, H. Lischka, Proc. Natl. Acad. Sci. USA **107**, 21453–21458 (2010)
14. A.L. Sobolewski, W. Domcke, C. Dedonder-Lardeux, C. Jouvet, Phys. Chem. Chem. Phys. **4**, 1093–1100 (2002)
15. D.R. Yarkony, Rev. Mod. Phys. **68**, 985–1013 (1996)

16. W. Domcke, D.R. Yarkony, H. Koppel (eds.), *Conical Intersections: Theory, Computation and Experiment* (World Scientific, Singapore, 2011)
17. S. Matsika, P. Krause, Annu. Rev. Phys. Chem. **62**, 621–643 (2011)
18. M.N.R. Ashfold, G.A. King, D. Murdock, M.G.D. Nix, T.A.A. Oliver, A.G. Sage, Phys. Chem. Chem. Phys. **12**, 1218–1238 (2010)
19. M.L. Hause, Y.H. Yoon, A.S. Case, F.F. Crim, J. Chem. Phys. **128**, 104307 (2008)
20. A. Iqbal, M.S.Y. Cheung, M.G.D. Nix, V.G. Stavros, J. Phys. Chem. A **113**, 8157–8163 (2009)
21. C.P. Schick, P.M. Weber, J. Phys. Chem. A **105**, 3725–3734 (2001)
22. D.A. Blank, S.W. North, Y.T. Lee, Chem. Phys. **187**, 35–47 (1994)
23. J. Wei, A. Kuczmann, J. Riedel, F. Renth, F. Temps, Phys. Chem. Chem. Phys. **5**, 315–320 (2003)
24. G.A. King, T.A.A. Oliver, M.G.D. Nix, M.N.R. Ashfold, J. Phys. Chem. A **113**, 7984–7993 (2009)
25. H. Lippert, H.H. Ritze, I.V. Hertel, W. Radloff, ChemPhysChem **5**, 1423–1427 (2004)
26. G.M. Roberts, C.A. Williams, M.J. Paterson, S. Ullrich, V.G. Stavros, Chem. Sci. **3**, 1192–1199 (2012)
27. G.A. Pino, A.N. Oldani, E. Marceca, M. Fujii, S.I. Ishiuchi, M. Miyazaki, M. Broquier, C. Dedonder, C. Jouvet, J. Chem. Phys. **133**, 124313 (2010)
28. R.N. Dixon, T.A.A. Oliver, M.N.R. Ashfold, J. Chem. Phys. **134**, 194303 (2011)
29. G.M. Roberts, A.S. Chatterley, J.D. Young, V.G. Stavros, J. Phys. Chem. Lett. **3**, 348–352 (2012)
30. M.N.R. Ashfold, B. Cronin, A.L. Devine, R.N. Dixon, M.G.D. Nix, Science **312**, 1637–1640 (2006)
31. H. Satzger, D. Townsend, M.Z. Zgierski, S. Patchkovskii, S. Ullrich, A. Stolow, Proc. Natl. Acad. Sci. USA **103**, 10196–10201 (2006)
32. N.L. Evans, S. Ullrich, J. Phys. Chem. A **114**, 11225–11230 (2010)
33. A. Iqbal, V.G. Stavros, J. Phys. Chem. Lett. **1**, 2274–2278 (2010)
34. S.T. Tsai, C.K. Lin, Y.T. Lee, C.K. Ni, Rev. Sci. Instrum. **72**, 1963–1969 (2001)
35. C.M. Tseng, Y.T. Lee, M.F. Lin, C.K. Ni, S.Y. Liu, Y.P. Lee, Z.F. Xu, M.C. Lin, J. Phys. Chem. A **111**, 9463–9470 (2007)
36. X.M. Yang, Int. Rev. Phys. Chem. **24**, 37–98 (2005)
37. A.T.J.B. Eppink, D.H. Parker, Rev. Sci. Instrum. **68**, 3477–3484 (1997)
38. A. Stolow, A.E. Bragg, D.M. Neumark, Chem. Rev. **104**, 1719–1757 (2004)
39. R. Spesyvtsev, O.M. Kirkby, H.H. Fielding, Faraday Discuss. **157**, 165–179 (2012)
40. R. Montero, A.P. Conde, V. Ovejas, R. Martinez, F. Castano, A. Longarte, J. Chem. Phys. **135**, 054308 (2011)
41. R. Montero, A.P. Conde, V. Ovejas, F. Castano, A. Longarte, J. Phys. Chem. A **116**, 2698–2703 (2012)
42. D. Proch, T. Trickl, Rev. Sci. Instrum. **60**, 713–716 (1989)
43. U. Even, J. Jortner, D. Noy, N. Lavie, C. Cossart-Magos, J. Chem. Phys. **112**, 8068–8071 (2000)
44. W.C. Wiley, I.H. McLaren, Rev. Sci. Instrum. **26**, 1150–1157 (1955)
45. J.H. Moore, C.C. Davis, M.A. Coplan, *Building Scientific Apparatus*, 4th edn. (Cambridge University Press, Cambridge, 2009)
46. M. Nisoli, S. Desilvestri, V. Magni, O. Svelto, R. Danielius, A. Piskarskas, G. Valiulis, A. Varanavicius, Opt. Lett. **19**, 1973–1975 (1994)
47. D.W. Chandler, P.L. Houston, J. Chem. Phys. **87**, 1445–1447 (1987)
48. M.N.R. Ashfold, N.H. Nahler, A.J. Orr-Ewing, O.P.J. Vieuxmaire, R.L. Toomes, T.N. Kitsopoulos, I.A. Garcia, D.A. Chestakov, S.M. Wu, D.H. Parker, Phys. Chem. Chem. Phys. **8**, 26–53 (2006)
49. S.J. Cavanagh, S.T. Gibson, M.N. Gale, C.J. Dedman, E.H. Roberts, B.R. Lewis, Phys. Rev. A **76**, 052708 (2007)

50. N.L. Evans, H. Yu, G.M. Roberts, V.G. Stavros, S. Ullrich, Phys. Chem. Chem. Phys. **14**, 10401–10409 (2012)
51. H. Yu, N.L. Evans, V.G. Stavros, S. Ullrich, Phys. Chem. Chem. Phys. **14**, 6266–6272 (2012)
52. A.T.J.B. Eppink, S.M. Wu, B.J. Whitaker, in *Imaging in Molecular Dynamics: Technology and Applications*, ed. by B.J. Whitaker (Cambridge University Press, Cambridge, 2003), pp. 65–112
53. G.A. Garcia, L. Nahon, I. Powis, Rev. Sci. Instrum. **75**, 4989–4996 (2004)
54. G.M. Roberts, J.L. Nixon, J. Lecointre, E. Wrede, J.R.R. Verlet, Rev. Sci. Instrum. **80**, 053104 (2009)
55. P.M. Regan, S.R. Langford, A.J. Orr-Ewing, M.N.R. Ashfold, J. Chem. Phys. **110**, 281–288 (1999)
56. G.M. Roberts, C.A. Williams, J.D. Young, S. Ullrich, M.J. Paterson, V.G. Stavros, J. Am. Chem. Soc. **134**, 12578–12589 (2012)
57. C.A. Williams, G.M. Roberts, H. Yu, N.L. Evans, S. Ullrich, V.G. Stavros, J. Phys. Chem. A **116**, 2600–2609 (2012)
58. H. Reisler, A.I. Krylov, Int. Rev. Phys. Chem. **28**, 267–308 (2009)
59. R.H. Qadiri, E.J. Feltham, E.E.H. Cottrill, N. Taniguchi, M.N.R. Ashfold, J. Chem. Phys. **116**, 906–912 (2002)
60. E.J. Feltham, R.H. Qadiri, E.E.H. Cottrill, P.A. Cook, J.P. Cole, G.G. Balint-Kurti, M.N.R. Ashfold, J. Chem. Phys. **119**, 6017–6031 (2003)
61. R.N. Zare, *Angular Momentum: Understanding Spatial Aspects in Chemistry and Physics* (Wiley, New York, 1988)
62. B. Cronin, M.G.D. Nix, R.H. Qadiri, M.N.R. Ashfold, Phys. Chem. Chem. Phys. **6**, 5031–5041 (2004)
63. G.A. King, T.A.A. Oliver, M.G.D. Nix, M.N.R. Ashfold, J. Chem. Phys. **132**, 064305 (2010)
64. T. Eicher, S. Hauptmann, *The Chemistry of Heterocycles: Structure, Reactions, Syntheses, and Applications*, 2nd edn. (Wiley-VCH, Berlin, 2003)
65. D.J. Hadden, K.L. Wells, G.M. Roberts, L.T. Bergendahl, M.J. Paterson, V.G. Stavros, Phys. Chem. Chem. Phys. **13**, 10342–10349 (2011)
66. M. Barbatti, H. Lischka, S. Salzmann, C.M. Marian, J. Chem. Phys. **130**, 034305 (2009)
67. R.P. Bell, *The Tunnel Effect in Chemistry* (Chapman & Hall, London & New York, 1980)
68. A. Kohen, J.P. Klinman, Chem. Biol. **6**, R191–R198 (1999)
69. L.M. Tolbert, K.M. Solntsev, Acc. Chem. Res. **35**, 19–27 (2002)
70. J.T. Hynes, T.H. Tran-Thi, G. Granucci, J. Photochem. Photobiol. A, Chem. **154**, 3–11 (2002)
71. A. Kohen, R. Cannio, S. Bartolucci, J.P. Klinman, Nature **399**, 496–499 (1999)
72. S.Y. Reece, J.M. Hodgkiss, J. Stubbe, D.G. Nocera, Philos. Trans. R. Soc. Lond. B, Biol. Sci. **361**, 1351–1364 (2006)
73. R.I. Cukier, D.G. Nocera, Annu. Rev. Phys. Chem. **49**, 337–369 (1998)
74. Y. Zhang, T.A.A. Oliver, M.N.R. Ashfold, S.E. Bradforth, Faraday Discuss. **157**, 141–163 (2012)
75. M.N.R. Ashfold, A.L. Devine, R.N. Dixon, G.A. King, M.G.D. Nix, T.A.A. Oliver, Proc. Natl. Acad. Sci. USA **105**, 12701–12706 (2008)
76. M.G.D. Nix, A.L. Devine, B. Cronin, R.N. Dixon, M.N.R. Ashfold, J. Chem. Phys. **125**, 133318 (2006)
77. C. Ratzer, J. Kupper, D. Spangenberg, M. Schmitt, Chem. Phys. **283**, 153–169 (2002)
78. R.J. Le Roy, W.K. Liu, J. Chem. Phys. **69**, 3622–3631 (1978)
79. H.D. Bist, J.C.D. Brand, D.R. Williams, J. Mol. Spectrosc. **24**, 413–467 (1967)
80. D.J. Hadden, G.M. Roberts, T.N.V. Karsili, M.N.R. Ashfold, V.G. Stavros, Phys. Chem. Chem. Phys. **14**, 13415–13428 (2012)
81. M.G.D. Nix, A.L. Devine, B. Cronin, M.N.R. Ashfold, J. Chem. Phys. **126**, 124312 (2007)
82. K.L. Wells, D.J. Hadden, M.G.D. Nix, V.G. Stavros, J. Phys. Chem. Lett. **1**, 993–996 (2010)
83. T.A.A. Oliver, G.A. King, M.N.R. Ashfold, Phys. Chem. Chem. Phys. **13**, 14646–14662 (2011)

84. R. Livingstone, O. Schalk, A.E. Boguslavskiy, G.R. Wu, L.T. Bergendahl, A. Stolow, M.J. Paterson, D. Townsend, J. Chem. Phys. **135**, 194307 (2011)
85. A.G. Sage, M.G.D. Nix, M.N.R. Ashfold, Chem. Phys. **347**, 300–308 (2008)
86. C.M. Tseng, Y.T. Lee, C.K. Ni, J. Phys. Chem. A **113**, 3881–3885 (2009)
87. D.J. Hadden, C.A. Williams, G.M. Roberts, V.G. Stavros, Phys. Chem. Chem. Phys. **13**, 4494–4499 (2011)
88. J.S. Lim, S.K. Kim, Nat. Chem. **2**, 627–632 (2010)
89. J.W. Hudgens, T.G. Digiuseppe, M.C. Lin, J. Chem. Phys. **79**, 571–582 (1983)
90. R. de Nalda, J.G. Izquierdo, J. Dura, L. Banares, J. Chem. Phys. **126**, 021101 (2007)
91. S.C. Althorpe, in *Conical Intersections: Theory, Computation and Experiment*, ed. by W. Domcke, D.R. Yarkony, H. Koppel (World Scientific, Singapore, 2011), pp. 155–194
92. A.L. Sobolewski, W. Domcke, ChemPhysChem **8**, 756–762 (2007)
93. M. Gauden, A. Pezzella, L. Panzella, M.T. Neves-Petersen, E. Skovsen, S.B. Petersen, K.M. Mullen, A. Napolitano, M. d'Ischia, V. Sundstrom, J. Am. Chem. Soc. **130**, 17038–17043 (2008)
94. S. Olsen, J. Riesz, I. Mahadevan, A. Coutts, J.P. Bothma, B.J. Powell, R.H. McKenzie, S.C. Smith, P. Meredith, J. Am. Chem. Soc. **129**, 6672–6673 (2007)
95. J.B. Fenn, Angew. Chem., Int. Ed. Engl. **42**, 3871–3894 (2003)
96. J. Lecointre, G.M. Roberts, D.A. Horke, J.R.R. Verlet, J. Phys. Chem. A **114**, 11216–11224 (2010)
97. A.R. McKay, M.E. Sanz, C.R.S. Mooney, R.S. Minns, E.M. Gill, H.H. Fielding, Rev. Sci. Instrum. **81**, 123101 (2010)
98. E. Nir, K. Kleinermanns, M.S. de Vries, Nature **408**, 949–951 (2000)
99. M. Smits, C.A. de Lange, S. Ullrich, T. Schultz, M. Schmitt, J.G. Underwood, J.P. Shaffer, D.M. Rayner, A. Stolow, Rev. Sci. Instrum. **74**, 4812–4817 (2003)
100. A. Gahlmann, I.R. Lee, A.H. Zewail, Angew. Chem., Int. Ed. Engl. **49**, 6524–6527 (2010)
101. J. Zhou, O. Kostko, C. Nicolas, X.N. Tang, L. Belau, M.S. de Vries, M. Ahmed, J. Phys. Chem. A **113**, 4829–4832 (2009)
102. C.R. Calvert, L. Belshaw, M.J. Duffy, O. Kelly, R.B. King, A.G. Smyth, T.J. Kelly, J.T. Costello, D.J. Timson, W.A. Bryan, T. Kierspel, P. Rice, I.C.E. Turcu, C.M. Cacho, E. Springate, I.D. Williams, J.B. Greenwood, Phys. Chem. Chem. Phys. **14**, 6289–6297 (2012)
103. T.A.A. Oliver, Y. Zhang, M.N.R. Ashfold, S.E. Bradforth, Faraday Discuss. **150**, 439–458 (2011)
104. M. Faubel, K.R. Siefermann, Y. Liu, B. Abel, Acc. Chem. Res. **45**, 120–130 (2012)
105. C.P. Schwartz, J.S. Uejio, A.M. Duffin, A.H. England, D.N. Kelly, D. Prendergast, R.J. Saykally, Proc. Natl. Acad. Sci. USA **107**, 14008–14013 (2010)
106. P. Slavicek, B. Winter, M. Faubel, S.E. Bradforth, P. Jungwirth, J. Am. Chem. Soc. **131**, 6460–6467 (2009)

Chapter 7
Ultrafast Laser-Induced Processes Described by Ab Initio Molecular Dynamics

Leticia González, Philipp Marquetand, Martin Richter, Jesús González-Vázquez, and Ignacio Sola

Abstract This chapter introduces theoretical methods that integrate the equations of motion of electrons and nuclei in molecules, including all degrees of freedom and all types of couplings. We are concerned with methods that treat the electronic motion quantum-mechanically, by expanding the electronic wave function in a relatively small basis of eigenstates of the Hamiltonian, and the nuclear motion classically, as an ensemble of trajectories each unfolding on a single electronic state at a given time, but allowing to switch between states. In particular, we focus on a quite novel method called the SHARC (Surface-Hopping in the Adiabatic Representation including arbitrary Couplings) scheme. The main novelty of SHARC consists in the evaluation of the transition probability between electronic states, which is performed by surface-hopping techniques in the adiabatic representation, essentially treating on the same footing both non-adiabatic beyond Born-Oppenheimer transitions (intersystem crossing, internal conversion) and laser-induced crossings. The choice of approximations and representation is particularly useful in evaluating the dynamics when the laser field or non-adiabatic couplings are strong. In the chapter we show examples of the performance of the scheme in two scenarios. In the first one, the dynamics of the system is simulated starting in the electronic excited state assuming an instantaneous excitation. In the second one, the interaction of the system with an external laser field is explicitly considered. This approach is necessary when deactivation occurs during the laser excitation. Moreover, the explicit consideration of the external field permits the use of quantum control schemes. We consider here two limiting cases, the impulsive and the adiabatic time-evolution, represented by two paradigmatic control schemes, the ultrafast pump-dump control and the APLIP (Adiabatic Passage by Light Induced Potentials) scheme, respectively.

L. González (✉) · P. Marquetand · M. Richter
Institute of Theoretical Chemistry, University of Vienna, Währinger Str. 17, 1090 Vienna, Austria
e-mail: leticia.gonzalez@univie.ac.at

J. González-Vázquez · I. Sola
Departamento de Química Física I, Universidad Complutense, 28040 Madrid, Spain

R. de Nalda, L. Bañares (eds.), *Ultrafast Phenomena in Molecular Sciences*,
Springer Series in Chemical Physics 107, DOI 10.1007/978-3-319-02051-8_7,

7.1 Introduction

Progress in monitoring and controlling the dynamics of molecules by means of ultrashort femtosecond pulses, and particularly photochemical reactions, has been spectacular over the last thirty years [1–16]. Moreover, the advent of strong pulses [17] has given access to highly excited states of molecules, increasing the complexity of the competing photochemical and photophysical processes [18–21] and thus making difficult to interpret the main mechanisms governing the dynamics based on simple models. Computational photochemistry is indispensable to unravel photoinduced phenomena, since predictions are put forward regarding the paths that are likely to be followed in a molecule under light irradiation, based on calculated potential energy curves (PES) with the corresponding couplings. However, and despite the inherent difficulties in calculating electronic excited states [22], averaged kinetic calculations based on the approximate evaluation and counting of the energy eigenstates of the molecule do not suffice to understand the dynamics driven by ultrashort pulses. In order to predict or understand the outcome of experiments, it is becoming indispensable to solve the time-dependent Schrödinger equation (TDSE) for all the electronic and nuclear degrees of freedom in the presence of an external field, beyond the usual Born-Oppenheimer approximation and weak-field perturbation regime. Unfortunately, an "exact" solution of the TDSE is computationally intractable except for the simplest systems [23]. The key to achieve successful numerical simulations depends then on the nature and extension of the approximations that are undertaken to solve this equation. Naturally, these approximations will condition the expected dynamics that is subject to the molecular Hamiltonian and the laser field.

Several methods, such as the multiconfigurational time-dependent Hartree method (MCTDH) [24], the multiple spawning approach [25–27] and other techniques [28–36] have emerged in the last years to describe multidimensional dynamics. Not all these methods are able to incorporate the laser field into the dynamics, but many efforts are being made in this direction [37–44]. An alternative to the full quantum mechanical solution of the TDSE is the use of semiclassical methods. A particularly extended approach is ab initio molecular dynamics [45–47] (MD), where an ensemble of independent semiclassical trajectories is used to describe the nuclear positions while the electronic structure is treated quantum mechanically, i.e. with ab initio methods. The most accurate version of this method is indeed the use of ab initio methods, but it is also possible to couple MD with time-dependent density functional theory (TD-DFT) or even semiempirical methods. Semiclassical strategies are particularly popular since they allow a complete full dimensional description of the system under study with by far much less computational effort than calculating PES and performing wavepacket propagations on them. The electronic structure calculations in MD are computed on-the-fly. Thus, the cost of such simulations is mainly related to the cost of the level of theory employed for the electronic structure and of course to the fact that a sufficiently large number of trajectories is required to obtain reliable quantum yields in the case of competing processes. In photochemistry, due to non-adiabatic and/or spin-orbit couplings, it is common

to obtain different branching ratios for competing pathways involving several PES. In the presence of non-adiabatic phenomena, it is usual to combine MD with the surface hopping (SH) method [48–50] so that the system is allowed to hop from one PES to another, as required to describe non-adiabatic photochemistry. Of course, SH requires the calculation of non-adiabatic coupling (NAC) terms within the given method, a task which is straightforward within ab initio methods [51] but has been derived only in the last decade for TD-DFT [52–55]. Several reviews highlight many of the applications that can be treated with the trajectory SH method [56–58]. In contrast, the use of MD in the presence of spin-orbit couplings is much less extended [59–62]. Moreover, up to our knowledge, as of 2011, there are no on-the-fly ab initio MD studies explicitly including both non-adiabatic and spin-orbit couplings in an ab initio framework. This shortcoming is mainly motivated by the fact that intersystem crossing (ISC) between PES of different multiplicity is typically believed to occur in a much longer time scale than internal conversion (IC) via conical intersections. Recent investigations, e.g. in benzene, revealed however that ISC can compete with IC in an ultrafast time scale [63, 64]. Therefore, it seems mandatory to have methods which can describe multidimensional dynamics in the presence of both non-adiabatic and spin-orbit couplings [65]. Additionally, to achieve quantitative agreement with experiments, it is desirable to couple nuclear and electronic degrees of freedom with an electromagnetic field, so that laser transitions can also be directly modeled in theory, as they happen in experiment. Some approaches have been derived to incorporate time-dependent external fields with MD [66–73], but there is no general scheme able to incorporate all types of couplings (non-adiabatic, spin-orbit, dipole couplings, etc.) into MD.

In this chapter we present a novel semiclassical scheme to integrate the equations of motion of electrons and nuclei in molecules, including all degrees of freedom and all types of couplings, that expands the electronic wave function in a relatively small basis of eigenstates of the Hamiltonian, and treats the nuclear motion as a classical trajectory unfolding on a single electronic state. The main novelty in the present approach consists in the evaluation of the transition probability between electronic states, which is performed by SH techniques in the adiabatic representation, essentially treating on the same footing both non-adiabatic beyond Born-Oppenheimer transitions (ISC, IC) and laser-induced crossings. The numerical method is called Surface-Hopping in the Adiabatic Representation including arbitrary Couplings, abbreviated SHARC [74, 75]. As it will be shown later in this chapter, the choice of the given approximations and representation is particularly advantageous in evaluating the dynamics when the laser field and NACs are strong.

The rest of this chapter is organized as follows. First, the basic ideas of semiclassical dynamics and in particular SH are explained in detail. SHARC is introduced and put into the context of the related FISH (Field-Induced SH) [71] method, which has been successfully used recently to interpret some control experiments [76–79]. In the following sections, the performance of SHARC will be illustrated in two scenarios depending on the way that the light interaction is considered. In the first scenario, the dynamics of the system is simulated starting in the electronic excited state assuming an instantaneous excitation. In the second scenario, the interaction

of the system with an external laser field is explicitly considered. The latter methodology is needed when the deactivation occurs during the laser excitation. Moreover, the explicit consideration of the external field allows one to use control techniques by changing the shape of the field. Here, we shall consider two limiting cases, the impulsive and the adiabatic time-evolution, represented by two paradigmatic control schemes, the ultrafast pump-dump control and the APLIP (Adiabatic Passage by Light Induced Potentials) scheme, respectively.

7.2 Methodologies for Ab Initio Molecular Dynamics

7.2.1 Surface Hopping vs. Ehrenfest Dynamics

In this section we shall concentrate on methods that treat the dynamics of the molecule by a mixed quantum-classical approach. In principle one could decide which degree of freedom follows which (classical or quantum) equation, but in practice all nuclear degrees of freedom will be considered classical variables, while all electronic degrees of freedom will be regarded as quantum operators. This practice follows the same criteria as the distinction between parameters and operators in the usual Born-Oppenheimer approximation. Then, the quantum Hamiltonian describing the quantum part can be identified with the so-called electronic Hamiltonian for the N_{el} electrons and N_{nuc} nuclear system,

$$\mathsf{H}^{\mathrm{el}} = \sum_{i}^{N_{el}} \left(-\frac{\hbar^2}{2m_e}\nabla_i^2 - \sum_{k}^{N_{nuc}} \frac{Z_k e^2}{4\pi\epsilon_0 |\vec{r}_i - \vec{R}_k|} + \frac{1}{2}\sum_{i\neq j}^{N_{el}} \frac{e^2}{4\pi\epsilon_0 |\vec{r}_i - \vec{r}_j|} \right), \tag{7.1}$$

where Z_k is the nuclear charge of atom k at position $\vec{R}_k$, and $\vec{r}_i$ are the electron coordinates; m_e is the electron mass and ϵ_0 the vacuum permittivity. In Eq. (7.1) the nuclear positions are regarded as parameters, i.e., they have fixed values when they operate on the electronic wave function.

Conversely, the classical Hamiltonian, describing the classical part, can be identified with the nuclear Hamiltonian function

$$H^{\mathrm{nuc}}(\mathbf{R}, \mathbf{P}) = \sum_{k}^{N_{nuc}} \left(\frac{1}{2M_k}\vec{P}_k^2 + \frac{1}{2}\sum_{l\neq k}^{N_{nuc}} \frac{Z_k Z_l e^2}{4\pi\epsilon_0 |\vec{R}_k - \vec{R}_l|} \right), \tag{7.2}$$

where $\vec{P}_k = M_k \dot{\vec{R}}_k$ is the momentum of nuclei k with mass M_k. Here and in the following, bold type letters succinctly denote sets of variables over all the particles. In the potential part, the nuclear Hamiltonian only contains the repulsive Coulomb potential between each pair of nuclei. To simplify the notation we will include the nuclear Coulomb potential in the electronic Hamiltonian. Here and in the following, bold type letters succinctly denote sets of variables over all the particles. Furthermore, when considering molecules under external fields, the electronic Hamiltonian will incorporate the molecule-radiation coupling interaction.

The energy of the mixed quantum-classical system can then be written as

$$E^{\text{tot}} = E^{\text{el}} + E^{\text{nuc}} = \langle \Psi(\mathbf{r};\mathbf{R}) | \mathsf{H}^{\text{el}} | \Psi(\mathbf{r};\mathbf{R}) \rangle + \sum_{k}^{N_{nuc}} \frac{1}{2} M_k \dot{\vec{R}}_k^2. \tag{7.3}$$

The equation of motion for the quantum particles is then

$$i\hbar \frac{\partial \Psi(\mathbf{r},t;\mathbf{R}(t))}{\partial t} = \mathsf{H}^{\text{el}}\big(\mathbf{r};\mathbf{R}(t)\big)\Psi\big(\mathbf{r},t;\mathbf{R}(t)\big), \tag{7.4}$$

while the equation of motion for the classical particles is

$$M_k \ddot{\vec{R}}_k = -\nabla_{\vec{R}_k} \langle \Psi\big(\mathbf{r},t;\mathbf{R}(t)\big) | \mathsf{H}^{\text{el}} | \Psi\big(\mathbf{r},t;\mathbf{R}(t)\big) \rangle, \tag{7.5}$$

If Ψ is a stationary (adiabatic) wave function, by the Hellmann-Feynman theorem one can write,

$$M_k \ddot{\vec{R}}_k = -\langle \Psi\big(\mathbf{r};\mathbf{R}(t)\big) | \nabla_{\vec{R}_k} \mathsf{H}^{\text{el}} | \Psi\big(\mathbf{r};\mathbf{R}(t)\big) \rangle. \tag{7.6}$$

In Eq. (7.4), the Hamiltonian is always implicitly time-dependent because of $\mathbf{R}(t)$, while Eqs. (7.5) or (7.6) give mean-field classical trajectories dependent on the electronic wave function. Together they determine the dynamics of the coupled electron-nuclear system in a mean-field approximation. This is the basis of the so-called Ehrenfest method [49, 80].

The main problem of the Ehrenfest method is that the mean-field trajectory follows an unphysical motion that misrepresents the dynamics in many cases. This is particularly distressful when transitions between different electronic states are likely, as it happens in excited states of molecules because of NACs and, as it might seem unavoidable when considering laser-excited molecules. While quantum mechanics deals with probability amplitudes, which may very well be in a superposition of multiple eigenfunctions of the system that describe different states, the classical description of the atomic nuclei binds them to one state at a time. An averaged quantum force, such as that given by Eq. (7.6), does not represent in general the quantum force exerted in each different state. However, when coherence effects like those induced by strong fields are in place, it is the averaged force, rather than the gradient of a particular PES, what mostly affects the nuclear motion [19, 81–86].

A different approach, initially proposed by Tully, is SH [48]. In SH one abandons the idea of trying to find the most representative mean-field trajectory and treats quantum jumps statistically, using stochastic methods. At each instant of time, the nuclei move under the force of a single electronic state. However, this state can be different in different trajectories, and an ensemble of trajectories must be calculated. On the other hand, Eq. (7.4) still holds for the electrons, because one needs to evaluate the probabilities of all the possible quantum transitions between the states. A "reference" electronic wave function is actualized at each time, that is used to calculate the quantum forces that act on the nuclei: $\Psi^{\text{el}}(\mathbf{r},t;\mathbf{R}) \to \Psi^{\text{ref}}(\mathbf{r},t;\mathbf{R})$, such that

$$M_k \ddot{\vec{R}}_k = -\langle \Psi^{\text{ref}}(\mathbf{r},t;\mathbf{R}) | \nabla_{\vec{R}_k} \mathsf{H}^{\text{el}} | \Psi^{\text{ref}}(\mathbf{r},t;\mathbf{R}) \rangle. \tag{7.7}$$

The SH approach imposes a "dual" following of the electron dynamics and a choice of representation by which one "a priori" decides what is the nature of the electronic states that will create the most convenient (the most "representative") quantum forces. The results will obviously depend on this choice of representation. In most SH studies, the reference state is a Born-Oppenheimer electronic state. Expanding the electronic wave function on this basis

$$\Psi^{\mathrm{el}}(\mathbf{r}, t; \mathbf{R}) = \sum_{\alpha} c_{\alpha}(t)\psi_{\alpha}^{\mathrm{BO}}(\mathbf{r}; \mathbf{R}), \tag{7.8}$$

the coefficients $c_{\alpha}^{*}(t)c_{\alpha}(t)$ give the probability of finding the system on state α. Next, one applies an stochastic approach to actualize these probabilities, "collapsing" the electronic wave function on a single reference state. However, the collapse does not affect the TDSE for the electrons [Eq. (7.4)]. In some approaches, one can also collapse the electronic wave function that enters into the TDSE after some time (but not at each instant of time, or the probability to remain in the same state will be one always!), breaking the unitary evolution [87].

Since the initial state is always well defined, the algorithm calculates the probability of hopping or jumping to all other possible states, deciding, by a random choice, whether the system remains in the same state or jumps: $\Psi^{\mathrm{ref}}(\mathbf{r}, t_1; \mathbf{R}) = \psi_{\beta}^{\mathrm{BO}}(\mathbf{r}; \mathbf{R}) \rightarrow \psi_{\alpha}^{\mathrm{BO}}(\mathbf{r}; \mathbf{R}) = \Psi^{\mathrm{ref}}(\mathbf{r}, t_1 + \Delta t; \mathbf{R})$. The algorithm most often employed to calculate the transition probabilities is the Tully's fewest switches criterion (TFS). In TFS the probability of hopping depends on the instantaneous rate of change of populations, which depends on the coupling strength, not on the accumulated probability.

In order to evaluate the probability of hopping, we need to calculate how the quantum amplitudes change in time. Introducing the Born-Oppenheimer expansion [Eq. (7.8)] on the TDSE [Eq. (7.4)] and projecting on each BO electronic state $\langle\psi_{\beta}^{\mathrm{BO}}|$, we obtain

$$\dot{c}_{\beta}(t) = -\sum_{\alpha}\left[\frac{i}{\hbar}\mathsf{H}_{\beta\alpha}^{\mathrm{el}} + \mathsf{K}_{\beta\alpha}\right]c_{\alpha}(t), \tag{7.9}$$

where $\mathsf{H}_{\beta\alpha}^{\mathrm{el}}$ are the matrix elements of the electronic Hamiltonian, and

$$\mathsf{K}_{\beta\alpha} = \left\langle \psi_{\beta}^{\mathrm{BO}}\big(\mathbf{r}; \mathbf{R}(t)\big) \middle| \frac{\partial}{\partial t}\psi_{\alpha}^{\mathrm{BO}}\big(\mathbf{r}; \mathbf{R}(t)\big) \right\rangle = \dot{\mathbf{R}}(t) \cdot \left\langle \psi_{\beta}^{\mathrm{BO}}\big(\mathbf{r}; \mathbf{R}(t)\big) \middle| \nabla_{\mathbf{R}}\psi_{\alpha}^{\mathrm{BO}}\big(\mathbf{r}; \mathbf{R}(t)\big) \right\rangle \tag{7.10}$$

is the matrix element responsible of the NACs.

Now, it is possible to calculate the hopping probability from a state β to another state within Δt as stated in [49]. Let us suppose we have a set of N_T trajectories, where $N_{\beta}(t_n)$ trajectories will populate state β at time t_n:

$$N_{\beta}(t_n) = c_{\beta}^{*}(t_n)c_{\beta}(t_n) \cdot N_T. \tag{7.11}$$

Without loss of generality, the population of state β is decreased by $\Delta N = N_{\beta}(t_n) - N_{\beta}(t_{n+1})$ to $N_{\beta}(t_{n+1})$ at a later time $t_{n+1} = t_n + \Delta t$. The minimum number

of switches required to go from $N_\beta(t_n)$ to $N_\beta(t_{n+1})$ is ΔN hops from state β to any other state and zero hops from any other state to state β. Therefore, the probability for a hop out of state β within the time interval $[t_n; t_{n+1}]$ is

$$P_{\beta\to\ldots} = \frac{\Delta N}{N_\beta(t_n)} = \frac{N_\beta(t_n) - N_\beta(t_{n+1})}{N_\beta(t_n)} = \frac{c^*_\beta(t_n)c_\beta(t_n) - c^*_\beta(t_{n+1})c_\beta(t_{n+1})}{c^*_\beta(t_n)c_\beta(t_n)}. \tag{7.12}$$

Assuming that we have a sufficiently small time step, we can approximate the above equation as:

$$P_{\beta\to\ldots} \approx -\frac{\frac{d}{dt}(c^*_\beta c_\beta)\Delta t}{c^*_\beta(t_n)c_\beta(t_n)}, \tag{7.13}$$

with

$$\frac{d}{dt}\big(c^*_\beta c_\beta\big) \approx \frac{c^*_\beta(t_{n+1})c_\beta(t_{n+1}) - c^*_\beta(t_n)c_\beta(t_n)}{\Delta t} = 2\Re\big(c^*_\beta \dot{c}_\beta\big), \tag{7.14}$$

with $\Re$ being the real part.

Thus, the final formula for calculating the hopping probability from a state β to any other state within the time step Δt is:

$$P_{\beta\to\ldots} = \frac{-2\cdot\Re(c^*_\beta \dot{c}_\beta)}{c^*_\beta c_\beta}\cdot\Delta t. \tag{7.15}$$

Including Eq. (7.9) into this formula gives:

$$P_{\beta\to\ldots} = \sum_\alpha \frac{2\cdot\Re(c^*_\beta c_\alpha(\frac{i}{\hbar}\mathsf{H}^{\mathrm{el}}_{\alpha\beta} + \mathsf{K}_{\alpha\beta}))}{c^*_\beta c_\beta}\cdot\Delta t. \tag{7.16}$$

The hopping probability from state β to a specific state α now is defined by simply removing the sum of the above equation as:

$$P_{\beta\to\alpha}(t) = 2\cdot\Re\left\{c^*_\beta c_\alpha\left[\frac{i}{\hbar}\mathsf{H}^{\mathrm{el}}_{\alpha\beta} + \mathsf{K}_{\alpha\beta}\right]\right\}\frac{\Delta t}{c^*_\beta c_\beta}. \tag{7.17}$$

7.2.2 Laser-Induced Dynamics: FISH vs. SHARC

Typically, the SH methodology has been used to follow the dynamics of molecules (or reactants) in electronically excited states, where many non-adiabatic crossings occur. However, it is also possible to use this approach to simulate laser-induced dynamics, as in the so-called FISH scheme [71]. The most straightforward approach is to incorporate the radiation-molecule coupling as a non-diagonal term of H^{el},

$$\mathsf{H}^{\mathrm{el}}_{\beta\alpha} = V^{\mathrm{BO}}_\alpha\big(\mathbf{R}(t)\big)\delta_{\beta\alpha} - \mu_{\beta\alpha}\big(\mathbf{R}(t)\big)\mathcal{E}(t), \tag{7.18}$$

where $V_\alpha^{\mathrm{BO}}(\mathbf{R}(t))$ are the Born-Oppenheimer PES, $\mu_{\beta\alpha}(\mathbf{R}(t))$ is the transition dipole moment and $\mathcal{E}(t)$ the external field. Equations (7.10) and (7.17) apply exactly as before. Given a reference state $\psi_\alpha^{\mathrm{BO}}$ at time t, the nuclear equation of motion will be

$$M_k \ddot{\vec{R}}_k = -\left\langle \psi_\alpha^{\mathrm{BO}}(\mathbf{r};\mathbf{R}) \middle| \nabla_{\vec{R}_k} \mathsf{H}^{\mathrm{el}} \middle| \Psi_\alpha^{\mathrm{BO}}(\mathbf{r};\mathbf{R}) \right\rangle, \tag{7.19}$$

where explicit time-dependence is omitted. In principle, one could incorporate other couplings, for instance, the spin-orbit couplings, as additional non-diagonal terms in H^{el}. In the current FISH scheme [71], Eqs. (7.9), (7.10), (7.17) and (7.19) determine the coupled electron-nuclear dynamics.

It has been shown that the choice of Born-Oppenheimer electronic states as the reference state for the SH quantum force is sufficiently accurate to represent the dynamics of systems driven by different laser pulses [71]. However, in this approach the gradients are evaluated directly in the laser-free potentials, and strong field effects like the Stark effect cannot be properly described. When the reference state departs largely from the true electronic wave function, the ensemble of trajectories needed to statistically reproduce the observed effects hugely raises. As previously stated, when strong fields act on the molecule, the mean-field trajectory can actually reproduce quite well the dynamics of the system, particularly in simpler systems. In the SH approach, this Ehrenfest-like trajectory can be incorporated in a better reference wave function. This is the basis of the SHARC method [74].

In SHARC, instead of expanding the wave function in the Born-Oppenheimer basis [Eq. (7.8)], one uses a "fully adiabatic" basis,

$$\Psi^{\mathrm{el}}\big(\mathbf{r},t;\mathbf{R}(t)\big) = \sum_\alpha a_\alpha(t)\psi_\alpha^{\mathrm{a}}\big(\mathbf{r},t;\mathbf{R}(t)\big), \tag{7.20}$$

that serves as a reference state. Notice that in general this reference state will be explicitly time-dependent. To simplify the notation, we will thereafter neglect the implicit time-dependence of $\mathbf{R}(t)$. This adiabatic basis is chosen to diagonalize the Hamiltonian in the presence of the additional couplings not included in the Born-Oppenheimer approximation, such as the spin-orbit and electron-radiation coupling:

$$\psi_\alpha^{\mathrm{a}}(\mathbf{r},t;\mathbf{R}) = \sum_\beta \mathsf{U}_{\alpha\beta}(t;\mathbf{R})\psi_\beta^{\mathrm{BO}}(\mathbf{r};\mathbf{R}). \tag{7.21}$$

U is the unitary rotation for each nuclear position and instant of time that makes

$$\mathsf{H}^{\mathrm{a}}_{\beta\alpha}(t) = \left\langle \psi_\beta^{\mathrm{a}}(\mathbf{r},t;\mathbf{R}) \middle| \mathsf{H}^{\mathrm{el}} \middle| \psi_\alpha^{\mathrm{a}}(\mathbf{r},t;\mathbf{R}) \right\rangle = V_\alpha^{\mathrm{a}}(\mathbf{R},t)\delta_{\beta\alpha}. \tag{7.22}$$

In the context of strong laser-molecule interaction, these truly adiabatic potentials, which are explicitly time-dependent, are called light-induced potentials (LIPs) $V_\alpha^{\mathrm{a}}(\mathbf{R},t) = V_\alpha^{\mathrm{LIP}}(\mathbf{R},t)$ and exhibit very interesting properties, including bond hardening and bond softening effects [19, 81–86]. In principle, distinct SHARC approaches could be followed depending on whether the adiabatic basis diagonalizes the full Hamiltonian at each instant of time, including the laser and spin-orbit couplings, or the laser coupling only.

In order to collapse the electronic wave function into one and only one reference state (per trajectory and instant of time), we need to calculate the quantum amplitudes

$$\dot{a}_\beta(t) = -\sum_\alpha \left[\frac{i}{\hbar} \mathsf{V}^{\mathrm{a}}_\alpha \delta_{\beta\alpha} + \mathsf{K}^{\mathrm{a}}_{\beta\alpha} \right] a_\alpha(t) \tag{7.23}$$

with

$$\mathsf{K}^{\mathrm{a}}_{\beta\alpha} = \mathsf{U}^\dagger_{\beta\alpha} \mathsf{K}_{\beta\alpha} \mathsf{U}_{\beta\alpha} + \mathsf{U}^\dagger_{\beta\alpha} \dot{\mathsf{U}}_{\beta\alpha}, \tag{7.24}$$

where K is the anti-Hermitian matrix responsible for the NAC [Eq. (7.10)] and U is the unitary matrix responsible for the change of representation, that is, for all the "non-adiabatic" transitions between the LIPs induced by the field. If the field envelope is smooth enough, as the field intensity becomes stronger, the second term in Eq. (7.24) becomes smaller in comparison with the energy difference (splitting) between the LIPs.

Following exactly the same procedure as before, by the TFS algorithm, one can decide the probability of remaining in the initial reference state β or hopping to a different reference state α

$$P^{\mathrm{a}}_{\beta\to\alpha}(t) = 2 \cdot \Re\left\{ a^*_\beta a_\alpha \left[\frac{i}{\hbar} \mathsf{H}^{\mathrm{a}}_{\alpha\beta} + \mathsf{K}^{\mathrm{a}}_{\alpha\beta} \right] \right\} \frac{\Delta t}{a^*_\beta a_\beta} \quad . \tag{7.25}$$

If the reference state is $\Psi^{\mathrm{ref}}(\mathbf{r}, t; \mathbf{R}) = \psi^{\mathrm{a}}_\alpha(\mathbf{r}, t; \mathbf{R}(t))$ then the nuclei will follow the equation of motion

$$M_k \ddot{\vec{R}}_k = -\nabla_{\vec{R}_k} \left\langle \psi^{\mathrm{a}}_\alpha\big(\mathbf{r}, t; \mathbf{R}(t)\big) \middle| \mathsf{H}^{\mathrm{a}} \middle| \psi^{\mathrm{a}}_\alpha\big(\mathbf{r}, t; \mathbf{R}(t)\big) \right\rangle. \tag{7.26}$$

Equations (7.23) to (7.26) determine the coupled electron-nuclear dynamics in the SHARC scheme. In the following sections of this chapter we will explore how this scheme reproduces the results of the dynamics, often comparing the results to those obtained by fully quantum dynamics (QD) or by the FISH scheme. Here, we show the dynamics on a very simple test system, in order to understand how FISH and SHARC imply different ways of following the dynamics. Both approaches are compared to the exact quantum dynamical approach for reference. As the test system, we treat a light-induced transition between two displaced harmonic oscillators within the rotating wave approximation (RWA), neglecting NACs. The one-dimensional potentials are defined as

$$V_g(R) = \frac{1}{2} k \, R^2 \tag{7.27}$$

$$V_e(R) = \frac{1}{2} k \, (R - R_e)^2 + D_{ge} \tag{7.28}$$

where $k = 2 = R_e = 2$ and $D_{ge} = 10$ in arbitrary units. Both the reduced mass of the system and the transition dipole moment are taken as unity, $m = \mu_{ge} = 1$. The

electronic Hamiltonian matrix mapped in the Born-Oppenheimer basis $\psi_\alpha^{\mathrm{BO}}$ (where $\alpha = g/e$, for the ground and excited state respectively) is

$$\mathsf{H}^{\mathrm{el}}(R) = \begin{pmatrix} V_g(R) & -\frac{1}{2}\mu_{ge}\mathcal{E}(t) \\ -\frac{1}{2}\mu_{ge}\mathcal{E}(t) & V_e(R) - \hbar\omega \end{pmatrix}. \tag{7.29}$$

Here $\mathcal{E}(t)$ is the field envelope and $\hbar\omega$ is taken as 13, so that the laser excitation if off-resonant by a blue-shift of $\Delta = D_{ge} - \hbar\omega = -3$ arbitrary units, compensates the displacements of the potentials and allows efficient excitation at the Franck-Condon window. The field envelope $\mathcal{E}(t)$ is zero in the beginning, raises in a sine-squared fashion and remains constant after $t \sim 25$, see Fig. 7.1a, representing a very strong, smoothly switched-on, CW laser field.

In FISH, at each nuclear position $R(t)$, we solve the TDSE for the electronic coefficients $c_g(t)$ and $c_e(t)$ using a fourth-order Runge-Kutta method with the Hamiltonian given by Eq. (7.29). We use a time-step of 0.0025. Applying Eq. (7.17) we calculate the probability of hopping and decide by a random algorithm at each instant of time which is the reference state (V_g or V_e), where the analytic gradients are calculated to integrate the nuclear equation of motion [Eq. (7.19)], using a velocity Verlet algorithm [88, 89]. To characterize the dynamics, we follow an ensemble of 200 trajectories.

In SHARC, the same approach is followed. However, instead of Eq. (7.29), the electronic Hamiltonian is first diagonalized, $\mathsf{H}^{\mathrm{a}}(R) = \mathsf{U}^\dagger(R)\mathsf{H}^{\mathrm{el}}(R)\mathsf{U}(R)$, and the TDSE is solved for the adiabatic coefficients $a_+(t)$ and $a_-(t)$ at each instant of time and thus for a given $R(t)$. Using Eq. (7.25) we evaluate the hopping probability and the nuclear equation of motion is solved using the gradients of the LIPs $V_\alpha^{\mathrm{LIP}}(R,t)$, where $\alpha = +/-$. Notice that only when $\mathcal{E}(t) = 0$, the LIPs correlate with the diabatic states $V_g \longleftrightarrow V_+$ and $V_e \longleftrightarrow V_-$. However, using the unitary transformation

$$\begin{pmatrix} a_+ \\ a_- \end{pmatrix} = U^\dagger \begin{pmatrix} c_g \\ c_e \end{pmatrix} \tag{7.30}$$

we can always calculate populations $P_\alpha = |c_\alpha|^2$, $P_\alpha^a = |a_\alpha|^2$, in the diabatic or adiabatic potentials respectively. In SHARC, we use the same time step and number of trajectories as in FISH.

The exact quantum dynamical results are obtained by integrating the TDSE with the nuclear Hamiltonian

$$\mathsf{H}^{\mathrm{nuc}} = \begin{pmatrix} \mathsf{T} + V_g(R) & -\frac{1}{2}\mu_{ge}\mathcal{E}(t) \\ -\frac{1}{2}\mu_{ge}\mathcal{E}(t) & \mathsf{T} + V_e(R) - \hbar\omega \end{pmatrix}, \tag{7.31}$$

where $\mathsf{T} = -\frac{\hbar^2}{2m}\frac{\partial^2}{\partial R^2}$ is the kinetic energy operator. Here, R is obviously a variable and the equation is only integrated once for a given initial state. The norm of

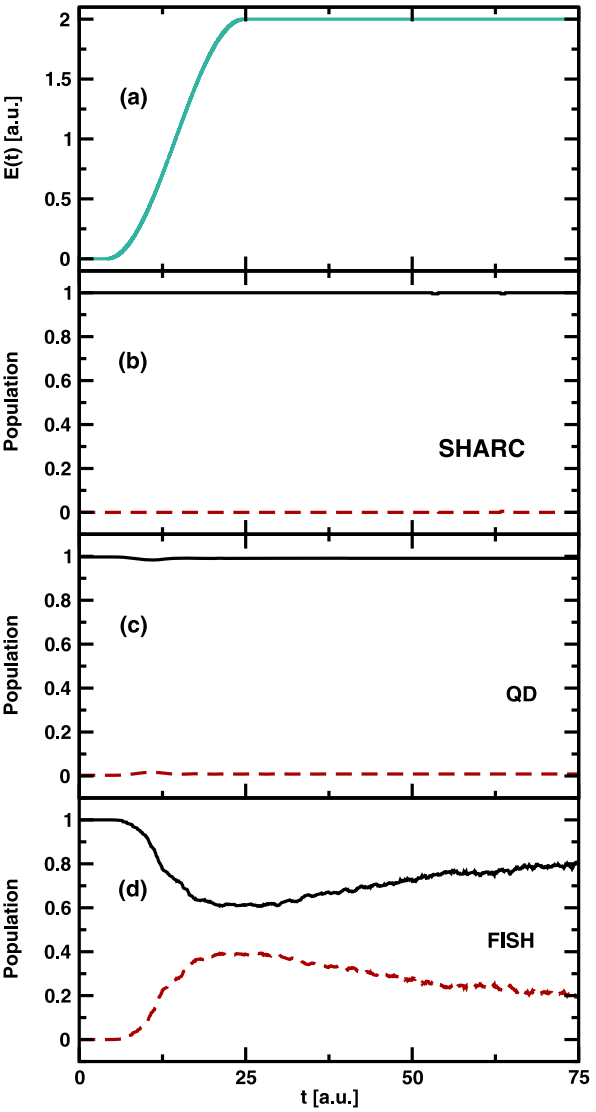

Fig. 7.1 Population in the states + (*black/solid*) and − (*red/dashed*) as calculated from SHARC (panel (**b**)), QD (panel (**c**)) and FISH (panel (**d**)) in the adiabatic representation. Additionally, the laser envelope as used in the RWA is shown in panel (**a**) (Color figure online)

the nuclear wave packets $\phi_g(R)$ and $\phi_e(R)$ gives the population in each electronic state. The TDSE is solved using the split-operator scheme [90–92]. As above, adiabatic populations can be calculated with the use of the unitary transformation of Eq. (7.30).

Figure 7.1 shows the results of the population dynamics obtained with the three methods mentioned above in the adiabatic representation, where SHARC naturally operates. A clear difference is noticeable between the SHARC and the FISH method, whereby SHARC gives the same behavior as the exact QD. Given the chosen pulse, the adiabatic population basically remains all the time in the initial LIP.

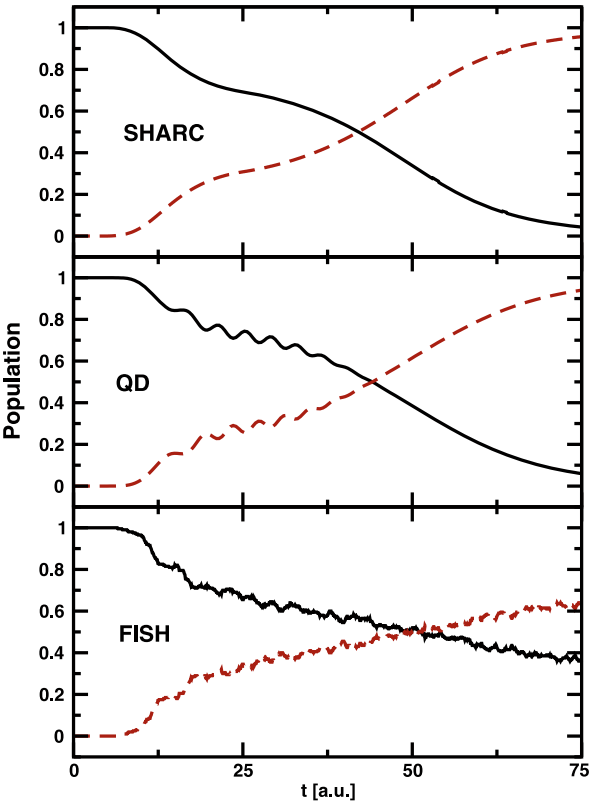

Fig. 7.2 Population in the states g (*black/solid*) and e (*red/dashed*) as calculated from SHARC (*upper panel*), QD (*middle panel*) and FISH (*lower panel*) in the diabatic representation (Color figure online)

The gradients of this LIP clearly better represent the electronic force that governs the nuclear motion. FISH works in the diabatic basis, where many transitions between the potentials occur and as Fig. 7.1d shows the statistics of 200 trajectories cannot represent properly the adiabatic populations.

In QD it is usual to work with diabatic states, which, in the absence of NACs and external fields, naturally coincide with the adiabatic ones. Therefore, in the following sections we will provide only diabatic (or Born-Oppenheimer states) populations. In Fig. 7.2 we have also displayed the population dynamics in the diabatic representation as triggered by the field of Fig. 7.1a. As it can be seen, even in the diabatic representation, natural to the FISH method, there is a difference between the final ratio of populations predicted by SHARC and FISH, whereby SHARC agrees almost perfectly with the result of QD. As observed, the differences in the gradients of the LIPs manifest in the dynamics of the trajectories and any associated property.

Although FISH and SHARC can give the same results for a number of problems, the technically different implementation of SH in the SHARC method compared to the one of FISH proves to be advantageous whenever one uses strong pulses. In Sect. 7.3 we shall provide a clear example of a strong-field process that SHARC can deal with successfully. The differences between SHARC and FISH grow as the

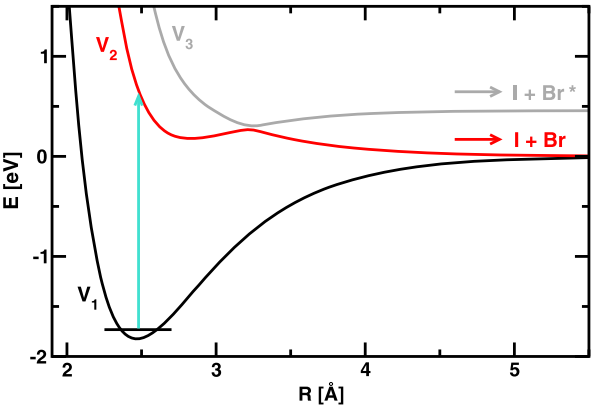

Fig. 7.3 Excitation scheme and potential energy curves of the IBr molecule. Population is transferred from the ground state potential V_1 (*black*) to an excited-state potential V_2 (*red*). From there, dissociation is possible leading to I + Br. Spin-orbit coupling opens up another channel on the potential curve V_3 (*grey*), resulting in I + Br* (Color figure online)

pulse amplitude and duration increases, *i.e.* as the laser-induced dynamics is more *adiabatic*. However we shall see that also in the opposite, *impulsive* regime, SHARC gives at least qualitatively correct results.

7.3 Examples of Laser-Free Dynamics

One advantage of the SHARC method over other SH schemes is that it allows to use SH in problems where the dynamics is influenced by spin-orbit coupling. In contrast, the original SH formulation will most likely fail in the presence of spin-orbit coupling because the regarded states are mixed by the spin-orbit interaction over a wide range in coordinate space. In such a case, a great number of hops would be necessary to account for the mixing. Such a situation where numerous hops take place precisely contradicts the underlying idea of the TFS criterion [48], so that the inclusion of spin-orbit coupling would lead to massive errors. Kinetic couplings—due to non-adiabatic interactions from states of the same multiplicity—are usually very localized in the coordinate space and therefore the original SH method works very satisfactorily.

In the following we will discuss the dissociation dynamics of the IBr molecule after photoexcitation, since this is a paradigmatic example of a reaction determined by strong spin-orbit coupling [19, 42, 86, 93, 94]. A photon in the visible regime can excite IBr from the electronic ground state $1^1\Sigma^+_{0^+}$ to the excited state $1^3\Pi_{0^+}$. Spin-orbit coupling with the excited state $1^3\Sigma^-_{0^+}$ leads to two dissociation channels: I + Br ($^3P_{3/2}$) and I + Br* ($^3P_{1/2}$), see Fig. 7.3. The energy difference of these two channels is only due to spin-orbit coupling, see Ref. [95].

The IBr system serves then as a perfect test case for the SHARC method [74] because being diatomic the results can be easily compared to exact QD simulations. For this comparison, we restrict ourselves to the model potentials from Ref. [96]. For systems possessing more degrees of freedom, SHARC can be coupled with elec-

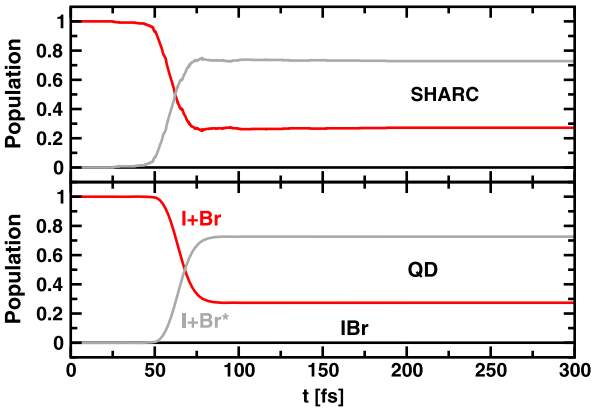

Fig. 7.4 Population dynamics in the excited states of IBr after excitation with a δ-pulse computed with the SHARC algorithm (*upper panel*) and QD (*lower panel*). After around 65 fs, an avoided crossing is passed, which gives rise to a branching ratio $Q = 72$ % of the products in the different dissociation channels (I + Br in state $i = 2$ and I + Br* in state $i = 3$) with both simulation types. The ground state ($i = 1$; *black*) is not populated (Color figure online)

tronic calculations computed on-the-fly. In the case of IBr, the QD calculations are carried out using the split-operator method [90–92] as in the previous section. The same technique is employed in imaginary time to obtain vibrational eigenstates [97]. From these solutions, Wigner distributions are calculated, which in turn serve to derive the initial conditions for the MD simulations. A time step of 0.002 fs was employed for both the SHARC and QD simulations. The MD calculations have been carefully benchmarked by using 500 trajectories. Convergence was obtained already after 100 trajectories.

In this application, the ground state population of IBr is excited to the excited state potential V_2 (see Fig. 7.3)—situation equivalent to an excitation with a δ-pulse. Such an scenario does not correspond to a real experiment because lasers have a finite duration. However, since laser interactions are not commonly integrated in MD packages, a δ-excitation is the usual approximated way of operating. We shall use these same conditions in SHARC and QD to investigate whether spin-orbit coupling is treated correctly within SHARC, decoupled from laser interactions (the latter will be incorporated explicitly in Sect. 7.4). The resulting population dynamics is depicted in Fig. 7.4. Population is initially in the state V_2 (I + Br) and after ca 50 fs starts decaying to V_1 (I + Br*) by virtue of the spin-orbit coupling. A comparison of the outcome from MD and QD reveals a very good agreement in the time evolution of the populations. It is possible to define the branching ratio of the dissociation products as $Q = \frac{[\mathrm{I+Br^*}]}{[\mathrm{I+Br}]+[\mathrm{I+Br^*}]}$. This branching is equal to 72 % in both cases, demonstrating the suitability of SHARC to work in the presence of spin-orbit couplings [74].

7.4 Examples of Laser-Induced Dynamics

The simulation of laser interactions is not trivial within the SH scheme. Although the first developments date back to the 1990s [66–68], few applications can be found in the literature until very recently. New implementations [70–72, 74] now make it possible to fulfill a long-time dream: Unraveling ultrafast laser-modulated molecular processes including all internal degrees of freedom.

When considering laser interactions, two extreme cases can be defined: The impulsive regime and the adiabatic regime. An ultrafast photoexcitation is referred to as impulsive if its time scale is short compared with a considered molecular event e.g. a vibrational period ($\tau_{laser} < \tau_{vib}$) [98]. A pictorial description is that the oscillator is kicked on a time scale shorter than its response time. In contrast, the oscillator can accommodate itself slowly to the perturbation of the laser in the adiabatic limit. In this case, the time scale of the electromagnetic interaction is long compared to the vibrational period ($\tau_{laser} > \tau_{vib}$). In some cases, not the time scale of the whole interaction but the time that is needed to switch on the laser—until the maximum intensity is reached—is classified under the above criteria.

In the following, we present some examples of ab initio MD simulations employing SHARC which are attributed to the two categories just described.

7.4.1 Impulsive Regime

As a first scenario, we shall use SHARC to treat spin-orbit and strong laser-field induced couplings at the same time. As in Sect. 7.3, we use the IBr molecule as a model system and QD calculations for comparison. However, we now incorporate all laser interactions explicitly in the simulations. As an extension to the model presented above, we shall also exert control on IBr via the non-resonant dynamic Stark effect (NRDSE), as originally implemented experimentally by Sussman *et al.* [19]. The Stark effect is produced when an electric field energetically shifts the potentials of a molecule. If the field is time dependent, the process is called dynamic Stark effect [99]. Especially interesting for control is the NRDSE case mentioned above when the frequency of the time-dependent electric field does not induce a one-photon transition but only induces potential shifts. Therefore, the effect is frequently described as a photonic catalysis [19, 42, 81–83, 86]. In order to influence the potentials significantly, the field strength is chosen as intermediate, compared to strong fields which would ionize the molecule, or weak fields which would introduce only a small perturbation.

In IBr, the control field is able to change the ratio Q (see Sect. 7.3) between the possible dissociation products after photoexcitation. The latter is induced by a first excitation pulse $\mathcal{E}_{\mathrm{e}}(t)$. The subsequent dynamics is then influenced by an infrared control pulse $\mathcal{E}_{\mathrm{c}}(t)$. We extend the model employed in Sect. 7.3 by using realistic polarizabilites α and dipole moments μ as given in Ref. [95].

The excitation pulse has a wavelength of 493.4 nm, a full width at half maximum of the Gaussian-shaped envelope of 50 fs and an intensity of 10 TW/cm^2.

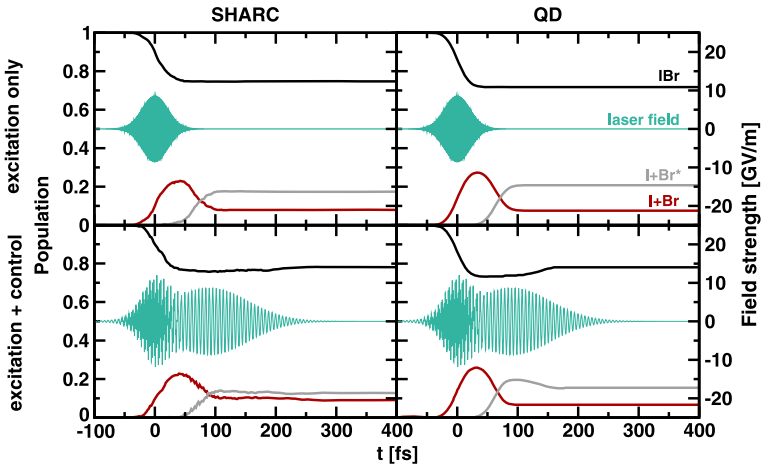

Fig. 7.5 Time-dependent populations as modeled by SHARC (*left panels*) or QD (*right panels*). In the *lower panels*, the dynamics is influenced by a control laser via the NRDSE while the unchanged dynamics is presented in the *upper panels* for comparison. The employed laser fields are overlaid in each *panel* (Color figure online)

The wavelength of the control laser is 1.73 μm, similar to the experiment [19], a full width at half maximum of the Gaussian-shaped envelope of 150 fs, an intensity of 10 TW/cm^2, and the delay $\Delta\tau$ between the pulses is set to 90 fs. A time step of 0.001 fs was used to propagate 500 trajectories or the quantum wave packet, respectively. Further computational details can be found in Ref. [86].

Figure 7.5 shows the dynamics induced by SHARC and with QD. As it can be seen, the populations obtained with SHARC are almost identical to those obtained with the exact QD in this complex control scenario. In the presence of the excitation field (upper panel), 26 % of the population is transferred from the ground state to the excited states according to SHARC, in agreement to 28 % according to QD. The branching ratio Q is given as 70 % by SHARC and 73 % by QD. When the control laser is added to the system (bottom panel), 22 % of the population is excited both in SHARC and in QD. The branching ratio Q is decreased to 59 % by the control field in the SHARC simulations, in agreement with the value of 65 % from QD.

The decrease in the ratio Q induced by the control field can be understood from the mean time-dependent momentum, presented in Fig. 7.6. The momentum is decreased by the control pulse compared to the case without control. The lower ratio Q can then by rationalized analogous to Landau-Zener theory where the change of an adiabatic potential is proportional to $e^{-\frac{1}{v}}$, v being the velocity along the considered coordinate [100, 101]. Again, in this case the agreement of the momentum calculated with SHARC and QD is excellent.

So far, we have focused on excited states. Now, we want to turn our attention to the ground state. In order to look at the full picture of NRDSE control in IBr, we plot the probability density ρ in the different states in Fig. 7.7. At a distance of $R \approx 3.8$ Å and approximately 90 fs, population is dumped to the ground state, where it starts

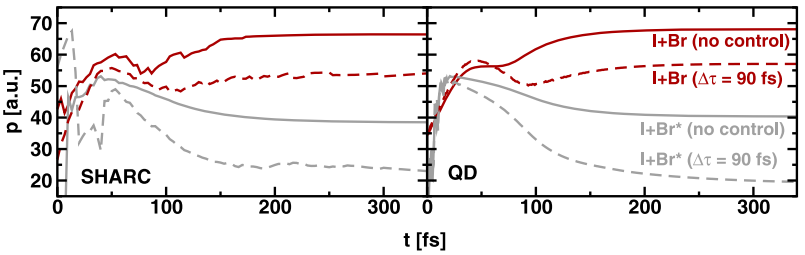

Fig. 7.6 Mean time-dependent momentum in the excited states. *Red curves* correspond to V_2 and *grey curves* to V_3. The dynamics without control field (*solid lines*) is compared to the one with a time delay of $\Delta\tau = 90$ fs (*dashed lines*) between excitation and control pulse for SHARC and QD (Color figure online)

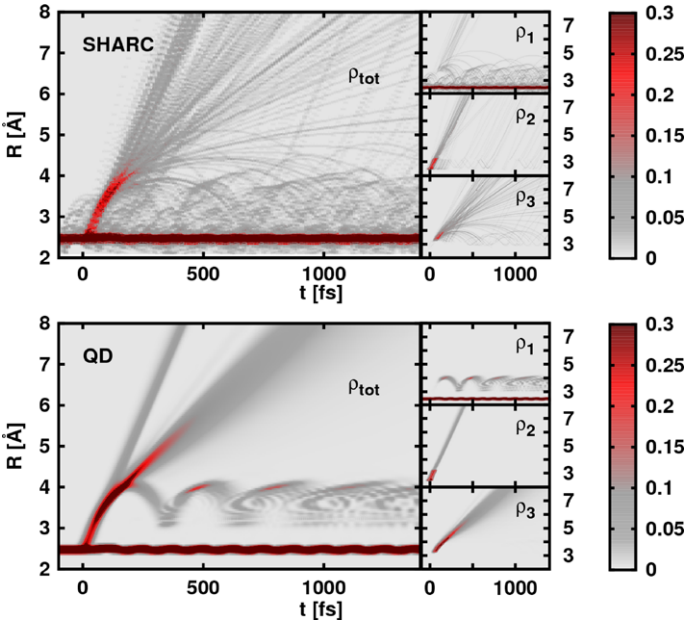

Fig. 7.7 Probability density for a time delay of 90 fs between excitation and control pulse. Results from SHARC are shown on the *top*, output from QD on the *bottom*. The respective *panel* on the *left* shows the total probability density and the *panels* on the *right* show the fractions of the same density belonging to the adiabatic states j as indicated. Adapted from Ref. [86] (Color figure online)

oscillating. The energy difference between V_2 and the ground state corresponds to the control laser frequency in this region. Hence, the control laser may still induce resonant transitions, although it is thought to be non-resonant in NRDSE control. This dump process as well as all other effects are nicely reproduced in the SHARC simulations, see Fig. 7.7.

Table 7.1 Fitting parameters employed in the construction of the model

$V = D_e[1 - \exp(-\alpha(R - R_0)^2)] + V_0$			
	V_1	V_2	V_3
α ($10^3\ a_0^{-2}$)	0.5937	0.4053	0.4698
D_e (10^3 Hartree)	27.0664	35.7438	24.1634
R_0 (a_0)	5.8250	6.8691	6.7426
V_0 (Hartree)	0.0000	0.0665	0.1167
$\mu = a_0 + a_1 \cdot R + a_2 \cdot R^2 + a_3 \cdot R^3 + \cdots$			
	μ_{12}		μ_{23}
a_0	3.018		100.276
a_1	−0.706		−99.8748
a_2	0.309		40.0344
a_3	−0.0393		−8.531
a_4	0.00202		1.061

In summary: the previous examples show that molecular dynamics influenced by relatively strong fields is possible within the SHARC method. In the next section, we shall focus on the adiabatic regime for the time scale of the pulses.

7.4.2 Adiabatic Regime

In this section we explore how efficiently the semiclassical methods simulate the dynamics under the influence of strong laser pulses in the adiabatic regime. As an example, we shall simulate the APLIP (Adiabatic Passage by Light-Induced Potentials) process in Na_2 [102–105], comparing the results of FISH, SHARC and quantum dynamics.

Since the model is one-dimensional, again in this case it suffices to provide potential energy curves and the dipole moments in advance and run the dynamics on the given potentials. The potentials employed in the model are the electronic states $^1\Sigma_g(3s)$, $^1\Sigma_u(3p)$ and $^1\Sigma_g(4s)$ of the Na_2 molecule, (named V_1, V_2 and V_3 hereafter). These as well as the dipole moments are taken from Ref. [103] and fitted to Morse oscillators, in the case of the potentials, and polynomial expansions, in the case of the transition dipoles. Table 7.1 collects the parameters used in the fitting.

The APLIP scheme is a two-photon absorption process, where two laser pulses with frequencies ω_1 and ω_2 partially overlapping in time are employed. Originally, only one pathway was considered in the APLIP scheme, the so-called counter-intuitive pathway (proposed by Garraway and coworkers [102]), where the laser closer to the resonant transition between V_2 and V_3, $\mathcal{E}_2(t)$ must be switched on ahead of the laser closer to the transition between V_1 and V_2, $\mathcal{E}_1(t)$. Additionally,

APLIP requires that the frequency of the first laser, ω_1, is shifted to the blue of the Franck-Condon transition. This shift must be compensated by the second frequency ω_2, so that the initial and target potentials, V_1 and V_3, are in two-photon resonance. In the simulations presented here we have chosen $\omega_1 = 0.981$ eV and $\omega_2 = 2.192$ eV. The APLIP scheme can be understood in the dressed state picture using only this pathway as follows (see Fig. 7.8a): the first laser pulse, with frequency ω_1, induces an electronic repulsion between the potentials $V_2 - \hbar\omega_2$ and $V_3 - \hbar(\omega_1 + \omega_2)$ modifying the target potential $V_3 - \hbar(\omega_1 + \omega_2)$. Then, the second pulse, with frequency ω_2, induces a second Stark shift between the potentials V_1 and $V_2 - \hbar\omega_2$, modifying the initial potential V_1. During the time both pulses overlap the barrier between the V_1 and $V_3 - \hbar(\omega_1 + \omega_2)$ in the LIP is removed and then a slow displacement from the well corresponding to V_1 to the well corresponding to $V_3 - \hbar(\omega_1 + \omega_2)$ is possible, accounting for a very robust and selective population transfer. This is the standard APLIP mechanism proposed by Garraway and coworkers [102]. However, a second two-photon resonant process cannot be neglected in this case. For this set of potentials the second pathway describes a "red-detuning" intuitive pulse sequence that also leads to an effective APLIP process [104, 105]. Here, we consider the effect of both pathways in the dynamics, by constructing the Hamiltonian matrix in the Floquet picture as:

$$\mathsf{H}^{\mathrm{el}} = \begin{pmatrix} V_1 & 0 & -\mu_{12}\mathcal{E}_1/2 & -\mu_{12}\mathcal{E}_2/2 \\ 0 & V_3 - \hbar(\omega_1+\omega_2) & -\mu_{23}\mathcal{E}_2/2 & -\mu_{23}\mathcal{E}_1/2 \\ -\mu_{21}\mathcal{E}_1/2 & -\mu_{32}\mathcal{E}_2/2 & V_2 - \hbar\omega_2 & 0 \\ -\mu_{21}\mathcal{E}_2/2 & -\mu_{32}\mathcal{E}_1/2 & 0 & V_2 - \hbar\omega_1 \end{pmatrix} \tag{7.32}$$

where μ_{ij} is the transition dipole moment between electronic states i and j. The envelopes in time domain of the laser pulses are chosen of the form $\cosh^{-2}((t-t_0)/\tau)$, centered at t_0 and with width τ in all simulations. Note that the first three rows and columns describe the blue-detunning pathway while the last column/row takes into account the red-detunning alternative. The potentials included in this Hamiltonian are shown in Fig. 7.8a.

As explained before, the success of the APLIP control scheme, and in general of adiabatic control schemes, relies on the nuclear wave function remaining in a single LIP and, for high selectivity, following in a quasi-static way the time-dependent structural changes of the LIP. Thus, it is necessary that the semiclassical dynamics follows the dynamics of LIPs, which is exactly the idea underlying the SHARC methodology [74, 85, 86]. As an example, Fig. 7.8b shows the time evolution of a particular trajectory in SHARC on top of the LIPs. This trajectory was created with zero momentum in the minimum of the potential V_1 (the most likely situation in the Wigner distribution) using the Hamiltonian of Eq. (7.32) and the following laser parameters: $\tau = 5.5$ ps, $\Delta\tau = 4.5$ ps and $\mathcal{E}_1 = \mathcal{E}_2 = 0.006$ e/a$_0^2$. Due to the electric field interaction, the molecule adapts to the minimum of the LIP and evolves following the light-induced gradients. In this special case, with almost no kinetic energy, the internuclear distance and the energy of the trajectory gives directly the position of the LIP equilibrium geometry and its energy.

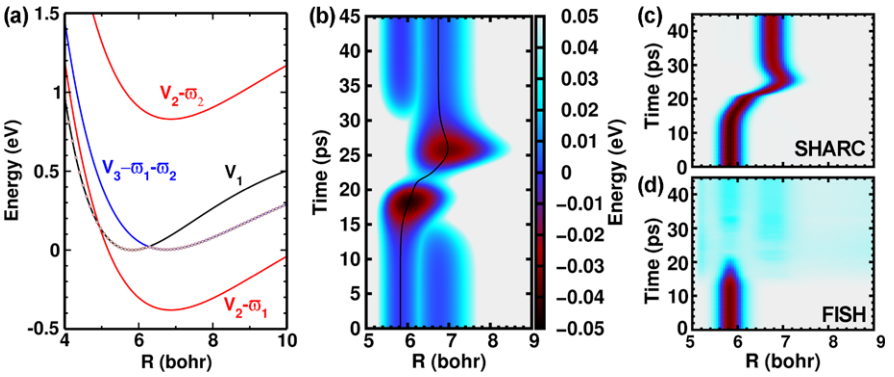

Fig. 7.8 APLIP scheme simulated with ab initio molecular dynamics, adapted from Ref. [85]. (**a**) The employed four potential model in the Floquet representation (as presented in Eq. (7.32)) fitted from the electronic states: $^1\Sigma_g(3s)$ (*black line*), $^1\Sigma_u(3p)$ (*red lines*, dressed with photons of frequency ω_1 and ω_2) and $^1\Sigma_g(4s)$ (*blue line*, dressed with the sum of ω_1 and ω_2 photons). (**b**) Time evolution of the Light Induced Potentials (LIPs) during the APLIP scheme (color map) and the position of a trajectory propagated using the SHARC method (see text). (**c**) Time evolution of the swarm of trajectories when they are propagated with SHARC. (**d**) Time evolution of the swarm of trajectories when they are propagated with FISH (Color figure online)

In order to mimic the behaviour of a vibrational quantum distribution, the evolution of the swarm of trajectories is shown in Fig. 7.8c and d. In case of Fig. 7.8c, the simulation of the dynamics using the SHARC method shows perfect adiabatic evolution of all the trajectories in the LIPs (see Fig. 7.8b) as expected in this adiabatic control scheme. However, if the reference electronic states are not adiabatic, that is, if H^{el} [Eq. (7.32)] is not diagonalized to calculate the LIPs (panel d), the trajectories follow the gradients of the diabatic (molecular) potentials. Then the ab initio MD method does not account directly for the laser-induced changes of the potential gradients and, as a consequence, the dynamics is not described correctly.

The failure of the FISH method can be attributed to the huge number of jumps that are induced by the field. However, not the whole population transferred from V_1 to V_2 is subsequently transferred from V_2 to V_3, as it would be expected in a correct simulation of the APLIP scheme. As a consequence, the net population of V_2 should remain close to zero at all times, which is not the case within the FISH simulation. In contrast, in the SHARC method the dynamics is correctly described because there are no jumps between the LIPs.

7.5 Summary and Prospect

In this chapter we have introduced the so-called SHARC scheme, in which we formulated the concept of ab initio molecular dynamics in the adiabatic representation, allowing to include non-adiabatic, spin-orbit, and laser-coupling interactions on the same footing. In this way, we have seen through different model examples that the

classical trajectories of the nuclei describe the most relevant features observed in quantum dynamical calculations subjected to laser fields, also strong ones. Without large statistical sampling the dynamics of the internuclear distance follows the average position of the wave packet. Additionally, the nuclei gain little kinetic energy during the dynamics and, although the method is classical and cannot reproduce the zero vibrational quantum energy, the final average vibrational energy only differs slightly from the quantum value. More importantly, SHARC can consistently reproduce the effects of non-adiabatic processes as the duration of the laser fields becomes smaller and the nuclei gain some extra vibrational energy.

In the presence of strong fields, the observed dynamics is equivalent to the Ehrenfest dynamics, although in the SHARC scheme, SH dynamics is included, allowing jumps between the different LIPs close to degeneration points. Moreover, the SHARC formalism recalculates the K matrix in the LIPs, by considering that the LIP is a combination of several "bare" potentials. In contrast, in the related FISH methodology [71] in which, with respect to the laser couplings, a diabatic representation is employed, the constant "hops" between the states (recall Figs. 7.1d and 7.8d) cannot correct the strong deviations of the dynamics from that given by the "bare" electronic gradients, even with high statistical sampling. The same behavior is expected whenever large Stark effects and laser-induced potential shaping affects the dynamics.

On the contrary, we expect that whenever the strong-field drives the dynamics of molecules with negligible ionization, and particularly if the time-variation of the field is slow enough that the nuclei respond to the average electronic forces, the SHARC scheme will be able to reproduce the results of fully quantum treatments, with the benefit of allowing for the calculation of the dynamics in many dimensions, as it is required for polyatomic molecules. More work along these lines, including the effects of rotation, alignment, and the influence of strong fields in systems governed by conical intersections is in prospect.

Acknowledgements This work is financed by the Deutsche Forschungsgemeinschaft (DFG) within the project GO 1059/6-1, by the German Federal Ministry of Education and Research within the research initiative PhoNa, the Dirección General de Investigación of Spain under Project No. CTQ2012-36184, a Juan de la Cierva contract, and the European COST Action CM0702.

References

1. S.A. Rice, M. Zhao, *Optical Control of Molecular Dynamics* (Wiley, New York, 2000)
2. M. Shapiro, P. Brumer, *Principles of Quantum Control of Molecular Processes* (Wiley, New York, 2003)
3. L. Wöste, J. Manz (eds.), *Femtosecond Chemistry, Vols. I, II* (VCH, Weinheim, 1995)
4. B. Whitaker (ed.), *Femtosecond Chemistry, Vols. I, II* (Cambridge University Press, Cambridge, 2003)
5. V. Sundström (ed.), *Femtochemistry and Femtobiology: Ultrafast Reaction Dynamics at Atomic-Scale Resolution* (Imperial College Press, London, 1996)
6. F.C.D. Schryver, S. DeFeyter, G. Schweitzer (eds.), *Femtochemistry* (Wiley-VCH, Weinheim, 2001)

7. M. Martin, J.T. Hynes (eds.), *Femtochemistry and Femtobiology: Ultrafast Events in Molecular Science* (Elsevier, Oxford, 2004)
8. A. Douhal, J. Santamaria (eds.), *Femtochemistry and Femtobiology* (World Scientific, Singapore, 2002)
9. W. Domcke, D.R. Yarkony, H. Köppel (eds.), *Conical Intersections: Electronic Structure, Dynamics and Spectroscopy* (World Scientific, Singapore, 2004)
10. M. Chergui (ed.), *Femtochemistry—Ultrafast Chemical and Physical Processes in Molecular Systems* (World Scientific, Singapore, 1996)
11. A.H. Zewail, *Femtochemistry, Vols. I, II* (World Scientific, Singapore, 1994)
12. A.H. Zewail, Femtochemistry: atomic-scale dynamics of the chemical bond. J. Phys. Chem. **104**, 5660–5694 (2000)
13. A. Assion, T. Baumert, M. Bergt, T. Brixner, V. Seyfried, M. Strehle, G. Gerber, Control of chemical reactions by feedback-optimized phase-shaped femtosecond laser pulses. Science **282**, 919–922 (1998)
14. C. Daniel, J. Full, L. González, C. Lupulescu, J. Manz, A. Merli, Štefan Vajda, L. Wöste, Deciphering the reaction dynamics underlying optimal control laser fields. Science **299**, 536–539 (2003)
15. M. Dantus, Ultrafast four-wave mixing in the gas phase. Annu. Rev. Phys. Chem. **52**, 639–679 (2001)
16. I.V. Hertel, W. Radloff, Ultrafast dynamics in isolated molecules and molecular clusters. Rep. Prog. Phys. **69**, 1897–2003 (2006)
17. A.D. Bandrauk (ed.), *Molecules in Laser Fields* (Marcel Dekker, New York, 1994)
18. R.J. Levis, G.M. Menkir, H. Rabitz, Selective bond dissociation and rearrangement with optimally tailored, Strong-field laser pulses. Science **292**, 709–713 (2001)
19. B.J. Sussman, D. Townsend, M.Y. Ivanov, A. Stolow, Dynamic Stark control of photochemical processes. Science **314**, 278–281 (2006)
20. O. Smirnova, S. Patchkovskii, Y. Mairesse, N. Dudovich, M.Y. Ivanov, Strong-field control and spectroscopy of attosecond electron-hole dynamics in molecules. Proc. Natl. Acad. Sci. USA **106**, 16556–16561 (2009)
21. K. Yamanouchi, The next frontier. Science **295**, 1659–1660 (2002)
22. L. González, D. Escudero, L. Serrano-Andrés, Progress and challenges in the calculation of electronic excited states. Comput. Phys. Commun. **13**, 28–51 (2012)
23. F. Martín, J. Fernández, T. Havermeier, L. Foucar, T. Weber, K. Kreidi, M. Schöffler, L. Schmidt, T. Jahnke, O. Jagutzki, A. Czasch, E.P. Benis, T. Osipov, A.L. Landers, A. Belkacem, M.H. Prior, H. Schmidt-Böcking, C.L. Cocke, R. Dörner, Single photon-induced symmetry breaking of H_2 dissociation. Science **315**, 629–633 (2007)
24. H.-D. Meyer, F. Gatti, G.A. Worth (eds.), *Multidimensional Quantum Dynamics* (Wiley, Weinheim, 2009)
25. M. Ben-Nun, J. Quenneville, T.J. Martinez, Ab initio multiple spawning: photochemistry from first principles quantum molecular dynamics. J. Phys. Chem. A **104**, 5161 (2000)
26. M. Ben-Nun, T.J. Martínez, *Ab Initio Quantum Molecular Dynamics* (Wiley, New York, 2002), pp. 439–512
27. A.M. Virshup, C. Punwong, T.V. Pogorelov, B.A. Lindquist, C. Ko, T.J. Martínez, Photodynamics in complex environments: ab initio multiple spawning quantum Mechanical/Molecular mechanical dynamics. J. Phys. Chem. B **113**, 3280–3291 (2009)
28. G.A. Worth, M.A. Robb, I. Burghardt, A novel algorithm for non-adiabatic direct dynamics using variational Gaussian wavepackets. Faraday Discuss. **127**, 307–323 (2004)
29. V.A. Rassolov, S. Garashchuk, Semiclassical nonadiabatic dynamics with quantum trajectories. Phys. Rev. A **71**, 032511 (2005)
30. J. Li, C. Woywod, V. Vallet, C. Meier, Investigation of the dynamics of two coupled oscillators with mixed quantum-classical methods. J. Chem. Phys. **124**, 184105 (2006)
31. R. Spezia, I. Burghardt, J.T. Hynes, Conical intersections in solution: non-equilibrium versus equilibrium solvation. Mol. Phys. **104**, 903–914 (2006)

32. B. Lasorne, M.A. Robb, G.A. Worth, Direct quantum dynamics using variational multi-configuration Gaussian wavepackets. Implementation details and test case. Phys. Chem. Chem. Phys. **9**, 3210–3227 (2007)
33. T. Yonehara, S. Takahashi, K. Takatsuka, Non-Born–Oppenheimer electronic and nuclear wavepacket dynamics. J. Chem. Phys. **130**, 214113 (2009)
34. T. Yonehara, K. Takatsuka, Non-Born–Oppenheimer quantum chemistry on the fly with continuous path branching due to nonadiabatic and intense optical interactions. J. Chem. Phys. **132**, 244102 (2010)
35. G. Granucci, M. Persico, A. Zoccante, Including quantum decoherence in surface hopping. J. Chem. Phys. **133**, 134111 (2010)
36. B.F.E. Curchod, I. Tavernelli, U. Rothlisberger, Trajectory-based solution of the nonadiabatic quantum dynamics equations: an on-the-fly approach for molecular dynamics simulations. Phys. Chem. Chem. Phys. **13**, 3231–3236 (2011)
37. J. Caillat, J. Zanghellini, M. Kitzler, O. Koch, W. Kreuzer, A. Scrinzi, Correlated multi-electron systems in strong laser fields: a multiconfiguration time-dependent Hartree-Fock approach. Phys. Rev. A **71**, 012712 (2005)
38. T. Yonehara, K. Takatsuka, Nonadiabatic electron wavepacket dynamics of molecules in an intense optical field: an ab initio electronic state study. J. Chem. Phys. **128**, 154104 (2008)
39. J. Kim, H. Tao, J.L. White, V.S. Petrović, T.J. Martinez, P.H. Bucksbaum, Control of 1,3-cyclohexadiene photoisomerization using light-induced conical intersections. J. Phys. Chem. A
40. L. Wang, H.-D. Meyer, V. May, Femtosecond laser pulse control of multidimensional vibrational dynamics: computational studies on the pyrazine molecule. J. Chem. Phys. **125**, 014102 (2006)
41. T.J. Penfold, G.A. Worth, C. Meier, Local control of multidimensional dynamics. Phys. Chem. Chem. Phys. **12**, 15616–15627 (2010)
42. C. Sanz-Sanz, G.W. Richings, G.A. Worth, Dynamic Stark control: model studies based on the photodissociation of IBr. Faraday Discuss. **153**, 275–291 (2011)
43. M. Schröder, J.-L. Carreon-Macedo, A. Brown, Implementation of an iterative algorithm for optimal control of molecular dynamics into MCTDH. Phys. Chem. Chem. Phys. **10**, 850–856 (2008)
44. M. Schröder, A. Brown, Realization of the cnot quantum gate operation in six-dimensional ammonia using the OCT-MCTDH approach. J. Chem. Phys. **131**, 034101 (2009)
45. R. Car, M. Parrinello, Unified approach for molecular dynamics and density-functional theory. Phys. Rev. Lett. **55**, 2471–2474 (1985)
46. N. Doltsinis, D. Marx, First principles molecular dynamics involving excited states and nonadiabatic transitions. J. Theor. Comput. Chem. **1**, 319–349 (2002)
47. D. Marx, J. Hutter (eds.), *Ab Initio Molecular Dynamics: Basic Theory and Advanced Methods* (Cambridge University Press, Cambridge, 2009)
48. J.C. Tully, Molecular dynamics with electronic transitions. J. Chem. Phys. **93**, 1061–1071 (1990)
49. N. Doltsinis, in *Computational Nanoscience: Do It Yourself!*, NIC Series, vol. 31 (John von Neumann Institute for Computing, Jülich, 2006), pp. 389–409
50. E. Tapavicza, I. Tavernelli, U. Rothlisberger, Trajectory surface hopping within linear response time-dependent density-functional theory. Phys. Rev. Lett. **98**, 023001 (2007)
51. M. Baer, *Beyond Born-Oppenheimer: Electronic Nonadiabatic Coupling Terms and Conical Intersections* (Wiley, Hoboken, 2006)
52. V. Chernyak, S. Mukamel, Density-matrix representation of nonadiabatic couplings in time-dependent density functional (TDDFT) theories. J. Chem. Phys. **112**, 3572–3579 (2000)
53. R. Baer, Non-adiabatic couplings by time-dependent density functional theory. Chem. Phys. Lett. **364**, 75–79 (2002)
54. I. Tavernelli, B.F.E. Curchod, U. Rothlisberger, On nonadiabatic coupling vectors in time-dependent density functional theory. J. Chem. Phys. **131**, 196101 (2009)

55. I. Tavernelli, E. Tapavicza, U. Rothlisberger, Nonadiabatic coupling vectors within linear response time-dependent density functional theory. J. Chem. Phys. **130**, 124107 (2009)
56. M.S. Topaler, T.C. Allison, D.W. Schwenke, D.G. Truhlar, What is the best semiclassical method for photochemical dynamics of systems with conical intersections? J. Chem. Phys. **109**, 3321–3345 (1998)
57. G.A. Worth, M.A. Robb, *Applying Direct Molecular Dynamics to Non-adiabatic Systems* (Wiley, New York, 2003), pp. 355–431
58. M. Barbatti, Nonadiabatic dynamics with trajectory surface hopping method. WIREs Comput. Mol. Sci. **1**, 620–633 (2011)
59. S. Garashchuk, V.A. Rassolov, G.C. Schatz, Semiclassical nonadiabatic dynamics based on quantum trajectories for the $O(^3P, ^1D) + H_2$ system. J. Chem. Phys. **124**, 244307 (2006)
60. W. Hu, G. Lendvay, B. Maiti, G.C. Schatz, Trajectory surface hopping study of the o(3p) + ethylene reaction dynamics. J. Phys. Chem. A **112**, 2093–2103 (2008)
61. I. Tavernelli, B.F.E. Curchod, U. Rothlisberger, Nonadiabatic molecular dynamics with solvent effects: a LR-TDDFT QM/MM study of ruthenium (II) tris (bipyridine) in water. Chem. Phys. **391**, 101–109 (2011)
62. M. Odelius, C. Ribbing, J. Kowalewski, Molecular dynamics simulation of the zero-field splitting fluctuations in aqueous Ni(II). J. Chem. Phys. **103**, 1800–1811 (1995)
63. D.S.N. Parker, R.S. Minns, T.J. Penfold, G.A. Worth, H.H. Fielding, Ultrafast dynamics of the s1 excited state of benzene. Chem. Phys. Lett. **469**, 43–47 (2009)
64. R.S. Minns, D.S.N. Parker, T.J. Penfold, G.A. Worth, H.H. Fielding, Competing ultrafast intersystem crossing and internal conversion in the "channel 3" region of benzene. Phys. Chem. Chem. Phys. **12**, 15607–15615 (2010)
65. B. Fu, B.C. Shepler, J.M. Bowman, Three-state trajectory surface hopping studies of the photodissociation dynamics of formaldehyde on ab initio potential energy surfaces. J. Am. Chem. Soc. **133**, 7957–7968 (2011)
66. K. Yamashita, K. Morokuma, Theoretical study of laser-catalyzed Na + HCl reaction: a possibility of transition state spectroscopy. Chem. Phys. Lett. **169**, 263–268 (1990)
67. H. Gai, G.A. Voth, A computer simulation method for studying the ablation of polymer surfaces by ultraviolet laser radiation. J. Appl. Phys. **71**, 1415–1420 (1992)
68. M. Thachuk, M.Y. Ivanov, D.M. Wardlaw, A semiclassical approach to intense-field above-threshold dissociation in the long wavelength limit. J. Chem. Phys. **105**, 4094–4104 (1996)
69. K. Yagi, K. Takatsuka, Nonadiabatic chemical dynamics in an intense laser field: electronic wave packet coupled with classical nuclear motions. J. Chem. Phys. **123**, 224103 (2005)
70. G.A. Jones, A. Acocella, F. Zerbetto, On-the-fly, electric-field-driven, coupled electron-nuclear dynamics. J. Phys. Chem. A **112**, 9650–9656 (2008)
71. R. Mitrić, J. Petersen, V. Bonačić-Koutecký, Laser-field-induced surface-hopping method for the simulation and control of ultrafast photodynamics. Phys. Rev. A **79**, 053416 (2009)
72. I. Tavernelli, B.F.E. Curchod, U. Rothlisberger, Mixed quantum-classical dynamics with time-dependent external fields: a time-dependent density-functional-theory approach. Phys. Rev. A **81**, 052508 (2010)
73. B.F.E. Curchod, T.J. Penfold, U. Rothlisberger, I. Tavernelli, Local control theory in trajectory-based nonadiabatic dynamics. Phys. Rev. A **84**, 042507 (2011)
74. M. Richter, P. Marquetand, J. González-Vázquez, I. Sola, L. González, SHARC—*ab initio* molecular dynamics with surface hopping in the adiabatic representation including arbitrary couplings. J. Chem. Theory Comput. **7**, 1253–1258 (2011)
75. M. Richter, P. Marquetand, J. González-Vázquez, I. Sola, L. González, Correction to SHARC: ab initio molecular dynamics with surface hopping in the adiabatic representation including arbitrary couplings [J. Chem. Theory Comput. 2011, 7, 1253–1258]. J. Chem. Theory Comput. **8**, 374 (2012)
76. J. Petersen, R. Mitrić, V. Bonačić-Koutecký, J. Wolf, J. Roslund, H. Rabitz, How shaped light discriminates nearly identical biochromophores. Phys. Rev. Lett. **105**, 073003 (2010)
77. R. Mitrić, J. Petersen, M. Wohlgemuth, U. Werner, V. Bonačić-Koutecký, Field-induced surface hopping method for probing transition state nonadiabatic dynamics of Ag_3. Phys. Chem.

Chem. Phys. **13**, 8690–8696 (2011)
78. R. Mitrić, J. Petersen, M. Wohlgemuth, U. Werner, V. Bonačić-Koutecký, L. Wöste, J. Jortner, Time-resolved femtosecond photoelectron spectroscopy by field-induced surface hopping. J. Phys. Chem. A **115**, 3755–3765 (2011)
79. P. Lisinetskaya, R. Mitrić, Simulation of laser-induced coupled electron-nuclear dynamics and time-resolved harmonic spectra in complex systems. Phys. Rev. A **83**(3) (2011)
80. X. Li, J.C. Tully, H.B. Schlegel, M.J. Frisch, Ab initio ehrenfest dynamics. J. Chem. Phys. **123**, 084106 (2005)
81. J. González-Vázquez, I.R. Sola, J. Santamaria, V.S. Malinovsky, Quantum control of spin-orbit coupling by dynamic Stark-shifts induced by laser fields. Chem. Phys. Lett. **431**, 231–235 (2006)
82. B.Y. Chang, S. Shin, J. Santamaria, I.R. Sola, Bond breaking in light-induced potentials. J. Chem. Phys. **130**, 124320 (2009)
83. B.Y. Chang, S. Shin, I.R. Sola, Further aspects on the control of photodissociation in light-induced potentials. J. Chem. Phys. **131**, 204314 (2009)
84. A. Präkelt, M. Wollenhaupt, C. Sarpe-Tudoran, T. Baumert, Phase control of a two-photon transition with shaped femtosecond laser-pulse sequences. Phys. Rev. A **70**, 063407 (2005)
85. J.J. Bajo, J. González-Vázquez, I.R. Sola, J. Santamaria, M. Richter, P. Marquetand, L. González, Mixed quantum-classical dynamics in the adiabatic representation to simulate molecules driven by strong laser pulses. J. Phys. Chem. A
86. P. Marquetand, M. Richter, J. González-Vázquez, I. Sola, L. González, Nonadiabatic ab initio molecular dynamics including spin-orbit coupling and laser fields. Faraday Discuss. **153**, 261–273 (2011)
87. O.V. Prezhdo, P.J. Rossky, Mean-field molecular dynamics with surface hopping. J. Chem. Phys. **107**, 825–834 (1997)
88. L. Verlet, Computer "experiments" on classical fluids. I. Thermodynamical properties of Lennard-Jones molecules. Phys. Rev. **159**, 98–103 (1967)
89. L. Verlet, Computer "experiments" on classical fluids. ii. Equilibrium correlation functions. Phys. Rev. **165**, 201–214 (1968)
90. M.D. Feit, J.A. Fleck Jr., A. Steiger, Solution of the Schrödinger equation by a spectral method. J. Comput. Phys. **47**, 412–433 (1982)
91. M.D. Feit, J.A. Fleck Jr., Solution of the Schrödinger equation by a spectral method ii: Vibrational energy levels of triatomic molecules. J. Chem. Phys. **78**, 301–308 (1983)
92. M.D. Feit, J.A. Fleck Jr., Wave packet dynamics and chaos in the Hénon-Heiles system. J. Chem. Phys. **80**, 2578–2584 (1984)
93. B.J. Sussman, M.Y. Ivanov, A. Stolow, Nonperturbative quantum control via the nonresonant dynamic Stark effect. Phys. Rev. A **71**, 051401 (2005)
94. D. Townsend, B.J. Sussman, A. Stolow, A Stark future for quantum control. J. Phys. Chem. A **115**4, 357–373 (2011)
95. S. Patchkovskii, Ab initio investigation of potential energy curves of the 23 electronic states of IBr correlating to neutral 2P atoms. Phys. Chem. Chem. Phys. **8**, 926–940 (2006)
96. H. Guo, The effect of nonadiabatic coupling in the predissociation dynamics of IBr. J. Chem. Phys. **99**, 1685–1692 (1993)
97. R. Kosloff, H. Tal-Ezer, A direct relaxation method for calculating eigenfunctions and eigenvalues of the Schrödinger equation on a grid. Chem. Phys. Lett. **127**, 223–230 (1986)
98. R.D. Levine, *Molecular Reaction Dynamics* (Cambridge University Press, Cambridge, 2005)
99. B.J. Sussman, Five ways to the nonresonant dynamic Stark effect. Am. J. Phys. **79**, 477–484 (2011)
100. L.D. Landau, Theory of energy transfer. Phys. Z. Sowjetunion **1**, 89 (1932)
101. C. Zener, Non-adiabatic crossing of energy levels. Proc. R. Soc. Lond. A **137**, 696–701 (1932)
102. B.M. Garraway, K. Suominen, Adiabatic passage by light-induced potentials in molecules. Phys. Rev. Lett. **80**, 932–935 (1998)

103. I.R. Solá, J. Santamaría, V.S. Malinovsky, Efficiency and robustness of adiabatic passage by light-induced potentials. Phys. Rev. A **61**, 043413 (2000)
104. I.R. Solá, B.Y. Chang, J. Santamaría, V.S. Malinovsky, J.L. Krause, Selective excitation of vibrational states by shaping of light-induced potentials. Phys. Rev. Lett. **85**, 4241–4244 (2000)
105. J.-L. Chang, R. Li, J.-C. Wu, J.-C. Shieh, Y.-T. Chen, Two-photon vibronic spectra of vinyl chloride at 7.3–10 eV. J. Chem. Phys. **115**, 5925–5931 (2001)

Chapter 8
Ultrafast Ionization and Fragmentation: From Small Molecules to Proteomic Analysis

Marcos Dantus and Christine L. Kalcic

Abstract Proteomic analysis offers great diagnostic relevance, because unlike DNA, different cells in an organism express different proteins. In fact, the cellular proteome can vary as a function of time or in response to stimuli. Beyond amino acid sequence, protein function depends on chemical modifications known as post-translational modifications (PTMs) that serve as "switches" and "signals" that activate or inhibit vital functions. Despite advances in mass spectrometry, which have led to the development of fully automated protein sequencing instruments, the mapping of PTMs remains a challenge. The interaction of intense near-infrared femtosecond laser pulses with isolated molecules or ions leads to the creation of radical-ion species through an ultrafast process known as tunnel ionization. The resulting unstable ions fragment according to predictable dissociation pathways. Progress analyzing and controlling the fundamental processes taking place during photoionization and fragmentation of small polyatomic molecules has led to the development of femtosecond laser-induced ionization/dissociation (fs-LID) for proteomic analysis. Fs-LID has been proven effective for the mapping of phosphorylation sites as well as other PTMs along the peptide backbone. The fundamental steps involved in fs-LID, which permits cleavage of strong bonds while leaving chemically labile bonds intact, are discussed. Numerous examples are given to illustrate this exciting new ion activation method, and potential applications are identified.

8.1 Ultrafast Field Ionization and Its Application to Analytical Chemistry

The utility of ultrafast photoionization in analytical chemistry stems from the mechanism by which energy is deposited into the population of molecules or ions being studied. While IR laser excitation is comparable to a slow-heating method, and UV laser excitation relies on resonant photon absorption, the femtosecond laser can cause ultrafast electron loss (oxidation) through a process known as tunnel ion-

M. Dantus (✉) · C.L. Kalcic
Michigan State University, East Lansing, MI, USA
e-mail: dantus@msu.edu

R. de Nalda, L. Bañares (eds.), *Ultrafast Phenomena in Molecular Sciences*, Springer Series in Chemical Physics 107, DOI 10.1007/978-3-319-02051-8_8,

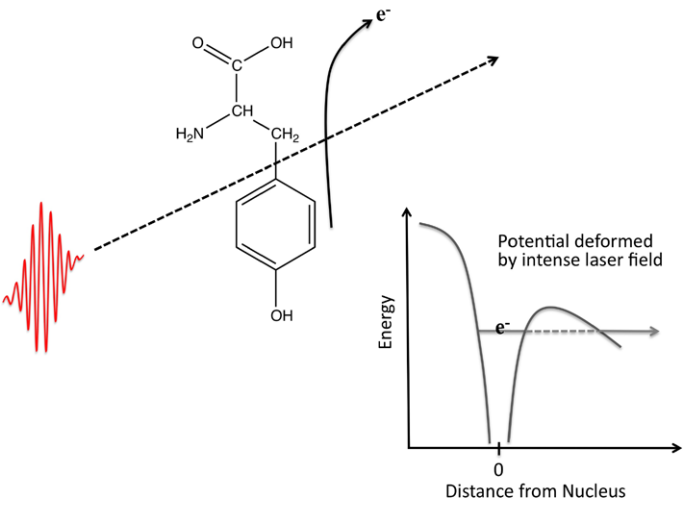

Fig. 8.1 [5] Tunnel Ionization of Tyrosine. When an ultrafast laser pulse passes by the target molecule or ion in the gas phase, the intense electric field deforms the potential felt by electrons within the molecule. As a result, the electron that is most polarizable is able to escape, leaving behind a photoionized radical site

ization [1]. Tunnel ionization is achieved when an electron, pulled by the electric field of the laser pulse, acquires sufficient energy to overcome its binding energy within a single optical cycle. This process is illustrated in Fig. 8.1. For an excitation wavelength near 800 nm, tunnel ionization requires a peak power density of 10^{14} W/cm^2 and pulse duration shorter than 35 fs. These estimates are based upon reported ionization thresholds for small molecules in an intense laser field, and have been generalized for larger molecules [2–4].

Lasers, especially those with UV and VUV wavelengths, have been used to induce bond photodissociation. Unfortunately, the most accessible chromophores present in biomolecules have a wide range of absorption maxima, as illustrated in Fig. 8.2. Therefore, wavelength tuning is typically necessary to optimize the photofragmentation process of different analytes. Unlike conventional photodissociation, tunnel ionization relies only on the presence of a polarizable electron, not a specific chromophore. In this sense, under tunneling ionization conditions, the femtosecond laser can serve as a universal excitation source.

Laser induced ionization has been a powerful method for studying the spectroscopy of weakly fluorescent molecules. When carried out with nanosecond laser pulses, ionization takes place through intermediate states that are resonant with the laser pulse energy. Given that most organic compounds have an ionization potential near 9 eV, ionization typically requires three UV photons. Such spectroscopic measurements are typically referred to as $2 + 1$ resonantly enhanced multiphoton processes (REMPI). The use of short (< 100 fs) pulses with near-IR wavelengths opens a new path for ionization that is less dependent on resonance excitation of intermediate states. The transition from multiphoton ionization (MPI) to tunneling ionization

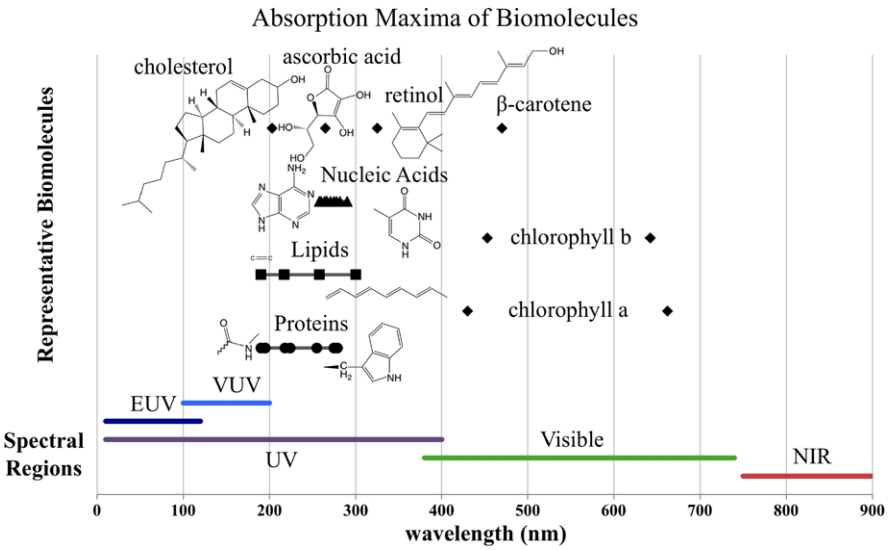

Fig. 8.2 The absorption maxima for several chromophores are plotted and grouped by classes of biomolecules. Note that larger pigments like chlorophyll have broad absorption spectra, and only the maxima are indicated in this figure

in atoms was studied by Mevel et al. who observed that distinct MPI features in the photoelectron spectra (separated by the photon energy hv) gradually disappear as tunneling ionization becomes dominant [6]. Similar work on large polyatomic molecules (benzene, naphthalene and anthracene), revealed broad featureless photoelectron spectra stretching up to 25 eV [7]. The larger the molecule, the smoother the spectrum, indicating that tunneling ionization is the dominant mechanism for above threshold ionization. The conditions of that study were 10^{13} W/cm^2, 780 nm, 170 fs. Based on those observations, the conditions of our experiments (larger molecules and much shorter pulses) place our approach in the tunneling ionization regime. Tunnel ionization is advantageous for analytical applications because it removes the need for wavelength tuning. Furthermore, as will be shown, tunnel ionization leads to ultrafast photodissociation processes that occur on a timescale faster than energy randomization. Therefore, tunnel ionization offers the ability to cleave strong bonds while leaving weaker bonds intact.

8.2 Mass Spectrometry Coupled to an Ultrafast Laser Source

8.2.1 Introduction

With the utility of soft ionization methods such as matrix-assisted laser desorption/ionization (MALDI) and electrospray ionization (ESI) which yield intact pseudomolecular ions [8, 9], tandem mass spectrometry is a robust tool for studying

molecular structure in the gas phase. The high-throughput capabilities are routinely used in the field of proteomics to efficiently analyze thousands of peptides. A typical MS/MS experiment first isolates the precursor ion population using a magnetic or electric field, and then activates this ion population to cause dissociation. The resulting product ions are recorded as the MS/MS spectrum [10]. A variety of ion activation methods can be employed, causing dissociation of the precursor ions along different pathways and leading to complementary MS/MS spectra [11]. These tandem mass spectra can be analyzed by hand or electronically using algorithms to map out the most likely structure of the original precursor ion. An ion activation method capable of breaking many different bonds within a molecule is desirable because the corresponding MS/MS spectrum will be more "information rich." In other words, it will contain a greater number of overlapping product ions that can be used to assign a more complete precursor structure with higher confidence. An ion activation method is suitable for peptide samples if it can generate sufficient product ions for unambiguous sequencing and mapping of structural modifications [12]. This structure determination can become problematic if certain regions in a peptide resist fragmentation, or if weakly bound peptide modifications dissociate preferentially to other bonds along the peptide backbone. In order to find a solution to these challenges, there is great interest in the development and characterization of new ion activation methods. Each method serves as an additional tool for tandem mass spectrometry experiments.

Given the expertise of our research group in ultrafast laser science and pulse shaping, the development of an ion activation method that utilized Femtosecond laser irradiation seemed fitting. The coupling of tandem mass spectrometry with a femtosecond laser was especially promising given developments in the field of femtosecond photoionization. In 1980, Zewail commented that the use of sufficiently short pulses would allow one to beat the timescale of energy redistribution, which typically takes place in tens of picoseconds [13]. As a result, a handful of research groups turned their focus to new experiments in laser control. The application of femtosecond lasers to study photodissociation processes in real time [14] led to the observation that bond dissociation can take place on a timescale of ~200 fs, which is two or three orders of magnitude faster than energy redistribution within a molecule. The optimization of laser fields to control chemical reactions and therefore the observed fragmentation patterns was proposed by Tannor and Rice [15]. Brumer and Shapiro realized that coherent light from the laser would cause interference between particular photochemical pathways, opening an attractive means for laser control of chemistry with nanosecond lasers [16]. The concept of creating a molecular wave packet that could be followed in time to cause selective chemistry by two or more carefully timed pulses was outlined by Rice, Kosloff and Tannor [17]. By the 1990's, scientists began to modify femtosecond laser pulses by adding linear chirp, first to control wave packet motion [18], and then to control the yield of chemical reactions [19].

The experimental work on adaptive quantum control was reviewed by Brixner and Gerber in 2003 [20]. Our group published a comprehensive review of modern (1997–2005) experimental results on coherent laser control of physicochemical processes [21]. The combination of shaped femtosecond pulses with mass spectrometry

(MS) has been hailed as the most promising technology for laser control of chemical reactions. However, despite all of the high hopes, there are only a handful of groups across the world that have conducted these types of experiments. The pioneers in this field are Gustav Gerber, who published a series of papers in 1998–2003 [22–26], Robert Levis and Hershel Rabitz [27–29], Ludger Wöste [30, 31], Thomas Weinacht [32–37], and Robert Jones [38]. All of their experiments are based on a closed-loop approach using learning algorithms to control the laser fields with feedback from the experimental signal [39]. A different strategy that has worked well on diatomic molecules is to exploit the influence of the laser field on the potential energy surfaces, through the dynamic Stark shift [40, 41]. Our group has followed a different approach, often called open-loop, in which sets of differently shaped but predefined pulses are evaluated for their ability to control chemistry [42–46].

In 2008, we published an article that reviewed the latest work in which shaped near-IR pulses were used to control molecular fragmentation [2]. In that work, we studied the laser fragmentation of 16 different molecules as a function of different phase functions, including linear chirp. We found that for several molecules the relative yield of certain fragment ions could be changed by almost two orders of magnitude. Interestingly, we found that linear chirping of the laser pulses was sufficient to cause these large changes. In those experiments, we found that vibrational coherence seemed to play a relatively small role (less than 30 % change in fragment abundance) while the pulse duration could change some fragment abundances by an order of magnitude. This observation led us to the conclusion that near-IR femtosecond laser pulses could play a very important role in the development of powerful analytical methods; however, the reproducibility of the results would depend on the implementation of methods to ensure that the pulse duration (< 40 fs) would always be the same. This goal became possible with the development of automated pulse compression by multiphoton intrapulse interference phase scan (MIIPS) [47, 48].

The combination of ultra-short intense femtosecond pulses with an ion-trap mass spectrometer led to the development of femtosecond laser-induced ionization/dissociation (fs-LID) by the Dantus and Reid groups [49]. By coupling ultrafast near-IR laser pulses with the MS^n capability of an ion trap mass spectrometer, extensive dissociation of peptides is achieved. The fs-LID instrumentation and method were first described in 2009, and the fs-LID spectra of four singly, doubly, and triply protonated peptides allowed for complete sequence determination [49]. We've found that, in positive ion mode, fs-LID is most efficient for singly protonated precursor ions, which is consistent with the estimate that ionization energy of peptides increases approximately 1.1 eV with each additional positive charge [50]. Fs-LID is also useful for the mapping of labile post-translational modifications along the peptide chain, such as phosphorylation, which was demonstrated on two synthetic phosphothreonine containing peptides. The non-ergodic dissociation patterns observed were due to the femtosecond time-scale of activation, which resulted in the ultrafast creation of a radical cation and for the ultrafast cleavage of chemical bonds faster than intramolecular energy redistribution. The applicability of fs-LID to phosphopeptide analysis was investigated further for singly protonated phosphopeptides

[51]. Radical-driven sequence ions (a, c, x, and z-ions) were observed for each phosphopeptide, and there was no dominant phosphate loss or phosphate group scrambling. The phosphorylation sites were characterized unambiguously from the fs-LID spectra [51]. Fs-LID has also been used for the analysis of protonated biomolecules other than peptides. The method works to dissociate fatty acid chains in lipids [52] and induce cross-ring cleavages in carbohydrate-based metabolites [53]. The technique was demonstrated to cleave the S–S bond in Arg^8-vasopressin, eliminating the need for wet chemistry prior to MS/MS analysis of peptides with strong disulfide bridges [54].

The most widely adopted ion activation method for MS/MS experiments is collision induced dissociation (CID), where collisions of the precursor ions with a helium bath gas causes fragmentation. As the energy gained through collisions is redistributed throughout the precursor ion, bond cleavage occurs according to bond dissociation energy. Therefore, the most abundant product ions in the MS/MS spectrum are those formed through the cleavage of the most labile bond or bonds in the analyte. For peptides, the amino acid composition greatly influences the observed dissociation pattern by affecting the amenability of the molecule to protonation, the most likely protonation sites, and proton mobility in the gas phase. These factors can influence the observed dissociation patterns by enhancing cleavage of specific bonds [55, 56]. For example, under mobile proton conditions, the backbone heteroatoms become protonated, making the peptide bonds labile [57]. This makes CID MS/MS spectra ideal for peptide sequencing when mobile protons are present, as a distribution of peptide bonds between each amino acid along the backbone chain dissociate. The mass-to-charge ratio of neighboring product ions in the MS/MS spectrum will differ by the mass of a single amino acid residue, allowing for reconstruction of the original sequence one amino acid at a time. However, this procedure is interrupted when unusually labile or non-labile bonds interfere with the standard dissociation patterns. Under non-mobile proton conditions, the proton or protons are typically sequestered at basic residues, reducing the observed sequence coverage by CID [58]. Another obstacle to sequencing are non-labile disulfide bonds between cysteine residues because they give some peptides a cyclic structure. In these cases, a single peptide bond cleavages fails to fragment the ion, as the two pieces remain linked at the disulfide bridge and the product is detected at the same m/z value as the precursor ion. For this reason, peptide samples known to contain S–S bonds are often chemically reduced prior to MS/MS analysis by CID [59]. While this retains complete or nearly complete sequence coverage, important structural information related to sulfur-sulfur connectivity in the native structure is lost. The presence of a labile chemical modification can interfere with peptide sequencing in a different manner. For example, during post-translational processing, a protein may become phosphorylated as part of a cell signaling regulation pathway. Under partially or non-mobile proton conditions, the covalent bond between the phosphate group and the amino acid side chain is more labile than the backbone peptide bonds. The H-bonding character of the phosphate group promotes proton transfer from basic side chains, leading to a charge-directed loss of H_3PO_4 [60]. This explains why, upon activation by CID, the phosphate group or groups are cleaved more readily than the

peptide backbone, and the dominant product ion reflects only this phosphoric acid loss, rather than a series of product ions containing sequence information. Phosphate group loss and position scrambling have been identified as being problematic in CID-MS^n studies [61].

The branch of proteomics that focuses on post-translational modification (PTM) analysis frequently deals with these more "problematic" samples, where comprehensive structural analysis requires cleaving strong bonds while leaving more labile bonds intact. A number of alternative ion activation methods have been introduced to achieve this required non-thermal fragmentation. Electron capture dissociation (ECD) [62] and electron transfer dissociation (ETD) [63, 64] activate the precursor ions through the formation of an unstable radical. The subsequent radical-directed fragmentation pathways are complementary to CID, and leave weakly bound PTMs intact. Photodissociation of trapped peptides in the ultraviolet [65–69] and vacuum ultraviolet [68, 70–74] regimes also generates MS/MS spectra that are similar to ETD and ECD spectra, and rely on photon absorption for ion activation rather than electron transfer [74, 75].

Fs-LID is a viable alternative to these non-statistical ion activation methods. Fs-LID differs from other laser-induced activation methods in that the laser is in the near IR region, far from the electronic excitation transitions of peptides. The ion activation is achieved through tunnel ionization, as discussed earlier. Upon ionization of a protonated peptide, the oxidized species formed is a distonic cation $[M + H]^+ \rightarrow [M + H]^{2+\bullet}$, which is susceptible to both proton- and radical-directed fragmentation pathways. As a result, fs-LID MS/MS spectra are often more information rich than CID spectra. While conservative predictions may expect product ion cleavages to occur at or near the original site of radical formation, reactive radicals have actually been demonstrated to migrate upon formation within a peptide cation. This means that the radical is mobile and that its migration is coupled with rearrangements within the molecule [76]. This can give rise to backbone cleavages and side chain losses that propagate several residues away from the initial radical site [77, 78]. This mechanism for ion activation is applicable to positive-mode MS/MS analysis of protonated peptides in any charge state and does not require a chromophore. Fs-LID is compatible with any ion trap mass spectrometer, and the interfacing of the laser can be done without compromising CID capability. Currently, the amplified laser is setup on a large optical table, but as ultrafast technology improves, the size and cost of these laser systems will decrease, making them more appealing. Ultimately, a compact femtosecond fiber laser could be brought into an existing mass spectrometry facility to make fs-LID an option for routine MS/MS analyses. Novel approaches to fiber laser design, for example self-similar evolution [79], has allowed for the development of compact fiber oscillators delivering peak power levels of 250 kW and 42 fs pulse duration [80].

Photofragmentation studies of biomolecules using UV radiation from nanosecond lasers led to the suggestion that the use of tunable fs-UV laser pulses might lead to efficient and non-ergodic dissociation of large molecules [81]. However, limited work has paired a femtosecond Ti:Sapphire laser with an ion trap mass spectrometer for such dissociation studies. Laarman et al. used a learning algorithm with pulse

shaping methods to optimize the cleavage of an acyl-N bond in Ac-Phe-NHMe to demonstrate the application of femtosecond pulse photodissociation for peptide sequencing [82]. Guyon et al. performed femtosecond pump-probe experiments on flavin, using the frequency doubled laser at 405 nm for resonant excitation of the inherent flavin chromophore [83]. Other experiments have interrogated the dissociation pathways of protonated aromatic amino acids and dipeptides using femtosecond pulses at 266 nm [84, 85]. Our work builds upon these previous experiments, but avoids the need for resonant excitation in the UV.

8.2.2 Experimental Methods

Fs-TOF Experiments on small neutral molecules were carried out using a regeneratively amplified Ti:Al_2O_3 laser seeded with a broad-band Ti:Al_2O_3 oscillator. The output was centered at 800 nm with the maximum pulse energy of 0.8 mJ. The bandwidth was ~28 nm (FWHM) resulting in ~35 fs (FWHM) transform-limited (TL) pulses. A MIIPS enabled pulse shaper [48] was placed before the amplifier to eliminate phase distortions from the laser and any optics in the setup, and to deliver arbitrary phases precisely at the target. Para-nitrotoluene (Aldrich > 99 %) was used without further purification. The fs-TOF experiments were carried out using a time-of-flight mass spectrometer (TOFMS) with a 0.5 meter field-free drift region (Fig. 8.3). Sample molecules were effused through an inlet valve into the chamber, where the pressure was maintained with a three stage differentially pumped system at 10^{-7} Torr with operational flexibility up to 10^{-5} Torr during experiments. Pulses with a 1 kHz repetition rate were focused by a 50 mm lens into the chamber to cause ionization and fragmentation of the molecules. The energy per pulse was attenuated to 100 μJ to reach a corresponding peak power density of 4.0×10^{15} W/cm^2.

Fs-LID of Trapped Ions Experiments on biomolecules were conducted by using a custom-built Quantronix (East Setauket, NY) Integra-HE amplified Ti:Al_2O_3 laser system. The broadband output of the Ti-Light oscillator is passed through a 128-pixel MIIPS-enabled pulse shaper (Biophotonic Solutions Inc, MI) before seeding a 2-stage amplifier. The system is capable of delivering a 3.0 W output with a repetition rate of 10 kHz. The pulse-shaper is used to measure and compensate phase distortions accumulated as the laser beam passes through optics in the setup, resulting in transform-limited (TL) pulses with a ~ 26 nm (FWHM) bandwidth and ~ 35 fs duration at the sample.

All samples were subjected to electrospray ionization for introduction into a Thermo Finnigan LCQ Deca XP Plus ion trap mass spectrometer. The LCQ was modified in-house to accommodate laser irradiation of the trapped ion samples. A ½″ diameter hole was drilled through the vacuum manifold in line with the ion trap, and a vacuum-sealed laser port was constructed with fused silica window. A 5 mm hole was drilled all the way through the ring electrode and the quartz spacers were notched accordingly to provide a clear path for the focused laser beam

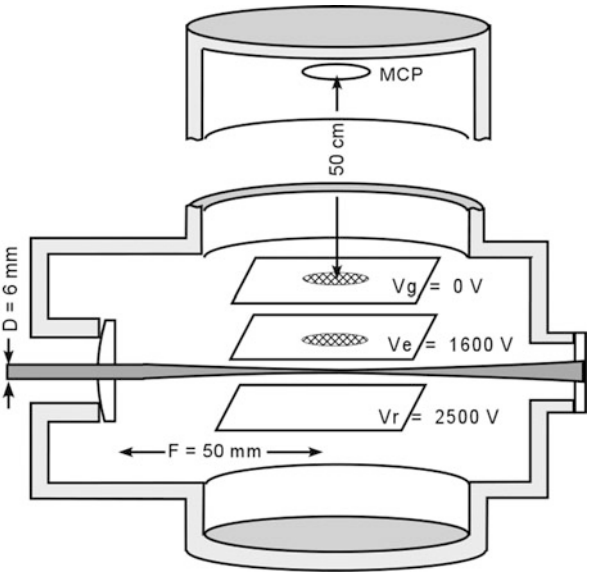

Fig. 8.3 [54] Schematic of the time-of-flight mass spectrometer. The laser beam is introduced into the chamber through a lens. Ions, generated between the repeller and extractor at high voltage, are detected by the dual microchannel plate detector after a 0.5-meter field free flying region

through the trap. Finally, a silver mirror was fixed to the vacuum manifold on the far side of the ion trap and used to direct the laser out another fused silica window in the back of the instrument. A manual flow controller was used to reoptimize the helium pressure within the trap following these structural modifications. A more detailed description of the modifications to the commercial mass spectrometer can be found elsewhere [49], and the setup is diagrammed in Fig. 8.4. The beam from the Ti-Light oscillator passes through a MIIPS Box pulse shaper equipped with a 128-pixel spatial light modulator (SLM) before seeding the amplifier. A computer is used to control the voltages across each SLM pixel, whereby the phase across the bandwidth of the laser pulse can be altered. This technology allows us to measure and compensate for phase distortions, which cleans up the laser pulses and shortens the pulse duration of the amplified system from > 70 fs to < 40 fs. The fs-LID setup utilizes this ability to ensure that the femtosecond pulses are as short as possible (transform limited) when they reach the ion packet inside the 3D ion trap. Past experiments have shown that delivering $\sim$35 fs pulses reproducibly is critical to fs-LID efficiency. The effects of dispersion, which leads to pulse broadening, severely reduces the tunnel ionization efficiency, as shown in Fig. 8.5.

The amplified laser beam is directed through a mechanical shutter, which is triggered to open and close when appropriate by the software that controls the mass spectrometer. A quarter wave plate and polarizer are used as a means of attenuating the amplified laser from the full 3.5 W output to an optimal fs-LID power. If the laser beam is too intense when it enters the vacuum manifold, the fs-LID signal-to-noise ratio suffers. This trend as a function of laser power is shown in Fig. 8.6 for a series of fs-LID spectra of protonated tryptophan. Finally, the amplified laser beam is directed up a periscope and focused through a lens before it enters the vacuum manifold via the fused silica window. Focusing the beam is necessary in order to

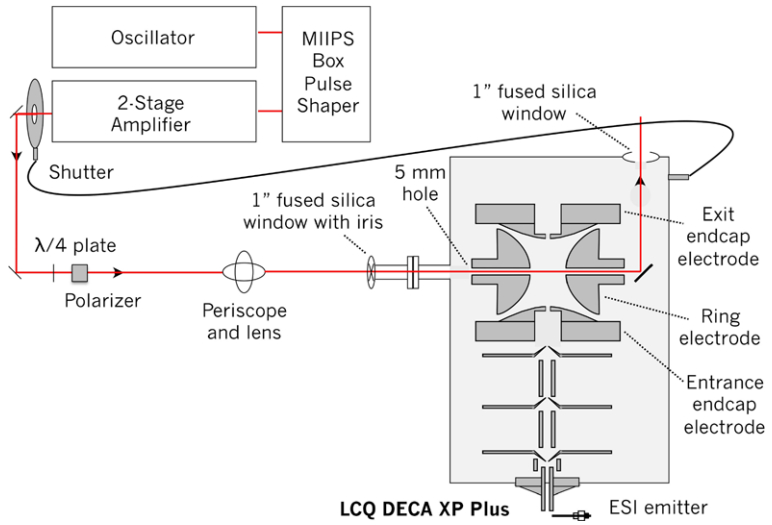

Fig. 8.4 [5] Instrumental setup of the amplified laser and 3D ion trap mass spectrometer

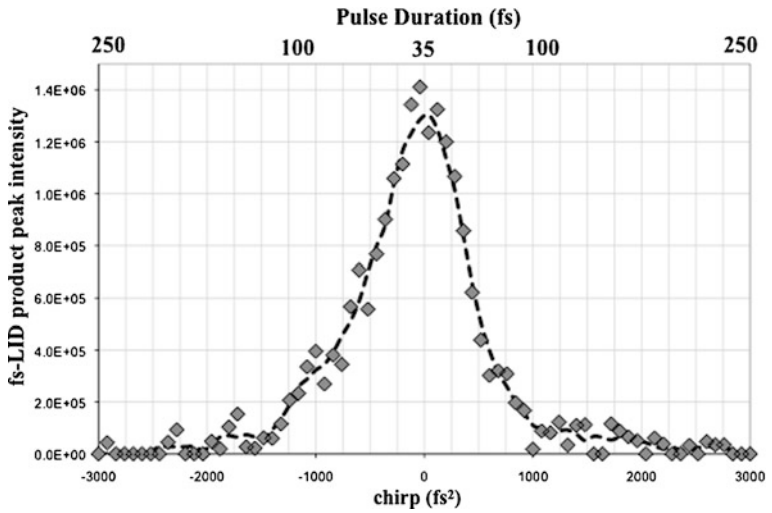

Fig. 8.5 [5] Short pulses are critical to fs-LID. Transform limited pulses with a duration of 35 fs maximize the intensity of the fs-LID product ion signal, while pulses that are stretched to 100 fs in duration result in a 80 % loss of signal intensity

pass the beam through the ion trap without hitting any of the metal surfaces, and it also provides a high peak power at the ion packet for ion activation. The unfocused beam (6.8×10^9 W/cm^2) does not provide a peak power sufficient to initiate fs-LID; experiments indicate that a peak power on the order of 10^{13} W/cm^2 must be achieved before an fs-LID product ion signal is observed (data not shown).

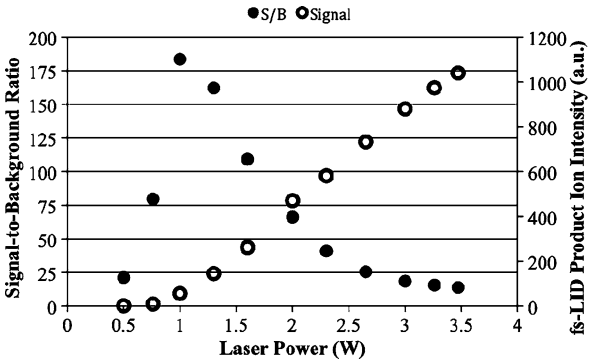

Fig. 8.6 [5] The intensity of the most abundant product ion in the fs-LID spectrum of protonated tryptophan ($[W + H]^+$) was monitored as a function of laser power (*open circles*). When the laser is allowed to irradiate a blank sample containing only MS Buffer, certain unidentified peaks are observed, most of which lie below 300 m/z (not shown). The most intense such peak observed in the $[W + H]^+$ fs-LID spectrum at 77.1 m/z was also monitored as a function of laser power. The ratio of the product ion to the 77.1 m/z ion is presented here, as the signal-to-background ratio (*closed circles*)

For these experiments, the laser was attenuated to 1.2 W (120 μJ/pulse), and focused into the ion trap using a 600 mm focal length lens, resulting in a peak laser power of 7.5×10^{13} W/cm^2. Samples were isolated using the Advanced Define Scan panel of the LCQ Tune Plus software at a q-value of 0.25. To collect fs-LID data, the normalized collision energy was set to 0 % and an activation time of 100–200 ms was used. Note that the exposure time on the shutter control box has to be manually set to match the activation time to maximize the laser-ion packet interaction without exceeding the activation window and bombarding the dynode with photons as the product ions are being ejected to generate the MS/MS spectrum. Additionally, we chose to use a 3 microscan setting and average spectra over 3–5 min for each data file.

Fs-LID data collection requires use of the built-in electronic triggering function to open and close the laser shutter during the appropriate ion activation step. To optimize our fs-LID signal before data collection, we adjust the ion trap fill time so that the isolation yields a precursor ion signal of approximately 10^6 counts. The Automatic Gain Control can be used to do this, or the fill time can be set manually. We also tweak the laser beam angle slightly off of the top periscope mirror while monitoring the photoionization product ion peak using the manual tune window. When this peak is maximized, we know we are getting the maximum laser-ion packet overlap and therefore see the best fs-LID efficiency. This slight steering of the mirror is only necessary when switching between samples that differ significantly (> 100 Da) in mass-to-charge ratio. This is likely because the ion packets are different sizes or the ion trajectories shift for precursor ions of different masses. Finally, note that fs-LID is a non-resonant ion activation method, so no wavelength tuning is necessary, nor do we modify our samples with chromophores.

8.3 Results from Small Polyatomic Molecules

8.3.1 Vibrational and Electronic Coherence

For over three decades short pulses have been used to create coherent superpositions of states and to observe quantum beats as a function of time delay. As shorter laser pulses have become available, it has become possible to create these vibrational wave packets involving vibrational modes of even the lightest atoms. Shorter pulses have also accessed the creation of superpositions of electronic states. When the vibrational or electronic wave packets are formed through excitation using a field that is one-photon resonant with the states, the formation and time evolution are well understood. Here, however, we focus on an application involving femtosecond lasers that are in the near-IR, and therefore not resonant with the dissociative or ionic states of the molecules being studied. If a typical organic molecule has an ionization-energy of 9 eV and the photon energy is ~1.5 eV, then at least 6 photons are needed to create the ion and several more are required to yield fragment ions. The focus of this section is to provide information about the vibrational and electronic coherence in small polyatomic molecules soon after they have been subjected to strong-field ionization by a near-IR femtosecond laser pulse. The extent of vibrational and electronic coherence that survives the strong-field ionization is relevant because it can be harvested in order to achieve coherent control using shaped pulses.

Strong field experiments in diatomic molecules have revealed that it is possible to form coherent vibrational and rotational wave packets. An example of such observations is the strong field ionization of deuterium to form D_2^+, and the observation of vibrational oscillations (~ 25 fs period) and rotational recurrences (~550 fs) [86, 87]. The vibrational oscillations were clearly visible when 12 fs pulses were used; however, when longer pulses were used the vibrational oscillations were no longer observed. More recently, the creation of superpositions of electronic and vibrational states has been observed following tunnel ionization of N_2, O_2, and CO with few-cycle pulses [88]. Results from the strong field ionization of CH_2I_2 show evidence of I–C–I bending coherent wave packet motion considered to arise through the formation of "multihole" wave packets. Interest in using tunnel ionization as a method for activating macromolecules being studied by mass spectrometry requires us to consider if vibrational and electronic coherence survive in larger molecules. Results from acetophenone and substituted acetophenones from our group showed evidence of coherent wave packet motion [89]. Of particular interest in that research was the effect of substituents in the aromatic ring. For example, Fig. 8.7 shows portions of the transients obtained for acetophenone (red) partially deuterated (CD_3) acetophenone (black), ortho (cyan), meta (indigo) and para (green)-methyl acetophenone. Ortho substitution increases the oscillation period from 0.7 ps to 1 ps, while meta substitution results in no oscillations. while meta substitution results in no oscillations. The observations are related to the preferred electronic configuration of the differently substituted compounds and the torsion of the carbonyl group.

Although it is suspected that the tunnel ionization process is capable of producing superpositions of electronic states, the evolution of the electronic wave packets

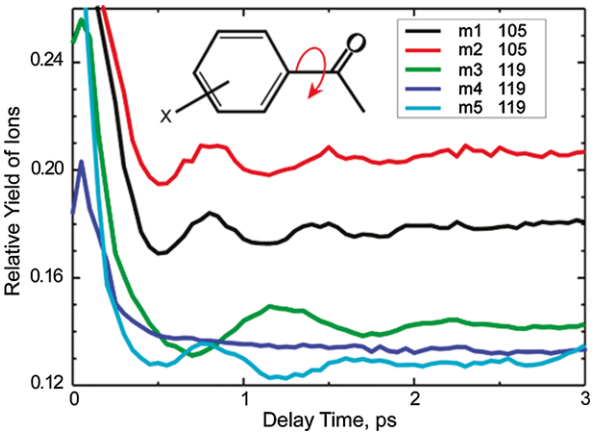

Fig. 8.7 [89] Transients obtained from acetophenone and methyl-acetophenone as a function of time delay between the pump (200 fs, 800 nm, chirped) and probe (35 fs, 800 nm, TL) pulses. Molecules are m1, acetophenone; m2, d-acetophenone; m3, 2-methyl-acetophenone; m4, 3-methyl-acetophenone; m5, 4-methyl-acetophenone. A schematic of the torsional vibration of the phenyl ring, which is thought to be responsible for the ion yield modulation, is shown

have not been observed. Electronic coherence is of particular importance because, at high energies, it could be used to control among various dissociation processes. Our group has been searching for evidence of electronic coherence following tunnel ionization of large organic molecules. Our early results indicated that the electronic coherence, if formed, was decaying within the pulse duration (∼35 fs). More recently we have found a method to detect electronic coherence following tunnel ionization. We are exploring cases in which the initial electronic coherence involves excited states in the neutral molecule and one case in which the electronic state involves the molecular ion (data not shown here). The coherence lasts for at least 100 fs and opens the window for coherent control experiments that will show large differences as a response to small differences in phase. It is becoming clear that the use of ultrashort intense pulses, lasting less than 5 optical cycles in duration, facilitates the creation of ions that exhibit coherent dynamics dictated by the coherent superposition of electronic and vibrational states. This observation has now been tested by our group with molecules with greater than 15 atoms, and we believe it will be correct for even larger molecules. The ability to create these initial coherent superpositions should allow coherent control of the fragmentation processes that is well beyond what could be achieved in the early experiments in the field involving pulse durations exceeding 50 fs.

8.3.2 Effect of Pulse Shaping

At the level of power density required for tunnel ionization, most of the molecules being subjected to fs-TOF are ionized/activated. Ionization saturation of most or-

ganic molecules is experimentally observed around 1–2 $\times$ 10^{14} W/cm^2 [3, 90]. Additionally, it was observed that shaping of the femtosecond laser pulses resulted in different product ion distributions, sparking several studies in laser control of molecular fragmentation [22]. Our group has reviewed these studies and followed up with a systematic evaluation of which field parameters are responsible for the changes observed in the fragmentation pathways [2]. We observed that the mass spectrum observed for polyatomic molecules under near-threshold ionization by transform limited sub-40 fs pulses was very similar to that obtained by electron-impact ionization (EIMS). In general, mechanisms for fragmentation following EIMS are well understood as radical-cation chemical reactions that proceed in the absence of molecular coherence. In order to better understand the system, the interaction of near-IR femtosecond laser pulses with small isolated molecules and cations was investigated through fs-TOF and fs-LID experiments on para-nitrotoluene (pNT) [54]. The different fragmentation pathways for the neutral and protonated forms of pNT were of particular interest.

Mass spectra of pNT obtained by electron ionization (EI), fs-TOF, CID, and fs-LID are shown in Fig. 8.8. The EI spectrum is obtained from the NIST database. Transform limited pulses with 35 fs time duration are used for fs-TOF and fs-LID experiments, with the peak power density of 4.0 $\times$ 10^{15} W/cm^2 and 1.6 $\times$ 10^{14} W/cm^2, respectively.

The photochemistry of pNT has been studied intensively. Although some controversy remains, the major pathways of dissociation are well established and are adopted here to explain our data. In the fs-TOF experiments, pNT molecules are tunnel ionized instantaneously. The molecular ions undergo isomerization of CH_3-f-NO_2 to CH_3-f-O-NO, as observed by the CH_3-f-O^+ product ion and the competitive production of NO_2 and NO through a common transition state [91]. In the presence of a strong field, the elimination of NO_2 is the predominant step following isomerization. The resulting $C_7H_7^+$ ions exist as an equilibrium of benzyl and tropylium ions, which was confirmed by their absorption bands at 263 and 353 nm respectively [92]. Sequential absorption of photons releases C_2H_2 fragments, giving rise to $C_5H_5^+$, $C_3H_3^+$, and C^+ ions.

The fragmentation pattern of pNT by electron ionization (Fig. 8.8) is very similar to that seen by fs-TOF with transform limited pulses. However, less molecular ion and more small fragments (C^+, H^+) are observed in the fs-TOF spectrum. This is due to the absorption of additional photons by larger fragments including molecular ions, resulting in sequential fragmentation

The fs-LID ion trap experiments on protonated pNT reveal that the even-electron, protonated molecule (MH^+) follows a slightly different fragmentation pathway than the ionized neutral ($M^{+\bullet}$). The fs-LID spectrum (Fig. 8.8) shows a combination of even- and odd-electron product ions, and is dominated by losses of heteroatoms from the nitro group. While the peak at 121 ($C_7H_7NO^{+\bullet}$), resulting from the loss of OH, is absent in the fs-TOF spectrum, all other fs-LID product ions match up with fs-TOF product ions, with an occasional shift of 1 m/z due to the retention of an extra proton. The tropylium ion is a minor product in fs-LID and therefore the benzene ring fragment ions (such as $C_5H_5^+$) are also in low abundance. While smaller

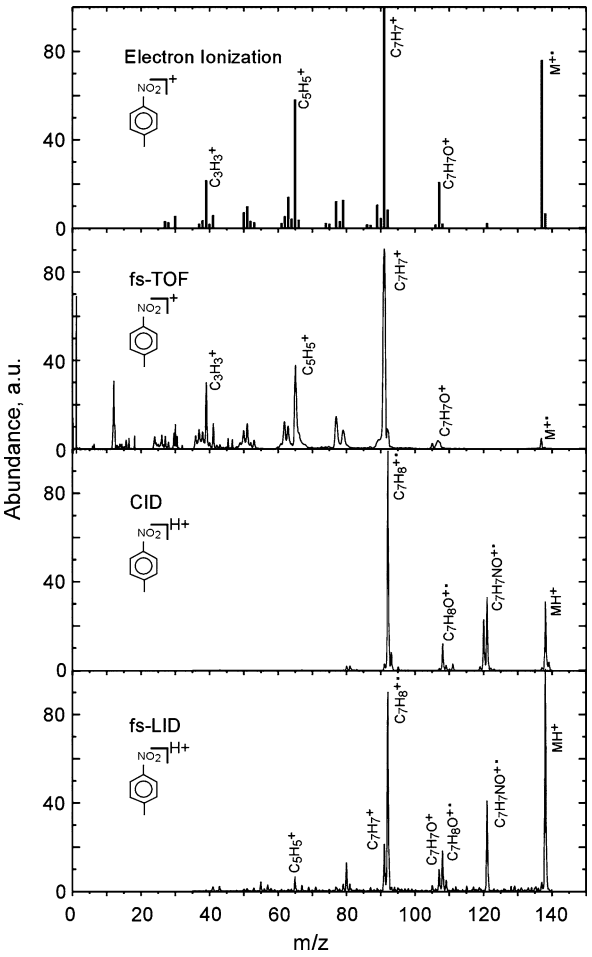

Fig. 8.8 [54] Mass spectra of para-nitrotoluene obtained by electron ionization, fs-TOF, CID, and fs-LID. Note that in the ion trap experiments (CID and fs-LID), the trapping potentials create a low mass cutoff of 35 m/z—any product ions generated below this point are ejected from the trap before the detection scan and therefore do not appear in the spectra

fragments may form upon activation with the femtosecond laser, the trapping voltages impose a low mass cutoff of 35 m/z in the ion trap; therefore, the smaller ions cannot be detected in this experiment.

While CID is a commonly employed activation method for biomolecules, it does not lead to extensive fragmentation of small organics like pNT. Nevertheless, the CID spectrum is included in Fig. 8.8 to provide an additional comparison to fs-LID. CID of pNT results in losses of OH, H_2O, NO, and NO_2. We see no tropylium ion, and therefore observe no benzene ring fragmentations. The only CID peak absent in the fs-LID spectrum corresponds to the water loss (peak 120), which comes from the protonated NO_2 group grabbing an additional proton from the benzene ring and kicking out a water molecule, leaving $C_7H_6NO^+$. This product ion provides no additional structural information.

Mass spectra of pNT were recorded as a function of linear chirp in the femtosecond laser pulses. A constant pulse energy was maintained so that larger linear chirp

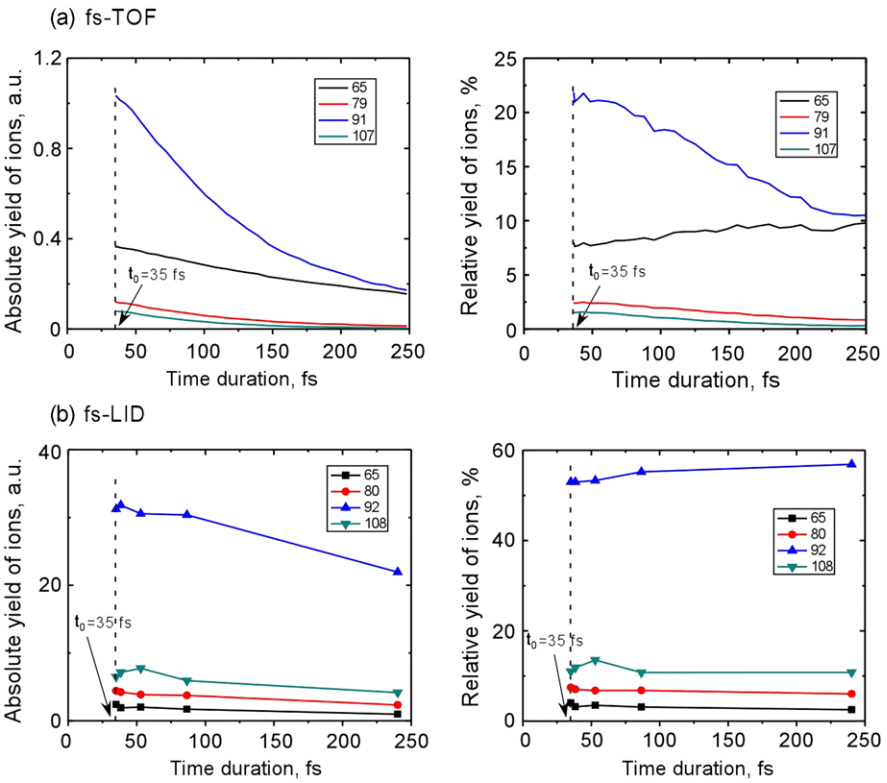

Fig. 8.9 [54] Chirp dependence of pNT fragmentation obtained by fs-TOF (panel **a**) and fs-LID (panel **b**). Absolute and relative yields of several major product ions are plotted as a function of the time duration

values result in longer pulses with lower peak intensity. The absolute and relative yields of several major product ions are plotted as a function of pulse duration in Fig. 8.9.

In the fs-TOF experiments, absolute yields of all product ions decrease with increasing pulse duration. For longer pulses, the volume in which the power density is higher than the ionization threshold is smaller, thus fewer molecules are ionized/activated and fragmented. On the other hand, the relative yields of larger fragments decrease while those of smaller fragments increase with pulse duration. This can be explained by the longer pulses giving ions more time to absorb additional photons and dissociate into smaller product ions.

Unlike the fs-TOF dependence on chirp, the fs-LID experiments show that TL pulses are ideal for ion activation in an ion trap. Longer chirped pulses result in a loss of overall fs-LID signal, with all product ion intensities decreasing uniformly (as seen by the constant relative yields in Fig. 8.9b). The difference between the TOF and ion trap data may be attributed to the different vacuum regimes utilized in each. Fragment ions are formed in the TOF-MS at 10^{-5} Torr and can continue to

dissociate into smaller and smaller pieces; however, a helium bath gas maintains a pressure around 1 mTorr in the ion trap, so as product ions are formed, they undergo collisional cooling and are stored until the detection period.

While it was known that pulse shaping led to changes in the relative yields of different fragments, it was yet to be determined if these changes were related to coherently controlled quantum mechanical interference or if they were related to ladder-switching mechanisms that were first identified when picosecond pulses were compared with nanosecond pulses. In other words, longer pulses can be absorbed by the molecule at different times, and thereby access different pathways.

In order to explore evidence of coherence in the fragmentation of p-NT using shaped laser pulses we first determined that laser intensity and central wavelength has little or no effect on the relative ion yields. We then evaluated the relative yield of several ions as a function of different families of shaped pulses (sinusoidal function, chirp, binary phases, cubic phases, etc.). The results from thousands of experiments were analyzed and there seemed to be no evidence of a vibrational or electronic coherence that had been selectively excited by one of the different shaped pulses. A selection of those results is shown in Fig. 8.10, where results are compared for four different types of shaped pulses and four different laser intensities. Note that the relative yields of $C_7H_7^+$ and $C_3H_3^+$, track closely, and show no intensity dependence.

When the study was submitted for publication the reviewer asked if p-NT was a particularly different molecule, and perhaps an exception. We then studied 16 other molecules, and our findings are best summarized in Fig. 8.11. The yield of the strongest peaks in the mass spectrum of the different molecules was tracked as a function of pulse shaping. Results are shown as a function of chirp (continuous line) and as a function of sinusoidal shaping (dotted lines). Correlation between chirp and sinusoidal shaping was achieved by matching the integrated (all masses) ion yield produced by the laser pulses. The close agreement shown in the data, evidenced as coincidence between chirped and sinusoidal shaped pulses, suggests to us that the spectral-temporal details of the pulse were not as important as the average duration of the pulses.

We concluded that pulse duration, in fact, was the most important predictor of fragmentation. One explanation for the observed effect on pulse duration is that ions are able to undergo further fragmentation through the absorption of additional photons of the incident field. Deviations from this conclusion are possible, especially when vibrational and electronic coherence survive the initial tunnel ionization process. We believe that coherent control of photofragmentation under tunnel ionization conditions should be possible, provided the excitation fields used are shorter than ~ 5 optical cycles.

8.4 Results from Peptides [5]

Here we analyze the fragmentation mechanism involved in fs-LID MS/MS of trapped peptides. We start with the protonated amino acids and several derivatives

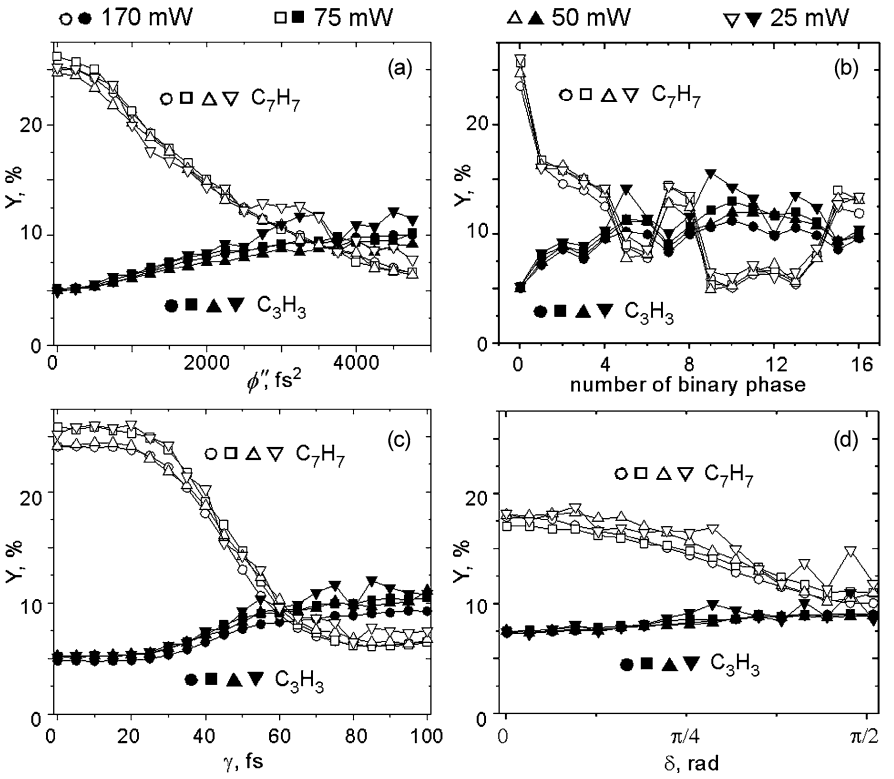

Fig. 8.10 [2] Percentage of total ionization measured at different laser powers (*dot*, *squares*, and *up* and *down triangle* for 170, 75, 50, and 25 μJ/pulse, respectively) for two main fragments of the dissociation of para-nitrotoluene, C_7H_7 (*open symbols*) and C_3H_3 (*filled symbols*), as a function of different methods of phase modulation, including (**a**) quadratic phase modulation, (**b**) 8-bit binary phase modulation, (**c**) sinusoidal phase modulation, as a function of modulation period, and (**d**) sinusoidal phase modulation as a function of phase factor. The difference of the signal for different powers is no more than the standard deviation of the measurements

to identify the most likely sites for photoionization. Further analysis of the fs-LID MS/MS spectra of a series of small peptides leads to the identification of principle cleavage pathways as well as some of the finer details of peptide dissociation by fs-LID.

8.4.1 Amino Acids

The fragmentation reactions of the protonated α-amino acids by CID have been described in detail, with dominant product ions corresponding to losses of NH_3, H_2O, and $H_2O + CO$ [93]. Fs-LID does not induce these same small molecule losses. Without derivatization, the only protonated amino acids that give rise to an fs-

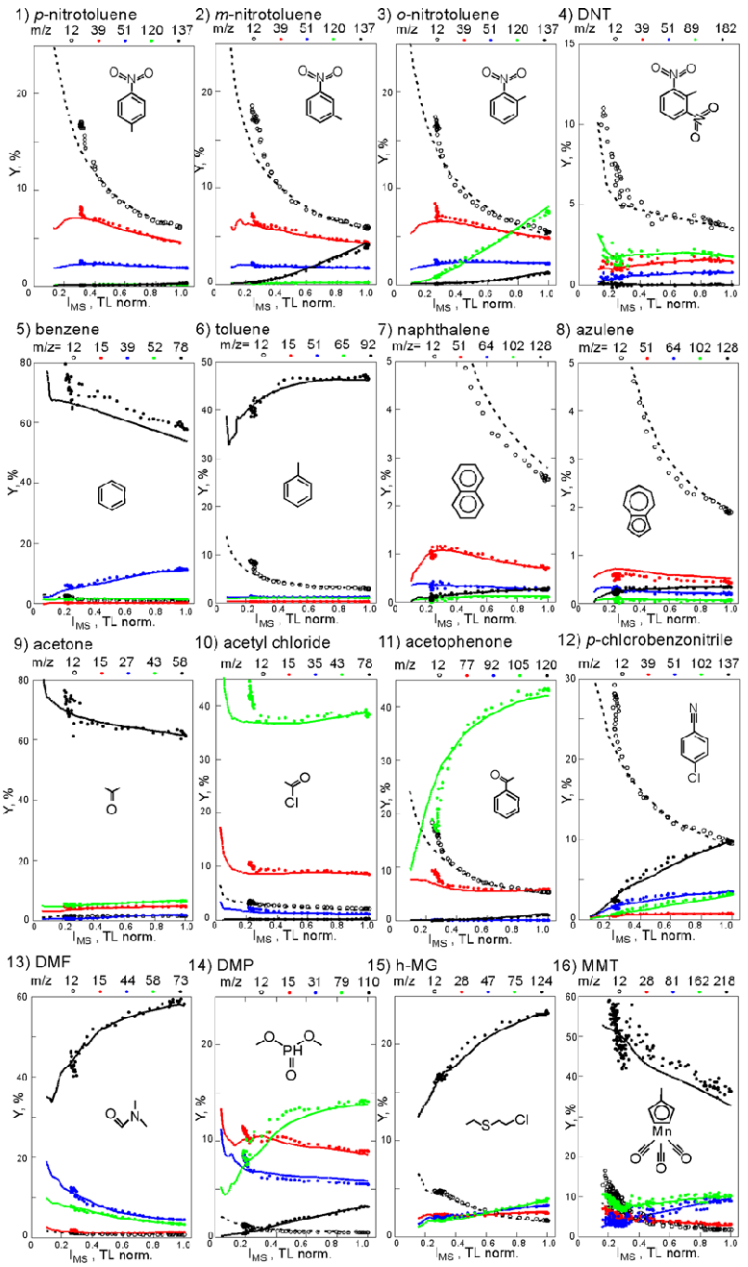

Fig. 8.11 [2] (1–16) Relative intensity of the most prominent ion products (Y), including C^+ (*open black*) and the molecular ion (*black dot*) as a function of the total yield of all ions (I_{MS}) for 16 different molecules as a function of linear chirp when the phase is scanned from 0 to 10,000 fs^2 (*lines*) and as a function of a sinusoidal phase modulation, where the period is scanned from 0 to 100 fs (*points*). Note the remarkable agreement between the two completely different types of phase modulation

Table 8.1 [5] The presence (Yes) or absence (No) of fs-LID signal is designated for each amino acid in the protonated $[M + H]^+$ form as well as the N-benzoyl and N-acetyl methyl ester derivatives. The calculated vertical ionization energies for several of the neutral amino acids in their low-lying conformations are reported [94] and experimental values from the NIST Chemistry Webbook are reported where possible

Amino Acid	IE of neutral (eV) [94]	$[M + H]^+$	N-benzoyl	N-acetyl methyl ester
A—Alanine	9.67 (NIST: 8.88)	No	No	No
C1—L-Cystine		No	No	Yes
C2—Cysteine	8.66 (NIST: 9–9.5)	No	No	Yes
D—Aspartic Acid	10.08	No	–	No
E—Glutamic Acid		No	No	No
F—Phenylalanine	8.40	Yes	Yes	Yes
G—Glycine	9.82 (NIST $\sim$ 9.2)	No	No	No
H—Histidine	7.76/8.34	No	No	No
I—Isoleucine	9.45 (NIST: 9.5)	No	No	Yes
K—Lysine	8.98 (NIST: 8.6–9.5)	No	No	Yes
L—Leucine	9.51 (NIST: 8.51)	No	Yes	Yes
M—Methionine	8.09 (NIST: 8.3–9.0)	Yes	Yes	Yes
N—Asparagine	9.31	No	Yes	No
P1—L-Proline	8.75 (NIST: 8.3–9.3)	No	Yes	Yes
P2—4-hydroxy-L-proline	(NIST: 9.1)	No	Yes	No
Q—Glutamine		No	No	No
R—Arginine	8.46	No	Yes	No
S—Serine	9.99 (NIST: 8.7–10)	No	Yes	No
T—Threonine	9.80 (NIST: < 10.2)	No	Yes	No
V—Valine	9.50 (NIST: 8.71)	No	No	No
W—Tryptophan	7.07 (NIST: < 7.5)	Yes	Yes	Yes
Y—Tyrosine	7.77 (NIST: < 8.4)	Yes	Yes	Yes

LID signal are methionine, phenylalanine, tryptophan, and tyrosine (see Table 8.1). These are the four amino acids with the lowest ionization energies, supporting the proposed photoionization mechanism for ion activation by fs-LID. However, ionization energy is not the sole predictor of fs-LID efficiency, as protonated phenylalanine gives rise to a more intense fs-LID signal than protonated methionine (data not shown) despite having a higher ionization energy. This suggests that polarizability of the precursor ions is critical to ion activation by fs-LID.

The CID and fs-LID MS/MS spectra for protonated tyrosine are compared in Fig. 8.12. As expected, the loss of NH_3 corresponds to the base peak observed in the CID spectrum, and $H_2O + CO$ losses are also observed. The same $H_2O + CO$ loss is observed following activation by fs-LID, but dissociation appears to proceed through the photoionized intermediate $[Y + H]^{2+\bullet}$, as confirmed by the MS^3 spec-

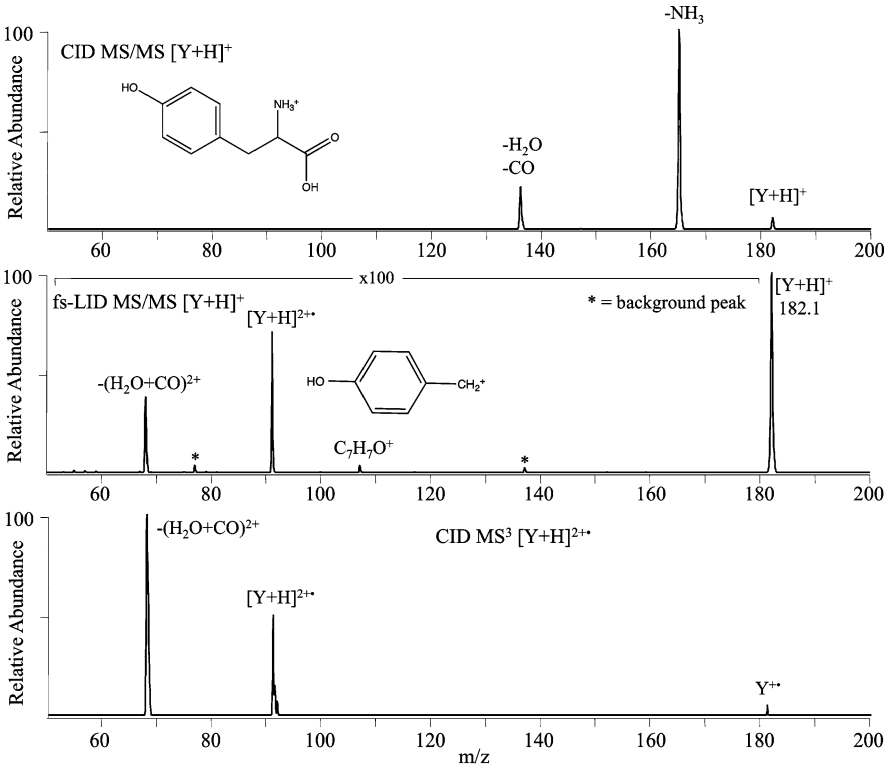

Fig. 8.12 [5] CID (*top*) and fs-LID (*middle*) spectra for protonated tyrosine illustrate the difference in dissociation pathways achieved by the two ion activation methods. CID MS^3 of the photoionization product (*lower* panel) indicates that $H_2O + CO$ loss proceeds through thermal excitation of the radical intermediate species

trum in the lower panel. NH_3 loss is absent in the fs-LID MS/MS spectrum and C_α–C_β bond dissociation gives rise to the $C_7H_7O^+$ product ion which was not observed by CID. Clearly, the two ion activation methods access different dissociation pathways.

Based on these results, which indicate that the presence of an aromatic ring enhances fs-LID activation, we evaluated all the amino acids after N-benzoyl derivatization. The presence of the benzoyl group led to a greater number of amino acids showing fs-LID ion activation events (see Table 8.1). The CID and fs-LID MS/MS spectra for N-benzoyl tyrosine are compared in Fig. 8.13. Once again, neutral losses dominate the CID spectrum while fs-LID ion activation proceeds through a radical intermediate. The photoionized $[BzY + H]^{2+\bullet}$ product ion is observed, as well as Bz^+ and $Y^{+\bullet}$, suggesting that the benzoyl group is a likely site of radical formation that leads to a radical-directed dissociation of the benzoyl group from the tyrosine molecule.

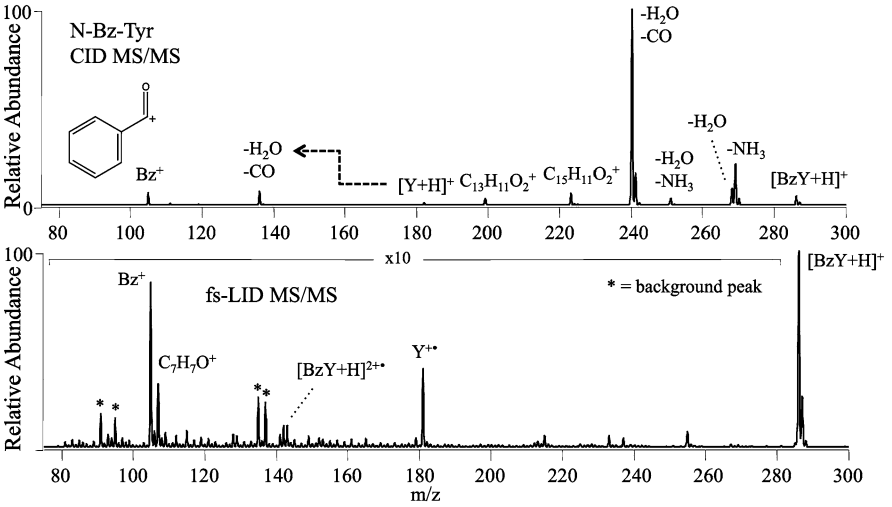

Fig. 8.13 [5] CID (*top*) and fs-LID (*bottom*) MS/MS spectra of N-benzoyl tyrosine. Note that NH_3 loss and minor product ions $C_{13}H_{11}O_2^+$ and $C_{15}H_{11}O_2^+$ in the CID spectrum indicate the presence of an isomeric impurity with the benzoyl addition occurring at the tyrosine side chain rather than the amine

We also evaluated N-acetyl methyl ester derivatized amino acids. This derivatization scheme was intended to simply lengthen each molecule, without the addition of a highly polarizable group. The CID and fs-LID MS/MS spectra for N-acetyl tyrosine methyl ester are shown in Fig. 8.14. The methyl ester and acetyl groups give rise to losses of CH_3OH, $CH_3OH + CO$, and CH_2CO following activation by CID, but these chemical modifications remain intact when ion activation is performed by fs-LID. The same $C_7H_7O^+$ fs-LID product ion is observed here as was seen for the other tyrosine-based precursors in Figs. 8.12 and 8.13.

Interestingly, between the two derivatization methods, we observed greater susceptibility to fs-LID for all amino acids except: alanine, aspartic acid, glutamic acid, glycine, histidine, glutamine and valine, as summarized in Table 8.1.

For a majority of the samples, the only product ion observed in the fs-LID MS/MS spectrum was the photoionization product, $[M + H]^{2+\bullet}$. However, the samples with the lowest ionization energies did demonstrate dissociation, primarily at the C_α–C_β bond. The series of spectra for the tyrosine samples provided in Figs. 8.12–8.14 are representative of the data for phenylalanine, methionine, and tryptophan. The photoionization product is observed in all three fs-LID MS/MS spectra, as is side chain product ion after cleavage of the C_α–C_β bond. Neutral losses of small molecules such as NH_3, H_2O, CO, CH_3OH, and CH_2CO dominate the CID spectra of these samples, but these thermal dissociation pathways are mitigated in fs-LID. These samples illustrate that fs-LID is complementary to CID, and that fs-LID spectra are rich in structural information, as the non-ergodic dissociation pathways lead to diagnostic product ions that are unique to the amino acid(s) in the

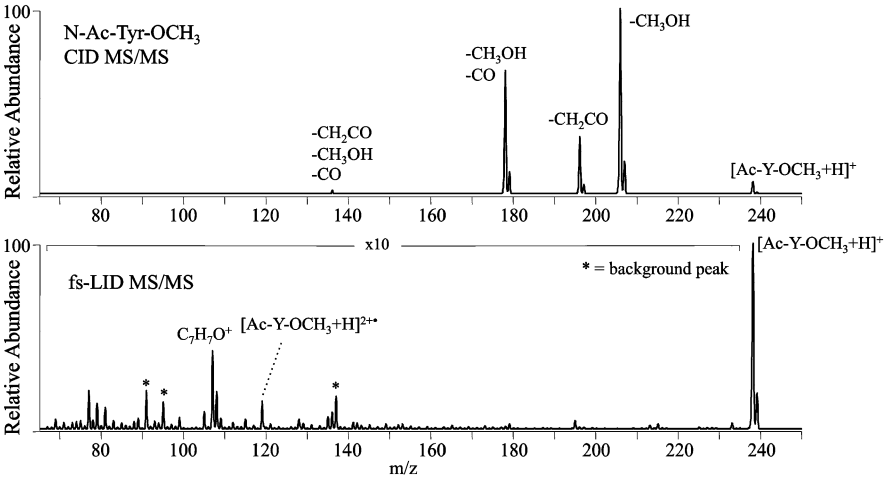

Fig. 8.14 [5] CID (*top*) and fs-LID (*bottom*) MS/MS spectra of the N-acetyl methyl ester tyrosine derivative

sample, rather than a series of small molecule losses that could be observed from any amino acid.

The fs-LID process is initiated by tunnel ionization of the most labile electron(s) in the molecule, and it leads to the formation of a radical cation. If no additional energy is deposited, the radical cation would fragment on a timescale long enough for intramolecular energy randomization leading to statistical bond breakage. Based on extensive experimental data, bond dissociation occurring in fs-LID is non-ergodic, suggesting that subsequent fragmentation occurs on a femtosecond timescale. We rationalize this by observing that the strong field acts on the entire macromolecule, pulling on most of the electrons. While usually only one electron is lost, one can assume that many other electrons are strongly perturbed by the field. This leads to energy being deposited on the macromolecule. This energy manifests as multiple bond breaking events recorded as a series of product ions for a particular peptide. The total energy deposited by the strong field on a typical singly protonated peptide can be estimated by adding the ionization energy (10.9 eV) [50] to the energy required to break one bond (4 eV) giving a total of $\sim$ 15 eV or $\sim$ 1450 kJ/mol. This amount of energy is equivalent to that of tens of photons and leads to ultrafast bond breaking. A more detailed analysis of the fs-LID process from single amino acids to peptides is given below.

8.4.2 Aromatics

Phenylalanine, tyrosine, and tryptophan all have ionization energies in the 7–8.5 eV range [94] and photoionize easily by fs-LID in both the protonated and derivatized

forms. While the delocalized pi systems stabilize the resulting radical, we do observe significant radical-directed cleavage of the C_α–C_β bonds in all three amino acids, giving rise to a singly charged product ion corresponding to the mass of the amino acid's side chain. The other major product in these fs-LID spectra is a doubly charged product ion that has lost neutral CO_2 from the carboxylic acid end of the molecule. Based on our observations, the aromatic amino acids are the most likely sites for radical formation when a peptide is subjected to fs-LID.

8.4.3 Acidic/Basic Amino Acids

Aspartic acid and glutamic acid show no ionization or dissociation into product ions via fs-LID, regardless of derivatization, which is consistent with their high ($\sim$ 10 eV) ionization energy. Histidine also gives rise to no fs-LID product ions, which is surprising given the low ($\sim$ 8 eV) estimated ionization energy of the neutral form. Most likely, protonation of the histidine side chain is interfering with the conjugated pi system of electrons, making them less polarizable and therefore less susceptible to strong field ionization.

Lysine and arginine show limited degrees of photoionization by fs-LID only after derivatization as an N-acetyl methyl ester and N-benzoyl derivative, respectively. Since the side chains of these residues are basic, they are probable sites of protonation, leaving few lone pair electrons susceptible to photoionization. Overall, the acidic and basic amino acids are unlikely origins for radical formation.

8.4.4 Polar Amino Acids

Glycine does not photoionize in any form, which is not surprising given that the hydrogen atom side chain does not enhance the polarizability of the amino acid backbone. More surprisingly, glutamine and its derivatives showed no fs-LID product ions, while asparagine gave rise to a small signal as an N-benzoyl derivative, as did serine and threonine. While the interaction of the benzoyl group with the backbone of each amino acid and the resulting stereochemistry are unique, the aromatic group does increase the polarizability of some of these previously inactive polar amino acids to the point that fs-LID signal can be observed. The bulky benzoyl group did not improve the amenability of cystine or cysteine to fs-LID, but a simple lengthening of the backbone in the N-acetyl methyl ester forms was sufficient to observe limited photoionization.

8.4.5 Non-polar Amino Acids

The susceptibility to fs-LID of the non-polar amino acids was found to increase with size and therefore polarizability. Alanine and valine were completely inactive,

while leucine, isoleucine, and proline could be photoionized upon derivatization (see Table 8.1). Methionine is the exception in this category—the S heteroatom in the side chain significantly lowers the ionization energy and accordingly, the activated sample gives rise to strong fs-LID product ions in all protonated and derivatized forms.

The fs-LID MS/MS analysis of single amino acids allowed us to elucidate the most likely origin of the $[M + H]^{2+\bullet}$ ion-radical pair. Methioinine and the aromatic residues are the most amenable to photoionization. Extending to slightly larger molecular systems, the fs-LID product ion signal seems to track with ionization potential or polarizability. Utilizing the benzoyl group as a chromophore was one successful method for generating fs-LID product ions from previously inactive samples. However, this sort of wet chemistry is unnecessary if the analyte is sufficiently large. The N-acetyl methyl ester derivatives were studied to mimic the lengthening of the backbone in a longer peptide or protein, and this modification also led to the observation of fs-LID product ions from previously inactive amino acids. Our conclusion is that longer peptides will be largely amenable to interrogation by fs-LID regardless of their sequence, without the need for any derivatization prior to MS/MS analysis.

8.4.6 Protein Sequencing

In proteomic MS/MS, the greater the number of assignable product ions observed, the more information-rich the spectrum can be considered. Peptide sequencing can be done manually or with the aid of software, whereby pairs of peaks that differ by the mass of a single amino acid are used to map out the identity and order of residues in the precursor sequence. If a specific region of the peptide does not fragment well, the exact sequence in that cannot be assigned. While some of the product ions corresponding to backbone cleavages may be redundant (in that we observe multiple cleavages between the same pair of residues), they increase our confidence in the ultimate sequence assignment. Therefore, it is advantageous to find an ion activation method that yields a greater variety of product ions, rather than simply a high intensity of product ions.

The robustness of fs-LID as an ion activation method is confirmed by the fs-LID spectrum of the peptide GAILAGAILA, which contains no aromatic or methionine residues (Fig. 8.15). The polarizability of the large molecule is sufficient for photoionization and gives rise to sufficient product ions for nearly 100 % sequence coverage. The most abundant product ions are the $-56^{2+\bullet}$ (side chain loss from Leu or Ile) and a nearly complete series of b-ions, limited only by the low mass cutoff (LMCO) associated with isolation of the precursor at 869.4 Da.

A single residue substitution at the C-terminal end of the peptide from alanine to arginine leads to a ∼7 % increase in dissociation efficiency by fs-LID (see Table 8.2) and also gives rise to more abundant a-ions near the C-terminal end of the

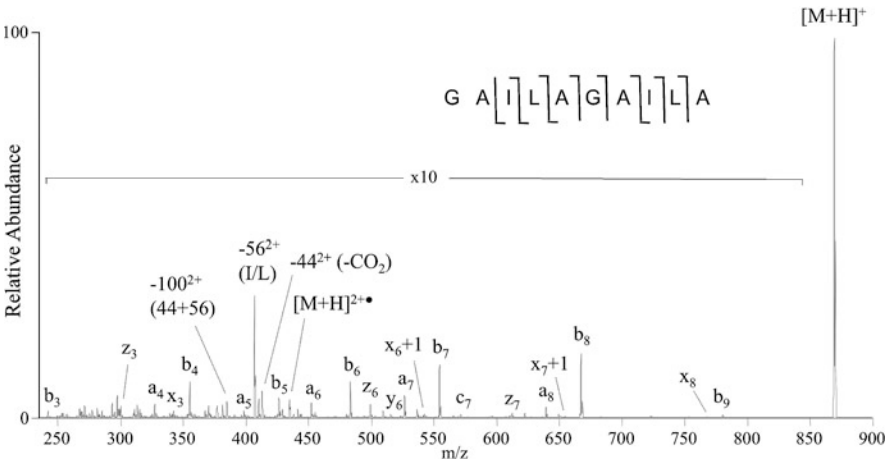

Fig. 8.15 [5] Fs-LID MS/MS spectrum for GAILAGAILA

Table 8.2 [5] Observed fs-LID dissociation efficiencies for a series of 12 synthetic peptides with sequence GAIL(X1)GAIL(X2). Efficiencies were calculated from the ratio of precursor ion abundances (normalized by the total ion current) in isolation and fs-LID spectra for each sample. Spectra for the three shaded samples can be found in Figs. 8.15–8.17

X1/**X2**	A	C	D	M
A	18.4 %	22.0 %	22.7 %	23.1 %
K	22.6 %	23.7 %	29.8 %	31.4 %
R	25.8 %	30.9 %	33.5 %	39.8 %

GAILAGAILR peptide (Fig. 8.16). This suggests that photoionization of the precursor occurs predominantly at the arginine residue. The -72^{2+} product ion corresponds to partial loss of the arginine side chain as a radical following cleavage of the C_β–C_γ bond while the rest of the peptide remains intact. Another notable feature in the fs-LID spectrum is the presence of satellite ions v_3, w_{b3}, w_{a7}, v_8, and w_{a8}, which can be used to differentiate between Ile and Leu residues when sequencing the peptide.

Alternatively, we can seed a likely origin for the radical into the peptide with a single residue substitution that places a methionine residue in the 5th position. This dramatically increases the fs-LID dissociation efficiency to nearly 40 % as shown in Table 8.2. This was expected given the fs-LID activity of protonated methionine observed earlier. Note that the fs-LID spectrum of GAILMGAILR (Fig. 8.17) has a base peak of $[M+H]^{2+\bullet}$ due to the stability of the radical formed at the methionine residue. This stability detracts slightly from the abundance of sequence ions, but also gives rise to strong side chain losses from methionine, -61^{2+} and $-74^{2+\bullet}$, that can be used as diagnostic indicators of methionine in unknown peptide or protein samples.

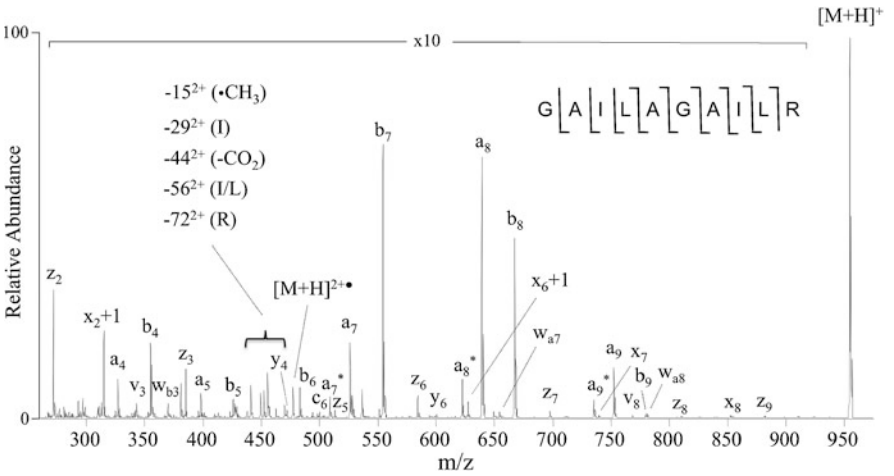

Fig. 8.16 [5] Fs-LID MS/MS spectrum for GAILAGAILR

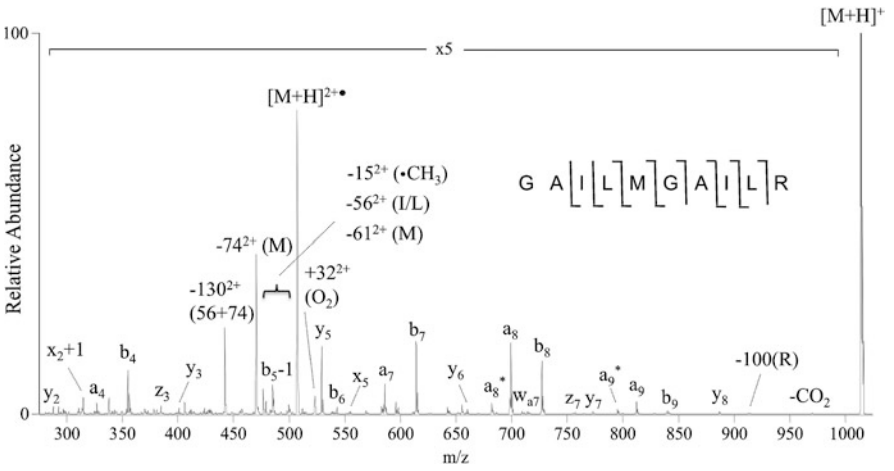

Fig. 8.17 [5] Fs-LID MS/MS spectrum for GAILMGAILR

The diagnostic side chain losses observed in fs-LID spectra of 12 synthetic peptides have been tabulated in Table 8.3 and are consistent with those reported in the literature [77, 78, 95]. Note that the neutral loss of even-electron species leaves a radical on the doubly charged peptide backbone, and can give rise to sequence ions, meaning that many of the side chain losses observed in fs-LID are intermediate rather than "dead-end" product ions. This opens the door for sequential dissociation, and also provides radical intermediates that can be isolated and subjected to MS^3 (or MS^n) for further analysis when present in sufficient abundance. The side chain losses from I, L, M, and R can be seen in the fs-LID spectra as noted in Figs. 8.15–8.17.

Table 8.3 [5] Observed fs-LID side chain losses from residues in the GAIL(X1)GAIL(X2) series

Residue	Mass of side chain loss (Da)	Chemical Formula
C	33	SH
D	44	CO_2
I	29, 56 (see Figs. 8.15–8.17)	$^{\bullet}C_2H_5$, C_4H_8
K	72	$^{\bullet}C_4H_{10}N$
L	43, 56 (see Figs. 8.15–8.17)	$^{\bullet}C_3H_7$, C_4H_8
M	61, 74 (see Figs. 8.17)	$^{\bullet}C_2H_5S$, C_3H_6S
R	72, 100 (see Figs. 8.16–8.17)	$^{\bullet}C_2H_6N_3$, $C_4H_{10}N_3^+$

The fs-LID dissociation efficiencies for the three peptide samples discussed above are combined with those of nine similar samples in Table 8.2. The peptide sequence is GAIL(X1)GAIL(X2) where X1 = alanine (A), cysteine (C), aspartic acid (D), or methionine (M) and X2 = alanine (A), lysine (K), or arginine (R). A two-way ANOVA test revealed that both the X1 effect and the X2 effect are statistically significant ($p = 0.0129$ and 0.0016, respectively). As the X1 residue changes from A to C to D to M, the polarizability of the peptide increases. As X2 changes from A to K to R, the proton mobility of the peptide decreases. Polarizability and proton mobility are not completely independent nor easily quantifiable for these samples, so the interaction effects cannot be analyzed.

In general, if the peptide being analyzed contains one or more F, M, W, or Y residues, we expect to see the photoionized $[M + H]^{2+\bullet}$ product as the base peak in the fs-LID MS/MS spectrum. In most other samples analyzed, products arising from side chain losses or sequence ions of type a and b are the most abundant, and all spectra contained a, b, x, y, and z-type ions. C-type sequence ions are the only product ions we do not observe regularly when using fs-LID for ion activation of these peptides. We also see an increase in sequence ion abundances near residues like C, K, and R, which have moderate ionization energies and are potential sites for side chain losses.

8.4.7 Bond Cleavage Pathways

Stabilization of the radical formed by photoionization can occur through H^+ or $H^{\bullet}$ abstraction. If the hydrogen atom comes from a side chain, the result is either a side chain loss, or propagation of the radical along the peptide chain. $H^{\bullet}$ transfer to a carbonyl along the peptide backbone as well as proton-driven chemistry will occur at the same time to produce sequence ions. A possible mechanism for each case is outlined in Fig. 8.18, where the ILM portion of the GAILMGAILR peptide is shown after undergoing photoionization. The radical is shown at its most likely origin, the S atom of the methionine side chain. Pathway (a) illustrates a potential $H^{\bullet}$ transfer which leads to migration of the radical two side chains down the peptide backbone to the C_β atom on the isoleucine side chain. This intermediate would

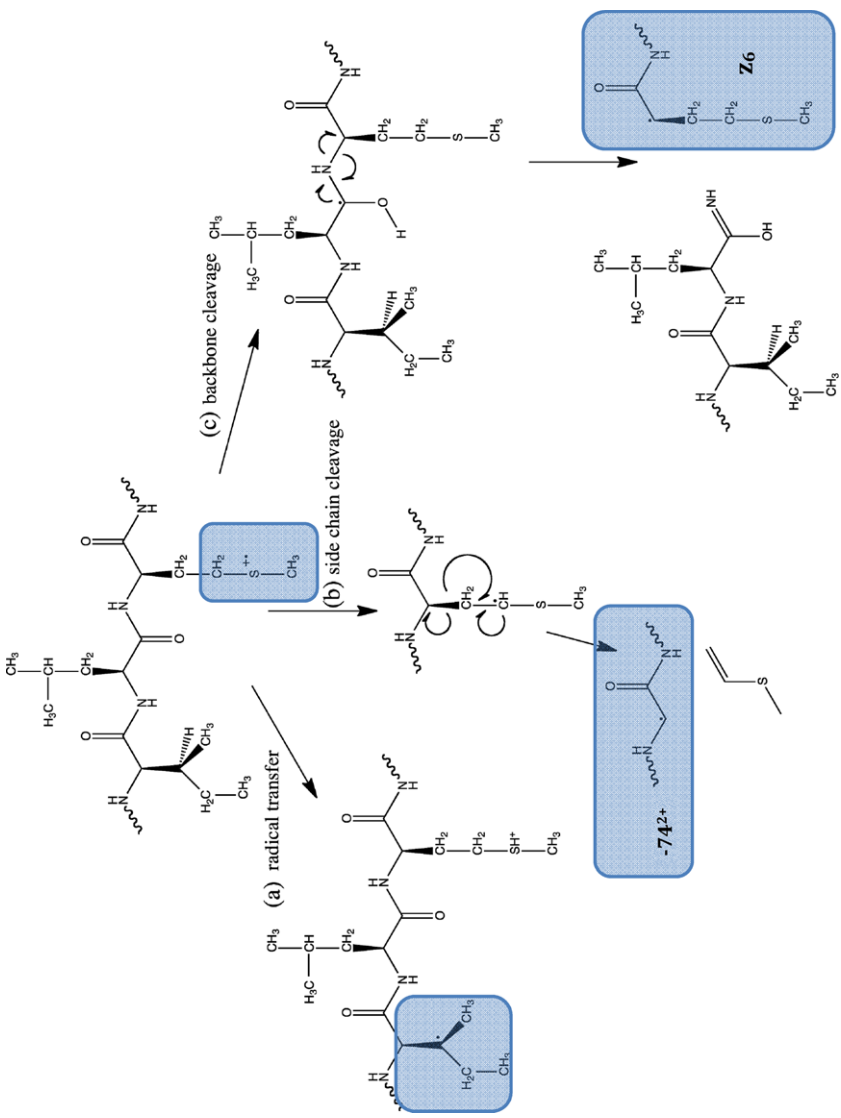

Fig. 8.18 [5] In the gas phase, the distonic species can dissociate via a number of pathways. The mechanisms shown here are meant to illustrate the variety of product ions that can form

then contribute to the -56^{2+} product ion abundance observed in Fig. 8.17. Pathway (b) follows the radical-directed cleavage of the C_α–C_β bond in the methionine side chain, resulting in the neutral loss of 74 Da, corresponding to the -74^{2+} product ion peak in Fig. 8.17. Finally, Pathway (c) illustrates one possible outcome of the radical migrating away from the methionine side-chain. The ion can now undergo a radical-directed backbone cleavage of the N–C_α bond in the peptide, resulting in c and/or z-type ions. Note that this mechanism is non-specific and could occur at various points along the peptide, giving rise to the z_3 and z_7 ions observed in Fig. 8.17. The mechanism is shown at the methionine residue here only for simplicity, in reality the resulting z_6 ion is a minor product ion and is not labeled in Fig. 8.17.

8.5 Discussion and Future Outlook

The ease with which femtosecond lasers are able to cause tunnel ionization in large isolated molecules and ions has led to the development of tools that have application in analytical chemistry. Already, fs-LID has been shown to generate information-rich MS/MS spectra. Through the analysis of protonated amino acids, we have identified the aromatic amino acids and methionine as the most likely sites of radical formation upon tunnel ionization, and have determined that ionization energy is not the sole predictor of sample amenability to fs-LID. As the fs-LID MS/MS spectra of the peptides illustrate, high polarizability and low proton mobility can boost fs-LID dissociation efficiency up above 35 %, even in samples with no aromatic chromophore to enhance ion activation. This makes fs-LID an attractive ion activation technique because it requires no chromophore or sample derivatization prior to MS/MS analysis. While a VUV laser can be used to efficiently photodissociate peptides due to the absorption maximum of peptide bonds around 190 nm [96], a femtosecond laser can activate any class of molecules via tunneling ionization, independent of their absorption spectra.

Another benefit of using femtosecond laser pulses is their ability to open several non-ergodic dissociation pathways, wherein stronger bonds are broken and more labile bonds remain intact. This observation has lead to a number of fundamental studies, and is a major attraction as an analytical tool. In particular, non-ergodic dissociation is valuable for the analysis of post-translational modification. There is an alternative method for inducing this type of gas phase radical known as electron capture or electron transfer dissociation (ECD/ETD), which reduces multiply charged gas phase ions to form hydrogen-abundant radical cations ($[M + 2H]^{2+} \rightarrow [M + 2H]^{+\bullet}$). By comparison, fs-LID intermediates are hydrogen-deficient ($[M + H]^{+} \rightarrow [M + H]^{2+\bullet}$), and therefore the technique does not need a multiply charged precursor to carry out ion activation in positive ion mode. This makes fs-LID appropriate for pairing with laser desorption sources such as MALDI, as the soft ionization method is known to generate singly protonated ions. Preliminary studies in negative ion mode using fs-LID have also shown promising results and higher product ion yields, indicating that fs-LID may one day be appropriate for high throughput proteomic and metabolomic studies.

In conclusion, fundamental studies on the strong-field interaction between femtosecond lasers and large organic molecules has resulted in important analytical tools that may one day advance diverse fields such as drug discovery and medical diagnosis.

Acknowledgements The instrument used for the fs-LID work was funded by grant 156 of the 21st Century Jobs Trust Fund of the SEIC Board from the State of Michigan. Additional support comes from grant CRIF ID 0923957 from the National Science Foundation. The results presented here would not be available without the work of very talented colleagues. We specifically thank Professors Gavin E. Reid and A. Daniel Jones who collaborated in the initial development of the fs-LID method. We are also thankful for the careful and persistent work on the effects of pulse shaping on molecular fragmentation by Xin Zhu, and the analysis and suggestion of multiple experiments by Dr. Vadim V. Lozovoy,

References

1. J.H. Posthumus, Rep. Prog. Phys. **67**, 623 (2004)
2. V.V. Lozovoy, X. Zhu, T.C. Gunaratne, D.A. Harris, J.C. Shane, M. Dantus, J. Phys. Chem. A **112**, 3789 (2008)
3. S.M. Hankin, D.M. Villeneuve, P.B. Corkum, D.M. Rayner, Phys. Rev. A **64** (2001)
4. C. Uiterwaal, C.R. Gebhardt, H. Schroder, K.L. Kompa, Eur. Phys. J. D **30**, 379 (2004)
5. C.L. Kalcic, G.E. Reid, V.V. Lozovoy, M. Dantus, J. Phys. Chem. A (2011)
6. E. Mevel, P. Breger, R. Trainham, G. Petite, P. Agostini, A. Migus, J.P. Chambaret, A. Antonetti, Phys. Rev. Lett. **70**, 406 (1993)
7. R.J. Levis, M.J. DeWitt, J. Phys. Chem. A **103**, 6493 (1999)
8. J.B. Fenn, M. Mann, C.K. Meng, S.F. Wong, C.M. Whitehouse, Science **246**, 64 (1989)
9. F. Hillenkamp, M. Karas, R.C. Beavis, B.T. Chait, Anal. Chem. **63**, A1193 (1991)
10. J.R. Yates, J. Mass Spectrom. **33**, 1 (1998)
11. L. Sleno, D.A. Volmer, J. Mass Spectrom. **39**, 1091 (2004)
12. V.H. Wysocki, K.A. Resing, Q.F. Zhang, G.L. Cheng, Methods **35**, 211 (2005)
13. A.H. Zewail, Phys. Today **33**, 27 (1980)
14. M. Dantus, M.J. Rosker, A.H. Zewail, J. Chem. Phys. **87**, 2395 (1987)
15. D.J. Tannor, S.A. Rice, J. Chem. Phys. **83**, 5013 (1985)
16. P. Brumer, M. Shapiro, Chem. Phys. Lett. **126**, 541 (1986)
17. D.J. Tannor, R. Kosloff, S.A. Rice, J. Chem. Phys. **85**, 5805 (1986)
18. J.L. Krause, R.M. Whitnell, K.R. Wilson, Y.J. Yan, S. Mukamel, J. Chem. Phys. **99**, 6562 (1993)
19. I. Pastirk, E.J. Brown, Q.G. Zhang, M. Dantus, J. Chem. Phys. **108**, 4375 (1998)
20. T. Brixner, G. Gerber, ChemPhysChem **4**, 418 (2003)
21. M. Dantus, V.V. Lozovoy, Chem. Rev. **104**, 1813 (2004)
22. A. Assion, T. Baumert, M. Bergt, T. Brixner, B. Kiefer, V. Seyfried, M. Strehle, G. Gerber, Science **282**, 919 (1998)
23. M. Bergt, T. Brixner, B. Kiefer, M. Strehle, G. Gerber, J. Phys. Chem. A **103**, 10381 (1999)
24. T. Brixner, B. Kiefer, G. Gerber, Chem. Phys. **267**, 241 (2001)
25. M. Bergt, T. Brixner, C. Dietl, B. Kiefer, G. Gerber, J. Organomet. Chem. **661**, 199 (2002)
26. T. Brixner, N.H. Damrauer, G. Krampert, P. Niklaus, G. Gerber, J. Mod. Opt. **50**, 539 (2003)
27. R.J. Levis, G.M. Menkir, H. Rabitz, Science **292**, 709 (2001)
28. R.J. Levis, H.A. Rabitz, J. Phys. Chem. A **106**, 6427 (2002)
29. P. Graham, G. Menkir, R.J. Levis, Spectrochim. Acta, Part B, At. Spectrosc. **58**, 1097 (2003)
30. C. Daniel, J. Full, L. Gonzalez, C. Kaposta, M. Krenz, C. Lupulescu, J. Manz, S. Minemoto, M. Oppel, P. Rosendo-Francisco, S. Vajda, L. Woste, Chem. Phys. **267**, 247 (2001)

31. C. Daniel, J. Full, L. Gonzalez, C. Lupulescu, J. Manz, A. Merli, S. Vajda, L. Woste, Science **299**, 536 (2003)
32. D. Cardoza, F. Langhojer, C. Trallero-Herrero, O.L.A. Monti, T. Weinacht, Phys. Rev. A **70** (2004)
33. F. Langhojer, D. Cardoza, M. Baertschy, T. Weinacht, J. Chem. Phys. **122** (2005)
34. D. Cardoza, M. Baertschy, T. Weinacht, J. Chem. Phys. **123** (2005)
35. D. Cardoza, C. Trallero-Herrero, F. Langhojer, H. Rabitz, T. Weinacht, J. Chem. Phys. **122** (2005)
36. D. Cardoza, B.J. Pearson, M. Baertschy, T. Weinacht, J. Photochem. Photobiol. A, Chem. **180**, 277 (2006)
37. D. Cardoza, M. Baertschy, T. Weinacht, Chem. Phys. Lett. **411**, 311 (2005)
38. E. Wells, K.J. Betsch, C.W.S. Conover, M.J. DeWitt, D. Pinkham, R.R. Jones, Phys. Rev. A **72** (2005)
39. R.S. Judson, H. Rabitz, Phys. Rev. Lett. **68**, 1500 (1992)
40. M. Wollenhaupt, A. Prakelt, C. Sarpe-Tudoran, D. Liese, T. Baumert, J. Opt. B, Quantum Semiclass. Opt. **7**, S270 (2005)
41. B.J. Sussman, D. Townsend, M.Y. Ivanov, A. Stolow, Science **314**, 278 (2006)
42. I. Pastirk, M. Kangas, M. Dantus, J. Phys. Chem. A **109**, 2413 (2005)
43. J.C. Shane, V.V. Lozovoy, M. Dantus, J. Phys. Chem. A **110**, 11388 (2006)
44. V.V. Lozovoy, M. Dantus, ChemPhysChem, **6**, 1970 (2005)
45. V.V. Lozovoy, T.C. Gunaratne, J.C. Shane, M. Dantus, ChemPhysChem **7**, 2471 (2006)
46. V.V. Lozovoy, M. Dantus, Annu. Rep. Prog. Chem., Sect. C, Phys. Chem. **102** (2006)
47. V.V. Lozovoy, I. Pastirk, M. Dantus, Opt. Lett. **29**, 775 (2004)
48. Y. Coello, V.V. Lozovoy, T.C. Gunaratne, B.W. Xu, I. Borukhovich, C.H. Tseng, T. Weinacht, M. Dantus, J. Opt. Soc. Am. B, Opt. Phys. **25**, A140 (2008)
49. C.L. Kalcic, T.C. Gunaratne, A.D. Jones, M. Dantus, G.E. Reid, J. Am. Chem. Soc. **131**, 940 (2009)
50. B.A. Budnik, Y.O. Tsybin, P. Hakansson, R.A. Zubarev, J. Mass Spectrom. **37**, 1141 (2002)
51. S.A. Smith, C.L. Kalcic, K.A. Safran, P.M. Stemmer, M. Dantus, G.E. Reid, J. Am. Soc. Mass Spectrom. **21**, 2031 (2010)
52. S.A. Smith, C.L. Kalcic, M. Dantus, G.E. Reid, Phospholipid analysis by femtosecond laser-induced ionization/dissociation mass spectrometry (fs-LID MS), in *57th ASMS Conference* (2009)
53. N.S. Winkler, C.L. Kalcic, A.D. Jones, M. Dantus, Study of metabolites including alpha-tomatine by femtosecond laser-induced ionization/dissociation (fs-LID), in *57th ASMS Conference* (2009)
54. X. Zhu, C.L. Kalcic, N. Winkler, V.V. Lozovoy, M. Dantus, J. Phys. Chem. A **114**, 10380 (2010)
55. A.R. Dongre, J.L. Jones, A. Somogyi, V.H. Wysocki, J. Am. Chem. Soc. **118**, 8365 (1996)
56. E.A. Kapp, F. Schütz, G.E. Reid, J.S. Eddes, R.L. Moritz, R.A. O'Hair, T.P. Speed, R.J. Simpson, J. Anal. Chem. **75**, 6251 (2003)
57. V.H. Wysocki, G. Tsaprailis, L.L. Smith, L.A. Breci, J. Mass Spectrom. **35**, 1399 (2000)
58. D. Pu, N.L. Clipston, C.J. Cassady, J. Mass Spectrom. **45**, 297 (2010)
59. J.J. Gorman, T.P. Wallis, J.J. Pitt, Mass Spectrom. Rev. **21**, 183 (2002)
60. A.M. Palumbo, J.J. Tepe, G.E. Reid, J. Proteome Res. **7**, 771 (2008)
61. A.M. Palumbo, G.E. Reid, Anal. Chem. **80**, 9735 (2008)
62. R.A. Zubarev, D.M. Horn, E.K. Fridriksson, N.L. Kelleher, N.A. Kruger, M.A. Lewis, B.K. Carpenter, F.W. McLafferty, Anal. Chem. **72**, 563 (2000)
63. L.M. Mikesh, B. Ueberheide, A. Chi, J.J. Coon, J.E.P. Syka, J. Shabanowitz, D.F. Hunt, Biochim. Biophys. Acta, Proteins Proteomics **1764**, 1811 (2006)
64. J. Wiesner, T. Premsler, A. Sickmann, Proteomics **8**, 4466 (2008)
65. J.J. Wilson, J.S. Brodbelt, Anal. Chem. **79**, 7883 (2007)
66. J.J. Wilson, G.J. Kirkovits, J.L. Sessler, J.S. Brodbelt, J. Am. Soc. Mass Spectrom. **19**, 257 (2008)

67. L. Joly, R. Antoine, M. Broyer, P. Dugourd, J. Lemoine, J. Mass Spectrom. **42**, 818 (2007)
68. S.H. Yoon, Y.J. Chung, M.S. Kim, J. Am. Soc. Mass Spectrom. **19**, 645 (2008)
69. M. Perot, B. Lucas, M. Barat, J.A. Fayeton, C. Jouvet, J. Phys. Chem. A **114**, 3147 (2010)
70. T.Y. Kim, J.P. Reilly, J. Am. Soc. Mass Spectrom. **20**, 2334 (2009)
71. R. Parthasarathi, Y. He, J.P. Reilly, K. Raghavachari, J. Am. Chem. Soc. **132**, 1606 (2010)
72. J.A. Madsen, D.R. Boutz, J.S. Brodbelt, J. Proteome Res. **9**, 4205 (2010)
73. J.A. Madsen, T.S. Kaoud, K.N. Dalby, J.S. Brodbelt, Proteomics **11**, 1329 (2011)
74. W.D. Cui, M.S. Thompson, J.P. Reilly, J. Am. Soc. Mass Spectrom. **16**, 1384 (2005)
75. J.P. Reilly, Mass Spectrom. Rev. **28**, 425 (2009)
76. B.N. Moore, S.J. Blanksby, R.R. Julian, Chem. Commun. **5015** (2009)
77. Q.Y. Sun, H. Nelson, T. Ly, B.M. Stoltz, R.R. Julian, J. Proteome Res. **8**, 958 (2009)
78. M.M. Savitski, M.L. Nielsen, R.A. Zubarev, Anal. Chem. **79**, 2296 (2007)
79. W.H. Renninger, A. Chong, F.W. Wise, Phys. Rev. A **82** (2010)
80. B. Nie, D. Pestov, F.W. Wise, M. Dantus, Opt. Express **19**, 12074 (2011)
81. W.J. Jia, K.W.D. Ledingham, C.T.J. Scott, C. Kosmidis, R.P. Singhal, Rapid Commun. Mass Spectrom. **10**, 1597 (1996)
82. T. Laarmann, I. Shchatsinin, P. Singh, N. Zhavoronkov, M. Gerhards, C.P. Schulz, I.V. Hertel, J. Chem. Phys. **127** (2007)
83. L. Guyon, T. Tabarin, B. Thuillier, R. Antoine, M. Broyer, V. Boutou, J.P. Wolf, P. Dugourd, J. Chem. Phys. **128** (2008)
84. H. Kang, C. Jouvet, C. Dedonder-Lardeux, S. Martrenchard, G. Gregoire, C. Desfrancois, J.P. Schermann, M. Barat, J.A. Fayeton, Phys. Chem. Chem. Phys. **7**, 394 (2005)
85. G. Gregoire, H. Kang, C. Dedonder-Lardeux, C. Jouvet, C. Desfrancois, D. Onidas, V. Lepere, J.A. Fayeton, Phys. Chem. Chem. Phys. **8**, 122 (2006)
86. T. Ergler, A. Rudenko, B. Feuerstein, K. Zrost, C.D. Schroter, R. Moshammer, J. Ullrich, Phys. Rev. Lett. **97** (2006)
87. W.A. Bryan, J. McKenna, E.M.L. English, J. Wood, C.R. Calvert, R. Torres, D.S. Murphy, I.C.E. Turcu, J.L. Collier, J.F. McCann, I.D. Williams, W.R. Newell, Phys. Rev. A **76** (2007)
88. S. De, M. Magrakvelidze, I.A. Bocharova, D. Ray, W. Cao, I. Znakovskaya, H. Li, Z. Wang, G. Laurent, U. Thumm, M.F. Kling, I.V. Litvinyuk, I. Ben-Itzhak, C.L. Cocke, Phys. Rev. A **84** (2011)
89. X. Zhu, V.V. Lozovoy, J.D. Shah, M. Dantus, J. Phys. Chem. A **115**, 1305 (2011)
90. S.M. Hankin, D.M. Villeneuve, P.B. Corkum, D.M. Rayner, Phys. Rev. Lett. **84**, 5082 (2000)
91. D.B. Galloway, J.A. Bartz, L.G. Huey, F.F. Crim, J. Chem. Phys. **98**, 2107 (1993)
92. P. Lablanquie, K. Ohashi, N. Nishi, J. Chem. Phys. **98**, 399 (1993)
93. N.N. Dookeran, T. Yalcin, A.G. Harrison, J. Mass Spectrom. **31**, 500 (1996)
94. D. Dehareng, G. Dive, Int. J. Mol. Sci. **5**, 301 (2004)
95. J. Laskin, Z.B. Yang, C.M.D. Ng, I.K. Chu, J. Am. Soc. Mass Spectrom. **21**, 511 (2010)
96. A.R. Goldfarb, L.J. Saidel, E. Mosovich, J. Biol. Chem. **193**, 397 (1951)

Chapter 9
On the Investigation of Excited State Dynamics with (Pump-)Degenerate Four Wave Mixing

Tiago Buckup, Jan P. Kraack, Marie S. Marek, and Marcus Motzkus

Abstract Multidimensional time-resolved spectroscopy allows disentangling particular aspects of the molecular dynamics, which are normally hidden from linear techniques. In this chapter, we show how third- and fifth-order techniques using sub-20 fs pulses can be applied to address coherence and population dynamics in the excited states of biomolecules. In particular, broadband four wave mixing is combined with an initial pump pulse to promote population to the excited state. With this approach, it is possible to interrogate the potential surface of the excited and ground states during the excited state evolution with a time resolution better than 20 fs. Three general aspects of the excited state dynamics are discussed. (1) The assignment of vibrational coherence to the respective excited state potential is illustrated for retinal in solution and in the protein environment. By changing the excitation wavelength and comparing low- and high-frequency vibrational coherence content, it is shown that low-frequency modes are predominantly originated in the excited state, while high-frequency modes belong to the ground state. (2) The temporal resolution of dark electronic states in lycopene is investigated with pump-DFWM. Contrasting to lower-order techniques, pump-DFWM allows to snapshot the ultrafast population relaxation directly after the excitation of the S_2 electronic state. (3) The evolution of the vibrational coherence in the excited state is demonstrated for β-carotene. This gives accurate information on the instantaneous frequency, populations and even anharmonicities of all relevant vibrational modes on the potential surface of the excited state.

9.1 Introduction

The evolution of photochemical transformations has been in the focal point of ultrafast time-resolved spectroscopy since its advent [1–6]. In this regard, the ability to follow the population and coherence dynamics in the femtosecond time scale

T. Buckup · J.P. Kraack · M.S. Marek · M. Motzkus (✉)
Physikalisch-Chemisches Institut, Universität Heidelberg, Im Neuenheimer Feld 229, 69120 Heidelberg, Germany
e-mail: marcus.motzkus@pci.uni-heidelberg.de

R. de Nalda, L. Bañares (eds.), *Ultrafast Phenomena in Molecular Sciences*, Springer Series in Chemical Physics 107, DOI 10.1007/978-3-319-02051-8_9,

with high resolution, particularly in excited states, is a major pre-requisite to fully understand how structural changes in (bio-)chromophores take place [7–10].

Time-resolved spectroscopy of excited potential surfaces is, though, more challenging than the ground state spectroscopy due to two major aspects. The first one is the number of excited molecules contributing to the signal. Under normal excitation regimes (i.e. well below saturation), the number of excited molecules is much smaller than the number of molecules in the ground state. Contributions from the excited state may therefore be weak and difficult to detect. This can be specially complicated in (self-)heterodyne detection methods if ground and excited state contributions spectrally overlap. In methods using such kind of detection, the intensities of different contributions add linearly, which can obscure, or even totally cancel, weak signals. Such an effect can be observed e.g. in transient absorption (TA) when a negative signal like stimulated emission (SE) overlaps with an excited state absorption (ESA). This contrasts to background-free third-order methods, where all contributions will be detected with a much higher sensitivity to small variations of the dynamics in the excited state.

The second aspect is related to the time scale of processes in the excited state. After excitation, population and coherence in the higher electronic states are not in equilibrium but evolve in many (bio-)chromophores often on a very fast time scale. Such time scales range from hundreds of femtoseconds as found for the isomerization of protein-bound retinal [11] to just some tens of femtoseconds as observed for the internal conversion between excited states of carotenoids [12]. While ultrafast transient population evolution can in principle be resolved by using state-of-the-art sub-10 fs pulses [13], following the evolution of the vibrational coherence is not trivial. Not just the amplitude of oscillatory phenomena contains information on the deactivation of the excited state, but also the frequency and the phase may offer important insight. Nevertheless, determination of frequency and phase during an ultrafast relaxation process is demanding, which has received a lot of attention recently. It requires accurate analysis in order to avoid phase and frequency changes due to pure analysis artifacts [14, 15].

One way of addressing these central aspects in time-resolved spectroscopy is to increase the dimensionality of the nonlinear optical interaction. Multidimensional time-resolved spectroscopy employs additional ultrashort pulses in order to open a new spectral and/or temporal observation window, which is normally hidden from lower-order techniques [16]. For example, this allows probing a specific molecular response without the need of complex fitting algorithms or assumptions [17, 18]. In this chapter, we show how four wave mixing methods with three beams like coherent anti-Stokes Raman scattering (CARS) and transient grating (TG) can be combined with an additional initial pump beam to be selective to excited state dynamics in the condensed phase (Fig. 9.1). The so called pump-degenerate four wave mixing (pump-DFWM) technique [19, 20] consists of two interactions with the initial pump pulse to produce coherences and populations in the excited state, which will be probed by the consecutive four wave mixing sequence. In this sense, pump-DFWM can be thought of as a “pump-probe” method, where the probe is not a single pulse, but is a nonlinear probe sequence of three ultrashort pulses. Due to their bandwidths,

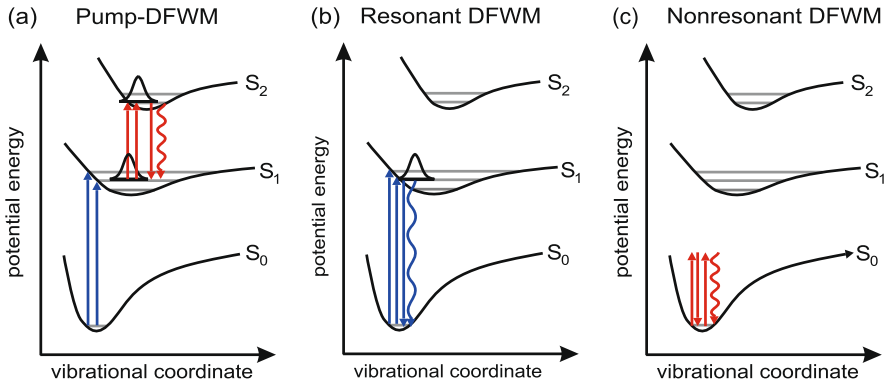

Fig. 9.1 Interaction scheme of (**a**) pump-DFWM, (**b**) electronically resonant DFWM and (**c**) non-resonant DFWM. In pump-DFWM (**a**), the excited potential can be exclusively investigated by pre-exciting the ground state population with the initial pump. This is not the case when using DFWM only: Resonant DFWM (**b**) excites and probes dynamics in both potential surfaces, i.e., excited and ground state dynamics

the pulses of the DFWM sequence generate both CARS (and its Stokes counterpart CSRS) and TG contributions.

Three fundamental aspects of the excited state dynamics found in several molecular systems are discussed using such nonlinear experiments. Firstly, the assignment of vibrational coherence to the respective electronic states is shown in the case of Retinal Protonated Schiff Base (RPSB) using DFWM (Fig. 9.1(b) and (c)) with sub-20 fs time resolution (Sect. 9.3.1). Tuning the excitation spectrum of the DFWM sequence is exploited with its high sensitivity to disentangle the origin of low- (<800 cm^{-1}) and high-frequency (>800 cm^{-1}) molecular modes. The second aspect is the detection of short-living dark electronic states, whose excitation via one-photon is forbidden. In Sect. 9.3.2, pump-DFWM (Fig. 9.1(a)) is applied to lycopene in order to unravel the presence of additional electronic states after the relaxation of the S_2 state. The focus is the unique capability of pump-DFWM to detect additional relaxation pathways due to its higher dimensionality. The experimental results are further supported by a simulation in the response function formalism. In the last experimental Sect. 9.3.3, vibrational coherences in a vibrationally excited electronic state are addressed with pump-DFWM. In particular the vibrational evolution of high-frequency modes are resolved with a high time and spectral resolution. This is demonstrated for β-carotene during the internal conversion between S_2 and S_1.

9.2 Pump-Degenerate Four Wave Mixing

9.2.1 Signal Generation

Pump-DFWM is an ultrafast technique able to obtain the complete vibrational spectra as well as electronic population and coherence relaxation in excited state poten-

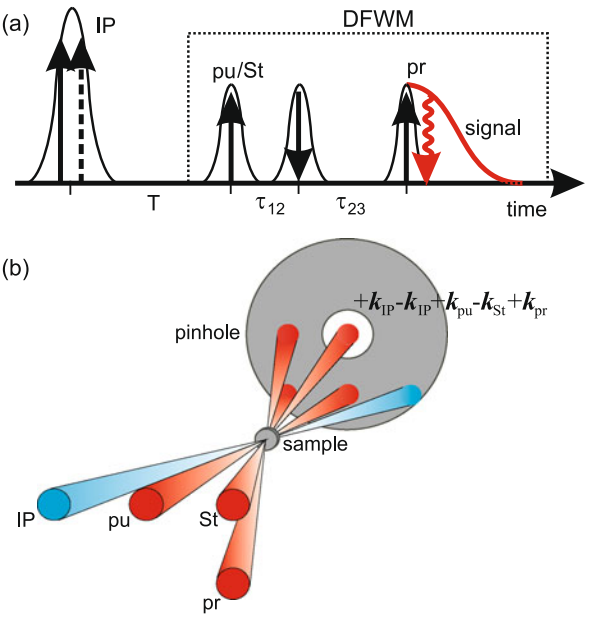

Fig. 9.2 (**a**) Scheme showing the respective delays between all beams. (**b**) Extended folded BOXCARS phase-matching scheme used in the (pump-)DFWM experiment

tials [21, 22]. The excitation with the initial pump (Fig. 9.2(a)) generates population and vibrational coherence in the excited state, which will be probed by the nonlinear interactions with the DFWM sequence. Several delay times between the excitation pulses can be defined (Fig. 9.2(a)). The first one is the delay T between the initial pump pulse and the DFWM sequence. During this delay, population as well as vibrational coherence induced by the initial pump will relax. The second time interval is the delay τ_{12} between the pump pulse and Stokes of the DFWM. During this time, as in pure DFWM, the electronic coherence between the participating states will evolve. This has been exploited by us to distinguish normal molecular modes from polarization beating [23]. The last time interval is the delay τ_{23} between the pump/Stokes and probe pulses of the DFWM sequence.

The higher dimensionality of pump-DFWM allows to follow the molecular dynamics in the excited PES with unprecedented time and spectral resolution (see also Sect. 9.2.2). The transient dynamics triggered by the initial pump pulse is selected and probed by the DFWM sequence. Therefore, each DFWM transient obtained at a given delay T after the excitation contains detailed information on transient populations and coherences [24–26]. The DFWM signal can be separated into two components, an oscillatory part related to the vibrational coherence and a non-oscillatory part. The amplitude of the whole DFWM scales with the electronic population squared of the excited state while the decay of the DFWM non-oscillatory signal gives information on the electronic population relaxation. The oscillatory signal contains information about the vibrational coherence like dephasing times, vibrational frequencies and phases of involved molecular Raman modes. This allows to build a snapshot of the structural changes during the relaxation of the chromophore and a precise picture of chemical transformations even in complex biomolecules

(Fig. 9.3). Here it is interesting to understand the interplay between the time and spectral resolution [27]. Although the time resolution of such snapshots is a priori given by the delay T and the pulse durations (Fig. 9.2(a)), the measurement of each vibrational spectrum also modifies the time resolution. In order to measure a spectrum, a DFWM transient with a given length (delay τ_{23}) must be Fourier transformed. The longer the DFWM transient, the higher will be the spectral resolution, but at the same time, the lower will be the time resolution of the snapshot, and vice-versa. In other words, the interplay between spectral and time resolution in pump DFWM may be fine adjusted by the length of the transient measured during the delay τ_{23}.

9.2.2 Setup Description

In our setup [21, 22, 28–31], the laser for the DFWM sequence is initially generated in a broadband noncollinear optical parametric amplifier (nc-OPA), which is pumped by a commercial femtosecond laser system (1 KHz, 300 μJ at 800 nm). After pulse compression in a prism compressor, typical pulse durations are about 11 and 15 fs depending on the central wavelength. After beam-splitting the nc-OPA output in three DFWM beams (pump, Stokes and probe beams), two delay stages are used to control the delay (Fig. 9.2(a)) between pump and Stokes (τ_{12}) and between Stokes and probe (τ_{23}). In general, the relative delay τ_{23} is scanned with a step length of about 2–3 fs in order to obtain enough data sampling for high-frequency modes. All three beams are focused using the same concave mirror ($f = 25$ cm) in a folded BOXCARS phase-matching geometry (Fig. 9.2(b)). Typical spot diameters are around 60–100 μm and the energies are 20 nJ for pump and Stokes and 15 nJ for the probe.

The combination of DFWM with an initial pump is straightforward. The IP pulse is generated in a second nc-OPA with similar pulse parameters as the DFWM nc-OPA. In such a way, the spectrum can be individually tuned from the DFWM's nc-OPA, which is an important requirement for the detection of excited electronic states (see Sect. 9.2.3). The delay T between the IP and the DFWM sequence is controlled by an additional delay stage. The IP beam is focused using an additional concave mirror in an extended folded BOXCARS phase-matching geometry. This allows controlling individually the spot size of the IP beam. Typical IP pulse energies used in pump-DFWM experiments depend on several parameters like spectral overlap between excitation and absorption spectra, which will be discussed below. In general, in order to achieve a high signal-to-noise-ratio (SNR), energies in the range between 30–80 nJ are used.

The detection of the (pump-)DFWM signal is performed using two photomultipliers at two different wavelengths. An interferometric filter with a FWHM of 10 nm is used in front of each detector. In order to avoid signal attenuation by using a 50 % beam splitter, the signal beam is split with high-pass filters into two beams. In this case, the low-frequency spectral region is reflected to one detector while the high-frequency spectral region is transmitted to the other detector. This always allows one

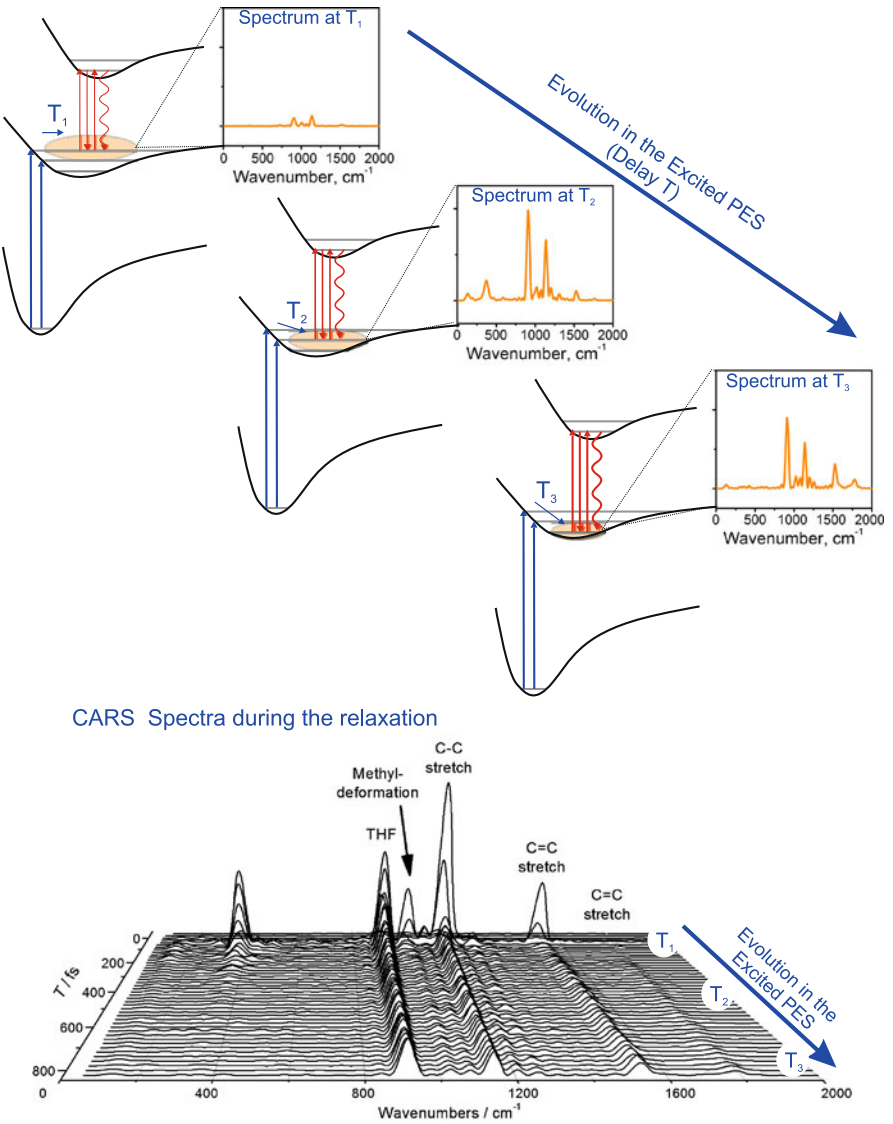

Fig. 9.3 Scheme of pump-DFWM in the excited potential surface and the generation of CARS (as well as CSRS) spectra during the relaxation. For each delay between the initial pump and the DFWM sequence (delay T), a DFWM transient is obtained by varying the delay τ_{23}. After Fourier transformation of each transient, snapshots of the vibrational spectra can be plotted during the relaxation on the excited potential surface

to measure two complementary wavelengths. The main drawback of this setup is that the signal amplitude at different detection wavelengths cannot be directly compared due to different detection parameters in each detector (e.g. photomultiplier amplifi-

cation, filter transmission, etc.). This can be easily overcome by spectrally resolving the signal in a spectrometer and detecting the signal with a CCD camera.

9.2.3 Role of Spectral Overlap

A central point in the investigation of excited state dynamics with (pump-)DFWM is the spectral overlap between excitation pulses and the molecular absorption. In this regard, there are two important aspects how DFWM and pump-DFWM can be tuned in order to separate different signal contributions.

The first aspect can be illustrated by a comparison between DFWM and transient absorption (TA). Both techniques are third-order time-resolved methods. DFWM, however, uses three beams and homodyne detection, while TA uses two beams and self-heterodyne detection by the probe beam. In principle, both methods are able to generate vibrational coherence: In DFWM, the first two pulses excite two or more different vibrational levels. Similarly, in transient absorption vibrational levels lying within the bandwidth of the pump pulse are excited. Except for these similarities, DFWM presents additional features not found for e.g. TA. One of these features is the possibility of efficient non-resonant excitation (Fig. 9.1(c)). DFWM can efficiently generate vibrational modes with non-resonant spectra in comparison to TA, which clearly contains only ground state modes. This can be contrasted to resonant (or even near-resonant) excitation, which potentially contains both excited and ground state modes. By comparing both signals, it is possible to assign modes to their electronic potential.

The second aspect is related to the detection of excited state dynamics without any interference of ground state contributions. The spectrum tuning of initial pump and DFWM allows detecting exclusively excited state dynamics. This is performed by making the initial pump spectrum resonant (or near-resonant if the molecular absorption is not perfectly within the nc-OPA wavelength range) which leads to the excitation of the excited state as well as ground state vibrational manifold. The suppression of ground state contributions is achieved by the correct tuning of the DFWM spectrum: It must be tuned to the excited state absorption (ESA) or stimulated emission (SE) spectral regions. If the ESA and SE do not overlap with the ground state absorption, this leads to a pure excited electronic state signal. This can be easily understood since the DFWM signal is nonresonant with the ground state absorption and the DFWM signal scales with the transition dipole moment μ^8. Non-resonant transition dipole moments are several orders of magnitude smaller than resonant transition dipole moments, generating resonant signals 10^6 stronger than non-resonant signals [32, 33].

For partially or totally overlapping ESA/SE and ground state absorption, the pump-DFWM will intrinsically have ground state contributions, which can be, however, strongly reduced by changing the energy relation of the initial pump and the DFWM sequence. Third order techniques with homodyne detection like DFWM signal provide two control knobs which are critical in this respect: The

signal depends (i) on the population difference squared between the involved states ($\Delta n^2 = (n_e - n_g)^2$) and (ii) on the intensity of each incoming beam ($I_{pu} I_{St} I_{pr} \sim I^3$). By decreasing the energy of the total DFWM sequence, the DFWM signal is automatically diminished. This overall decrease of the DFWM can be compensated by increasing the energy of the initial pump pulse, which also leads easily to a suppression of the ground state contributions. This can be easily understood since the population difference between the excited state and ground state diminishes.

9.3 Results and Discussion

In the following, three different applications will be presented. Firstly, pure DFWM is applied to RPSB in order to disentangle ground from excited state vibrational coherence. This first experiment is followed then by two experiments using pump DFWM applied to carotenoids, where the excited dynamics is exclusively investigated.

9.3.1 Assignment of Vibrational Coherence to Electronic States Using Pure DFWM

9.3.1.1 Introduction

Oscillations in the DFWM signal contains important information about vibrational coherence dynamics. In this context, a major issue of the signal analysis is the assignment of such modulations to specific electronic states of the sample molecule, since resonant excitation generates vibrational coherences in both ground as well as excited electronic states. In order to achieve this goal, spectral tuning of the excitation spectra together with spectral resolution of the signal light in DFWM experiments have previously been used for investigations on coherence dynamics in Bacteriorhodopsin (BR) and retinal protonated Schiff-bases (RPSB) [29, 30].

Particular interest resides in the characterization of wave packet dynamics in these samples because of the occurring photo-isomerization reactions which are important model reactions in terms of their biological relevance [3] as well as technical applications as photo-chemical switches [34]. The observed vibrational dynamics embrace a large energetic region ranging from around 100 cm^{-1} to more than 1500 cm^{-1}. High-frequency modes (> 800 cm^{-1}) reflect single- and double-bond stretching or substituent wagging motion where the vibrational frequency is dependent on the specific structure of the chromophore and its environment. Contrary to that, low-frequency modes (< 800 cm^{-1}) represent delocalized motion from groups of atoms. By following the evolution of the vibrational frequencies accompanying, e.g. photo-induced chemical reactions, one may hope to directly identify the chemically relevant modes [14, 35]. In this context, ground state vibrational modes which

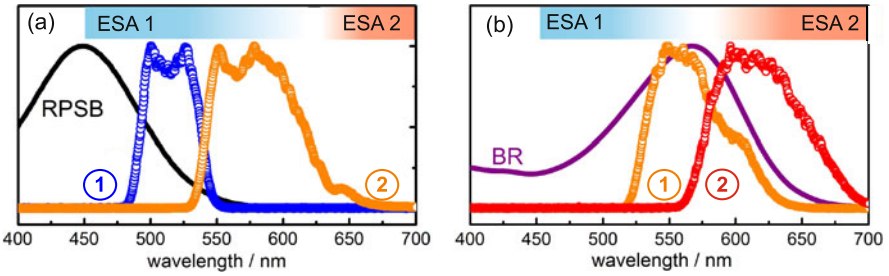

Fig. 9.4 (**a**) Absorption spectrum of all-*trans* RPSB in ethanol (*black*) together with the experimental excitation spectra (*blue* (1), *orange* (2)). (**b**) Absorption spectrum of BR (*purple*) in aqueous HEPES-buffer together with the experimental excitation spectra (*orange* (1) and *red* (2)) (Color figure online)

are directly activated by the excitation pulses do generally not contain important information about the photo-induced reaction but mainly report on vibrational dephasing caused by solvent-solute interactions. Excited state vibrational coherences on the other hand, are more useful for following photo-induced structural evolution as such dynamics can take place directly in the excited state. Therefore, a clear separation between ground and excited state signal contributions is desirable.

9.3.1.2 Results

Excitation spectra for RPSB (Fig. 9.4(a)) were located in the red wing of the ground state absorption and centred at 510 nm (spectrum 1) and 570 nm (spectrum 2). Both spectra access different vibrational manifolds in the excited state, however, both have strong overlap with an intense ESA band (500–600 nm) [36, 37]. Spectrum 2 also covers the spectral region of such a excited state emission. Based on these spectral characteristics, both excitation spectra can induce ground as well as excited state coherences. Due to a reduced overlap with high-frequency excited state vibrational manifolds, spectrum 2 can only give rise to low-frequency excited state coherences.

The excitation spectra for BR are tuned to cover the centre and the red part of the absorption spectrum. Similar to the RPSB experiments, this allows the different excitation spectra to access different vibrational manifolds in the excited state which then give rise to different vibrational coherence dynamics. Differing from the RPSB excitation, the excitation spectra used with BR partially overlap with two excited state absorption bands (ESA 1 ($S_4 \leftarrow S_1$) and ESA 2 ($S_3 \leftarrow S_1$) in Fig. 9.4(b)) of retinal in BR located at around 500 nm and around 650 nm, respectively. In particular, spectrum 1 overlaps with the red wing of ESA 1 and also with the blue wing of ESA 2. Excitation spectrum 2 overlaps only with the ESA 2.

Figures 9.5(a) and (b) show for RPSB that high- and low-frequency modes contribute to the total signal with different relative intensities compared to the non-oscillatory population dynamics. High relative contributions of high-frequency modes are observed for spectrum NR. For this excitation spectrum, no clear low-frequency modulations of RPSB are observed throughout the spectrally-resolved

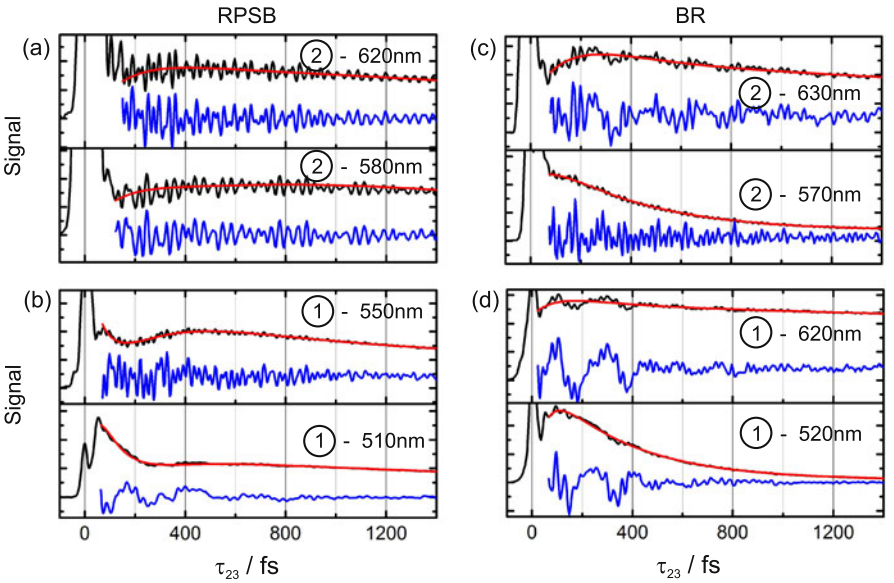

Fig. 9.5 Representative spectrally-resolved DFWM dynamics for RPSB (**a**) and (**b**) and BR (**c**) and (**d**). *Black lines* indicate the experimental data, *red lines* represent exponential fits to the population dynamics. *Blue lines* give residual oscillatory dynamics after subtraction of the exponential fit (Color figure online)

signal dynamics. The application of spectrum 1, on the other hand, reduces the relative intensity of high-frequency modes. In addition, intense low-frequency modulations appear in the dynamics. The low-frequency modulations are particularly strong for signal detection around the centre of the excitation spectrum.

Figures 9.5(c) and (d) show similar transient data from the spectrally-resolved DFWM experiments on BR. Again, clear high- as well as low-frequency vibrational coherence dynamics can be discerned for the different excitation spectra. However, the modes contribute to the dynamics with different relative intensities between the non-oscillatory population dynamics and the vibrational coherence dynamics. For instance, high-frequency modes are observed with high relative intensity when BR is excited in the red wing of its ground state absorption whereas similar modes decrease in their relative intensities when the excitation spectrum is tuned towards the centre of the ground state absorption. Importantly, different observations are made for the low-frequency modes which most strongly contribute to the dynamics for excitation spectrum 1 while their relative contributions are only low for excitation with spectrum 2.

The described observations can clearly be visualized by calculating FFT spectra from the transient data of RPSB and BR after subtraction of a multi-exponential fit to the non-oscillatory population dynamics. For RPSB and BR samples mainly three and four high-frequency modes show strong intensities in the FFT spectra, respectively (Fig. 9.6). These high-frequency modes (at about 1565 cm^{-1}, 1200 cm^{-1}

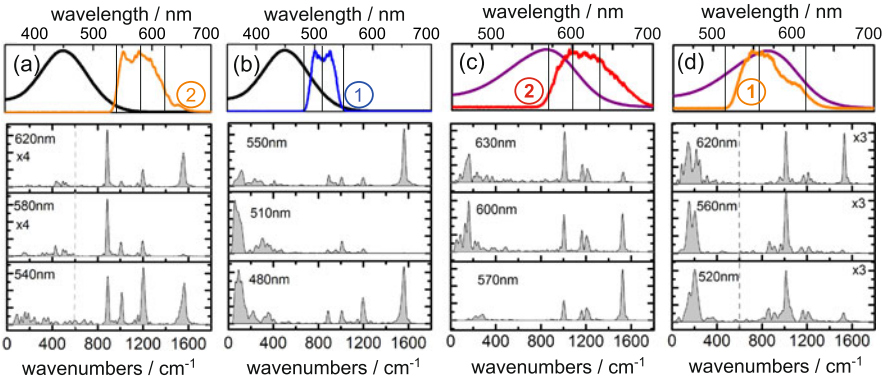

Fig. 9.6 FFT spectra of RPSB ((**a**) and (**b**)) and BR ((**c**) and (**d**)) for selected excitation spectra. For RPSB, low-frequency modes only contribute to the signal for excitation spectrum 1 (**b**). For BR, low-frequency modes strongly increase in their relative intensities for spectrum 1 (**d**) in comparison to spectrum 2 (**c**)

and 1000 cm^{-1} for RPSB and 1525 cm^{-1}, 1200 cm^{-1}, 1155 cm^{-1} and 1010 cm^{-1} for BR) reflect mainly retinal chain single- and double-bond stretching modes [38]. The vibrational frequencies of the modes do not depend on the different excitation spectra and nor on the different spectral regions of signal detection. Only four BR additional bands in the energetic region between 800–1000 cm^{-1} appear in the FFT spectra for excitation with spectrum 1 and detection wavelengths on the blue side of the excitation spectrum (Fig. 9.6(d)). These modes reflect primarily out-of-plane wagging motion of retinal chain substituents [15, 38]. Such modes are absent in all FFT spectra for RPSB (note that the 885 cm^{-1} is a solvent mode from ethanol).

For both RPSB as well as BR intense low-frequency modes can be discerned in the energetic region between 100–300 cm^{-1} (Fig. 9.6). For RPSB one broad dominant band is located at approximately 120 cm^{-1} only for spectrum 1. Contrasting to that, two clear bands are found for BR at 160 cm^{-1} and 210 cm^{-1} for both spectra 1 and 2. However, the contributions of these two modes are much stronger for spectrum 1.

9.3.1.3 Discussion

The protein-environment strongly reduces the lifetime of the S_1 state of all-*trans* retinal in BR by nearly one order of magnitude compared to RPSB [36, 39, 40]. This effect has previously been discussed to originate from either electrostatic or steric interactions [14, 15, 36, 39–41]. It may thus be expected that band positions and dephasing time constants from vibrational coherence dynamics in both ground as well as excited electronic states will also be affected by the highly different environmental interactions in both molecules. The energetic positions of the most prominent high-frequency modes (Fig. 9.6) closely match the ground state vibrational frequencies of RPSB which are known from resonance Raman measurements [38]. Beside

the energetic positions of the high frequency modes, the lack of changes in the vibrational frequencies and their lifetimes (not shown) [29, 30] when the different excitation spectra were used, helps to assign high-frequency modes to ground-state wave packet motion.

The experimentally observed dependence of the relative contributions of the high-frequency modes on the detection wavelength for a specific excitation spectrum exactly matches theoretical expectations for spectrally-resolved DFWM [29]. The highest relative contributions are expected on both blue- as well as red-detuned detection wavelengths while these contributions are at a minimal level near the centre of the excitation spectrum. The decreasing intensity of the high-frequency modes for spectrum 1 of RPSB (Fig. 9.6(b)) and spectrum 1 and blue-detuned detection wavelengths for BR (Fig. 9.6(b)) has, however, different origins [29]. The first origin is based on the fact that red-detuned excitation spectra, for which a large part of the applied spectral intensity is off-resonant (e.g. spectrum 2 for RPSB and spectrum 2 for BR), favour the excitation of ground state vibrational coherences over the induction of excited state population. The second effect is based on interference between ground and excited state response pathways which is due to the homodyne signal detection in DFWM: In spectral regions of intense ESA, the relative intensity of ground state dynamics is controlled by an interference term between ground state and excited state response pathways. The intensity of ground state dynamics is determined by the different ratios of transition dipole moments for ground state bleach and ESA.

In contrast to the high-frequency dynamics, the observed out-of-plane modes (only for BR, 800–1000 cm^{-1}), which are observed only for excitation spectrum 1, exhibit negligible Franck-Condon activity [38]. For out-of-plane modes from the ground state, one would expect such dynamics to contribute to both excitation spectra for BR, which is, however, not observed. As the modes are observed with high relative intensity only in spectral regions of ESA 1 (500–570 nm) this indicates that the out-of-plane modes are detected through a probing pathway exploiting ESA transitions. In total, the above mentioned points show that the out-of-plane modes originate from excited state dynamics in agreement with earlier speculations on the basis of pump-probe experiments [15].

In this context, it is interesting to note that out-of-plane modes are clearly observable for excited state dynamics of BR while similar vibrational dynamics seem to be negligible for RPSB even for signal detection in spectral regions throughout the intense ESA band centred at 500 nm (Fig. 9.6). The importance of this observation concerns information about the excitation mechanism of these modes: For a direct excitation of the modes by the laser pulse in the excited state, these modes need to be normal modes of the all-*trans* retinal chromophore. However, retinal normal modes cannot simply be absent in case of RPSB in comparison to the BR dynamics. This, together with the clear dependence of the out-of-plane modes on the excitation wavelength, indicates that the activation of such modes in BR play an important role in the relaxation pathway of the excited state leading to double bond isomerization. This point will be discussed in more detail below in the context of the low-frequency modes.

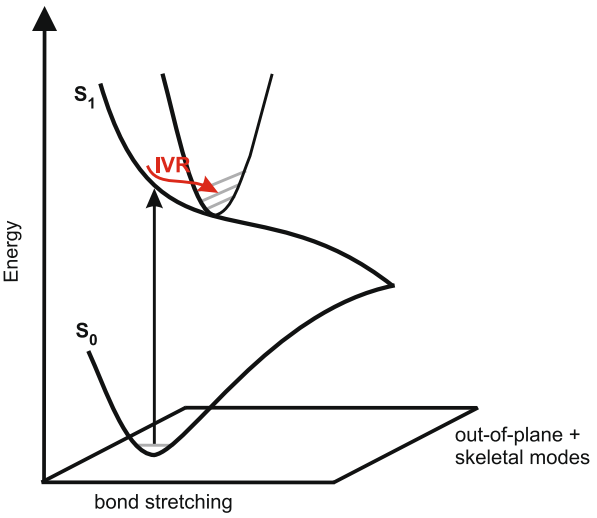

Fig. 9.7 Proposed activation mechanism for low-frequency and out-of-plane excited state vibrational coherences in RPSB and BR. The initial intramolecular vibrational energy redistribution (IVR) takes place between Franck-Condon active modes and non-Franck-Condon active out-of-plane and low-frequency modes

Similar to the out-of-plane modes, the band positions of the low-frequency modes (Fig. 9.6) do not match with previously reported resonance Raman experiments of Schiff bases in BR or in solution [38]. Also for these modes the pronounced dependence of their observation on the excitation wavelengths together with very short lifetime of the low-frequency coherences for both RPSB and BR (< 600 fs) indicates that the modes reflect excited state dynamics. In addition, these observations and conclusions are in perfect agreement with previous results for BR and RPSB in pump-probe experiments and time-resolved fluorescence experiments [39, 40]. The spectral region of observation of the low-frequency modes which is highly correlated to the spectral region of ESA in both RPSB and BR additionally substantiates that the modulations stem from excited state vibrational coherences. These observations extend the current picture of excited state wave packet dynamics of RPSB and BR by showing that the modes are observable in both spectral regions of excited state stimulated emission [39, 40] and also via multiple electronic transitions of ESA. Hence, the reported DFWM experiments resolve long standing inconsistencies for excited state dynamics of RPSB and BR: Previously, such excited state wave packet dynamics were only resolved for excited state emission [39, 40] for RPSB and only for the ESA 1 band in BR [15].

In the following we discuss the origin of the dependence of the low-frequency modes on the excitation and detection wavelength (Fig. 9.6). Low frequency modes in RPSB can only be observed with resonant excitation spectrum (spectrum 1 in Fig. 9.4(a)). For BR, low-frequency modes have a stronger relative intensity (when compared to high-frequency modes) for excitation with excess photon energy (spectrum 1 in Fig. 9.4(b)). The observation that the modulation intensity depends on the excitation wavelength indicates that the modulations are not directly activated by the excitation pulses.

This holds as long as the spectral shape of the ESA bands at the detection wavelengths of interest do not change significantly for the applied excitation spectra what

has been demonstrated previously for RPSB [36]. An alternative activation mechanism of the low-frequency modes compared to a direct excitation through light-matter interaction can be given as coherent internal vibrational energy redistribution starting from directly excited high-frequency vibrational levels in the S_1 state [40] (Fig. 9.7). Such an activation mechanism has been proposed for RPSB previously based on the need for a huge amount of excess vibrational energy ($\sim 5000\ cm^{-1}$) in order to observe the low-frequency modes [40]. However, our DFWM experiments reveal that such a threshold can only be on the order of a few hundreds of wavenumbers (200–500 cm^{-1}). In the context of the activation of the low-frequency modes, it is important to note that very similar observations have been determined for the out-of-plane modes for BR (Fig. 9.6). This observation is indicative for a conclusion that both types of modes are acceptor modes for access vibrational energy deposition in the excited state and are therefore responsible for ultrafast relaxation possibly along the reaction coordinate. Their specific observation only for BR can be indicative for the conclusion that these modes are responsible for the much faster isomerization in the protein environment compared to the chromophore in solution and also for the much higher selectivity and quantum yield for photoproduct formation [42].

9.3.2 Detection of Dark States

9.3.2.1 Introduction

The identification and characterization of dark electronic states is of the greatest challenges in spectroscopy of excited dynamics. Since these states cannot be excited directly, as the denotation 'dark state' already implies, identification of dark states on photochemical processes in biological systems is often difficult. Nonetheless, the processes that cannot be explained without the presence of dark states are numerous and the examples range from photo-damage of DNA [43] to light-harvesting [44]. In the latter case, a long standing and still ongoing debate is held on the possible participation of dark electronic states in the energy dissipation pathway in carotenoids. It is well known that the first bright electronic singlet state (S_2) of these natural pigments that is excited via absorption of light in the green-blue region of the visible spectrum is not the lowest lying excited singlet state. The first excited singlet state S_1 is indeed a very well characterized dark state, whose energy, electronic lifetime and vibrational spectra [12] have been determined in many spectroscopic investigations. However, several experimental findings such as the deviation of the S_2 lifetime dependence on the conjugation length of the carotenoids from the energy gap law raise the question whether additional dark states between the S_2 and S_1 states exist and potentially participate in the relaxation pathway [45, 46]. Such states have already been predicted by theory [47] but are extremely difficult to detect spectroscopically, since they cannot even be excited via two-photon absorption, as is the case for the S_1 state [48], and have very short lifetimes.

Applying pump-DFWM to lycopene, a carotenoid with 11 conjugated double bonds, we find direct evidence for the contribution of an additional electronic state

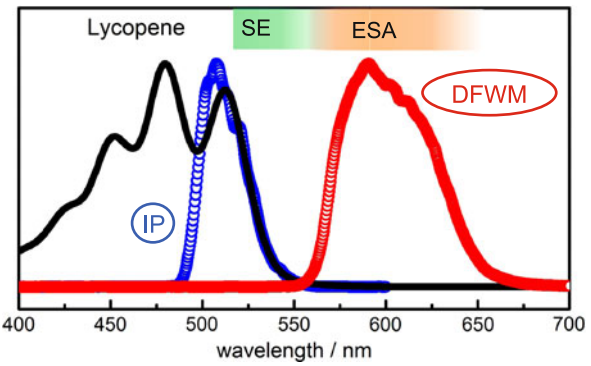

Fig. 9.8 Excitation spectra (DFWM: *red*; initial pump: *blue*) together with lycopene's ground state absorption spectrum (*black line*) in THF (Color figure online)

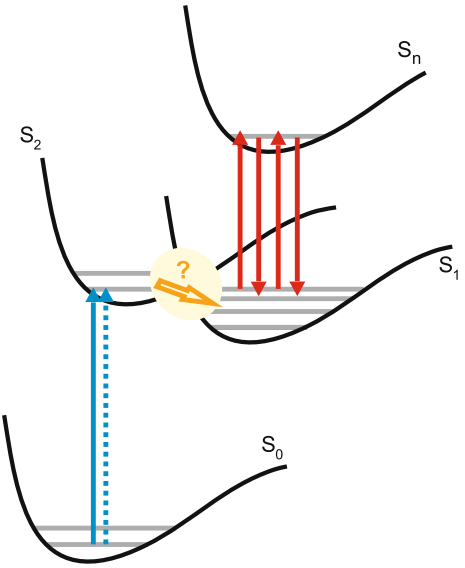

Fig. 9.9 Excitation scheme for the pump-DFWM experiments in lycopene

in the rapid deactivation from the S_2 to the S_1 state [31]. This contribution manifests itself in a long-living signal that appears at short delay times T between the initial pump pulse and the DFWM sequence and it can be assigned to an additional dark state by numerical model simulations of lycopene's pump-DFWM signal.

9.3.2.2 Results

The excitation spectra for the pump-DFWM experiments on lycopene are shown in Fig. 9.8 together with lycopene's linear absorption spectrum. The spectrum of the initial pump pulse overlapped with the ground state absorption to the first bright electronic singlet state S_2 (Fig. 9.9). The DFWM spectrum was centered at 600 nm corresponding to the S_1–S_n excited state absorption.

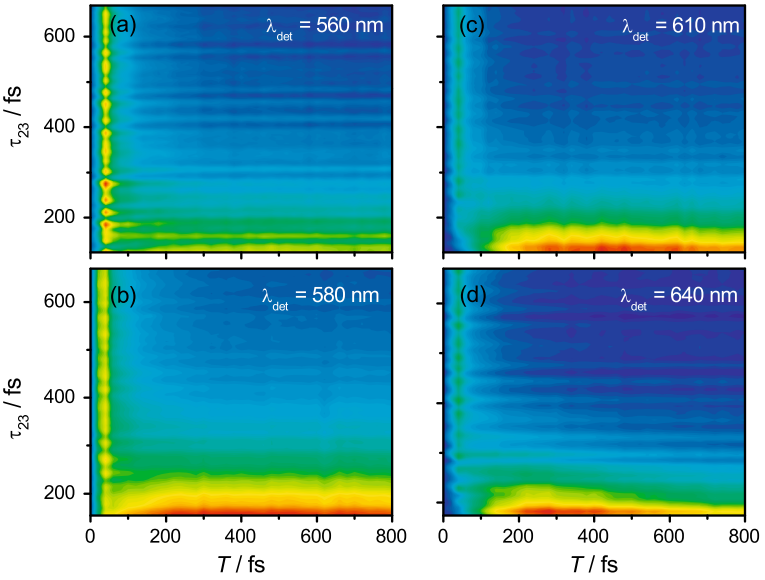

Fig. 9.10 Spectrally resolved pump-DFWM signal of lycopene at different detection wavelengths

The pump-DFWM signal was detected at several different wavelengths ranging from the blue edge (560 nm) of the S_1 absorption to the far red edge (640 nm) and is shown in Fig. 9.10 as 2D plots of the probe delay τ_{23} against the initial pump delay T (see Fig. 9.2 for definition of delays).

The plots in Fig. 9.10 clearly show a slow rise of the signal along the T axis at small probe delays τ_{23} for all detection wavelengths. This rise illustrates the flow of population from the initially excited S_2 state into the S_1 state where resonant DFWM takes place [12]. Exponential fitting of the rise gives a time constant of 140 fs. The oscillatory and non-oscillatory contributions of the DFWM signal emerge along the delay τ_{23} between the DFWM probe pulse and the temporally overlapped pump and Stokes pulses. Along the τ_{23}-axis of Fig. 9.10, the expected exponential decay of the slowly varying component of the signal is visible for late initial pump delays ($T > 100$ fs). In a narrow time window between $T = 10$ fs and $T = 80$ fs, however, a signal with a long lifetime in τ_{23} (> 2 ps) occurs. This component has a maximum at about $T = 40$ fs and has larger amplitude at blue-detuned detection wavelengths (560 nm) than at red-detuned detection wavelengths (640 nm), compared to the rapidly decaying S_1 signal at later T delays.

9.3.2.3 Discussion

The pump-DFWM signal of carotenoids for late initial pump delays T (~ 800 fs) can easily be explained in the framework of the relaxation from the initially excited S_2 state to the S_1 state including the process of vibrational relaxation in the S_1

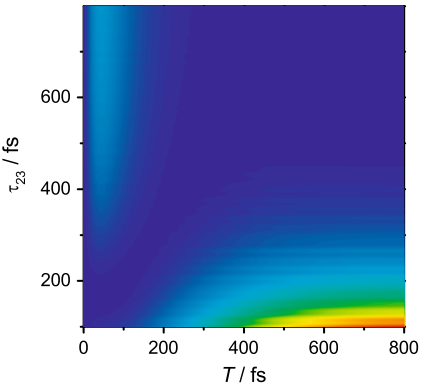

Fig. 9.11 Simulated pump-DFWM signal of lycopene

state (see also the following Sect. 9.3.3). The interpretation of the long living signal at $T = 40$ fs requires a more detailed discussion. The temporal evolution of this signal is striking since its very long lifetime in τ_{23} (2.5 ps) and is paired with a rapid decay along the T-axis. The latter aspect reveals this signal stemming from a process taking place during the relaxation from S_2 to S_1. However, none of these two states can account for such a signal: At $T = 40$ fs the S_1 state has almost negligible population. Since the DFWM signal depends on the squared population difference (Δn^2) between the involved states, the S_1 state can definitely be ruled out as source for such strong signal. On the other hand, the S_2 state is instantaneously populated by the initial pump pulse so that any signal from this state should appear directly at time zero and not delayed by 40 fs.

In order to clarify the origin of this unique signal at early initial pump delays we performed numerical model simulations based on the Brownian oscillator model [31, 49]. Details for the simulations can be found in [31]. The simulation results are shown in Fig. 9.11. Note that the laser pulses in the simulations are approximated by δ-functions. The signal in Fig. 9.11 hence displays integration over all wavelengths and can be just qualitatively compared to the spectrally resolved experimental signals in Fig. 9.10. Nevertheless, the prominent features of the experimental data shown in Fig. 9.10 are well reproduced.

In order to reproduce all features of the experimental pump-DFWM signal, several different models were tested [31]. Nevertheless, the only way to reproduce the long-living signal at $T = 40$ fs in our simulations was to introduce a stimulated emission pumping DFWM (SEP-DFWM) [50] process between an additional state (X in Fig. 9.12) and a vibrationally hot ground state (hot-S_0). This additional state is located energetically directly below the S_2 state and is populated extremely rapidly with a time constant of 20 fs. The decay from S_2 to X leads to the delay of 40 fs of the signal along the T-axis, and since X decays into the S_1 state, the signal is vanished before significant S_1 excited state absorption appears. The long lifetime in τ_{23} on the other hand is due to the slow decay of the hot ground state (6 ps). The assignment of the signal to a hot ground state is supported by the temporal evolution of the vibrational modes (not shown here) [31]. All other tested models beginning with the simplest model considering only S_2 and S_1 over models including either

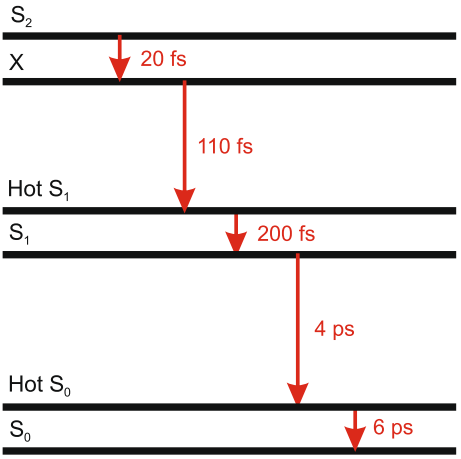

Fig. 9.12 Time constants for the relaxation pathway in lycopene underlying the model simulations

SEP-DFWM between S_2 and hot-S_0 or relaxation via an additional 'X state' without SEP-DFWM up to models incorporating S_2–S_m absorption processes did not lead to a successful replication of the experimental signal [31].

The relaxation scheme shown in Fig. 9.12 implies that the 'X state' corresponds to such an additional dark electronic state discussed in literature. However, X could as well be thought of as the approach of a Franck-Condon window for the S_2–hot-S_0 transition within the first 40 fs after excitation. Measurements in lycopene using different initial pump spectra showed no dependence of the temporal position of the long-living signal on the energy of the IP. Since a shift of the IP spectrum leads to excitation to another position on the S_2 electronic hypersurface, this lack of dependence actually argues for X being an electronic state between S_2 and S_1 as already suggested in other experimental investigations [45, 46, 51, 52].

In our model the generally accepted S_2 lifetime of 130 fs in lycopene, which is normally determined either by fluorescence or via the rise time of the S_1 excited state absorption, is composed of the ultrafast relaxation from S_2 to X (20 fs) and the X lifetime (110 fs). Similar time constants were found in sub-picosecond absorption spectroscopy in carotenoids with varying conjugation lengths [53]. In this study, the intermediate state in lycopene was identified to be of $3A_g^-$ symmetry and lifetimes of 20 fs and 150 fs were determined for S_2 and $3A_g^-$, respectively. Further indication for the S_2–S_1 relaxation via an additional state was given in a recent femtosecond transient absorption study of lutein and β-carotene combined with quantum chemical calculations [46]. In this case, the existence of the intermediate state was inferred from the observation that the fluorescence spectra of these carotenoids differ from a direct mirror image of the absorption. The authors assigned a long lifetime to the S_2 state (100–170 fs, depending on the solvent) and a shorter one (80 fs and 50 fs for lutein and β-carotene, respectively) to the intermediate state, determined by quantum chemical calculations as $1B_u^-$. Another indirect hint for a dark state was found in femtosecond time-resolved absorption and Kerr-gate fluorescence experiments on different β-carotene homologues [52]. The behavior of the S_2 relaxation

rates depending on the conjugation length could only be explained by the existence of an additional state located between S_2 and S_1. Similar to studies on lutein and β-carotene [46], the longer lifetime of about 100 fs was assigned to the S_2 state while the identical rise time of the S_1 state was explained with a very fast S_x–S_1 relaxation (10 fs). The dark nature of the additional state in combination with the extremely rapid relaxation from S_2 to S_1 in carotenoids makes it very difficult to observe this state in spectroscopic studies using transient absorption and to differentiate between the time constants of the S_2 state and the dark state. Using the method of pump-DFWM, however, we can distinguish between these two adjacent states and unambiguously assign of the longer lifetime of 110 fs to the dark state due to its intense stimulated emission that leads to a unique signal in this technique.

9.3.3 Vibrational Coherence Evolution in the Excited State

9.3.3.1 Introduction

Among the incoherent population relaxation (Sect. 9.3.2), the evolution of the ultrafast vibrational coherence in the excited state is an additional but very important aspect in understanding chemical transformations. Not just the frequency of oscillatory phenomena can give significant hints on the flow of a given reaction, but also how the frequencies change during the relaxation process may also help to re-construct the relaxation pathway and the participating molecular degrees of freedom. The high temporal and spectral resolution of pump-DFWM make this technique an ideal tool for the analysis of the shift of the vibrational frequencies in time. Another important aspect of the vibrational dynamics is the population time of individual modes. Rise and decay times of vibrational mode amplitudes present us a better picture on how modes are populated and depopulated and, sometimes, allow for the identification of vibrational modes specific for a given electronic state. In pump-DFWM, the evolution of the vibrational population can be measured by detecting the vibrational mode intensity for several initial pump delays T.

In this section, we apply pump-DFWM to resolve the evolution of the vibrational coherence in the excited states of carotenoids. Similar to lycopene investigated on the last section, the S_1 state will be populated with excess vibrational energy, given the considerable difference in zero-point energies between S_1 and S_2. McCamant et al. [54] proposed a two-stage mechanism for internal vibrational redistribution (IVR) on S_1 for β-carotene in solution. The authors employed femtosecond stimulated Raman scattering and explained their results without invoking any intermediate states between S_1 and S_2 in β-carotene. Rondonuwu et al. [55] however, investigated polyenes of similar conjugation length by sub-picosecond time-resolved Raman scattering. The authors suggested the following energetic pathway upon excitation of S_2 ($1B_u^+$): $1B_u^+ \rightarrow 3A_g^- \rightarrow 1B_u^- \rightarrow 2A_g^- \rightarrow 1A_g^-$. Hence, the puzzle of carotenoid's deactivation network is not resolved by either time dependent vibrational or transient absorption spectroscopy.

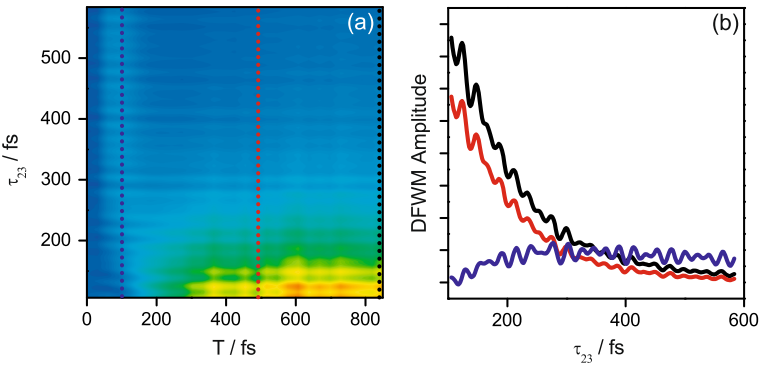

Fig. 9.13 (**a**) Typical 2D scan for β-carotene; (**b**) Selected DFWM transients for three values of delay T: 100 fs (*blue*), 490 fs (*red*) and 850 fs (*black*). The *color* used for the *dotted lines* in (**a**) correspond to the *color* of the respective transients in (**b**)

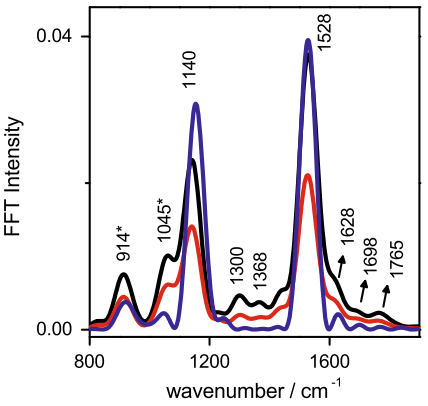

Fig. 9.14 Fast Fourier transform spectra of DFWM transients for three values of delay T (100, 490 and 850 fs). The *colors* used correspond to the same *color* coding used in Fig. 9.13

9.3.3.2 Results

A typical 2D transient data set for β-carotene is shown in Fig. 9.13. The non-oscillatory dynamics of the pump-DFWM signal along the T-axis in β-carotene show similar characteristics found for lycopene (Sect. 9.3.2). The long-lived signal at T-delays ($T = 100$–130 fs) can be related to the same feature observed for lycopene at shorter T-delays. This contribution comes also from a vibrationally excited ground state (hot-S_0), which is excited via a dark state X by the DFWM sequence via SEP-DFWM [50] directly after the relaxation of the S_2 state. The longer vibrational dephasing time of this signal is additional evidence that this contribution does not come from the excited state, but must be related to a long time vibrational dynamics in the ground state.

In Fig. 9.14, the Fourier transformation of the oscillatory contribution detected at the red wing of the absorption ($\lambda_{det} = 610$ nm) is shown. Two major vibrational contributions can be distinguished: (i) the vibration at 1140 cm^{-1} can be associated

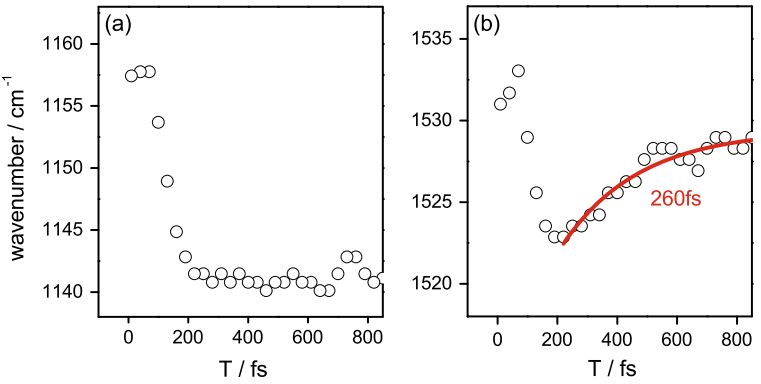

Fig. 9.15 Dependence of the central frequency of two vibrational modes of β-carotene on the delay time between initial pump and the DFWM sequence: (**a**) 1140 cm^{-1} C–C single-bond stretching, (**b**) 1528 cm^{-1} C=C double-bond stretching

with the C–C single-bond stretch mode and (ii) the vibration at 1528 cm^{-1} is related to the C=C double bond stretch mode. Besides these two major contributions, several additional modes are observed. One of them, at 1765 cm^{-1}, is a typical contribution which is associated with the C=C stretch mode characteristic for the S_1 state [54]. This mode cannot be found for any other electronic state, dark or bright, in carotenoids. Other small contributions at 1368 cm^{-1}, 1626 cm^{-1} and 1698 cm^{-1} were recently proposed to be related to the formation of dark states in lycopene ($N = 11$) and spheroidene ($N = 10$) [55]. The two peaks at about 915 cm^{-1} and 1045 cm^{-1} are modes of the solvent (THF).

As shown in Fig. 9.15(a), the C–C stretch mode evolves from its corresponding wavenumber in the ground state ($\sim$ 1160 cm^{-1}) to a lower wavenumber in the excited state at 1140 cm^{-1} within the lifetime of the S_2 state in THF ($\sim$ 170 fs). After this time the frequency does not change during the population time of the S_1 state. The C=C stretch mode evolves initially (Fig. 9.15(b)) similarly compared to the evolution of the C–C mode, i.e., the central wavenumber varies from its value in the ground state 1532 cm^{-1} down to 1522 cm^{-1} during the lifetime of the S_2 state. After this time, different to the C–C mode dynamics, the wavenumber of the C=C mode drifts to 1528 cm^{-1} with a time scale of 260 ± 20 fs.

9.3.3.3 Discussion

The evolution of the C=C stretch mode at 1528 cm^{-1} after $T \sim 200$ fs can be explained in terms of vibrational energy relaxation in the excited state. For earlier values of T, the molecule is still vibrationally excited. As T increases and the system relaxes, lower vibrational levels will be eventually populated and, due to vibrational anharmonicity, wavepackets generated by the DFWM sequence will show a higher vibrational energy. For β-carotene in THF the time constant associated with the relaxation of this mode is 260 fs. A similar behavior cannot

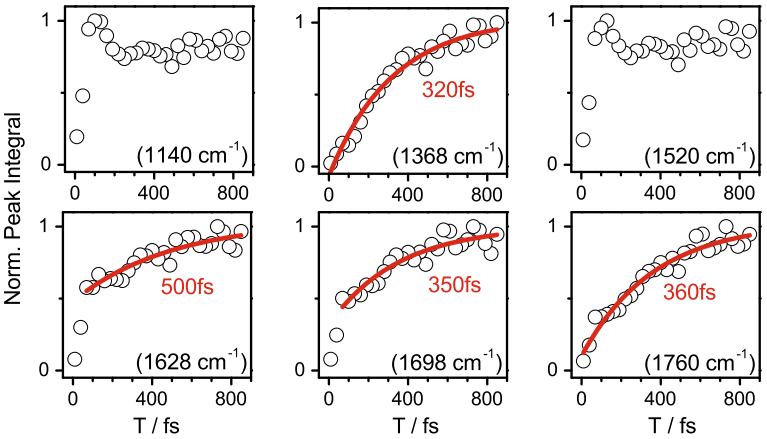

Fig. 9.16 Variation of selected FFT peaks depicted in Fig. 9.14. The integral of the peaks, was calculated with 10 cm^{-1} width around the given wavenumber and its value was normalized

be observed for the C–C vibrational mode. The absence of any evolution for the C–C mode at later T values and the significant variation of the central frequency of the C=C mode are two central features in understanding the internal conversion between S_2 and S_1. The frequency of strongly coupled vibrational modes shifts more than for modes which are weakly coupled. Therefore, it becomes clear that the C=C stretching mode is the strongest coupled mode in the early times during the internal conversion between S_2 and S_1. This assignment is in good agreement with other experimental observations [54]. A similar behavior is also present for the C=C mode at 1765 cm^{-1} (not shown), although the shift seems to be much smaller [21].

The excited state potential surface can be further mapped by plotting the peak area of each individual Raman mode (Fig. 9.16). The evolution of the area of a CARS/CSRS peak is directly related to the changes of population in the mode [49] and, therefore, indicates the relaxation pathway on the multidimensional PES. The peak area is calculated around the center wavenumber with 10 cm^{-1} width. The two main vibrational contributions to the signal at 1140 cm^{-1} and 1528 cm^{-1} rise almost instantaneously with a maximum value at 100–130 fs. At this time delay, as depicted in Fig. 9.13, the stimulated pump excitation (SEP) mechanism is present. After this delay the peak integral remains almost constant during the relaxation of the system. This merely confirms that the C–C and the C=C modes are present in hot-S_0 as well as in the excited electronic states. The behavior of the other vibrational modes is different. As expected, the S_1-specific C=C stretch mode at 1760 cm^{-1} has negligible magnitude for early values of T, but then increases with a time constant of 360 ± 20 fs. The other modes at 1368 cm^{-1}, 1628 cm^{-1} and 1698 cm^{-1} show a similar behavior with time constants of 320 ± 20 fs, 500 ± 30 fs and 350 ± 20 fs, respectively. The last two modes show an additional fast rise which peaks at about 100 fs. This is explained by the absence of these modes in the ground

state, generating a fast rising signal as soon as the system is excited and starts to relax.

The lack of a clear vibrational signature specific to a dark state in β-carotene is in agreement with the picture obtained for other carotenoids using pump-DFWM. The dark state observed between the S_2 and the S_1 state has a lifetime which is between 20–80 fs, depending on the carotenoid length. In the lifetime of such a dark state, the C–C or C=C modes will barely be able to oscillate two times before the electronic state has completely decayed, which will lead to a contribution very short in duration in the DFWM signal. Therefore, the signal of such a dark state will be hardly detectable with DFWM (as well as in TA or other any other third-order technique). This demonstrates the power of a pump DFWM: By using an initial pump pulse to excite the molecule, the presence of such ultrafast transient states can be clearly resolved in the deactivation.

9.4 Conclusions

Multidimensional time-resolved spectroscopy methods use additional laser-matter interactions to open new temporal and/or spectral observation windows. This allows observing molecular phenomena normally hidden from time-resolved techniques with low-dimensionality. We have exploited third- and fifth-order nonlinear methods based on four wave mixing to investigate the excited state of biomolecules. This was demonstrated to Schiff-bases in BR and solution as well as for different carotenoids in solution. With (pump-) DFWM, it is possible to resolve the activation and deactivation of Raman modes and electronic population, leading to a better understanding of the chemical changes, in particular in electronically excited states.

References

1. M. Dantus, M.J. Rosker, A.H. Zewail, Real-time femtosecond probing of transition-states in chemical-reactions. J. Chem. Phys. **87**(4), 2395–2397 (1987)
2. J. Dobler et al., Excited-state reaction dynamics of bacteriorhodopsin studied by femtosecond spectroscopy. Chem. Phys. Lett. **144**(2), 215–220 (1988)
3. R.A. Mathies et al., Direct observation of the femtosecond excited-state cis-trans isomerization in bacteriorhodopsin. Science **240**(4853), 777–779 (1988)
4. P.F. Barbara, G.C. Walker, T.P. Smith, Vibrational-modes and the dynamic solvent effect in electron and proton-transfer. Science **256**(5059), 975–981 (1992)
5. J.L. Herek et al., Femtosecond real-time probing of reactions. 9. Hydrogen-atom transfer. J. Chem. Phys. **97**(12), 9046–9061 (1992)
6. K. Lenz et al., Resonance Raman and femtosecond absorption studies of vibrational-relaxation initiated by ultrafast intramolecular proton-transfer. Chem. Phys. Lett. **229**(4–5), 340–346 (1994)
7. A.H. Zewail, Femtochemistry: recent progress in studies of dynamics and control of reactions and their transition states. J. Phys. Chem. **100**(31), 12701–12724 (1996)

8. W. Fuss, W.E. Schmid, S.A. Trushin, Time-resolved dissociative intense-laser field ionization for probing dynamics: femtosecond photochemical ring opening of 1, 3-cyclohexadiene. J. Chem. Phys. **112**(19), 8347–8362 (2000)
9. M. Dantus, Coherent nonlinear spectroscopy: from femtosecond dynamics to control. Annu. Rev. Phys. Chem. **52**, 639 (2001)
10. W. Wohlleben et al., Coherent control for spectroscopy and manipulation of biological dynamics. ChemPhysChem **6**(5), 850–857 (2005)
11. R.W. Schoenlein et al., The 1st step in vision—femtosecond isomerization of rhodopsin. Science **254**(5030), 412–415 (1991)
12. T. Polívka, V. Sundström, Ultrafast dynamics of carotenoid excited states—from solution to natural and artificial systems. Chem. Rev. **104**(4), 2021–2071 (2004)
13. D. Polli et al., Broadband pump-probe spectroscopy with sub-10-fs resolution for probing ultrafast internal conversion and coherent phonons in carotenoids. Chem. Phys. **350**(1–3), 45–55 (2008)
14. T. Kobayashi, T. Saito, H. Ohtani, Real-time spectroscopy of transition states in bacteriorhodopsin during retinal isomerization. Nature **414**(6863), 531–534 (2001)
15. A. Kahan et al., Following photoinduced dynamics in bacteriorhodopsin with 7-fs impulsive vibrational spectroscopy. J. Am. Chem. Soc. **129**(3), 537–546 (2007)
16. S. Mukamel, Multidimensional femtosecond correlation spectroscopies of electronic and vibrational excitations. Annu. Rev. Phys. Chem. **51**, 691–729 (2000)
17. W. Wohlleben et al., Multichannel carotenoid deactivation in photosynthetic light harvesting as identified by an evolutionary target analysis. Biophys. J. **85**(1), 442–450 (2003)
18. I.H.M. Vanstokkum et al., Conformational dynamics of flexibly and semirigidly bridged electron donor-acceptor systems as revealed by spectrotemporal parameterization of fluorescence. J. Phys. Chem. **98**(3), 852–866 (1994)
19. J. Oberle et al., Enhancement and subpicosecond dynamics of optical nonlinearities of excited-states—trans-stilbene in solution. Chem. Phys. Lett. **241**(4), 281–289 (1995)
20. M. Motzkus, S. Pedersen, A.H. Zewail, Femtosecond real-time probing of reactions. 19. Nonlinear (DFWM) techniques for probing transition states of uni- and bimolecular reactions. J. Phys. Chem. **100**(14), 5620–5633 (1996)
21. T. Buckup et al., Multidimensional spectroscopy of beta-carotene: vibrational cooling in the excited state. Arch. Biochem. Biophys. **483**(2), 219–223 (2009)
22. J. Hauer, T. Buckup, M. Motzkus, Pump-degenerate four wave mixing as a technique for analyzing structural and electronic evolution: multidimensional time-resolved dynamics near a conical intersection. J. Phys. Chem. A **111**(42), 10517–10529 (2007)
23. J.P. Kraack, M. Motzkus, T. Buckup, Selective nonlinear response preparation using femtosecond spectrally resolved four-wave-mixing. J. Chem. Phys. **135**, 224505 (2011)
24. T. Joo, A.C. Albrecht, Electronic dephasing studies of molecules in solution at room-temperature by femtosecond degenerate 4-wave-mixing. Chem. Phys. **176**(1), 233–247 (1993)
25. T.H. Joo, A.C. Albrecht, Vibrational frequencies and dephasing times in excited electronic states by femtosecond time-resolved 4-wave-mixing. Chem. Phys. **173**(1), 17–26 (1993)
26. B.I. Grimberg et al., Ultrafast nonlinear spectroscopic techniques in the gas phase and their density matrix representation. J. Phys. Chem. A **106**(5), 697–718 (2002)
27. S. Mukamel, J.D. Biggs, Communication: Comment on the effective temporal and spectral resolution of impulsive stimulated Raman signals. J. Chem. Phys. **134**(16) (2011)
28. T. Hornung, H. Skenderovic, M. Motzkus, Observation of all-trans-beta-carotene wavepacket motion on the electronic ground and excited dark state using degenerate four-wave mixing (DFWM) and pump-DFWM. Chem. Phys. Lett. **402**(4–6), 283–288 (2005)
29. J.P. Kraack et al., Ground- and excited-state vibrational coherence dynamics in bacteriorhodopsin probed with degenerate four-wave-mixing experiments. ChemPhysChem **12**(10), 1851–1859 (2011)
30. J.P. Kraack, T. Buckup, M. Motzkus, Vibrational analysis of ground and excited electronic states of all-trans retinal protonated Schiff-bases. Phys. Chem. Chem. Phys. **13**, 21402–21410

(2011)
31. M.S. Marek, T. Buckup, M. Motzkus, Direct observation of a dark state in lycopene using pump-DFWM. J. Phys. Chem. B **115**(25), 8328–8337 (2011)
32. G. Beadie et al., Towards a FAST-CARS anthrax detector: analysis of cars generation from DPA. J. Mod. Opt. **51**(16–18), 2627–2635 (2004)
33. M. Mehendale et al., All-ultraviolet time-resolved coherent anti-Stokes Raman scattering. Opt. Lett. **31**(2), 256–258 (2006)
34. N. Hampp, Bacteriorhodopsin as a photochromic retinal protein for optical memories. Chem. Rev. **100**(5), 1755–1776 (2000)
35. I. Iwakura, A. Yabushita, T. Kobayashi, Observation of transition state in Raman triggered oxidation of chloroform in the ground state by real-time vibrational spectroscopy. Chem. Phys. Lett. **457**(4–6), 421–426 (2008)
36. O. Bismuth et al., Photochemical dynamics of all-trans retinal protonated Schiff-base in solution: excitation wavelength dependence. Chem. Phys. **341**(1–3), 267–275 (2007)
37. B. Loevsky et al., A new spectral window on retinal protein photochemistry. J. Am. Chem. Soc. **133**(6), 1626–1629 (2011)
38. A.B. Myers, R.A. Harris, R.A. Mathies, Resonance Raman excitation profiles of bacteriorhodopsin. J. Chem. Phys. **79**(2), 603–613 (1983)
39. B.X. Hou et al., Comparing photoinduced vibrational coherences in bacteriorhodopsin and in native and locked retinal protonated Schiff bases. Chem. Phys. Lett. **381**(5–6), 549–555 (2003)
40. G. Zgrablic, S. Haacke, M. Chergui, Vibrational coherences of the protonated Schiff base of all-trans retinal in solution. Chem. Phys. **338**(2–3), 168–174 (2007)
41. J. Léonard et al., Functional electric field changes in photoactivated proteins revealed by ultrafast Stark spectroscopy of the Trp residues. Proc. Natl. Acad. Sci. USA **106**(19), 7718–7723 (2009)
42. S.P. Balashov et al., Quantum yield ratio of the forward and back light reactions of bacteriorhodopsin at low-temperature and photosteady-state concentration of the bathoproduct-k. Photochem. Photobiol. **54**(6), 955–961 (1991)
43. I. Vaya et al., Fluorescence of natural DNA: from the femtosecond to the nanosecond time scales. J. Am. Chem. Soc. **132**(34), 11834–11835 (2010)
44. R. Nakamura et al., Dark excited states of carotenoid regulated by bacteriochlorophyll in photosynthetic light harvesting. J. Phys. Chem. B (2011)
45. Y. Koyama et al., Excited-state dynamics of overlapped optically-allowed $1B(u)(+)$ and optically-forbidden $1B(u)(-)$ or $3A(g)(-)$ vibronic levels of carotenoids: possible roles in the light-harvesting function. Int. J. Mol. Sci. **11**(4), 1888–1929 (2010)
46. E. Ostroumov et al., Electronic coherence provides a direct proof for energy-level crossing in photoexcited lutein and beta-carotene. Phys. Rev. Lett. **103**(10) (2009)
47. P. Tavan, K. Schulten, The low-lying electronic excitations in long polyenes: a PPP-MRD-CL study. J. Chem. Phys. **85**(11), 6602–6609 (1986)
48. P.J. Walla et al., Excited-state kinetics of the carotenoid S-1 state in LHC II and two-photon excitation spectra of lutein and beta-carotene in solution: efficient car S-1 $\rightarrow$ Chl electronic energy transfer via hot S-1 states? J. Phys. Chem. A **106**(10), 1909–1916 (2002)
49. S. Mukamel, *Principles of Nonlinear Optical Spectroscopy* (Oxford University Press, New York, 1995), p. 543
50. P.H. Vaccaro, *Advanced Series in Physical Chemistry: Molecular Dynamics and Spectroscopy by Stimulated Emission Pumping* (World Scientific, New York, 1994)
51. G. Cerullo et al., Photosynthetic light harvesting by carotenoids: detection of an intermediate excited state. Science **298**(5602), 2395–2398 (2002)
52. D. Kosumi et al., The dependence of the ultrafast relaxation kinetics of the S-2 and S-1 states in beta-carotene homologs and lycopene on conjugation length studied by femtosecond time-resolved absorption and Kerr-gate fluorescence spectroscopies. J. Chem. Phys. **130**(21) (2009)
53. R. Fujii et al., Two different pathways of internal conversion in carotenoids depending on the length of the conjugated chain. Chem. Phys. Lett. **369**(1–2), 165–172 (2003)

54. D.W. McCamant, P. Kukura, R.A. Mathies, Femtosecond time-resolved stimulated Raman spectroscopy: application to the ultrafast internal conversion in beta-carotene. J. Phys. Chem. A **107**(40), 8208–8214 (2003)
55. F.S. Rondonuwu et al., Singlet internal conversion processes in the order of IBu → 3A(g) (−) → IBu → 2A(g) (−) → IA (g) (−) in all-trans-spheroidene and lycopene as revealed by subpicosecond time-resolved Raman spectroscopy. Chem. Phys. Lett. **429**(1–3), 234–238 (2006)

Chapter 10
Surface-Aligned Femtochemistry: Molecular Reaction Dynamics on Oxide Surfaces

Mihai E. Vaida and Thorsten M. Bernhardt

Abstract In this contribution the application of ultrafast laser pulses to reveal the dynamics of chemical reactions on metal oxide surfaces will be discussed. A combination of an optical pump-probe configuration with time-of-flight mass spectrometry is employed to monitor the mass and the relative velocity of intermediates and products of a photoinduced surface reaction in real time. Starting from a well defined reactant adsorption geometry representing the initial "collision complex" of the reactive encounter, this approach enables the observation of the coherent nuclear motion through the transition state to the emerging reaction products and thus provides insight into the elementary steps of complex surface chemical reaction mechanisms. Results will be presented for the application of this technique to the photodissociation dynamics of methyl iodide and methyl bromide adsorbed on magnesia ultrathin films on a Mo(100) single crystal surface.

10.1 Introduction

The influence of a solid support on the dynamics of a molecular encounter is of fundamental interest to all aspects of surface chemistry and catalysis [1, 2]. An issue of central importance in this respect is the geometrical alignment of the initial collision complex, which determines the passage through the transition state and ultimately the outcome of the desired chemical reaction [3, 4]. The motion involved in this process occurs on the ultrafast timescale of nuclear movement and its understanding is fundamental to the perception of chemical reaction mechanisms on surfaces of, e.g., catalytic materials. However, in order to be able to unravel the decisive molecular dynamics, the averaging over an ensemble of impact parameters and trajectories originating from variations in the starting geometry has to be minimized [5].

In gas phase experiments this can be realized by employing van der Waals complexes of reactants with defined geometry that are prepared in a supersonic molec-

M.E. Vaida · T.M. Bernhardt (✉)
Institute of Surface Chemistry and Catalysis, University of Ulm, Albert-Einstein-Allee 47, 89069 Ulm, Germany
e-mail: thorsten.bernhardt@uni-ulm.de

R. de Nalda, L. Bañares (eds.), *Ultrafast Phenomena in Molecular Sciences*, Springer Series in Chemical Physics 107, DOI 10.1007/978-3-319-02051-8_10,

ular beam [6–8]. On surfaces a complementary approach has been pioneered by John C. Polanyi which was termed "surface-aligned reaction" and which relies on an ordered adsorbate structure on a solid surface [5, 9, 10]. This approach will be described in more detail below.

To detect the resulting dynamics subsequent to the excitation of a molecular complex in aligned geometry in the gas phase, pump-probe mass spectrometry employing ultrafast lasers in combination with molecular beams is a widely applied experimental technique that has considerably advanced the field of femtochemistry [11]. Different experimental approaches are employed to study molecular reaction dynamics in surface femtochemistry, such as two photon photoemission, time-resolved sum frequency generation, or two pulse correlation spectroscopy [12]. In the present contribution, we report results of a novel alternative experimental approach for direct mass resolved monitoring of surface transition states and products adapting the gas phase pump-probe methodology.

The investigations presented here were motivated by a seminal contribution of John C. Polanyi and Ahmed H. Zewail in 1995 in which they proposed the investigation of surface transition state dynamics via direct detection of reaction intermediates and products in a femtosecond (fs) pump-probe schema similar to gas-phase femtochemistry investigations [4]. They termed this new approach that relies on a well defined reactant adsorption geometry 'surface-aligned femtosecond photoreaction'. A great deal of both, surface-aligned reaction studies (not time-resolved) [5, 10] as well as real-time surface femtochemistry investigations (see, e.g., Refs. [12–25]) have since provided insight into surface reaction dynamics. Nevertheless, the direct time- and mass-resolved detection of the transition state and the product formation dynamics of a surface reaction as proposed by Polanyi and Zewail has been realized only very recently employing the new approach of surface pump-probe fs-laser mass spectrometry [26–28].

This technique, which will be described in detail in Sect. 10.2, relies on the combination of time-of-flight mass spectrometry with non-resonant or resonance enhanced multi-photon ionization (REMPI) detection and fast surface preparation by a pulsed molecular beam [28]. Ultrathin oxide films serve as versatile substrates that interact only weakly with adsorbed molecules. Yet, the molecular adsorption structure on the substrate provides the geometrical alignment that determines the reaction dynamics subsequent to photoexcitation. Escaping fragments might, e.g., directly desorb into the gas phase or inelastically exchange energy via collisional interaction with the substrate surface depending on the adsorption geometry. Furthermore, collisional encounters with neighboring adsorbate molecules might lead to the formation of new reaction products.

In the following, first, the concept of surface-aligned chemistry will be described and the investigated methyl halide adsorbate systems as well as their photochemistry will be briefly presented. Second, the technique of surface pump-probe fs-laser mass spectrometry will be explained. In the third section of this chapter, the data obtained from the investigated methyl halide molecules on magnesia and the resulting insights into the photoinduced uni- and bimolecular surface reaction dynamics will be discussed.

10.1.1 Surface-Aligned Chemistry

The idea of surface-aligned chemistry (or surface-aligned reaction) originated, as stated by Ning and Polanyi in a recent contribution [5], from an early investigation of the light-induced dissociation of CH_3Br molecules adsorbed on a LiF(001) surface [29]. The recoiling methyl radical fragments exhibited 1.5 eV of excess translational energy which was proposed to enable subsequent reactive encounters of CH_3 with co-adsorbate molecules. Yet, due to the initial adsorbate alignment on the surface a specific geometry of the internuclear collision would be defined, thus restricting the ranges of collision energies, collision angles, and impact parameters and thus selecting specified dynamical trajectories rather than averaging over a multitude of collisional possibilities [5]. In this way, considerably more detailed insight into the single reactive collisional events would be attainable.

Several groups have since demonstrated the viability of this approach employing photoexcitation (e.g., Refs. [30–42]), electron injection with, e.g., the tip of a scanning tunneling microscope (STM) (e.g., Refs. [43–47]), electron beams [48, 49], or even collisions with accelerated atom beams [50] to trigger the initial ejection of a surface-aligned molecular fragment.

In particular the atomic resolution capabilities of the STM have impressively revealed real-space views on the effect of molecular alignment on surface reactions. As an example, the electron-induced dissociation of CH_3SSCH_3 molecules adsorbed on a gold surface is illustrated in Fig. 10.1 [45]. The adsorption structure of a CH_3SSCH_3 molecule is depicted in Fig. 10.1a. Following a low-current voltage pulse that is applied between the STM tip and the sample the CH_3S fragments are separated along the parent direction of the S–S bond by two lattice spacings (5.5 Å) and the S–C bond directions in the CH_3S species match closely those of the parent CH_3SSCH_3 molecule as can be seen from Fig. 10.1b. Therefore, the authors call the dissociation of CH_3SSCH_3 bond-aligned because the products are ejected along the S–S bond direction as well as surface-aligned because the products are trapped on the surface sites aligned with the breaking bond [45].

In a succeeding investigation also reactions of the emerging CH_3S fragments could be observed [51]. For this purpose, CH_3SSCH_3 molecules were allowed to self-assemble into linear chains on the gold surface. The electron-induced dissociation reaction of individual molecules in the self-assembled structures subsequently led to a propagating chemical reaction along the molecular chain in which S–S bonds were broken and then reformed to produce new CH_3SSCH_3 molecules.

Comparable localized atomic reactions have been reported by the Polanyi group as well [52–55]. In addition, it has been realized that the alignment effect can be utilized to imprint self-assembled molecular patterns on surfaces [56, 57].

In their seminal contribution Zewail and Polanyi already proposed that such an adsorbate surface alignment also presents an ideal starting structure for coherent excitation and fs-time-resolved dynamical investigations. A prospective schema for transition state spectroscopy by fs-laser excitation of the surface-aligned reaction $H + H_2S \rightarrow H_2 + HS$ induced in co-adsorbed H_2S molecules on LiF(001) is illustrated in Fig. 10.2.

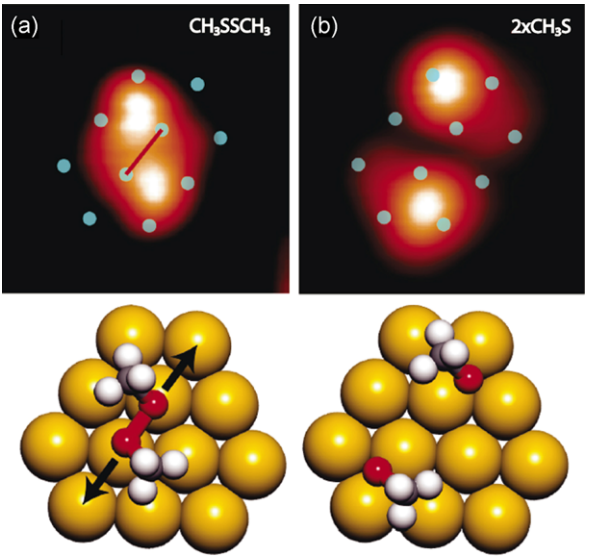

Fig. 10.1 STM images and structural models (*below*) of (**a**) the undissociated CH_3SSCH_3 molecule on Au(111) (*red line* is the direction of the S–S bond, *blue dots* mark the gold atoms in the lattice) and (**b**) the *trans*-pair of CH_3S fragments produced by electron-induced dissociation of (**a**). The models show the schematic of the surface-aligned dissociation of CH_3SSCH_3. The width of the STM images is 12 Å (adapted from [45])

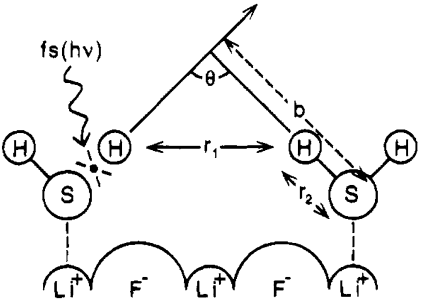

Fig. 10.2 Schematic representation of the prospective surface-aligned femtosecond photoreaction in the system H_2S/LiF(001) starting at time t_0 via fs-laser excitation. The molecular adsorption structure provides the necessary restriction of the initial state geometry with the atomic distances r_1(H–H), r_2(HS–H), the collision angle Θ, and the impact parameter b (adapted from [4])

The initial photodissociation of one H_2S molecule at time zero, t_0, defines the direction, in which the reactive H-atom is released, while the co-adsorbate geometry restricts the possible impact parameters and thus the observable trajectories of the reaction dynamics which is subsequently probed by time-delayed product detection. However, the direct time- and mass-resolved monitoring of the transition state and the product formation dynamics of such a surface-aligned reaction has only been realized recently via surface pump-probe fs-laser mass spectrometry as already stated above [27, 28].

Whereas most surface femtochemistry investigations so far have been performed on metal surfaces, for the surface-aligned femtochemistry approach presented in this chapter an insulating magnesium oxide substrate is used to ensure direct pho-

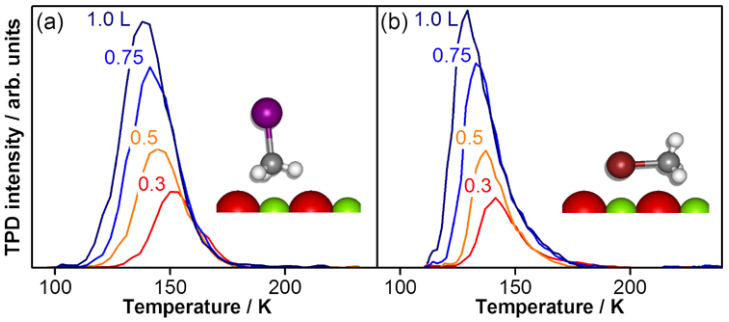

Fig. 10.3 TPD spectra of the molecular desorption of (**a**) CH_3I and (**b**) CH_3Br from sub-monolayer coverages on 8 ML MgO(100)/Mo(100) (heating rate: 2 K/s) [68]. The numbers indicated at the spectra represent the exposure in units of Langmuir ($1\ L = 1 \cdot 10^{-6}$ torr s = 0.25 ML for both molecules [36, 69]). The *insets* illustrate the proposed molecular adsorption structures. Please see text for more details

toexcitation of the adsorbate molecules. In the following section the properties of the employed photochemical model system of methyl halide molecules adsorbed at sub-monolayer coverages on MgO(100) will be discussed.

10.1.2 Molecular Adsorption on a Single Crystalline Oxide Surface

In the experiments presented here, the molecular reaction dynamics on weakly interacting oxide surfaces is addressed by studying methyl halide molecules (CH_3I and CH_3Br) as photochemically well characterized models systems (see, e.g., [58–63] and references therein). These molecules are adsorbed at sub-monolayer coverages on a single crystalline MgO(100) surface. This surface is prepared in situ as an insulating ultrathin film on a Mo(100) single crystal substrate [28, 64]. For the generation of the MgO(100) films (typical thickness: 8–10 monolayers (ML)) magnesium metal is evaporated (0.15 ML/min) in an atmosphere of $2 \cdot 10^{-7}$ mbar of oxygen with the substrate held at 600 K [65–67]. The MgO films grow epitaxially on the Mo(100) surface with a lattice mismatch of 5.4 % [65]. The (100) plane of MgO is parallel, but rotated by 45°, with respect to the (100) plane of Mo(100).

Temperature programmed desorption (TPD) spectroscopy is employed to characterize the interaction of the adsorbate molecules with the surface as a function of the molecular coverage. Both investigated molecules exhibit very similar desorption properties as can be seen from the graphs in Fig. 10.3.

Figure 10.3a displays TPD spectra recorded after dosing different amounts of CH_3I onto an MgO/Mo(100) film at 90 K substrate temperature [26, 68]. Methyl iodide adsorbs molecularly on the MgO(100) single crystal surface and desorbs without decomposition [69] already below 200 K which reflects the weak bonding of these molecules to the insulating oxide surface. The maximum of the CH_3I

desorption signal in Fig. 10.3a shifts with increasing coverage to lower temperatures indicating a desorption activation energy that further decreases with increasing coverage. On MgO single crystals [69–71] the similar temperature dependence was interpreted in terms of a repulsive adsorbate-adsorbate interaction due to an adsorbate structure with the CH_3I symmetry axis and hence the permanent dipole moment of the molecules aligned parallel to each other and parallel to or slightly tilted from the surface normal. On bulk magnesia an adsorption structure with the I-atom facing the surface was proposed earlier [70, 71]. On magnesia ultrathin films on Mo(100), however, an orientation was reported previously with the methyl group heading toward the substrate surface [26]. This adsorption geometry is in accordance with the time-resolved investigations and it is illustrated schematically in the inset of Fig. 10.3a. However, it has to be noted that neither the adsorption site, nor the exact tilt angle of the molecules with respect to the surface normal are known [27].

In Fig. 10.3b a series of TPD spectra are shown that have been recorded after dosing different amounts of CH_3Br onto an 8 ML MgO/Mo(100) film at 90 K [68]. No evidence for methyl bromide dissociation subsequent to adsorption on the MgO/Mo(100) substrate was found. No reaction products such as ethane or molecular bromine, which could be formed due to methyl bromide dissociation on the surface, were observed. Hence, methyl bromide also adsorbs molecularly on the MgO/Mo(100) surface and desorbs without decomposition. Also in the case of methyl bromide the maximum of the desorption signal shifts to lower temperatures with increasing coverage indicating a repulsive adsorbate-adsorbate interaction between the molecules. The same behavior had been observed previously for CH_3Br adsorbed at low coverages on bulk MgO(100) [36] and on LiF(100) [72]. However, angular distributions of methyl fragments emerging from CH_3Br photodissociation on MgO(100) lead to the assignment of an adsorbate structure in which the C–Br axes of the adsorbed CH_3Br molecules lay close to the plane of the substrate surface as indicated by the inset in Fig. 10.3b [36].

10.1.3 Laser-Induced Molecular Desorption and Reaction on the Magnesium Oxide Surface

The adsorbate alignment on the surface that has been discussed in the previous section determines the photoinduced reaction dynamics of the methyl halide molecules on magnesia. Light-induced fragmentation and photoreactions are commonly studied experimentally via angularly resolved time-of-flight quadrupole mass spectrometry. This technique has also been applied by several groups in the past to investigate the photoreaction of methyl iodide molecules adsorbed on a magnesium oxide single crystal surface [70, 71, 73–77]. For sub-monolayer coverages [70, 71], the most striking experimental observation was the considerably reduced I^*/I branching ratio as compared to the gas phase photodissociation, indicating a particular substrate

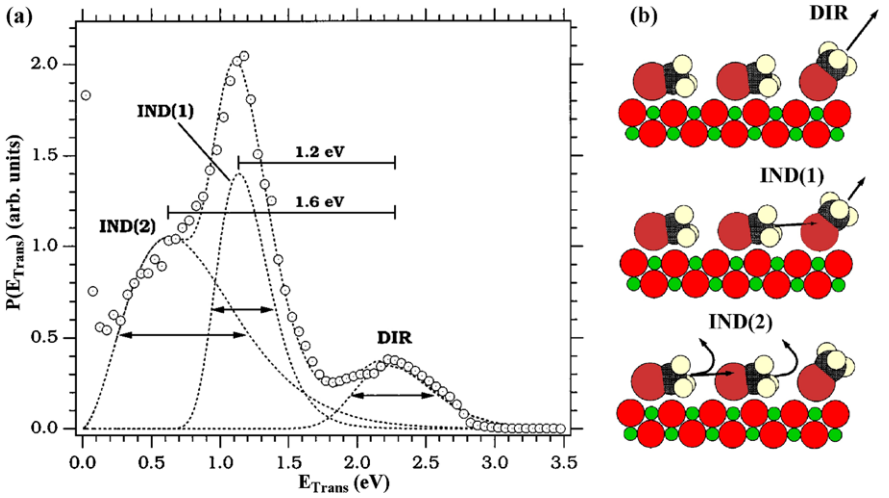

Fig. 10.4 (**a**) Methyl photofragment translational energy distribution derived from a time-of-flight profile (here 10 ML dose), collected at an angle of 20° from the surface normal. *Dotted lines* are fits to the three components of photodissociation: DIR, IND(1), and IND(2). The total fit is also shown as a *solid line*. Full widths at half-maximum (FWHM) for each component are indicated by *horizontal arrows*. (**b**) Schematic illustrations of the dynamics involved in the three photodissociation channels. *Top*: DIR CH_3 escapes without collisions with neighboring adsorbate molecules. *Middle*: IND(1) CH_3 are formed in an exchange reaction, preserving the prior Br–C bond direction. *Bottom*: IND(2) CH_3 undergo nonreactive inelastic collisions which broaden their energy and angular distributions (adapted from [36])

induced de-excitation mechanism for I^* in the methyl iodide photochemistry on magnesia [78–82]. This issue will be addressed again in Sect. 10.3.2 below.

The photoreaction pathways of methyl bromide adsorbed at different insulating substrates have been investigated in detail as well [72, 83–91]. For the case of CH_3Br on MgO(100) Polanyi and co-workers performed photodissociation experiments at 193 nm wavelength [36]. As an example, the result of this study is illustrated in Fig. 10.4. Via TPD spectroscopy and angularly resolved photofragment detection it could be shown that the CH_3Br molecules are adsorbed with their C–Br axis lying down, i.e., at an angle approximately parallel to the surface plane [36] (see also the previous section and the inset in Fig. 10.3b). The translational energy distribution of the emerging methyl fragments after photoexcitation that result from such an adsorption structure is presented in Fig. 10.4a. Clearly, three distinct pathways for the production of CH_3 from CH_3Br/MgO(100) are apparent from the measured energy profile. These three reaction channels have been observed for all investigated methyl bromide coverages from sub-monolayer up to 10 ML.

The direct ejection channel (termed DIR in Fig. 10.4) has a translational energy distribution comparable to that of the gas phase dissociation. This suggests that these photofragments did not suffer strong collisions as they departed the adsorbate layer. This is illustrated in the top graphics of Fig. 10.4b. In addition, two indirect methyl desorption channels have been assigned to the measured energy distribution. The

IND(1) pathway exhibits a maximum at a translational energy 1.2 eV below that of the DIR channel. This shift was attributed to a strong collision suffered by the CH_3 on leaving the molecular layer. In addition, the IND(1) fragments exhibit a similar angular dependence as those of the DIR channel (peaking around 40° from the surface normal for 0.75 ML coverage). This means that the IND(1) CH_3 maintain the memory of the prior Br–C bond direction, similar to the DIR CH_3, despite having collided strongly enough to lose 45 % of their initial translational energy. A molecular mechanism that would be consistent with these observations is a methyl exchange reaction as shown schematically in the middle graphics of Fig. 10.4b.

Finally, the methyl fragments produced via the third pathway IND(2) exhibit the lowest translational energy. More importantly, however, the angular distribution of these fragments has been determined to be broad with approximately a $\cos^2$ distribution, which indicates that these fragments did not retain memory of the prior Br–C bond direction. These photofragments were attributed to CH_3 escaping from adsorbed CH_3Br molecules with their C–Br bond axes nearly parallel to the surface plane, which inevitably leads to strong collisions with neighboring adsorbate molecules prior to desorption. Potential exchange reactions might also be feasible as illustrated in the bottom graphics of Fig. 10.4b.

This example demonstrates that photoreactions induced in surface-aligned adsorbate layers might indeed exhibit fairly complex, yet nevertheless distinguishable reaction pathways. The question whether the corresponding molecular reaction dynamics in these systems can be revealed by coherent excitation and time-resolved detection on the timescale of the molecular motion, namely with fs resolution, will be addressed in Sect. 10.3 of this chapter. For this purpose, in the subsequent section an experimental technique will be put forward which permits to monitor surface-aligned reactions with fs-time-, mass-, and fragment velocity-resolution.

10.2 Surface Pump-Probe Fs-Laser Mass Spectrometry

The major novelty of the experimental time-resolved laser-spectroscopy approach presented in this chapter consists in the detection of neutral photoreaction products via fs time-delayed multi-photon ionization directly at the surface. A schematic illustration of the experimental arrangement used for the surface pump-probe fs-laser mass spectrometry investigations is presented in Fig. 10.5.

The experiments are carried out in an ultra high vacuum (UHV) surface science apparatus (base pressure $< 1 \times 10^{-10}$ mbar) equipped with standard tools for surface preparation and analysis [92]. The fs-laser light is produced with a commercial Ti:Sapphire oscillator continuously pumped by a 6 W Spectra Physics Millennia Nd:YVO4 laser. The 800 nm laser pulses are amplified with a Nd:YLF laser pumped Ti:Sapphire amplifier (Spectra Physics Spitfire XP) to yield 35 fs pulses with a typical power of 3 W at a repetition rate of 1 kHz. The pump laser pulses at 266 nm are generated by frequency tripling of the fundamental wavelength in a homebuilt third harmonic generator. The probe laser beam is tuned to a central wavelength

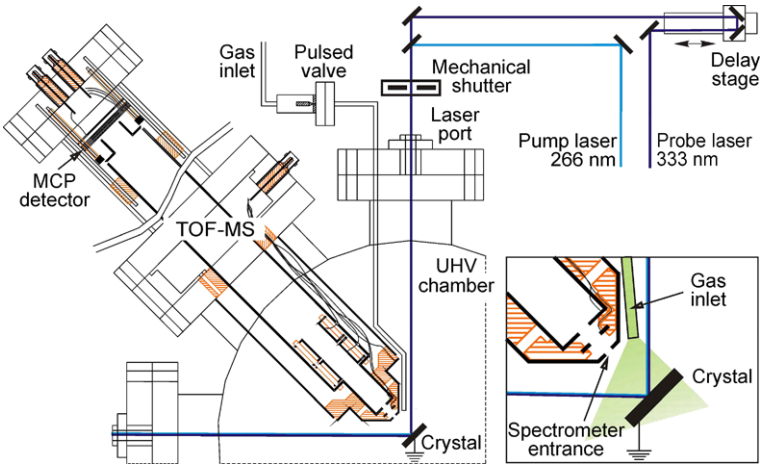

Fig. 10.5 Schematic layout of the experimental arrangement employed for the investigation of ultrafast reactions at oxide surfaces (see text for more details). The *inset* shows a magnified view of the TOF-MS head and of the surface position

of 333 nm (for resonant methyl radical detection) by means of a commercial optical parametric amplifier (Spectra-Physics OPA-800). The average laser power at the surface is 1–2 mW/cm^2 and 60–600 mW/cm^2 for pump and probe, respectively. The pump and probe laser beams collinearly irradiate the surface at an incidence angle of 45°. The temporal width of the pump and the probe laser pulses are about 80 fs and both laser beams are p-polarized. The time zero in the experiments is determined in situ by monitoring of the integral pump-probe time dependent two photon electron emission signal from the molybdenum single crystal surface [28].

A homebuilt Wiley/McLaren-type time-of-flight mass spectrometer (TOF-MS) [93] is employed to analyze both the mass and the relative velocity of the photoreaction products. The crystal surface is an integral part of the mass spectrometer because it constitutes the repeller electrode of the TOF-MS. It is grounded and positioned perpendicular to the spectrometer axis at a distance of 8 mm from the first spectrometer electrode. A bias voltage of 500 V is applied to this spectrometer entrance, which creates a static electric field (first acceleration region). Hence, subsequent to ionization, the reaction products are instantaneously removed from the sample surface and attracted into the TOF-MS. A second acceleration of the ions is accomplished inside the spectrometer. Depending on the relative acceleration field strengths the spectrometer can be operated either in optimal "mass-resolution" mode or in a "velocity-resolution" mode to analyze initial kinetic energy differences between ions of similar mass (see, e.g., [58, 94]).

After acceleration, the ions pass the field free drift tube with different velocity according to their mass to charge ratio and to their initial kinetic energy (in the "velocity-resolution" mode) and are detected by a micro-channel plate (MCP) amplifier detector arrangement as a function of their flight time. The time-of-flight signal acquisition is carried out by a multi-channel scaler electronics.

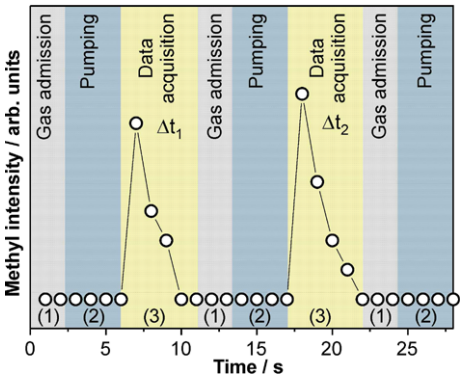

Fig. 10.6 Transient recording routine: (1) Methyl iodide is admitted to the surface by the pulsed valve. During the admission time the laser beam is blocked; (2) the non-adsorbed molecules are pumped and the delay time Δt between the pump and the probe laser pulses is adjusted. The laser beam remains blocked; (3) the surface is exposed to laser light and the methyl mass peak intensity is integrated until all molecules are dissociated/desorbed from the irradiated area. The initial surface coverage in this experiment was 0.5 ML and the laser exposure time 5 s (5000 laser pulses) [28]

To monitor in real-time the methyl halide dissociation dynamics at sub-monolayer coverage on the magnesia ultrathin films, the following transient recording routine, which is exemplified here for the methyl iodide molecule (illustrated in Fig. 10.6), is applied while the MgO/Mo(100) surface is positioned in the front of the TOF-MS (as shown in Fig. 10.5) and cooled to 90 K. (1) An initial coverage of 0.25 ML to 0.5 ML CH_3I is dosed onto the surface with the pulsed valve while the laser is blocked by a computer controlled mechanical shutter (see Fig. 10.5) so that no methyl signal can be detected by the mass spectrometer as indicated in Fig. 10.6. (2) A short pumping brake of a few seconds follows. (3) Subsequently, the laser shutter is opened and the mass peak of interest (methyl cation in Fig. 10.6) is detected and summed over 2500 to 5000 laser shots at one fixed pump-probe delay time.

After 2500 to 5000 laser shots, depending on the initial coverage, essentially all molecules are dissociated and desorbed from the irradiated surface area. Subsequently the laser beams are blocked again and the surface is covered with an identical amount of molecules as before. During the following short pumping brake the pump-probe delay time is adjusted and the described data acquisition procedure is repeated for a new pump-probe delay time [28]. Several of the thus obtained transients were averaged to yield the data shown below.

10.3 Femtosecond Dynamics of Surface Aligned Reactions

The technique of surface pump-probe fs-laser mass spectrometry is now applied to reveal in real-time the photoinduced reaction dynamics of methyl halide molecules

that are adsorbed in a surface aligned geometry on the magnesium oxide substrate (cf. Sect. 10.1.2). In the following, the employed laser excitation schema is first discussed for the case of methyl iodide molecules on MgO. Time-delayed probing of the emerging methyl fragments enables the monitoring of the unimolecular decomposition dynamics of the adsorbed molecules. The thus obtained results are then compared to the unimolecular decomposition dynamics of methyl bromide molecules on the same substrate to elucidate the influence of the different initial adsorption geometries. Furthermore, also light-induced bimolecular reactions are detected in these model systems and in the final section the dynamics involved in the formation of the halide molecules (I_2 and Br_2) on the surface will be discussed.

10.3.1 Unimolecular Photodissociation

10.3.1.1 Methyl Iodide on MgO(100)/Mo(100)

To monitor the real-time dissociation dynamics of the methyl iodide molecules adsorbed at sub-monolayer coverage on the MgO/Mo(100) surface, the following pump-probe schema is applied. The pump laser pulse is centered at a wavelength of 266 nm to electronically excite the adsorbed methyl iodide molecules to the A-band by means of direct one photon adsorption. In Fig. 10.7a the measured spectrum of the pump laser beam is presented. The one photon absorption spectrum of methyl iodide in the A-band region [95] is also displayed in Fig. 10.7a.

The relevant potential energy curves of the methyl iodide molecule are depicted in Fig. 10.7c. As the exact influence of the surface on the methyl iodide potentials is not known, and because the methyl iodide molecules do only weakly bind to the magnesia surface [78], the shown gas-phase potentials are assumed to be almost unperturbed by the surface to a first approximation. The A-band dissociation of CH_3I (see recent contributions [58, 59, 61, 96–103] and references therein) is prompt and involves primarily the two dissociative excited electronic states denoted as $^3Q_{0+}$ and $^1Q_1$ by Mulliken [104]. One 266 nm photon (pump) excites the CH_3I molecule almost exclusively to the $^3Q_{0+}$ state of the A-band and prepares the initial wave packet at time zero. Close to the point of the initial excitation, at a C–I bond distance of 2.35 to 2.40 Å, the $^3Q_{0+}$ potential leading to CH_3 and spin-orbit excited $I^*(^2P_{1/2})$ crosses the $^1Q_1$ potential that correlates diabatically with CH_3 and ground state $I(^2P_{3/2})$. At this point a bifurcation of the wave packet is possible and an experimental gas phase $I(^2P_{3/2})$ yield of about 30 % [107] points toward an efficient coupling between the $^3Q_{0+}$ and $^1Q_1$ states.

In previous photodissociation experiments with methyl iodide adsorbed at sub-monolayer coverage on MgO(100) single crystal surfaces the direct photoexcitation (in contrast to a surface mediated excitation) has been shown to be the exclusive excitation mechanism [70, 71]. In the present experiments, an ultrathin magnesia film on Mo(100) has been employed instead of a magnesia single crystal. Still, all experimental evidence indicates that the direct photoexcitation clearly dominates over a surface mediated process [28].

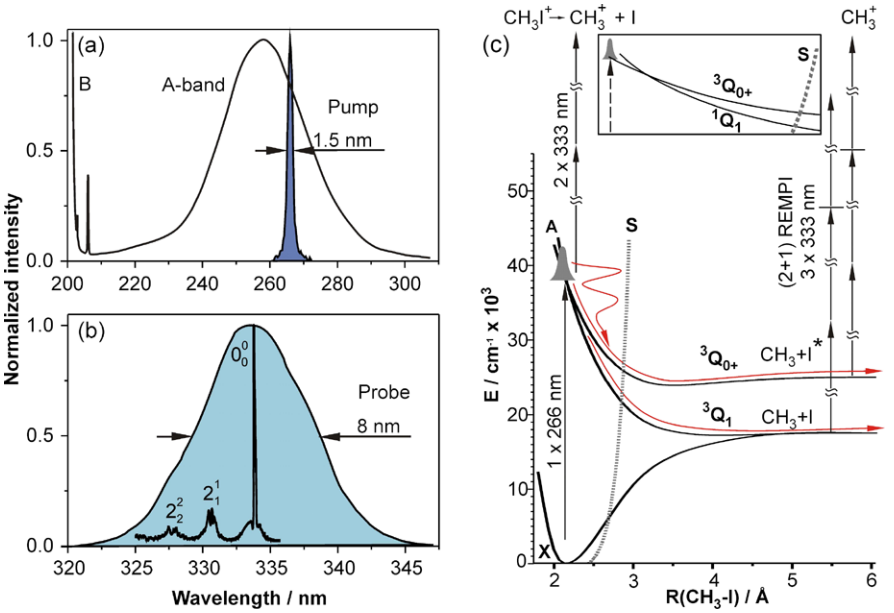

Fig. 10.7 (**a**) Single photon adsorption spectrum (A-band) of methyl iodide near the region of excitation by the pump pulse (adapted from Ref. [95]). The peak highlighted in *blue* represents the measured pump laser beam spectrum employed for the methyl iodide dissociation. (**b**) Two photon resonant ionization spectrum of CD_3 radicals (adapted from Ref. [105]) displaying the three vibronic transitions in the probe wavelength region. The measured spectrum of the probe laser beam is represented by the spectrum highlighted in *light blue*. (**c**) Potential energy diagrams of free methyl iodide [98, 106]. The *curved red arrows* illustrate the propagation of the wave packet after photodissociation. The *vertical arrows* represent the excitation and the detection laser pulses (detection energies not drawn to scale). The potential S reflects the Lennard-Jones interaction between the methyl group and the magnesia surface [82]. The *inset* shows a magnification of the methyl iodide A-band excitation region [28] (Color figure online)

Subsequent to the A-band dissociation, the probe pulse at a central wavelength of 333 nm is employed to sensitively detect the methyl fragments through resonance enhanced multi-photon ionization ((2 + 1)-REMPI) [59, 60, 105]. The experiments have been performed with both deuterated and non-deuterated methyl iodide [26] (333.4 nm for CH_3 and 333.9 nm for CD_3 detection, respectively). Two photons are employed for excitation from the $2p^2A_2''$ ground state to the $3p^2A_2''$ Rydberg state, followed by absorption of a third photon to ionize the methyl fragments. Figure 10.7b displays the probe laser beam spectrum together with the (2 + 1) REMPI transitions of CD_3I around 333 nm [105]. Due to the bandwidth of 8 nm (FWHM), the probe pulse is able to excite simultaneously the 0_0^0, 2_1^1, and 2_2^2 vibronic transitions (cf. Fig. 10.7b).

It should be emphasized that the experiment in this way is able to probe the dynamics of *neutral* products emerging from photoexcitation and dissociation at the surface. The REMPI process occurs only when the electronic states of the methyl

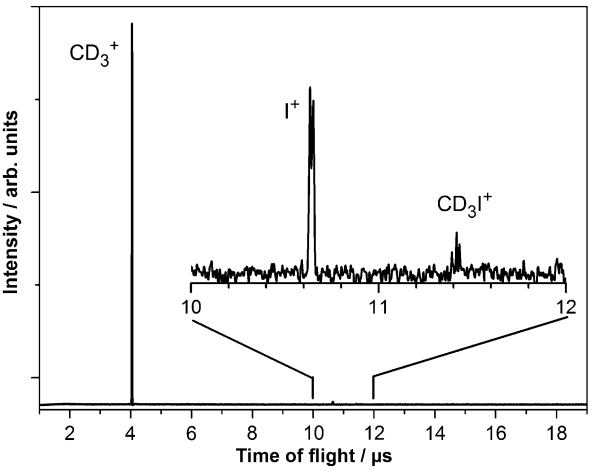

Fig. 10.8 Time-of-flight mass spectrum obtained from 0.25 ML CD_3I adsorbed on 10 ML MgO/Mo(100) at 130 fs pump-probe delay time. The *inset* presents a magnified view of the mass spectrum between 10 and 12 µs flight time [28]

fragment involved in the resonant transitions are not perturbed, neither by the iodine fragment nor by the substrate. Consequently, the real-time evolution of the REMPI probability reflects the dynamics of the methyl liberation from the iodine and surface force fields.

A time-of-flight mass spectrum obtained at 130 fs pump-probe delay time from methyl iodide adsorbed on MgO/Mo(100) is displayed in Fig. 10.8 [28]. Apart from an intense methyl ion peak, small peaks corresponding to iodine atoms and methyl iodide molecules are present.

By monitoring the intensity of the methyl cation signal as a function of the pump-probe delay time transients were obtained that reflect the photodissociation dynamics of CH_3I and CD_3I adsorbed on MgO/Mo(100), respectively. Figure 10.9a shows the result for CH_3I molecules on MgO/Mo(100) measured with a probe laser power of 70 mW/cm^2. The transient signal exhibits a steep rise starting at zero time delay with a maximum reached around 130 fs. It subsequently decays but does not reach the initial value measured at negative delay times again. Instead, a small but clearly apparent offset is observed which stays constant at longer positive delay times. Fitting of a kinetic exponential 'rise and decay'-model (with subsequent offset) to the experimental data gave similar time constants of $\tau_1 = \tau_2 = 90$ fs for the rise and the decay component of the observed peak, respectively. The transient signal obtained for CD_3^+ at comparable laser conditions is displayed in Fig. 10.9b. The appearance is identical to the CH_3^+ signal in Fig. 10.9a: a peak followed by a signal offset at positive delay times. Fitting of the 'rise and decay'-model to the peak structure also resulted in identical time constants as in the non-deuterated case. No clear indication for the expected isotope mass effect of about 20 % on the dynamics could be detected within the accuracy of the time resolution of the experiment.

Figure 10.9c shows the transient CD_3^+ signal recorded with the same pump power as above, but with the probe power increased to 600 mW/cm^2. While the peak structure at short delay times is still present, the offset at longer delay times is now

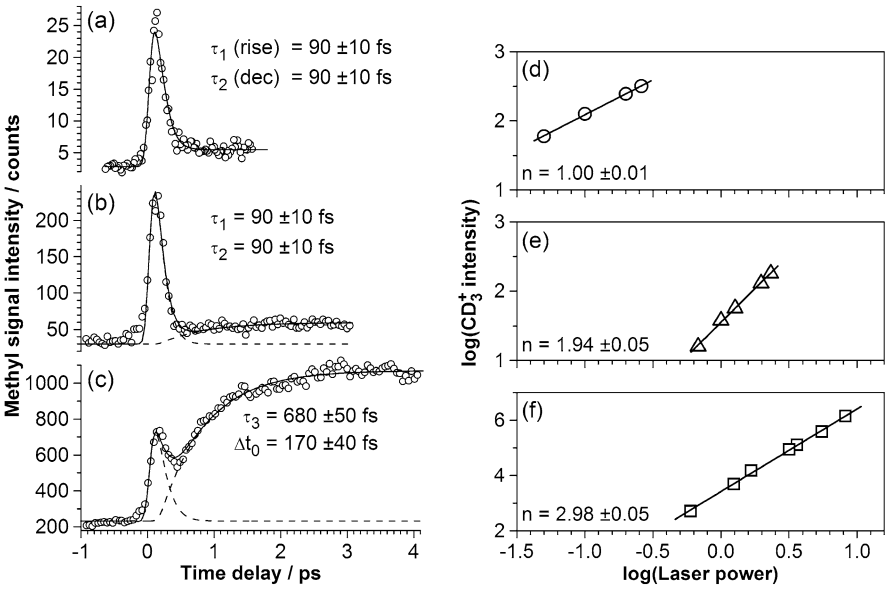

Fig. 10.9 *Left column*: Transients obtained by monitoring the methyl cation signal as a function of the pump-probe delay time. (**a**) CH_3I transient (pump laser power: 1 mW/cm^2; probe: 70 mW/cm^2). (**b**) CD_3I transient obtained with comparable laser conditions (pump: 2 mW/cm^2; probe: 70 mW/cm^2). (**c**) CD_3I transient obtained with 600 mW/cm^2 probe laser power (pump power: 2 mW/cm^2). The *solid lines* are the best fit of the sum of an exponential 'rise and decay'- and a 'delayed exponential rise'-model to the experimental data (convoluted with the pump-probe autocorrelation function). The separated components corresponding to the two models are indicated by the *dashed lines*. The time constants τ_1 and τ_2 result from the fitting of the 'rise and decay'-model which are identical for all three transients. The initial delay Δt_0 and the time constant τ_3 of the 'delayed exponential rise'-component are indicated in (**c**). *Right column*: Dependence of the methyl cation signal on the laser power (n represents the slope of the linear fit to the data): (**a**) Pump laser beam intensity variation (130 fs pump-probe delay time; 2500 fs (not shown) is similar). (**b**) Probe laser beam intensity variation at 130 fs pump-probe delay time; (**c**) probe laser beam intensity variation at 2500 fs pump-probe delay time [26, 28]

considerably enhanced and exhibits an exponential rise. The strong probe pulse energy dependence of this latter rising signal supports its attribution to the resonant ionization ((2 + 1)-REMPI) of methyl fragments resulting from the A-band dissociation.

To quantify this effect, the dependence of the CD_3^+ signal intensity on the pump and the probe laser power was measured at pump-probe time delays of 130 fs and of 2500 fs (corresponding to the maximum intensity of the peak structure and to the plateau in the CD_3^+ transient, respectively). The results are displayed in Fig. 10.9d–f in a double-logarithmic representation. The slope n of the linear fit to the measured data reflects the number of photons involved in the respective excitation and detection processes. No indications of saturation effects have been observed at the employed laser intensities. From these investigations it can be concluded that the excitation of the methyl iodide that initiates the molecular dissociation requires one

pump photon (Fig. 10.9d), while the detection of the methyl signal through ionization involves two probe photons at 130 fs time delay (Fig. 10.9e) and three probe photons at 2500 fs delay time (Fig. 10.9f) [28].

The fitting of a 'rise and decay'—in conjunction with a 'delayed exponential rise'-model to the transient in Fig. 10.9c resulted in similar rise and decay time constants for the peak as in Figs. 10.9a and 10.9b. For the exponential rise at longer delay times, a time constant of $\tau_3 = 680 \pm 50$ fs with an initial coherent delay of $\Delta t_0 = 170$ fs was obtained from the fitting procedure. The two separate components of the fit, peak and delayed rise, respectively, are indicated by the dashed lines in Fig. 10.9c. Identical fitting parameters with adjusted amplitudes also fitted the transient CD_3^+ signal obtained at lower probe laser power (see dashed curves in Fig. 10.9b). For the interpretation of these transient data the gas phase dissociation dynamics reported in the literature in conjunction with the respective potential energy curves displayed in Fig. 10.7c will be considered.

First gas-phase time-resolved investigations of CH_3I photodissociation dynamics via A-band employing fs pump-probe technique in conjunction with mass spectrometry were performed by Zewail and coworkers [58, 102]. The transient data obtained in these experiments indeed exhibited a similar appearance of a peak structure followed by an exponential rise as the transients shown in Fig. 10.9, however, with completely different time constants [58]. In the gas-phase investigations, the peak structure was attributed to the dynamics of the dissociating excited transition state of methyl iodide, $CH_3I^{*\ddagger}$, which was directly ionized by the probe pulse immediately after A-band excitation. Subsequent, rapid decomposition of the CH_3I^{+*} ion leads to the observed CH_3^+ fragment. The escape of the wavepacket from the $CH_3I^{*\ddagger}$ transition state Franck-Condon region was determined to be about 50 fs or even faster [58, 62, 102].

In contrast, the delayed rise of the transient signal was attributed to the direct REMPI detection of the emerging neutral fragments (I [58, 102] or CH_3 [59, 60]) reflecting the dynamics of their liberation from the force field of each other in coherent motion along the dissociative potential energy surfaces (cf. Fig. 10.7c). A dissociation time of 120 fs could be established for the $CH_3 + I^*$ channel by monitoring the I^+ signal intensity by means of $(2 + 1)$ REMPI detection at 304 nm [58].

Recent gas-phase investigations performed by Bañares and coworkers employing fs-laser pump-probe spectroscopy in conjunction with velocity map imaging have monitored several well defined channels of the C–I bond breakage of the CH_3I molecule via A-band excitation by detecting the methyl radical via $(2 + 1)$ REMPI at 333.5 nm [59, 60]. Bañares and coworkers, found that the CH_3I dissociation yielding vibrationless methyl radicals as well as ground and spin-orbit excited iodine atoms occurs in 40 fs and 80 fs, respectively. The CH_3I dissociation yielding the iodine fragments in the ground state and vibrationally excited methyl radicals $(CH_3(1_1^1))$ occurs in 135 fs.

Because of the similar appearance of the measured methyl transient signals (cf. Fig. 10.9a–c), our interpretation is based on the gas-phase explanation of the molecular dynamics of transition state and emerging fragments, respectively. On the basis of this assignment and by considering the potential energy diagram of methyl iodide

(Fig. 10.7c) an interpretation of the measured reaction times of the methyl iodide surface reaction will be proposed in the following discussion.

First, the peak structure with the rise and decay time constants of 90 fs, apparent in all observed transients (cf. Fig. 10.9a–c), will be discussed. In accordance with the gas-phase interpretation, the peak structure is assigned to the ionization of the excited methyl iodide before complete decomposition according to the schema:

$$CH_3I_{ads} \xrightarrow{266\ nm} CH_3I^{*\ddagger}_{ads} \rightarrow CH_3I^{+*} \xrightarrow{2\times 333\ nm} CH_3^+ + I \qquad (10.1)$$

The peak structure of the methyl ion signal therefore reflects the passage of the wave packet initially launched on the $^3Q_{0+}$ state through the transition state Franck-Condon region of the two-photon ionization (cf. Fig. 10.7c). The methyl iodide cation thus generated immediately decomposes leading to the observed methyl ion signal

In the direct gas-phase dissociation the $CH_3I^{*\ddagger}$ transition state was detected instantaneously after excitation and decayed faster than 50 fs [58, 60, 102]. In the case of methyl iodide adsorbed on MgO, however, a 90 fs rise is observed with a maximum signal around 130 fs followed by a 90 fs decay. This indicates that the presence of the magnesia surface has a fundamental impact on the dynamics of the transition state: (1) It influences the excited electronic state structure of methyl iodide so that the optimal Franck-Condon window for $CH_3I^{*\ddagger}$ detection is reached only after 130 fs. (2) The process of methyl iodide dissociation is considerably delayed by the presence of the surface. This indicates a strong inelastic interaction of the $CH_3I^{*\ddagger}$ transition state with the surface prior to decomposition. (3) If the methyl iodide molecules would be adsorbed with the iodine facing the magnesia surface [70, 71], the dissociation of $CH_3I^{*\ddagger}$ would lead to the prompt ejection of the light methyl fragments resulting in a time constant for the $CH_3I^{*\ddagger}$ decay identical to the gas-phase [78–80]. Thus, the observed dynamics support the adsorption structure with the methyl heading toward the surface. Further evidence in this respect is provided by the measured dynamics of the methyl fragments emerging from the A-band dissociation, which will be presented in the following.

The second part of the discussion will be concerned with the delayed exponential rise that is particularly apparent at high probe laser flux (see Fig. 10.9c). It is assigned, again in accordance with the gas-phase interpretation, to the $(2+1)$ REMPI detection of methyl radicals emerging from the A-band dissociation of the adsorbed methyl iodide molecules according to the reaction schema (cf. Fig. 10.7c):

$$CH_3I_{ads} \xrightarrow{266\ nm} CH_3I^{*\ddagger}_{ads} \rightarrow CH_3I + I/I^* \xrightarrow{(2+1)\times 333\ nm} CH_3^+ + I/I^* \qquad (10.2)$$

The initial delay of $\Delta t_0 = 170$ fs (cf. Fig. 10.9c) of this part of the methyl ion signal reflects the liberation of the methyl fragments from the molecular force field and from the force field of the magnesia surface. Gas-phase investigations showed a 120 fs coherent delay in the methyl fragment appearance [59, 60]. Because of the considerably prolonged initial delay observed here, the direct ejection of methyl as in the free molecule can be ruled out. Instead, the data are again in favor of a CH_3I adsorption structure with the methyl facing the magnesia substrate (cf. Fig. 10.3a).

The extended time needed for the liberation of the methyl thus reveals the effect of the magnesia surface that manifests itself in the trapping of the $CH_3I^{*\ddagger}$ transition state. The subsequent growth of the methyl signal with a time constant of $\tau_3 = 680$ fs (Fig. 10.9c) is consequently interpreted as the average lifetime of all trajectories leading from the transition state to the release of the methyl fragment. For the free molecule, due to the strongly repulsive nature of the dissociation and thus well focused wave packet, this rise is instantaneous [58, 59].

At the surface, however, the wave packet spreads due to the inelastic interaction with the surface. The corresponding trajectories therefore include the motion of methyl toward the surface leading to the inelastic collision and the recoil away from the surface followed potentially by a collision with the slowly moving, heavy iodine atom. This interaction with both, the surface and the iodine atom, was predicted theoretically and was termed as 'chattering' motion [78–80]. The scenario might proceed until the methyl trajectory is rotated away from the iodine trajectory far enough so that the fragment can escape.

In addition to the mass-resolved detection, the time-of-flight technique also enables the measurement of the relative initial velocity of the reaction products, i.e. here, of the methyl fragments emerging from the methyl iodide photodissociation at different reaction times [58, 94]. In this way, additional information concerning the dynamic processes of the supported molecules can be obtained. In the present work the velocity-resolved detection is accomplished by lowering the acceleration voltage between the surface and the mass spectrometer entrance electrode by about a factor of 4 compared to the settings for optimal mass resolution (cf. Fig. 10.5). Under these experimental conditions, the shape and the relative position of a mass peak reflect the initial kinetic energy distribution of the corresponding reaction products [58, 94].

Figure 10.10 displays the methyl ion time-of-flight mass signal recorded under these 'velocity-resolved' conditions as a function of the pump-probe delay time in a contour as well as a 3D-surface plot representation. A longer ion flight time (ToF-scale in Fig. 10.10) corresponds to a smaller initial ion velocity or initial kinetic energy, respectively. Clearly, the peak and the exponential rise structures originate from methyl ions with different initial kinetic energy. This strongly supports the above interpretation that the methyl transient signal reflects the concurrency of two different processes occurring at different delay times ((10.1) and (10.2), respectively) after photoexcitation at surface.

The liberated methyl radicals in the two processes would, in addition, be expected to appear with two different initial kinetic energies corresponding to the two dissociation channels along the ${}^3Q_{0+}$ and the ${}^1Q_1$ potentials, respectively (cf. Fig. 10.7c). However, this difference is not resolved in the data of Fig. 10.10 which might be due to the energy loss during the interaction with the surface. In contrast, the heavy iodine atoms are assumed to remain almost immobile during the dissociation time period and might be released in the spin-orbit excited as well as the electronic ground state.

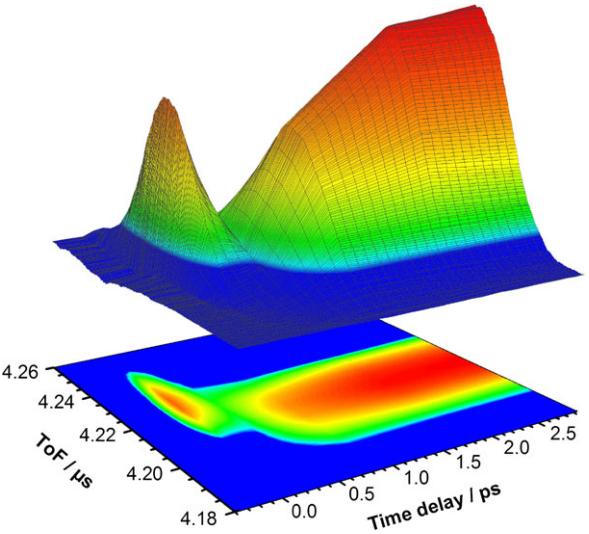

Fig. 10.10 Enlarged methyl cation time-of-flight (ToF) mass signals as a function of the pump-probe time delay. The normalized signal intensity is color coded in the contour and the 3D-surface plot representation from *blue* (0 %) to *red* (100 %). In order to enable the velocity resolution of the spectrometer, the first accelerating potential of mass spectrometer was reduced (cf. Fig. 10.5) [27, 28]

10.3.1.2 Methyl Bromide on MgO(100)/Mo(100)

The technique of surface pump-probe fs-laser mass spectrometry was applied in a similar manner also to study the photodissociation dynamics of methyl bromide molecules adsorbed on a MgO ultrathin film surface [68]. The pump laser wavelength was again 266 nm and the probe laser was tuned to the center wavelength of 333 nm to sensitively detect the methyl fragments [105]. The resulting time-of-flight mass spectrum measured at 2 ps pump-probe delay time is displayed in Fig. 10.11a. The exclusive reaction product observed in the mass spectrum in this case is the methyl fragment. No other reaction products are detected under these conditions independent of laser intensity or pump-probe delay time.

The temporal evolution of the methyl cation signal intensity a function of the pump-probe delay time is shown in Fig. 10.11b (open circles). No transient signal is observed up to 150 fs. Subsequently, the CH_3^+ signal presents an exponential rise with the maximum reached around 1.2 ps. Through fitting of the experimental data by a 'delayed exponential rise'-model (solid line in Fig. 10.11b) a time constant of $\tau = 320 \pm 60$ fs was obtained for the rise of the methyl cation transient.

The known electronic structure of the free CH_3Br molecule will now be considered here as well to discuss the molecular surface photodissociation because to a first approximation the methyl bromide molecules are also only weakly disturbed by the interaction with the magnesia surface as evidenced by TPD (Fig. 10.3b).

In contrast to methyl iodide, which was extensively studied in the past, few reports are available on the methyl bromide photodissociation. Previous investigations [108, 109] assumed that the potentials of methyl bromide and methyl iodide molecules are similar, but due to the shorter C–Br bond length of methyl bromide (1.939 Å) compared to the C–I bond length of methyl iodide (2.1396 Å), the A-band maximum of CH_3Br is shifted to higher energy. The A-band of CH_3Br, i.e. the first

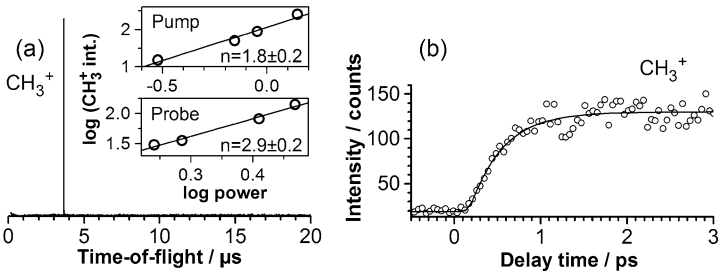

Fig. 10.11 (**a**) Time-of-flight mass spectrum obtained after photoexcitation of methyl bromide adsorbed at sub-monolayer coverage (0.25 ML) on 8 ML MgO/Mo(100) at 266 nm (6 mW/cm^2) and probing at 333 nm (600 mW/cm^2, 2 ps pump-probe delay time) through (2 + 1)-REMPI via the $3p^2A_2''$ Rydberg state [105]. *Upper inset*: Methyl cation signal intensity as a function of the 266 nm pump power. *Lower inset*: Methyl cation signal intensity as a function of the 333 nm probe laser power (both also measured at 2 ps pump-probe delay time, both in a double logarithmic representation). The slopes *n* of the linear fits to the data are indicated in the plots. (**b**) Temporal evolution of the methyl cation signal as a function of the pump-probe delay time (*open circles*). The *solid line* represents the best fit of a single exponential rise model to the data [68]

absorption continuum, can be accessed in the 170–270 nm spectral range with an absorption maximum around 200 nm [95, 110].

The excitation of methyl bromide to the A-band also leads to two dissociative channels: (1) the Br-channel giving rise to the formation of a methyl radical and a bromine atom in the ground state (Br($^2P_{3/2}$)), and (2) the Br*-channel giving rise to methyl and a bromine atom in the spin-orbit excited state (Br($^2P_{1/2}$)). Five dissociative electronic states are correlated with these two channels. Using the Mulliken notation [104, 111, 112], these states are labeled in ascending energy order $^3Q_2$, $^3Q_1$, $^3Q_{0+}$, $^3Q_{0-}$, and $^1Q_1$. The $^3Q_1$ and $^1Q_1$ states can be accessed from the ground state via single photon excitation in a perpendicular electric dipole transition and they adiabatically correlate with the Br-channel. The $^3Q_{0+}$ state can be accessed in a parallel transition by single photon excitation and it is correlated with the Br*−channel. The single photon excitation of the $^3Q_2$ and $^3Q_{0-}$ states is electric dipole forbidden. A curve crossing occurs between the $^1Q_1$ and $^3Q_{0+}$ states [113, 114] which is possible due to the different symmetries of these states. However, in contrast to the methyl iodide molecule, where the A-band absorption occurs mainly via a parallel transition to the $^3Q_{0+}$ state which correlates with I* (cf. Fig. 10.7c), in the case of methyl bromide, magnetic-circular-dichroism investigations show that the $^1Q_1$ state is more strongly populated than the $^3Q_1$ and $^3Q_{0+}$ states [115].

In order to clarify the initial excitation mechanism that eventually leads to the dissociation of methyl bromide adsorbed on the magnesia surface, the CH_3^+ yield at 2 ps pump-probe delay time was monitored as a function of the pump laser power. The result is displayed in the upper inset of Fig. 10.11a and clearly shows that the photodissociation process requires more than one single photon. The slope value of 1.8 ± 0.2 of a linear fit to the measured power dependence data in the double logarithmic plot indicates that the photodissociation is most likely initiated by two

pump photons. According to Ref. [113], a $^3A_1$ dissociative A-band state can be accessed near the C–Br equilibrium distance by two-photon excitation at 266 nm. When spin-orbit interactions are considered, this $^3A_1$ state gives rise to two states corresponding to $^3Q_0$, and $^3Q_1$, respectively. As discussed in detail previously [68], these states represent the most probable two-photon excitation channel of the CH_3Br molecule which lead to dissociation.

The emerging methyl radicals are subsequently detected via (2 + 1) REMPI at a wavelength of 333 nm. This is confirmed by the probe power dependence measurements shown in the lower inset of Fig. 10.11a. Similar to CH_3I/MgO, the initial coherent delay of $\Delta t_0 = 150 \pm 50$ fs of the methyl ion signal emerging from CH_3Br (Fig. 10.11b) is proposed to reflect the liberation of the methyl fragments from the molecular force field and from the force field of the magnesia surface. The subsequent growth of the methyl signal with a time constant of $\tau = 320 \pm 60$ fs is consequently interpreted as the average lifetime of all trajectories leading form the initial excitation to the release of the methyl fragment.

Surprisingly, the time constant of $\tau = 320 \pm 60$ fs for the rise of the CH_3^+ signal in Fig. 10.11b is considerably shorter compared to the one obtained for the exponential rise of the methyl cation signal in the case of CH_3I photodissociation on MgO (680 ± 50 fs, see previous section). As mentioned above, no direct measurement of the CH_3Br photodissociation time has been performed until now. However, based on the method provided by Sander and Wilson [116] to calculate the lifetime of a dissociative state using the anisotropy parameter β which is deduced from the angular distribution of the photofragments, Gougousi et al. [117] estimated that the lifetime of the CH_3Br A-band is 120 ± 40 fs. If this method is applied to CH_3I, an upper limit for the lifetime of the A-band of 70 fs can be estimated [118]. This means that in the gas-phase the methyl bromide A-band photodissociation takes longer than the methyl iodide A-band photodissociation. However, in the present investigation the methyl bromide appears to photodissociate faster than methyl iodide, if adsorbed on MgO.

In Sect. 10.1.3, the investigations of Polanyi and coworkers of the 193 nm photodissociation of CH_3Br adsorbed on a bulk MgO(100) surface by means of angular resolved time-of-flight quadrupole mass spectrometry have been discussed [36]. This experiment indicates that the emerging methyl photofragments can be either directly liberated into the gas-phase (DIR CH_3 fragments; see Fig. 10.4) or they can lose a significant part of their total kinetic energy released from the A-band photodissociation in a collision process with neighboring molecules (IND(1) and IND(2) CH_3 fragments; see Fig. 10.4). These latter indirect mechanisms represent the dominant methyl release channel in this system in which the escaping methyl fragments have to experience a collision with adjacent molecules due to an adsorption geometry in which the C–Br axis is nearly parallel to the surface (cf. inset in Fig. 10.3b and Fig. 10.4b). These results provide the basis for a reasonable explanation why the methyl photofragment appearance time on MgO, measured in our experiment, is much faster for methyl bromide (320 ± 60 fs) compared to methyl iodide (680 ± 50 fs) despite of the theoretical prediction of a longer dissociation time for free CH_3Br.

The different appearance times can be connected to the different adsorption geometries of the methyl halide molecules on the magnesia surface. As discussed in Sect. 10.1.2 methyl iodide molecules are proposed to be adsorbed with the methyl-end heading toward the surface. This leads to a trapping of the methyl group between the MgO surface and the I atom subsequent to the photodissociation and the liberation of the methyl fragment from the surface takes a considerable time in the case of methyl iodide. In contrast, according to Polanyi and coworkers [36], the methyl bromide molecules are adsorbed with their C–Br axis almost parallel to the MgO substrate. Therefore, the methyl photofragment can escape much easier and faster, suffering in most cases only one collision with the adjacent molecule, which would explain the faster appearance time of 320 ± 60 fs for CH_3Br. This time constant thus reflects the integral methyl desorption dynamics represented by the three reaction channels illustrated in Fig. 10.4b. The distinction of the DIR, IND(1), and IND(2) mechanisms in the time-resolved experiment should now be possible due to the clearly distinguishable translational energy of the emerging methyl fragments (see Fig. 10.4a) and work is in progress to apply surface pump-probe fs-laser mass spectrometry in the velocity-resolution mode (cf. Fig. 10.10) to accomplish this task.

10.3.2 Bimolecular Surface Reactions

The formation of a new chemical bond in, or between, molecules that are attached to a substrate constitutes the elementary step of a bimolecular surface chemical reaction and also occurs on the ultrafast timescale of nuclear motion. The comprehension of the involved molecular dynamics is fundamental to the perception of chemical reaction mechanisms on surfaces of, e.g., catalytic materials [1]. The key to a molecular level insight of a bimolecular reactive encounter, however, is the knowledge about the structure and the dynamics of the transition state of the reaction [3, 4].

Employing the model system of methyl iodide adsorbed at sub-monolayer coverages on a magnesia ultrathin film it could be demonstrated that with the technique of surface pump-probe fs-laser mass spectrometry it is indeed possible to directly probe the transition state and the product formation dynamics of a bimolecular surface reaction by time-, mass-, and velocity-resolved multi-photon ionization on the surface [27]. The starting configuration is again obtained by a well defined reactant adsorption geometry that represents the initial ‘collision complex’ of the reactive bimolecular encounter as proposed by Polanyi (see Sect. 10.1.1 [4, 5, 10]). In the following it will be shown that in this way unprecedented insight into the elementary steps of a complex bimolecular surface chemical reaction mechanism can be obtained.

Methyl iodide adsorption layers were prepared under similar conditions as described in the previous section at which the mass spectrum displayed in Fig. 10.8 was obtained at a pump-probe delay time of 130 fs. If the delay time was changed to 2 ps, the mass spectrum shown in Fig. 10.12a could be recorded (photoexcitation with 266 nm, 1 mW/cm^2, and multi-photon ionization detection with 333 nm,

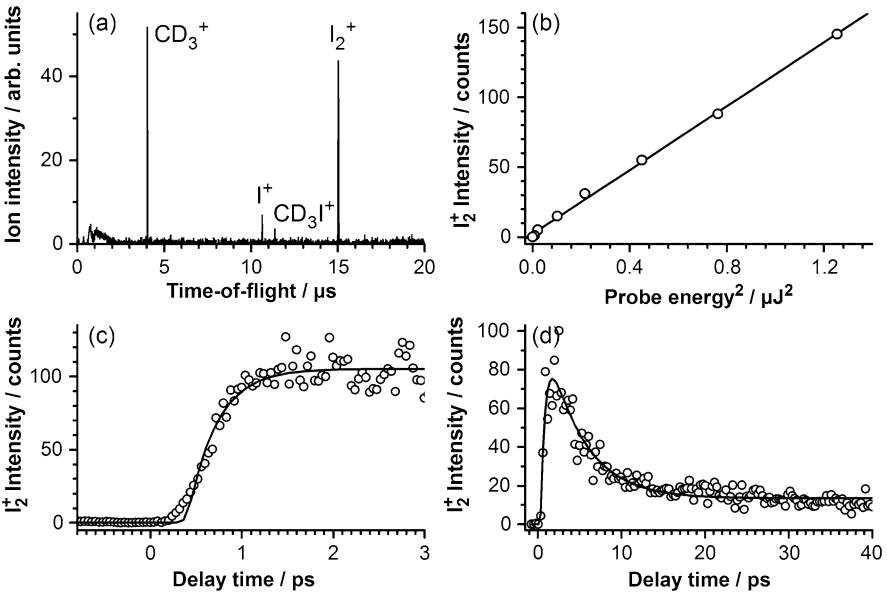

Fig. 10.12 (**a**) Time-of-flight fs-laser desorption/ionization mass spectrum obtained from 0.25 ML of (deuterated) methyl iodide on MgO/Mo(100). The conditions are comparable to those of Fig. 10.8, however, the spectrum was recorded at a pump-probe delay time of 2 ps. (**b**) Intensity of the I_2 signal as a function of the squared probe pulse energy at 2 ps delay time. *Open circles* represent the experimental data; the *solid line* is a linear fit to the data. The *bottom graphs* display the time-resolved signal intensity of I_2 at early delay times (**c**) and up to 40 ps pump-probe delay (**d**). *Open circles* represent the experimental data; the *solid lines* are fits of a kinetic exponential rise and decay model (please see text for more details) [27]

600 mW/cm^2). In addition to the signals observed at 130 fs delay time (Fig. 10.8), a pronounced peak of molecular iodine, I_2^+, is apparent in Fig. 10.12a. This signal exhibits a quadratic probe laser power dependence as can be seen from Fig. 10.12b. This indicates that the I_2^+ signal is due to a two-photon ionization process, which will be important to the interpretation below.

The temporal evolution of the I_2^+ mass signal is displayed in Fig. 10.12c and d. Iodine molecules are detected after a pump-probe delay time of about 200 fs. Subsequently, the signal rises exponentially and reaches its maximum value at 1.2 ps. The fit of an exponential growth model (convoluted with the pump-probe autocorrelation function, solid line in Fig. 10.12c) to the experimental data yields a rise time constant of $\tau_1(I_2) = 310 \pm 30$ fs. However, the signal only stays constant until a few ps and then decays again with a time constant of $\tau_2(I_2) = 5.0 \pm 0.3$ ps as can be seen from Fig. 10.12d.

The interpretation of these data is based on the respective (gas phase) potential energy curves of methyl iodide and molecular iodine as displayed in Fig. 10.13 [98, 106, 119]. It is again assumed that the weak interaction of the molecules with the insulating substrate does, to a first approximation, not influence the relevant potentials. Photoexcitation of adsorbed methyl iodide with 266 nm leads to the dis-

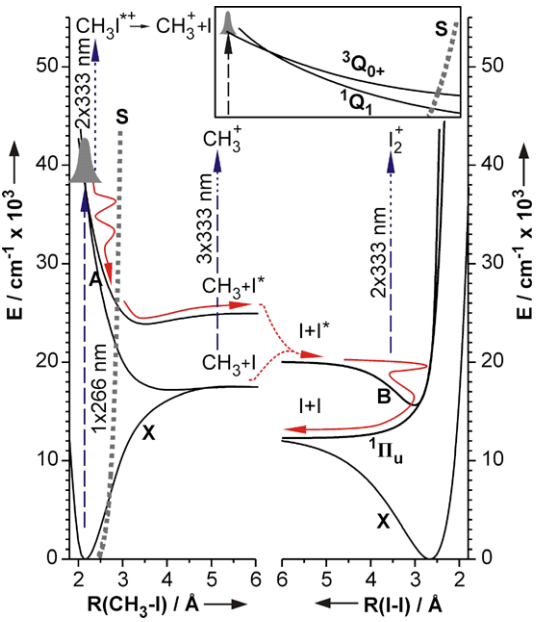

Fig. 10.13 Potentials of CH_3I (*left*) and I_2 (*right*) [98, 106, 119]. The *solid arrows* illustrate the propagation of the wave packet. The *dashed arrows* represent the excitation and the detection laser pulses (detection energies not drawn to scale). The potential S reflects the Lennard-Jones interaction between the methyl group and the magnesia surface [82]. The *inset* shows a magnification of the CH_3I–A-band excitation region [27]. Please compare also to Fig. 10.7c

sociative A-band states as detailed above (cf. Fig. 10.13, left hand side). Two of the thus generated I-atom fragments might now be assumed to recombine in order to form the observed I_2 molecules. This assumption is, however, contradicted by the measured laser power dependences. Most strikingly, the probe power dependence depicted in Fig. 10.12b shows that the I_2^+ signal is due to a two-photon ionization process. Yet, the X- and A-states of I_2 are both not accessible for two-photon ionization with 333 nm.

Therefore, it is most likely that the I_2^+ signal originates from the ionization of iodine molecules in the electronically excited B-state. The respective potential energy curves are displayed on the right hand side of Fig. 10.13 [119]. I_2(B) might be formed in a bimolecular reaction of emerging spin-orbit excited I* with ground state I atoms (indicated by the dashed arrow connecting the CD_3I with the I_2 potentials in Fig. 10.13). However, power dependent measurements of the I_2 signal also indicate the predominance of a single photon excitation (pump) mechanism for the bimolecular reaction [27]. In previous gas phase experiments with methyl iodide clusters, a four-center bimolecular reaction had been proposed to account for the observed I_2 formation [102]. In this mechanism two adjacent methyl iodide molecules act as reaction center with the photoexcitation leading to a cooperative nuclear motion of both C–I bonds via a transition state of the form $[CD_3–I^*–I–CD_3]^‡$ finally resulting in the elimination of I_2(B).

The transient data in Fig. 10.12c and d thus are interpreted to reflect the real-time dynamics of the bimolecular interaction of I* with I via a favorable surface-aligned geometry that enables the four-center transition state. The fastest release of I_2 molecules in this reaction is observed within 200 to 300 fs. The average time

constant for all trajectories leading from the bimolecular transition state to I_2 is represented by the 310 fs rise of the molecular iodine signal.

Molecular iodine is bound in the B-state and the radiative lifetime of the molecule in this state is on the order of microseconds [120]. However, the transient data in Fig. 10.12d exhibit a decay of the I_2^+ signal starting after several ps. This decay is attributed to a coupling between the B-state and a $^1\Pi_u$ dissociative state induced by the presence of the surface in the vicinity of the iodine molecule (see Fig. 10.13). Thus, the breaking of the $D_{\infty h}$ symmetry of I_2 at the surface leads to molecular predissociation on the ps timescale [121]. As a result, only ground state iodine atoms are released after several ps. Interestingly, this also provides a new mechanism for the previously observed pronounced and puzzling I^* quenching in surface photodissociation experiments (cf. Sect. 10.1.3 [71]).

Thus, the mass spectrometric detection of intermediates and products in a pump-probe scheme is able to reveal rich details of the bimolecular surface photoreaction dynamics. In this respect the influence of the insulating surface on the reaction dynamics can be shown to manifests itself in the unimolecular decomposition by (1) the alignment of the reactants prior to photoreaction, (2) the trapping of the dissociative transition state preventing direct decomposition as in the gas-phase and in this way (3) enhancing the possibility for a non-adiabatic transition of the wave packet through the conical intersection. Furthermore, the presence of the substrate (4) provides an additional energy dissipation pathway for the bimolecular reaction to proceed, and finally (5) leads to a breaking of the molecular symmetry of the I_2(B) state to enable predissociation and thus opening a new channel for I^* de-excitation at the surface.

Also in the case of a methyl bromide adsorption layer on a magnesia surface the bimolecular reaction of the emerging halide atoms could be detected [68] and a similar reaction dynamics as in the case of methyl iodide might be assumed. However, the assignment of the bimolecular dynamics, i.e. of the actual detection excitation pathways, remains so far to be confirmed by detailed laser power and wavelength dependent measurements.

10.4 Conclusion and Prospects

In this contribution it was demonstrated that fs-laser induced excitation of a surface-aligned molecular adsorbate layer on an oxide surface in conjunction with time delayed direct ionization and mass spectrometric detection of reaction products on the surface can provide detailed insight into the molecular surface reaction dynamics. As examples the photoreactions of methyl iodide and methyl bromide adsorbed on ultrathin MgO(100) films on Mo(100) have been studied. A pronounced difference in the appearance times of the methyl radical fragments was observed for the two different methyl halides. This observation was related to the different molecular adsorption structures on magnesia. Furthermore, the adsorption geometry on the surface also defined the alignment of the encounter complex for the observed bimolecular formation of the halide molecules I_2 and Br_2.

The findings presented here demonstrate the potential of the new experimental technique of surface pump-probe fs-laser mass spectrometry to reveal the detailed dynamics of a wide variety of bimolecular surface-aligned reactions. The unique possibility to measure directly the surface transition state and product formation dynamics is of importance to the revelation of even complex reaction mechanisms in surface chemistry and heterogeneous catalysis. In recent experiments the investigations were extended to reactions on metallic surfaces [122, 123] and oxide supported metal particles [92, 124]. Furthermore, future investigations will include different co-adsorbate molecules like O_2, N_2O and CO_2 in addition to the methyl halides. In this respect it could be shown most recently that the irradiation of co-adsorption layers of CH_3I and CH_3Br lead to the detection of IBr molecules. This result confirms that the observation of a reaction dynamics involving fragments from different adsorbates is indeed feasible [68].

Acknowledgement The research presented in this contribution was supported by the Deutsche Forschungsgemeinschaft (DFG), the Fonds der Chemischen Industrie (FCI), and by Deutscher Akademischer Austauschdienst (DAAD).

References

1. G. Ertl, Reactions at surfaces: from atoms to complexity (Nobel lecture). Angew. Chem., Int. Ed. Engl. **47**, 3524–3535 (2008)
2. G. Ertl, *Reactions at Solid Surfaces* (Wiley, New York, 2009)
3. R.D. Levine, R.B. Bernstein, *Molecular Reaction Dynamics* (Oxford University Press, Oxford, 1988)
4. J.C. Polanyi, A.H. Zewail, Direct observation of the transition state. Acc. Chem. Res. **28**, 119–132 (1995)
5. Z. Ning, J.C. Polanyi, Surface aligned reaction. J. Chem. Phys. **137**, 091706 (2012)
6. S. Buelow, G. Radhakrishnan, J. Catanzarite, C. Wittig, The use of van der Waals forces to orient chemical reactants: the $H + CO_2$ reaction. J. Chem. Phys. **83**, 444–445 (1985)
7. S. Buelow, M. Noble, G. Radhakrishnan, H. Reisler, C. Wittig, G. Hancock, The role of initial conditions in elementary gas-phase processes involving intermediate "complexes". J. Phys. Chem. **90**, 1015–1027 (1986)
8. N.F. Scherer, C. Sipes, R.B. Bernstein, A.H. Zewail, Real-time clocking of bimolecular reactions: application to $H + CO_2$. J. Chem. Phys. **92**, 5239–5259 (1990)
9. J.C. Polanyi, H. Rieley, Photochemistry in the adsorbed state, in *Dynamics of Gas-Surface Interactions*, ed. by C.T. Rettner, M.N.R. Ashfold (Royal Chem. Soc., London, 1991), p. 329
10. J.C. Polanyi, Y. Zeiri, Dynamics of adsorbate photochemistry, in *Laser Spectroscopy and Photochemistry on Metal Surfaces*, ed. by H.-L. Dai, W. Ho (World Scientific, Singapore, 1995), p. 1241
11. A.H. Zewail, Femtochemistry: atomic-scale dynamics of the chemical bond. J. Phys. Chem. A **104**, 5660–5694 (2000)
12. C. Frischkorn, M. Wolf, Femtochemistry on metal surfaces: nonadiabatic reaction dynamics. Chem. Rev. **106**, 4207–4233 (2006)
13. H.-L. Dai, W. Ho (eds.), *Laser Spectroscopy and Photochemistry on Metal Surfaces* (World Scientific, Singapore, 1995)
14. H. Petek, S. Ogawa, Surface femtochemistry: observation and quantum control of frustrated desorption of alkali atoms from noble metals. Annu. Rev. Phys. Chem. **53**, 507–531 (2002)

15. W. Ho, Femtosecond laser-induced dynamical quantum processes on solid surfaces (DQPSS). Surf. Sci. **363**, 166–178 (1996)
16. J.A. Misewich, A. Kalamarides, T.F. Heinz, U. Hoefer, M.M.T. Loy, Vibrationally assisted electronic desorption: femtosecond surface chemistry of O_2/Pd(111). J. Chem. Phys. **100**, 736–739 (1994)
17. P. Szymanski, A.L. Harris, N. Camillone III., Efficient subpicosecond photoinduced surface chemistry: the ultrafast photooxidation of CO on palladium. J. Phys. Chem. C **112**, 15802–15808 (2008)
18. M. Bonn, S. Funk, C. Hess, D.N. Denzler, C. Stampfl, M. Scheffler, M. Wolf, G. Ertl, Phonon-versus electron-mediated desorption and oxidation of CO on Ru(0001). Science **285**, 1042–1045 (1999)
19. J.A. Prybyla, H.W.K. Tom, G.D. Aumiller, Femtosecond time-resolved surface reaction: desorption of CO from Cu(111) in $<$ 325 fsec. Phys. Rev. Lett. **68**, 503–506 (1992)
20. I.M. Lane, D.A. King, Z.-P. Liu, H. Arnolds, Real-time observation of nonadiabatic surface dynamics: the first picosecond in the dissociation of NO on iridium. Phys. Rev. Lett. **97**, 186105 (2006)
21. P. Szymanski, S. Garrett-Roe, C.B. Harris, Time- and angle-resolved two-photon photoemission studies of electron localization and solvation at interfaces. Prog. Surf. Sci. **78**, 1–39 (2005)
22. C. Reuss, I.L. Shumay, U. Thomann, M. Kutschera, M. Weinelt, T. Fauster, U. Hofer, Control of the dephasing of image-potential states by CO adsorption on Cu(100). Phys. Rev. Lett. **82**, 153–156 (1999)
23. M. Bauer, C. Lei, K. Reak, R. Tobey, J. Gland, M.M. Murnane, H.C. Kapteyn, Direct observation of surface chemistry using ultrafast soft-X-ray pulses. Phys. Rev. Lett. **87**, 025501 (2001)
24. C.D. Lindstrom, X.-Y. Zhu, Photoinduced electron transfer at molecule-metal interfaces. Chem. Rev. **106**, 4281–4300 (2006)
25. A. Foehlisch, P. Feulner, F. Hennies, A. Fink, D. Menzel, D. Sanchez-Portal, P.M. Echenique, W. Wurth, Direct observation of electron dynamics in the attosecond domain. Nature **436**, 373–376 (2005)
26. M.E. Vaida, P.E. Hindelang, T.M. Bernhardt, Femtosecond real-time probing of transition state dynamics in a surface photoreaction: methyl desorption from CH_3I on MgO(100). J. Chem. Phys. **129**, 011105 (2008)
27. M.E. Vaida, T.M. Bernhardt, Surface-aligned femtochemistry: real-time dynamics of photoinduced I_2 formation from CD_3I on MgO(100). ChemPhysChem **11**, 804–807 (2010)
28. M.E. Vaida, T.M. Bernhardt, Surface pump-probe femtosecond-laser mass spectrometry: time-, mass-, and velocity-resolved detection of surface reaction dynamics. Rev. Sci. Instrum. **81**, 104103 (2010)
29. E.B.D. Bourdon, J.P. Cowin, I. Harrison, J.C. Polanyi, J. Segner, C.D. Stanners, P.A. Young, UV photodissociation and photodesorption of adsorbed molecules. 1. Methyl bromide on lithium fluoride(001). J. Phys. Chem. **88**, 6100–6103 (1984)
30. E.B.D. Bourdon, P. Das, I. Harrison, J.C. Polanyi, J. Segner, C.D. Stanners, R.J. Williams, P.A. Young, Photodissociation, photoreaction and photodesorption of adsorbed species, Part 2. CH_3Br and H_2S on LiF(001). Faraday Discuss. **82**, 343–358 (1986)
31. I. Harrison, J.C. Polanyi, P.A. Young, Photochemistry of adsorbed molecules. IV. Photodissociation, photoreaction, photoejection, and photodesorption of H_2S on LiF(001). J. Chem. Phys. **89**, 1498–1523 (1988)
32. W.D. Mieher, W. Ho, Photochemistry of oriented molecules coadsorbed on solid surfaces: the formation of $CO_2 + O$ from photodissociation of O_2 coadsorbed with CO on Pt(111). J. Chem. Phys. **91**, 2755–2756 (1989)
33. E.B.D. Bourdon, C.-C. Cho, P. Das, J.C. Polanyi, C.D. Stanners, G.-Q. Xu, Photochemistry of adsorbed molecules. IX. Ultraviolet photodissociation and photoreaction of HBr on LiF(001). J. Chem. Phys. **95**, 1361–1377 (1991)

34. V.J. Barclay, D.B. Jack, J.C. Polanyi, Y. Zeiri, Dynamics of surface-aligned photochemistry (theory). 2. Localized h-atom scattering in the HBr(ad)/LiF(001) + hν system. J. Chem. Phys. **97**, 9458–9467 (1992)
35. J. Kiss, D.J. Alberas, J.M. White, Surface-aligned photoreaction of DBr with C_2H_4 on Pt(111). J. Am. Chem. Soc. **114**, 10486–10492 (1992)
36. S.J. Garrett, D.V. Heyd, J.C. Polanyi, Photochemistry of adsorbed molecules. XVIII. Photodissociation and exchange reaction in CH_3Br/MgO(001) at 193 nm. J. Chem. Phys. **106**, 7847–7855 (1997)
37. T. Yamanaka, Y. Inoue, T. Matsushima, An aligned oxidation of carbon monoxide induced by 193 nm irradiation on platinum(113). Chem. Phys. Lett. **264**, 180–185 (1997)
38. J.B. Giorgi, R. Kühnemuth, J.C. Polanyi, Surface-aligned photochemistry: photolysis of HCl adsorbed on LiF(001) studied by Rydberg-atom time-of-flight spectroscopy. J. Chem. Phys. **110**, 598–605 (1999)
39. J.B. Giorgi, F.Y. Naumkin, J.C. Polanyi, S.A. Raspopov, N.S.K. Sze, Surface aligned photochemistry: photodissociation of Cl_2 and $Cl_2\cdots Cl$ adsorbed on LiF(001). J. Chem. Phys. **112**, 9569–9581 (2000)
40. J.B. Giorgi, R. Kühnemuth, J.C. Polanyi, Surface-aligned photochemistry: photodissociation of H_2S adsorbed on LiF(001) studied by Rydberg-atom time-of-flight spectroscopy. J. Chem. Phys. **113**, 807–814 (2000)
41. C.E. Tripa, J.T. Yates Jr., Surface-aligned reaction of photogenerated oxygen atoms with carbonmonoxide targets. Nature **398**, 591–593 (1999)
42. M. Kim, J.N. Hohman, Y. Cao, K.N. Houk, H. Ma, A.K.-Y. Jen, P.S. Weiss, Creating favorable geometries for directing organic photoreactions in alkanethiolate monolayers. Science **331**, 1312–1315 (2011)
43. S.-W. Hla, L. Bartels, G. Meyer, K.H. Rieder, Inducing all steps of a chemical reaction with the scanning tunneling microscope tip: towards single molecule engineering. Phys. Rev. Lett. **85**, 2777–2780 (2000)
44. S.W. Hla, G. Meyer, K.H. Rieder, Inducing single-molecule chemical reactions with a UHV-STM: a new dimension for nano-science and technology. Chem. Phys. Chem. **2**, 361–366 (2001)
45. P. Maksymovych, J.T. Yates Jr., Propagation of conformation in the surface-aligned dissociation of single CH_3SSCH_3 molecules on Au(111). J. Am. Chem. Soc. **128**, 10642 (2006)
46. K.R. Harikumar, J.C. Polanyi, A. Zabet-Khosousi, P. Czekala, H. Lin, W.A. Hofer, Directed long-range molecular migration energized by surface reaction. Nat. Chem. **3**, 400–408 (2011)
47. K. Huang, I.R. McNab, J.C. Polanyi, S.Y. Yang, Adsorbate alignment in surface halogenation: standing up is better than lying down. Angew. Chem., Int. Ed. Engl. **51**, 9061–9065 (2012)
48. J.-G. Lee, S.-H. Hong, J. Ahner, J.T. Yates Jr., Surface aligned ion-molecule reaction: direct observation of initial and final ion momenta. Phys. Rev. Lett. **89**, 253202 (2002)
49. J.-G. Lee, J.T. Yates Jr., Surface-aligned ion-molecule reaction on the surface of a molecular crystal $CD_3^+ + CD_3I \rightarrow C_2D_5^+ + DI$. J. Am. Chem. Soc. **126**, 13071–13078 (2004)
50. C. Akerlund, I. Zoric, B. Kasemo, A collision induced reaction: CO_2 production on O_2 and CO covered Pt(111). J. Chem. Phys. **104**, 7359–7362 (1996)
51. P. Maksymovych, D.C. Sorescu, K.D. Jordan, J.T. Yates Jr., Collective reactivity of molecular chains self-assembled on a surface. Science **322**, 1664–1667 (2008)
52. S. Dobrin, K.R. Harikumar, J.C. Polanyi, An STM study of the localized atomic reaction of 1, 2- and 1, 4-dibromobenzene at Si(111) $-$ 7 $\times$ 7. Surf. Sci. **561**, 11–24 (2004)
53. S. Dobrin, K.R. Harikumar, C.F. Matta, J.C. Polanyi, An STM study of the localized atomic reaction of 1, 2- and 1, 4-dibromoxylene with Si(111) $-$ 7 $\times$ 7. Surf. Sci. **580**, 39–50 (2005)
54. H. Guo, J. Wei, J.C. Polanyi, S.Y. Yang, Molecular dynamics of localized reaction, experiment and theory: methyl bromide on Si(111) $-$ 7 $\times$ 7. ACS Nano **2**, 699–706 (2008)
55. L. Leung, T. Lim, Z. Ning, J.C. Polanyi, Localized reaction at a smooth metal surface: p-diiodobenzene at Cu(110). J. Am. Chem. Soc. **134**, 9320–9326 (2012)

56. I.R. McNab, J.C. Polanyi, Patterned atomic reaction at surfaces. Chem. Rev. **106**, 4321–4354 (2006)
57. K.R. Harikumar, I.R. McNab, J.C. Polanyi, A. Zabet-Khosousi, W.A. Hofer, Imprinting self-assembled patterns of lines at a semiconductor surface, using heat, light, or electrons. Proc. Natl. Acad. Sci. USA **108**, 950–955 (2011)
58. D.P. Zhong, A.H. Zewail, Femtosecond real-time probing of reactions. 23. Studies of temporal, velocity, angular, and state dynamics from transition states to final products by femtosecond-resolved mass spectrometry. J. Phys. Chem. A **102**, 4031–4058 (1998)
59. R. de Nalda, J.G. Izquierdo, J. Durá, L. Bañares, Femtosecond multichannel photodissociation dynamics of CH_3I from the A band by velocity map imaging. J. Chem. Phys. **126**, 021101 (2007)
60. R. de Nalda, J. Durá, A. Garcia-Vela, J.G. Izquierdo, J. González-Vázquez, L. Bañares, A detailed experimental and theoretical study of the femtosecond A-band photodissociation of CH_3I. J. Chem. Phys. **128**, 244309 (2008)
61. J. Durá, R. De Nalda, J. Álvarez, J.G. Izquierdo, G.A. Amaral, L. Bañares, Femtosecond transition-state imaging of the A-band CH_3I photodissociation. Chem. Phys. Chem. **9**, 1245–1249 (2008)
62. J. Durá, R. de Nalda, G.A. Amaral, L. Bañares, Imaging transient species in the femtosecond A-band photodissociation of CH_3I. J. Chem. Phys. **131**, 134311 (2009)
63. L. Rubio-Lago, J.D. Rodrigues, A. García-Vela, M.G. Gonzàlez, G.A. Amaral, L. Bañares, A slice imaging and multisurface wave packet study of the photodissociation of CH_3I at 304 nm. Phys. Chem. Chem. Phys. **13**, 8186–8194 (2011)
64. M.E. Vaida, T. Gleitsmann, R. Tchitnga, T.M. Bernhardt, Femtosecond-laser photoemission spectroscopy of Mo(100) covered by ultrathin MgO(100) films of variable thickness. J. Phys. Chem. C **113**, 10264–10268 (2009)
65. M.-C. Wu, J.S. Corneille, C.A. Estrada, J.-W. He, D.W. Goodman, Synthesis and characterization of ultra-thin MgO films on Mo(100). Chem. Phys. Lett. **182**, 472–478 (1991)
66. U. Heiz, F. Vanolli, L. Trento, W.-D. Schneider, Chemical reactivity of size-selected supported clusters: an experimental setup. Rev. Sci. Instrum. **68**, 1986–1994 (1997)
67. M. Sterrer, E. Fischbach, T. Risse, H.-J. Freund, Geometric characterization of a singly charged oxygen vacancy on a single-crystalline MgO(001) film by electron paramagnetic resonance spectroscopy. Phys. Rev. Lett. **94**, 186101 (2005)
68. M.E. Vaida, T.M. Bernhardt, Surface-aligned femtochemistry: photoinduced reaction dynamics of CH_3I and CH_3Br on MgO(100). Faraday Discuss. **157**, 437–449 (2012)
69. V.P. Holbert, S.J. Garrett, J.C. Bruns, P.C. Stair, E. Weitz, A novel method for determining absolute coverages by temperature programmed desorption with application to the adsorption of CH_3I on MgO(100). Surf. Sci. **314**, 107–113 (1994)
70. D.H. Fairbrother, K.A. Trentelman, P.G. Strupp, P.C. Stair, E. Weitz, Orientation of methyliodide adsorbed on MgO(100)—results from 257 nm photodissociation studies. J. Vac. Sci. Technol. A **10**, 2243–2247 (1992)
71. K.A. Trentelman, D.H. Fairbrother, P.G. Strupp, P.C. Stair, E. Weitz, 257 nm photoinduced chemistry of methyl iodide adsorbed on MgO(100). J. Chem. Phys. **96**, 9221–9232 (1992)
72. S.J. Garrett, D.V. Heyd, J.C. Polanyi, Photochemistry of adsorbed molecules. XVII. Photodissociation at 193 nm of CH_3Br adsorbed on LiF(001) and NaCl(001). J. Chem. Phys. **106**, 7834–7846 (1997)
73. J. Kutzner, G. Lindeke, K.H. Welge, D. Feldmann, Dissociative desorption from CH_3I by ultraviolet-laser radiation. J. Chem. Phys. **90**, 548–555 (1989)
74. K.A. Trentelman, D.H. Fairbrother, P.C. Stair, P.G. Strupp, E. Weitz, A photofragment spectrometer for studying photodissociation of molecules adsorbed on surfaces: the 257 nm photolysis of CD_3I on MgO(100). J. Vac. Sci. Technol. A **9**, 1820–1822 (1991)
75. D.H. Fairbrother, K.A. Briggman, P.C. Stair, E. Weitz, Molecular orientation and surface morphology in methyl iodide films grown on MgO(100) probed by photodissociation. J. Phys. Chem. **98**, 13042–13049 (1994)

76. D.H. Fairbrother, K.A. Briggman, P.C. Stair, E. Weitz, The role of adsorbate structure in the photodissociation dynamics of adsorbed species: methyl iodide/MgO(100). J. Chem. Phys. **102**, 7267–7276 (1995)
77. K.A. Briggman, P.C. Stair, E. Weitz, Surface residence time measurements of transient methyl radicals. Chem. Phys. Lett. **334**, 1–6 (2001)
78. H. Guo, G.C. Schatz, A mechanism for the quenching of I^* in photodissociation of methyl iodide adsorbed on a MgO surface. Chem. Phys. Lett. **184**, 245–250 (1991)
79. J.Y. Fang, H. Guo, Multiconfiguration time-dependent Hartree studies of the CH_3I/MgO photodissociation dynamics. J. Chem. Phys. **101**, 5831–5840 (1994)
80. J.V. Setzler, Z.H. Huang, H. Guo, Theoretical modeling of photodissociation dynamics of CH_3I on MgO(001). J. Chem. Phys. **103**, 4300–4311 (1995)
81. M.I. McCarthy, R.B. Gerber, K.A. Trentelman, P. Strupp, D.H. Fairbrother, P.C. Stair, E. Weitz, Photodissociation dynamics of CH_3I adsorbed on MgO(100)—theory and experiment. J. Chem. Phys. **97**, 5168–5176 (1992)
82. J.-Y. Fang, H. Guo, Four-dimensional quantum dynamics of the CH_3I/MgO photodissociation. Chem. Phys. Lett. **235**, 341–346 (1995)
83. F.L. Tabares, E.P. Marsh, G.A. Bach, J.P. Cowin, Laser photofragmentation and photodesorption of physisorbed CH_3Br on lithium fluoride. J. Chem. Phys. **86**, 738–744 (1987)
84. I. Harrison, J.C. Polanyi, P.A. Young, Photochemistry of adsorbed molecules. III. Photodissociation and photodesorption of CH_3Br adsorbed on LiF(001). J. Chem. Phys. **89**, 1475–1497 (1988)
85. Z.-H. Huang, H. Guo, Dynamical simulations of the photodissociation of CH_3Br on a LiF(001) surface. J. Chem. Phys. **97**, 2110–2118 (1992)
86. G.N. Robinson, N. Camillone III, P.A. Rowntree, G.-Y. Liu, J. Wang, G. Scoles, Low energy helium diffraction studies of CH_3Br overlayers physisorbed on C(0001), NaCl(001), and LiF(001) surfaces. J. Chem. Phys. **96**, 9212–9220 (1992)
87. D.V. Heyd, E.T. Jensen, J.C. Polanyi, Photochemistry of adsorbed molecules. XIV. Photoejection of CH_3X (X=Cl, Br) from CH_3Br/LiF(001). J. Chem. Phys. **103**, 461–464 (1995)
88. N. Camillone III, K.A. Kahn, P.J. Lasky, L. Wu, J.E. Moryl, R.M. Osgood Jr., The wavelength dependence of photoinduced hot electron dissociative attachment to methyl bromide adsorbed on gallium arsenide (110). J. Chem. Phys. **109**, 8045–8057 (1998)
89. N. Camillone III, K.A. Khan, J.A. Yarmoff, R.M. Osgood Jr., Surface-reconstruction-switched adsorbate photofragmentation dynamics. Phys. Rev. Lett. **87**, 056101 (2001)
90. S. Dobrin, X. Lu, F.Y. Naumkin, J.C. Polanyi, S.Y. Yang, Imprinting Br-atoms at Si(111) from a SAM of CH_3Br(ad) with pattern retention. Surf. Sci. **573**, L363–L368 (2004)
91. R. Osgood, Photoreaction dynamics of molecular adsorbates on semiconductor and oxide surfaces. Chem. Rev. **106**, 4379–4401 (2006)
92. M.E. Vaida, T.M. Bernhardt, Adsorption and photodissociation dynamics of methyl iodide on magnesia supported gold nano-particles. Eur. Phys. J. D **52**, 119–122 (2009)
93. W.C. Wiley, I.H. McLaren, Time-of-flight mass spectrometer with improved resolution. Rev. Sci. Instrum. **26**, 1150–1157 (1955)
94. D. Zhong, T.M. Bernhardt, A.H. Zewail, Femtosecond real-time probing of reactions. 24. Time, velocity and orientation mapping of the dynamics of dative bonding in bimolecular electron transfer reactions. J. Phys. Chem. A **103**, 10093–10117 (1999)
95. W.S. Felps, K. Rupnik, S.P. McGlynn, Electronic spectroscopy of the cyanogen halides. J. Phys. Chem. **95**, 639–656 (1991)
96. G. Li, H.J. Hwang, State-to-state correlated study of CD_3I photodissociation at 266 and 304 nm. J. Chem. Phys. **124**, 244306 (2006)
97. C. Hu, S. Pei, Y.-L. Chen, K. Liu, Photoelectron imaging of atomic iodine following A-band photolysis of CH_3I. J. Phys. Chem. A **111**, 6813–6821 (2007)
98. A.B. Alekseyev, H.-P. Liebermann, R.J. Buenker, S.N. Yurchenko, An ab initio study of the CH_3I photodissociation. I. Potential energy surfaces. J. Chem. Phys. **126**, 234102 (2007)
99. A.B. Alekseyev, H.-P. Liebermann, R.J. Buenker, An ab initio study of the CH_3I photodissociation. II. Transition moments and vibrational state control of the I^* quantum yields.

J. Chem. Phys. **126**, 234103 (2007)
100. J.L. Knee, L.R. Khundkar, A.H. Zewail, Picosecond monitoring of a chemical reaction in molecular beams: photofragmentation of $R - I \rightarrow R^{\ddagger} + I$. J. Chem. Phys. **83**, 1996–1998 (1985)
101. L.R. Khundkar, A.H. Zewail, Picosecond MPI mass spectrometry of CH_3I in the process of dissociation. Chem. Phys. Lett. **142**, 426–432 (1987)
102. D.P. Zhong, P.Y. Cheng, A.H. Zewail, Bimolecular reactions observed by femtosecond detachment to aligned transition states: inelastic and reactive dynamics. J. Chem. Phys. **105**, 7864–7867 (1996)
103. A. García-Vela, L. Bañares, Wave packet calculations on the effect of the femtosecond pulse width in the time-resolved photodissociation of CH_3I in the A-band. Phys. Chem. Chem. Phys. **13**, 2228–2236 (2011)
104. R.S. Mulliken, Intensities in molecular electronic spectra. X. Calculations on mixed-halogen, hydrogen halide, alkyl halide, and hydroxyl spectra. J. Chem. Phys. **8**, 382–395 (1940)
105. J.W. Hudgens, T.G. DiGiuseppe, M.C. Lin, Two photon resonance enhanced multiphoton ionization spectroscopy and state assignment of the methyl radical. J. Chem. Phys. **79**, 571–582 (1983)
106. M. Tadjeddine, J.P. Flament, C. Teichtel, Non-empirical spin-orbit calculation of the CH_3I ground state. Chem. Phys. **118**, 45–55 (1987)
107. K.Q. Lao, M.D. Person, P. Xayariboun, L.J. Butler, Evolution of molecular dissociation through an electronic curve crossing: polarized emission spectroscopy of CH_3I at 266 nm. J. Chem. Phys. **92**, 823–841 (1990)
108. G.N.A. Van Veen, T. Baller, A.E. De Vries, Photofragmentation of CH_3Br in the A band. Chem. Phys. **92**, 59–65 (1985)
109. W.P. Hess, D.W. Chandler, J.W. Thoman Jr., Photofragment imaging: the 205-nm photodissociation of CH_3Br and CD_3Br. Chem. Phys. **163**, 277–286 (1992)
110. L.T. Molina, M.J. Molina, F.S. Rowland, Ultraviolet absorption cross sections of several brominated methanes and ethanes of atmospheric interest. J. Phys. Chem. **86**, 2672–2676 (1982)
111. R.S. Mulliken, Nature of electronic levels in ultraviolet spectra of hydrogen and alkyl halides. Phys. Rev. **61**, 277–283 (1942)
112. R.S. Mulliken, E. Teller, Interpretation of the methyl iodide absorption bands near λ2000. Phys. Rev. **61**, 283–296 (1942)
113. C. Escure, T. Leininger, B. Lepetit, Ab initio study of methyl-bromide photodissociation in the A band. J. Chem. Phys. **130**, 244305 (2009)
114. D. Ajitha, M. Wierzbowska, R. Lindh, P.A. Malmqvist, Spin-orbit ab initio study of alkyl halide dissociation via electronic curve crossing. J. Chem. Phys. **121**, 5761–5766 (2004)
115. A. Gedanken, M.D. Rowe, Magnetic circular dichroism spectra of the methyl halides. Resolution of the $n \rightarrow \sigma^*$ continuum. Chem. Phys. Lett. **34**, 39–43 (1975)
116. R.K. Sander, K.R. Wilson, Double absorption photofragment spectroscopy: a new tool for probing unimolecular processes. J. Chem. Phys. **63**, 4242–4251 (1975)
117. T. Gougousi, P.C. Samartzis, T.N. Kitsopoulos, Photodissociation study of CH_3Br in the first continuum. J. Chem. Phys. **108**, 5742–5746 (1998)
118. M. Dzvonik, S. Yang, R. Bersohn, Photodissociation of molecular beams of aryl halides. J. Chem. Phys. **61**, 4408–4421 (1974)
119. K.P. Huber, G. Herzberg, *Molecular Spectra and Molecular Structure. IV. Constants of Diatomic Molecules* (Van Nostrand, New York, 1979)
120. G.A. Capelle, H.P. Broida, Lifetimes and quenching cross sections of $I_2(B^3\Pi_{0u}^+)^*$. J. Chem. Phys. **58**, 4212–4222 (1973)
121. E.D. Potter, Q. Liu, A.H. Zewail, Femtosecond reaction dynamics in macroclusters. Effect of solvation on wave-packet motion. Chem. Phys. Lett. **200**, 605–614 (1992)
122. M.E. Vaida, T.M. Bernhardt, Femtosecond two photon photoemission spectroscopy of methyl iodide adsorbed on a gold surface. AIP Conf. Proc. **1387**, 146–154 (2011)

123. M.E. Vaida, R. Tchitnga, T.M. Bernhardt, Femtosecond time-resolved photodissociation dynamics of methyl halide molecules on ultrathin gold films. Beilstein J. Nanotechnol. **2**, 618–627 (2011)
124. M.E. Vaida, T. Gleitsmann, R. Tchitnga, T.M. Bernhardt, Femtosecond-laser photoemission and photodesorption from magnesia supported gold clusters. Phys. Status Solidi B **247**, 1139–1146 (2010)

Chapter 11
Optical Diagnostics with Ultrafast and Strong Field Raman Techniques

Frederic Chaussard, Bruno Lavorel, Edouard Hertz, and Olivier Faucher

Abstract In this chapter, we will discuss some coherent techniques, namely Raman Induced Polarization Spectroscopy (RIPS) and femtosecond Coherent Raman Anti-Stokes Spectroscopy (fs-CARS). We will demonstrate their ability to be used as non-invasive optical diagnostic tools for temperature, density, or concentration measurements, as well as a means of testing collision induced energy transfer models (in a low field regime), and studying the so-called inhomogeneous lineshape effects that are particularly enhanced in the case of hydrogen. We will also show how molecular alignment achieved in a strong field regime can provide additional information about collisional relaxation processes. In all cases, a precise knowledge of the collisional effects is required, and so a general modeling of collisional relaxations will be detailed.

11.1 Introduction

Nonlinear coherent interactions of molecules with ultrashort laser pulses remain outstanding means to deduce the properties of gas-phase species (such as spectroscopic constants), as well as to get information about the environment of molecules. This is generally performed in a low field regime (perturbative regime). On the other hand, with intense laser fields, the spatial manipulation of molecules, especially molecular alignment and orientation, becomes possible, even under field-free conditions. Though seemingly different at first sight, these top-

F. Chaussard · B. Lavorel · E. Hertz · O. Faucher (✉)
Laboratoire Interdisciplinaire CARNOT de Bourgogne (ICB), UMR 6303 CNRS–Université de Bourgogne, BP 47870, 21078 Dijon Cedex, France
e-mail: olivier.faucher@u-bourgogne.fr

F. Chaussard
e-mail: frederic.chaussard@u-bourgogne.fr

B. Lavorel
e-mail: bruno.lavorel@u-bourgogne.fr

E. Hertz
e-mail: edouard.hertz@u-bourgogne.fr

R. de Nalda, L. Bañares (eds.), *Ultrafast Phenomena in Molecular Sciences*, Springer Series in Chemical Physics 107, DOI 10.1007/978-3-319-02051-8_11,

ics share in common similar techniques, which rely on the coherent superposition of rovibrational states, created by a very short laser pulse, resulting in quantum beats that can be recorded over time. The different dephasing processes experienced by the molecules affect the dynamics of such wave packets that can be tracked on a picosecond time scale in order to access to the relevant information.

In the first part of this chapter, we will discuss the use of such coherent techniques for temperature and concentration diagnostics in the low field limit by focusing on Raman Induced Polarization Spectroscopy (RIPS) [1, 2] and femtosecond Coherent Anti-Stokes Raman Spectroscopy (fs-CARS) [3]. The principle of the two techniques relies on the impulsive electronically non-resonant Raman excitation of a manifold of rotational states with an ultrashort polarized pump laser. In both cases, the signal contains information about the molecular structure, the density, the temperature, and the concentration. In the former, the initial vibrational level of the molecule (generally the ground one) is not changed and the rotational superposition of states leads to transient alignments appearing with a time period determined by the rotational constant B. In the latter, the signal arises from the interferences between rovibrational transitions [4] and exhibits recurrences with a time period, which in the case of Q-branch transitions is given by $T_r = 1/2\alpha_e$, where α_e is the first order rotational anharmonicity of the potential. RIPS is suitable for molecules such as N_2, CO_2, O_2, or N_2O with small rotational constants and for which rotational transitions are in the range of tenths of wavenumbers, whereas CARS will be preferred in the case of lighter molecules such H_2 with a larger rotational constant and a rotational spectrum spreading over a large wave number domain. Moreover, in contrast to RIPS or other techniques, CARS is able to probe not only the ground state, but also the dynamics of excited states.

Besides the oscillating contribution coming from the interferences, the molecules undergo collisions and collisional relaxation, which manifests itself on the signal by a time decay. Taking precisely into account these complex mechanisms is of great importance for temperature and pressure measurements.

The case of hydrogen will be discussed apart. Indeed, this molecule exhibits unusual behaviours due to the speed-dependence of the collisional parameters and requires specific models to describe the CARS time response.

In the second part of this chapter, we will explore the extension of short pulse induced alignment to dissipative environments. Although there are a real fundamental interest and practical applications of alignment in a dissipative medium, field-free alignment has been mainly studied in low-density conditions. We will show that performing measurement in a dissipative medium is a way to get independent information about the rotational population relaxation and the pure phase decoherence effects. In this context, a quantum mechanical density matrix formalism, using the Liouville equation and the relaxation matrix, will be described. Results obtained on the CO_2 molecule in mixture with Ar at room temperature will be presented.

11.2 Optical Diagnostic by Means of Femtosecond Spectroscopy

11.2.1 Temperature and Concentration Measurement in Gas Mixtures Using Rotational Coherence Spectroscopy Techniques

11.2.1.1 Raman Induced Polarization Spectroscopy (RIPS)

Principles In a RIPS experiment, the principle of the measurement relies on the observation of the depolarization experienced by a weak probe pulse, due to the birefringence resulting from the alignment rephasing of the molecules induced by the pump pulse. In a homodyne detection scheme, the detected RIPS signal is given by [1, 2]

$$I \propto \int_{-\infty}^{+\infty} \left|E_{\mathrm{s}}(t)\right|^2 dt, \tag{11.1}$$

with $E_{\mathrm{s}}(t)$ being the signal electric field. Its envelope is directly proportional to the third order nonlinear polarization $P^{(3)}(t)$, and can be written as [1, 2, 5]

$$E_{\mathrm{s}}(t) \propto \omega P^{(3)}(t) \propto \omega E_{\mathrm{d}}(t) \int_{-\infty}^{+\infty} \left|E_{\mathrm{p}}(\tau)\right|^2 R(t-\tau) d\tau. \tag{11.2}$$

In this equation, $R(t-\tau)$ is the rotational molecular response, $E_{\mathrm{d}}(t)$ the probe time envelope, $E_{\mathrm{p}}(\tau)$ the pump electric field, and ω the pulsation of both electric fields.

The rotational nonlinear response $R(t-\tau)$ of a given linear molecule i in a mixture of n molecules can be expressed as

$$R_i(t-\tau) \propto N_i \sum_{J_i} \Delta\alpha_i^2 (\rho_{J_i} - \rho_{J_i'}) g_{J_i} \frac{(J_i+1)(J_i+2)}{(2J_i+3)} \exp\left[-\gamma_{J_i}(t-\tau)\right] \times \sin\left[\omega_{J_i}(t-\tau)\right] \tag{11.3}$$

when absorption is neglected.

In this expression, N_i is the partial gas density, $\Delta\alpha_i$ is the difference between the polarizabilities along the molecular symmetry axis and along any axis perpendicular to the former ($\Delta\alpha_i = \alpha_{||} - \alpha_{\perp}$), J_i and J_i' are the rotational quantum numbers ($\Delta J = J_i' - J_i = 2$ for a S-branch Raman transition), $\rho_{J_i} = \exp(-E_{J_i}/T)/Q_i$ the population density with E_{J_i} being the rotational energy and Q_i the rotational partition function, and g_{J_i} is the nuclear spin degeneracy factor. ω_{J_i} is the frequency of the Raman S-branch transition given by $\omega_{J_i} = 4\pi B_i(2J_i+3)$ (with B_i the rotational constant of the vibrational level in which the superposition state is excited) when the centrifugal distortion is neglected, which can be no longer the case at high temperature if accurate calculations are needed. γ_{J_i} is the linewidth of the mentioned

transition, which can be described by the usual linear mixing rule for a mixture of n molecules

$$\gamma_{J_i} = \sum_{k=1}^{n} c_k \gamma_{J_i}^{k-i} \tag{11.4}$$

where c_k are the mole fractions of molecules k, $\gamma_{J_i}^{i-i}$ are the self-perturbed linewidths, and $\gamma_{J_i}^{k-i}$ are the linewidths of molecule i perturbed by molecule k.

As it can be seen in Eq. (11.3), the signal measured in a gas mixture is the sum of each component contributions (consisting in series of transients) whose amplitudes are proportional to the square anisotropy polarizability $\Delta\alpha_{J_i}$ and their concentrations N_i. The latter can thus be deduced from the experimental total signal, as soon as the anisotropy polarizabilities $\Delta\alpha_i$ are known, whereas the temperature can be determined thanks to the signal dependence versus the population distribution and linewidth parameters.

Accidental temporal coincidences between transients of two or more molecules due to the value of their molecular constants can exist and lead to macroscopic interferences, which exhibit a more sensitive shape with respect to the concentration [6]. When no such overlaps occur, it is still possible to induce them by using a multiple pump pulses sequence and tuning the delay between these pulses so as to improve the concentration dependence on the resulting transient [7].

In order to calculate the RIPS signal using Eqs. (11.1)–(11.3), the values of collisional linewidths γ_J are needed. These ones are the diagonal elements of the real part of the relaxation matrix W, whereas the off-diagonal elements $k_{JJ'}$ describe the coupling of the lines through rotational energy transfer. Such transfers are important when the pressure is increasing and one observes then the so-called line-mixing effect, which results in the fact that in the frequency domain the lineshape is not the sum of individual lines. The relaxation matrix is usually obtained by inversion of experimental or calculated linewidths with fitting or scaling laws. There exist several relaxation models to do so, but one of the most suitable is based on the energy corrected sudden (ECS) formalism [8]. Following this formalism, the relaxation matrix is written as

$$k_{JJ'} = \mathrm{Re}(W_{JJ'}) = \left(2J'+1\right)\frac{\rho_{J_>}}{\rho_J}\sum_L (2L+1)\begin{pmatrix} J & L & J' \\ 0 & 0 & 0 \end{pmatrix}^2 \frac{\Phi_L(\omega_{JJ'})^2}{\Phi_L(\omega_{L0})^2} Q_L, \tag{11.5}$$

with

$$\gamma_J = \mathrm{Re}(W_{JJ}) = -\sum_{J'\neq J} \mathrm{Re}(W_{JJ'}), \tag{11.6}$$

where (11.6) is known as the sum rule. In this expression, ρ_J is the population of the J level, $J_>$ is the upper value of (J, J'), L is the coupled angular momentum between J and J', Φ_L is an adiabatic correction term accounting for the finite collision duration [8], and $\begin{pmatrix} \cdots \\ \cdots \end{pmatrix}$ is a $3J$-symbol.

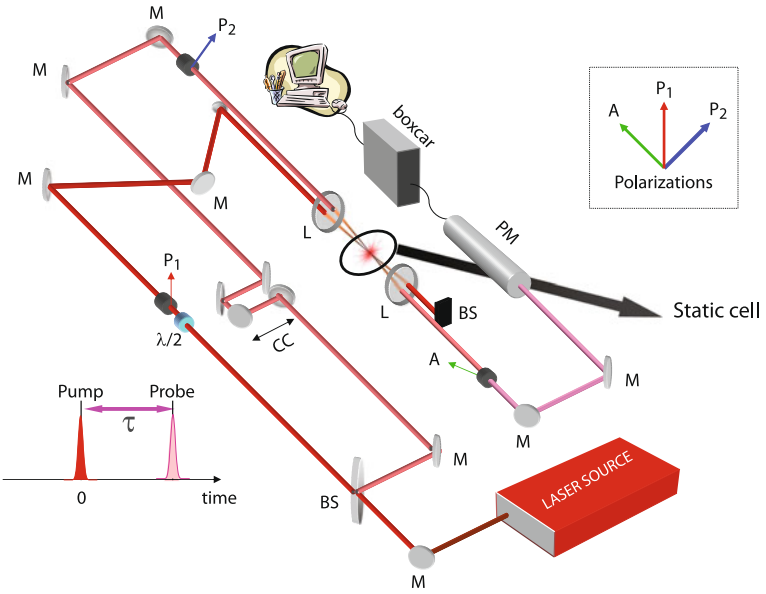

Fig. 11.1 Setup for RIPS experiment: P_i polarizers, M mirror, BS beam splitter, CC corner cube, L lens, PM photomultiplier. The polarizations of the beams are called back at the *top right*

Equation (11.5) also depends on a subset of state to state rates Q_L obtained either through experiments or modeled with semi-empirical scaling laws [9], among which the ECS-P law, using a polynomial law for the basis relaxation rates, or the ECS-E using an exponential law, or a mix of the two ECS-EP. In all cases, the expressions of the basis rates Q_L are parametrized and the values of these parameters are fitted on experimental or calculated values.

As it shows, RIPS can be a powerful tool to get accurate information about collisional relaxation, as it has been shown in the case of N_2 and CO_2 [5].

Experimental Procedure The experimental arrangement for RIPS measurements is a standard pump-probe set-up (Fig. 11.1). The pump and the probe beams are derived from a chirped pulsed amplified Ti:Sapphire femtosecond laser. They are both linearly polarized at 45° with respect to each other and are crossed at a small angle in the cell containing the studied species. The pump-probe delay is tuned thanks to a corner cube reflector mounted on a motorized stage. The probe signal is detected by a photomultiplier through an analyzer oriented at 90° with respect to the initial polarization of the probe beam.

Results As an example of the potential of RIPS for simultaneous temperature and concentration measurements, some results on CO_2–N_2 mixtures are shown [10]. Experiments were performed at three temperatures: 297, 423, and 573 K for pressures

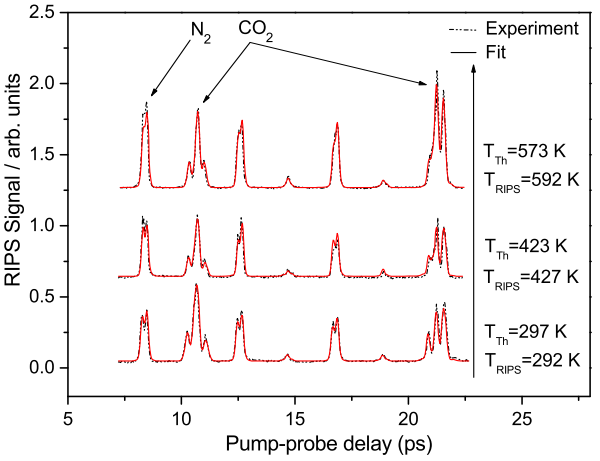

Fig. 11.2 RIPS signal as a function of pump-probe delay in a CO_2–N_2 mixture. The pressure was 1.21, 1.52, and 1.73 bar from *top* to *bottom*. The concentration of CO_2 was 0.1478, deduced from measurements of partial pressures

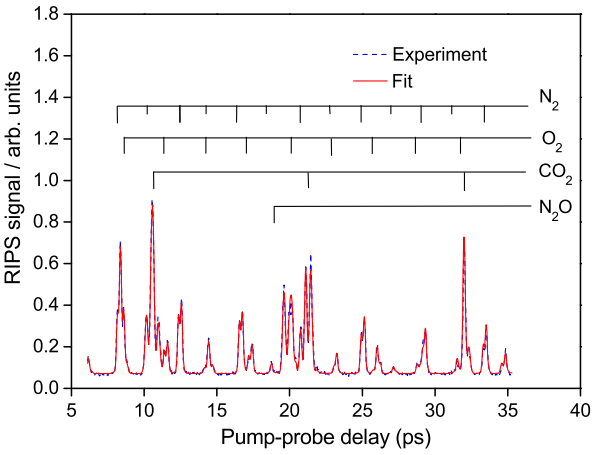

Fig. 11.3 RIPS signal as a function of pump-probe delay in N_2O–CO_2–O_2–N_2 mixture at 1.21 bar and room temperature. The fitted concentrations are $C(N_2O) = 0.058$, $C(CO_2) = 0.127$, $C(O_2) = 0.164$, and $C(N_2) = 0.637$, whereas the concentrations deduced from measurements of partial pressures are 0.064, 0.124, 0.162 and 0.635

below 2 bar, and CO_2 concentration of roughly 15 %. Figure 11.2 shows the comparison between the experimental and the theoretical signals. The temperature was compared to the temperature given by a thermocouple, and the actual concentration was obtained from partial pressures measurements. As it can be seen, the fitting procedure led to concentration and temperatures in good agreement with the actual ones.

Measurements of concentration in three and four molecular components mixtures have also been performed [11]. The case of N_2O–CO_2–O_2–N_2 is presented in Fig.11.3. The time response consists of many transients that have been assigned to the four components of the mixture. The fitted concentrations were in good agreement with the actual ones.

11.2.1.2 Coherent Anti-Stokes Raman Spectroscopy (CARS)

Principles In femtosecond Coherent Anti-Stokes Raman Spectroscopy, synchronized pump and Stokes pulses create a coherent superposition of Q-branch transitions ($\Delta J = 0$) between the ground and the first vibrational state ($\Delta v = 1$) of H_2. Each transition oscillates with a frequency $\omega_J = \Delta E_J/\hbar$, with ΔE_J the energy of the Raman transition. The time evolution of the coherent excitation is probed by a time-delayed third pulse, which under phase matching conditions completes the CARS scheme and leads to the anti-Stokes signal.

If the lineshapes are described by Lorentzian profiles in the frequency domain, the CARS signal at a given delay τ is given by [4, 12]:

$$I_{\mathrm{CARS}}(\tau) \propto \left| \sum_{J=0}^{J_{\max}} f_J \exp\left(\mathrm{i}\frac{\Delta E_J}{\hbar} - 2\pi\gamma_J \right)\tau \right|^2 . \tag{11.7}$$

The weighting coefficients f_J are proportional to the rotational population and to the convolution of the pump and the Stokes pulses in the frequency domain. For a diatomic molecule the Q-branch Raman transitions energies ΔE_J can be expressed by the molecular constants ω_e, $\omega_e x_e$, α_e, β_e, and the density shift coefficients.

As said above, when the pressure increases, line overlaps occur in the frequency domain, leading to the so-called *line-mixing* effect. As a consequence, the non-diagonal terms of the matrix cannot be neglected anymore. The most convenient way to include those off-diagonal terms is to use the G-matrix formalism [13], in which the G-matrix, given by

$$\mathsf{G} = \mathrm{i}\omega_J \mathsf{I} - \mathsf{W}, \tag{11.8}$$

where I is the identity matrix and W is the relaxation matrix defined in Eq. (11.5). This G matrix can be diagonalized so as to have the following form:

$$\widetilde{\mathsf{G}} = \mathsf{A}^{-1}\mathsf{G}\mathsf{A} = (\mathrm{i}\widetilde{\omega_J} - 2\pi\widetilde{\gamma_J})\mathsf{I}. \tag{11.9}$$

In this expression, A is the change of basis matrix constructed from the eigenvectors of G, $\widetilde{\omega_J}$ are the new shifted eigenvalues of the transition frequencies, and $\widetilde{\gamma_J}$ are the new eigenvalues for the collisional linewidths.

The final CARS signal can then be written as [14]

$$I_{\mathrm{CARS}}(\tau) \propto \left| \sum_{J=0}^{J_{\max}} (\mathbf{b}\mathsf{A})_J \left(\mathsf{A}^{-1}\mathsf{P}\mathbf{b}\right)_J \exp\left[(\mathrm{i}\widetilde{\omega}_J - 2\pi\widetilde{\gamma}_J)\tau\right] \right|^2 , \tag{11.10}$$

where P is a diagonal matrix which accounts for the initial population difference, and **b** is a vector including the transition strength.

As the RIPS technique, fs-CARS happens to be a powerful tool to investigate collisional relaxation processes, as well as to measure temperature, pressure, and concentration for instance in combustion media. Several works have been devoted to these issues, especially in the case of nitrogen (see for example [14–17]).

Some experimental results will be presented in the next section, in which we will focus our attention on the case of molecular hydrogen.

11.2.2 Hydrogen Rovibrational Femtosecond CARS

Over the past decades, a lot of frequency-resolved spectroscopic studies have been performed to determine the vibrational line profiles of pure or foreign gas broadened H_2, because of its particular interest in combustion diagnostic, especially in thermometry in H_2/air flames. Moreover, H_2 is a particular molecule that exhibits unusual spectral features. The origin of these spectral signatures has unambiguously been found in the radiator speed dependence of the collisional parameters, coupled to the velocity and speed (velocity modulus) changes due to collisions [18–20]. Though these effects also exist in other molecules, the lightness of H_2 enhances them and makes this molecule an ideal candidate for a detailed study of such collisional processes. For example, the collisional shifting value is particularly important (more than two times the broadening) and strongly depends on the relative speed. As a consequence, the spectral lines become asymmetric for weak concentration of H_2 in mixtures, and the broadening coefficients are no longer linear functions of the perturber mole fraction. None of the usual profiles such as the weighted sum of Lorentzian or Voigt profiles can correctly model the frequency response and would lead to important errors if used for temperature diagnostic, these effects being enhanced when the temperature increases. Several lineshape models have been developed in the frequency domain to describe these effects [18, 19, 21, 22], and a particularly interesting approach to derive such lineshapes relies on the use of a kinetic model based on the time evolution of the autocorrelation function, which uses the so-called Keilson-Storer function [23] and the concept of speed-memory to model the velocity and speed changes due to collisions. Corresponding extended approaches have been developed to model the CARS time response in the whole density range, running from the low density or Doppler regime, to the high density or collisional regime [22, 24]. They will be briefly recalled in the following subsection.

11.2.2.1 Modelization of Collisional Effects: KS-3D Biparametric Model

Following the works of Keilson *et al*. [23] and Robert *et al*. [22, 24], the modelization of the time response uses the so-called memory function $f(\mathbf{v}|\mathbf{v}') = f_{KS}$ which describes the probability per time unit for the optically active molecule, with velocity v' to have a velocity v after a collision. As a generalization of Eq.(11.7), the temporal response takes the form

$$I_{\mathrm{CARS}}(\tau) \propto \left| \sum_J f_J d_J(\tau) \exp\left[(i \Delta E_J / \hbar) \tau \right] \right|^2 , \tag{11.11}$$

where $\mathrm{d}_J(\tau)$ is the normalized autocorrelation function of the polarizability responsible for the J line. $d_J(\tau)$ is given by the integration over the radiator velocity $\mathbf{v}$ of the corresponding quantity $d_J(\mathbf{v}, \tau)$. The time evolution of the former is given by the following equation:

$$\frac{\mathrm{d}_J(\mathbf{v}, t)}{\mathrm{d}t} = -\left[\nu_{\mathrm{VC}} + \mathrm{i}\mathbf{k}.\mathbf{v} + \Gamma_J^{\mathrm{coll}}(\mathrm{v}) + i\,\Delta_J^{\mathrm{coll}}(\mathrm{v})\right] d_J(\mathbf{v}, t) + \int\int\int f_{KS}(\mathbf{v}, \mathbf{v}') d_J(\mathbf{v}', t) \mathrm{d}^3\mathbf{v}', \tag{11.12}$$

where ν_{VC} is the frequency of velocity changing collisions (independent of v), $\mathrm{i}\mathbf{k}.\mathbf{v}$ is the dephasing due to the Doppler effect, $\Gamma_J^{\mathrm{coll}}(\mathrm{v})$ and $\Delta_J^{\mathrm{coll}}(\mathrm{v})$ are respectively the speed-dependent collisional width and shift of the optical transition.

Molecular dynamic simulations have shown [25] that in general, and especially in systems such as H_2–X (X = N_2, Ar, He), the orientation and the modulus change with very different time scales, and thus cannot be described with a unique phenomenological parameter characterizing the strength of the collision in the memory function f_{KS}. For this reason, Bonamy *et al.* have developed a biparametric memory model in which the memory function $f_{KS}(\mathbf{v}, \mathbf{v}')$ is written as a product of a function describing the changes of the modulus and a function describing the changes of the orientation [24, 25]

$$f_{KS}(\mathbf{v}, \mathbf{v}') = \nu_{VC} f_m(x, x') f_o(\mathbf{v}^o, \mathbf{v}^{o'}) \tag{11.13}$$

with

$$f_m(x, x') = \overline{f}_M(x) \sum_n \gamma_m^{2n} \overline{L}_n^{1/2}(x) \overline{L}_n^{1/2}(x') \tag{11.14}$$

and

$$f_o(\mathbf{v}^o, \mathbf{v}^{o'}) = \sum_{l,m} \gamma_o^l Y_{l,m}(\theta, \varphi) Y_{l,m}^*(\theta', \varphi'), \tag{11.15}$$

with $x = (\mathrm{v}/\widetilde{\mathrm{v}})^2 = m\mathrm{v}^2/2kT$, $x' = (v'/\widetilde{\mathrm{v}})^2 = m\mathrm{v}'^2/2kT$, $\overline{f}_M(x) = 4e^{-x}/\sqrt{\pi}$, $Y_{l,m}(\theta, \varphi)$ the spherical harmonics, and $\overline{L}_n^{1/2}(x)$ the Laguerre polynomials [26, 27]. f_m and f_o depend respectively on the memory parameters γ_m and γ_o describing the radiator velocity changes (in modulus and orientation). The values of those parameters have been calculated by molecular dynamic simulations [25]. In the case of systems such as H_2–X, they have only a slight dependence versus temperature, and therefore this dependence can be neglected.

When considering the limit case $\nu_{VC} = 0$ one retrieves the usual speed dependent Voigt profiles [28], or the simple Voigt profiles when neglecting the speed dependence of Γ^{coll} and Δ^{coll}. When the orientation changes can be disregarded (as it is the case in the high density limit), the memory function only depends on one memory parameter, γ, and yields the KS-1D model [22]. The limit values for the memory parameter are then

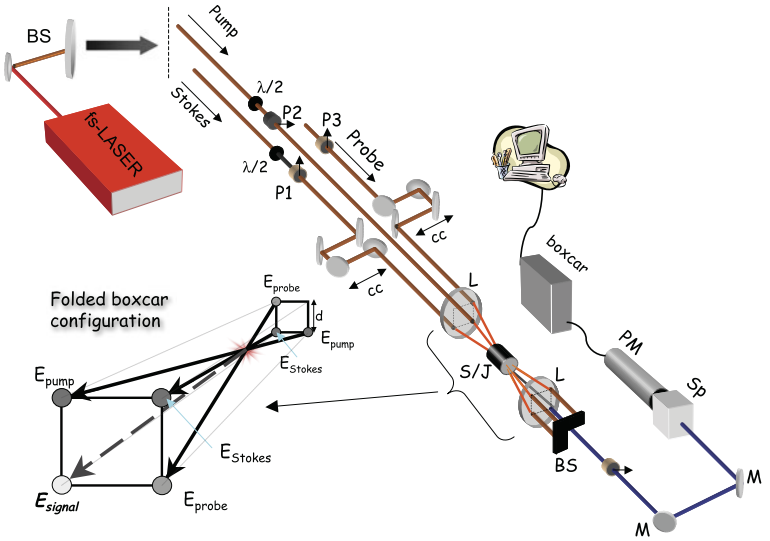

Fig. 11.4 Setup for CARS experiment: P_i polarizers, M mirror, BS beam splitter, CC corner cube, L lens, PM photomultiplier. The folded BOXCARS configuration is recalled on the *left*

- $\gamma = 0$, that corresponds to the hard collision approximation [29];
- and $\gamma = 1$, corresponding to the soft collision model [30].

The values of ν_{VC} and of the collisional parameters Γ^{coll} and Δ^{coll} have been determined from previous studies performed in the frequency domain [19, 20, 31, 32].

Experimental Procedure In the CARS experiment on molecular hydrogen [33, 34], the frequencies of the synchronized pump and Stokes pulses are chosen so as their difference matches a Q-branch transition $(v = 0, J) \rightarrow (v = 1, J)$ frequency. This excitation process creates a Raman coherence in the medium, monitored by a time-delayed probe pulse which mixed with the pump/Stokes pulses generates an Anti-Stokes signal described by the interaction with the third order non-linear polarization of the medium.

A scheme of the experimental set-up is shown on Fig. 11.4. The laser system is a chirped pulsed amplified Ti:Sapphire laser (pulse duration 100 fs, repetition rate 1 kHz) centered at 800 nm. The output beam is split into two parts, one of which serves as a Stokes beam (800 nm), while the second after frequency doubling, is used as a pumping beam for a noncolinear optical parametric amplifier (NOPA) (which does not appear on the scheme). The laser beam from the NOPA (pulse duration 30–40 fs) is centered at 600 nm and split into two parts to yield the pump and the probe beam for the CARS signal generation. The beams, linearly polarized and parallel to each other, are focused with a first lens and crossed at a small angle in the gas cell. In order to satisfy the phase-matching condition the folded BOXCARS configuration [35] is used. In this condition, the anti-Stokes signal, centered at 480 nm propagates in a different direction from that of the incoming beams and

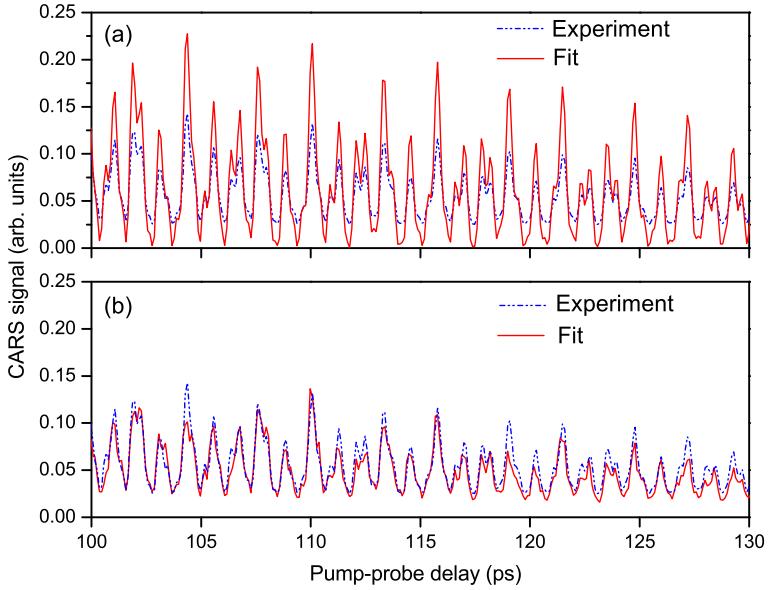

Fig. 11.5 CARS signal of 20 % H_2 diluted in 80 % of N_2 at 900 K and a density of 9.25 amagat. The *dash line* represents the experimental signal, the *full one* represents the calculated signal by the Lorentzian profile (**a**) and by the KS-1D model (**b**) [*NB*: *An amagat* (*Am*) *is a practical unit of number density. It is defined as the number of ideal gas molecules per unit volume at 1 atm and 273.15 K. One has, for an ideal gas,* $n(atm) = [T(K)/273.15] \times n(Am)$]

thus can be easily selected by a diaphragm, collimated by a second lens, and then detected by a photomultiplier.

Results So as to evidence the role and influence of the speed-effects on the CARS signal, and therefore on the temperature and/or density diagnostic, several examples can be shown.

In the high density limit [33], comparisons between experimental signals and calculated ones using the KS-1D model [22] have been made, depending on the value of the memory parameter γ: $\gamma = 0$ for the Lorentzian limit (no speed-effect) or the γ value deduced from molecular dynamics simulations [25, 36]. As it can be seen on Fig. 11.5, a strong disagreement between the experimental signal and the calculated signal from the Lorentzian model is observed, whereas this disagreement is strongly reduced when using the KS-1D model with the adequate value of γ. Temperature can also be deduced from the experimental signals through three kind of thermometry procedures: using the Lorentzian limit and neglecting or not the speed-dependence of the collisional parameters, or using the KS-1D model. The results are reported in Table 11.1. The higher the N_2 concentration, the more important is the discrepancy between the temperature deduced with the Lorentzian models and the reference value. On the contrary, when fully taking into account the speed-effects using the KS-1D model, the discrepancy is strongly reduced and falls down to 2 %.

Table 11.1 Thermometry procedure in H_2–N_2 mixtures, using the KS-1D model (T_{KS-1D}), or the Lorentzian limit without the speed-dependence of the collisional parameters ($T_{Lorentz(1)}$), or with the speed-dependence of the collisional parameters ($T_{Lorentz(2)}$). The reference temperature is measured by a thermocouple. The values in parentheses are standard deviations

H_2–N_2	5 % H_2, 95 % N_2	50 % H_2, 50 % N_2
T_{Th}	593	899
$T_{Lorentz(1)}$	741(1)	929(8)
$T_{Lorentz(2)}$	557(5)	864(7)
T_{KS-1D}	602(5)	885(7)

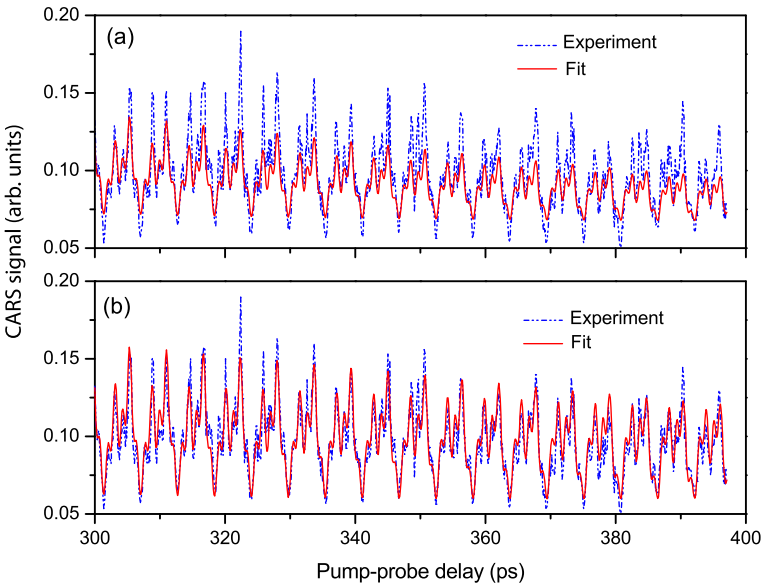

Fig. 11.6 CARS signal of 20 % H_2 diluted in 80 % of N_2 at 296 K and a density of 0.893 amagat. The *dash line* represents the experimental signal, the *full one* represents the calculated signal by the Voigt profile (**a**) and by the KS-3D biparametric model (**b**)

In the low density regime [26], density retrievals from measured signals can be performed, using two similar procedures as above, namely with or without taking into account the influence of the velocity effects. When neglecting the velocity memory effects, the KS-3D [24] yields the usual speed-dependent Voigt profile, and as it can be seen on Fig. 11.6 a quite important disagreement can be observed between the experimental signals and the calculated ones, especially at long delay ranges. When retrieving the total density through a least squares fitting procedure with the KS-3D biparametric model, the results exhibit a relatively good agreement with the measured ones (which are calculated from the gas state equation using the second Virial correction), as it is shown on Fig. 11.7

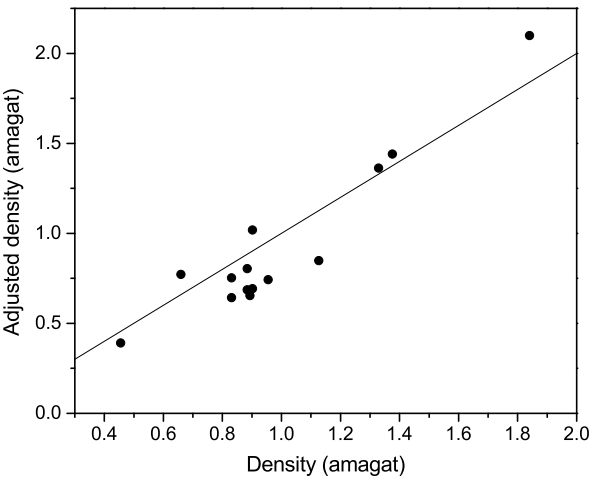

Fig. 11.7 Densities (*full circles*) obtained by fitting experimental CARS signals using the KS-3D biparametric model, in function of the measured densities (see text for details)

11.3 Field-Free Molecular Alignment in Dissipative Environment and Strong Field Regime

11.3.1 Alignment in a Dissipative Medium

Manipulating external degrees of freedom of molecules by intense laser fields is of great importance for chemistry, nonlinear and molecular optics, or quantum processes. For all these fields, molecular alignment plays a key role. It is known for long that an anisotropic polarizability allows for aligning molecules by nonresonant pulses, and one can distinguish between two kinds of regimes, the adiabatic one for which the pulse duration is longer than the rotational period of the molecule, and the nonadiabatic or sudden regime for which it is the opposite. In the latter, a periodic alignment is observed even after the pulse turns off, corresponding to the rephasing of the rotational wavepacket created by a pump pulse through the nonresonant Raman excitation of the molecular polarizability [37]. So far, most of experiments of short-pulsed induced alignment have been performed in a low density regime, although it is of practical interest to work at higher densities, and generally speaking in dissipative media.

Such an extension to dissipative media has been theoretically proposed by Ramakrishna and Seideman [38–40]. In particular, the authors highlighted the ability of such studies to get independent informations about the rotational population relaxation and the pure-phase decoherence effects. They developed a theory of nonadiabatic alignment in dissipative media using a quantum mechanical density matrix formalism that will be briefly recall in the following subsection.

11.3.1.1 Theoretical Description: Liouville-von Neumann Equation

It is usual to quantify the degree of alignment by using the mean value of $\cos^2\theta$, where θ is the angle between the molecular axis and the polarization direction of the laser field. In order to describe the influence of the surrounding environment, it is convenient to use the framework of the density operator $\rho(t)$ which can be expanded in terms of the rigid rotor eigenstates $|J, M\rangle$. Within this framework, the expectation value $\langle\cos^2\theta\rangle$ is given by $\mathrm{Tr}[\rho(t)\cos^2\theta]$ where Tr stands for the trace of the operator. The time evolution of the density operator is assumed to obey the Liouville-von Neumann equation [41]. Within the multilevel Bloch-Redfield model, it writes [38]

$$\frac{\mathrm{d}\rho(t)}{\mathrm{d}t} = -\frac{\mathrm{i}}{\hbar}\big[H_0 + H_1(t), \rho(t)\big] + \left(\frac{\mathrm{d}\rho(t)}{\mathrm{d}t}\right)_{\mathrm{diss}}, \tag{11.16}$$

where $[\cdot,\cdot]$ indicates a commutator. In this expression, H_0 is given by $H_0 = BJ^2 - DJ^4$, $H_1(t) = -1/4E^2(t)\Delta\alpha\cos^2\theta$ is the interaction term, J is the angular momentum operator, B is the rotational constant, D is the centrifugal distortion, $\Delta\alpha$ is the polarizability anisotropy, and $E(t)$ is the envelope of the laser electric field, which will be assumed to be Gaussian in our case.

The last term of Eq. (11.16) describes the dissipation due to elastic and inelastic collisions between the aligned molecule and its perturbers. It can be split into two sets of coupled differential equations, corresponding to off-diagonal and diagonal elements of the density operator:

$$\left(\frac{\mathrm{d}\rho_{JMJ'M'}}{\mathrm{d}t}\right)_{\mathrm{diss}} = -\frac{1}{2}\sum_{(J_1,M_1)\neq(J,M)}[K_{JMJ_1M_1} + K_{J'M'J_1M_1}]\rho_{JMJ'M'}(t) - \gamma^{(\mathrm{pd})}_{JMJ'M'}\rho_{JMJ'M'}(t), \tag{11.17}$$

$$\left(\frac{\mathrm{d}\rho_{JMJM}}{\mathrm{d}t}\right)_{\mathrm{diss}} = -\sum_{(J_1,M_1)\neq(J,M)}\big[K_{JMJ_1M_1}\rho_{JMJM}(t) - K_{J_1M_1JM}\rho_{J_1M_1J_1M_1}\big]. \tag{11.18}$$

The coefficients $K_{JMJ'M'}$ are the rate of population transfer from state $|J, M\rangle$ to state $|J', M'\rangle$. The additional term $\gamma^{(\mathrm{pd})}_{JMJ'M'}$ is the pure decoherence rate of phase between $|J, M\rangle$ and $|J', M'\rangle$.

The decomposition of the Liouville equation into diagonal and off-diagonal elements leads to recast $\langle\cos^2\theta\rangle(t)$ as

$$\big\langle\cos^2\theta\big\rangle(t) = \big\langle\cos^2\theta\big\rangle_{\mathrm{p}}(t) + \big\langle\cos^2\theta\big\rangle_{\mathrm{c}}(t) \tag{11.19}$$

The first term of the second member of the above egality is referred as the permanent alignment and gives rise to the time evolution of alignment due to the population of the rotational states, whereas the second one leads to the time evolution of alignment due to coherence and is referred as the transient alignment. Before laser excitation, at

thermal equilibrium, one has $\langle\cos^2\theta\rangle_{\rm p} = 1/3$ and $\langle\cos^2\theta\rangle_{\rm c} = 0$. After the coherent excitation of the rotational levels, $\langle\cos^2\theta\rangle_{\rm p}$ goes beyond the 1/3 isotropic value, whereas $\langle\cos^2\theta\rangle_{\rm c} \neq 0$. In a non-dissipative media, $\langle\cos^2\theta\rangle_{\rm p}$ remain constant, and $\langle\cos^2\theta\rangle_{\rm c}$ oscillates at the rotational period as long as the coherence is maintained, but in presence of collisional relaxation, both decay to their equilibrium values.

If one makes the assumption of M-independent $K_{JMJ'M'}$ [38] (i.e., the orientation of the angular momentum is randomize by collisions), then the latter can be constructed with the usual ECS approach [8] and Eq. (11.6) can be applied. Using Eqs. (11.17)–(11.18), one can write

$$\frac{{\rm d}\langle\cos^2\theta\rangle_{\rm p}(t)}{{\rm d}t} = -\sum_{J,M}\gamma_J\rho_{JMJM}(t)V_{JMJM} + \sum_{J,M}\sum_{J'M'}K_{J'MJM}\rho_{J'MJ'M}V_{J'MJM} \tag{11.20}$$

and

$$\frac{{\rm d}\langle\cos^2\theta\rangle_{\rm c}(t)}{{\rm d}t} = -\sum_{J\neq J',M}\left(\frac{1}{2}[\gamma_J+\gamma_{J'}] + \gamma_{JJ'}^{\rm (pd)}\right)\rho_{JMJ'M}V_{JMJ'M} \tag{11.21}$$

where $V_{JMJ'M}$ are the elements of the $\cos^2\theta$ operator. In the case of CO_2, the collisional linewidths γ_J only depend slightly on the J value, so that they can be replaced by an averaged value $\overline{\gamma}$.

As expected from Eqs. (11.20)–(11.21), $\langle\cos^2\theta\rangle_{\rm c}$ should not decay at the same rate as $\langle\cos^2\theta\rangle_{\rm p}$, the latter decreasing with a time constant of $1/\overline{\gamma}$, the former decaying with a time constant of $1/(\overline{\gamma}+\overline{\gamma}^{\rm (pd)})$ (if one replaces the $\gamma_{JJ'}^{\rm (pd)}$ by an averaged value). Thus, it would be possible to experimentally evidence these two different temporal decays, providing the contribution of $\gamma_{JJ'}^{\rm (pd)}$ term can be separately predicted.

Thanks to a classical approach [42, 43], it is indeed possible to disentangle the elastic and inelastic contributions to the collisional linewidths, and then to construct the relaxation rates by fitting the scaling laws mentioned in Sect. 11.2.1 on the inelastic part only. Comparing computed values of $\langle\cos^2\theta\rangle(t)$ with experimental data should therefore provides a way of questioning the calculated value of $\gamma_{JJ'}^{\rm (pd)}$.

11.3.1.2 Experimental Procedure and Results

The time evolution of the alignment is monitored by a technique based upon a birefringence measurement and thus the same setup as the RIPS experiment [44] depicted in Fig. 11.1 is used. It is indeed possible to show that the detected signal (in the case of an homodyne detection) is given by [44]

$$I_{\rm Align}(\tau) \propto \left[\left(\langle\cos^2\theta\rangle(t) - \frac{1}{3}\right)^2 \otimes E_{\rm probe}^2(t)\right]_{t=\tau} \tag{11.22}$$

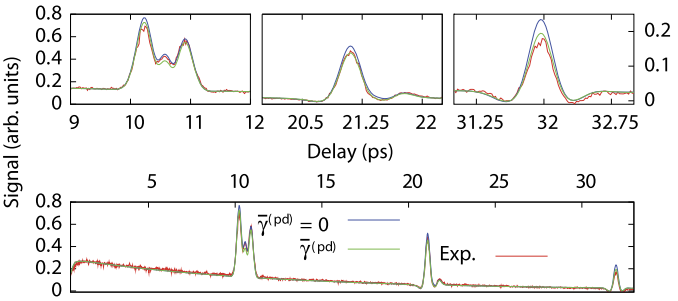

Fig. 11.8 Homodyne alignment signal versus pump-probe delay recorded in CO_2–Ar mixture with 10 % CO_2 at room temperature and 5 bar, for a peak intensity of 54 TW/cm^2. The *straight lines* correspond to numerical simulations with setting the elastic contribution $\gamma^{(pd)}_{JJ'}$ to 0 or including a Boltzmann J-averaged value of $\gamma^{(pd)}_{JJ'}$

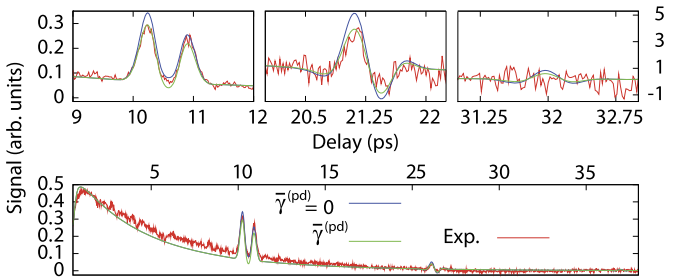

Fig. 11.9 Same as Fig. 11.9, but at a pressure of 15 bar and a peak intensity of 51 TW/cm^2

where $\otimes$ refers to a convolution product and E_{probe} is the electric field of the probe beam. The signal is then directly related to the degree of alignment.

Preliminary experiments and analysis have been performed for CO_2–Ar mixtures, at pressures up to 20 bar. As depicted on Figs. 11.8 and 11.9, the decay of both permanent and transient components of the signal is observable. The model described in the previous subsection reproduces to a relatively good extend the experimental signal, especially the shape of the transients, and the signal decay as long as the pressure is not too high (up to 5 bar in this case). Obviously the agreement is slightly improved whatever the pressure when the elastic contribution is included. However, one can also noticed on Fig. 11.9 that the decay of the permanent alignment remains uncorrectly described with an over damped calculated value.

It is noteworthy that in the model used for the numerical simulations, the assumption is made that collisions totally randomize the orientation of the angular momentum, leading to consider that the relaxation rates $K_{JMJ'M'}$ do not depend on the quantum number M. On the opposite, an alternative approach [45] would be to

assume that the orientation of the angular momentum is preserved by the collisions (more precisely the M/J value is conserved). The use of classical molecular dynamics calculations could be a way to assess the validity of either one or the other assumption [45].

11.4 Conclusion

In this chapter, we have reviewed some time-resolved ultrafast nonlinear coherent techniques and their application to the diagnostic of concentration/temperature, and their reliability to provide information about collisional relaxation processes, the knowledge of the latter being crucial for the success of practical applications. Owing to the large spectral width of femtosecond pulses, a superposition of rotational or rovibrational states can be prepared through a non-resonant Raman excitation resulting in a coherent wavepacket that can be probed over time and that provides dynamical information on the system. Besides, strong fields values offer the possibility to investigate specific processes such as molecular alignment. Due to the absence of resonance conditions, Raman Induced Polarization Spectroscopy (RIPS) is particularly suitable to the detection of several number of molecules simultaneously, providing they have a anisotropic polarizability. In this case, a simultaneous thermometry procedure is also possible. The RIPS signal being sensitive to pure rotational relaxation, the accuracy of the diagnostic will directly depends on that of the relaxation processes description. At the same time it can be a powerful tool to precisely get information on collisional relaxation by allowing to test rotational energy transfer models. When RIPS measurements are not possible, as for molecular hydrogen, femtosecond Coherent Anti-Stokes Raman Spectroscopy (fs-CARS) is an alternative technique which proves to be not only a tool for accurate temperature diagnostics, but also capable to study sophisticated effects such as the consequences of collision-induced radiator velocity changes and of the speed dependence of collisional parameters.

When using strong fields values, the production of molecular alignment happens to be a unique way of probing the dissipative properties of the studied media and yielding information which are difficult if not inaccessible to obtain by conventional frequency-resolved and low field techniques. In particular, it should be possible to disentangle the elastic and inelastic contributions of the relaxation rates within a single measurement, and get insight on the reorientation of the angular momentum under collisions.

Acknowledgements The authors would like to thank Ha Tran, P. Joubert, L. Bonamy, D. Robert, R. Saint-Loup, D. Sugny, Th. Vieillard, and V. Renard for their contributions to the results presented here.

References

1. M. Morgen, W. Price, L. Hunziker, P. Ludowise, M. Blackwell, Y. Chen, Chem. Phys. Lett. **209**, 1 (1993)
2. M. Morgen, W. Price, P. Ludowise, Y. Chen, J. Chem. Phys. **102**, 8780 (1995)
3. R. Leonhardt, W. Holzapfel, W. Zinth, W. Kaiser, Chem. Phys. Lett. **133**, 373 (1987)
4. T. Lang, K.L. Kompa, M. Motzkus, Chem. Phys. Lett. **310**, 65 (1999)
5. B. Lavorel, O. Faucher, M. Morgen, R. Chaux, J. Raman Spectrosc. **31**, 77 (2000)
6. E. Hertz, B. Lavorel, O. Faucher, R. Chaux, J. Chem. Phys. **113**, 6629 (2000)
7. E. Hertz, R. Chaux, O. Faucher, B. Lavorel, J. Chem. Phys. **115**, 3598 (2001)
8. A.E. DePristo, S.D. Augustin, R. Ramaswamy, H. Rabitz, J. Chem. Phys. **71**, 850 (1979)
9. G. Millot, J. Chem. Phys. **93**, 8001 (1990)
10. H. Tran, B. Lavorel, O. Faucher, R. Saint-Loup, P. Joubert, J. Raman Spectrosc. **34**, 994 (2003)
11. H. Tran, B. Lavorel, O. Faucher, R. Saint-Loup, P. Joubert, J. Raman Spectrosc. **33**, 872 (2002)
12. H. Skenderovic, T. Buckup, W. Wohlleben, M. Motzkus, J. Raman Spectrosc. **33**, 866 (2002)
13. M.L. Koszykowski, R.L. Farrow, R.E. Palmer, Opt. Lett. **10**, 478 (1985)
14. G. Knopp, P. Radi, M. Tulej, T. Gerber, P. Beaud, J. Chem. Phys. **118**, 8223 (2003)
15. P. Beaud, H.-M. Frey, T. Lang, M. Motzkus, Chem. Phys. Lett. **344**, 407 (2001)
16. G. Knopp, P. Beaud, P. Radi, M. Tulej, B. Bougie, D. Cannavo, T. Gerber, J. Raman Spectrosc. **33**, 861 (2002)
17. P. Beaud, T. Gerber, P.P. Radi, M. Tulej, G. Knopp, Chem. Phys. Lett. **373**, 251 (2003)
18. R.L. Farrow, L.A. Rahn, G.O. Sitz, G.J. Rosasco, Phys. Rev. Lett. **63**, 746 (1989)
19. J.Ph. Berger, R. Saint-Loup, H. Berger, J. Bonamy, D. Robert, Phys. Rev. A **49**, 3396 (1994)
20. P.M. Sinclair, J.-P. Berger, X. Michaut, R. Saint-Loup, R. Chaux, H. Berger, J. Bonamy, D. Robert, Phys. Rev. A **54**, 402 (1996)
21. D. Robert, J.M. Thuet, J. Bonamy, S. Temkin, Phys. Rev. A **47**, R771 (1993)
22. D. Robert, L. Bonamy, Eur. Phys. J. D **2**, 245 (1998)
23. J. Keilson, J.E. Storer, Q. Appl. Math. **10**, 243 (1952)
24. L. Bonamy, H. Tran, P. Joubert, D. Robert, Eur. Phys. J. D **31**, 459 (2004)
25. P. Joubert, P.N.M. Hoang, L. Bonamy, D. Robert, Phys. Rev. A **66**, 042508 (2002)
26. H. Tran, J.M. Hartmann, J. Chem. Phys. **130**, 094301 (2009)
27. M. Abramowitz, *Handbook of Mathematical Functions* (Dover, New York, 1970)
28. J.M. Hartmann, *Collisional Effects on Molecular Spectra. Laboratory Experiments and Model, Consequences for Applications* (Elsevier, Amsterdam, 2008)
29. S.G. Rautian, I.I. Sobel'man, Sov. Phys. Usp. **9**, 701 (1967)
30. L. Galatry, Phys. Rev. **122**, 1218 (1961)
31. F. Chaussard, X. Michaut, R. Saint-Loup, H. Berger, P. Joubert, B. Lance, J. Bonamy, D. Robert, J. Chem. Phys. **112**, 158 (2000)
32. F. Chaussard, R. Saint-Loup, H. Berger, P. Joubert, X. Bruet, J. Bonamy, D. Robert, J. Chem. Phys. **113**, 4951 (2000)
33. H. Tran, P. Joubert, L. Bonamy, B. Lavorel, V. Renard, F. Chaussard, O. Faucher, B. Sinardet, J. Chem. Phys. **122**, 194317 (2005)
34. H. Tran, F. Chaussard, N. Le Cong, B. Lavorel, O. Faucher, P. Joubert, J. Chem. Phys. **131**, 174310 (2009)
35. J.A. Shirley, R.J. Hall, A.C. Eckbreth, Opt. Lett. **5**, 380 (1980)
36. P.N.M. Hoang, P. Joubert, D. Robert, Phys. Rev. A **89**, 012507 (2002)
37. H. Stapelfeldt, T. Seideman, Rev. Mod. Phys. **75**(2), 543 (2003)
38. S. Ramakrishna, T. Seideman, J. Chem. Phys. **124**, 034101 (2006)
39. S. Ramakrishna, T. Seideman, Phys. Rev. Lett. **95**, 113001 (2005)
40. S. Ramakrishna, T. Seideman, J. Chem. Phys. **122**, 084502 (2005)

41. U. Weiss, *Quantum Dissipative Systems* (World Scientific, Singapore, 1999)
42. S. Ivanov, L. Nguyen, J. Buldyreva, J. Mol. Spectrosc. **233**, 60 (2005)
43. S. Ivanov, O. Buzykin, Mol. Phys. **106**, 1291 (2008)
44. O. Faucher, B. Lavorel, E. Hertz, F. Chaussard *Progress in Ultrafast Intense Laser Science VII*, vol. 79 (Springer, Berlin, 2011)
45. J.-M. Hartmann, C. Boulet, J. Chem. Phys. **136**, 184302 (2012)

Index

Symbols
$^1\pi\sigma^*$, 136
$(1+1)$-REMPI, 37, 42
β-carotene, 207, 223

A
A-band dissociation, 242
A-band of methyl iodide, 242
Ab initio calculations, 85
Ab initio MD, 159, 164
Ab initio molecular dynamics, 146, 164
Abel inversion, 8
Abel-inverted images, 71
Abel-inverted velocity maps, 76
Adenine, 136
Adiabatic alignment, 8
Adsorbate alignment, 236
Adsorbate-adsorbate interaction, 236
Alignment, 92, 264
Alignment and orientation, 8
Alignment laser pulse, 5
Alignment revivals, 8
Amino acids, 187
Angular distribution, 6, 66, 68, 72
Anions, 113
Anisotropy, 85, 128
Anisotropy parameter, 73
Anisotropy polarizability, 266
APLIP, 148, 162–164
Aromatic, 128
Asymmetry parameter, 44
AT effect, 40
Attosecond, 26, 105
Attosecond laser pulses, 6
Attosecond streak camera, 17
Autler-Townes splitting, 39
Autoionization, 32, 36
Available kinetic energy, 85
Azole, 130

B
Bacteriorhodopsin, 212
Beyond Born-Oppenheimer approximation, 59
Bimolecular surface reactions, 251
Biochemistry, 120
Biomolecules, 119
Birefringence, 265
Born-Oppenheimer, 152
Born-Oppenheimer approximation, 30, 69, 146, 148, 152
Born-Oppenheimer expansion, 150
BOXCARS, 209
Br_2, 13
Branching ratio, 85
Brillouin-Kramers-Wentzel, 136
Brownian oscillator model, 221

C
CARS, 264
CD_3I, 243
Center-of-mass (CM) translational energy distributions, 72
CH_3Br/MgO(100), 237
CH_3I A-band, 69
CH_3I photodissociation, 245
$CH_3I^{*\ddagger}$ transition state, 246
CH_3SSCH_3, 233
'Chattering' motion, 247
Chromophores, 120
Clocking, 86
"Clocking" times, 62
Cluster-specific chemistry, 83
Clusters, 83
CO_2, 9

R. de Nalda, L. Bañares (eds.), *Ultrafast Phenomena in Molecular Sciences*,
Springer Series in Chemical Physics 107, DOI 10.1007/978-3-319-02051-8,

Coherent control, 45
Coherent diffractive imaging, 2
Coherent internal vibrational energy redistribution, 218
Coherent superposition, 269
Coherent wave packet motion, 182
Coincidence, 100
Coincidence momentum imaging, 49
Collision complex, 231
Collisional relaxation, 264
Conical intersections, 99, 121, 165
Contributions to the images, 67
Control of single ionization, 37
Coulomb explosion, 13, 49
Coulomb-Corrected SFA (CCSFA), 18
Couplings, 138

D
Dark states, 218
De Broglie wavelength, 4, 6
Delay time, 79
Delayed decay, 36
Density operator, 276
Deuterated, 134
Dimerization, 85
Direct photoionization and autoionization, 34
Dissipative medium, 264
Dissociation pathways, 191
Dissociative, 123
Dissociative ionization, 13
Doubly excited states, 31
Doubly excited states of H_2, 33
Dynamic alignment, 7
Dynamics, 134

E
Electron correlation, 32
Electron dynamics, 26
Electronic Hamiltonian, 148, 150, 154
Electronic relaxation, 113
Electrospray ionization, 140
Energy redistribution, 174
Energy-degenerate paths, 45
Excited state, 146, 149, 151, 160, 206
Excited state vibrational coherences, 217

F
FELICE, 4, 15
Femtochemistry, 2, 74, 77
Femtosecond, 26
Femtosecond laser-induced ionization/dissociation (fs-LID), 175
Femtosecond pump-probe detection, 64
Femtosecond pump-probe schemes, 94
Feshbach formalism, 31
Feshbach theory, 29
Few-photon single ionization, 37
Fifth-order nonlinear methods, 227
FLASH, 5, 12
FLASH free electron laser, 4
Franck-Condon, 139
Franck-Condon window, 222
Free electron lasers, 105
Frequency domain, 135
Full coincidence detection, 34

H
H/D exchange, 53
H_2S, 233
Half revival, 82
Hard collision, 272
Harmonic generation, 64
Harmonic imaging, 15
Hemispherical electron energy analysers, 108
Heteroaromatic, 121
HHG, 5, 6, 12, 15, 17
High harmonics, 113
Holographic interference, 5, 15, 17, 18, 20
Hydrogen migration, 49
Hydrogen scrambling, 54

I
I_2 molecules, 253
IBr, 255
Illuminating a molecule from within, 4
Imidazole, 130
Impulsive alignment, 8
Incoherent population relaxation, 223
Internal conversion (IC), 147
Intersystem crossing (ISC), 147
Intramolecular vibrational energy redistribution (IVR), 108
Ion activation, 174, 200
Ion trap, 178
Ionization, 100
Ionization amplitudes, 31
Ionization energies, 198
Ionization-enhancing resonances, 76
ISC, IC, 147

K
Koopmans-type correlations, 102

L
Laser desorption, 140
Laser photochemistry, 61
Laser-induced molecular alignment, 81
Laser-induced molecular desorption, 236
Laser-induced processes, 26
Laser-molecule interactions, 45

LCLS, 4–6, 12
Least-squares procedure, 67
LiF(001), 233
Lifetime, 136
Light-induced potentials (LIPs), 152
Line-mixing effect, 266
Lineshape, 270
LIP, 153–156
Liquid jets, 107
Lorentzian, 273
Lycopene, 218

M
Magnetic bottle electron spectrometer, 107
Mass spectrometry, 123
MD, 146, 147, 158
Memory function, 270
Mequinol, 136
Methyl bromide, 237, 248
Methyl fragments, 242
Methyl halide, 62, 235
Methyl iodide, 241
Methyl radical detection, 239
Methylacetylene, 49
MFPAD, 6, 11
MgO(100), 235
Molecular autoionization, 32, 36
Molecular axis alignment, 109
Molecular frame asymmetry, 44
Molecular movie, 6
Molecular photoionization, 27, 28
Molecular single ionization, 29
Molecules, 235
Momentum correlation map, 57
Multidimensional data, 67
Multidimensional time-resolved spectroscopy, 206
Multiphoton, 130
Multiphoton intrapulse interference phase scan (MIIPS), 175
Multiphoton ionization, 45, 71, 94
Multiphoton single-ionization, 26
Multiple-centered wave function, 59

N
NAC, 147, 149, 150, 153, 156
Newton sphere, 125
Newton spheres, 66
Nobel prize in chemistry, 2
Non-adiabatic, 122
Non-adiabatic coupling (NAC), 100, 101, 147
Non-adiabatic curve crossing, 69
Non-ergodic, 192
Non-ergodic dissociation, 200
Non-linear effects, 39
Non-resonant, 181
Non-resonant dynamic Stark effect (NRDSE), 159
Non-resonant excitation, 211
Noncollinear optical parametric amplifier, 209
NRDSE, 160
Nuclear Hamiltonian, 148, 154
Nuclear motion, 28
Nuclear wave packets, 40, 43

O
Off-resonance probe laser pulse, 78
Orbital tomography, 15
Out-of-plane modes, 217

P
Parallel transition, 11
Partial waves, 12
Permanent alignment, 276
Perpendicular transition, 11
PES, 146, 147, 149
Phenol, 133
Photochemical reaction, 99
Photochemistry, 184
Photodamage, 120
Photodetachment, 113
Photodissociation, 61, 62, 81, 83, 111, 126, 172
Photoelectron angular distribution, 6, 8, 12, 13, 103
Photoelectron hologram, 4, 16
Photoelectron imaging, 100
Photoelectron kinetic energy and angular distribution, 9
Photoelectron spectra, 93
Photoelectron spectroscopy, 123
Photoexcitation, 126
Photofragment, 123
Photofragment translational energy distribution, 237
Photofragmentation, 187
Photoionization, 195, 198
Photostability, 119
Polarizability, 194
Polyatomic molecules, 182
Ponderomotive acceleration, 14
Position sensitive detector, 50
Post-translational modifications, 175
Potential energy curves, 146
Potential energy curves for H_2, 32
Predissociation, 63, 91, 94, 254
Product ions, 174
Protein sequencing, 195

Proteomics, 177
Proton distribution map, 52
Proton kinetic energy release, 36
Pulse shaping, 174
Pump-degenerate four wave mixing, 206
Pump-probe, 27, 126
Pump-probe laser schemes, 63
Pump-probe mass spectrometry, 232
Pyrazole, 130
Pyrrole, 129

Q
Quantum control, 174
Quantum dynamical calculations, 165
Quantum dynamics (QD), 153, 155–160, 162
Quantum yield, 218

R
Rabi frequency, 40
Rabi oscillation, 40, 41
Rabi-type oscillations, 39
Radical, 196
Radical formation, 194, 200
Radical intermediates, 197
Reaction microscope, 6
Reaction times, 75
Reduced-dimensionality theoretical treatments, 75
Relaxation matrix, 266
REMPI, 138
Resonance enhanced multi-photon ionization, 232
Resonant enhancement, 79
Resonant multiphoton ionization, 61
Retinal protonated Schiff base, 207, 212
RIPS, 264
Rotational coherences, 110
Rotational wavepacket, 275
Rydberg, 127
Rydberg state, 91

S
Saddle-point method, 17
Scaling laws, 266
Second absorption band, 88
SH, 149–152, 157, 159
Single ionization probabilities, 38
Soft collision, 272
Spectral methods, 29
Spectral overlap, 211
Spectral-temporal, 187
Spectrally-resolved DFWM, 214
Speed-memory, 270
Spin-orbit, 152, 159, 164
Spin-orbit coupling, 146, 147, 152, 157, 158
Stark effect, 152, 159, 165
Stark shift, 163
Step-ladder mechanism, 41
Stimulated emission pumping DFWM, 221
Stimulated pump excitation (SEP) mechanism, 226
Strong field, 149, 152, 159, 162, 165
Strong laser pulses, 162
Strong laser-molecule interaction, 152
Strong pulses, 146, 156
Strong-field approximation, 17
Strong-field control, 95
Structural changes, 206
Superposition of two states, 43
Supersonic expansion, 65
Supersonic molecular beam, 106
Surface hopping (SH), 147
Surface pump-probe fs-laser mass spectrometry, 238
Surface-aligned chemistry, 233
Surface-aligned femtochemistry, 231
Surface-aligned femtosecond photoreaction, 234
Surface-aligned reaction, 232, 233
Symmetry breaking, 43

T
TDSE, 29, 146, 150, 154, 155
TFS, 157
TFS algorithm, 153
Three-body decomposition, 52
Three-step mechanism, 5
Time of flight, 107
Time zero, 66
Time-delayed two-photon ionization, 43
Time-dependent Schrödinger equation (TDSE), 17, 146
Time-dependent structural changes, 2
Time-dependent theoretical approaches, 29
Time-of-flight mass spectrometer, 178, 239
Time-of-flight mass spectrometry, 232
Time-resolved, 88
Time-resolved electron diffraction, 4
Time-resolved imaging, 27
Time-resolved photoelectron spectroscopy, 99
Time-resolved X-ray diffraction, 2
Total kinetic energy release, 122
Transient alignment, 276
Transition dipole moment, 128
Tully's fewest switches (TFS), 150
Tunnel ionization, 172

Tunneling, 123
Tyrosine, 133

U
Ultrafast, 139
Ultrafast electron diffraction experiments, 5
Ultrafast electron dynamics, 17
Ultrafast internal conversion, 108
Ultrafast photoionization, 171
Ultrashort femtosecond pulses, 146
Ultrashort laser pulses, 26
Ultrathin film, 235
Ultraviolet, 119
Unimolecular, 127
Up-down (or left-right) asymmetry, 43

V
Velocity map imaging, 13, 15, 16, 61, 107
Velocity map imaging detector, 8
Velocity map ion imaging, 125
Velocity mapping, 50, 65
Vibrational coherence, 211
Vibrational energy relaxation, 225
Vibrational relaxation, 220
Vibrational selectivity, 38
Vibrationally excited CH_3, 74
Vibronic level, 89
Vibronic wave packets, 37

W
Wave packet, 79
Wavelength tuning, 173
Wavepacket, 134

X
XUV/X-ray free electron laser (FEL), 5
XUV/X-ray photo-ionization, 4

Z
Zero point energy, 133